Partial Synthetic Models of the FeMoco Nitrogenase Cluster with Bridging C-Based Ligands

Thesis by

Linh Nguyen Vuong Le

In Partial Fulfillment of the Requirements for the Degree of
Doctor of Philosophy

CALIFORNIA INSTITUTE OF TECHNOLOGY
Pasadena, California

2024
(Defended April 12th, 2024)

© 2024

Linh Nguyen Vuong Le
ORCID: 0000-0003-1451-2675

ACKNOWLEDGEMENTS

The PhD journey is difficult and cannot be taken alone without the help of others. For the past six years, I was fortunate to have been supported by several people within the Caltech community and outside, who have made this experience a memorable and fulfilling part of my life.

First, I would like to thank my advisor, Prof. Theodor Agapie. His enthusiasm for research always motivated me to work hard and contribute my small efforts to science. Theo always had so many helpful advice and suggestions to improve my experiments, especially when I faced obstacles. He was also very patient with me when we drafted papers or proposals, correcting my mistakes and improving all my writing. I also learned a lot from him in terms of teaching and mentoring, as he was very devoted to ensuring a high quality in the classes he taught and to welcoming undergraduates or new graduate students to the lab. I am grateful to have had the opportunity to conduct my PhD studies in the Agapie group.

My PhD would not be complete without the support of my committee members. My committee chair, Prof. Harry Gray, had been incredibly encouraging ever since I was a first-year student. He gave me great advice on selecting a lab group, pursuing new ideas when I encountered obstacles, or choosing a career path. Harry was always available and excited to talk to me. Prof. Douglas Rees was also a great resource with a lot of knowledge on nitrogenase. I enjoyed our collaboration in conjunction with Dr. Jens Kaiser and Prof. Limei Zhang on crystallography, where I learned many new aspects of X-ray diffraction and absorption. Furthermore, I was lucky to have been the TA for Doug's class Ch14 twice. Not only did I strengthen my knowledge of chemical equilibrium, but I also learned from Doug's curiosity about other fields outside his expertise, especially during the field trips to different labs on campus. Lastly, Prof. Garnet Chan helped me in many ways, such as research and career options, even when he was busy attending conferences or traveling abroad. I must thank Garnet for introducing me to some members of his group when I wanted to learn more about computation.

Next, I would like to acknowledge the past and present members of the Agapie group, who have helped me in tremendous ways over the years. Dr. Manar Shoshani and Dr. Gwen Bailey were my mentors during my rotation and my first year, respectively. They always supported me and taught me so much, both inside and outside the lab, especially Gwen who collaborated with me on the cluster project. Dr. Anna Scott, who shared the glovebox with me for five years, was also a great resource, and many parts of the nitrogenase project would not have been possible without her contribution. Dr. Angela Shiau and Tianyi He also provided much feedback on experimental design and data interpretation. Other members of the lab have also helped me in various ways.

I have had opportunities to work with many internal and external collaborators, all of whom have enriched my scientific knowledge. Dr. Paul Oyala helped me with all the EPR experiments, retrieving my samples from the storage Dewar, running them, and providing thoughts on the interpretation. I would also like to thank Prof. Serena DeBeer (Max Planck Institute) and her lab for computational and spectroscopic studies on my clusters to illuminate many interesting properties. Dr. Jens Kaiser and Prof. Limei Zhang (University of Nebraska – Lincoln) helped me with shipping, data collection, and refinement for the single-crystal XAS experiments, and always responded promptly when I contacted them.

In addition, many members of the Caltech and Pasadena community had helped me in various ways. I would like to thank Profs. Jonas Peters, Kimberly See, and Ryan Hadt, whose classes I took during my first year. Alison Ross, many thanks for keeping the PhD program running and helping us with all the administrative tasks. I cannot forget the administrative assistants, namely Margarita Davis, Ann Mao, and Aracely Sustaita, who helped me schedule many meetings. Caltech International Offices had been a great resource for international students like me, in terms of both immigration and daily life at Caltech. The Caltech gym also played a very important part in my Caltech experience, especially my spin class teacher Ms. Maria Mukai, who taught me to keep on moving and keep climbing. Thanks to my roommate Reynold Watkins who would watch a movie with me every Thursday night. I would also like to thank all the friends I made at Caltech for the technical and emotional support throughout the years, particularly Alex Barth who was my “big sib” and helped me navigate life at Caltech, and Christian Johansen for all the spectroscopic assistance and our conversations on a myriad of topics. Takk for å være en god venn og for å hjelpe meg i seks år.

I could not have done any of this without my past mentors. Many thanks to Prof. Anthony Chianese, my undergraduate research advisor, for teaching me so much about experimental inorganic chemistry, along with Prof. Jason Keith and the late Prof. Ephraim Woods who were my undergraduate Chemistry professors. I would also like to acknowledge Prof. Brad Carrow who allowed me to conduct lab work in Summer 2017 at Princeton University and offered me a glimpse into graduate research.

My deep interest in pop music constituted an indispensable component of my life. I would like to thank Miley Cyrus, Lady Gaga, Lana Del Rey, and other artists for their mental support throughout my PhD, even in my darkest days and even in my lowest place. Thanks for all the great music that gave me the radical optimism when faced with obstacles.

In addition, I was very lucky to enter Caltech with a great cohort of amazing scientists, who were also supportive friends. Thanks to Taleen Dilanyan (and her husband Arsani) for hanging out with me every weekend for five years to catch up and release all our stress during the week. Jaron Tong helped me in many ways, from discussing experimental ideas to getting the COVID vaccine at Cal State LA. Thanks to Marta Gonzalvo and Manni He for coming to my lunches every other Thursday. I will also remember the rest of our friend group, namely Roman Korol, Ruben Mirzoyan, Jonathan Michelsen, Bryce Hickam, Isabel Klein, Sean Byrne, Reina Buenconsejo, Liam Hadt, and Connor Lee, and all the social events we had in the past six years.

My Caltech experience would not have been complete without the Vietnamese community. I would like to thank Cấn Trần Thành Trung, Đặng Hoàng Hà, Lê Quang Luận, Nguyễn Hoàng Mai, and other Vietnamese PhD students and postdocs who helped me settle into graduate school. I must also mention newer members of the group, namely Nguyễn Ngọc Mai Vy, Lê Bá Khoa, Đồng Thanh Hải, and Tôn Nữ Minh Thư, for always inviting me to try different restaurants. I will never forget all the times we got bubble tea and shared our teaching experiences when facing a difficult situation, our lunch at Aikan Sushi, or our debate over whether the table in Red Door Café was made of oak.

Additionally, I feel very fortunate to be surrounded by many old friends that I knew before graduate school. I would like to thank my friend Phua Yu Yu, whom I first met in 2012 in Singapore. We went to Anglo-Chinese School (Independent) together for high school in 2012 and 2013, and it was unbelievable that we met again at Caltech eight years later in 2021. Furthermore, I must also mention all my undergraduate friends from Colgate who always supported me, especially our Lambda Tau Plus group. Now it has been years since I left New York, but I still had so many Colgate friends in

Southern California. Tianyi He, who was in the Chianese lab with me at Colgate and coincidentally also joined the Agapie lab one year after me, helped a lot with EPR studies of my clusters. Thanks to Will Rosencrans, who was also at Caltech in the BMB program, for meeting me during our Friday lunches for four years. I would like to thank many other Colgate students affiliated with Caltech, namely Ryan de Silva, Nadia Houerbi, Joshua Liberman, and Tony Yap. Thanks to Yingqi Zhang from the University of Southern California who always gave me encouragements, and Cindy Vuong who would meet me from time to time when she came back to the LA area. Lastly, I would like to thank my Colgate/University of California – Los Angeles friend group with Vũ Thái Hà, Angela Jang, Shelley Chen, Soo Bin Kwon, Zach Abt, Leah Briscoe, Michael Kleinman, and Alec Chiu, for all the memories we had together at our many lunches, dinners, or trips.

The great lyricist Lana Del Rey once said: “When you leave all you take is your memory, and I’m gonna take mine of you with me”. It is sad to leave Caltech, but I cherish all the time I had with everyone in Southern California. I will always remember us this way, and I hope we will meet again.

ABSTRACT

Biological N_2 reduction to NH_3 occurs in microorganisms using the enzyme nitrogenase. This complex system consists of several iron-sulfur clusters, where the active site contains a MFe_7S_9C cluster (M = Mo, V, Fe) known as FeM cofactor (FeMco). The cluster includes an unusual interstitial carbide ligand, which is rare in both inorganic chemistry and biology. In addition, the role of this motif within the enzyme is not well-understood, and studies on synthetic model complexes are limited due to the absence of any previously reported iron-sulfur cluster systems bearing a carbon-based ligand that bridges the Fe atoms. Thus, this thesis focuses on developing strategies to insert a bridging carbon-based ligand into an iron-sulfur cluster platform.

Chapter 1 provides a general introduction and overview of complex biologically relevant iron-sulfur clusters and their corresponding synthetic analogs, with focus on NiFe CO dehydrogenase (CODH), acetyl CoA synthase (ACS), [FeFe] hydrogenase, P-cluster, and M-cluster of nitrogenase. Chapter 2 discusses the formation of a cluster with a μ_3-carbyne ligand resulting from the ring-opening of a bisaminocyclipropenylidene ligand. Electrochemical studies on this system and related species suggest that a chelating μ_3-carbyne leads to clusters with highly negative reduction potentials compared to μ_3-N or S ligands, suggesting that the interstitial carbide in FeMco may play a role in modulating the redox potential of the cluster to allow for the reduction of difficult substrates like N_2. Chapter 3 focuses on the binding of CO to the cluster with a μ_3-carbyne fragment, resulting in a high level of CO activation at 1851 cm^{-1} in the neutral cluster and 1782 cm^{-1} in the reduced cluster, Computational studies suggest that the bridging carbyne stabilizes the intermediate spin state at the Fe sites, resulting in more electrons in orbitals that can backbond with CO and greater activation. This suggests that the carbide in FeMco might play a role in modulating the electronic structure at the Fe sites to allow for greater activation of substrates. Chapter 4 highlights the synthesis of a cluster bearing a μ_4-carbide ligand using a previously reported terminal Mo carbide complex, with a bridging CO ligand that resembles the lo-CO form. The S = 1/2 spin state provides an opportunity to study the metal-carbon interaction by pulse EPR spectroscopy. In Chapter 5, a cluster ligated by an anthracene-bridged bisphenoxide ligand is described. Upon reduction, the anthracene bridge moves closer to one Fe site and interacts with it in an η^2 manner. This species can catalyze the electrochemical reduction of proton to form H_2, possibly through a protonated cluster intermediate.

The studies demonstrate the ability of the cluster to catalyze a biologically relevant reaction, and possibility for future studies on protonated species that have only been proposed in reactions of synthetic iron-sulfur clusters.

PUBLISHED CONTENT AND CONTRIBUTIONS

Le, L. N. V.; Bailey, G. A.; Scott, A. G.; Agapie, T. Partial Synthetic Models of FeMoco with Sulfide and Carbyne Ligands: Effect of Interstitial Atom in Nitrogenase Active Site. *Proc. Natl. Acad. Sci. U.S.A.* **2021**, *118* (49), e2109241118. https://doi.org/10.1073/pnas.2109241118.

L.N.V.L participated in the conception of the project, conducted the experiments, analyzed the data, and participated in the writing of the manuscript.

Le, L. N. V.; Joyce, J. P.; Oyala, P. H.; DeBeer, S.; Agapie, T. Highly Activated Terminal Carbon Monoxide Ligand in an Iron–Sulfur Cluster Model of FeMco with Intermediate Local Spin State at Fe. *J. Am. Chem. Soc.* **2024**, *146* (8), 5045–5050. https://doi.org/10.1021/jacs.3c12025.

L.N.V.L participated in the conception of the project, conducted the experiments, analyzed the experimental data, and participated in the writing of the manuscript.

TABLE OF CONTENTS

LIST OF FIGURES AND TABLES

Figures *Page*

Chapter 1

Chapter 2

Chapter 3

Chapter 4

Chapter 5

Appendix A

Tables

Chapter 2

Chapter 3

Chapter 1

SYNTHETIC MODELS OF ENZYME ACTIVE SITES BEARING IRON-SULFUR CLUSTERS

1.1 ABSTRACT

Iron-sulfur clusters are a ubiquitous motif in biological systems, with a variety of functions such as electron transfer, structural support, or catalysis for the redox conversion of small molecules. These clusters also possess interesting electronic properties, owing to the multimetallic nature that results in a large extent of metal-metal interactions. Synthetic chemistry offers an opportunity to access analogs of these biological active sites amenable to systematic modifications to test certain hypotheses, without having to drastically alter the protein backbone. Here, we present examples of reported synthetic clusters that mimic iron-sulfur-containing biologically active sites involved in the conversion of small molecule substrates. We focus on complex systems that have multiple metal centers (more than two), some of which include heterometals, namely NiFe CO dehydrogenase (CODH), acetyl CoA synthase (ACS), [FeFe] hydrogenase, and nitrogenase.

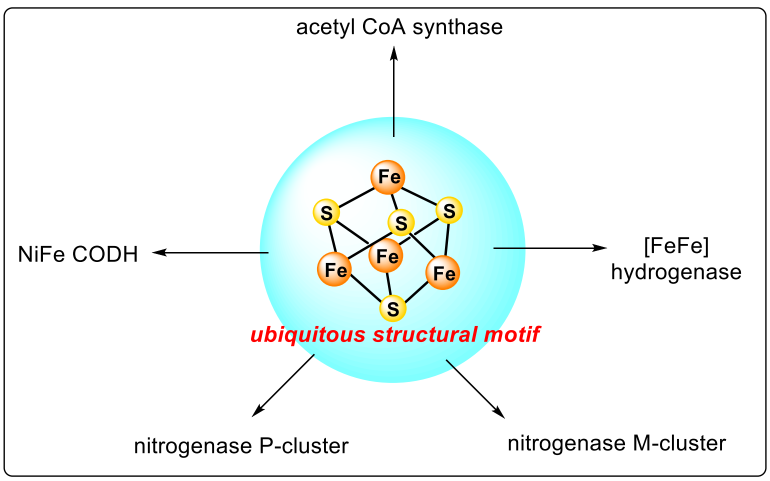

Representative examples of synthetic models

1.2 INTRODUCTION

Nature often employs systems consisting of multiple metal atoms in the form of metal clusters to achieve small molecule activation and transformation,[1–4] in order to exploit the synergy between different metal centers. This is achieved by the cooperation of many metal centers, for instance in the activation of substrate by sequential or concerted interaction with two or more metal sites. In addition, one metal center can modulate the electronic, geometric, or redox properties of the active metal that binds to the substrate to carry out the desired reaction. Clusters with multiple metals can also promote multielectron processes by distributing the charges among different metal atoms, instead of placing the burden on a highly oxidized or reduced metal site.

One commonly found multimetallic motif is the iron-sulfur cluster, where two or more Fe atoms are bridged by sulfide ligands. A variety of Fe-S compositions can exist, leading to systems with different geometries (Figure 1.1). For instance, the simplest iron-sulfur cluster of the 2Fe-2S type has a diamond-shaped structure, and the 4Fe-4S cluster forms a cube. The rare 3Fe-4S cluster possesses an incomplete cubane geometry.[5] These systems participate in a wide range of cellular processes, such as electron transport, small molecule activation and catalysis, iron/sulfur storage, and regulation of gene expression.[6,7]

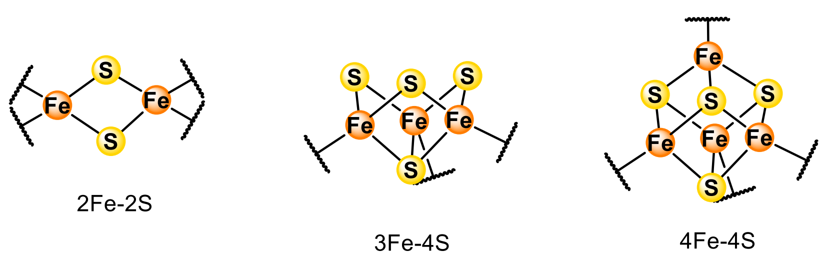

Figure 1.1. Examples of iron-sulfur cluster structures.

Owing to their complex structures, iron-sulfur clusters have been challenging synthetic targets for model systems to study their properties.[8] In addition, the 4Fe-4S form is a frequently encountered motif in enzymes, which exists as either the cubane form or building blocks for more complex structures. As synthetic models of 4Fe-4S clusters have been reviewed previously,[9] this discussion will place greater emphasis on active sites with more complicated bonding motifs, such as clusters with double cubane geometry, heterometals, dangling metal sites, or unusual interstitial ligands, which are still lacking in terms of synthetic modeling. Thus, the enzymes of primary interest will be nickel-iron carbon monoxide dehydrogenase (NiFe CODH), acetyl CoA synthase (ACS), iron-iron (FeFe) hydrogenase, and the P- and M-clusters of nitrogenase.

Arguably, there exist many plausible ways to model a biologically relevant metal cluster to study certain properties, especially because of their complicated structures that are hard to replicate. However, the closer the models are to the original version, the better it captures the relevant chemistry. Thus, since the clusters discussed often have many model systems that mimic a small part or the entire structure, we will focus on systems that bear the most resemblance to the native active site. The models should have multiple metal centers (more than two), include heterometals where possible, and preserve important topologies of the enzymatic cluster, such as the $[M_4X_4]$ cubane geometry. Furthermore, good models should contain biologically relevant donor atoms on the metal centers. Lastly, other important structural features such as interstitial bridging ligands should also be present.

1.3 COMPLEX IRON-SULFUR CLUSTERS AND SYNTHETIC MODELS

a) Nickel-iron carbon monoxide dehydrogenase (NiFe CODH) and acetyl CoA synthase (ACS)

i) Structure and function

The NiFe CODH enzyme reversibly oxidizes CO to CO_2, allowing microorganisms to utilize CO as a source or carbon and energy. In some organisms, the CO produced after CO_2 reduction is subsequently used in the synthesis of acetyl CoA, a key metabolic intermediate, using ACS.[10] Consequently, both NiFe CODH and ACS can be tightly associated in the same enzyme complex in some microbes.

Early spectroscopic studies using techniques such as ENDOR, EPR, IR, and Mössbauer spectroscopy of NiFe CODH suggest that it contains an $[Fe_4S_4]$ cluster, linked to an external Ni atom through an unidentified bridging ligand X, altogether referred to as the C-cluster.[11–13] Further EXAFS data suggest that the Ni center has a distorted square planar geometry, likely ligated by two cysteine residues and two N/O based ligands.[14] Subsequent X-ray crystallographic studies have established that the C-cluster actually consists of an unusual $[NiFe_3S_4]$ cluster, with an additional fifth Fe site connected to the cluster through sulfide[15,16] or thiolate bridges (Figure 1.2).[17]

In comparison, the A-cluster of the ACS site contains a cubane [Fe_4S_4] cluster, with two additional metal sites bridged to the cluster at one Fe vertex through a Cys residue.[18] Later studies have assigned these metal ions to be Ni.[15,19] The proximal Ni_p atom can adopt either a tetrahedral or a square planar geometry,[19,20] while the distal Ni_d site is in a square planar coordination environment bound by an N_2S_2 motif from a Cys-Gly-Cys segment in the protein backbone (Figure 1.2).[18–20]

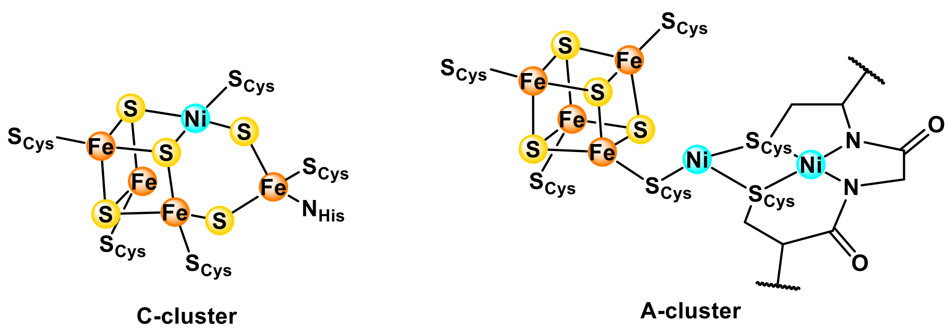

Figure 1.2. Structures of the C-cluster in NiFe CODH (PDB 1SU8) and the A-cluster in ACS (PDB 1OAO).

ii) Synthetic models

NiFe CODH

After the establishment of the [$NiFe_3S_4$] cluster from the X-ray structures of NiFe CODH, synthetic heterometallic cubane systems became more relevant. The Holm group reported a reductive rearrangement of a linear Fe_3 cluster **1.1** with $Ni(PPh_3)_4$ to yield a series of cubane species **1.2/1.3** with a [$NiFe_3S_4$] motif (Figure 1.3).[21] A cuboidal [Fe_3S_4] cluster can also be generated from the site-differentiated [Fe_4S_4] cluster **1.4** upon treatment with $(NEt_4)_2$(Meida) (Meida = N-methylimidodiacetate) to abstract the unique Fe atom as $[Fe(Meida)_2]^{2-}$ and form the incomplete cubane **1.5**.[22] Subsequently, a Ni vertex can be installed in **1.6** using $Ni(PPh_3)_4Cl$ (Figure 1.3).[23]

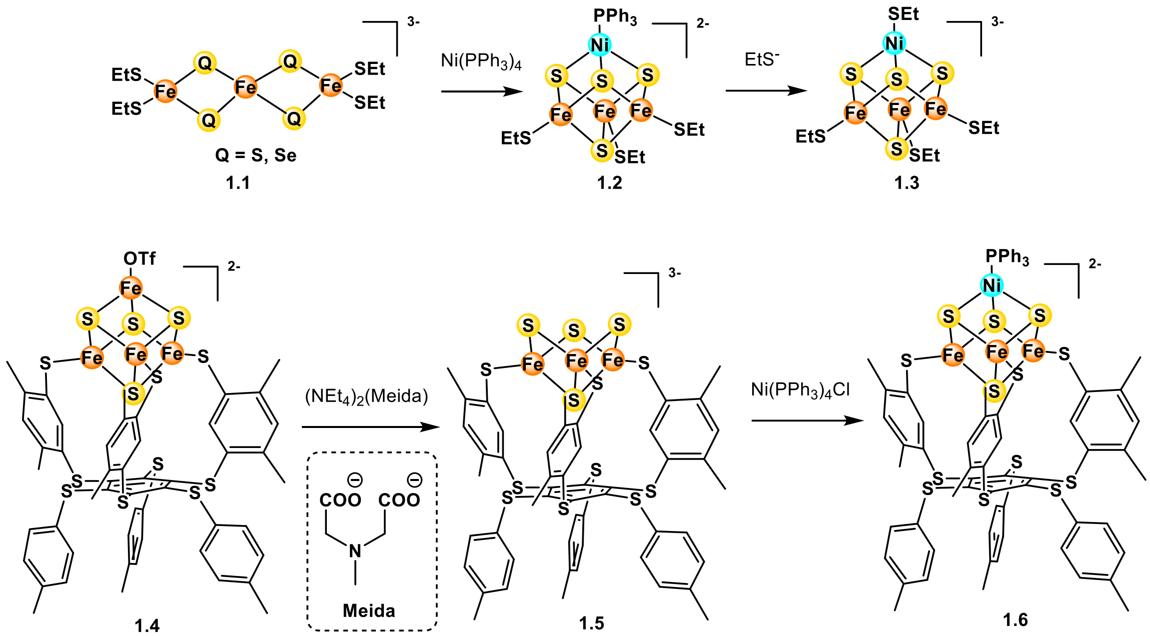

Figure 1.3. Preparation of $[NiFe_3S_4]$ clusters.

In both cases, spectroscopic studies of the electronic structures indicate that the clusters consist of a tetrahedral, high spin Ni^{II} (S = 1), antiferromagnetically coupled to a $[Fe_3S_4]^-$ (S = 5/2) fragment, resulting in a $[NiFe_3S_4]^+$ cluster with S = 3/2.[23,24] In contrast, the Ni center in CODH of *C. hydrogenoformans* possesses a square planar coordination sphere, characteristic of a diamagnetic Ni^{II} atom.[15] Furthermore, while the C-cluster has been observed in four different oxidation states[10], these synthetic clusters are less stable to redox chemistry as they exhibit one reversible reduction and one irreversible oxidation[21,23], reflecting the lower tendency for the cluster to be oxidized which will not favor the incorporation of the heterometal. For **1.6**, attempts have been made to substitute the PPh_3 ligand on Ni with the more biologically relevant SEt, but further characterization data are still lacking, possibly because of difficulties in its isolation.[21]

The tetrahedral Ni site in **1.6** can be converted to a square planar site closer to the biological analog using a sufficiently strong ligand that induces spin pairing. Treatment of **1.6** with the chelating phosphine dmpe results in the substitution of the PPh_3 ligand and yields **1.7** (Figure 1.4). X-ray crystallography confirms the distorted square planar coordination sphere of the Ni center (Figure 1.5, left). This suggests a diamagnetic Ni^{II} site like in the C-cluster. Furthermore, the Mössbauer spectrum of **1.7** is similar to prior reports of a $[ZnFe_3S_4]^+$ cluster with S = 5/2. Thus, the authors assign **1.7** to an S = 5/2 ground state, which is consistent with the conversion of the S = 1 tetrahedral Ni^{II} center in **1.6** to an S = 0 planar Ni^{II} in **1.7**, along with the loss of the antiferromagnetic coupling with the S = 5/2 $[Fe_3S_4]^-$ fragment.[25]

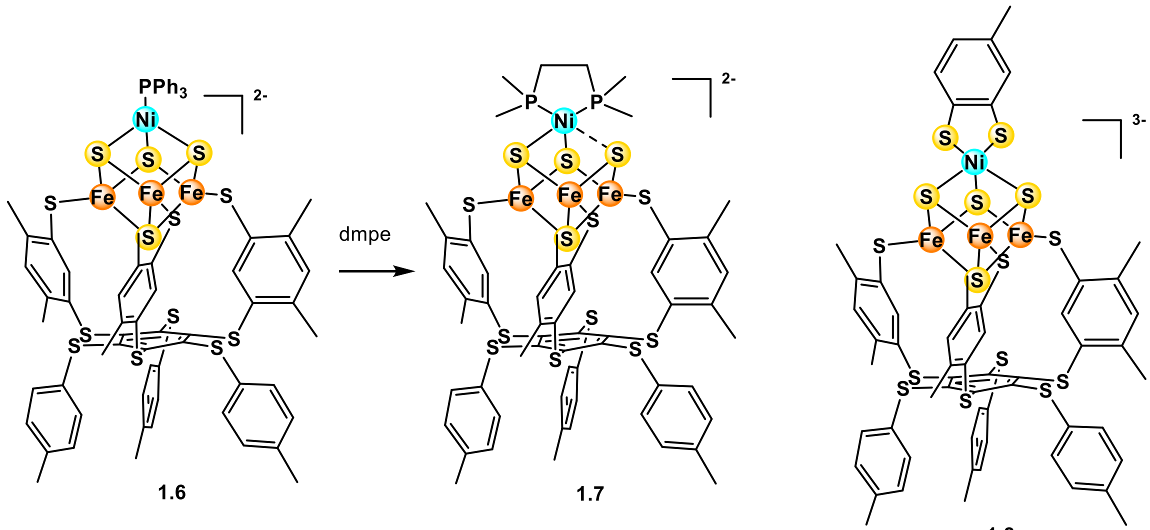

Figure 1.4. Substitution of the apical ligand on $[NiFe_3S_4]$ clusters.

One other significant geometric feature in **1.7** observed from X-ray crystallography is the loss of an edge in the cubane structure, and the Ni-S interaction has elongated beyond bonding distances, leading to a weak axial coordination of the S atom to nickel. However, the average Ni-S separation of 2.71 Å[25] (averaged from the corresponding distances in four different crystalline forms of the cluster) is still much shorter than the value of 3.75 Å in the C-cluster.[26] The axial M-S distance in the synthetic cluster can be tuned to approach this value by changing the metal to Pd (M-S = 3.02, 3.27 Å in two crystalline forms) or Pt (M-S = 3.11, 3.39 Å in two crystalline forms) while maintaining the planar coordination at the heterometal. However, this change can simply be attributed to the larger radius of the metal atom going down the group. Excluding the heterometal and the axial S, the remaining Fe_3S_3 portion compares well geometrically with the biological analog, with only 0.088 Å in the weighted rms deviation (Figure 1.5, right). This suggests that the protein environment and secondary sphere interactions play an important role in dictating the Ni-S separation in the C-cluster.[26]

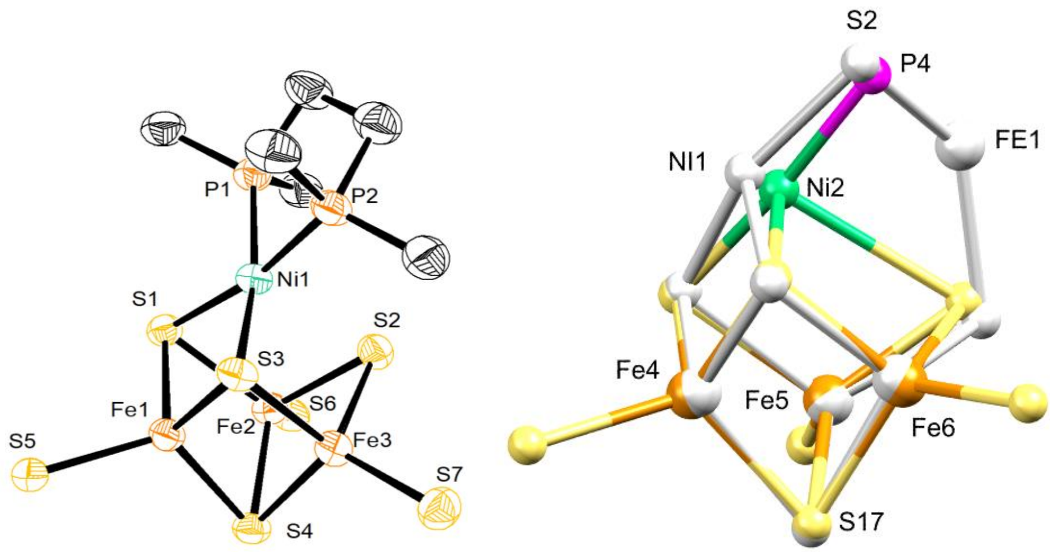

Figure 1.5. Structure of **1.7**. Left: Crystal structure of the [$NiFe_3S_4$] cluster in **1.7**. Hydrogen atoms, countercations and most of the thiolate ligand are omitted for clarity. Ellipsoids are shown at 50% probability level. Right: Overlay of **1.7** (colored) onto the NiFe CODH cluster (grey).

The closest model of the $NiFe_3S_4$ fragment results from the substitution of the PPh_3 ligand in **1.6** by toluene-2,3-dithiolate (tdt) to form **1.8** (Figure 1.4). The thiolate ligand reproduces the S_{Cys} atoms bound to the Ni in the enzyme, and its rigid structure also imposes an approximate square planar environment at the heterometal. Mössbauer and ^{1}H NMR spectroscopic studies indicate that the cluster has an S = 2 ground state resulting from the diamagnetic Ni^{II} and an S = 2 $[Fe_3S_4]^0$ unit, which is one-electron oxidized compared to **1.6** and **1.7**. Furthermore, the axial Ni-S distance has lengthened to 3.15 Å, closer to the value in the C-cluster without using a metal with a larger atomic radius.[27]

However, all of the aforementioned clusters fail to incorporate the fourth *exo* Fe atom. Taniyama *et al.* described the heterometallic VFe_4S_4 cluster **1.9** consisting of a VFe_3S_4 cubane and a dangling Fe atom linked to the cubane through a μ_2-thiolate, obtained in 8-10% using two different methods (Figure 1.6). These features of **1.9** capture some salient geometric properties of the C-cluster of NiFe CODH. However, apart from this similarity, it is hard to draw comparisons regarding other aspects such as electronics, as the properties of V are different from Ni, the external Fe should be bridged by a sulfide ligand from the cubane instead of a thiolate, and this atom in **1.9** is linked to the heterometal through an (O,O,O) motif much more complicated than in the biological case.[28]

Nevertheless, this example demonstrates the possibility of ligating an *exo* Fe atom to a heterometallic MFe_3S_4 cubane, a feat that still proves synthetically challenging.

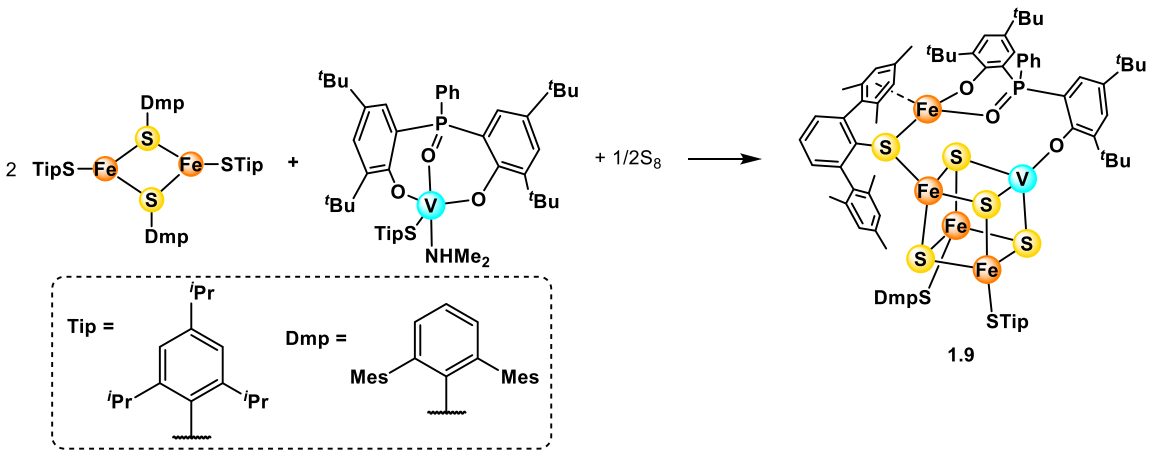

Figure 1.6. Synthesis of a Fe-VFe_3S_4 cluster.

While the examples presented show some synthetic cluster models that may resemble the C-cluster geometrically, they still fall short of a *functional* model. So far, none of these clusters have been studied in the presence of substrates or other related small molecules. Consequently, little can be learned about the mechanism of CO dehydrogenase from the present models. The challenge of the field now rests in the design of a multimetallic compound that is also capable of relevant biological transformations.

ACS

Clusters bearing a $[Fe_4S_4]$ cubane linked to a Ni center through a sulfur bridge have been prepared, which resemble the active site of ACS (Figure 1.7). Cluster **1.10** was generated from the reaction between the anionic cubane $[Fe_4S_4I_4]^{2-}$ and the nickel aminodithiolate complex [NiL] [L = -$SCH_2CH_2N(Et)CH_2CH_2CH_2N(Et)CH_2CH_2S^-$], where two Ni fragments substitute two iodide ligands on two adjacent vertices of the Fe_4S_4 unit. Another related cluster **1.11** was also identified by X-ray crystallography despite reproducibility issues, which contains one Ni center instead of two as in **1.10**. Some features of ACS were present in these models. The Ni centers are located within an N_2S_2 coordination sphere like in the distal Ni_d of the A-cluster, with a distorted square planar geometry. In addition, the Fe and Ni sites are either four- or five-coordinate, highlighting their open nature and the possibility of substrate binding at these atoms in related biological clusters.[29]

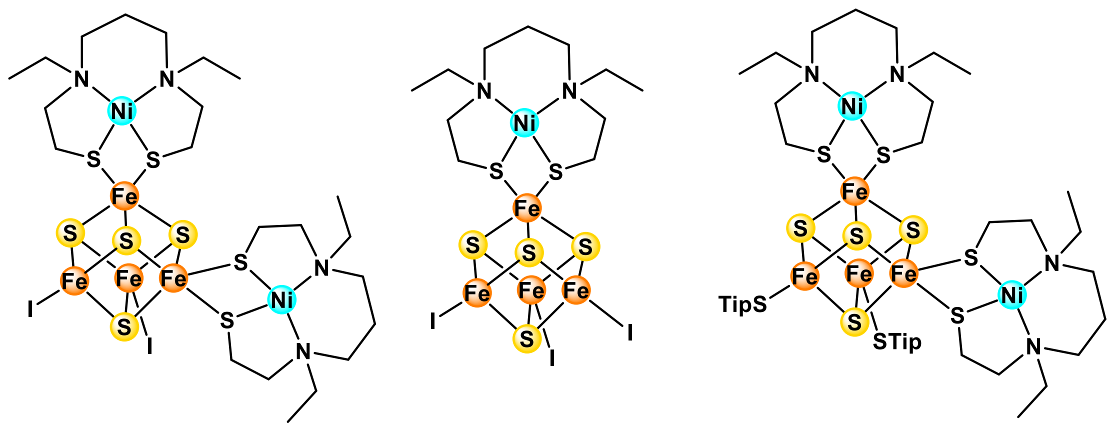

Figure 1.7. [Fe_4S_4] cubane clusters linked to an external Ni center.

Attempts have also been made to convert the halide ligands on the [Fe_4S_4] cluster to more biologically relevant thiolates, as this unit is usually bound to Cys residues in enzymes. On reacting **1.10** with two equivalents of KSTip, cluster **1.12** is formed from the ligand substitution between I and STip. This cluster can also be formed directly by reacting two equivalents of the same nickel precursor [NiL] with [$Fe_4S_4(STip)_2(tap)_2$] (tap = thioantipyrine = 2,3-dimethyl-1-phenyl-3-pyrazoline-5-thione). In **1.12**, the Ni centers also maintain the distorted square planar geometry (Figure 1.7). However, clusters **1.10** – **1.12** have been neither studied in the presence of substrates and related compounds nor characterized by spectroscopic methods such as EPR or Mössbauer spectroscopy to compare their electronic structures with the biological counterpart. However, the Ni(μ_2-SR)[Fe_4S_4] motif presented here had previously eluded synthetic attempts, since the μ_2-thiolate groups tend to bridge multiple Ni centers.[30] This model suggests that this structure is synthetically accessible and points to the plausibility of sulfur as the bridging X ligand in the C-cluster.

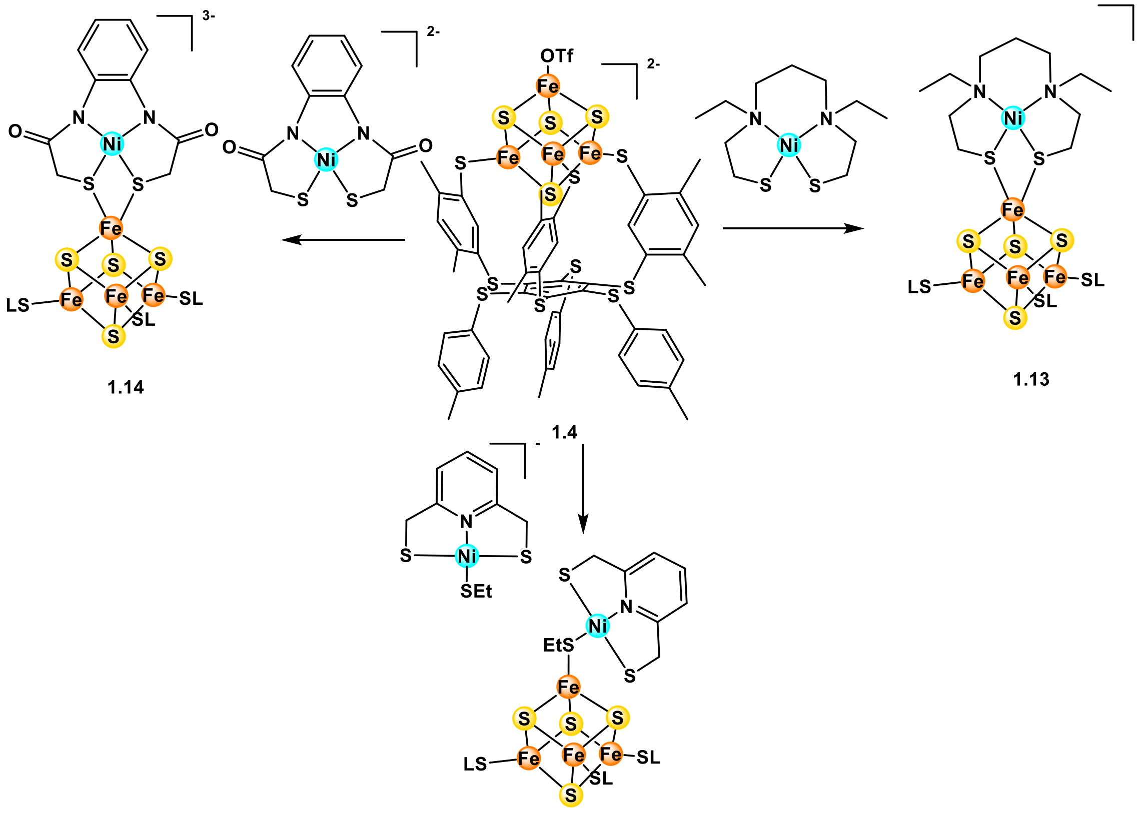

Figure 1.8. Thiolate-bound $[Fe_4S_4]$ clusters linked to an external Ni center.

The Holm group also reported related structures **1.13** and **1.14** with a Ni center bound to a thiolate-supported site-differentiated $[Fe_4S_4]$ cluster starting from **1.4** (Figure 1.8). Similarly, the Ni atom is stabilized by a chelating S_2N_2 environment, with two μ_2-S bridges. Interestingly, using a Ni precursor supported by pyridinedithiolate and ethanethiolate ligands, the authors reported a new product **1.15** with a single μ_2-S bridge based on NMR spectroscopy (Figure 1.8). While the Ni center in other systems resembles Ni_d, **1.15** represents progress in modeling the proximal Ni_p that is bridged by only one Cys residue in the A-cluster. However, **1.15** quickly decomposes in the presence of coordinating solvents such as MeCN, suggesting that a single unsupported bridge is less robust.[31] Possibly, the protein environment contributes greatly to the stabilization of the $[Fe_4S_4]$−(μ_2-S_{Cys})−Ni motif in the A-cluster. Consequently, it remains a challenge to develop a synthetic model of ACS that incorporates both the Ni_d and Ni_p sites within the same cluster.

b) [FeFe] hydrogenase

i) Structure and function

Hydrogenases are enzymes found in microorganisms that catalyze the reduction of proton to H_2, as well as the reverse conversion of H_2 into protons and electrons.[32] The enzyme can be classified into three different types depending on the structure of the active site: [FeFe], [NiFe], and [Fe] hydrogenases.[32,33] In [Fe] hydrogenase, the active site contains only one Fe center, and it requires methenyltetrahydromethanopterin to activate H_2, while [NiFe] hydrogenase contains a bimetallic Ni-Fe complex.[32] Only [FeFe] hydrogenase possesses an iron-sulfur cluster structure at the active site, and therefore it is the subject of our discussion.

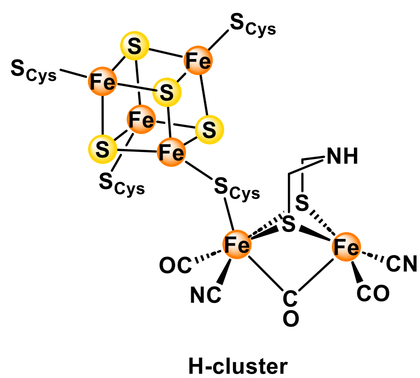

Figure 1.9. Structures of the H-cluster in [FeFe] hydrogenase from *Clostridium pasteurianum* (PDB 3C8Y).

The hexametallic cluster of [FeFe] hydrogenase, also known as the H-cluster, consists of a $[Fe_4S_4]$ cluster bridged to a Fe_2 complex through the S atom of a Cys residue (Figure 1.9). The remaining Fe sites on the $[Fe_4S_4]$ portion are ligated by Cys thiolates. Both Fe atoms of the [2Fe] subunit contain one terminal CO and one terminal CN ligand each.[34] In addition, the two Fe sites in the Fe_2 complex are also bridged by one CO ligand and an unusual azadithiolate moiety.[35,36]

ii) Synthetic models

Modeling of the active site of the [FeFe] hydrogenase enzyme usually focuses on the [2Fe] butterfly cluster, as this is considered the site of catalytic activity. There have been hundreds of model systems based on this motif and the readers are encouraged to refer to the corresponding articles discussing their significance.[37–39] However, the [Fe_4S_4] unit that assists in electron transfer must play an important part in the catalytic cycle, as it tunes the reactivity of the active site. Hence, a faithful synthetic model of [FeFe] hydrogenase should incorporate this unit into the compound in some way, leading to clusters with more than two Fe atoms. Thus, we will focus on models of this type, which have not been explored as widely in the literature.

So far, only one cluster has been reported which contains both the [2Fe] unit and the [Fe_4S_4] cubane bridged by a thiolate similarly to the H-cluster (Figure 1.10). The [2Fe] cluster **1.17** was synthesized by metalating the dithiolate ligand **1.16** bearing a pendant thioester group with $Fe_3(CO)_{12}$. This cluster was then appended to the unique Fe site of the site-differentiated [Fe_4S_4] cluster reported by the Holm group[40] to yield **1.18**, which was assigned based on mass spectrometry. Remarkably, the results are consistent with the presence of a [Fe_{cubane}(μ-SR)$Fe_{subsite}$] linkage like in the H-cluster, indicating that the pendant thioester has not only lost the COMe group, but it also displaces one CO ligand on the [2Fe] cluster. The Mössbauer spectrum also supports this assignment, as it shows four different Fe environments: two associated with the site-differentiated cubane and two with the [2Fe] butterfly cluster. Using more equivalents of **1.17** results in the complete substitution of the [Fe_4S_4] unit by the [2Fe] cluster (**1.19**). [41]

However, **1.16** was not characterized in the solid state by methods such as X-ray crystallography, so the bond metrics cannot be compared with those of the native enzyme. Nevertheless, DFT optimization of the assigned structure reveals a very short Fe-Fe distance of 2.6 Å in the [2Fe] unit, indicative of Fe-Fe bonding and significant Fe-Fe interaction. Calculations also predict the electronic structure of the cluster as Fe^{I}-Fe^{I}-[Fe_4S_4]$^{2+}$. The Mössbauer parameters of **1.16** show many similar features to those of the reduced form of *Clostridium pasteurianum* hydrogenase II, supporting a reassignment of the oxidation state of this cluster as Fe^{I}-Fe^{I}-[Fe_4S_4]$^{2+}$ compared to Fe^{II}-Fe^{II}-[Fe_4S_4]$^{2+}$ as previously reported.[42] In addition, the cyclic voltammogram of **1.16** exhibits a reversible one-electron reduction event at -0.65 V vs. Ag/AgCl, which is assigned to the reduction of the [Fe_4S_4]$^{2+}$ core, and an irreversible multi-electron reduction at -1.58 V associated with the [2Fe] unit. This result suggests that the Fe^{I} centers are typically harder to reduce than the [Fe_4S_4]$^{2+}$ cubane, so the [Fe_4S_4]$^{+}$ state may be biologically relevant. This state was subsequently identified in the superreduced in hydrogenase from *Chlamydomonas reinhardtii* at about 150 mV more negative than the $H_{ox/red}$ couple.[43] Consequently, some models have invoked this H_{sred} state in addition to the $H_{ox/red}$ species to account for the two electrons required for the $H_2/2H^+$ interconversion.[39]

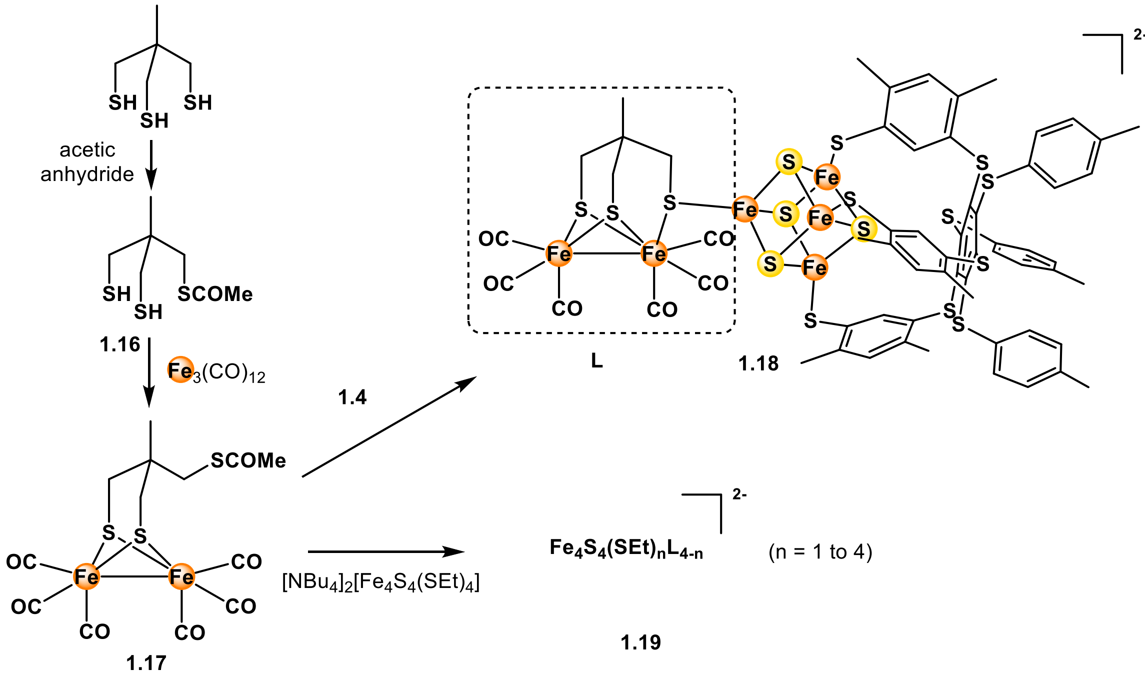

Figure 1.10. Attachment of a [2Fe] fragment to a $[Fe_4S_4]$ cluster. The [2Fe] fragment highlighted by a box is abbreviated as **L**.

Cluster **1.18** also shows electrocatalytic response for proton reduction. The cyclic voltammogram of **1.18** in the presence of the 4,6-dimethylpyridinium cation as the proton source shows a 20-fold increase in peak current, as well as a 200 mV shift to a more positive potential.[41] While this model still lacks some important features of the H-cluster like the CN ligands or the azadithiolate bridge, it demonstrates the possibility of linking the [2Fe] and $[Fe_4S_4]$ units to result in a mildly active catalyst for proton reduction.

Other efforts have focused on simplifying the $[Fe_4S_4]$ unit into an Fe-containing group capable of electron transfer. Song *et al.* reported cluster **1.20** where the [2Fe] unit is linked to the third Fe through a thiolate bridge similarly to the H-cluster (Figure 1.11). However, the third Fe is not biologically significant, as its electronic structure likely differs from the $[Fe_4S_4]$ units due to the inclusion of strong field ligands such as Cp and CO instead of the weak field thiolates.[44] Another model based on this motif replaces the thiophenolate ligand with a Boc-protected L-cysteinyl ester to mimic the [Fe_{cubane}(μ-cysteinyl-S)$Fe_{subsite}$] linkage (**1.21**, Figure 1.11). The IR spectrum of this cluster indicates a shift of about 30 – 35 cm^{-1} toward lower values for ν_{CO} compared to the parent cluster with CO in place of the cysteinyl thiolate.[44] In comparison, ν_{CO} shifts by 15 cm^{-1} toward lower values for **1.18**,[41] suggesting that the combination of the CpFe unit and the L-cysteinyl linkage results in more efficient electronic communication between the [2Fe] subsite and the third Fe atom. Furthermore, **1.21** (X = ^{t}BuN) also displays mild electrocatalytic activity for proton reduction using HOAc, with a turnover number of 8.7 and H_2 yield of about 90%.[45]

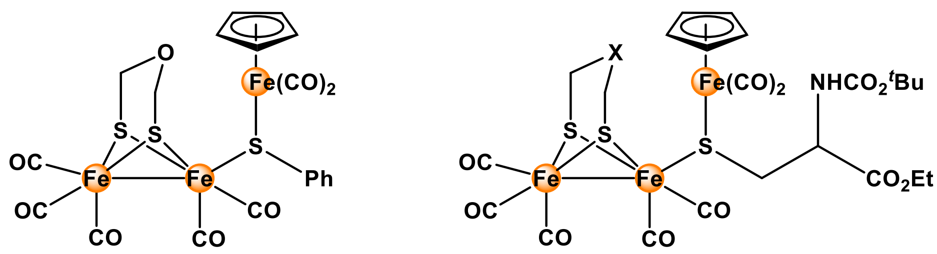

1.20

1.21

X = CH_2, ^{t}BuN, *p*-MeOC_6H_4N

Figure 1.11. Clusters bearing a [2Fe] unit and a CpFe fragment.

The role of the CpFe group has also been explored using other ligand architectures, which attempt to replicate the electron transfer properties of the [Fe_4S_4] cubane. Hu *et al.* reported complex **1.22** where two identical [2Fe] units are bridged by an Fe-sip unit (sip = sulfanylpropyliminomethyl-pyridine) through the sulfur atoms (Figure 1.12). The cyclic voltammogram of **1.22** shows a very anodic shift of the first reduction ($Fe^{I}Fe^{I}/Fe^{I}Fe^{0}$ in one [2Fe] unit) to -1.13 V compared to the parent [2Fe] cluster (μ-pdt)$Fe_2(CO)_6$ (pdt = propanedithiolate) and other reported [2Fe] models. This points to the electron-withdrawing effect of the Fe-sip unit, decreasing the electron density at the [2Fe] centers and making them accept electrons from reduction more easily. The second $Fe^{I}Fe^{I}/Fe^{I}Fe^{0}$ reduction in the other [2Fe] unit occurs more cathodically at -1.35 V, similarly to other monosubstituted [2Fe] systems. This can be attributed to the increase in electron density on one [2Fe] side after the first reduction, resulting in σ-donation by the Fe-sip bridge to the other [2Fe] side and making it accept another electron less readily.[46] Another cluster **1.23** utilizes the redox active ferrocene moieties as electron donors/acceptors, linked through the [2Fe] units through bridging phosphorus atoms (Figure 1.12). **1.23** shows electrocatalytic activities for proton reduction through cyclic voltammetry in the presence of *p*-toluenesulfonic acid, but mechanistic details suggest that H_2 production may result from the coupling of hydrogen atoms from a protonated phosphorus and a Fe center in the [2Fe] unit.[47] However, the importance of this process is inconclusive because of the presence of strong field phosphorus-based bridges that may change the electronic structures at the [2Fe] core.

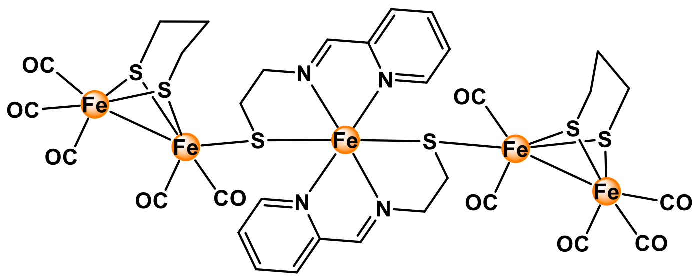

1.22

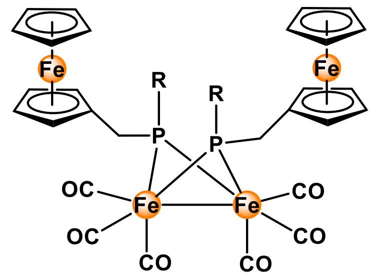

1.23
R = H, Me

Figure 1.12. Other models bearing redox-active pendant groups.

The oxidized cluster H_{ox} has also been modeled using a similar strategy and tested for H_2 oxidation, the reverse reaction also catalyzed by [FeFe]-hydrogenase. In addition to the importance of the $[Fe_4S_4]$ unit, the azadithiolate bridge also plays a crucial role in the catalytic cycle as the nitrogen atom can act as a proton relay,[48] but many of the models discussed earlier lack this feature. Compound **1.24** (Figure 1.13) was designed to incorporate this group, as well as pendant group with a mild redox couple between -0.3 and 1.0 V vs Fc/Fc^+, closer to that of the H_2/H^+ pair. The oxidation state of the [2Fe] unit is Fe^IFe^I as in H_{red}, and the Fc fragment exists as Fe^{II}. The first oxidation occurs at the [2Fe] cluster, resulting in an Fe^IFe^{II}-Fe^{II} state. The second oxidation occurs at the Fc unit, giving the assignment Fe^IFe^{II}-Fe^{III}. Thus, both [**1.24**]$^+$ and [**1.24**]$^{2+}$ exhibit the same oxidation states in the [2Fe] core as H_{ox}. Unlike other simpler models, [**1.24**]$^{2+}$ reacts with CO to yield a diamagnetic cluster, suggesting the conversion of the Fe centers to the $Fe^{II}Fe^{II}$-Fe^{II} form.[49] This parallels the observation that when H_{ox} from *Clostridium pasteurianum* and *Desulfovibrio desulfuricans* react with CO, the distal Fe becomes partially oxidized;[50,51] in this case, it is internally oxidized by the Fc^+ unit to become Fe^{II}. [**1.24**]$^+$ also catalyzes H_2 oxidation in the presence of excess $FcBAr^F_4$ oxidant and excess P(*o*-tolyl)$_3$ as the base, a marked activity compared to simpler [2Fe] models. Although the turnover of 0.4 h^{-1} is several orders of magnitude lower than the native enzyme,[49] this finding emphasizes that functional mimics of the H-cluster should contain the azadithiolate bridge and a redox active side group to act as proton/electron relays.

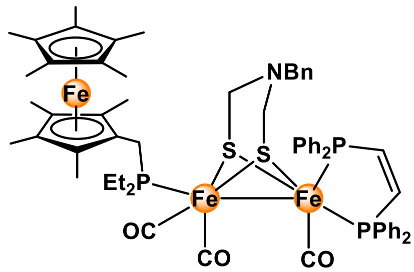

1.24

Figure 1.13. H-cluster model that catalyzes H_2 oxidation.

Recently, a new two-part method has been reported leading to a model cluster containing an $[Fe_4S_4]$ cubane, the [2Fe] cluster with an azadithiolate bridge, and CN^- ligands on the Fe centers. The $[Fe_4S_4]$ is assembled from $FeCl_3$, Na_2S and a 16 amino acid synthetic peptide H_2N-KL**C**EGG**C**IA**C**GA**C**GGW-$CONH_2$ (FdM) that has been shown to support an $[Fe_4S_4]$ cubane. The resultant EPR-silent peptide-$[Fe_4S_4]^{2+}$ cluster is formed as expected. Reduction by sodium dithionite leads to the $[Fe_4S_4]^+$-FdM species that is nucleophilic enough to displace a CO ligand from the synthetic cluster **1.25**, yielding the "miniaturized hydrogenase" **1.26** detected by spectroscopic techniques but without solid state characterization (Figure 1.14). The absence of an EPR signal suggests that **1.26** consists of an Fe^IFe^{II} core (S = 1/2) antiferromagnetically coupled to an $[Fe_4S_4]^+$ (S = 1/2) unit to give an S = 0 cluster.[52] This electronic configuration has been suggested as another plausible form of the H_{red} cluster based on FTIR spectroscopy.[53] Possessing all the salient features of the reduced H_{red} cluster, **1.26** exhibits catalytic activity for H_2 evolution from methyl viologen ($E_{0,\ MV^+/2^+} \approx -0.45$ V), despite a low turnover of 10 h^{-1}.[52] However, this cluster is the first active synthetic model bearing cyanide ligands at the [2Fe] unit, and it illustrates the importance of the 4Fe-4S cluster for the catalytic properties of the [2Fe] portion.

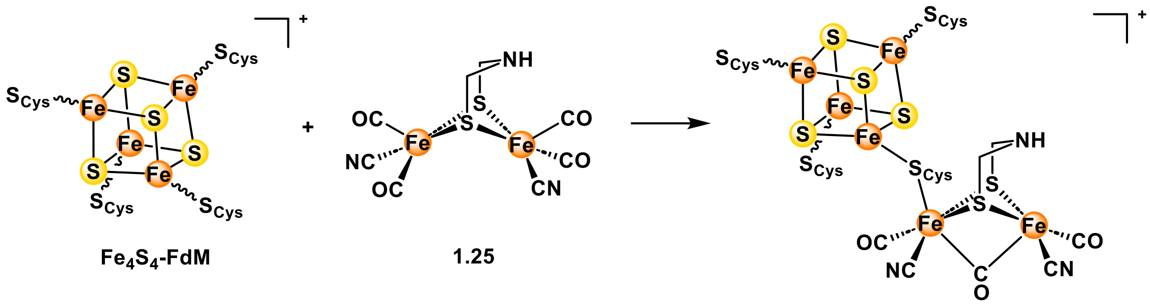

Figure 1.14. Synthesis of the miniaturized hydrogenase **1.26**.

All these models suggest that it is possible to achieve a functional synthetic model of the H-cluster closer to the biological structure, which involves incorporating the correct ligands in the primary coordination sphere of the [2Fe] unit, as well as including a fragment capable of electron transfer. However, this still does not guarantee a high level of activity. Cluster **1.26**, for instance, decomposes very quickly within about 1 h, limiting its usefulness as a catalyst. Perhaps the proficiency of [FeFe]-hydrogenase is tuned even further by the secondary coordination sphere consisting of the surrounding amino acid residues in the active site, which stabilize it and lead to other important interactions in the catalytic cycle.

c) P-cluster of nitrogenase

i) Structure and function

Nitrogenase is an enzyme found in microorganisms that catalyzes the conversion of atmospheric N_2 into NH_3.[54,55] This multielectron reaction requires 16 ATP molecules for every N_2 molecule reduced, with the release of two equivalents of NH_3 and one equivalent of H_2:

$$N_2 + 8e^- + 8\ H^+ + 16\ ATP \rightarrow 2\ NH_3 + H_2 + 16\ ADP + 16\ P_i$$

The reaction occurs at a complex metal cluster called the M-cluster in the active site. However, the enzyme also consists of two other clusters that form part of the electron transport chain to the M-cluster: a $[Fe_4S_4]$ cluster and the complex P-cluster with an $[Fe_8S_7]$ composition, which mediates the delivery of electrons from the $[Fe_4S_4]$ cluster to the active site.[56,57]

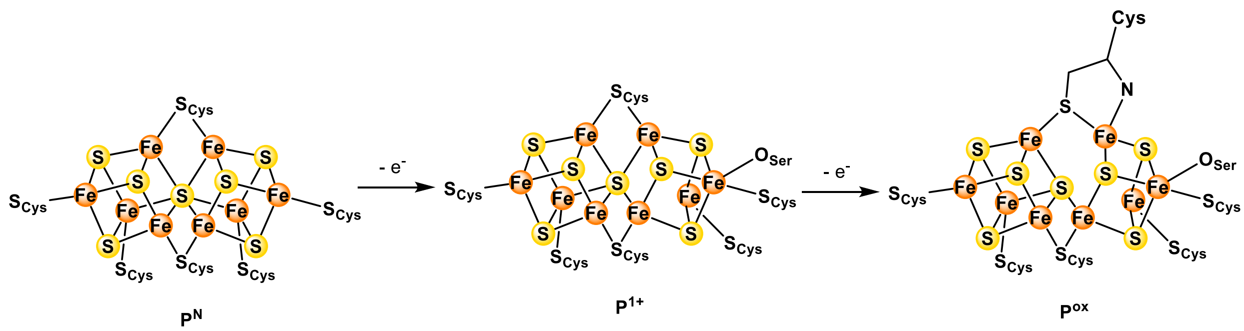

Figure 1.15. Structure of the P-cluster in 3 oxidation states (PDB 3U7Q for P^N and P^{ox}, 6CDK for P^{1+}).

The octanuclear P-cluster can be described as two [Fe_4S_4] fragments fused together at one S vertex (Figure 1.15).[58] Different oxidation states of this system have been characterized by crystallography, with some variations in geometry. In the as-isolated, neutral P^N state, the two halves are supported by two bridging thiolate ligands from Cys residues, with the remaining Fe sites terminally ligated by thiolates. In the two-electron oxidized form P^{ox}, the cluster becomes more open, where two Fe-S bonds with the central sulfide have been cleaved, and an N atom from a backbone amide and an O atom from a Ser residue now coordinate to the cluster.[59] A transient one-electron oxidized form P^{1+} has also been observed by spectroscopic methods,[60,61] which was characterized by X-ray crystallography after electrochemical generation. In this form, only one Fe-S bond to the central sulfide has been cleaved compared to P^N, while a Ser residue also coordinates to the cluster.[62] Consequently, the P^{1+} structure is a transition between the P^N and P^{ox} states.

ii) Synthetic models

Synthetic models of the P-clusters have only focused on the P^N geometry. Earliest examples of octametallic clusters with a μ_6-sulfide were reported by Zhang *et al.* after the rearrangement of an edge-bridged double cubane **1.27** (Figure 1.16).[63,64] The edge-bridged double cubane motif is known to rearrange into multimetallic clusters that contain up to 26 metal atoms;[65] however, the Tp-capped heterometals Mo and V are presumably less reactive, directing subsequent transformations to the Fe sites where rearrangement can occur in a more controlled manner. The product **1.28** contains many structural features of P^N, such as a μ_6-sulfide, an octametallic core, and two terminal hydrosulfide ligands that model terminal cysteine ligands, although the two halves are bridged by sulfides instead of thiolates. In addition, **1.28** also comprises heterometals Mo or V, which are not found in any form of the P-cluster.

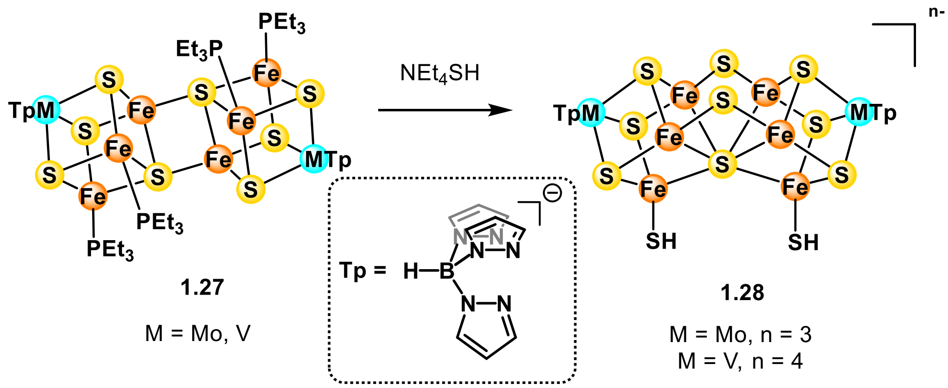

Figure 1.16. Synthesis of $M_2Fe_6S_9$ cluster with a μ_6-sulfide ligand.

Another strategy toward the synthesis of multimetallic clusters relies on self-assembly, where simple precursors aggregate to form more complex structures. In a nonpolar environment such as toluene as solvent, the combination of $Fe(N(SiMe_3)_2)_2$, TipSH (Tip = 2,4,6-tri(isopropyl)phenyl), tetramethylthiourea, and S_8 leads to the formation of the octametallic cluster **1.29** (Figure 1.17).[66] This product also contains a μ_6-sulfide, but with only Fe as the metal centers. However, the remaining ligands bound to Fe sites are not biologically relevant, such as amide and thiourea. These ligands can be substituted with thiolates using appropriate reagents. Using $CpFe(C_6H_5S)$, the authors can replace the two thiourea moieties with terminal thiolates to form **1.30**, which can then be converted into **1.31** using the bulky thiolate TbtSH (Tbt = 2,4,6-tris[bis(trimethylsilyl)methyl]phenyl) using protonolysis to remove the two terminal $N(SiMe_3)_2$ ligands (Figure 1.17).[67] In contrast, the replacement of the bridging $N(SiMe_3)_2$ groups with thiolates starting from these species has not been achieved.

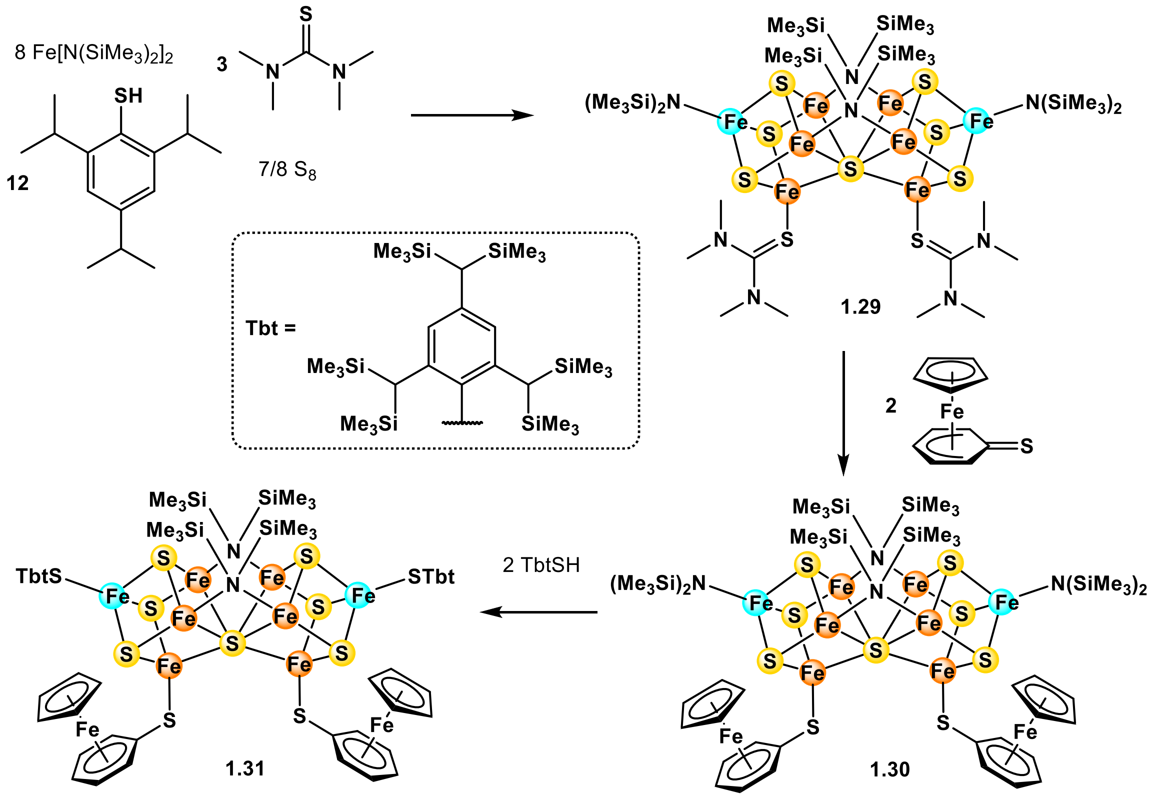

Figure 1.17. Syntheses of **1.29** – **1.31**.

In a similar manner, a cluster with a μ_6-sulfide ligand and all thiolate ligands can be prepared using self-assembly. A mixture of $Fe(N(SiMe_3)_2)_2$, TipSH (Tip = 2,4,6-tri(isopropyl)phenyl), DmpSH (Dmp = 2,6-(mesityl)$_2C_6H_3$), and S_8 leads to the formation **1.32**, which contains a μ_6-sulfide (Figure 1.18).[68] The two [Fe_4S_4] halves are now bridged by three thiolates: one STip and two SDmp moieties, while the two terminal Fe sites are ligated by SDmp groups. Despite the successful installation of thiolates, **1.32** contains one fewer terminal thiolate than the P-cluster, as it possesses one extra bridging thiolate ligand. One possible direction to convert this into a P-cluster structure is to add one thiolate ligand along with an appropriate amount of reductant, as **1.32** has a higher formal oxidation state ($Fe^{II}_5Fe^{III}_3$) than P^N (Fe^{II}_8) and P^{ox} ($Fe^{II}_6Fe^{III}_2$).

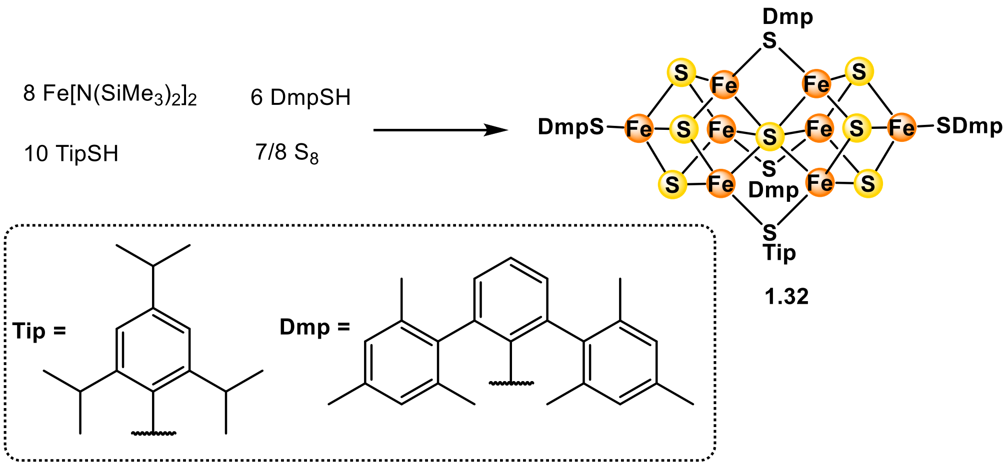

Figure 1.18. Synthesis of **1.32**.

Recently, Moula *et al.* successfully incorporated two bridging thiolate moieties into an Fe_8 cluster architecture.[69] Using a self-assembly strategy in toluene as the nonpolar solvent with $Fe(N(SiMe_3)_2)_2$, TbtSH, and S_8, the authors isolated **1.33**, where the two $[Fe_4S_4]$ halves are joined by a μ_6-sulfide and two bridging STbt ligands (Figure 1.19). In addition, the two ends of the cluster are also coordinated by STbt. Interestingly, two Fe centers are bound by Et_2O from the crystallization solvent. This provides a promising avenue for the completion of the P^N geometry by substitution of these solvent molecules with an appropriate thiolate.

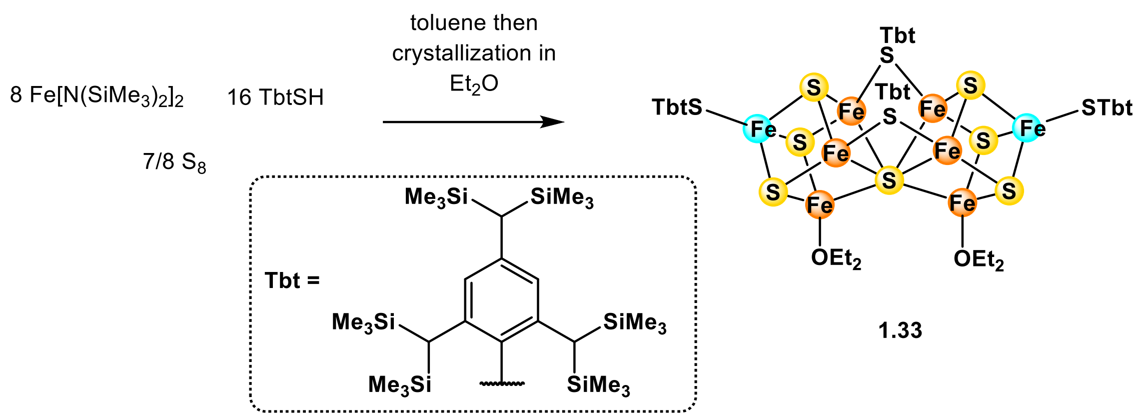

Figure 1.19. Synthesis of **1.33**.

d) M-cluster of nitrogenase

i) Structure and function

The site of N_2 reduction in the nitrogenase enzyme is the heterometallic MFe cluster cofactor (M = Mo, V, Fe), also known as the M-cluster, where the most efficient version, the iron-molybdenum cofactor (FeMoco), contains molybdenum.[54] Arguably, the M-cluster constitutes the most complex inorganic assembly found in biology, because of many aspects. This cluster consists of a $[Fe_4S_3]$ and a $[MFe_3S_3]$ partial cubanes, joined together by an unusual interstitial μ_6-C atom (Figure 1.20).[70–72] In addition, the two halves are also bridged by three belt sulfides (for M = Mo, Fe)[70,73,74] or two belt sulfides and one carbonate (for M = V).[75] The M site is ligated by a bidentate homocitrate and one N atom of a His residue, while the Fe site at the opposite end of the cluster is coordinated by a Cys thiolate.

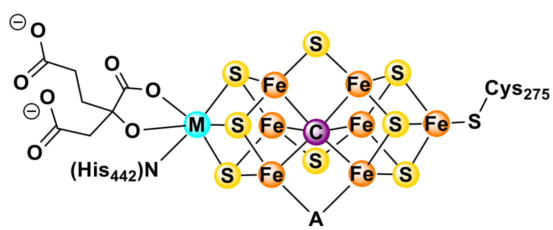

Figure 1.20. Structure of the M-cluster or FeMco of nitrogenase (PDB 3U7Q for M = Mo, 5N6Y for M = V, 8BOQ for M = Fe).

ii) Synthetic models

Due to the complexity of FeMco, no synthetic model reported to date has been able to capture all the essential elements of the cluster, such as the fused cubane geometry, heterometal, interstitial carbide, or bridging sulfides. Hence, most systems attempt to replicate some salient, but not all, aspects of FeMco.

Few synthetic clusters contain a fused cubane octametallic core. An example is **1.32** (*vide supra*), with an Fe_8 structure, three bridging thiolates, and a central μ_6-sulfide. While the cluster has the same topology as FeMco, the incorporation of a rather big interstitial sulfide leads to significant structural distortions compared to the M-cluster. The Fe-Fe distances within two halves in **1.32** are much longer than in FeMco (2.816 Å vs 2.69 Å). Furthermore, the two halves of **1.32** point away from each other, while in FeMco they are relatively symmetric about the interstitial carbide. Thus, the cage formed by the inner six Fe atoms in FeMco is designed such that it only fits a light element like carbon instead of the bigger sulfide.

Only one other Fe_8 cluster that contains an interstitial 2p atom has been reported so far. Ohta *et al.* isolated **1.34** from the reaction between a diiron precursor, S_8, and H_2O, which supplies the central O atom (Figure 1.34).[76] However, the crystal structure of **1.34** highlights structural differences compared to FeMoco. Out of the six Fe-O distances between the central O and the surrounding Fe atoms, only four are within bonding distances (1.910(6)–2.190(5) Å), while two are much longer at 3.361(5) Å, suggesting that the O atom only forms bonds with four Fe centers in a μ_4 mode instead of μ_6. As a result, the cluster becomes distorted, with one Fe site adopting a trigonal pyramidal structure instead of approximately tetrahedral like in FeMoco. Thus, the authors propose that the interstitial atom in FeMoco might allow the cluster to maintain its structural flexibility in different states without breaking apart.

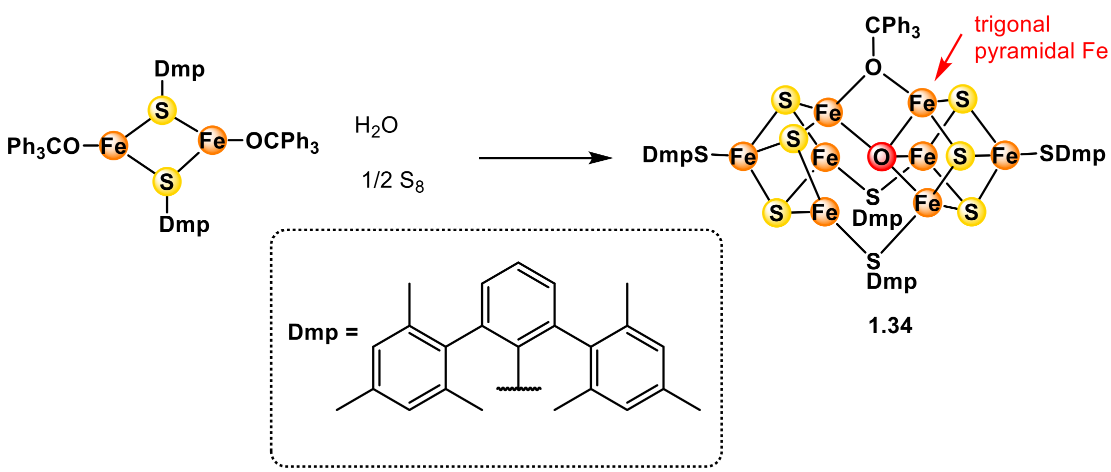

Figure 1.21. Synthesis of **1.34**.

In addition, heterometals have also been incorporated into some synthetic models of the M-cluster that attempt to reconstruct the [MFe_3] half that contains the heterometal such as **1.35** and **1.36** (Figure 1.22).[77–80] These clusters are generally prepared from a MS_3 complex supported by a tridentate ligand such as trispyrazolylborate or triazacyclohexane, and the Fe atoms are provided by $FeCl_2$. A variety of different neutral and anionic terminal ligands can be installed on the Fe sites, including the biologically relevant thiolates. However, a number of these clusters contain a

μ_3-S supplied by S_8 during the synthesis at the vertex opposite to the heterometal, instead of a smaller 2p element such as carbon like in nitrogenase. With Se^{2-} instead of S_8, this atom can be replaced with Se in **1.37**,[80] but the resulting Fe-Se distance of about 2.4 Å is much greater than the Fe-C distance in nitrogenase of about 2.00 Å,[70] making it difficult to draw a parallel in terms of the effects of the interstitial atoms on the properties of the clusters.

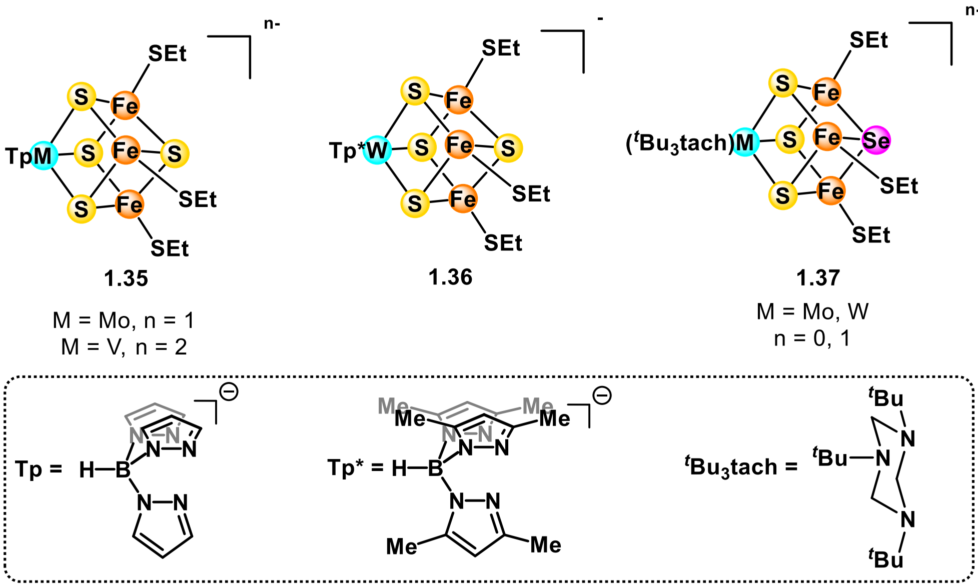

Figure 1.22. Representative examples of clusters containing heterometals.

The incorporation of a 2p element into the μ_3-bridging position was first realized by Chen *et al.* by the assembly of the binuclear complex **1.38** and the cubane $[Fe_4S_4Cl_4]^{2-}$ (Figure 1.23).[81] The resulting cluster **1.39** with a $[Fe_4S_3(\mu_3\text{-}NSiMe_3)]$ cubane core maps well onto half of FeMoco, with structural metrics within about 2% difference. Remarkably, the Fe-(μ_3-N) bond length of 1.95 Å is relatively close to the Fe-C distance of 2.00 – 2.01 Å in FeMco.[70,73,75] However, a *tert*-butyl imide motif still has low biological relevance, as the interstitial ligand in nitrogenase is monoatomic. Subsequently, an improved model **1.40** was reported from the reaction between the Tp^*WS_3 platform and $FeCl_2$ in the presence of ketyl as a reductant, where one Cl atom is now incorporated into the μ_3-bridging position.[82] This represents a great advance in the installation of different small ligands at this position, as the Cl ligand is much more labile than sulfide or imide. Indeed, the authors could replace it with an imide or sulfide group to form **1.41** through an oxidative ligand metathesis strategy with N_3SiMe_3 or S_8, respectively. Thus, this platform provides a potential entry into the installation of small monoatomic ligands like nitride or more importantly carbon-based ligands like carbide.

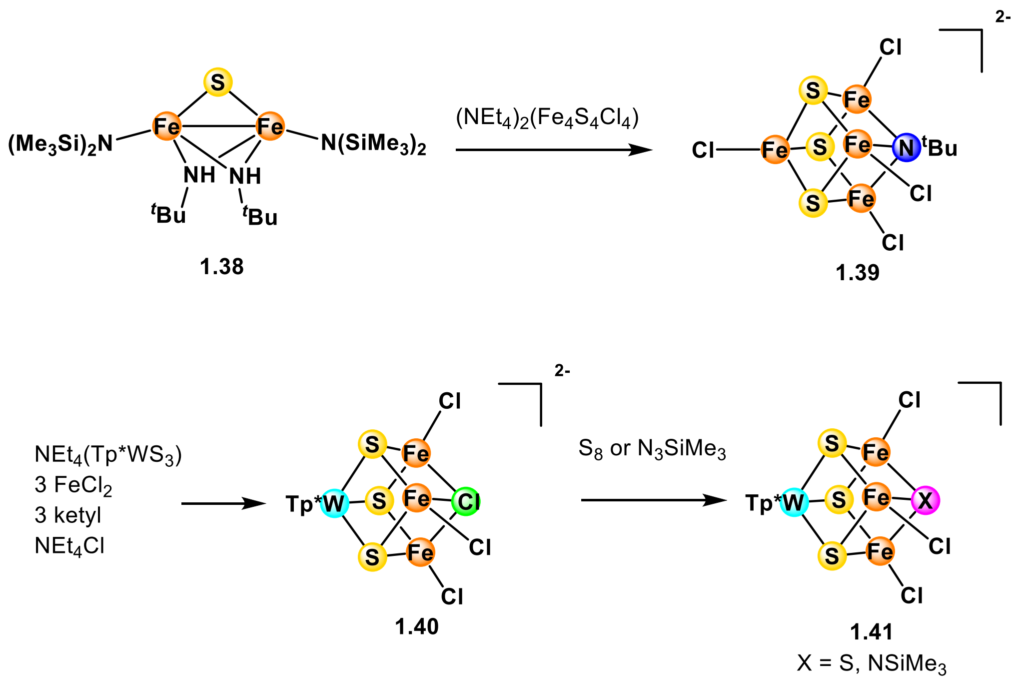

Figure 1.23. Incorporation of 2p bridging ligand into a cubane structure.

While no N_2-bound forms of nitrogenase have been conclusively described in the native enzyme, N_2 can also coordinate to synthetic clusters in a well-characterized example from the Suess lab (Figure 1.24).[83] In the $[MoFe_3S_4]$ cubane **1.42** where two Fe sites are ligated by the bulky N-heterocyclic carbene (NHC) 1,3-bis(2,6-diisopropylphenyl)imidazol-2-ylidene (IPr), the remaining open Fe center can bind N_2 in a terminal, end-on bridging manner between two $[MoFe_3S_4]$ units. This cluster possesses a strongly activated N_2 ligand, with ν_{N2} = 1830 cm^{-1}. One $[MoFe_3S_4]$ half can be substituted with a Ti^{III} radical fragment, leading to even stronger N_2 activation in **1.43** (ν_{N2} = 1768 cm^{-1}). However, no further functionalization of N_2 was reported. Nevertheless, this result suggests that a bridging C-based ligand is not required for N_2 binding, since this reaction occurs in **1.42** which contains μ_3-S atoms.

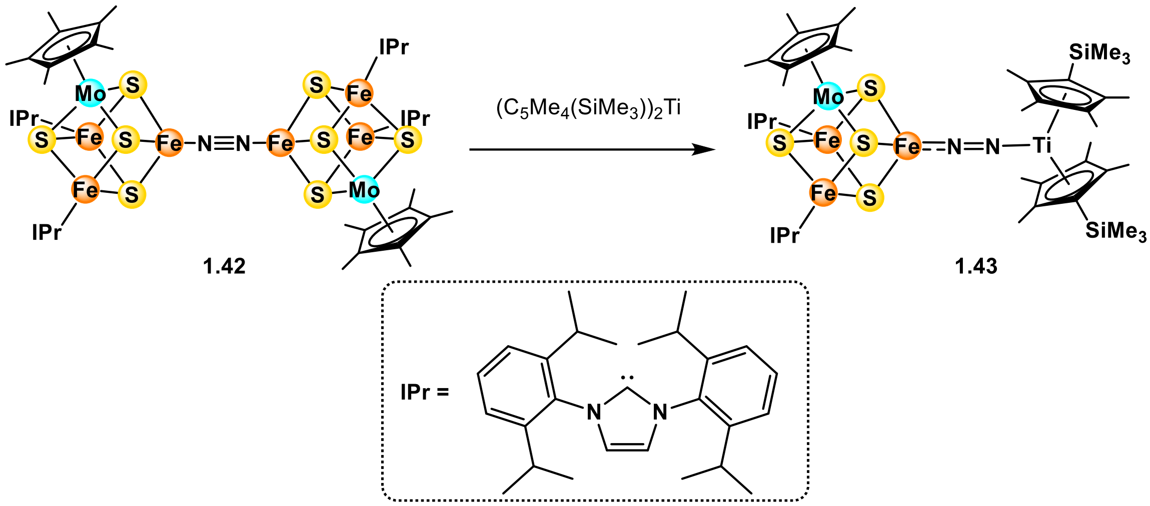

Figure 1.24. N_2 binding to a [$MoFe_3S_4$] cluster.

Due to the asymmetrical nature of the M-cluster, the incorporation of both the heterometal and Fe at the two ends of the cluster remains a substantial challenge. One successful example was reported by Tanifuji *et al.*, where the authors isolated **1.44** from a combination of relatively simple precursors [Cp^*MoS_3]$^-$, $FeCl_2$, and NEt_4SH (Figure 1.25).[84] The hexametallic product bears resemblance to the lower half of FeMoco, with one belt sulfide and two Fe atoms missing, and a sulfide in the central bridging position instead of carbide. Interestingly, in the presence of the reductant SmI_2 and an acid, **1.44** catalyzes the reductive coupling of C_1 substrates such as CN^-, CO, and CO_2 into short-chain hydrocarbons, albeit with lower efficiency than in nitrogenase where similar reactions have been observed.[85] The authors attributed this difference to the lack of two Fe sites in **1.44**, which have been invoked in substrate coordination and catalysis.[55]

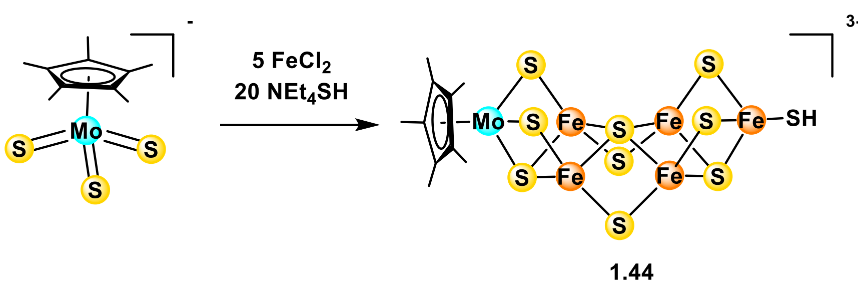

Figure 1.25. Synthesis of **1.44**.

Despite progress in various aspects of nitrogenase modeling, synthetic chemists are far from developing satisfactory models of this highly complicated system. Most prominently, no functional model capable of N_2 reduction to NH_3 has been reported, and no synthetic system so far has successfully incorporated a C-based ligand at the bridging position. Further work is required to understand how this unusual ligand is employed by biology in the challenging nitrogen fixation process.

1.4 CONCLUSION

Iron-sulfur clusters play a very important role in biological systems, particularly the conversion of small molecule substrates. However, due to their complex nature, their mechanistic details remain elusive. Model systems using synthetic chemistry have helped elucidate a small fraction of these aspects, but a large portion of the field is still unexplored. Using strategies such as self-assembly or rational construction from simple building blocks, chemists have attempted to mimic these enzymes in various ways, with different degrees of success. Thus, we hope that these strategies will continue to be explored or refined to achieve more realistic models that represent these biological systems in more authentic ways.

1.5 REFERENCES

(1) Bigness, A.; Vaddypally, S.; Zdilla, M. J.; Mendoza-Cortes, J. L. Ubiquity of Cubanes in Bioinorganic Relevant Compounds. *Coord. Chem. Rev.* **2022**, *450*, 214168. https://doi.org/10.1016/j.ccr.2021.214168.

(2) Venkateswara Rao, P.; Holm, R. H. Synthetic Analogues of the Active Sites of Iron−Sulfur Proteins. *Chem. Rev.* **2004**, *104* (2), 527–560. https://doi.org/10.1021/cr020615+.

(3) Buchwalter, P.; Rosé, J.; Braunstein, P. Multimetallic Catalysis Based on Heterometallic Complexes and Clusters. *Chem. Rev.* **2015**, *115* (1), 28–126. https://doi.org/10.1021/cr500208k.

(4) Swiegers, G. F.; Clegg, J. K.; Stranger, R. Structural Similarities in Enzymatic, Homogeneous and Heterogeneous Catalysts of Water Oxidation. *Chem. Sci.* **2011**, *2* (11), 2254–2262. https://doi.org/10.1039/C1SC00298H.

(5) Cardenas-Rodriguez, M.; Chatzi, A.; Tokatlidis, K. Iron–Sulfur Clusters: From Metals through Mitochondria Biogenesis to Disease. *J. Biol. Inorg. Chem.* **2018**, *23* (4), 509–520. https://doi.org/10.1007/s00775-018-1548-6.

(6) Johnson, D. C.; Dean, D. R.; Smith, A. D.; Johnson, M. K. Structure, Function, and Formation of Biological Iron-Sulfur Clusters. *Annu. Rev. Biochem.* **2005**, *74* (1), 247–281. https://doi.org/10.1146/annurev.biochem.74.082803.133518.

(7) Beinert, H.; Holm, R. H.; Münck, E. Iron-Sulfur Clusters: Nature's Modular, Multipurpose Structures. *Science* **1997**, *277* (5326), 653–659. https://doi.org/10.1126/science.277.5326.653.

(8) Lee, S. C.; Holm, R. H. The Clusters of Nitrogenase: Synthetic Methodology in the Construction of Weak-Field Clusters. *Chem. Rev.* **2004**, *104* (2), 1135–1158. https://doi.org/10.1021/cr0206216.

(9) Lee, S. C.; Lo, W.; Holm, R. H. Developments in the Biomimetic Chemistry of Cubane-Type and Higher Nuclearity Iron–Sulfur Clusters. *Chem. Rev.* **2014**, *114* (7), 3579–3600. https://doi.org/10.1021/cr4004067.

(10) Can, M.; Armstrong, F. A.; Ragsdale, S. W. Structure, Function, and Mechanism of the Nickel Metalloenzymes, CO Dehydrogenase, and Acetyl-CoA Synthase. *Chem. Rev.* **2014**, *114* (8), 4149–4174. https://doi.org/10.1021/cr400461p.

(11) Lindahl, P. A.; Ragsdale, S. W.; Münck, E. Mössbauer Study of CO Dehydrogenase from Clostridium Thermoaceticum. *J. Biol. Chem.* **1990**, *265* (7), 3880–3888.

(12) Fan, C.; Gorst, C. M.; Ragsdale, S. W.; Hoffman, B. M. Characterization of the Nickel-Iron-Carbon Complex Formed by Reaction of Carbon Monoxide with the Carbon Monoxide Dehydrogenase from Clostridium Thermoaceticum by Q-Band ENDOR. *Biochemistry* **1991**, *30* (2), 431–435. https://doi.org/10.1021/bi00216a018.

(13) Kumar, M.; Ragsdale, S. W. Characterization of the Carbon Monoxide Binding Site of Carbon Monoxide Dehydrogenase from Clostridium Thermoaceticum by Infrared Spectroscopy. *J. Am. Chem. Soc.* **1992**, *114* (22), 8713–8715. https://doi.org/10.1021/ja00048a062.

(14) Xia, J.; Dong, J.; Wang, S.; Scott, R. A.; Lindahl, P. A. EXAFS, EPR, and Electronic Absorption Spectroscopic Study of the .Alpha. Metallo Subunit of CO Dehydrogenase from Clostridium Thermoaceticum. *J. Am. Chem. Soc.* **1995**, *117* (27), 7065–7070. https://doi.org/10.1021/ja00132a004.

(15) Dobbek, H.; Svetlitchnyi, V.; Gremer, L.; Huber, R.; Meyer, O. Crystal Structure of a Carbon Monoxide Dehydrogenase Reveals a [Ni-4Fe-5S] Cluster. *Science* **2001**, *293* (5533), 1281. https://doi.org/10.1126/science.1061500.

(16) Dobbek, H.; Svetlitchnyi, V.; Liss, J.; Meyer, O. Carbon Monoxide Induced Decomposition of the Active Site [Ni−4Fe−5S] Cluster of CO Dehydrogenase. *J. Am. Chem. Soc.* **2004**, *126* (17), 5382–5387. https://doi.org/10.1021/ja037776v.

(17) Drennan, C. L.; Heo, J.; Sintchak, M. D.; Schreiter, E.; Ludden, P. W. Life on Carbon Monoxide: X-Ray Structure of Rhodospirillum Rubrum Ni-Fe-S Carbon Monoxide Dehydrogenase. *Proc. Natl. Acad. Sci. U.S.A.* **2001**, *98* (21), 11973–11978. https://doi.org/10.1073/pnas.211429998.

(18) Doukov, T. I.; Iverson, T. M.; Seravalli, J.; Ragsdale, S. W.; Drennan, C. L. A Ni-Fe-Cu Center in a Bifunctional Carbon Monoxide Dehydrogenase/Acetyl-CoA Synthase. *Science* **2002**, *298* (5593), 567–572. https://doi.org/10.1126/science.1075843.

(19) Svetlitchnyi, V.; Dobbek, H.; Meyer-Klaucke, W.; Meins, T.; Thiele, B.; Römer, P.; Huber, R.; Meyer, O. A Functional Ni-Ni-[4Fe-4S] Cluster in the Monomeric Acetyl-CoA Synthase from Carboxydothermus Hydrogenoformans. *Proc. Natl. Acad. Sci. U.S.A.* **2004**, *101* (2), 446–451. https://doi.org/10.1073/pnas.0304262101.

(20) Darnault, C.; Volbeda, A.; Kim, E. J.; Legrand, P.; Vernède, X.; Lindahl, P. A.; Fontecilla-Camps, J. C. Ni-Zn-[Fe_4-S_4] and Ni-Ni-[Fe_4-S_4] Clusters in Closed and Open α Subunits of Acetyl-CoA Synthase/Carbon Monoxide Dehydrogenase. *Nat. Struct. Mol. Biol.* **2003**, *10* (4), 271–279. https://doi.org/10.1038/nsb912.

(21) Ciurli, S.; Ross, P. K.; Scott, M. J.; Yu, S. B.; Holm, R. H. Synthetic Nickel-Containing Heterometal Cubane-Type Clusters with $NiFe_3Q_4$ Cores (Q = Sulfur, Selenium). *J. Am. Chem. Soc.* **1992**, *114* (13), 5415–5423. https://doi.org/10.1021/ja00039a063.

(22) Zhou, J.; Hu, Z.; Münck, E.; Holm, R. H. The Cuboidal Fe_3S_4 Cluster: Synthesis, Stability, and Geometric and Electronic Structures in a Non-Protein Environment. *J. Am. Chem. Soc.* **1996**, *118* (8), 1966–1980. https://doi.org/10.1021/ja9537843.

(23) Zhou, J.; Raebiger, J. W.; Crawford, C. A.; Holm, R. H. Metal Ion Incorporation Reactions of the Cluster $[Fe_3S_4(LS_3)]^{3-}$, Containing the Cuboidal $[Fe_3S_4]^0$ Core. *J. Am. Chem. Soc.* **1997**, *119* (27), 6242–6250. https://doi.org/10.1021/ja9704186.

(24) Zhou, J.; Scott, M. J.; Hu, Z.; Peng, G.; Munck, E.; Holm, R. H. Synthesis and Comparative Reactivity and Electronic Structural Features of $[MFe_3S_4]^{Z+}$ Cubane-Type Clusters (M = Iron, Cobalt, Nickel). *J. Am. Chem. Soc.* **1992**, *114* (27), 10843–10854. https://doi.org/10.1021/ja00053a021.

(25) Panda, R.; Zhang, Y.; McLauchlan, C. C.; Venkateswara Rao, P.; Tiago de Oliveira, F. A.; Münck, E.; Holm, R. H. Initial Structure Modification of Tetrahedral to Planar Nickel(II) in a Nickel−Iron−Sulfur Cluster Related to the C-Cluster of Carbon Monoxide Dehydrogenase. *J. Am. Chem. Soc.* **2004**, *126* (20), 6448–6459. https://doi.org/10.1021/ja030627s.

(26) Panda, R.; Berlinguette, C. P.; Zhang, Y.; Holm, R. H. Synthesis of MFe_3S_4 Clusters Containing a Planar MII Site (M = Ni, Pd, Pt), a Structural Element in the C-Cluster of Carbon Monoxide Dehydrogenase. *J. Am. Chem. Soc.* **2005**, *127* (31), 11092–11101. https://doi.org/10.1021/ja052381s.

(27) Sun, J.; Tessier, C.; Holm, R. H. Sulfur Ligand Substitution at the Nickel(II) Sites of Cubane-Type and Cubanoid $NiFe_3S_4$ Clusters Relevant to the C-Clusters of Carbon Monoxide Dehydrogenase. *Inorg. Chem.* **2007**, *46* (7), 2691–2699. https://doi.org/10.1021/ic062362z.

(28) Taniyama, N.; Ohki, Y.; Tatsumi, K. Synthesis of V/Fe/S Clusters Using Vanadium(III) Thiolate Complexes Bearing a Phenoxide-Based Tridentate Ligand. *Inorg. Chem.* **2014**, *53* (11), 5438–5446. https://doi.org/10.1021/ic4030603.

(29) Osterloh, F.; Saak, W.; Haase, D.; Pohl, S. Nickel(II) Complexes Bound to an [Fe_4S_4] Cluster via Bridging Thiolates: Synthesis and Crystal Structure of Model Compounds for the Active Site of Nickel CO Dehydrogenase. *Chem. Commun.* **1996**, No. 6, 777–778. https://doi.org/10.1039/CC9960000777.

(30) Osterloh, F.; Saak, W.; Pohl, S. Unidentate and Bidentate Binding of Nickel(II) Complexes to an Fe_4S_4 Cluster via Bridging Thiolates: Synthesis, Crystal Structures, and Electrochemical Properties of Model Compounds for the Active Sites of Nickel Containing CO Dehydrogenase/Acetyl-CoA Synthase. *J. Am. Chem. Soc.* **1997**, *119* (24), 5648–5656. https://doi.org/10.1021/ja970194r.

(31) Rao, P. V.; Bhaduri, S.; Jiang, J.; Hong, D.; Holm, R. H. On $[Fe_4S_4]^{2+}$−(μ_2-SR)−M^{II} Bridge Formation in the Synthesis of an A-Cluster Analogue of Carbon Monoxide Dehydrogenase/Acetylcoenzyme A Synthase. *J. Am. Chem. Soc.* **2005**, *127* (6), 1933–1945. https://doi.org/10.1021/ja040222n.

(32) Lubitz, W.; Ogata, H.; Rüdiger, O.; Reijerse, E. Hydrogenases. *Chem. Rev.* **2014**, *114* (8), 4081–4148. https://doi.org/10.1021/cr4005814.

(33) Fontecilla-Camps, J. C.; Amara, P.; Cavazza, C.; Nicolet, Y.; Volbeda, A. Structure–Function Relationships of Anaerobic Gas-Processing Metalloenzymes. *Nature* **2009**, *460* (7257), 814–822. https://doi.org/10.1038/nature08299.

(34) Peters, J. W.; Lanzilotta, W. N.; Lemon, B. J.; Seefeldt, L. C. X-Ray Crystal Structure of the Fe-Only Hydrogenase (CpI) from Clostridium Pasteurianum to 1.8 Angstrom Resolution. *Science* **1998**, *282* (5395), 1853–1858. https://doi.org/10.1126/science.282.5395.1853.

(35) Rohac, R.; Martin, L.; Liu, L.; Basu, D.; Tao, L.; Britt, R. D.; Rauchfuss, T. B.; Nicolet, Y. Crystal Structure of the [FeFe]-Hydrogenase Maturase HydE Bound to Complex-B. *J. Am. Chem. Soc.* **2021**, *143* (22), 8499–8508. https://doi.org/10.1021/jacs.1c03367.

(36) Pandey, A. S.; Harris, T. V.; Giles, L. J.; Peters, J. W.; Szilagyi, R. K. Dithiomethylether as a Ligand in the Hydrogenase H-Cluster. *J. Am. Chem. Soc.* **2008**, *130* (13), 4533–4540. https://doi.org/10.1021/ja711187e.

(37) Heinekey, D. M. Hydrogenase Enzymes: Recent Structural Studies and Active Site Models. *J. Organomet. Chem.* **2009**, *694* (17), 2671–2680. https://doi.org/10.1016/j.jorganchem.2009.03.047.

(38) Rauchfuss, T. B. Diiron Azadithiolates as Models for the [FeFe]-Hydrogenase Active Site and Paradigm for the Role of the Second Coordination Sphere. *Acc. Chem. Res.* **2015**, *48* (7), 2107–2116. https://doi.org/10.1021/acs.accounts.5b00177.

(39) Schilter, D.; Camara, J. M.; Huynh, M. T.; Hammes-Schiffer, S.; Rauchfuss, T. B. Hydrogenase Enzymes and Their Synthetic Models: The Role of Metal Hydrides. *Chem. Rev.* **2016**, *116* (15), 8693–8749. https://doi.org/10.1021/acs.chemrev.6b00180.

(40) Stack, T. D. P.; Holm, R. H. Subsite-Differentiated Analogs of Biological $[4Fe\text{-}4S]^{2+}$ Clusters: Synthesis, Solution and Solid-State Structures, and Subsite-Specific Reactions. *J. Am. Chem. Soc.* **1988**, *110* (8), 2484–2494. https://doi.org/10.1021/ja00216a023.

(41) Tard, C.; Liu, X.; Ibrahim, S. K.; Bruschi, M.; Gioia, L. D.; Davies, S. C.; Yang, X.; Wang, L.-S.; Sawers, G.; Pickett, C. J. Synthesis of the H-Cluster Framework of Iron-Only Hydrogenase. *Nature* **2005**, *433* (7026), 610–613. https://doi.org/10.1038/nature03298.

(42) Popescu, C. V.; Münck, E. Electronic Structure of the H Cluster in [Fe]-Hydrogenases. *J. Am. Chem. Soc.* **1999**, *121* (34), 7877–7884. https://doi.org/10.1021/ja991243y.

(43) Silakov, A.; Kamp, C.; Reijerse, E.; Happe, T.; Lubitz, W. Spectroelectrochemical Characterization of the Active Site of the [FeFe] Hydrogenase HydA1 from Chlamydomonas Reinhardtii. *Biochemistry* **2009**, *48* (33), 7780–7786. https://doi.org/10.1021/bi9009105.

(44) Song, L.-C.; Yang, Z.-Y.; Bian, H.-Z.; Hu, Q.-M. Novel Single and Double Diiron Oxadithiolates as Models for the Active Site of [Fe]-Only Hydrogenases. *Organometallics* **2004**, *23* (13), 3082–3084. https://doi.org/10.1021/om049752i.

(45) Song, L.-C.; Ge, J.-H.; Yan, J.; Wang, H.-T.; Luo, X.; Hu, Q.-M. Iron-Only Hydrogenase Active Site Models Containing a Cysteinyl Group Coordinated through Its Sulfur Atom to One Iron Atom of the Diiron Subsite. *Eur. J. Inorg. Chem.* **2008**, *2008* (1), 164–171. https://doi.org/10.1002/ejic.200700821.

(46) Hu, M.-Q.; Wen, H.; Ma, C.-B.; Li, N.; Yan, Q.-Y.; Chen, H.; Chen, C.-N. Synthesis, Structures and Electrochemistry Studies of 2Fe2S–Fe(II)(S–2N)$_2$ Models for H-Cluster of [FeFe]-Hydrogenase. *Dalton Trans.* **2010**, *39* (40), 9484–9486. https://doi.org/10.1039/C0DT00505C.

(47) Gimbert-Suriñach, C.; Bhadbhade, M.; Colbran, S. B. Bridgehead Hydrogen Atoms Are Important: Unusual Electrochemistry and Proton Reduction at Iron Dimers with Ferrocenyl-Substituted Phosphido Bridges. *Organometallics* **2012**, *31* (9), 3480–3491. https://doi.org/10.1021/om201126w.

(48) Barton, B. E.; Olsen, M. T.; Rauchfuss, T. B. Aza- and Oxadithiolates Are Probable Proton Relays in Functional Models for the [FeFe]-Hydrogenases. *J. Am. Chem. Soc.* **2008**, *130* (50), 16834–16835. https://doi.org/10.1021/ja8057666.

(49) Camara, J. M.; Rauchfuss, T. B. Combining Acid–Base, Redox and Substrate Binding Functionalities to Give a Complete Model for the [FeFe]-Hydrogenase. *Nat. Chem.* **2012**, *4* (1), 26–30. https://doi.org/10.1038/nchem.1180.

(50) Telser, J.; Benecky, M. J.; Adams, M. W.; Mortenson, L. E.; Hoffman, B. M. An EPR and Electron Nuclear Double Resonance Investigation of Carbon Monoxide Binding to Hydrogenase I (Bidirectional) from Clostridium Pasteurianum W5. *J. Biol. Chem.* **1986**, *261* (29), 13536–13541.

(51) Silakov, A.; Reijerse, E. J.; Albracht, S. P. J.; Hatchikian, E. C.; Lubitz, W. The Electronic Structure of the H-Cluster in the [FeFe]-Hydrogenase from *Desulfovibrio desulfuricans*: A Q-Band ^{57}Fe-ENDOR and HYSCORE Study. *J. Am. Chem. Soc.* **2007**, *129* (37), 11447–11458. https://doi.org/10.1021/ja072592s.

(52) Esmieu, C.; Guo, M.; Redman, H. J.; Lundberg, M.; Berggren, G. Synthesis of a Miniaturized [FeFe] Hydrogenase Model System. *Dalton Trans.* **2019**, *48* (7), 2280–2284. https://doi.org/10.1039/C8DT05085F.

(53) Sommer, C.; Adamska-Venkatesh, A.; Pawlak, K.; Birrell, J. A.; Rüdiger, O.; Reijerse, E. J.; Lubitz, W. Proton Coupled Electronic Rearrangement within the H-Cluster as an Essential Step in the Catalytic Cycle of [FeFe] Hydrogenases. *J. Am. Chem. Soc.* **2017**, *139* (4), 1440–1443. https://doi.org/10.1021/jacs.6b12636.

(54) Burgess, B. K.; Lowe, D. J. Mechanism of Molybdenum Nitrogenase. *Chem. Rev.* **1996**, *96* (7), 2983–3012. https://doi.org/10.1021/cr950055x.

(55) Hoffman, B. M.; Lukoyanov, D.; Yang, Z.-Y.; Dean, D. R.; Seefeldt, L. C. Mechanism of Nitrogen Fixation by Nitrogenase: The Next Stage. *Chem. Rev.* **2014**, *114* (8), 4041–4062. https://doi.org/10.1021/cr400641x.

(56) Cao, L.; Börner, M. C.; Bergmann, J.; Caldararu, O.; Ryde, U. Geometry and Electronic Structure of the P-Cluster in Nitrogenase Studied by Combined Quantum Mechanical and Molecular Mechanical Calculations and Quantum Refinement. *Inorg. Chem.* **2019**, *58* (15), 9672–9690. https://doi.org/10.1021/acs.inorgchem.9b00400.

(57) Rupnik, K.; Hu, Y.; Lee, C. C.; Wiig, J. A.; Ribbe, M. W.; Hales, B. J. P+ State of Nitrogenase P-Cluster Exhibits Electronic Structure of a $[Fe_4S_4]^+$ Cluster. *J. Am. Chem. Soc.* **2012**, *134* (33), 13749–13754. https://doi.org/10.1021/ja304077h.

(58) Tanifuji, K.; Ohki, Y. Recent Advances in the Chemical Synthesis of Nitrogenase Model Clusters. In *Metallocofactors that Activate Small Molecules: With Focus on Bioinorganic Chemistry*; Ribbe, M. W., Ed.; Structure and Bonding; Springer International Publishing: Cham, 2019; pp 33–61. https://doi.org/10.1007/430_2018_26.

(59) Peters, J. W.; Stowell, M. H. B.; Soltis, S. M.; Finnegan, M. G.; Johnson, M. K.; Rees, D. C. Redox-Dependent Structural Changes in the Nitrogenase P-Cluster. *Biochemistry* **1997**, *36* (6), 1181–1187. https://doi.org/10.1021/bi9626665.

(60) Tittsworth, R. C.; Hales, B. J. Detection of EPR Signals Assigned to the 1-Equiv-Oxidized P-Clusters of the Nitrogenase MoFe-Protein from Azotobacter Vinelandii. *J. Am. Chem. Soc.* **1993**, *115* (21), 9763–9767. https://doi.org/10.1021/ja00074a050.

(61) Chan, J. M.; Christiansen, J.; Dean, D. R.; Seefeldt, L. C. Spectroscopic Evidence for Changes in the Redox State of the Nitrogenase P-Cluster during Turnover. *Biochemistry* **1999**, *38* (18), 5779–5785. https://doi.org/10.1021/bi982866b.

(62) Keable, S. M.; Zadvornyy, O. A.; Johnson, L. E.; Ginovska, B.; Rasmussen, A. J.; Danyal, K.; Eilers, B. J.; Prussia, G. A.; LeVan, A. X.; Raugei, S.; Seefeldt, L. C.; Peters, J. W. Structural Characterization of the P^{1+} Intermediate State of the P-Cluster of Nitrogenase. *J. Biol. Chem.* **2018**, *293* (25), 9629–9635. https://doi.org/10.1074/jbc.RA118.002435.

(63) Zhang, Y.; Holm, R. H. Synthesis of a Molecular $Mo_2Fe_6S_9$ Cluster with the Topology of the P^N Cluster of Nitrogenase by Rearrangement of an Edge-Bridged $Mo_2Fe_6S_8$ Double Cubane. *J. Am. Chem. Soc.* **2003**, *125* (13), 3910–3920. https://doi.org/10.1021/ja0214633.

(64) Zhang, Y.; Zuo, J.-L.; Zhou, H.-C.; Holm, R. H. Rearrangement of Symmetrical Dicubane Clusters into Topological Analogues of the P Cluster of Nitrogenase: Nature's Choice? *J. Am. Chem. Soc.* **2002**, *124* (48), 14292–14293. https://doi.org/10.1021/ja0279702.

(65) Osterloh, F.; Sanakis, Y.; Staples, R. J.; Münck, E.; Holm, R. H. A Molybdenum–Iron–Sulfur Cluster Containing Structural Elements Relevant to the P-Cluster of Nitrogenase. *Angew. Chem. Int. Ed.* **1999**, *38* (13–14), 2066–2070. https://doi.org/10.1002/(SICI)1521-3773(19990712)38:13/14<2066::AID-ANIE2066>3.0.CO;2-K.

(66) Ohki, Y.; Sunada, Y.; Honda, M.; Katada, M.; Tatsumi, K. Synthesis of the P-Cluster Inorganic Core of Nitrogenases. *J. Am. Chem. Soc.* **2003**, *125* (14), 4052–4053. https://doi.org/10.1021/ja029383m.

(67) Ohki, Y.; Imada, M.; Murata, A.; Sunada, Y.; Ohta, S.; Honda, M.; Sasamori, T.; Tokitoh, N.; Katada, M.; Tatsumi, K. Synthesis, Structures, and Electronic Properties of [8Fe-7S] Cluster Complexes Modeling the Nitrogenase P-Cluster. *J. Am. Chem. Soc.* **2009**, *131* (36), 13168–13178. https://doi.org/10.1021/ja9055036.

(68) Ohki, Y.; Ikagawa, Y.; Tatsumi, K. Synthesis of New [8Fe-7S] Clusters: A Topological Link between the Core Structures of P-Cluster, FeMo-Co, and FeFe-Co of Nitrogenases. *J. Am. Chem. Soc.* **2007**, *129* (34), 10457–10465. https://doi.org/10.1021/ja072256b.

(69) Moula, G.; Nagasaki, A.; Matsumoto, T.; Miehlich, M. E.; Meyer, K.; Cramer, R. E.; Tatsumi, K. Synthesis of a Nitrogenase PN-Cluster Model with $[Fe_8S_7(\mu\text{-}S_{thiolate})_2]$ Core from the All-Ferric $[Fe_4S_4(S_{thiolate})_4]$ Cubane Synthon. *Angew. Chem. Int. Ed.* **2021**, *60* (29), 15792–15797. https://doi.org/10.1002/anie.202102369.

(70) Spatzal, T.; Aksoyoglu, M.; Zhang, L.; Andrade, S. L. A.; Schleicher, E.; Weber, S.; Rees, D. C.; Einsle, O. Evidence for Interstitial Carbon in Nitrogenase FeMo Cofactor. *Science* **2011**, *334* (6058), 940. https://doi.org/10.1126/science.1214025.

(71) Einsle, O.; Tezcan, F. A.; Andrade, S. L. A.; Schmid, B.; Yoshida, M.; Howard, J. B.; Rees, D. C. Nitrogenase MoFe-Protein at 1.16 Å Resolution: A Central Ligand in the FeMo-Cofactor. *Science* **2002**, *297* (5587), 1696. https://doi.org/10.1126/science.1073877.

(72) Lancaster, K. M.; Roemelt, M.; Ettenhuber, P.; Hu, Y.; Ribbe, M. W.; Neese, F.; Bergmann, U.; DeBeer, S. X-Ray Emission Spectroscopy Evidences a Central Carbon in the Nitrogenase Iron-Molybdenum Cofactor. *Science* **2011**, *334* (6058), 974. https://doi.org/10.1126/science.1206445.

(73) Trncik, C.; Detemple, F.; Einsle, O. Iron-Only Fe-Nitrogenase Underscores Common Catalytic Principles in Biological Nitrogen Fixation. *Nat. Catal.* **2023**, *6* (5), 415–424. https://doi.org/10.1038/s41929-023-00952-1.

(74) Schmidt, F. V.; Schulz, L.; Zarzycki, J.; Prinz, S.; Oehlmann, N. N.; Erb, T. J.; Rebelein, J. G. Structural Insights into the Iron Nitrogenase Complex. *Nat. Struct. Mol. Biol.* **2024**, *31* (1), 150–158. https://doi.org/10.1038/s41594-023-01124-2.

(75) Sippel, D.; Einsle, O. The Structure of Vanadium Nitrogenase Reveals an Unusual Bridging Ligand. *Nat. Chem. Biol.* **2017**, *13* (9), 956–960. https://doi.org/10.1038/nchembio.2428.

(76) Ohta, S.; Ohki, Y.; Hashimoto, T.; Cramer, R. E.; Tatsumi, K. A Nitrogenase Cluster Model [Fe_8S_6O] with an Oxygen Unsymmetrically Bridging Two Proto-Fe_4S_3 Cubes: Relevancy to the Substrate Binding Mode of the FeMo Cofactor. *Inorg. Chem.* **2012**, *51* (21), 11217–11219. https://doi.org/10.1021/ic301348f.

(77) Fomitchev, D. V.; McLauchlan, C. C.; Holm, R. H. Heterometal Cubane-Type MFe_3S_4 Clusters (M = Mo, V) Trigonally Symmetrized with Hydrotris(Pyrazolyl)Borate(1−) and Tris(Pyrazolyl)Methanesulfonate(1−) Capping Ligands. *Inorg. Chem.* **2002**, *41* (4), 958–966. https://doi.org/10.1021/ic011106d.

(78) Hong, D.; Zhang, Y.; Holm, R. H. Heterometal Cubane-Type WFe_3S_4 and Related Clusters Trigonally Symmetrized with Hydrotris(3,5-Dimethylpyrazolyl)Borate. *Inorg. Chim. Acta* **2005**, *358* (7), 2303–2311. https://doi.org/10.1016/j.ica.2004.11.051.

(79) Scott, T. A.; Holm, R. H. VFe_3S_4 Single and Double Cubane Clusters: Synthesis, Structures, and Dependence of Redox Potentials and Electron Distribution on Ligation and Heterometal. *Inorg. Chem.* **2008**, *47* (8), 3426–3432. https://doi.org/10.1021/ic702372f.

(80) Majumdar, A.; Holm, R. H. Specific Incorporation of Chalcogenide Bridge Atoms in Molybdenum/Tungsten-Iron-Sulfur Single Cubane Clusters. *Inorg. Chem.* **2011**, *50* (21), 11242–11251. https://doi.org/10.1021/ic2018117.

(81) Chen, X.-D.; Duncan, J. S.; Verma, A. K.; Lee, S. C. Selective Syntheses of Iron−Imide−Sulfide Cubanes, Including a Partial Representation of the Fe−S−X Environment in the FeMo Cofactor. *J. Am. Chem. Soc.* **2010**, *132* (45), 15884–15886. https://doi.org/10.1021/ja106478k.

(82) Xu, G.; Wang, Z.; Ling, R.; Zhou, J.; Chen, X.-D.; Holm, R. H. Ligand Metathesis as Rational Strategy for the Synthesis of Cubane-Type Heteroleptic Iron–Sulfur Clusters Relevant to the FeMo Cofactor. *Proc. Natl. Acad. Sci. U.S.A.* **2018**, *115* (20), 5089. https://doi.org/10.1073/pnas.1801025115.

(83) McSkimming, A.; Suess, D. L. M. Dinitrogen Binding and Activation at a Molybdenum–Iron–Sulfur Cluster. *Nat. Chem.* **2021**, *13* (7), 666–670. https://doi.org/10.1038/s41557-021-00701-6.

(84) Tanifuji, K.; Sickerman, N.; Lee, C. C.; Nagasawa, T.; Miyazaki, K.; Ohki, Y.; Tatsumi, K.; Hu, Y.; Ribbe, M. W. Structure and Reactivity of an Asymmetric Synthetic Mimic of Nitrogenase Cofactor. *Angew. Chem. Int. Ed.* **2016**, *55* (50), 15633–15636. https://doi.org/10.1002/anie.201608806.

(85) Gerlach, D. L.; Lehnert, N. Fischer–Tropsch Chemistry at Room Temperature? *Angew. Chem. Int. Ed.* **2011**, *50* (35), 7984–7986. https://doi.org/10.1002/anie.201102979.

Chapter 2

PARTIAL SYNTHETIC MODELS OF FEMOCO WITH SULFIDE AND CARBYNE LIGANDS: EFFECT OF INTERSTITIAL ATOM IN NITROGENASE ACTIVE SITE

Le, L. N. V.; Bailey, G. A.; Scott, A. G.; Agapie, T. Partial Synthetic Models of FeMoco with Sulfide and Carbyne Ligands: Effect of Interstitial Atom in Nitrogenase Active Site. *Proc. Natl. Acad. Sci. U.S.A.* **2021**, *118* (49), e2109241118. https://doi.org/10.1073/pnas.2109241118.

2.1 ABSTRACT

Nitrogen-fixing organisms perform dinitrogen reduction to ammonia at an Fe-M (M = Mo, Fe, or V) cofactor (FeMco) of nitrogenase. FeMco displays eight metal centers bridged by sulfides and a carbide having the MFe_7S_8C cluster composition. The role of the carbide ligand, a unique motif in protein active sites, remains poorly understood. Toward addressing how the carbon bridge affects the physical and chemical properties of the cluster, we isolated synthetic models of subsite MFe_3S_3C displaying sulfides and a chelating carbyne ligand. We developed synthetic protocols for structurally related clusters, $[Tp^*M'Fe_3S_3X]^{n-}$, where M' = Mo or W, the bridging ligand X = CR, N, NR, S, and Tp* = tris(3,5-dimethyl-1-pyrazolyl)hydroborate, to study the effects of the identity of the heterometal and the bridging X group on structure and electrochemistry. While the nature of M' results in minor changes, the chelating, μ_3-bridging carbyne has a large impact on reduction potentials, being up to 1 V more reducing compared to nonchelating N and S analogs. This work was done in collaboration with Dr. Gwendolyn Bailey (Mo-containing species) and Dr. Anna Scott (cluster **2.8**).

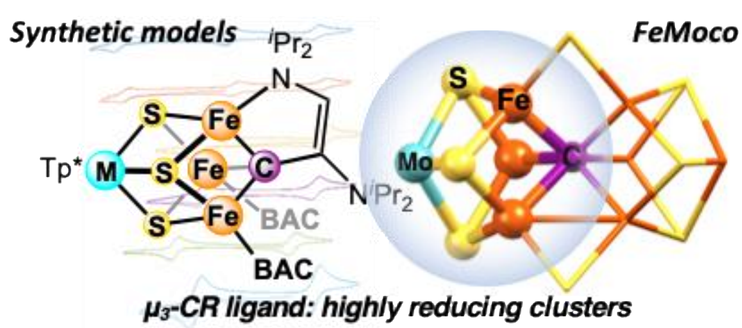

2.2 INTRODUCTION

Biological dinitrogen conversion to ammonia is performed by nitrogenases, a class of enzymes displaying several complex iron-sulfur clusters.[1] The site of N_2 reduction in the most efficient nitrogenase is a heterometallic cluster displaying Fe and Mo, the iron-molybdenum cofactor (FeMoco).[1] Two other nitrogenases are known where Fe or V are found at the Mo position. FeMoco consists of Fe_4S_3C and $MoFe_3S_3C$ cubanes with μ_3-sulfides joined together by a shared interstitial μ_6-carbide and three additional sulfides that bind in μ_2-fashion (Figure 2.1).[2] The impact of the carbide ligand on the electronic structure and reactivity of the cofactor, and therefore its role in the catalytic cycle of N_2-to-NH_3 conversion, is unclear.[3] The carbide ligand is not lost during catalysis, and it has been suggested that it becomes protonated before N_2 activation.[3] To address the effect of carbon-based ligands for N_2 activation, such as providing electronic stabilization and structural flexibility to accommodate multielectron redox processes, synthetic models have included arene,[4] N-heterocyclic carbene,[5] aryl,[6], and alkyl[7,8] donors in mononuclear iron complexes.

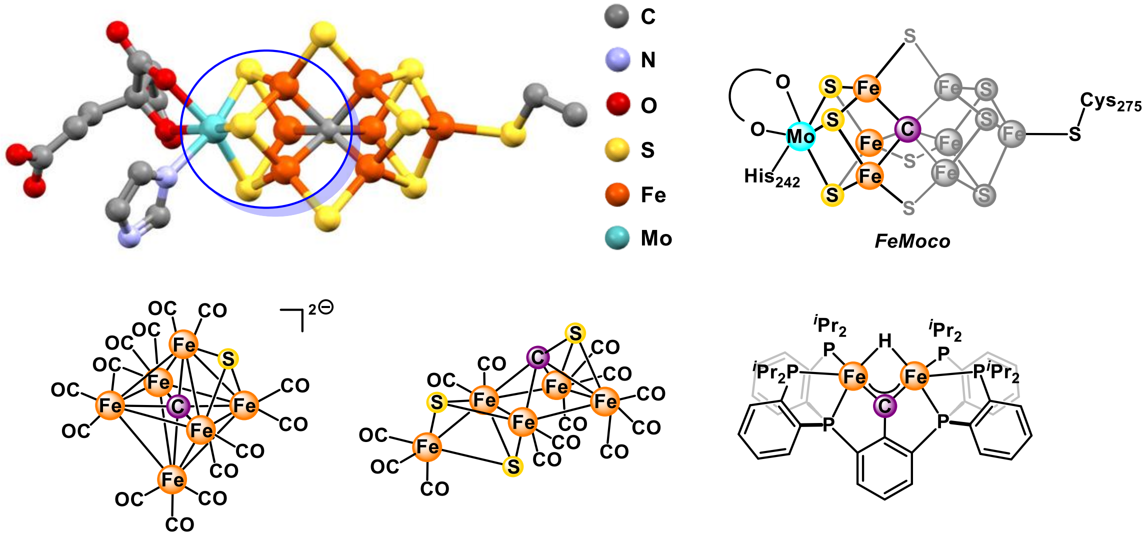

Figure 2.1. Top: Structure of FeMoco in Mo-dependent nitrogenase from the Protein Data Bank structure 3U7Q with a blue circle emphasizing the cubane subsite and its schematic representation highlighting in color the subsite of focus in this study. Bottom: Carbyne and carbide-containing model complexes.[9–11]

Bi- and multimetallic synthetic analogs focused on interrogating the role of the interstitial atom and multimetallic effects have been targeted,[7,9–23] but complexes that display bridging carbide[11,24–

[27] or even carbyne[9,10,28] ligands are rare. Carbide-containing Fe clusters display four to six metal centers, but invariably are rich in CO ligands.[24,25,27] The presence of this strong field donor limits the comparison to FeMoco given the significantly different electronic structure conferred by the weak field sulfides. Moreover, the formal oxidation state of the Fe centers is significantly more reduced, between Fe^{0} and Fe^{II}, than in the protein, between Fe^{II} and Fe^{III}.[2] Recent promising advances have been made toward the incorporation of sulfide ligands into carbide-containing iron carbonyl clusters.[10,11] In order to gain a more accurate understanding of the impact of the carbide on the properties of clusters related to FeMoco, metal complexes structurally related to the biological active site that are multimetallic, have multiple sulfide ligands and few CO ligands, and display bridging carbon-based ligands and oxidation states of Fe^{II}-Fe^{III} are desirable.

Toward developing synthetic methodologies to structures analogous to FeMoco that include a bridging carbon donor, we focus our initial efforts on the cubane subsite, $MoFe_3S_3C$ (Figure 2.1, *top row*). Because the nature of the μ_2-bridging ligands in FeMoco is variable, with sulfide, selenide,[29] CO,[30] or NH[31] (for FeVco) moieties at these positions as characterized by crystallography, the primary target was to match the composition of the cubane core. In this work, we present the preparation of a series of heterometallic iron-sulfur cubane-type clusters containing Mo or W with biologically relevant μ_3 bridging ligands X (X = N, NR, CR, and S) incorporated at the Fe_3 face—including examples bearing a bridging CR ligand. These variations in the bridging ligand result in a large shift in the biologically relevant $M'Fe_3^{11+}/M'Fe_3^{10+}$ redox couple of up to 2 V, with the most reducing system occurring for the cluster bearing a bridging carbyne. These results suggest an important role of the interstitial carbide ligand in FeMoco in modulating the electronic properties of the cluster toward rendering it more reducing and potentially more reactive in N_2 activation and conversion into NH_3.

2.3 RESULTS AND DISCUSSION

To rationally incorporate different ligands at the μ_3-bridging position corresponding to the carbide, a WFe_3S_3 cluster supported by a W-coordinated Tp* ligand, **2.1-W**, was selected as precursor bearing a μ_3-Cl at the carbide position (Figure 2.2).[32] Although heterometallic iron-sulfur clusters of the MFe_3 types have been reported with M = V, Mo, and W, they typically display a μ_3-S vertex opposite the heterometal that is difficult to substitute with other donor types relative to chloride.[33,34] Indeed, starting from a μ_3-Cl precursor offers a versatile route to incorporating biologically relevant light atoms at the bridging position by ligand metathesis reactions.[32] As an example, the μ_3-Cl ligand can be substituted with μ_3-S or μ_3-NSiMe$_3$ by oxidative metathesis with S_8 or Me_3SiN_3, respectively.[32]

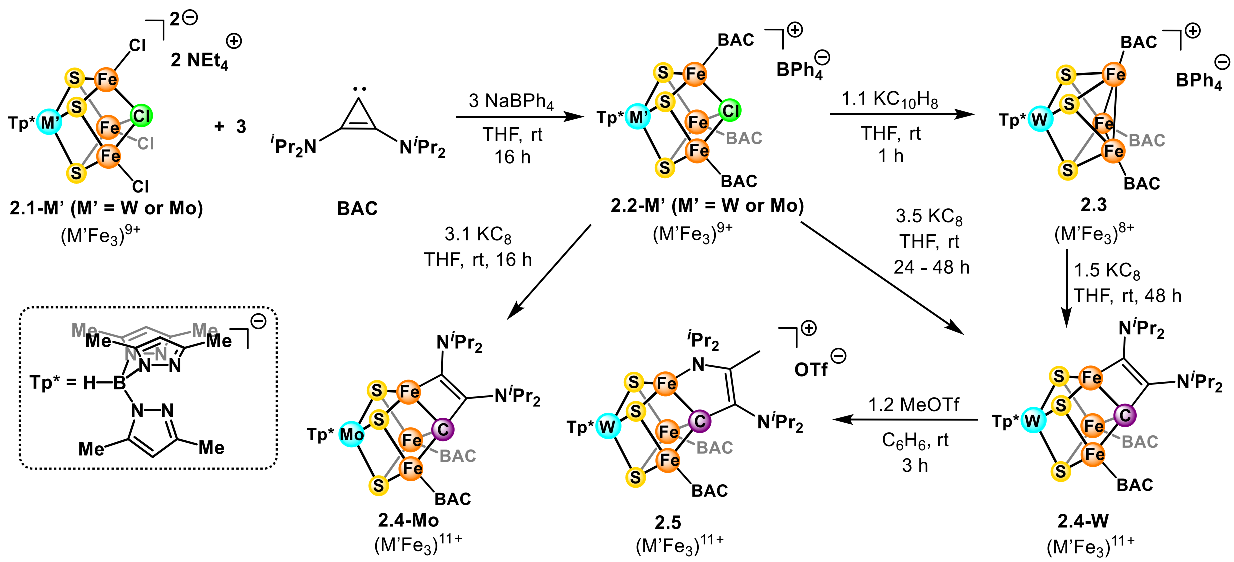

Figure 2.2. Synthesis of carbyne-containing clusters.

For the installation of a carbon-based ligand at the μ_3 position, we were inspired by the utilization of the strained carbene bis(diisopropylamino)cyclopropenylidene (BAC)[35] for promoting C-atom transfer to the Fe≡N bond of the iron(IV) nitride [{PhB(^{i}Pr$_2$Im)$_3$}Fe(N)] (^{i}Pr$_2$Im = 1,2-diisopropylimidazolylidene).[36] This ultimately generated a cyanide ligand, with the release of alkyne ^{i}Pr$_2$NC≡CN^{i}Pr$_2$ as the side product. Mixing **2.1-W** with 3 equivalents of BAC in tetrahydrofuran (THF) in the presence of NaBPh$_4$ as a chloride abstracting agent results in the gradual disappearance of the insoluble **2.1-W** to form a dark red solution, along with the precipitation of a colorless solid, assigned as NaCl (Figure 2.2). Upon filtration, the vapor diffusion of pentane into the filtrate over one day leads to the formation of dark purple needles. A single crystal X-ray diffraction (XRD) study of these crystals confirmed the structure of the product, where the three terminal chlorides have been substituted with BAC to give a monocationic cluster, **2.2-W**, with a BPh$_4$ counteranion (Figure 2.2). Although MFe$_3$S$_3$ clusters supported by carbene ligands have not been structurally characterized, the Fe-C distances are in the range of Fe$_4$S$_4$ clusters supported by NHC ligands.[15,37]

In order to promote the delivery of a C atom or CR group, at least one C-C bond has to be cleaved, which can be achieved by methods such as heating,[38] photolysis,[38] or reduction.[36,39] While **2.2-W** remains unchanged when irradiated with a 75-W Xe lamp and decomposes when heated at reflux in THF under an inert atmosphere, reduction with one equivalent of a strong reducing agent like potassium naphthalenide leads to the new cluster **2.3**. Instead of generating a neutral, one-electron reduced form of **2.2-W** and $KBPh_4$ as byproduct, product **2.3** loses the μ_3-Cl ligand as KCl likely driven by precipitation, leaving an open triangular Fe_3 face, as demonstrated by XRD characterization (Figure 2.2).

Cluster **2.3** possesses a rare incomplete cubane geometry for iron-sulfur clusters. The related $[Fe_4S_3]$ geometry has only been reported in the anion $[Fe_4S_3(NO)_7]^-$ of Roussin's black salt[40] in inorganic compounds, and an oxygen-tolerant [NiFe]-hydrogenase in biology.[41] Incomplete heterometallic cubanes of the form $M'Fe_3S_3$ have only been observed for M' = Mo in a synthetic system, where the Fe atoms are ligated by multiple CO ligands.[42] The open-face Fe_3 triangle resembles the sulfide-free triiron systems supported by multinucleating trisamide ligands, which can bind μ_3-nitride or μ_3-imide moieties.[14,43] Thus, the open nature of the Fe_3 cluster face in **2.3** makes it a promising platform for the rational installation of various bridging ligands in a μ_3 mode.

Cluster **2.3** can further be reduced with an excess of KC_8 to form the neutral, Et_2O soluble cluster **2.4-W**. Gratifyingly, under these highly reducing conditions, the C-C bond in the BAC ligand is cleaved and the cyclopropene ring opens, delivering a carbyne ligand to the bridging position. The cluster loses its C_3 symmetry, resulting in two Fe atoms ligated by BAC and a unique Fe center, to which the rest of the ring-opened BAC ligand anchors as a vinyl fragment. This is an example of a synthetic iron-sulfur cluster without CO ligands that displays a carbyne donor. Aside from the bridging carbyne ligand, the terminal hydrocarbyl ligand is also notable, given the role of such ligands in SAM enzymes[44] and their scarcity in iron-sulfur cluster synthetic chemistry.[45] Conveniently, **2.4-W** can also be synthesized directly from **2.2-W** using an excess of KC_8 or potassium naphthalenide without isolating **2.3**. This reaction stops at **2.3** if conducted at −78 °C for 1 h, while appreciable conversion to **2.4-W** can only be achieved at room temperature over longer reaction times, suggesting that the ring opening and rearrangement of the BAC ligand is rate-limiting. The vinyl ligand in **2.4-W** can be alkylated with MeOTf, leading to a five-membered amine-carbyne chelate with N^iPr_2 bound to the unique Fe (Figure 2.2). Cluster **2.5** is reminiscent of a putative NH_3-bound form of FeMoco, as it displays a bridging C-based ligand and a nitrogen donor at one of the Fe centers.

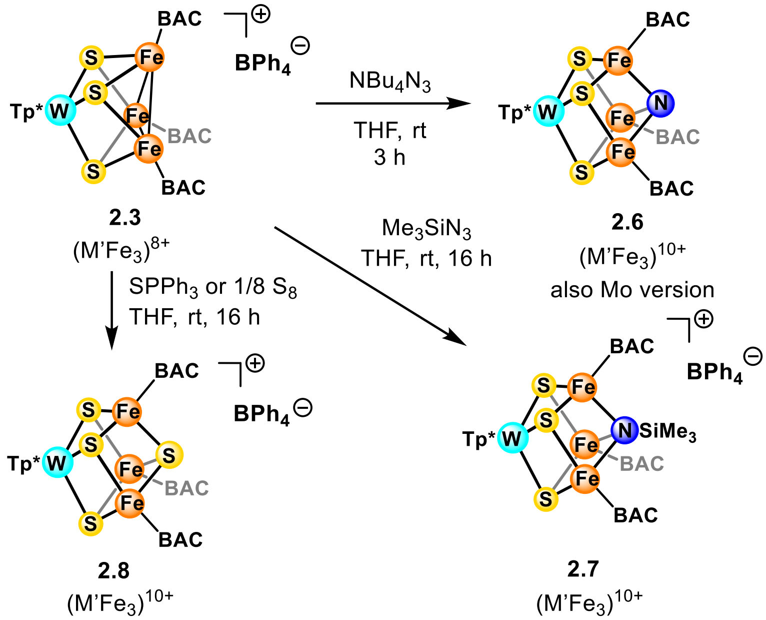

Figure 2.3. Synthesis of nitride, imide, and sulfide-containing clusters.

Toward preparing structural analogs of the μ_3-carbyne ligand, **2.3** was investigated as a precursor to a cluster bearing N or S at the bridging position. Treatment of **2.3** with NBu_4N_3, Me_3SiN_3, and PPh_3S (or S_8) leads to the formation of the corresponding nitride- (**2.6**), imide- (**2.7**), and sulfide- (**2.8**) bridged clusters (Figure 2.3). Complexes **2.6**, **2.7**, and **2.8** are isostructural, with a WFe_3S_3X (X = N or S) cubane supported by Tp* at W and one BAC ligand bound to each iron center (Figure 2.4). The presence of three BAC ligands is a distinct feature relative to **2.4-W**. Targeting a carbyne analog with the same number of BAC donors, we treated compound **2.5** with BAC; however, no reaction was observed, likely due to a combination of steric constraints and stability of the chelate.

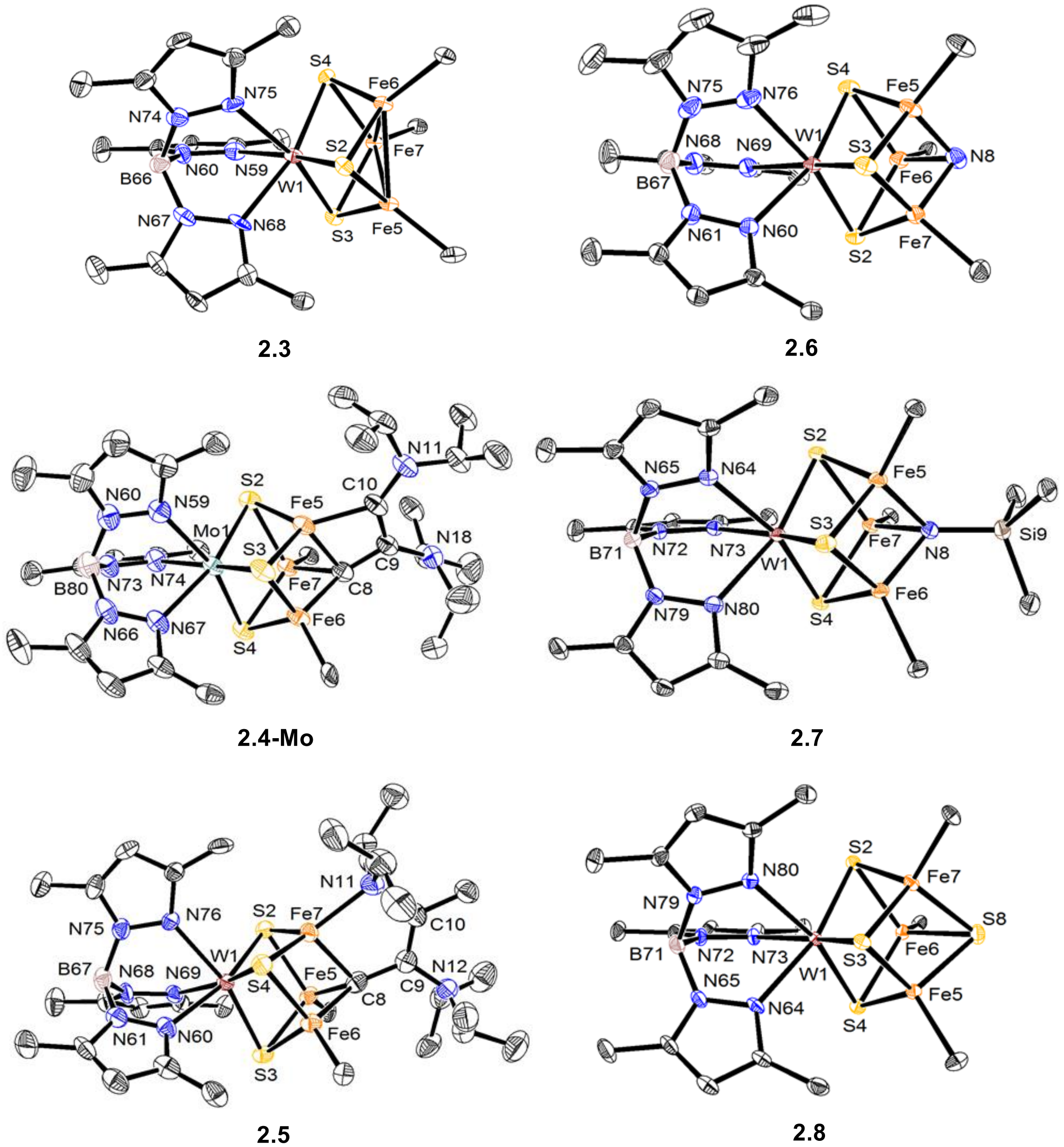

Figure 2.4. Crystal structures of **2.3**, **2.4-Mo**, and **2.5** to **2.8** (reference Supporting Information for the isostructural cluster **2.4-W**). Ellipsoids are shown at 50% probability level. Hydrogen atoms, counteranions (for **2.3**, **2.5**, **2.7**, and **2.8**), and the BAC ligand except for the carbene C are omitted for clarity.

For closer similarity to FeMoco, a Mo variant of the above clusters was targeted. The Mo-containing precursor **2.1-Mo** was conveniently synthesized from **[NEt$_4$][Tp*MoS$_5$]** via **[NEt$_4$][Tp*MoS$_3$]** generated by sulfur abstraction with PPh$_3$ (Supporting Information).[46] Adapting the synthetic protocol developed for **2.2-W**, chloride substitution with BAC from **2.1-Mo** allowed for the isolation of **2.2-Mo**. Ring opening upon reduction with KC_8 resulted in the formation of **2.4-Mo** (Figure 2.2). Notably, the MoS_3Fe_3C cluster core of **2.4-Mo** reproduces one half of the structure of FeMoco, including the bridging carbon donor. Furthermore, the geometry of the unique Fe in the C-bridged clusters **2.4-W**, **2.4-Mo**, and **2.5** reproduces the four-coordinate, distorted trigonal pyramidal geometry found in the belt sites of FeMoco (Figure 2.2). The S-Fe-S-C and S-Fe-S-N torsion angles in **2.4-W** (173.2°) and **2.5** (154.2°) approach 180°, bringing these four atoms close to coplanar, which corresponds to a distorted trigonal pyramidal geometry at Fe, leaving the axial site open for potential substrate coordination, as has been previously invoked for N_2 binding in FeMoco.[17] In addition, the Fe-N distance in **2.5** is 2.16 Å, close to the Fe-N bond length in the previously characterized NH-bound FeVco (2.01 ± 0.04 Å).[31] Further studies are being conducted to investigate reactivity at this site.

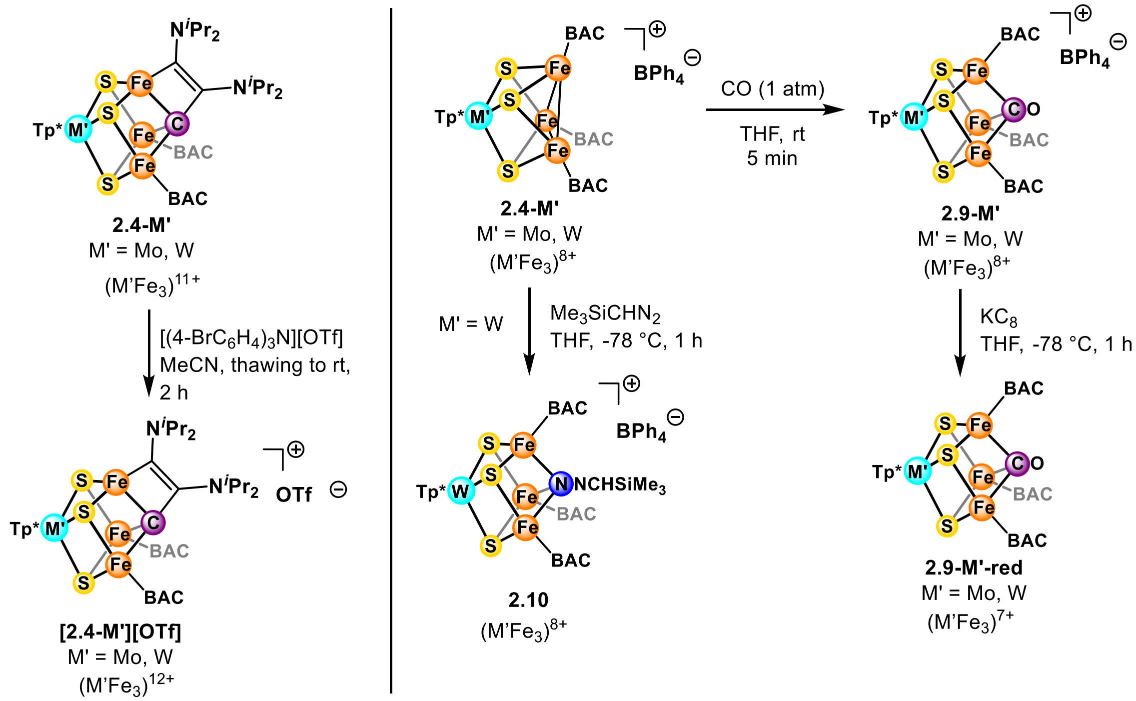

Figure 2.5. Oxidation of **2.4** (left) and installation of other ligands at the bridging position (right).

Both **2.4-W** and **2.4-Mo** can be oxidized by one electron using $[(4\text{-}BrC_6H_4)_3N][OTf]$ as the oxidant, whose structures were confirmed by X-ray diffraction after crystallization from THF/pentane vapor diffusion (see Supporting Information). In addition, other μ_3 bridges can also be installed from **2.3** such as CO and Me_3SiCHN_2 (Figure 2.5) to form **2.9-W** and **2.10**. The CO adduct **2.9-W** can be reduced by one electron using KC_8 or $KC_{10}H_8$, leading to the neutral cluster **2.9-W-red**. Analogous Mo versions have also been prepared for **2.6-Mo**, **2.9-Mo**, and **2.9-Mo-red** from the Mo analog **2.3-Mo** (prepared by Dr. Gwendolyn Bailey). While these species are not the focus of subsequent discussions, they demonstrate the ability to deliver a wide variety of bridging ligands to the open Fe_3 face.

A comparison of the structural aspects of the reported clusters and the corresponding subsite of FeMoco is informative (Table 2.S5). The W/Mo-S distances vary modestly (2.36 to 2.39 Å) in the series of cubane complexes, suggesting that the metal oxidation state remains unchanged. Although the total redox state of the metal core varies from $(M'Fe_3)^{8+}$ to $(M'Fe_3)^{11+}$, it is likely that the formal oxidation state for M' lies within the 3+/4+ range, based on literature assignments for $MoFe_3S_4$[47] and WFe_3S_4[48] in two redox states, $(M'Fe_3)^{10+}$ and $(M'Fe_3)^{11+}$, as well as the trend in M'-S bond length as a function of oxidation states of M' from related species (Table 2.S6). Comparison of bond lengths within the organic fragment supporting the carbyne ligand reveals notable differences in **2.4-W/2.4-Mo** versus **2.5**. In **2.4-W/2.4-Mo**, the C10-N11 (average 1.36 Å) and C9-N18 (average 1.46 Å) distances are significantly different, suggesting multiple bonding character in C10-N11, while in **2.5** C10-N11 and C9-N12 are more similar [1.47(1) and 1.43(1) Å, respectively]. The orientation of N11 in **2.4-W/2.4-Mo** is such that the lone pair can engage in delocalization within the olefin π bond, increasing the N-C bond order and lowering the C9-C10 bond order (Figure 2.6). Because the carbyne is directly bonded to the olefin, its character is linked to the propensity of the amine lone pair to delocalize, therefore rendering **2.4-W/2.4-Mo** more Fischer-like than **2.5**.[49] The possible changes in the character of the carbyne makes oxidation states ambiguous, but for consistency, herein the carbyne is assigned in the same way in all of the compounds. It is worth noting that the nature of the carbide ligand in FeMoco may also vary as a function of changes in the interactions with the other, remote metal centers. Additional experiments will be necessary to determine the overall redox states and distribution between metals; nevertheless, these compounds are in the range assigned for FeMoco.[2] The structural parameters for the W and Mo analogs **2.4-W** and **2.4-Mo** are very similar, which suggests analogous redox distribution within the cluster despite different heterometals M'. The Fe-C distances in **2.4-W**, **2.4-Mo**, and **2.5** are in the range of 1.94 to 1.95 Å, which are close to the average Fe-C bond length in

FeMoco of 2.00 Å,[50] though shorter, likely due to bridging of the carbide between more metal centers in the biological system.

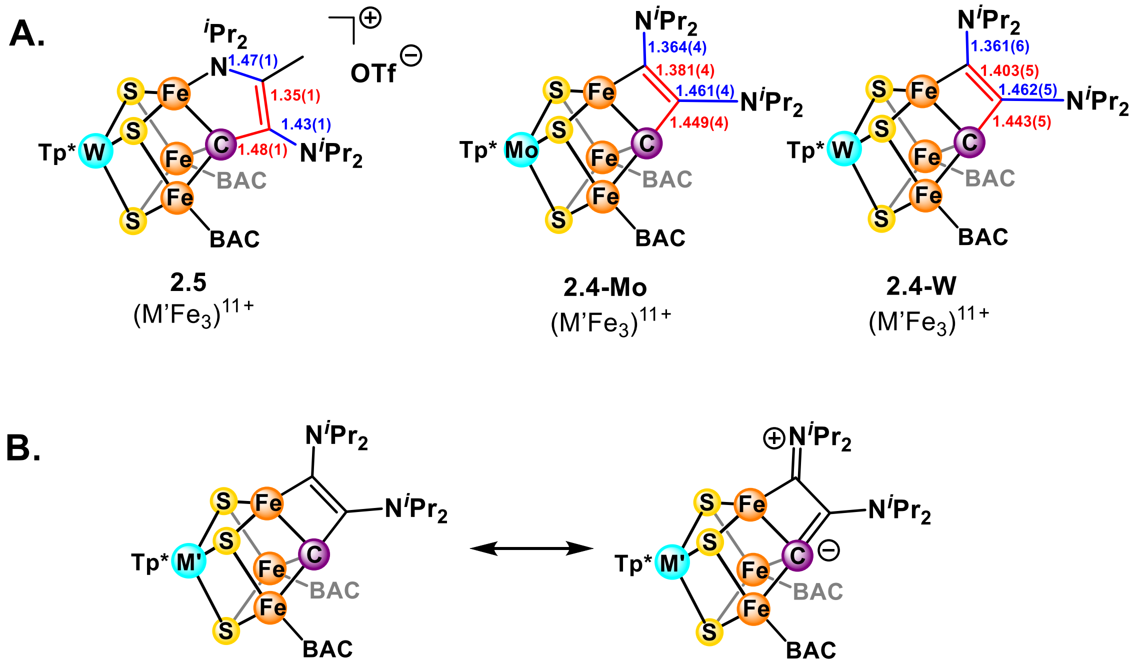

Figure 2.6. Bonding discussion. a) Bond length comparison between the chelating portion of **2.4-W**/**2.4-Mo** and **2.5**. b) Resonance structures for **2.5**.

In order to probe the impact of structure on the redox potentials of the cubane models of FeMoco, we carried out a comparative cyclic voltammetry (CV) study of compounds **2.4** to **2.8** (Figure 2.7). Each cluster displays at least one oxidation and one reduction event, both reversible. To assign the redox waves to the corresponding redox couple, starting from the structurally characterized complexes, the open-circuit potential of the system was determined prior to scanning reductively. For **2.6**, **2.7**, and **2.8**, the two CV features are assigned to the $(M'Fe_3)^{11+}/(M'Fe_3)^{10+}$ and $(M'Fe_3)^{10+}/(M'Fe_3)^{9+}$ couples. For **2.4-W**, **2.4-Mo**, and **2.5**, they correspond to $(M'Fe_3)^{12+}/(M'Fe_3)^{11+}$ and $(M'Fe_3)^{11+}/(M'Fe_3)^{10+}$. Compounds **2.4-W** and **2.4-Mo** show an additional reversible event at more positive potentials, assigned to $(M'Fe_3)^{13+}/(M'Fe_3)^{12+}$, which might be an indication of the carbyne ligand's ability to accommodate expanded redox capabilities. Compounds **2.4** to **2.8** can be compared using the $(M'Fe_3)^{11+}/(M'Fe_3)^{10+}$ couple (highlighted by boxes in Figure 2.7), which they all display.

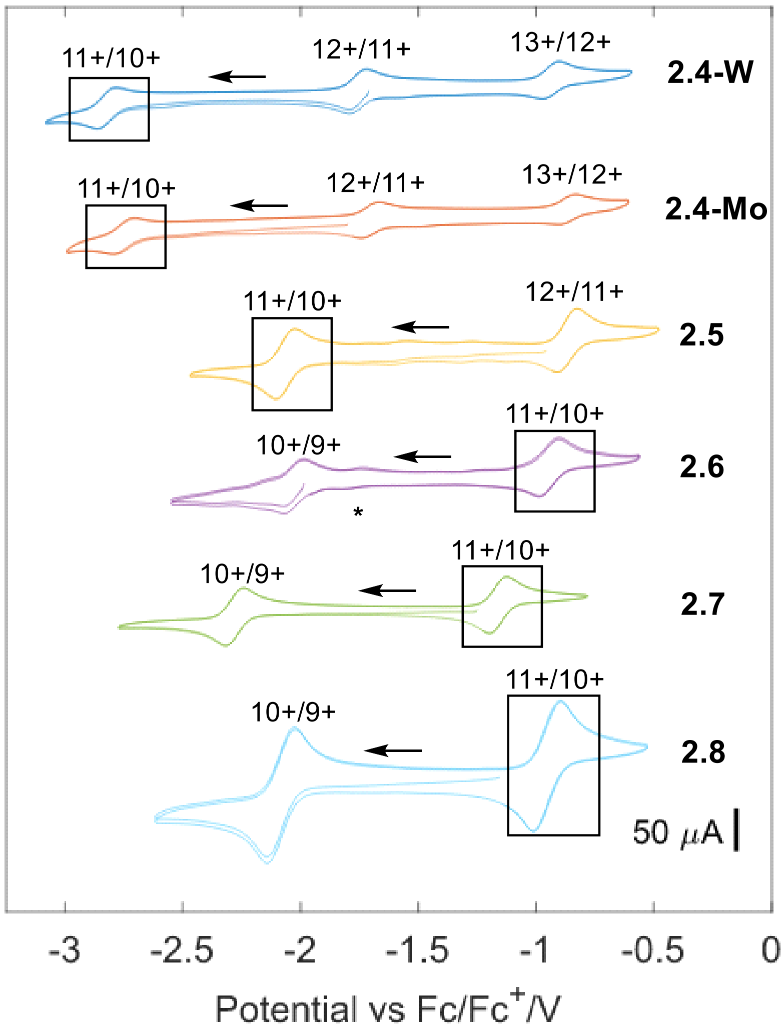

Figure 2.7. CV scans for compounds **2.4** to **2.8**. Each voltammogram starts from the open-circuit potential, and the boxed peaks correspond to the $(M'Fe_3)^{11+}/(M'Fe_3)^{10+}$ couples of interest. The redox assignment is indicated above each wave in terms of the charge of the $(M'Fe_3)$ metal core. Conditions: ~2.5 mM cluster in MeCN with 0.2 M $TBAPF_6$, scan rates of 200 mV s^{-1} (**2.4-W**, **2.5** to **2.8**) or 250 mV s^{-1} (**2.4-Mo**). The asterisk indicates small amounts of **2.4-W** impurity in samples of **2.6**.

Although the compared redox event corresponds to the same formal oxidation state and metal coordination number across all clusters, there are several structural changes that can impact the reduction potentials and convolute interpretation: the identity of the bridging atom (C versus N versus S), the presence and nature of a chelate attached to the bridge, and the character of the bridging ligand stemming from its substituents (i.e., rotation of the amine and delocalization of its lone pair). Within the carbyne-containing clusters there is little impact of the identity of the Group 6 metal (M' = Mo versus W) on the reduction potentials, with a slight increase in redox potential of 70 mV on changing W to Mo, although the other biologically relevant Fe or V variants remain to be pursued. In biomimetic group transfer chemistry with Mo and W, a similarly modest increase in potentials of about 120 mV is also observed for a nicotinic acid hydroxylase synthetic analog when Mo is replaced with W.[51] The redox couple shifts positively by about 0.75 V between **2.4-W** and **2.5**, and a combination of structural changes support this trend: the positive charge of **2.5**, the weaker electron donating capability of the $N^{i}Pr_2$ group compared to the vinyl ligand, and the donation of the amine lone pair into the olefin π system. The size of the carbyne chelate may also impact redox chemistry by changing the electronic character of the ligand. Osmium compounds supported by dppe versus dppm ligands show a relatively small change of 30 mV,[52] but we could not find specific precedent for the potential range of such effect for carbynes.

The $(M'Fe_3)^{11+}/(M'Fe_3)^{10+}$ couple for the C-containing clusters **2.4-W**, **2.4-Mo**, and **2.5** appear at potentials below −2 V, significantly more negative than for **2.6** to **2.8** at −0.87 V to −1.16 V. While **2.6** to **2.8** contain three BAC ligands and **2.4-W**/**2.5** only have two, complicating comparison, compound **2.5** displays a weaker donor in the tertiary amine compared to BAC in **2.6** to **2.8**. Although a less ambiguous analysis would benefit from an analog of **2.5** with a BAC ligand instead of the amine, which could not be accessed (*vide supra*), the greater electron donation ability of the NHC ligand compared to the tertiary amine is expected to render that hypothetical version of **2.5** even more reducing. Compounds **2.4-W**, **2.4-Mo**, and **2.5** all display chelates, unlike **2.6** to **2.8**. Multidentate phosphines and pyridines show shifts of less than 0.3 V in redox potentials relative to monodentate variants.[52] Although this difference is much smaller than the differences observed here, because the carbyne interactions may be more strongly impacted by changes in bond angles, we cannot rule out that changes in reduction potentials are primarily due the presence of chelates in **2.4-W**, **2.4-Mo**, and **2.5**. Overall, the combination of carbyne and chelate results in a remarkable redox potential difference. Compounds **2.5** and **2.6** maintain the same formal charge for the bridging ligand (3-) as carbyne versus nitride. Still, a difference in the $(M'Fe_3)^{11+}/(M'Fe_3)^{10+}$ redox potentials of 1.12 V is observed, a substantial impact of the chelating C- versus N-based, though nonchelating, ligands. Changing the donor from nitride (**2.6**) to imide (**2.7**) or sulfide (**2.8**) shifts the redox potential less than 200 mV, highlighting the similar effect of S and N donors on the redox chemistry, in contrast to the chelating carbyne.

These electrochemical results suggest that the interstitial carbon ligand in FeMoco may play an important role in increasing the reductive power of the clusters. While the specific oxidation states of the metal centers cannot be verified without additional spectroscopic studies, the reduced form, $(M'Fe_3)^{10+}$, corresponds to an average metal oxidation state of 2.5 (or 2 if a Fischer carbyne resonance is considered), close to the resting state of FeMoco as $Fe^{II}_3Fe^{III}_4Mo^{III}$ (average metal oxidation state 2.6).[2] Additional reduction steps lower the average formal oxidation state of FeMoco, but not below 2, and do not bring it in the range typically observed for mononuclear Fe complexes studied for N_2 activation.[53] Therefore, the ability of the biological cofactor to perform N_2 activation at high oxidation states is unusual. A possible explanation is charge redistribution within the cluster to increase reducing equivalents at the site of substrate binding or electronic communication between different metal sites.[21–23,54] We find here that the chelating carbyne ligand has a remarkable impact on the cluster reduction potentials, with very reducing potentials for relatively high, biologically relevant metal oxidation states. Moreover, the chelating carbyne clusters are significantly more reducing for the same redox state compared to N and S analogs. It is important to note that the chelation present in all carbynes reported here and the delocalization of amine lone pair in some of them may have a substantial effect on the redox chemistry by tuning the electronic properties of the carbon ligand; conceptually related, changes in the coordination environment of distal iron centers in FeMoco may have similar effects on the carbide.

Toward addressing the effect of the interstitial ligands of FeMoco, we have reported studies of tetranuclear Fe clusters with μ_4-fluoride and oxide ligands.[21] In those cases, the oxide makes the cluster about 1 V more reducing compared to fluoride for the same redox state while also promoting NO activation. Additionally, remote metal centers affect reactivity through interactions with the bridging moiety (O or F). In those systems, the charge of the interstitial atom could play a role in changing the potential. Here, this series of clusters accounts for changes in ligand charge. Chelating carbyne (**2.5**) and nitride (**2.6**) ligands have the same formal charge but result in ~1 V difference in reducing power, in contrast with the nitride (**2.6**), imide (**2.7**), and sulfide (**2.8**) species that have reduction potentials within 300 mV. The ability of the chelating carbyne to increase the reduction power is likely a consequence of its stronger interaction with the metal centers. In comparison, for the $(WFe_3)^{12+/11+}$ redox couple, the cluster $[NEt_4]_2[Tp^*WFe_3S_3(\mu_3\text{-}CSiMe_3)Cl_3]$ bearing a nonchelating μ_3-C atom reported by our group displays a redox potential of 480 mV more negative than the μ_3-S-bridged analog $[NEt_4][Tp^*WFe_3S_3(\mu_3\text{-}S)Cl_3]$,[55] suggesting that even in a nonchelating environment, a μ_3-C bridge still results in highly negative redox potentials.

In the context of N_2 reduction, the redox tuning observed here suggests that the interstitial carbon may allow FeMoco to access higher reducing power, enabling more facile transfer of electrons to the N_2 substrate for conversion to NH_3. This parallels the results from experiments using synthetic iron catalysts for N_2 reduction, many of which require strong external reducing agents like KC_8.[8,56] Considering the potential impact of replacing the bridging carbyne with a more biologically inexpensive sulfide, a much less reducing cluster (**2.8**) is generated for the same redox state, $(M'Fe_3)^{10+}$, and even an additional reducing equivalent in $(M'Fe_3)^{9+}$ does not match with the $(M'Fe_3)^{10+}$ carbyne system. Therefore, an interstitial sulfide may not provide sufficient reducing power to efficiently convert N_2 into NH_3, leading instead to the preference for the unusual bridging carbide motif.

2.4 CONCLUSION

In summary, we have described the synthesis of a series of heterometallic iron-sulfur clusters of the form $M'Fe_3S_3X$ (M' = Mo or W and X = CR, N, NR, and S) with the cubane geometry matching the structure of the MFe_3S_3C subsite of FeMco. These include examples of iron-sulfur clusters containing a chelating carbon-based ligand bridging the Fe_3 face. Importantly, electrochemical studies indicate that the presence of a bridging C-donor in combination with electronic tuning (by chelation and amine lone pair delocalization) allows the clusters to reach highly reducing states, with potential implications for N_2 reduction chemistry. These studies shed light on possible structural and electrochemical roles of the interstitial carbide ligand in nitrogenase.

2.5 SUPPORTING INFORMATION

A) Synthetic details

1. General considerations:

All reactions were performed at room temperature in a N_2-filled MBraun glovebox or using standard Schlenk techniques unless otherwise specified. Glassware was oven-dried at 140 °C for at least 2 h prior to use and allowed to cool under vacuum. **BAC**,[35,57] **[NEt$_4$][Tp*MoS$_5$]**[58] and KC_8[59] were prepared according to literature procedures, while **2.1-W** was prepared as reported[32] with minor modifications. Diethyl ether, benzene, tetrahydrofuran (THF), acetonitrile (CH_3CN), hexanes, and pentane were dried by sparging with N_2 for at least 15 min and then passing through a column of activated A2 alumina under positive N_2 pressure, and stored over 3 Å molecular sieves prior to use. Dimethylformamide (DMF) was purchased in anhydrous form from MilliporeSigma®, cannula-transferred to an oven-dried Schlenk tube, degassed via several consecutive cycles of active vacuum and agitation on the Schlenk line, brought into the glove box and stored over 3 Å molecular sieves prior to use. ^{1}H spectra were recorded on a Varian 300 MHz or 400 MHz spectrometer. ^{13}C NMR spectra were recorded on a Varian 400 MHz spectrometer. Deuterated acetonitrile (CD_3CN) and deuterated benzene (C_6D_6) were purchased from Cambridge Isotope Laboratories, dried over calcium hydride (for CD_3CN) or sodium/benzophenone ketyl (for C_6D_6), degassed by three freeze–pump–thaw cycles, and vacuum-transferred prior to use.

2. Procedures:

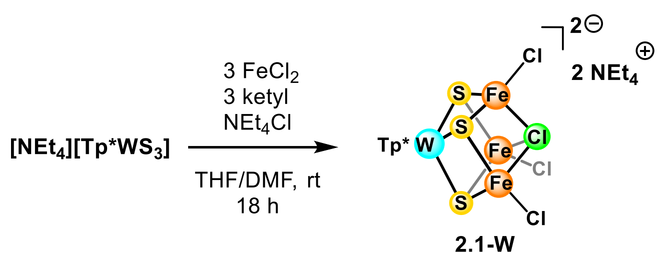

Synthesis of **2.1-W**. In a glovebox, **[NEt$_4$][Tp*WS$_3$]** (prepared as reported,[60] with an additional round of precipitation of the crude material from DMF/Et_2O before recrystallization in MeCN/Et_2O) (1.500 g, 2.12 mmol, 1 eq), $FeCl_2$ (0.807 g, 6.36 mmol, 3 eq) and NEt_4Cl (0.351 g, 2.12 mmol, 1 eq) were dissolved in DMF (90 mL). To this solution, sodium benzophenone ketyl monoanion (63.6 mL, 0.1 M in THF, 6.36 mmol, 3 eq) (freshly prepared by stirring 1 eq Na^0 in a THF solution of 1 eq benzophenone for several hours until all the Na^0 is consumed) was added slowly with stirring. The reaction mixture was stirred at room temperature for 18 h, after which the crude product was collected as a dark purple precipitate on a frit and washed with THF. This solid was purified by dissolving in ~200 mL MeCN, filtering and removing the solvent *in vacuo*. Additional material could be collected by vapor diffusion of Et_2O into the mother liquor from the first filtration. Total yield: 1.98 g (81%). NMR data for **2.1-W** prepared by this method are identical to previous reports.[32]

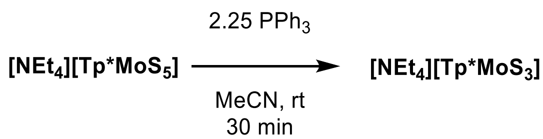

Synthesis of **[NEt_4][Tp*MoS_3]**. To a solution of **[NEt_4][Tp*MoS_5]** (10.0 g, 14.6 mmol, 1 eq) in acetonitrile (400 mL) was added solid triphenylphosphine (8.62 g, 32.9 mmol, 2.25 eq). The reaction was stirred for 30 min, and then concentrated to 50 mL and then precipitated with diethyl ether (300-400 mL) and filtered. Repeating this protocol twice, followed by washing with diethyl ether (250 mL) afforded **[NEt_4][Tp*MoS_3]** as a brown-green solid (7.1 g, 78%). ^{1}H NMR (400 MHz, CD_3CN): δ 5.78 (s, 3H, pyrazole-*H*), 3.14 (q, $^3J_{HH}$ = Hz, 8H, NCH_2), 3.09 (s, 9H, pyrazole-CH_3), 2.35 (s, 9H, pyrazole-CH_3), 1.19 (m, 12H, NCH_2CH_3) ppm. ^{13}C{^{1}H} NMR (101 MHz, CD_3CN): δ 153.00 (s, pyrazole-C), 143.18 (s, pyrazole-C), 107.41 (s, pyrazole-*C*H), 53.05 (s, N*C*H_2), 16.77 (s, pyrazole-*C*H_3), 12.89 (s, pyrazole-*C*H_3), 7.64 (s, NCH_2*C*H_3) ppm. Elemental analysis data for samples of **[NEt_4][Tp*MoS_3]** prepared in this fashion reproducibly shows the anticipated content for H and N, but low content for C, even following subsequent recrystallizations, possibly due to incomplete carbon combustion.[61] Representative data are as follows. Anal. calcd (%) for $C_{23}H_{42}BMoN_7S_3$ (M_r = 619.58): C, 44.59; H, 6.83; N, 15.83. Found: C, 43.50; H, 6.65; N, 15.39.

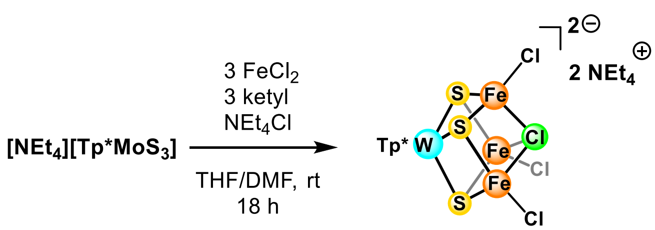

2.1-Mo

Synthesis of **2.1-Mo**. In the glovebox, a solution of **[NEt_4][Tp^*MoS_3]** (1.00 g, 1.61 mmol, 1 eq), $FeCl_2$ (0.614 g, 4.84 mmol, 3 eq), and NEt_4Cl (0.268 g, 1.61 mmol, 1 eq) was prepared in DMF (6.0 mL). Separately, a solution of benzophenone (0.882 g, 4.84 mmol, 3 eq) in THF (50 mL) was reduced over Na^0 (0.111 g, 4.84 mmol, 3 eq) by vigorous stirring over 3 h with a magnetic stir bar. The resulting blue solution of benzophenone ketyl radical was added dropwise to the brown reaction solution. After 16 h, the resulting suspension was filtered, and the blue filter cake was washed with THF (25 mL). This solid was recrystallized by vapor diffusion of diethyl ether into acetonitrile to yield **9** as an analytically pure, blue crystalline solid (1.37 g, 80%). ^{1}H NMR (400 MHz, CD_3CN): δ 3.10 (br s), 1.40 (br s), -21.87 (br s) ppm. Anal. calcd (%) for $C_{31}H_{62}BCl_4Fe_3MoN_8S_3$ (M_r = 1059.17): C, 35.15; H, 5.90; N, 10.58. Found: C, 34.96; H, 5.81; N, 10.29. X-ray quality needles were grown via repeated crystallizations by vapor diffusion, identically as above.

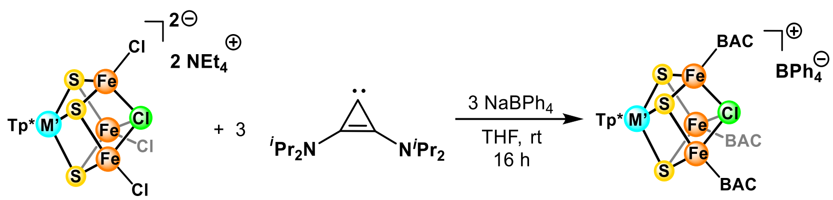

2.1-M' (M' = W or Mo) BAC 2.2-M' (M' = W or Mo)

Synthesis of **2.2-W**. In a glovebox, **2.1-W** (0.867 g, 0.76 mmol, 1 eq), **BAC** (0.536 g, 2.27 mmol, 3 eq) and $NaBPh_4$ (0.776 g, 2.27 mmol, 3 eq) were placed in a flask with a stir bar. To this mixture was added THF (35 mL) with stirring. The solids dissolved to form a dark red solution, along with the formation of a white precipitate. After 16 h, the mixture was filtered through Celite inside the box and the filtrate was evaporated to give a dark red solid. The solid was washed in C_6H_6 to remove a dark brown impurity and recrystallized by vapor diffusion with THF/pentane to yield X-ray quality brown needles. Yield: 1.22 g (89%). ^{1}H NMR (300 MHz, CD_3CN) δ 18.16, 7.39, 7.25, 6.98, 6.85, 1.30, 1.18, 1.13, -0.15, -10.03. Anal. calcd (%) for $C_{84}H_{126}N_{12}B_2ClWS_3Fe_3$ (M_r = 1808.61): C, 55.78; H, 7.02; N, 9.29. Found: C, 55.65; H, 7.12; N, 9.13.

Synthesis of **2.2-Mo**. In a glovebox, **2.1-Mo** (0.375 g, 0.354 mmol, 1 eq) and **BAC** (0.251 g, 1.06 mmol, 3 eq) were combined in THF (15 mL), forming a blue suspension. Then, $NaBPh_4$ (0.364 g, 1.06 mmol, 3 eq) was added dropwise as a solution in THF. A darkening of the reaction color to black was observed, concomitant with formation of a white precipitate. After 16 h, the mixture was filtered through Celite, and the filtrate was evaporated to yield a black solid. This solid was washed with diethyl ether (3 × 5 mL) and C_6H_6 (2 × 1 mL) to remove a brown impurity. The solid was then recrystallized by vapor diffusion of diethyl ether into THF to yield **2.2-Mo** as a black crystalline solid (0.450 g, 74%). On a 40 mg scale, the crystal quality was sufficient for structural identification by XRD. ^{1}H NMR (400 MHz, CD_3CN) δ 7.25 (s), 6.97 (s), 6.84 (s), 0.32 (br s), -10.89 (br s). Analytically pure samples of **2.2-Mo** were prepared via a second recrystallization by identical means. Anal. calcd (%) for $C_{84}H_{126}B_2ClFe_3MoN_{12}S_3$ (M_r = 1720.75): C, 58.63; H, 7.38; N, 9.77. Found: C, 58.50; H, 7.27; N, 9.57.

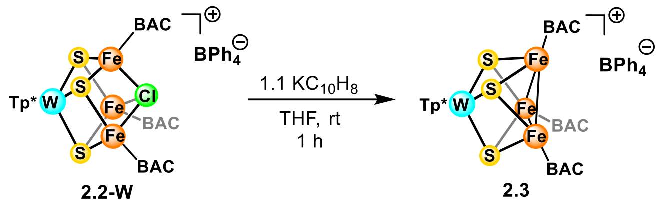

Synthesis of **2.3**. In a glovebox, **2.2-W** (364.0 mg, 0.201 mmol, 1 eq) was dissolved in THF (30 mL), making sure that all the solid goes into solution. Potassium naphthalenide (2.2 mL, 0.1 M in THF, 0.221 mmol, 1.1 eq) was added to the reaction dropwise while stirring using a syringe at room temperature. After 1 h, the reaction mixture was filtered through Celite and evaporated to dryness. The dark brown residue was washed with Et_2O and the crude product was recrystallized by vapor diffusion of pentane into a concentrated THF solution to give X-ray quality dark hexagons. Yield: 274.0 mg (77%). ^{1}H NMR (300 MHz, CD_3CN) δ 41.79, 10.81, 8.44, 7.30, 7.02, 6.87, -0.08, -23.02. Anal. calcd (%) for $C_{84}H_{126}N_{12}B_2WS_3Fe_3$ (M_r = 1773.18): C, 56.90; H, 7.16; N, 9.48. Found: C, 57.30; H, 7.32; N, 8.99.

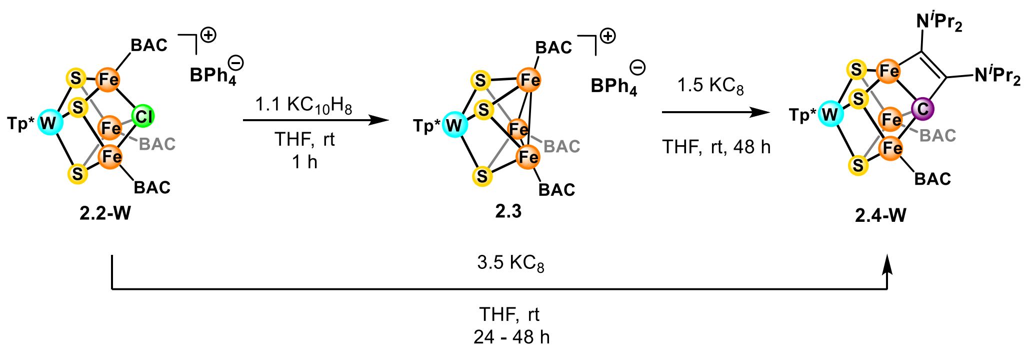

Synthesis of **2.4-W**. From **2.2-W**: In a glovebox, **2.2-W** (1.53 g, 0.85 mmol, 1 eq) and excess KC_8 (0.400 g, 2.96 mmol, 3.5 eq) were placed in a flask with a stir bar along with THF (35 mL). The dark brown solution was stirred at room temperature for 24 h or until no more **2.2-W** is seen by NMR spectroscopy. The mixture was then filtered through Celite inside the box and the filtrate was evaporated to give a dark brown solid. The product was extracted into Et_2O, filtered and the solvent removed to yield a dark brown solid. Yield: 1.08 g (88%).

From **2.3**: In a glovebox, **2.3** (0.376 g, 0.21 mmol, 1 eq) and excess KC_8 (0.043 g, 3.18 mmol, 1.5 eq) were placed in a flask with a stir bar along with THF (20 mL). The dark brown solution was stirred at room temperature for 24 h or until no more **2.3** is seen by NMR spectroscopy. The mixture was then filtered through Celite inside the box and the filtrate was evaporated to give a dark brown solid. The product was extracted into Et_2O, filtered and the solvent removed to yield a dark brown solid. Yield: 0.259 g (84%).

X-ray quality crystals of **2.4-W** were grown by placing a concentrated pentane solution at -35 °C for several days. Pure crystalline material for cyclic voltammetry can also be prepared by vapor diffusion of pentane into a concentrated solution of **2.4-W** in Et_2O at -35°C over several days. ^1H NMR (300 MHz, C_6D_6) δ 19.24, 10.20, 9.12, 5.15, 5.06, 3.94, 3.27, 2.78, 2.44, 1.24, -1.60, -4.84, -7.23, -11.00. Elemental analysis data for samples of **2.4-W** prepared in this fashion reproducibly shows the anticipated content for H and N, but low content for C, even following subsequent recrystallizations. This could be due to incomplete carbon combustion, a known problem for the analysis of metal complexes by combustion analysis.[61] Representative data are as follows. Anal. calcd (%) for $C_{60}H_{106}N_{12}BWS_3Fe_3$ (M_r = 1453.95): C, 49.56; H, 7.35; N, 11.56. Found: C, 48.50; H, 7.18; N, 11.34.

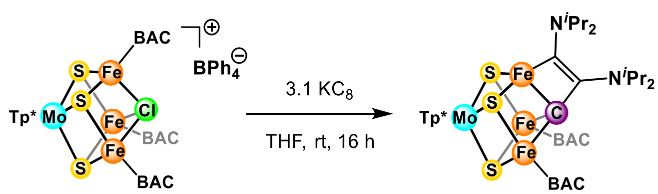

Synthesis of **2.4-Mo**. In a glovebox, KC_8 (0.041 g, 0.30 mmol, 3.1 eq) was added to a solution of **2.2-Mo** (0.167 g, 0.097 mmol, 1 eq) in THF (5 mL) with stirring. A color change to brown was immediately apparent. After stirring overnight (16 h), the reaction was filtered through Celite and the filtrate was concentrated to dryness *in vacuo*. Extraction into diethyl ether, filtration, and removal of the solvent from the filtrate provided **2.4-Mo** as a brown solid (0.130 g, 99%). X-ray quality crystals of **2.4-Mo** were grown by vapor diffusion of pentane into a concentrated THF solution at room temperature over several days. ^1H NMR (400 MHz, C_6D_6) δ 16.14, 11.70, 8.30, 5.88, 5.46, 4.14, 1.73, 1.12, 0.42, -2.55, -4.74, -5.87, -13.31 ppm. Elemental analysis data for samples of **2.4-Mo** prepared in this fashion reproducibly shows the anticipated content for H and N, but low content for C, possibly due to incomplete carbon combustion.[61] Representative data are as follows. Anal. calcd (%) for $C_{60}H_{106}BFe_3MoN_{12}S_3$ (M_r = 1366.07): C, 52.75; H, 7.82; N, 12.30. Found: C, 51.80; H, 7.73; N, 12.38.

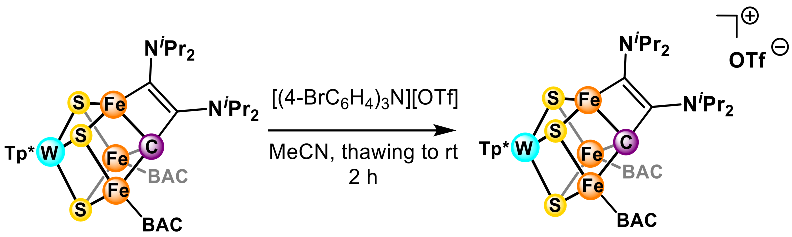

2.4-W **[2.4-W][OTf]**

Synthesis of **[2.4-W][OTf]**. In a glovebox, **2.4-W** (0.0300 g, 0.021 mmol, 1 eq) and [(4-BrC$_6$H$_4$)$_3$N][OTf] (0.0130 g, 0.021 mmol, 1 eq) were placed in a vial a stir bar and cooled to -78 °C in the cold well. To this vial was added thawing MeCN (2 mL), leading to a dark red solution with a white precipitate. The solution was stirred for 2 h at room temperature, then filtered and the solvent removed *in vacuo*. The dark solid was washed with Et_2O and crystallized by THF/pentane vapor diffusion, whose structure was confirmed by connectivity using X-ray crystallography. Yield: 30.8 mg (93%). ^{1}H NMR (400 MHz, THF-h$_8$, solvent suppression) δ 13.95, 7.07, 6.33, 6.18, 5.64, 1.20, 0.26, -1.26.

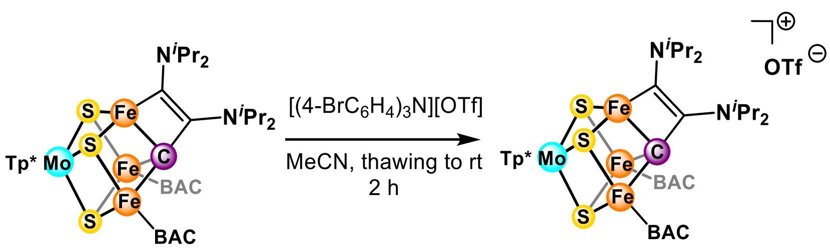

2.4-Mo **[2.4-Mo][OTf]**

Synthesis of **[2.4-Mo][OTf]**. In a glovebox, **2.4-Mo** (0.0800 g, 0.059 mmol, 1 eq) and [(4-BrC$_6$H$_4$)$_3$N][OTf] (0.0370 g, 0.059 mmol, 1 eq) were placed in a vial a stir bar and cooled to -78 °C in the cold well. To this vial was added thawing MeCN (10 mL), leading to a dark red solution with a white precipitate. The solution was stirred for 2 h at room temperature, then filtered and the solvent removed *in vacuo*. The dark solid was washed with Et_2O and crystallized by THF/pentane vapor diffusion, whose structure was assigned based on the similarities in its NMR spectrum compared to the W version. Yield: 60.0 mg (68%). [1]H NMR (400 MHz, THF-h_8, solvent suppression) δ 15.24, 9.21, 7.77, 6.55, 6.46, 0.82, 0.30, -3.06.

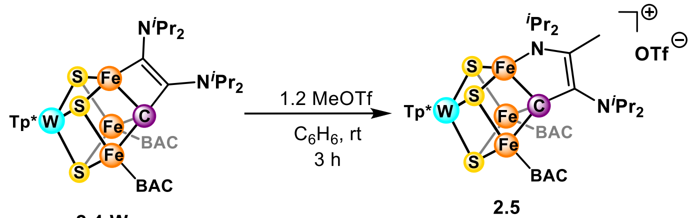

2.4-W

2.5

Synthesis of **2.5**. In a glovebox, **2.4-W** (prepared from **2.3**) (0.0200 g, 0.14 mmol, 1 eq) was dissolved in C_6H_6 (2 mL). To this solution, MeOTf (0.14 mL, 0.1 M solution in toluene, 0.14 mmol, 1 eq) was added dropwise with stirring using a syringe. A dark brown precipitate appeared immediately. The reaction was stirred for 3 h, after which the mother liquor became very light brown and the crude **2.5** precipitate was collected by filtration. This solid was the further purified by vapor diffusion of pentane into a concentrated solution in THF to deposit a dark microcrystalline powder. Yield: 0.0205 g (92%). When conducted on larger scales, the product becomes less pure even after crystallization and the yield drops to 50 – 60%. Despite the scale, however, samples of **2.5** still contain small amounts of unidentified impurities, which are observed in the cyclic voltammogram. X-ray quality crystals can be grown by slow evaporation of a concentrated MeCN solution of **2.5** at room temperature. [1]H NMR (300 MHz, CD_3CN) δ 15.64, 14.28, 10.87, 8.64, 8.32, 7.01, 6.45, 6.31, 5.57, 5.17, 3.55, 1.39, 0.99, -0.03, -0.18, -2.58, -5.38, -90.01. Anal. calcd (%) for $C_{62}H_{109}N_{12}O_3F_3BWS_4Fe_3$ (M_r = 1618.05): C, 46.02; H, 6.79; N, 10.39. Found: C, 43.60; H, 6.95; N, 9.78.

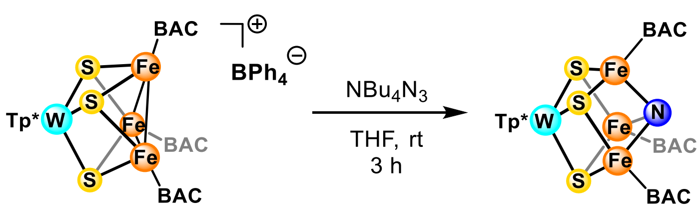

2.3

2.6

Synthesis of **2.6**. In a glovebox, **2.3** (40.0 mg, 0.023 mmol, 1 eq) and NBu_4N_3 (6.4 mg, 0.023 mmol, 1 eq) were dissolved in THF (2 mL) in a vial with a stir bar. The dark brown solution was stirred at room temperature for 3 h, after which the solvent was removed *in vacuo*. The product was extracted into Et_2O, which was left to evaporate at room temperature over the course of the day to yield dark X-ray quality crystal. When almost all the solvent has evaporated, the remaining supernatant was discarded and the crystals were washed with pentane. Yield: 18.2 mg (55%). Samples of **2.6** typically contain small amounts of impurities including **2.4-W**, which could not be removed due to similar solubilities. [1]H NMR (300 MHz, C_6D_6) δ 5.82, 2.03, 1.54, 1.13. Anal. calcd (%) for $C_{60}H_{106}N_{13}BWS_3Fe_3$ (M_r = 1467.96): C, 49.09; H, 7.28; N, 12.40. Found: C, 48.91; H, 7.57; N, 11.41.

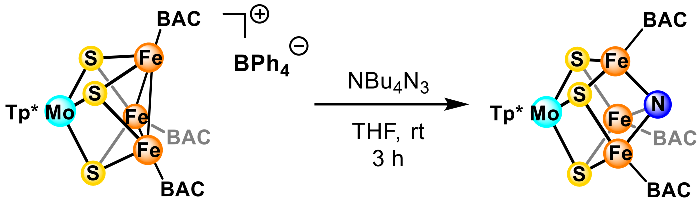

2.3-Mo (by Dr. Gwendolyn Bailey) **2.6-Mo**

Synthesis of **2.6-Mo**. In a glovebox, **2.3-Mo** (prepared analogously to the W version by Dr. Gwendolyn Bailey) (110.0 mg, 0.065 mmol, 1 eq) and NBu_4N_3 (18.6 mg, 0.065 mmol, 1 eq) were dissolved in THF (5 mL) in a vial with a stir bar. The dark brown solution was stirred at room temperature for 3 h, after which the solvent was removed *in vacuo*. The product was extracted into C_6H_6 and crystallized by C_6H_6/pentane vapor diffusion. Yield: 40.0 mg (44%). Low-quality crystals can be grown from vapor diffusion of pentane into a concentrated solution of **2.6-Mo** in Et_2O, which confirms the structural assignment. [1]H NMR (400 MHz, THF-h_8, solvent suppression) δ 5.41, 2.07, 1.13, 0.80.

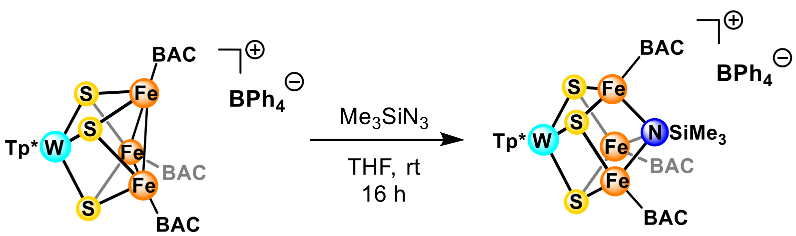

2.3 **2.7**

Synthesis of **2.7**. In a glovebox, **2.3** (89.3 mg, 0.050 mmol, 1 eq) was dissolved in THF (5 mL). To this solution was added Me_3SiN_3 (0.504 mL, 0.1 M in THF, 0.050 mmol, 1 eq) using a syringe. The dark brown solution was stirred at room temperature for 2 h, after which the solvent was removed *in vacuo*. The product was washed with Et_2O, then recrystallized by vapor diffusion of Et_2O into a concentrated THF solution to yield X-ray quality dark diamonds. Yield: 76.1 mg (81%). [1]H NMR (300 MHz, CD_3CN) δ 10.39, 7.27, 6.98, 6.85, 5.83, 0.52, -1.39. Anal. calcd (%)

for $C_{87}H_{135}N_{13}B_2SiWS_3Fe_3$ (M_r = 1860.37): C, 56.17; H, 7.31; N, 9.79. Found: C, 56.12; H, 7.33; N, 9.85.

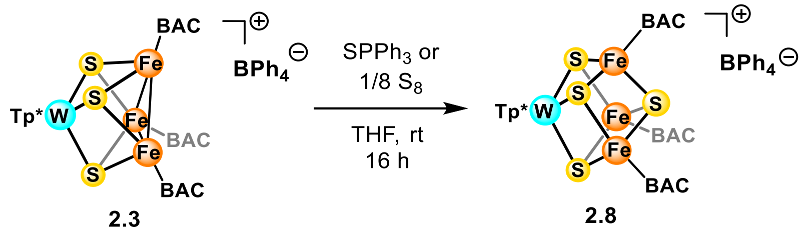

Synthesis of **2.8**. In a glovebox, **2.3** (150 mg, 0.085 mmol, 1 eq) was dissolved in THF (10 mL). To this solution was added $SPPh_3$ (25 mg, 0.085 mmol, 1 eq) in portions. The dark brown solution was stirred at room temperature for 6 h, after which the reaction mixture was filtered, and the solvent was then removed *in vacuo*. The product was washed with Et_2O, then recrystallized by vapor diffusion of Et_2O into a concentrated THF solution to yield X-ray quality dark rods. Yield: 84.0 mg (55%). ^{1}H NMR (300 MHz, CD_3CN) δ 14.35, 7.07, 6.79, 6.64, 5.23, 2.01, 1.90, 1.85, 1.58, -1.94. Anal. calcd (%) for $C_{84}H_{126}N_{12}B_2WS_4Fe_3$ (M_r = 1805.25): C, 55.89; H, 7.04; N, 9.31. Found: C, 55.82; H, 6.86; N, 10.17.

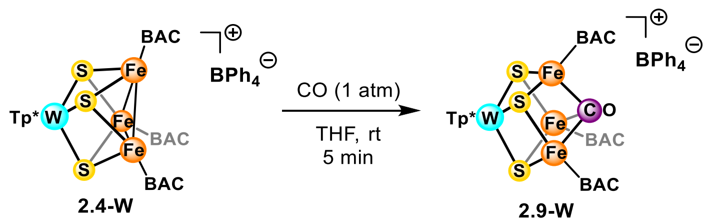

Synthesis of **2.9-W**. In a glovebox, **2.3** (83.5 mg, 0.047 mmol, 1 eq) was dissolved in THF (10 mL) in a 50 mL Schlenk tube. The tube was capped and degassed on the Schlenk line using three freeze-pump-thaw cycles. The headspace of the tube was then replaced with 1 atm CO at room temperature and stirred. The dark red solution quickly changed to dark brown after 5 min, after which the solvent was removed *in vacuo* and the tube transferred to the glovebox. The product was dissolved in a minimal amount of THF and crystallized by THF/pentane vapor diffusion. X-ray quality crystals were grown by vapor diffusion of Et_2O into a concentrated solution of **2.9-W** in C_6H_6. Yield: 82.9 mg (98%). ^{1}H NMR (400 MHz, THF-h_8, solvent suppression) δ 32.63, 7.05, 6.62, 6.53, 4.81, -5.69.

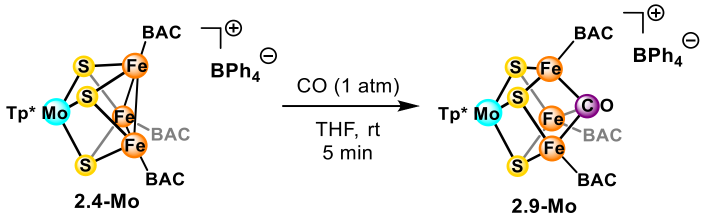

Synthesis of **2.9-Mo**. In a glovebox, **2.3-Mo** (prepared by Dr. Gwendolyn Bailey) (80.0 mg, 0.047 mmol, 1 eq) was dissolved in THF (10 mL) in a 50 mL Schlenk tube. The tube was capped and degassed on the Schlenk line using three freeze-pump-thaw cycles. The headspace of the tube was then replaced with 1 atm CO at room temperature and stirred. The dark red solution quickly changed to dark brown after 5 min, after which the solvent was removed *in vacuo* and the tube transferred to the glovebox. The product was dissolved in a minimal amount of THF and crystallized by THF/pentane vapor diffusion, which yielded weakly diffracting crystals but the structural assignment is supported by similarities in the NMR spectrum compared to the W version. Yield: 70.0 mg (86%). ^{1}H NMR (400 MHz, THF-h_8, solvent suppression) δ 14.61, 7.22, 6.79, 6.64, 5.70, -2.19.

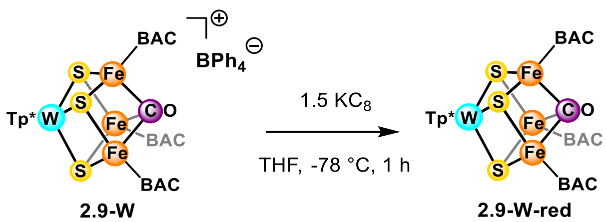

Synthesis of **2.9-W-red**. In a glovebox, **2.9-W** (40.0 mg, 0.022 mmol, 1 eq) was dissolved in THF (2 mL) and cooled to -78 °C in the cold well. To this reaction was added KC_8 (4.5 mg, 0.033 mmol, 1.5 equiv) and the reaction quickly changed to dark greenish brown. The reaction was stirred in the cold well for 1 h then filtered through Celite and dried *in vacuo*. The product was then extracted into Et_2O and C_6H_6, followed by vapor diffusion with pentane. Yield: 21.6 mg (66%). X-ray quality crystals were grown by vapor diffusion of pentane into a concentrated solution of the product in Et_2O. ^{1}H NMR (400 MHz, THF-h_8, solvent suppression) δ 10.63, -3.26, -21.75.

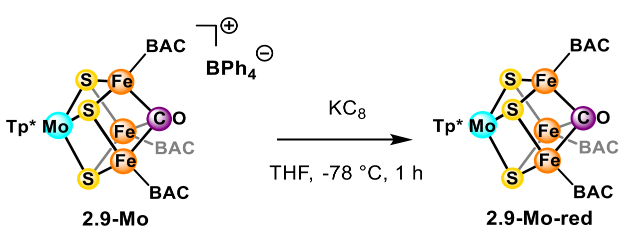

Synthesis of **2.9-Mo-red**. In a glovebox, **2.9-Mo** (70.0 mg, 0.041 mmol, 1 eq) was dissolved in THF (3 mL) and cooled to -78 °C in the cold well. To this reaction was added KC_8 (5.5 mg, 0.041 mmol, 1 equiv) and the reaction quickly changed to dark greenish brown. The reaction was stirred in the cold well for 1 h then filtered through Celite and dried *in vacuo*. The product was then extracted into C_6H_6, followed by vapor diffusion with pentane to yield X-ray quality crystals as dark blocks. Yield: 40.8 mg (71%). ^{1}H NMR (400 MHz, THF-h_8, solvent suppression) δ 12.56, -0.50, -17.86.

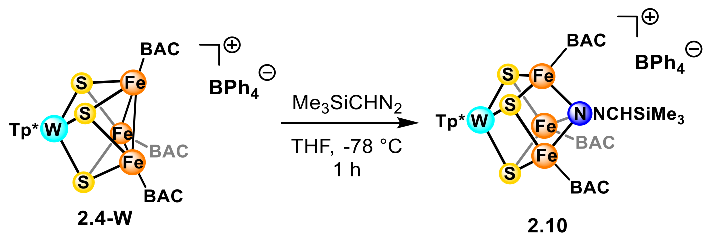

Synthesis of **2.10**. In a glovebox, **2.3** (20.0 mg, 0.011 mmol, 1 eq) was dissolved in THF (2 mL) and cooled to -78 °C. To this solution was added Me_3SiCHN_2 (6 μL, 2 M in hexanes, 0.011 mmol, 1 eq) and the reaction was stirred at -78 °C for 1 h. The solvent was then removed *in vacuo* and the solid was washed with cooled Et_2O. The product was dissolved in a minimal amount of THF and crystallized by THF/Et_2O vapor diffusion at -35 °C. The crystals obtained diffract weakly but a connectivity can be established, and they were not isolated in bulk due to their tendency to decompose at higher temperatures. ^{1}H NMR (400 MHz, THF-h_8, solvent suppression) δ 22.09, 7.64, 7.20, 6.76, 6.56, 5.61, 0.09, -2.73.

3. NMR spectra:

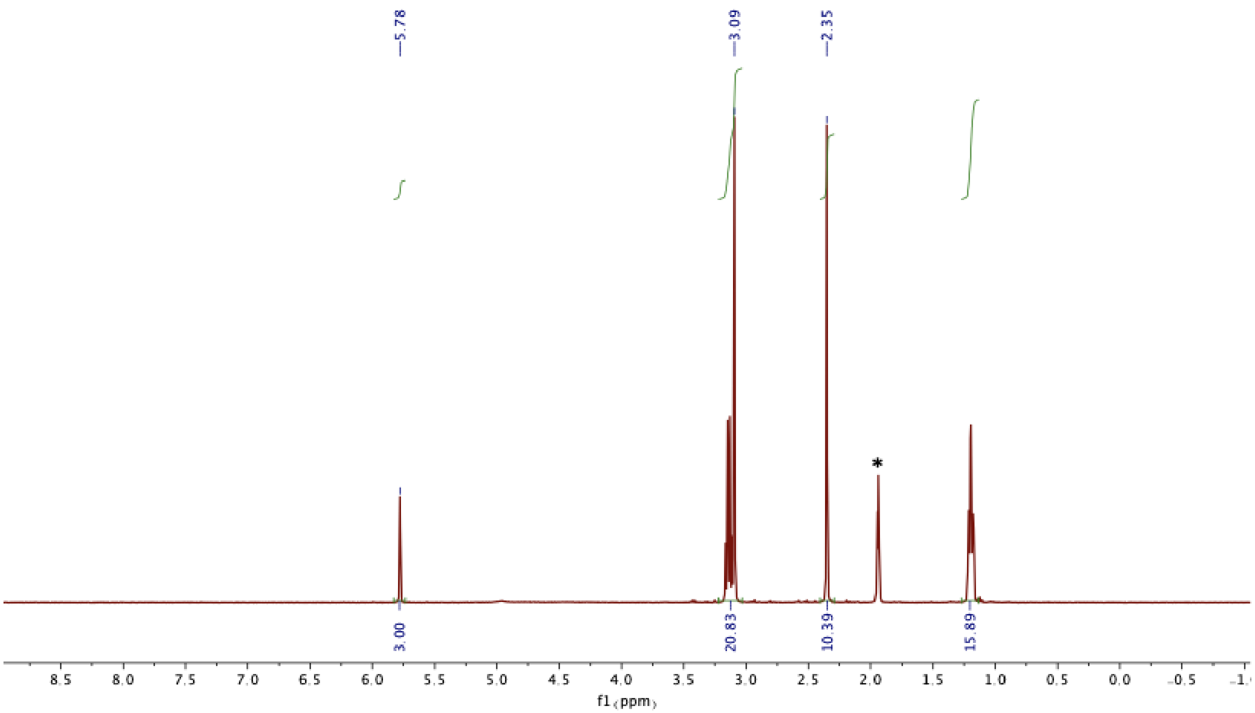

Figure 2.S1. ^{1}H NMR spectrum (400 MHz, CD_3CN) of **[NEt_4][Tp*MoS_3]**. Solvent peak is indicated by asterisk (*).

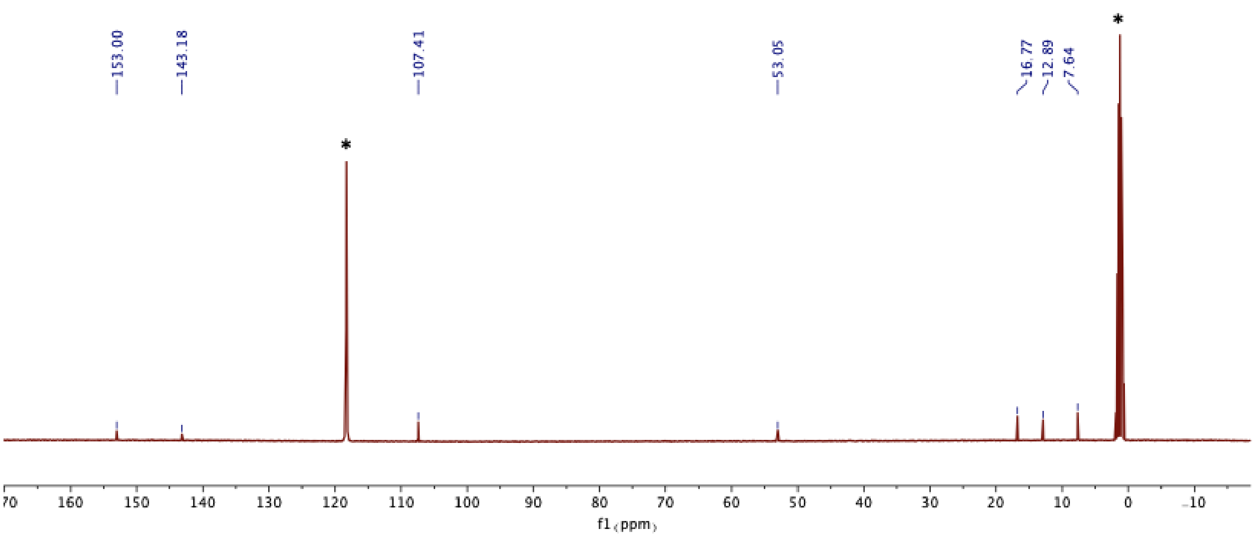

Figure 2.S2. $^{13}C\{^{1}H\}$ NMR spectrum (101 MHz, CD_3CN) of **[NEt_4][Tp*MoS_3]**. Solvent peaks are indicated by asterisks (*).

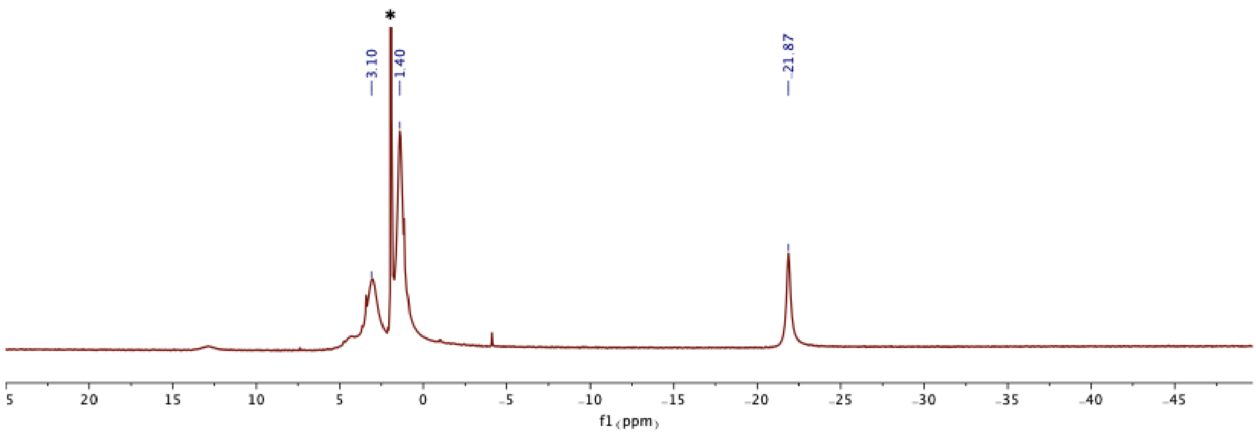

Figure 2.S3. [1]H NMR spectrum (400 MHz, CD_3CN) of **2.1-Mo**. Solvent peak is indicated by asterisk (*).

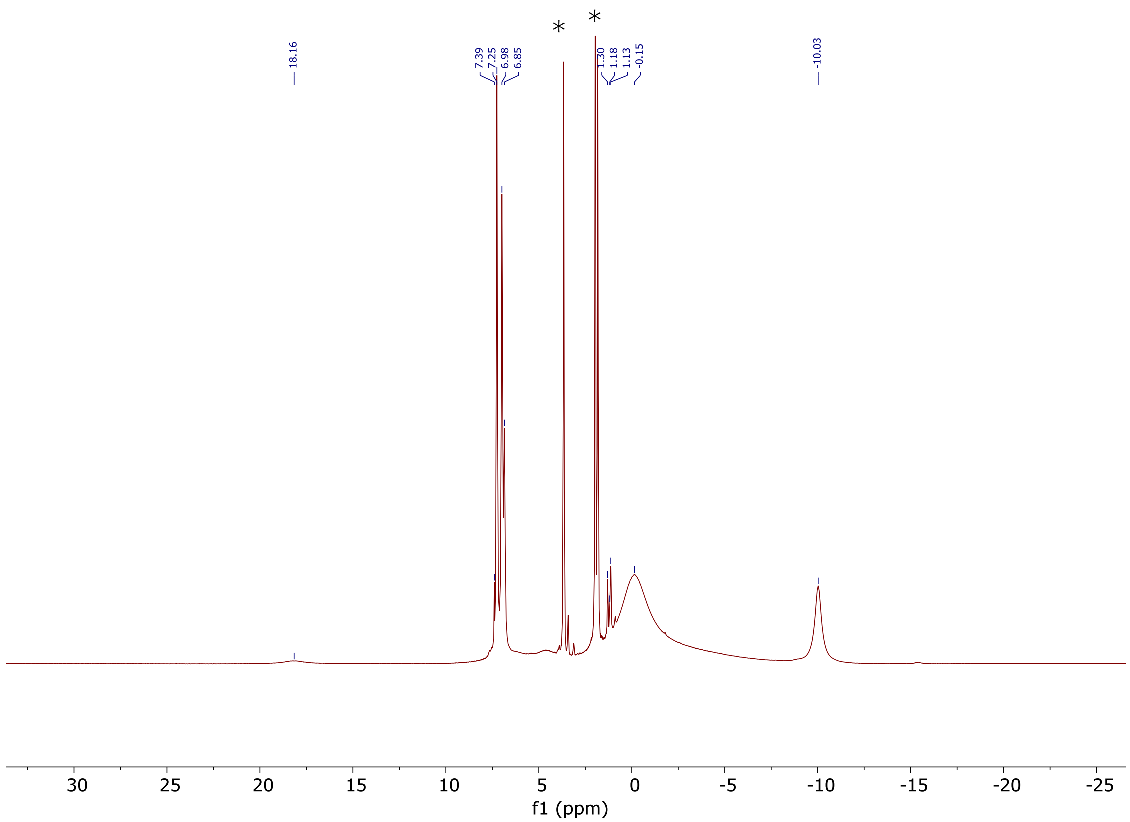

Figure 2.S4. [1]H NMR (300 MHz, CD_3CN) spectrum of **2.2-W**. Solvent peaks are indicated by asterisks (*).

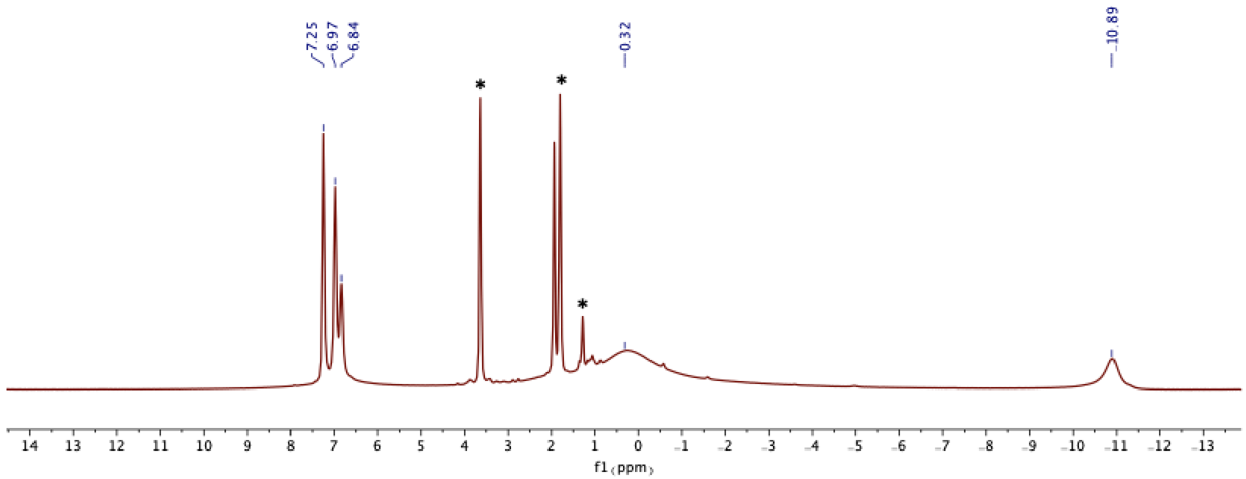

Figure 2.S5. [1]H NMR spectrum (400 MHz, CD_3CN) of **2.2-Mo**. Solvent peaks are indicated by asterisks (*).

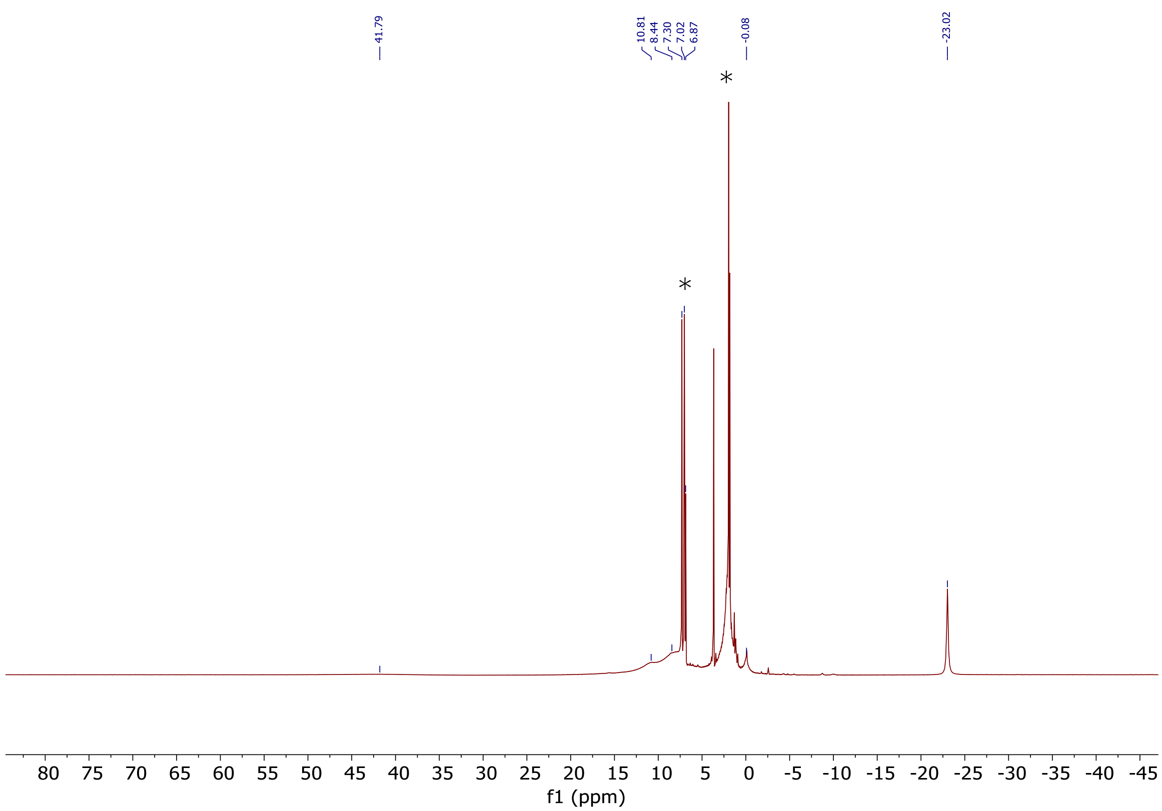

Figure 2.S6. [1]H NMR (300 MHz, CD_3CN) spectrum of **2.3**. Solvent peaks are indicated by asterisks (*).

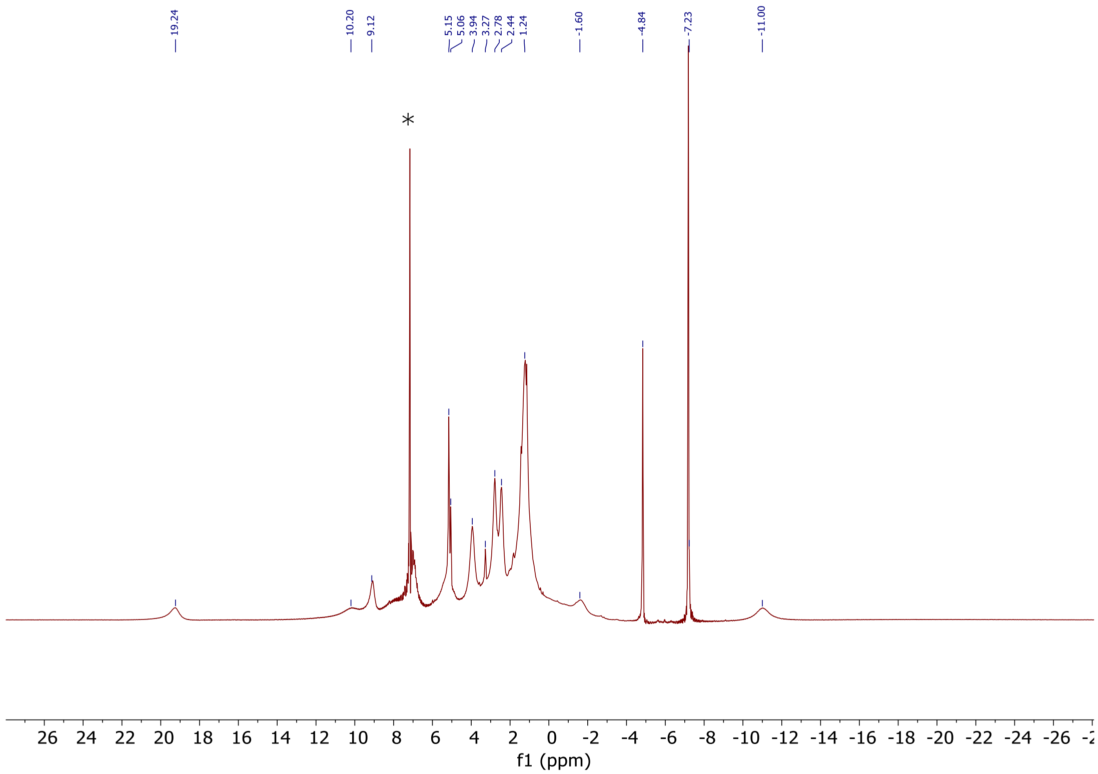

Figure 2.S7. ^{1}H NMR (300 MHz, C_6D_6) spectrum of **2.4-W**. Solvent peak is indicated by asterisk (*).

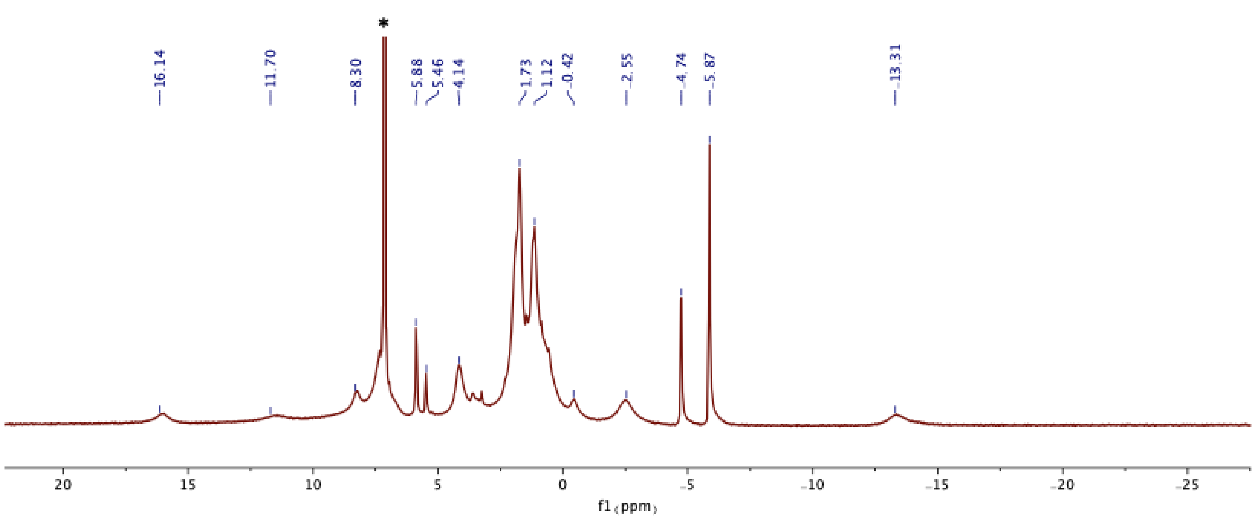

Figure 2.S8. ^{1}H NMR (400 MHz, C_6D_6) spectrum of **2.4-Mo**. Solvent peak is indicated by asterisk (*).

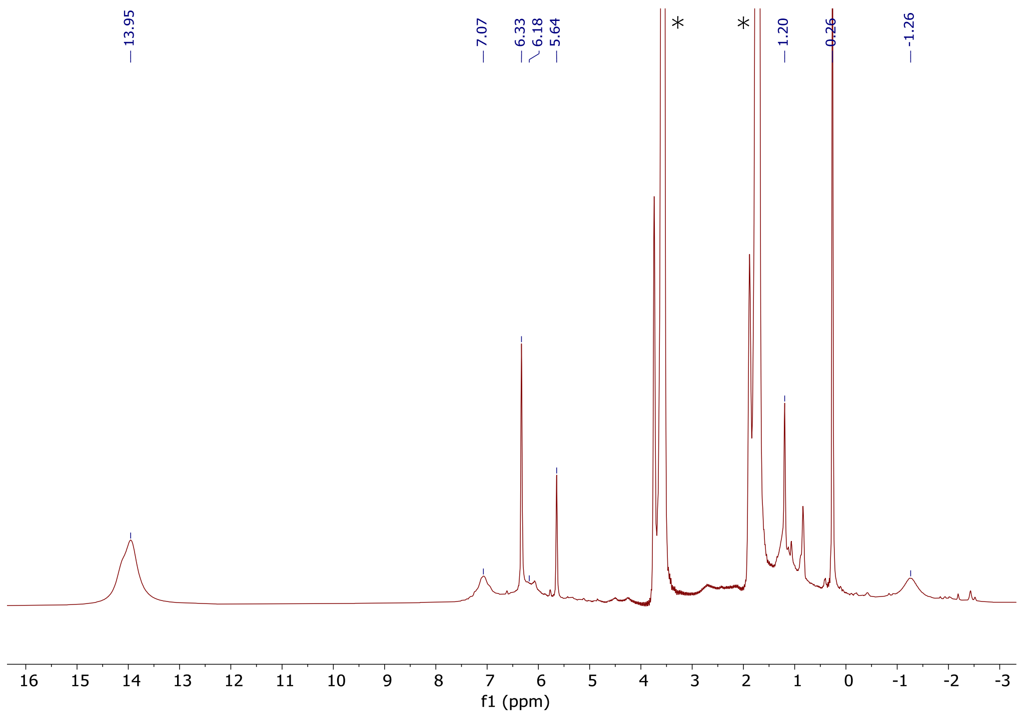

Figure 2.S9. ^{1}H NMR (400 MHz, THF-h_8, solvent suppression) spectrum of **[2.4-W][OTf]**. Solvent peaks are indicated by asterisks (*).

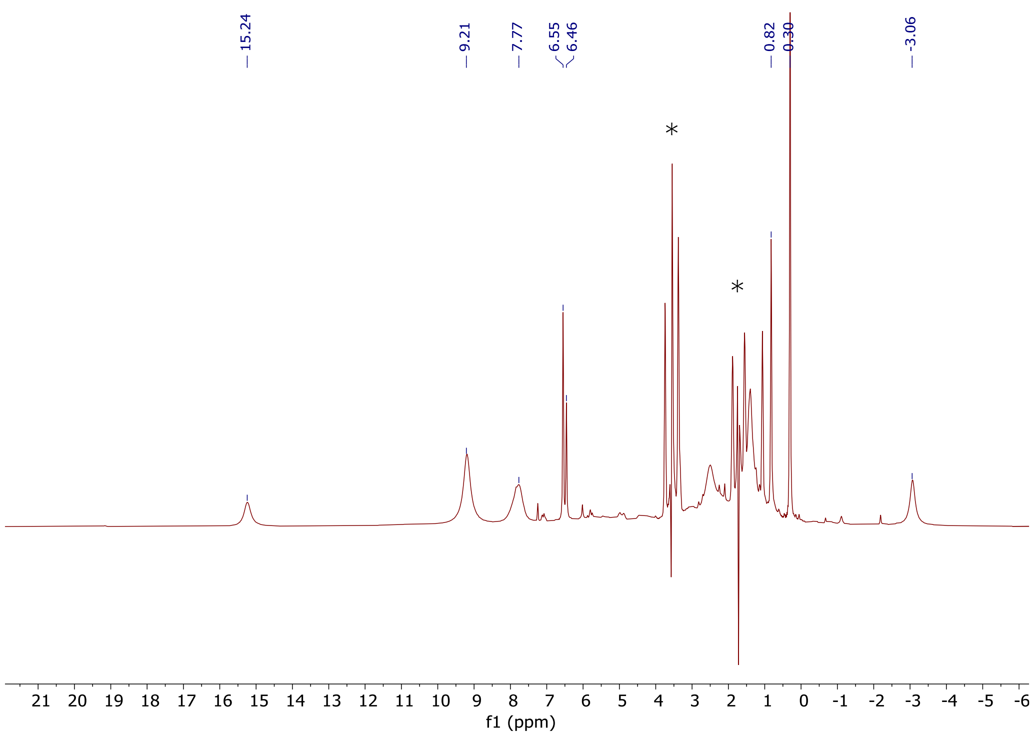

Figure 2.S10. ^{1}H NMR (400 MHz, THF-h_8, solvent suppression) spectrum of **[2.4-Mo][OTf]**. Solvent peaks are indicated by asterisks (*).

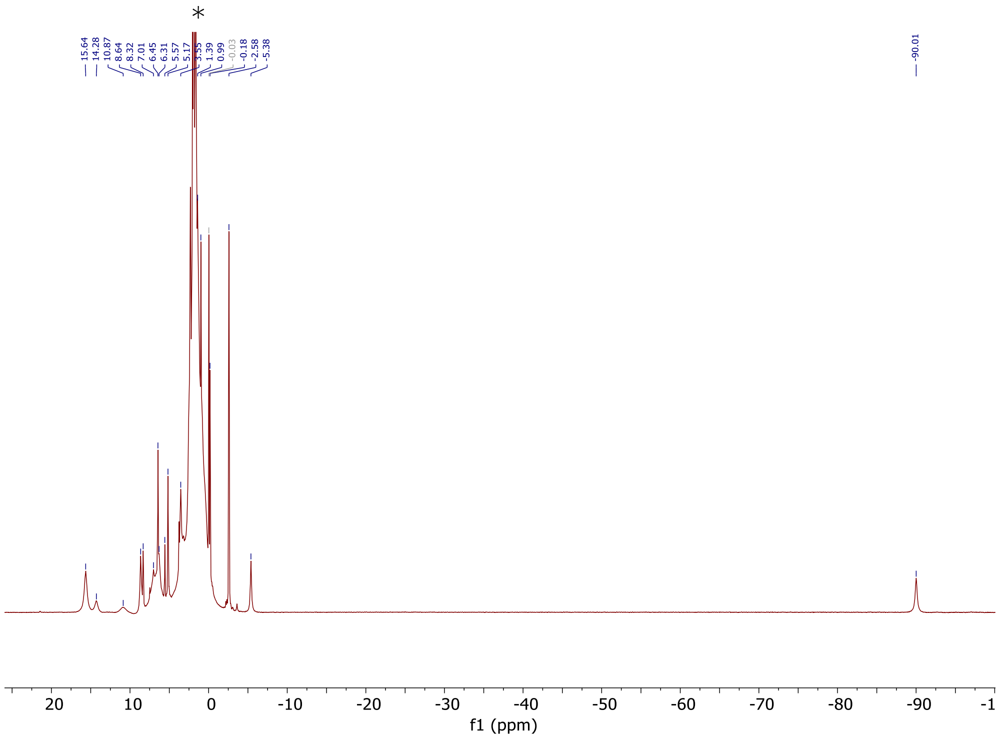

Figure 2.S11. ^{1}H NMR (300 MHz, CD_3CN) spectrum of **2.5**. Solvent peak is indicated by asterisk (*).

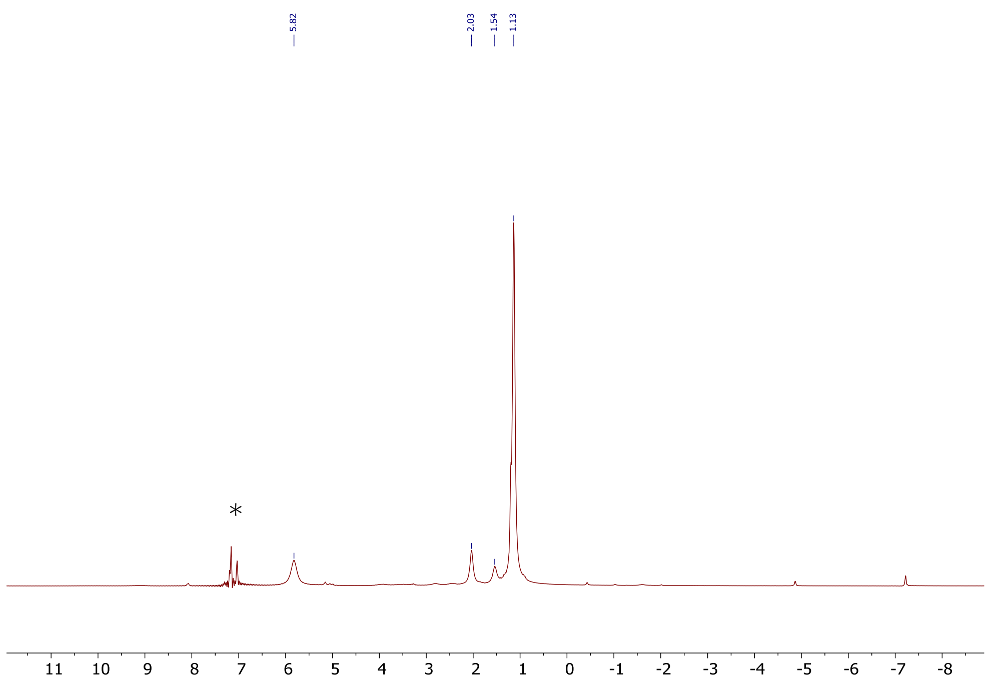

Figure 2.S12. ^{1}H NMR (300 MHz, C_6D_6) spectrum of **2.6**. Solvent peak is indicated by asterisk (*).

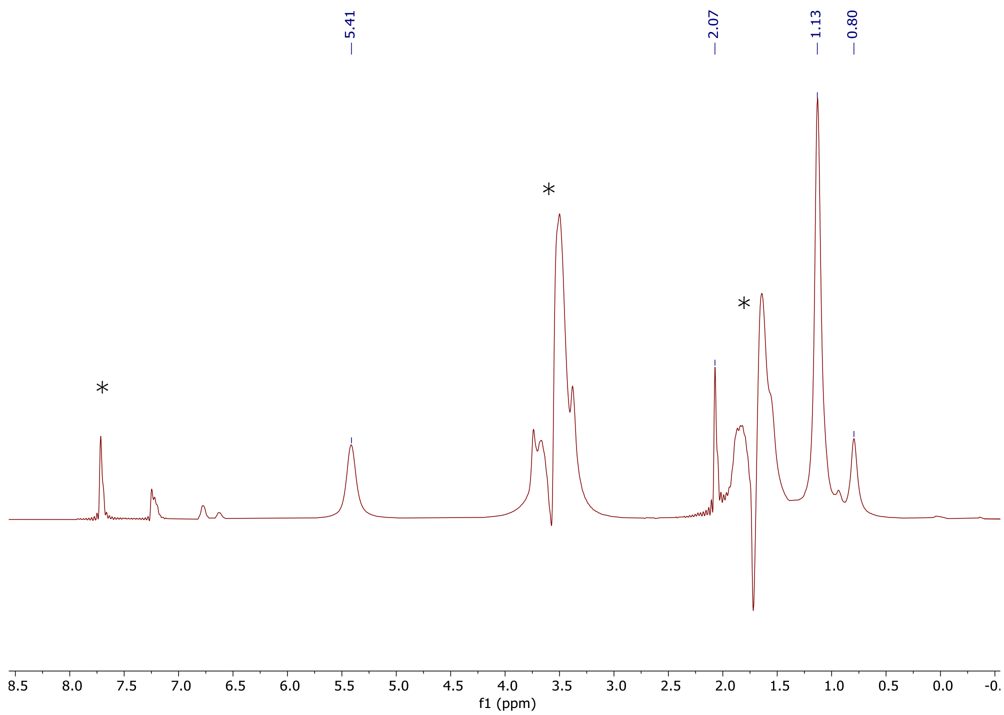

Figure 2.S13. ^{1}H NMR (400 MHz, THF-h_8, solvent suppression) spectrum of **2.6-Mo**. Solvent peaks are indicated by asterisks (*).

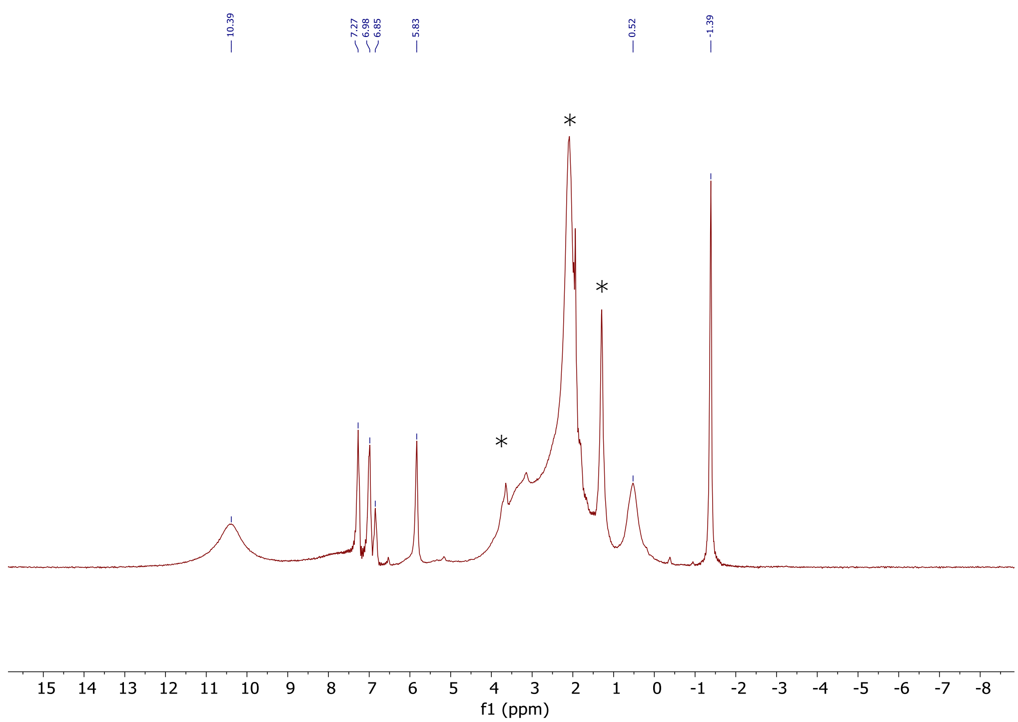

Figure 2.S14. ^{1}H NMR (300 MHz, CD_3CN) spectrum of **2.7**. Solvent peaks are indicated by asterisks (*).

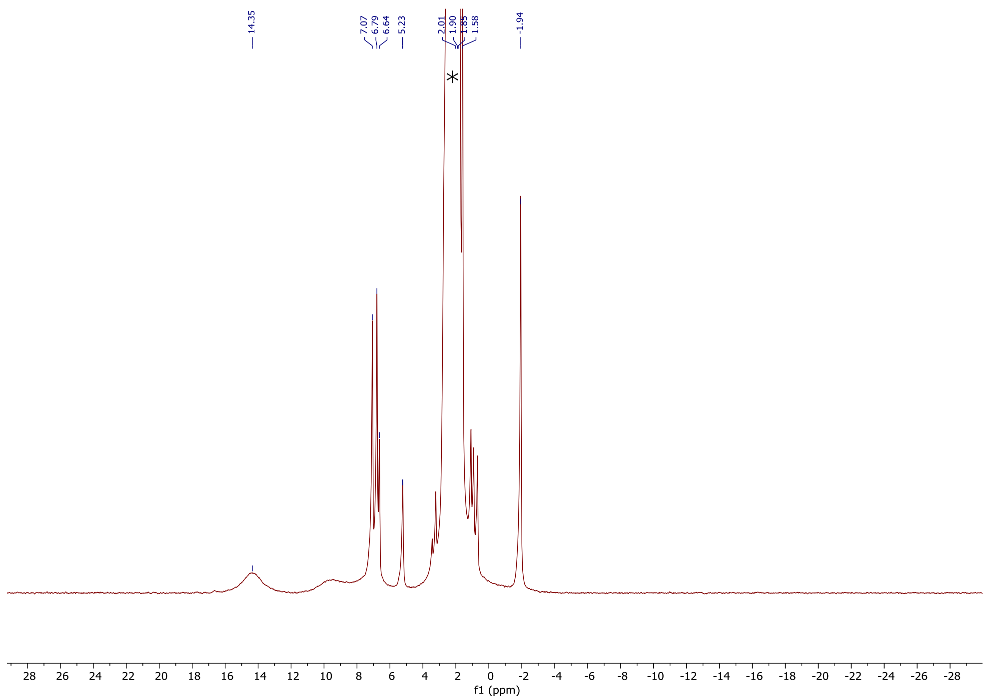

Figure 2.S15. ^{1}H NMR (400 MHz, CD_3CN) spectrum of **2.8**. Solvent peak is indicated by asterisk (*).

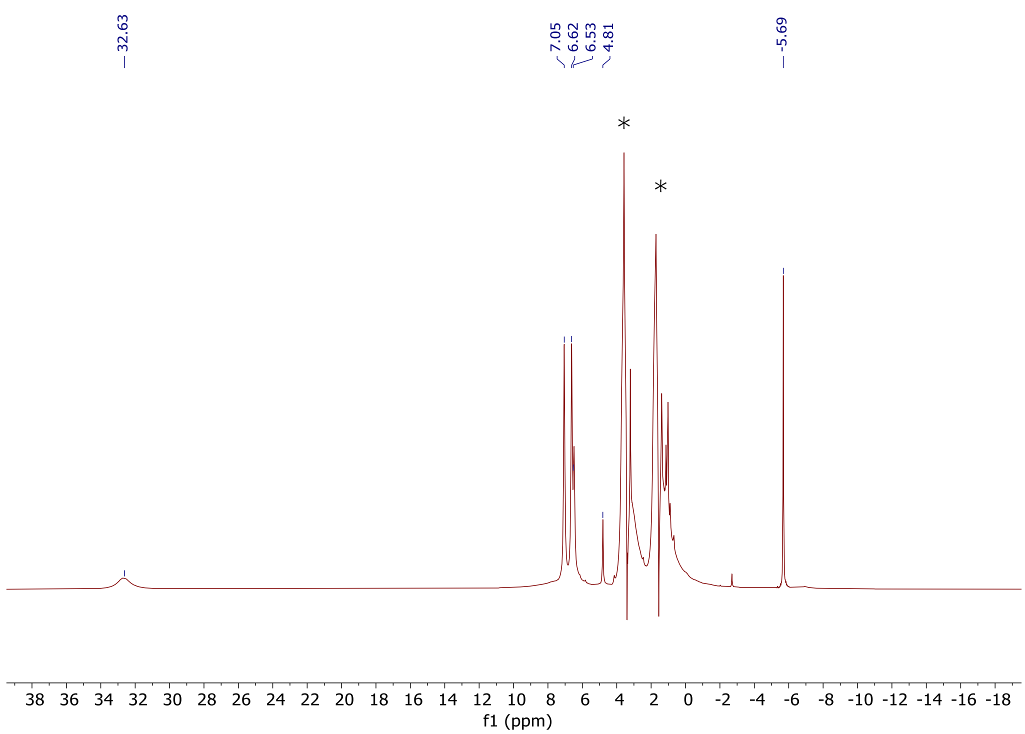

Figure 2.S16. ^{1}H NMR (400 MHz, THF-h_8, solvent suppression) spectrum of **2.9-W**. Solvent peaks are indicated by asterisks (*).

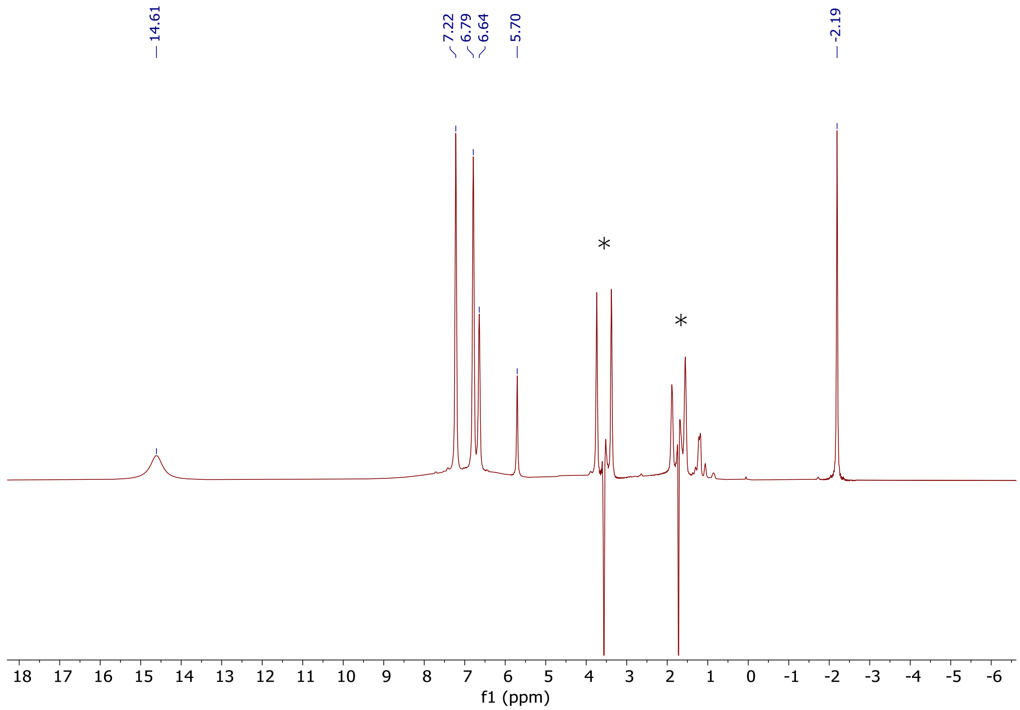

Figure 2.S17. ^{1}H NMR (400 MHz, THF-h_8, solvent suppression) spectrum of **2.9-Mo**. Solvent peaks are indicated by asterisks (*).

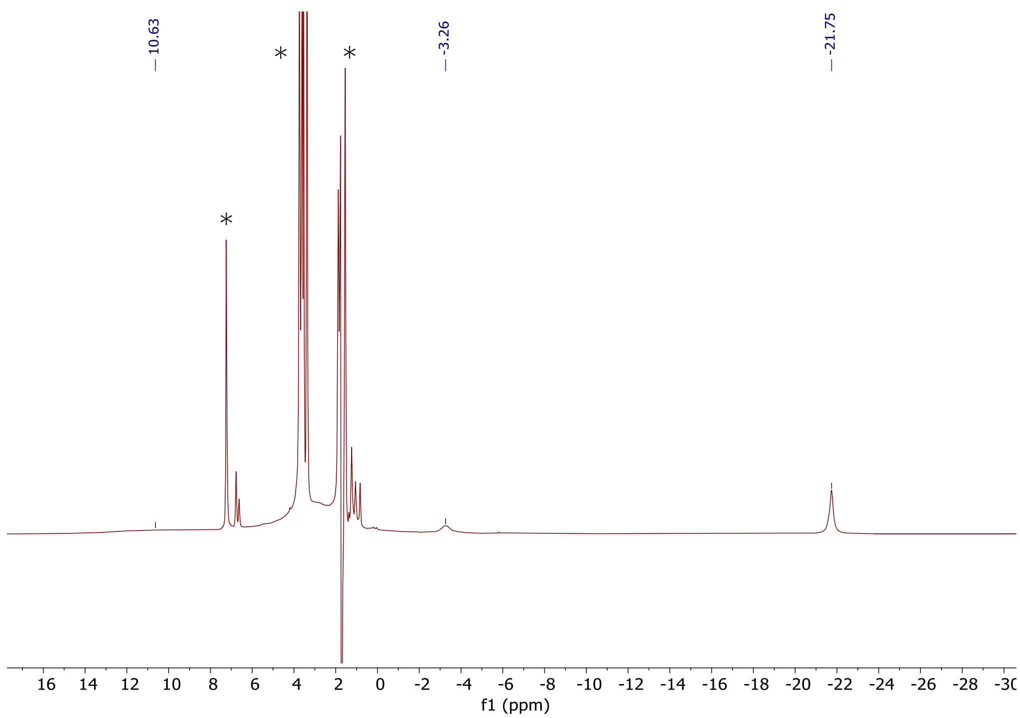

Figure 2.S18. ^{1}H NMR (400 MHz, THF-h_8, solvent suppression) spectrum of **2.9-W-red**. Solvent peaks are indicated by asterisks (*).

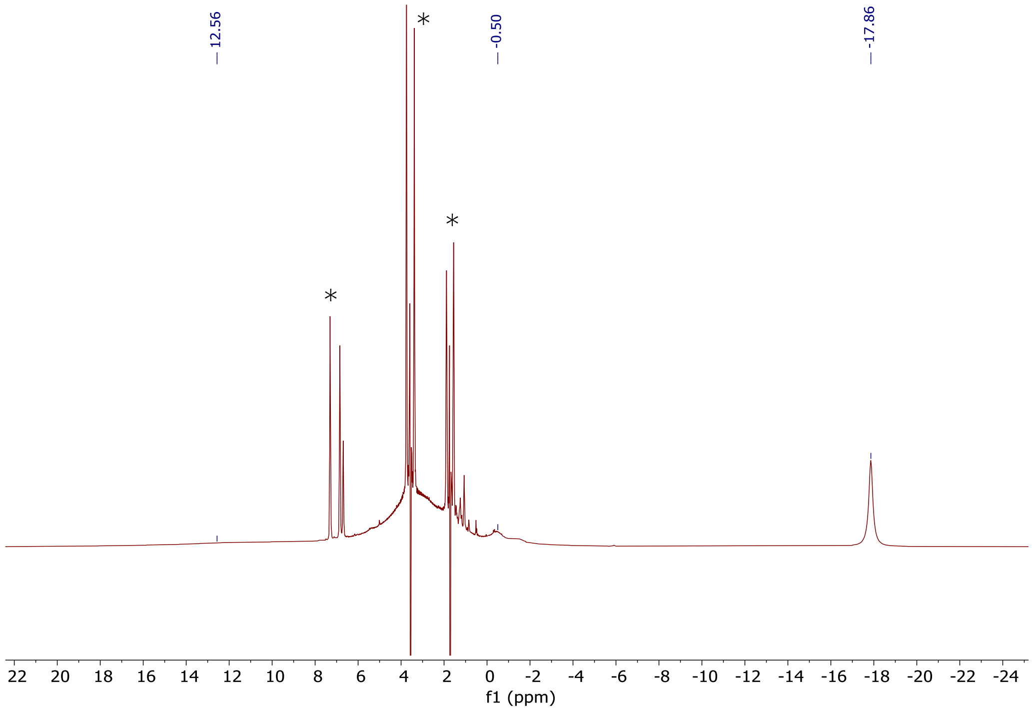

Figure 2.S19. ^{1}H NMR (400 MHz, THF-h_8, solvent suppression) spectrum of **2.9-Mo-red**. Solvent peaks are indicated by asterisks (*).

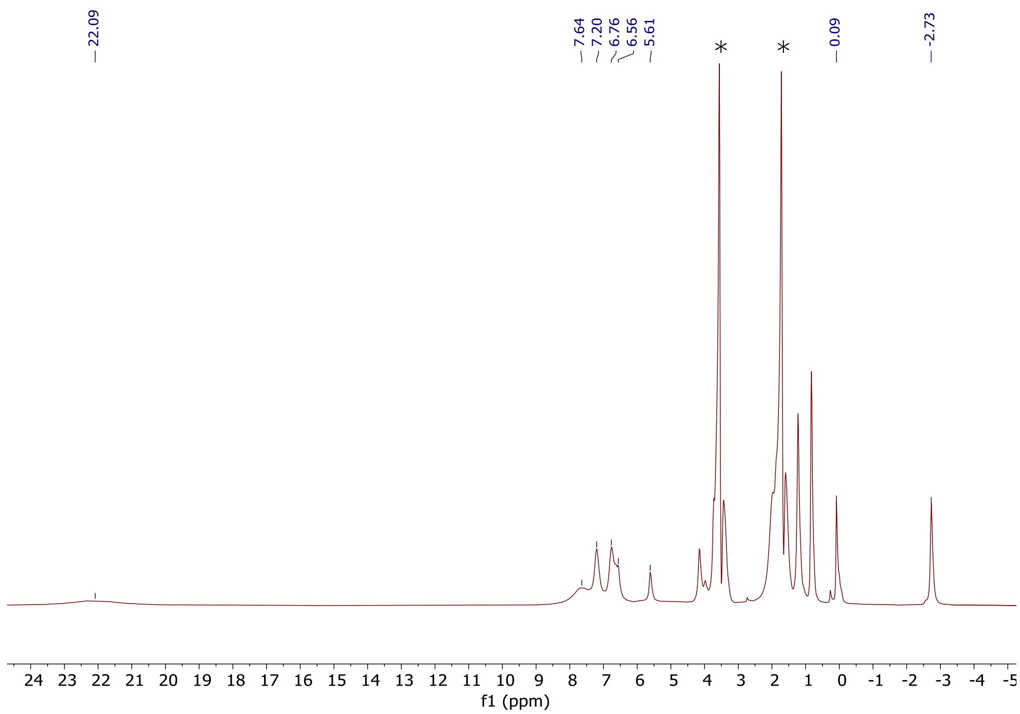

Figure 2.S20. ^{1}H NMR (400 MHz, THF-h_8, solvent suppression) spectrum of **2.10**. Solvent peaks are indicated by asterisks (*).

B) Electrochemical information

1. Electrochemical measurements:

Cyclic voltammetry experiments were performed with a Pine Instrument Company AFCBP1 biopotentiostat with the *AfterMath* software package. All measurements were performed in a three-electrode cell, which consisted of glassy carbon (working; ⌀ = 3.0 mm), Ag wire (reference), and bare Pt wire (counter), in a N_2-filled MBraun glovebox at room temperature. Dry CH_3CN that contained ~0.2 M $[Bu_4N][PF_6]$ was used as the electrolyte solution. Redox potentials are reported relative to the ferrocene/ferrocenium redox wave (Fc/Fc^+; ferrocene added as an internal standard). The open circuit potential was measured prior to each voltammogram being collected. Voltammograms were scanned reductively in order to minimize the oxidative damage that was frequently observed on scanning more oxidatively.

2. Additional electrochemical plots:

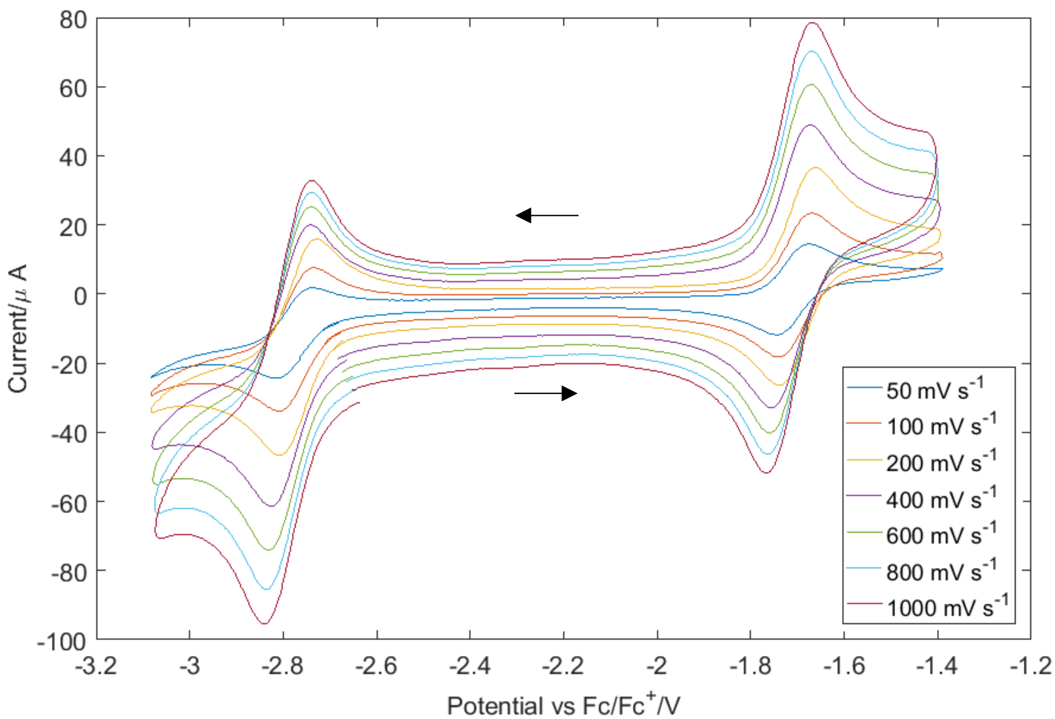

Figure 2.S21. CV of **2.4-W** at different scan rates, showing the two most negative redox events.

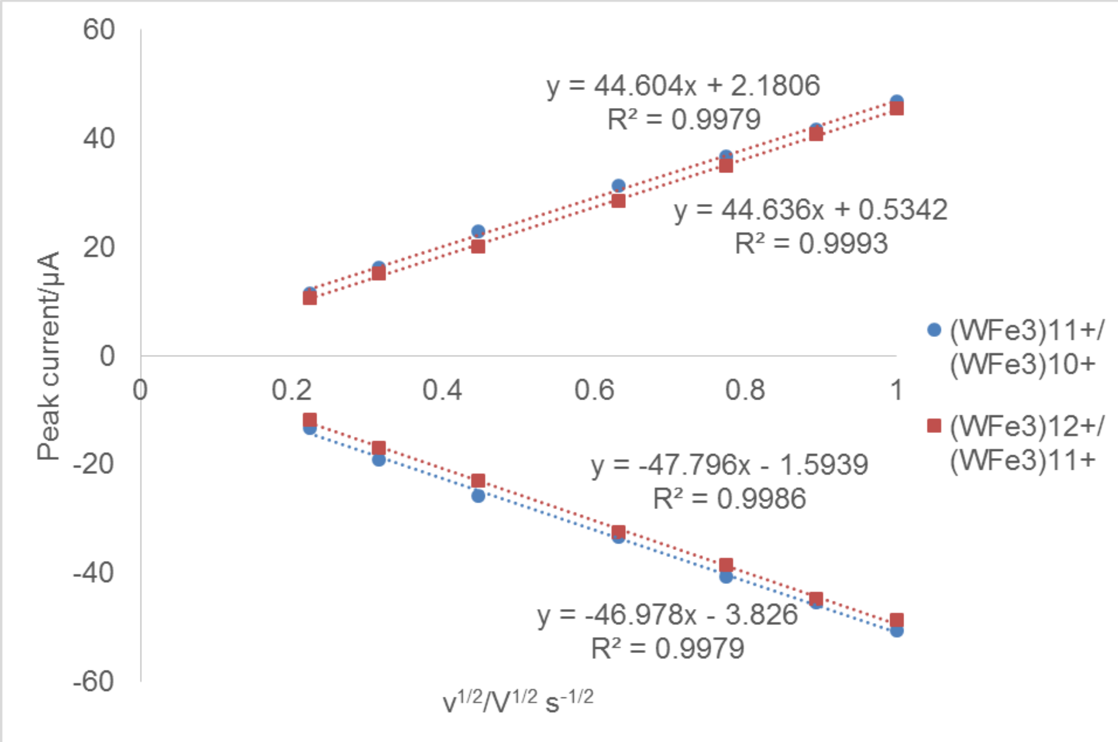

Figure 2.S22. Peak current vs. square root of scan rate for the two most negative redox features in **2.4-W**.

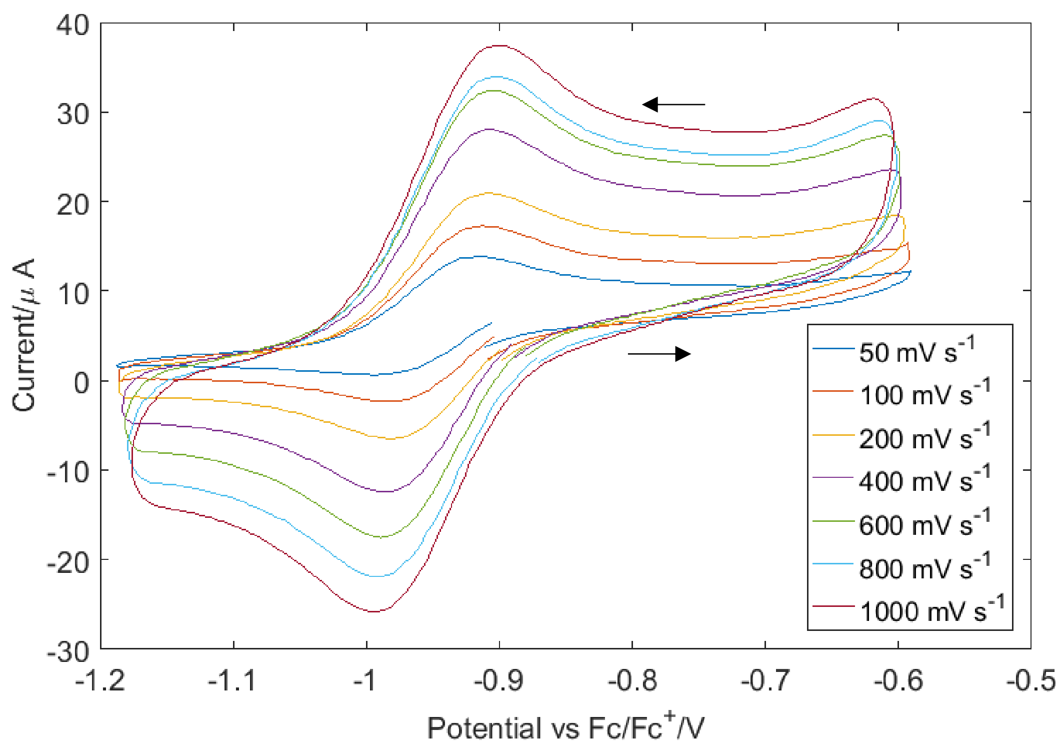

Figure 2.S23. CV of **2.4-W** at different scan rates for the most positive redox event.

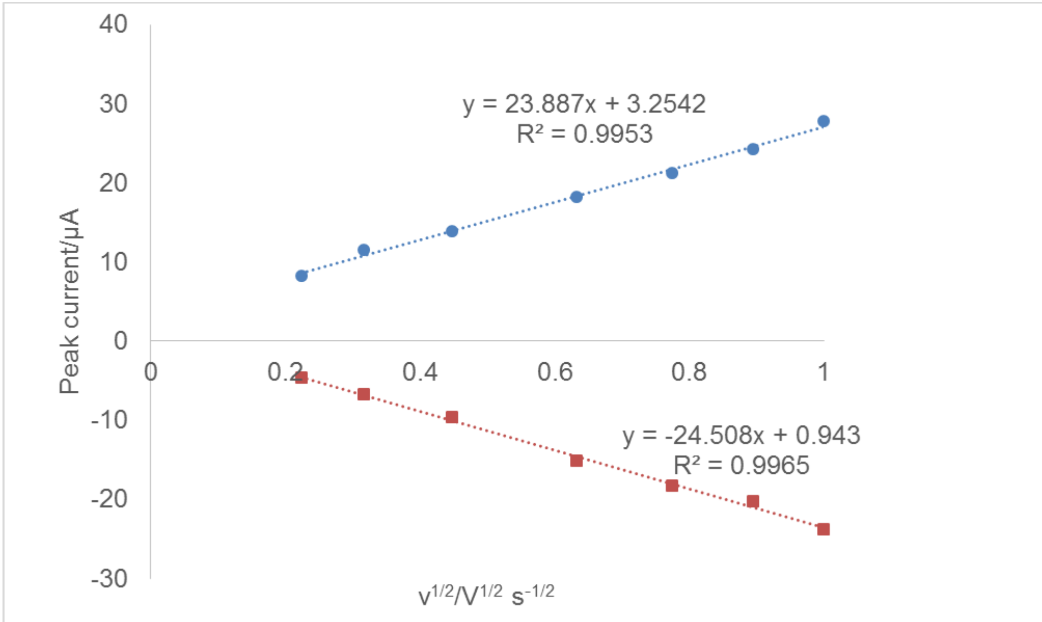

Figure 2.S24. Peak current vs. square root of scan rate for the most positive redox feature in **2.4-W**.

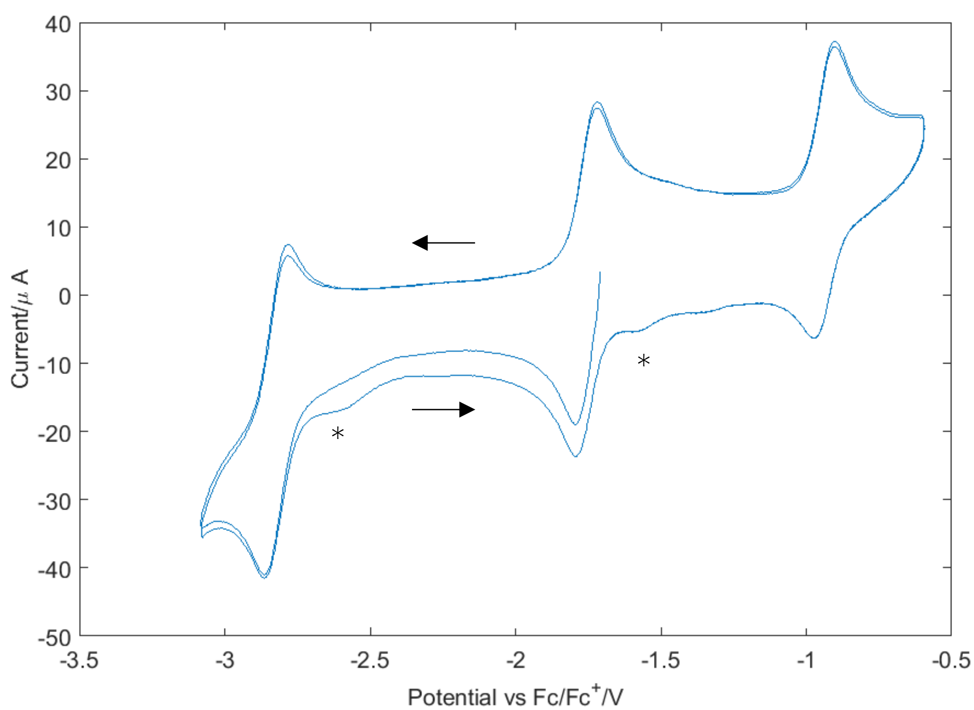

Figure 2.S25. CV of **2.4-W** including all 3 redox events at 200 mV s^{-1}. Note the appearance of decomposition products marked by asterisks (*), compared to CVs with only the two most negative redox events.

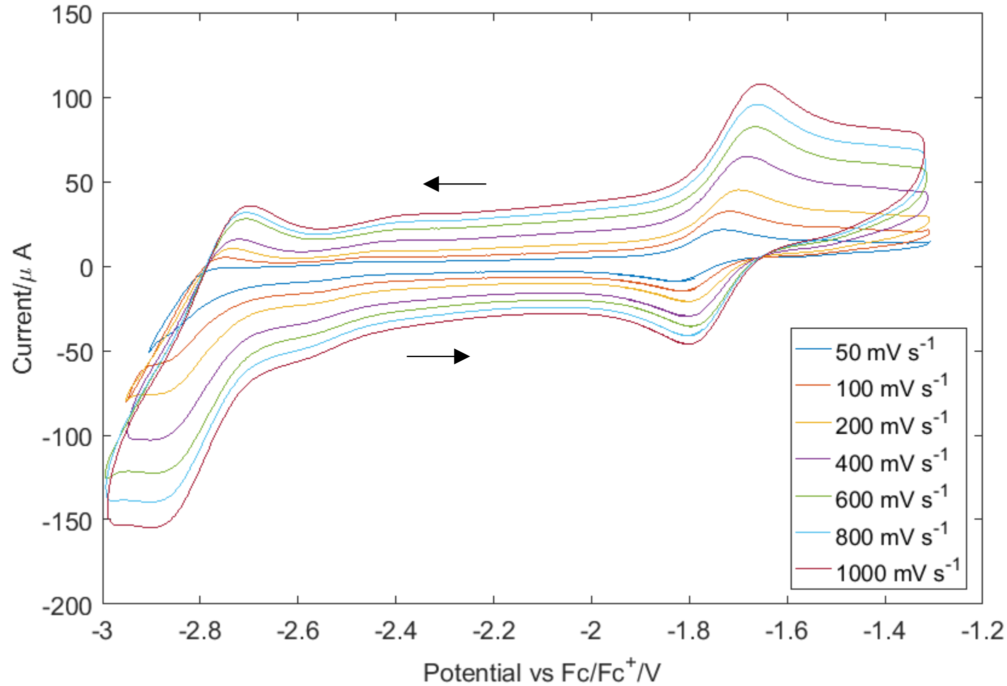

Figure 2.S26. CV of **2.4-Mo** at different scan rates, showing the two most negative redox events.

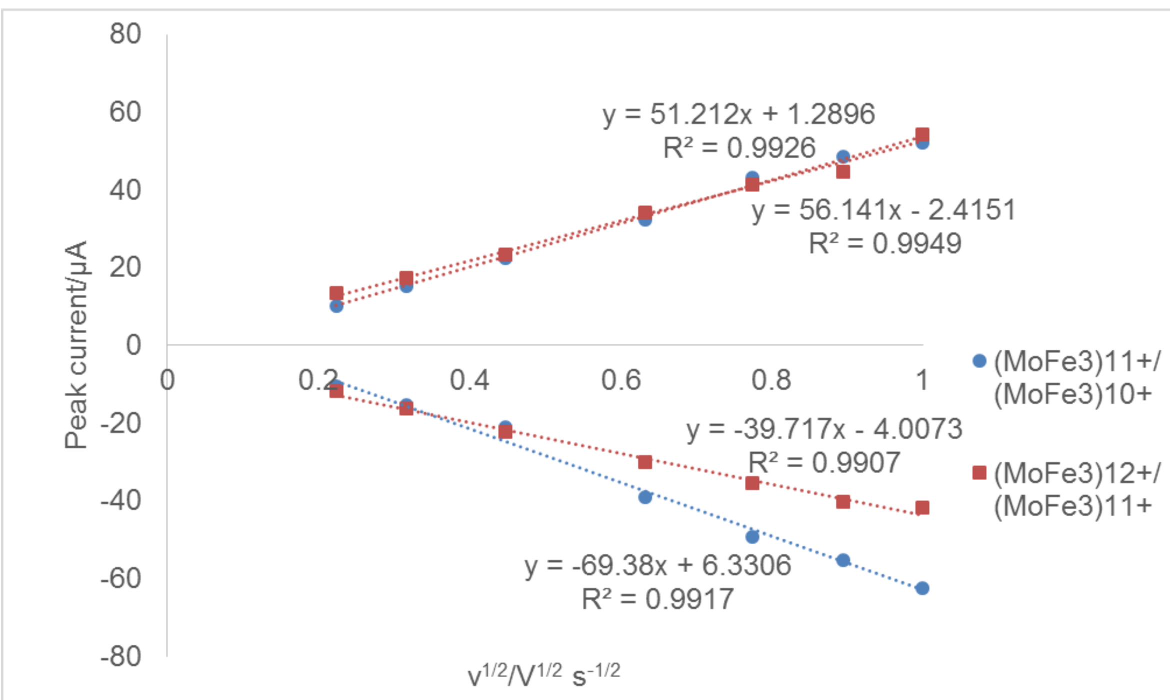

Figure 2.S27. Peak current vs. square root of scan rate for the two most negative redox features in **2.4-Mo**.

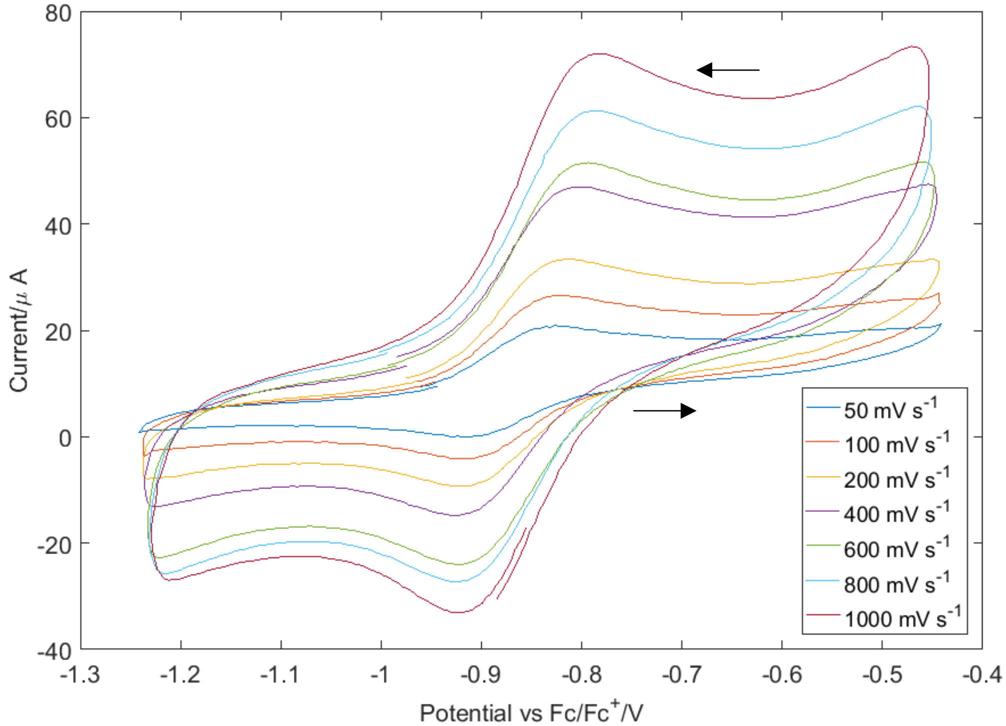

Figure 2.S28. CV of **2.4-Mo** at different scan rates for the most positive redox event.

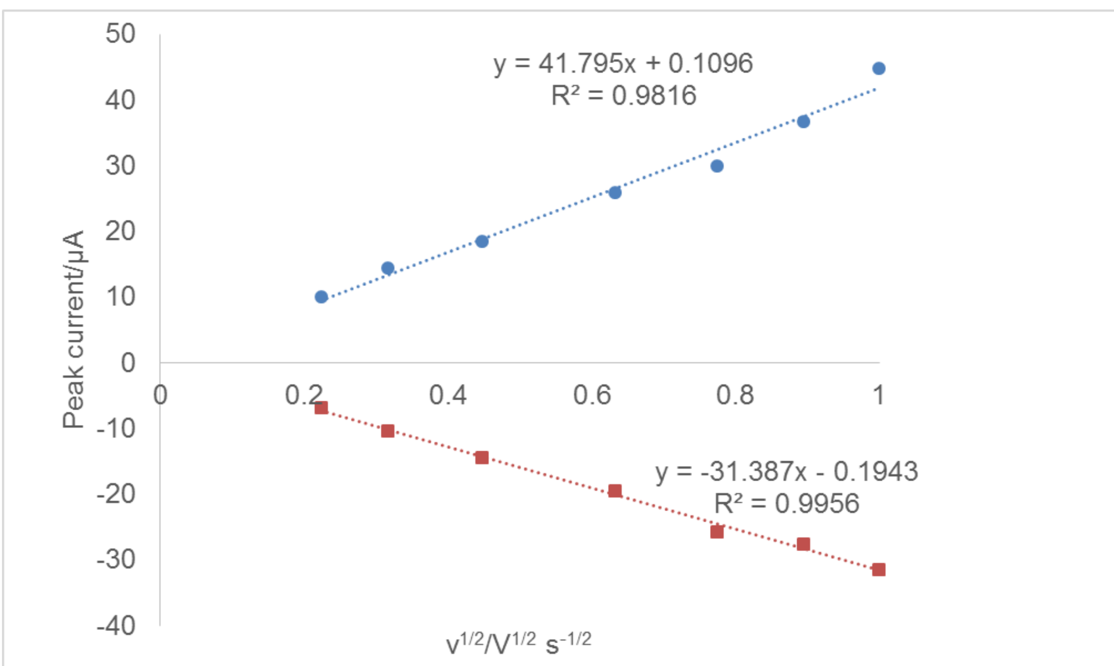

Figure 2.S29. Peak current vs. square root of scan rate for the most positive redox feature in **2.4-Mo**.

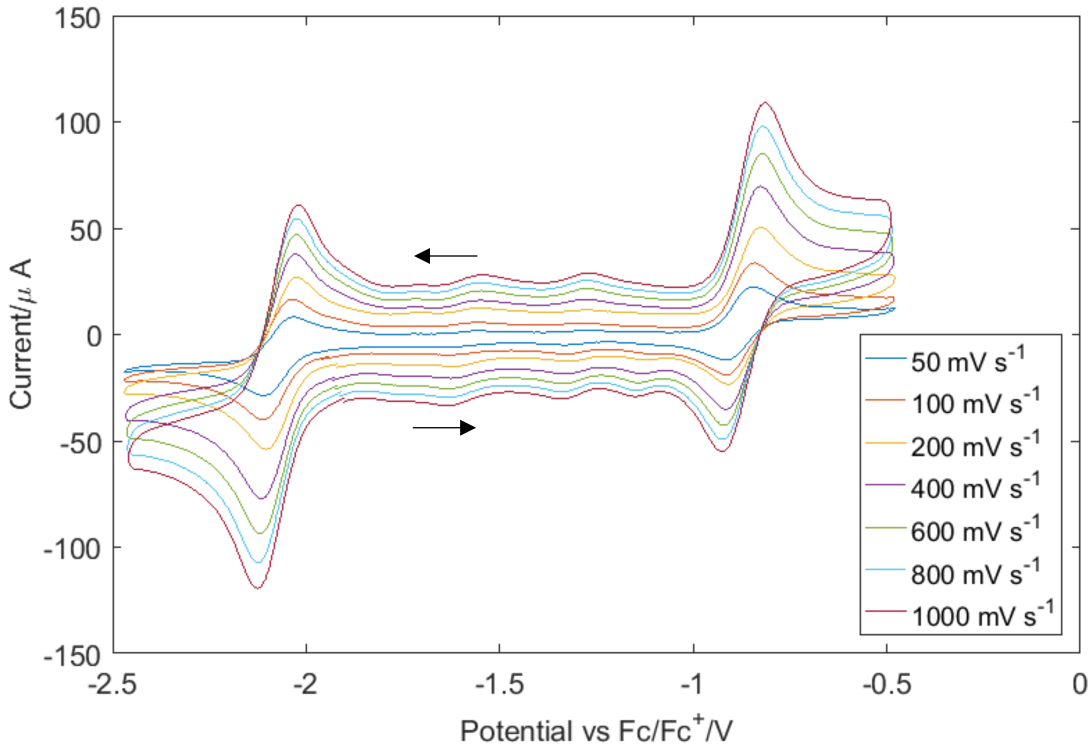

Figure 2.S30. CV of **2.5** at different scan rates.

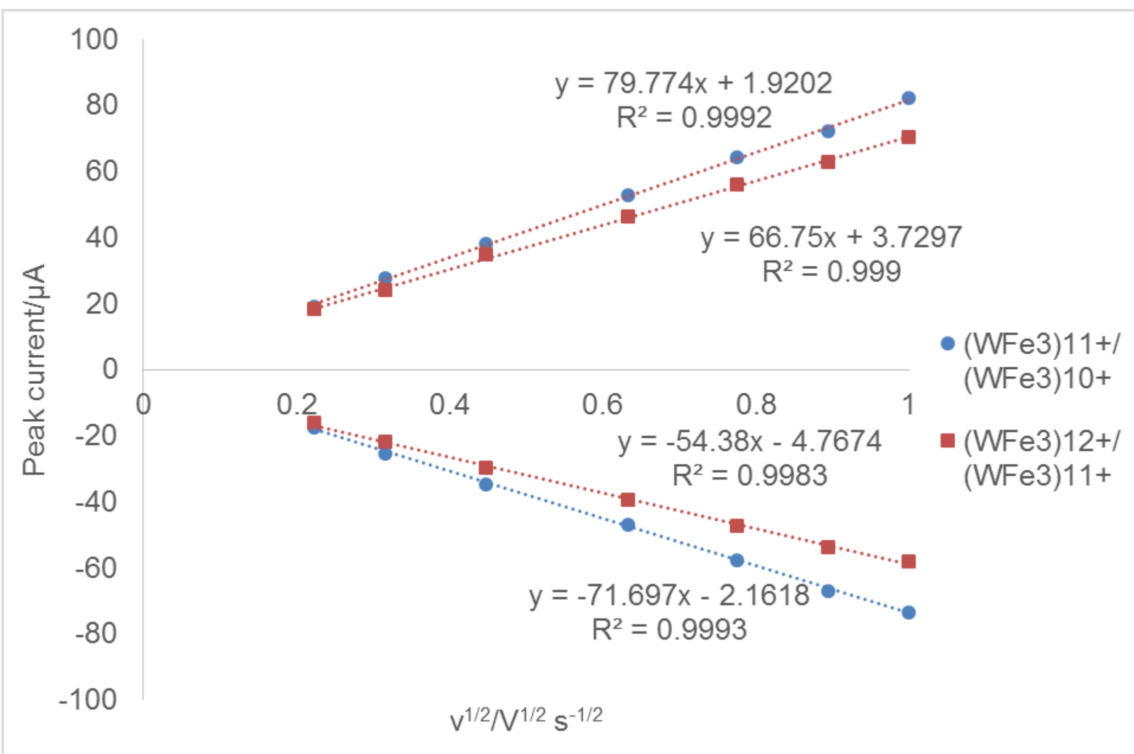

Figure 2.S31. Peak current vs. square root of scan rate for the redox features in **2.5**.

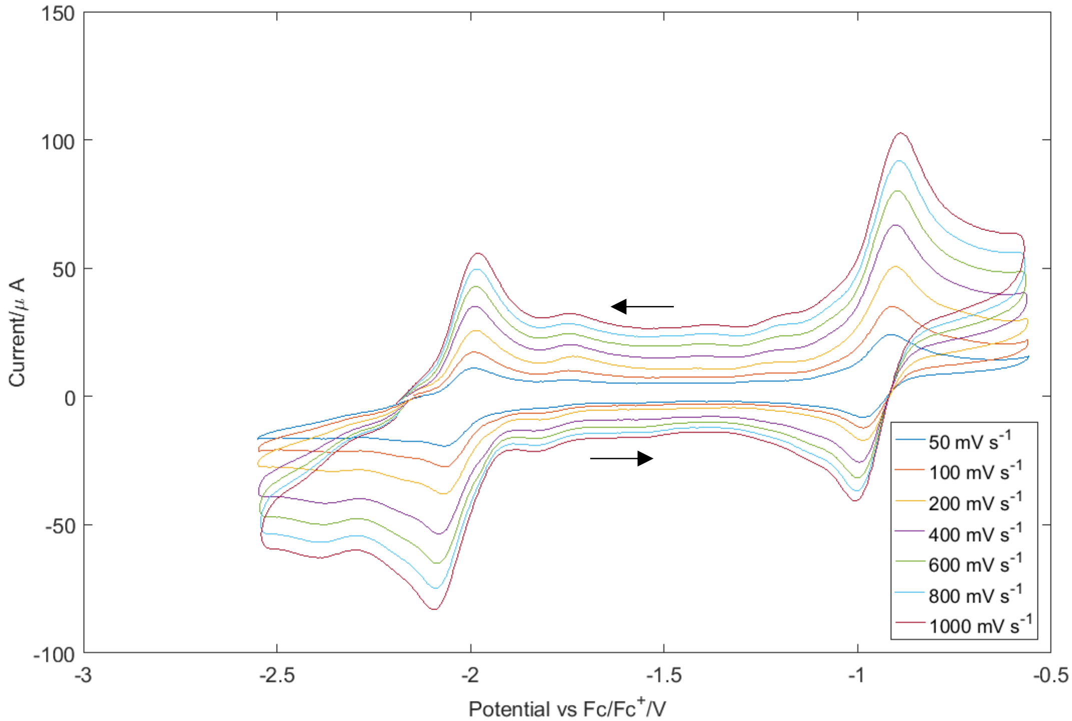

Figure 2.S32. CV of **2.6** at different scan rates.

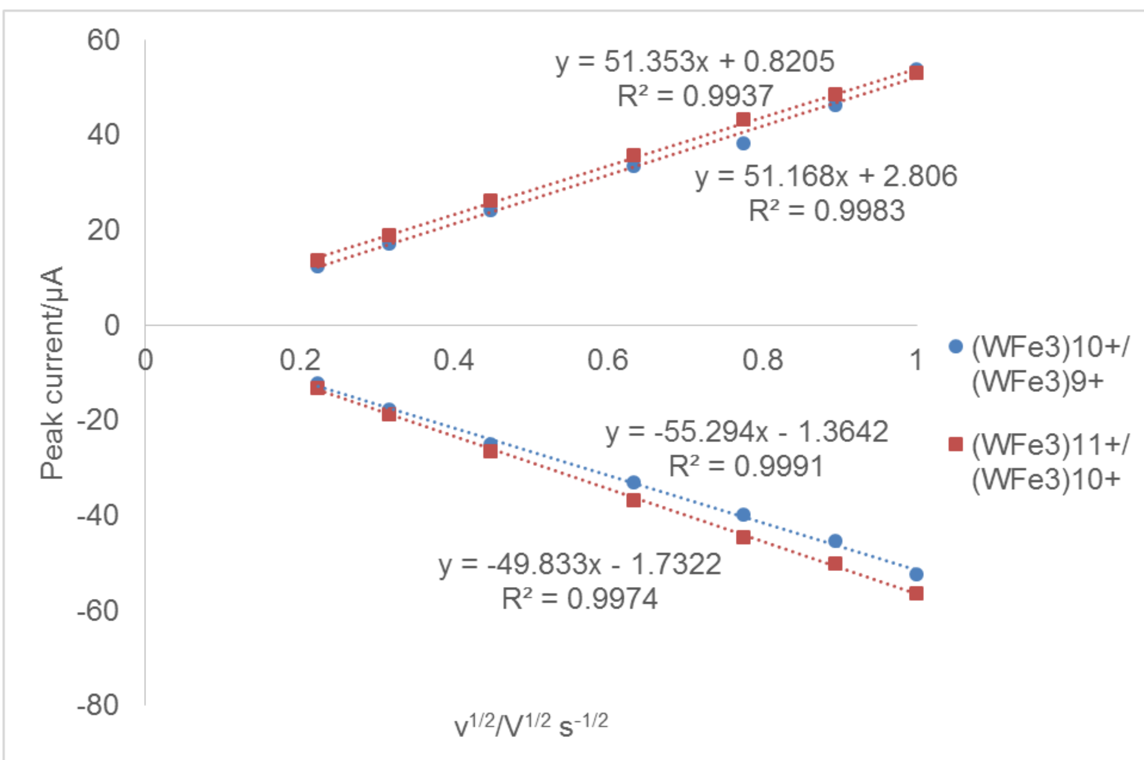

Figure 2.S33. Peak current vs. square root of scan rate for the redox features in **2.6**.

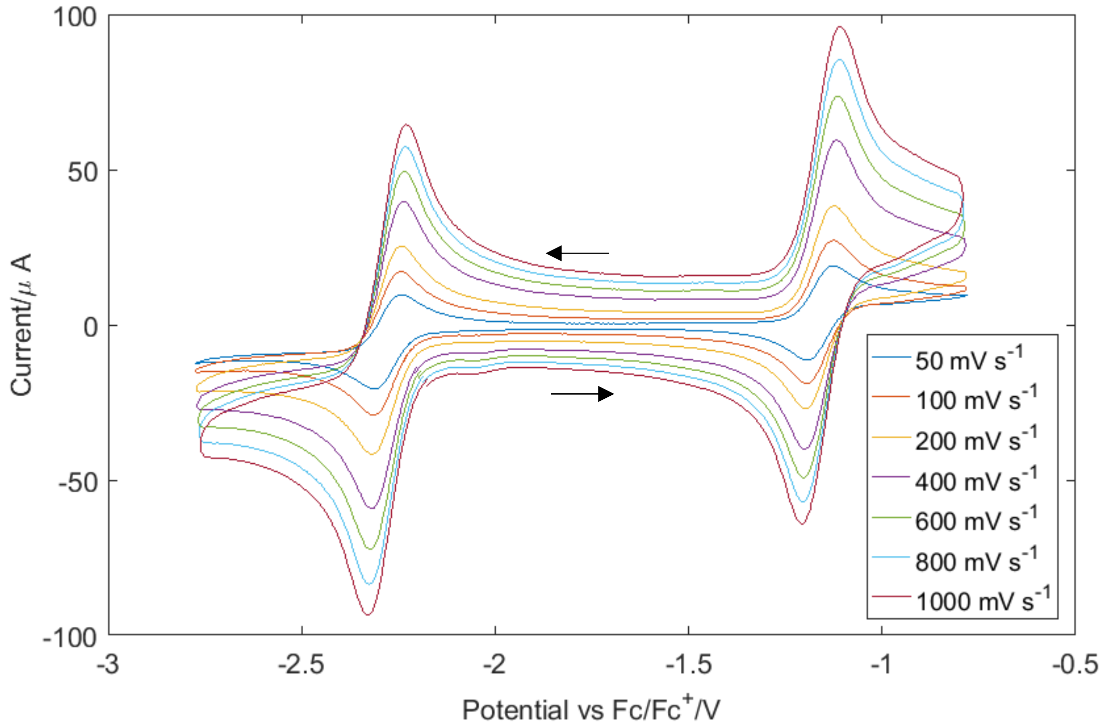

Figure 2.S34. CV of **2.7** at different scan rates.

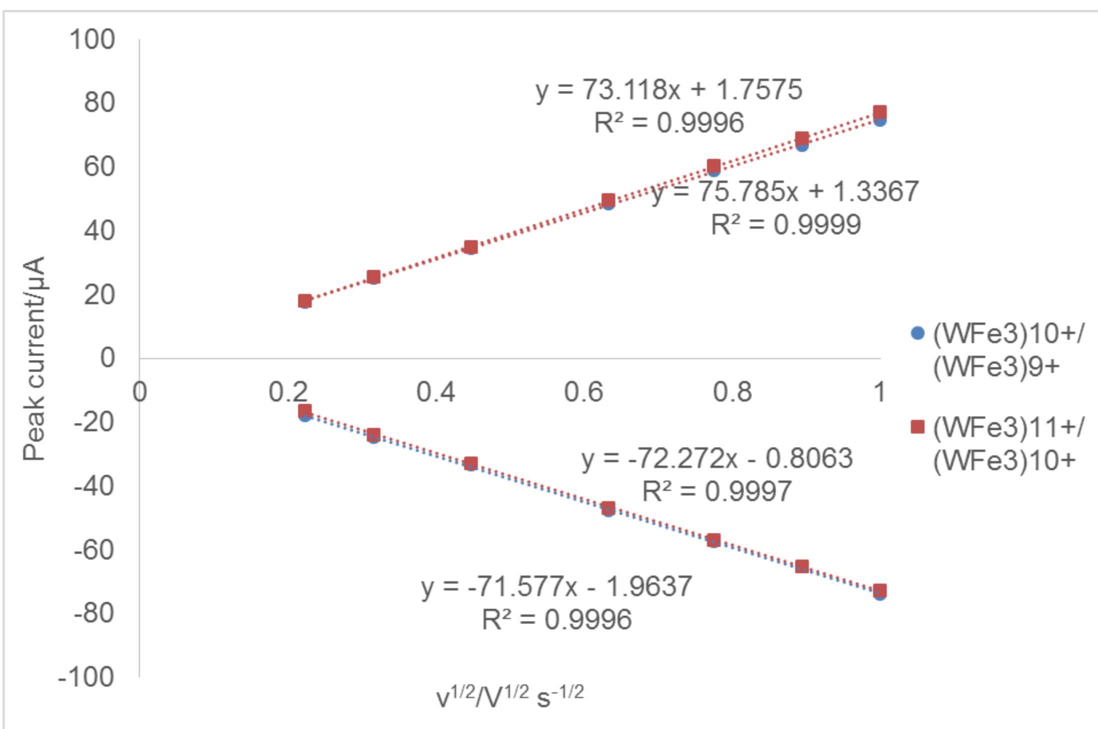

Figure 2.S35. Peak current vs. square root of scan rate for the redox features in **2.7**.

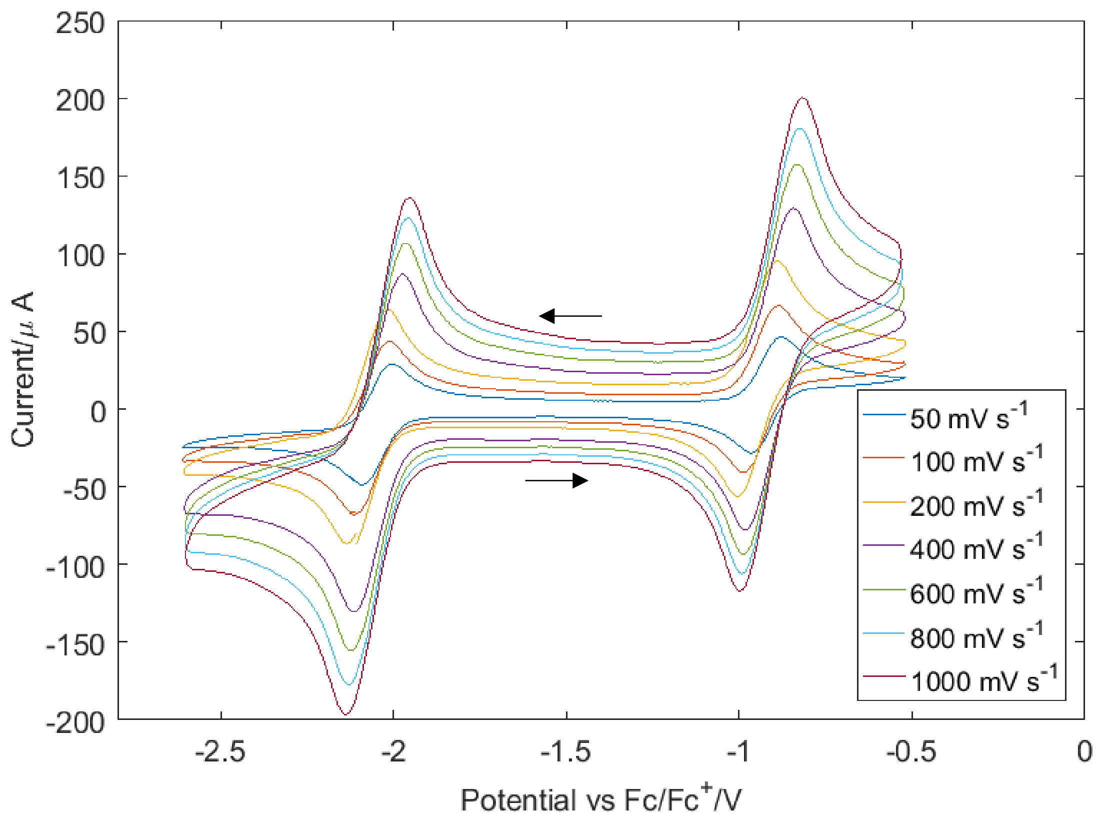

Figure 2.S36. CV of **2.8** at different scan rates.

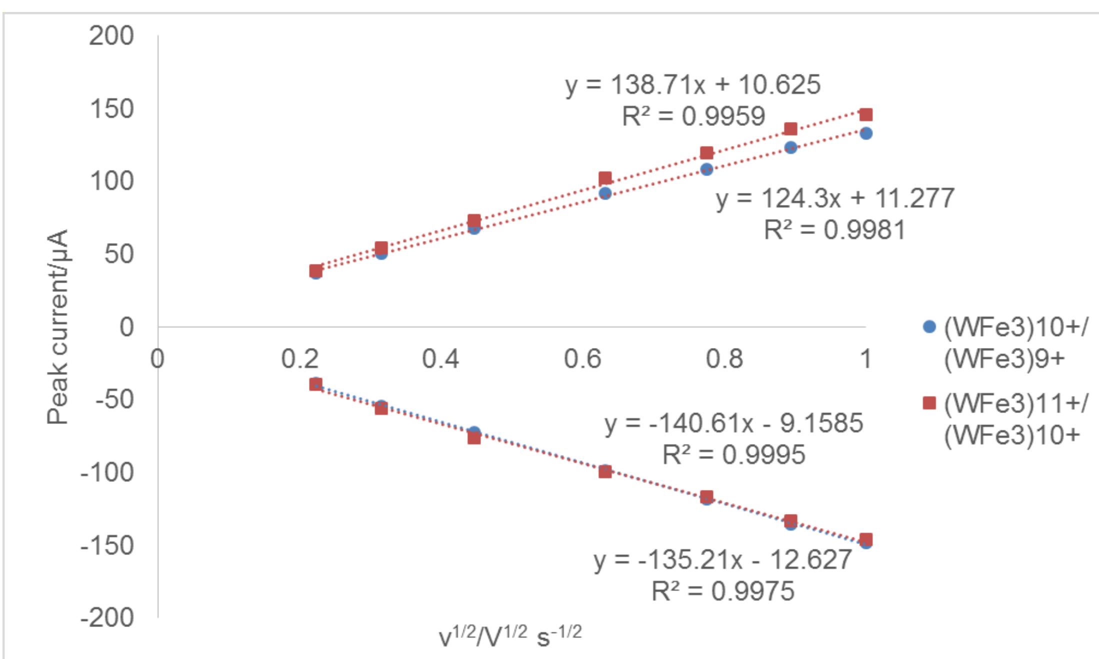

Figure 2.S37. Peak current vs. square root of scan rate for the redox features in **2.8**.

C) Crystallographic information

1. X-ray crystallography:

XRD data were collected at 100 K on a Bruker AXS D8 KAPPA or Bruker AXS D8 VENTURE diffractometer [microfocus sealed X-ray tube, λ(Mo Kα) = 0.71073 Å or λ(Cu Kα) = 1.54178 Å]. All manipulations, including data collection, integration, and scaling, were carried out using the Bruker *APEX3* software.[62] Absorption corrections were applied using *SADABS*.[63] Structures were solved by direct methods using *XS* (incorporated into *SHELXTL*),[64] *Sir92*[65] or *SUPERFLIP*[66] and refined using full-matrix least-squares on *CRYSTALS*[67] or *Olex2*[68] to convergence. All non-H atoms were refined using anisotropic displacement parameters. H atoms were placed in idealized positions and refined using a riding model. Because of the size of the compounds, most crystals included solvent-accessible voids that contained a disordered solvent. The solvent could be either modeled satisfactorily or accounted for using either the *SQUEEZE* procedure in the *PLATON* software package,[69] or a solvent mask in *Olex2*.[68]

2. Additional information:

Special refinement details for **2.1-Mo**. The asymmetric unit contains three co-crystallized acetonitrile molecules, whose disorder across the infinite rotation axis could not be modelled satisfactorily. Therefore, a solvent mask was calculated in *Olex2*[68] whereby 60 electrons were found in a volume of 67 Å^3, consistent with the presence of 3[C_2H_3N] per asymmetric unit.

Special refinement details for **2.2-W**. The asymmetric unit of the structure contains five co-crystallized THF solvent molecules. Bond lengths restraints and similarity restraints for anisotropic displacement parameters (ADPs) were applied to one THF molecule to obtain a stable model. When refined freely, atom C31 on one ^{i}Pr moiety becomes unstable and physically unreasonable in terms of ADPs, so similarity restraints were applied for the ADPs of atoms C30 – C32 on that ^{i}Pr group.

Special refinement details for **2.2-Mo**. The asymmetric unit of the structure contains diffuse solvent peaks, which could not be modelled satisfactorily. Therefore, the electron density for co-crystallized solvent molecules were accounted for using the *SQUEEZE* procedure in *PLATON*,[69] whereby 1000 electrons were found in a volume of 4699 Å^3, consistent with the presence of 3[$C_4H_{10}O$] in the asymmetric unit.

Special refinement details for **2.3**. The asymmetric unit of the structure contains one co-crystallized THF solvent molecule, which is disordered over two positions with occupancies of 60% and 40%. The BPh_4 counteranion is also disordered over two positions, with occupancies of 45% and 55%.

Special refinement details for **2.4-W**. The asymmetric unit of the structure contains diffuse solvent peaks, which could not be modeled satisfactorily. Therefore, the electron density for co-crystallized solvent molecules were accounted for using the *SQUEEZE* procedure in *PLATON*,[69] whereby 2312 electrons were found in a volume of 14735 Å^3, consistent with the presence of 3[C_5H_{12}] in the asymmetric unit.

Special refinement details for **2.4-Mo**. The asymmetric unit of the structure contains two co-crystallized THF solvent molecules. One THF molecule is disordered over two positions, with occupancies of 69% and 31%. One BAC ligand is also disordered over two positions, with occupancies of 64% and 36%.

Special refinement details for **2.6**. The asymmetric unit of the structure contains one co-crystallized Et_2O solvent molecule, which could be modeled with geometric and ADP restraints. The remaining solvent molecules are heavily disordered and could not be modeled satisfactorily. Therefore, the electron density for co-crystallized solvent molecules were accounted for using the *SQUEEZE* procedure in *PLATON*,[69] whereby 50 electrons were found in a volume of 540 Å^3, consistent with the presence of 0.5[$C_4H_{10}O$] in the asymmetric unit.

Special refinement details for **2.7**. The asymmetric unit of the structure contains three co-crystallized THF and 1 Et_2O solvent molecules. Bond lengths restraints and similarity restraints for ADPs were applied to the Et_2O molecule to obtain a stable model.

Special refinement details for **2.8**. The asymmetric unit of the structure contains highly disordered solvent molecules, which could not be modeled satisfactorily. Therefore, the electron density for co-crystallized solvent molecules were accounted for using the *SQUEEZE* procedure in *PLATON*,[69] whereby 662 electrons were found in a volume of 2495 Å^3, consistent with the presence of $4[C_4H_{10}O]$ in the asymmetric unit. One N^iPr_2 group is disordered over two positions, with occupancy of 50% each.

Special refinement details for **2.9-W**. The asymmetric unit of the structure contains two co-crystallized Et_2O and 1.5 C_6H_6 solvent molecules that could be modeled with geometric and ADP restraints. The remaining solvent molecules are highly disordered, which could not be modeled satisfactorily. Therefore, the electron density for co-crystallized solvent molecules were accounted for using the *SQUEEZE* procedure in *PLATON*,[69] whereby 72 electrons were found in a volume of 235 $Å^3$, consistent with the presence of $1[C_4H_{10}O]$ in the asymmetric unit.

Special refinement details for **2.9-W-red**. The asymmetric unit of the structure contains 1/3 of a cluster and one co-crystallized pentane solvent molecule, which could be modeled with geometric and ADP restraints. The remaining solvent molecules are highly disordered, which could not be modeled satisfactorily. Therefore, the electron density for co-crystallized solvent molecules were accounted for using the *SQUEEZE* procedure in *PLATON*,[69] whereby 316 electrons were found in a volume of 1788 $Å^3$, consistent with the presence of $0.5[C_5H_{12}]$ in the asymmetric unit.

Special refinement details for **2.9-Mo-red**. The asymmetric unit of the structure contains four co-crystallized benzene solvent molecules, which could be modeled with geometric and ADP restraints.

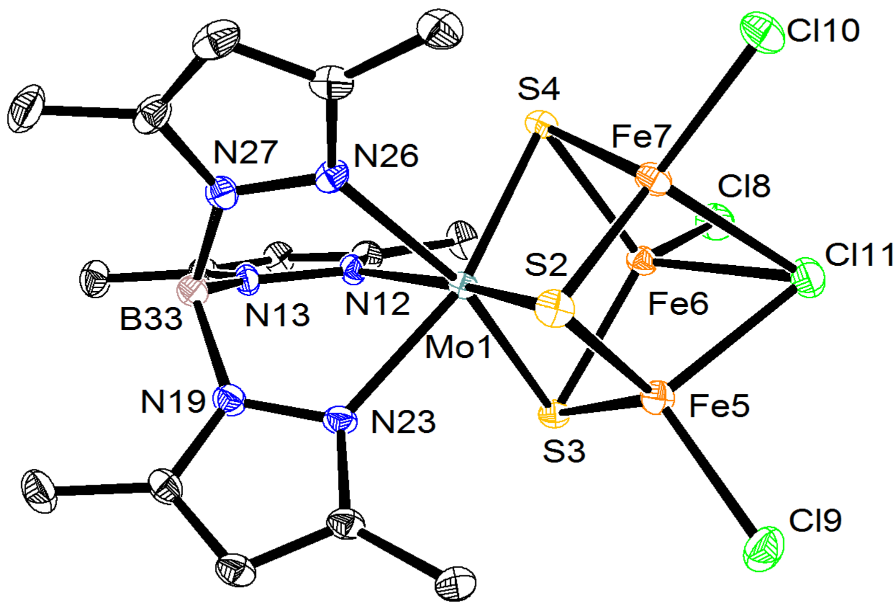

Figure 2.S38. Crystal structure of **2.1-Mo**. Ellipsoids are shown at 50% probability level. Hydrogen atoms, solvent molecules, and countercations are omitted for clarity.

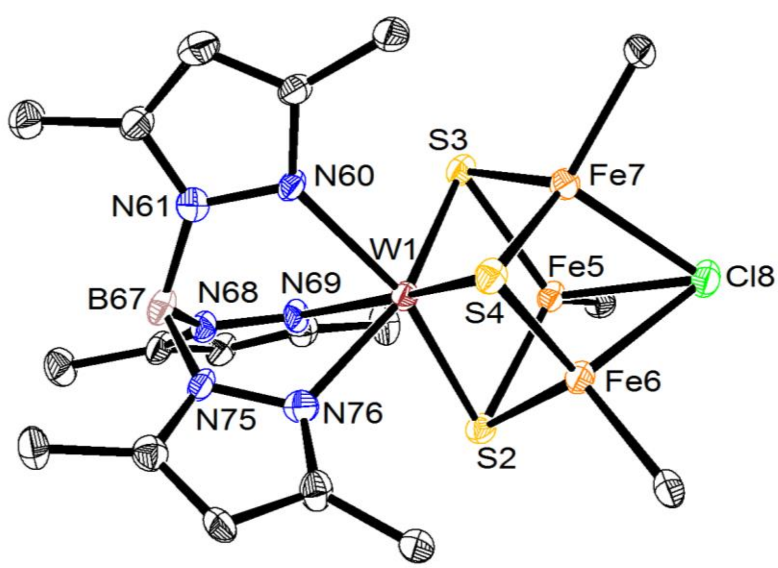

Figure 2.S39. Crystal structure of **2.2-W**. Ellipsoids are shown at 50% probability level. Hydrogen atoms, solvent molecules, counteranions, and the BAC ligand except for the carbene C are omitted for clarity.

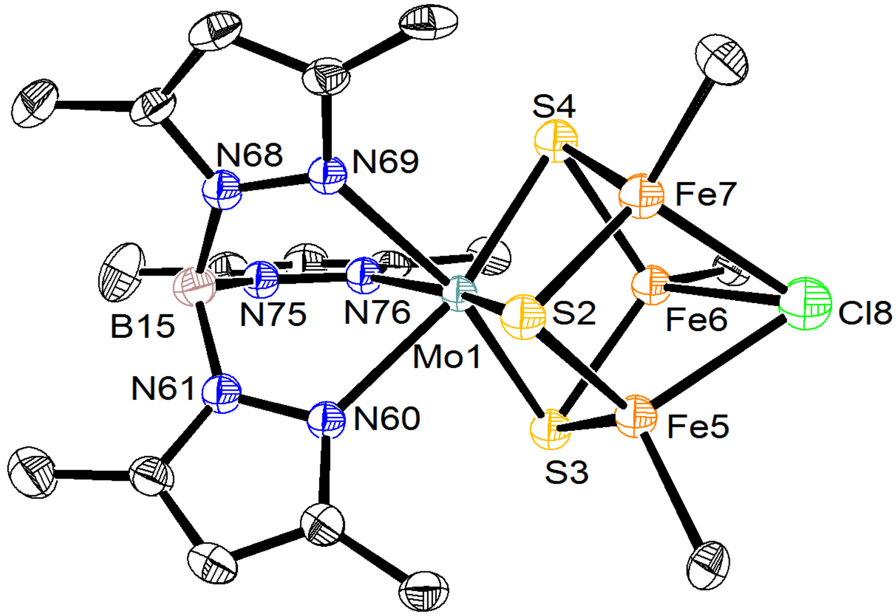

Figure 2.S40. Crystal structure of **2.2-Mo**. Ellipsoids are shown at 50% probability level. Hydrogen atoms, solvent molecules, counteranions, and the BAC ligand except for the carbene C are omitted for clarity.

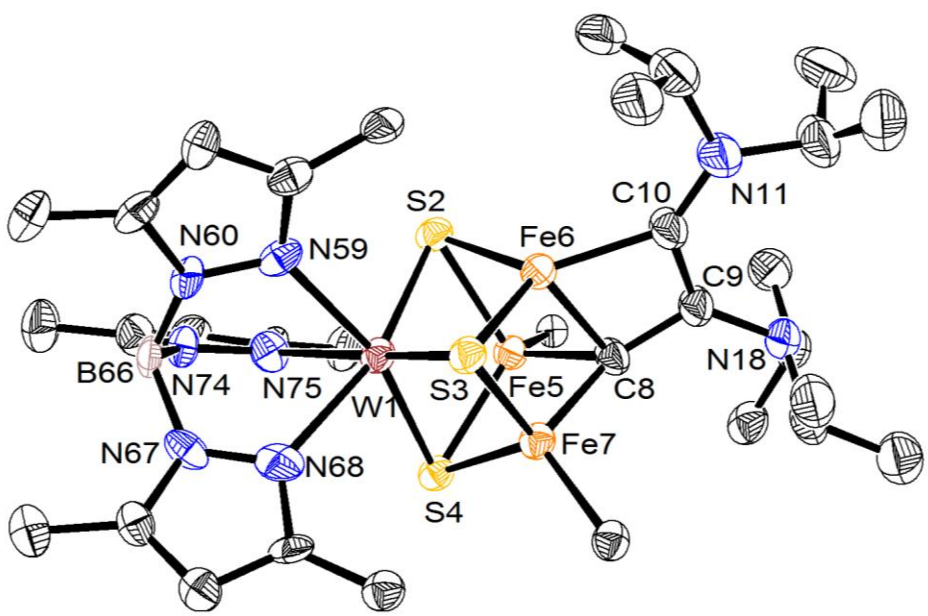

Figure 2.S41. Crystal structure of **2.4-W**. Ellipsoids are shown at 50% probability level. Hydrogen atoms and the BAC ligand except for the carbene C are omitted for clarity.

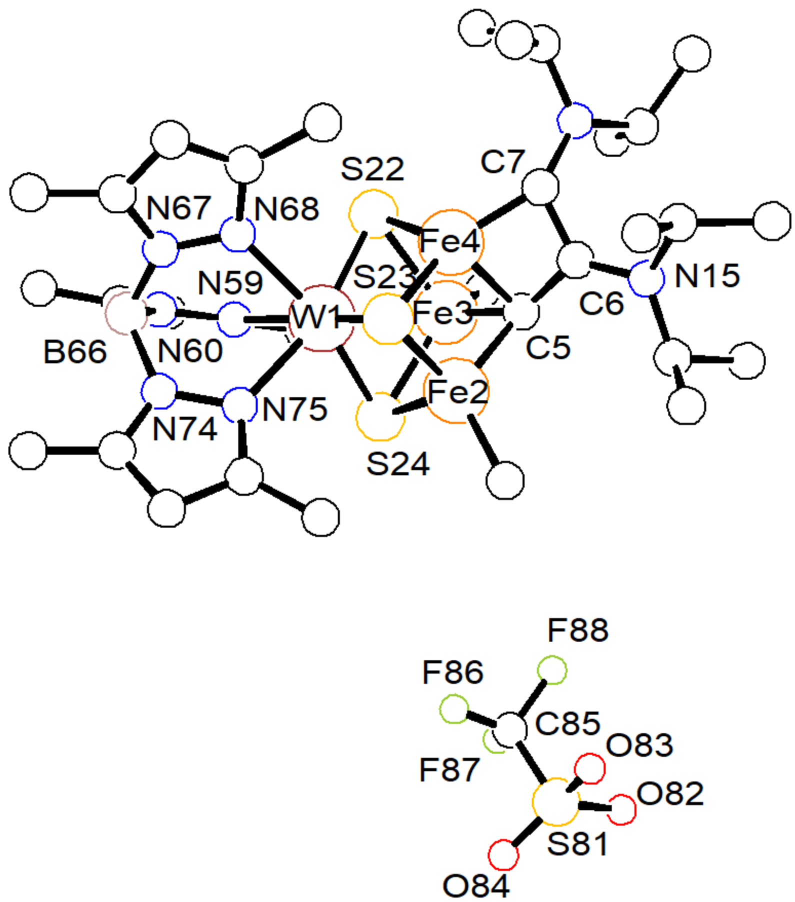

Figure 2.S42. Connectivity of of **[2.4-W][OTf]**. Spheres are shown at 50% probability level. Hydrogen atoms, solvent molecules, and the BAC ligand except for the carbene C are omitted for clarity.

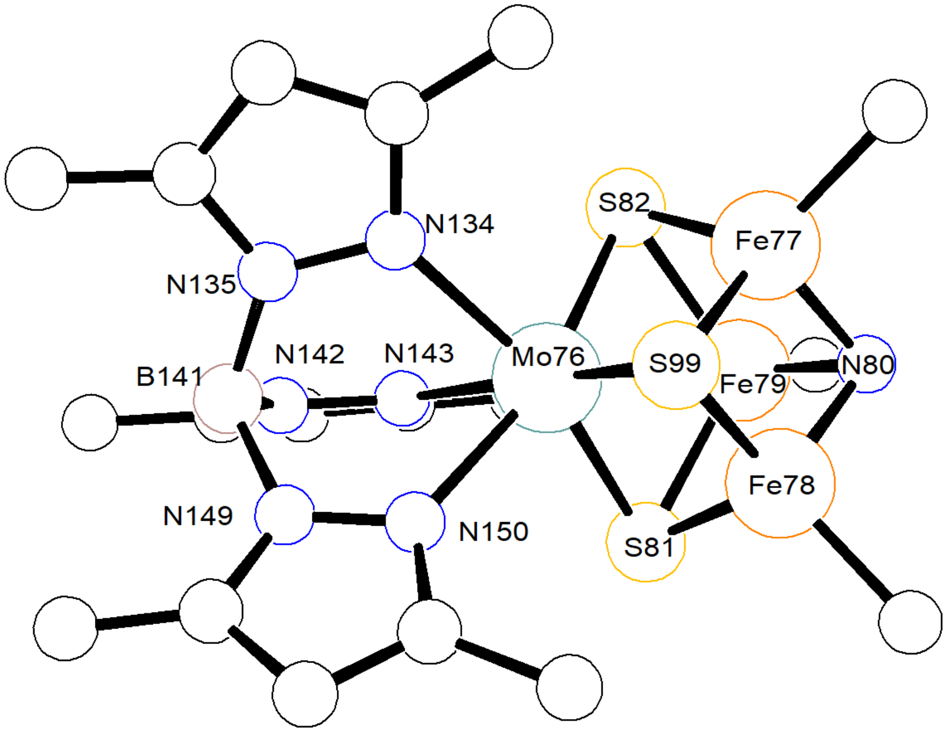

Figure 2.S43. Connectivity of **2.6-Mo**. Spheres are shown at 50% probability level. Hydrogen atoms, solvent molecules, and the BAC ligand except for the carbene C are omitted for clarity.

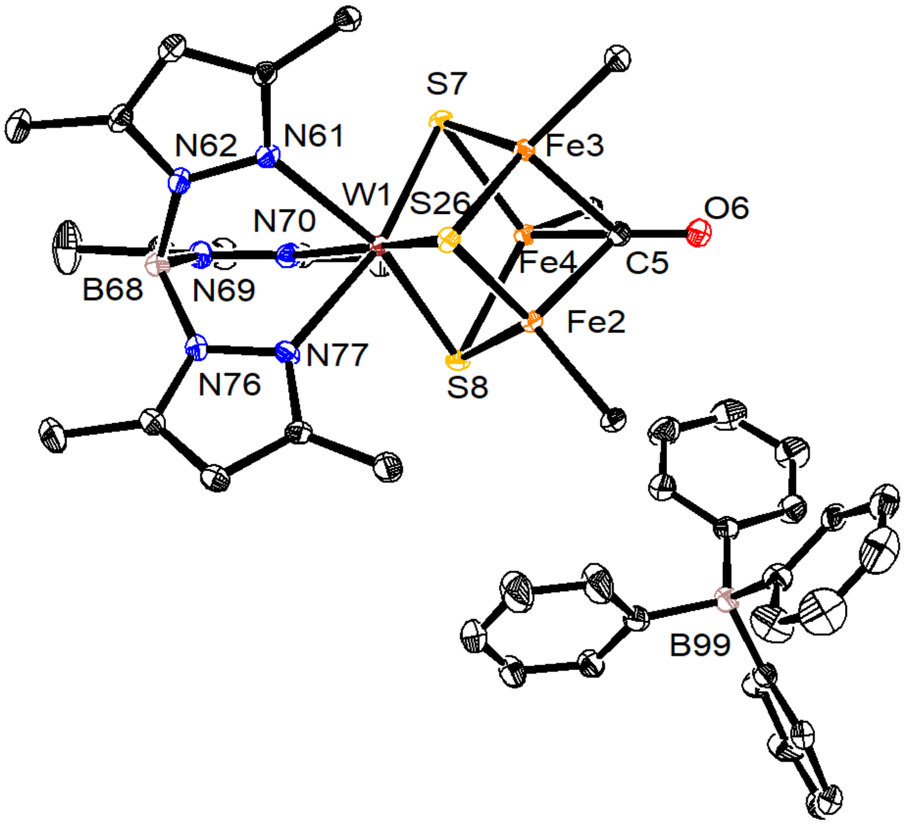

Figure 2.S44. Crystal structure of **2.9-W**. Ellipsoids are shown at 50% probability level. Hydrogen atoms, solvent molecules, and the BAC ligand except for the carbene C are omitted for clarity.

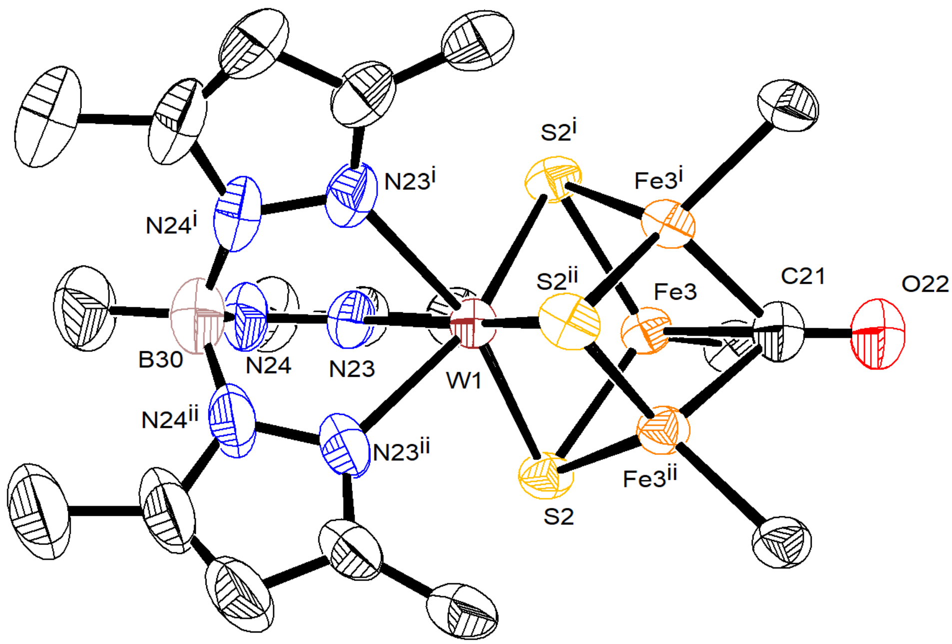

Figure 2.S45. Crystal structure of **2.9-W-red**. Ellipsoids are shown at 50% probability level. Hydrogen atoms, solvent molecules, and the BAC ligand except for the carbene C are omitted for clarity.

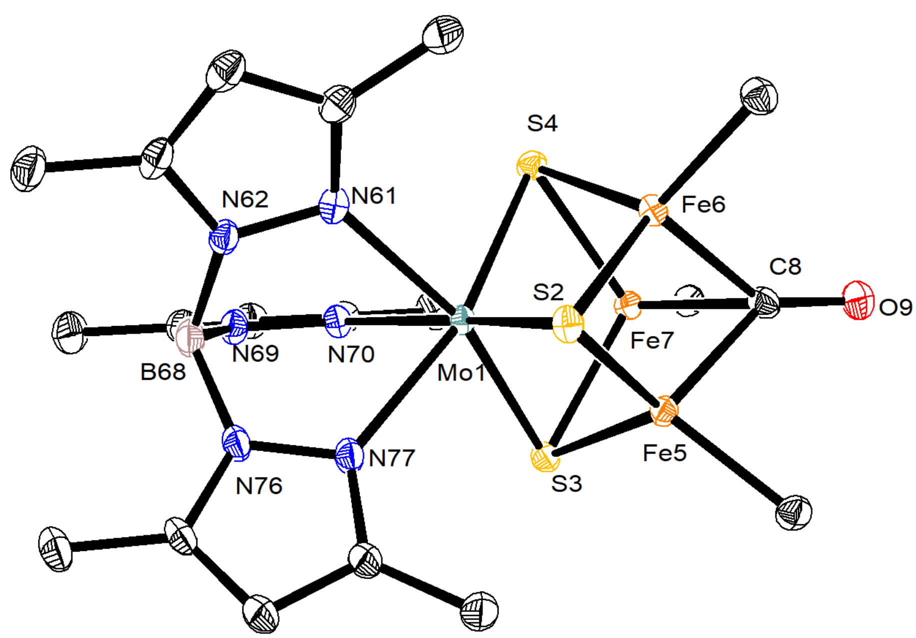

Figure 2.S46. Crystal structure of **2.9-Mo-red**. Ellipsoids are shown at 50% probability level. Hydrogen atoms, solvent molecules, and the BAC ligand except for the carbene C are omitted for clarity.

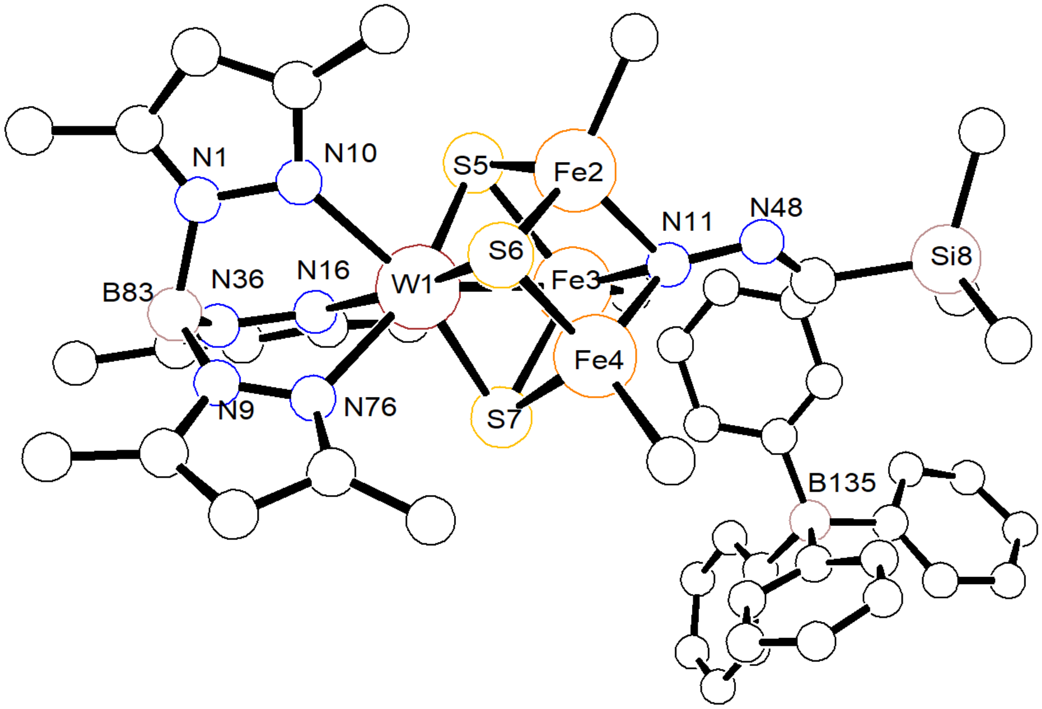

Figure 2.S47. Connectivity of **2.10**. Spheres are shown at 50% probability level. Hydrogen atoms, solvent molecules, and the BAC ligand except for the carbene C are omitted for clarity.

Table 2.S1. Summary of statistics for diffraction data for **2.1** to **2.3**

Cluster	**2.1-Mo**	**2.2-W**	**2.2-Mo**	**2.3**
CCDC	2084246	2081620	2084269	2081619
Empirical formula	$C_{31}H_{62}BCl_4Fe_3MoN_8S_3$	$C_{104}H_{166}B_2ClFe_3N_{12}O_5SW$	$C_{84}H_{126}B_2ClFe_3MoN_{12}S_3$	$C_{88}H_{134}B_2Fe_3N_{12}OS_3W$
Formula weight	1059.16	2169.22	1720.71	1845.32
Temperature/K	100	100	100	100
Crystal system	Tetragonal	Monoclinic	Monoclinic	Triclinic
Space group	I4	$P2_1/c$	C2/c	P-1
a/Å	27.911(5)	11.6866(11)	34.166(4)	17.663(2)
b/Å	27.911(5)	23.432(2)	18.991(2)	17.720(2)
c/Å	11.774(4)	40.384(3)	34.269(7)	20.505(3)
α/°	90	90	90	92.992(4)
β/°	90	90.747(7)	110.407(5)	101.822(4)
γ/°	90	90	90	119.269(3)
Volume/Å^3	9172(4)	11057.7(18)	20840(5)	5392.0(12)
Z	8	4	8	2
ρ_{calc}/g cm^{-3}	1.534	1.30	1.097	1.14
μ/mm^{-1}	1.599	6.135	5.357	1.559
F(000)	4360	4564	7272	1928
Crystal size/mm^3	0.28 × 0.04 × 0.04	0.17 × 0.27 × 0.33	0.23 × 0.15 × 0.05	0.04 × 0.25 × 0.26
Radiation	Mo Kα	Cu Kα	Cu Kα	Mo Kα
θ_{max}/°	34.988	79.7254	77.576	32.1002
Index ranges	$-44 \le h \le 35$, $-43 \le k \le 43$, $-18 \le l \le 17$	$-14 \le h \le 14$ $-28 \le k \le 29$ $-50 \le l \le 51$	$-43 \le h \le 40$, $-21 \le k \le 23$, $-42 \le l \le 42$	$-24 \le h \le 23$ $-24 \le k \le 24$ $-28 \le l \le 29$
Reflections measured	127007	125819	143808	208940
Independent reflections	18003	23705	21798	29857
Restraints/Parameters	1/474	82/1180	0/955	460/1263
GOF on F^2	1.093	1.10	0.989	1.05
R-factor	0.0412	0.101	0.0714	0.100
Weighted R-factor	0.0932	0.228	0.1621	0.255
Largest diff. peak/hole/e Å^{-3}	0.78/-0.67	3.83/-4.70	2.83/-1.48	5.92/-6.19

Table 2.S2. Summary of statistics for diffraction data for **2.4** to **2.6**

Cluster	**2.4-W**	**2.4-Mo**	**2.5**	**2.6**
CCDC	2081616	2084247	2081621	2081617
Empirical formula	$C_{60}H_{106}BFe_3N_{12}S_3W$	$C_{68}H_{121}BFe_3MoN_{12}O_2S_3$	$C_{62}H_{109}BF_3Fe_3N_{12}O_3S_4W$	$C_{64}H_{116}BFe_3N_{13}OS_3W$
Formula weight	1453.98	1509.24	1618.08	1542.11
Temperature/K	100	100	100	100
Crystal system	Tetragonal	Monoclinic	Monoclinic	Monoclinic
Space group	$I4_1/a$	$P2_1/c$	$P2_1/n$	$P2_1/n$
a/Å	40.2240(7)	14.928(3)	16.8020(7)	17.5730(8)
b/Å	40.2240(7)	19.995(6)	24.7882(11)	15.7090(6)
c/Å	23.9730(7)	26.171(7)	17.5431(8)	28.3510(11)
α/°	90	90	90	90
β/°	90	92.691(9)	100.328(3)	98.7120(14)
γ/°	90	90	90	90
Volume/Å^3	38787.6(18)	7804(3)	7188.2(6)	7736.1(5)
Z	16	4	4	4
ρ_{calc}/g cm^{-3}	1.00	1.285	1.50	1.32
μ/mm^{-1}	1.719	0.832	9.201	2.160
F(000)	12080	3208	3348	3216
Crystal size/mm^3	0.16 × 0.19 × 0.26	0.4 × 0.3 × 0.25	0.06 × 0.17 × 0.17	0.10 × 0.19 × 0.23
Radiation	Mo Kα	Mo Kα	Cu Kα	Mo Kα
θ_{max}/°	33.542	30.563	79.5220	34.1147
Index ranges	$-58 \leq h \leq 60$ $-62 \leq k \leq 55$ $-36 \leq l \leq 33$	$-21 \leq h \leq 19$, $-28 \leq k \leq 28$, $-37 \leq l \leq 37$	$-21 \leq h \leq 21$ $-30 \leq k \leq 31$ $-22 \leq l \leq 21$	$-27 \leq h \leq 27$ $-24 \leq k \leq 23$ $-44 \leq l \leq 44$
Reflections measured	547051	327729	87210	373952
Independent reflections	34786	23838	15019	29843
Restraints/Parameters	0/721	1270/1033	0/802	45/775
GOF on F^2	0.99	1.104	1.02	1.00
R-factor	0.049	0.0499	0.073	0.031
Weighted R-factor	0.151	0.1219	0.192	0.080
Largest diff. peak/hole/e Å^{-3}	2.27/-1.05	1.28/-0.96	2.88/-3.09	2.17/-1.17

Table 2.S3. Summary of statistics for diffraction data for **2.7** and **2.8**

Cluster	**2.7**	**2.8**
CCDC	2081622	2084054
Empirical formula	$C_{103}H_{169}B_2Fe_3$ $N_{13}O_4S_3SiW$	$C_{84}H_{126}B_2Fe_3$ $N_{12}O_2S_4W$
Formula weight	2150.87	1805.28
Temperature/K	100	100
Crystal system	Monoclinic	Monoclinic
Space group	$P2_1/c$	$P2_1/c$
a/Å	18.1176(19)	17.1740(15)
b/Å	34.458(4)	33.780(3)
c/Å	18.0735(18)	18.1970(17)
α/°	90	90
β/°	100.237(4)	94.158(3)
γ/°	90	90
Volume/Å^3	11103.7(20)	10529.0(16)
Z	4	4
ρ_{calc}/g cm^{-3}	1.29	1.14
μ/mm^{-1}	1.537	1.614
F(000)	4536	3760
Crystal size/mm^3	0.05 × 0.15 × 0.15	0.30 × 0.40 × 0.50
Radiation	Mo Kα	Mo Kα
θ_{max}/°	33.5348	38.337
Index ranges	$-28 \leq h \leq 28$ $-53 \leq k \leq 52$ $-28 \leq l \leq 24$	$-29 \leq h \leq 29$ $-54 \leq k \leq 58$ $-31 \leq l \leq 27$
Reflections measured	289936	408974
Independent reflections	43588	56363
Restraints/Parameters	26/1171	86/992
GOF on F^2	1.02	0.99
R-factor	0.037	0.047
Weighted R-factor	0.095	0.111
Largest diff. peak/hole/e Å^{-3}	2.30/-1.79	3.17/-2.45

Table 2.S4. Summary of statistics for diffraction data for **2.9-W** and **2.9-M'-red**

Cluster	2.9-W	2.9-W-red	2.9-Mo-red
Empirical formula	$C_{102}H_{155}B_2Fe_3N_{12}O_3S_3W$	$C_{76}H_{139}BFe_3N_{12}OS_3W$	$C_{85}H_{130}BFe_3MoN_{12}OS_3$
Formula weight	2066.64	1695.37	1706.54
Temperature/K	100	100	100
Crystal system	Triclinic	Cubic	Monoclinic
Space group	P-1	Pa-3	$P2_1/n$
a/Å	16.659(1)	26.2390(3)	18.245(8)
b/Å	19.0650(12)	26.2390(3)	25.101(6)
c/Å	19.5440(12)	26.2390(3)	19.343(6)
α/°	112.5000(18)	90	90
β/°	103.8500(19)	90	91.104(18)
γ/°	99.1140(19)	90	90
Volume/Å^3	5347.4(6)	18065.2(6)	8857(5)
Z	2	8	4
ρ_{calc}/g cm^{-3}	1.283	1.247	1.280
μ/mm^{-1}	1.581	1.856	0.741
F(000)	2170.0	7136.0	3620.0
Crystal size/mm^3	0.20 × 0.20 × 0.20	0.10 × 0.10 × 0.20	0.20 × 0.20 × 0.20
Radiation	Mo Kα	Mo Kα	Mo Kα
θ_{max}/°	38.307	30.000	31.584
Index ranges	$-28 \le h \le 28$ $-33 \le k \le 32$ $-33 \le l \le 34$	$-36 \le h \le 35$ $-35 \le k \le 36$ $-31 \le l \le 36$	$-26 \le h \le 26$ $-36 \le k \le 36$ $-28 \le l \le 28$
Reflections measured	215021	128663	116702
Independent reflections	55985	8796	29608
Restraints/Parameters	48/1135	91/294	102/955
GOF on F^2	0.98	1.00	1.00
R-factor	0.046	0.084	0.059
Weighted R-factor	0.113	0.220	0.160
Largest diff. peak/hole/e Å^{-3}	4.64/-2.01	3.09/-2.23	2.07/-1.42

Table 2.S5. Comparison of bond metrics for the clusters discussed. For **2.8**, the average Fe-S distance is reported for the sulfides in the WS_3 fragment, which is separate from the Fe-(μ_3-X) distance involving the sulfide bridging all the Fe atoms. Data for FeMoco are based on structure 3U7Q from the Protein Data Bank; bond metrics reported for this structure are from the MoS_3Fe_3C cubane.

Bond/Å	2.2-W $(WFe_3)^{9+}$	2.3 $(WFe_3)^{8+}$	2.4-W $(WFe_3)^{11+}$	2.4-Mo $(MoFe_3)^{11+}$	2.5 $(WFe_3)^{11+}$	2.6 $(WFe_3)^{10+}$	2.7 $(WFe_3)^{10+}$	2.8 $(WFe_3)^{10+}$	FeMoco
Fe-S	2.275(2)	2.246(2)	2.2791(9)	2.255(1)	2.260(2)	2.2356(6)	2.2800(6)	2.2660(6)	2.26
	2.272(2)	2.246(2)	2.2663(9)	2.254(1)	2.254(2)	2.2469(5)	2.2754(6)	2.2625(6)	2.26
	2.280(2)	2.256(2)	2.2689(9)	2.275(1)	2.281(2)	2.2504(6)	2.2750(7)	2.2953(6)	2.24
	2.261(2)	2.247(2)	2.2699(10)	2.246(1)	2.260(3)	2.2481(5)	2.2835(7)	2.2767(5)	2.22
	2.273(2)	2.246(2)	2.2663(9)	2.246(1)	2.294(2)	2.2350(5)	2.2850(6)	2.2707(6)	2.25
	2.262(2)	2.248(2)	2.2703(9)	2.267(1)	2.255(3)	2.2476(5)	2.2813(7)	2.2582(6)	2.22
avg.	**2.27**	**2.24**	**2.27**	**2.25**	**2.26**	**2.24**	**2.28**	**2.27**	**2.24**
M-S (M = W/Mo)	2.377(2)	2.391(2)	2.3590(8)	2.378(1)	2.352(2)	2.3580(4)	2.3543(5)	2.3457(5)	2.35
	2.370(2)	2.398(3)	2.3745(7)	2.377(1)	2.360(2)	2.3568(5)	2.3597(5)	2.3605(5)	2.36
	2.370(2)	2.390(2)	2.3607(8)	2.380(1)	2.360(2)	2.3627(5)	2.3524(6)	2.3585(5)	2.37
avg.	**2.37**	**2.39**	**2.36**	**2.38**	**2.36**	**2.36**	**2.36**	**2.36**	**2.36**
Fe-Fe	2.651(2)	2.521(2)	2.5186(7)	2.516(1)	2.516(2)	2.5043(4)	2.5721(4)	2.6593(4)	2.63
	2.633(2)	2.526(1)	2.5122(6)	2.506(1)	2.564(2)	2.4877(4)	2.5767(5)	2.6064(4)	2.59
	2.634(2)	2.522(2)	2.4854(7)	2.499(1)	2.542(2)	2.5155(4)	2.5723(5)	2.6605(4)	2.63
avg.	**2.64**	**2.52**	**2.51**	**2.51**	**2.54**	**2.50**	**2.57**	**2.64**	**2.62**
Fe-BAC	2.066(9)	2.013(8)	2.000(3)	1.997(2)	2.040(9)	1.979(2)	2.044(2)	2.045(2)	
	2.069(9)	2.023(9)	1.987(4)	2.021(6)	2.057(8)	1.998(2)	2.041(2)	2.019(2)	-
	2.073(9)	2.029(8)	-	-	-	1.990(2)	2.055(2)	2.052(2)	
avg.	**2.07**	**2.02**	**1.99**	**2.01**	**2.05**	**1.99**	**2.05**	**2.04**	
Fe-(μ_3-X)	2.480(2)		1.958(4)	1.953(3)	1.94(1)	1.8524(17)	1.961(2)	2.2873(6)	2.01
	2.488(2)	-	1.945(3)	1.956(3)	1.96(1)	1.851(2)	1.947(2)	2.3126(7)	2.01
	2.471(2)		1.943(3)	1.939(3)	1.96(1)	1.8447(18)	1.939(2)	2.2240(6)	1.98
avg.	**2.48**		**1.95**	**1.95**	**1.95**	**1.85**	**1.95**	**2.27**	**2.00**

Table 2.S6. Summary of M'-S bond lengths (M' = Mo or W) for relevant compounds bearing the $M'S_3$ moiety in different oxidation states of M'.

Compound	M' oxidation state	M'-S bond length range/Å	Average M'-S bond length/Å	Method of oxidation state determination for M'	Reference
$[NEt_4][Tp^*WS_3]$	W(VI)	2.192 – 2.194	2.19	charge balance	60
$[NBu_4][Tp^*MoS_3]$	Mo(VI)	2.173 – 2.192	2.18	charge balance	46
$[NEt_4][Tp^*W(\mu\text{-}S)_3Mo(CO)_3]$	W(VI) Mo(0)	2.240 – 2.250 (W(VI)) 2.549 – 2.577 (Mo(0))	2.25 (W(VI)) 2.56 (Mo(0))	bond length comparison with related species	70
$[NEt_4][(Tp^*WS_3)_2Co]$	W(V)	2.255 – 2.281	2.27	Mössbauer spectroscopy of related species	71
$[NEt_4]_2[Tp^*{}_2W_2Fe_6(\mu_4\text{-}N)_2S_6Cl_4]$	W(IV)	2.348 – 2.372	2.36	Mössbauer spectroscopy for Fe and charge balance	18
$[NEt_4][Tp^*MoS_5]$	Mo(IV)	2.172 – 2.254	2.22	charge balance	60
2.1-W	W(III)	2.370 – 2.390	2.38	Mössbauer spectroscopy for Fe and charge balance	18,32,71
$(tBu_3tach)MoFe_3S_4(SPh)_3$	Mo(III)	2.311 – 2.339	2.33	Mössbauer spectroscopy for Fe and charge balance	48
$[NEt_4][TpMoS_4Fe_3Cl_3]$	Mo(III)	2.343 – 2.344	2.34	Mössbauer spectroscopy for Fe and charge balance	33

2.6 REFERENCES

(1) Burgess, B. K.; Lowe, D. J. Mechanism of Molybdenum Nitrogenase. *Chem. Rev.* **1996**, *96* (7), 2983–3012. https://doi.org/10.1021/cr950055x.

(2) Spatzal, T.; Schlesier, J.; Burger, E.-M.; Sippel, D.; Zhang, L.; Andrade, S. L. A.; Rees, D. C.; Einsle, O. Nitrogenase FeMoco Investigated by Spatially Resolved Anomalous Dispersion Refinement. *Nat. Commun.* **2016**, *7* (1), 10902. https://doi.org/10.1038/ncomms10902.

(3) Siegbahn, P. E. M. Model Calculations Suggest That the Central Carbon in the FeMo-Cofactor of Nitrogenase Becomes Protonated in the Process of Nitrogen Fixation. *J. Am. Chem. Soc.* **2016**, *138* (33), 10485–10495. https://doi.org/10.1021/jacs.6b03846.

(4) Čorić, I.; Mercado, B. Q.; Bill, E.; Vinyard, D. J.; Holland, P. L. Binding of Dinitrogen to an Iron–Sulfur–Carbon Site. *Nature* **2015**, *526* (7571), 96–99. https://doi.org/10.1038/nature15246.

(5) Ung, G.; Peters, J. C. Low-Temperature N2 Binding to Two-Coordinate L_2Fe^0 Enables Reductive Trapping of $L_2FeN_2^-$ and NH_3 Generation. *Angew. Chem. Int. Ed.* **2015**, *54* (2), 532–535. https://doi.org/10.1002/anie.201409454.

(6) McWilliams, S. F.; Broere, D. L. J.; Halliday, C. J. V.; Bhutto, S. M.; Mercado, B. Q.; Holland, P. L. Coupling Dinitrogen and Hydrocarbons through Aryl Migration. *Nature* **2020**, *584* (7820), 221–226. https://doi.org/10.1038/s41586-020-2565-5.

(7) Nagelski, A. L.; Fataftah, M. S.; Bollmeyer, M. M.; McWilliams, S. F.; MacMillan, S. N.; Mercado, B. Q.; Lancaster, K. M.; Holland, P. L. The Influences of Carbon Donor Ligands on Biomimetic Multi-Iron Complexes for N_2 Reduction. *Chem. Sci.* **2020**. https://doi.org/10.1039/D0SC03447A.

(8) Creutz, S. E.; Peters, J. C. Catalytic Reduction of N_2 to NH_3 by an Fe–N_2 Complex Featuring a C-Atom Anchor. *J. Am. Chem. Soc.* **2014**, *136* (3), 1105–1115. https://doi.org/10.1021/ja4114962.

(9) Arnett, C. H.; Agapie, T. Activation of an Open Shell, Carbyne-Bridged Diiron Complex Toward Binding of Dinitrogen. *J. Am. Chem. Soc.* **2020**, *142* (22), 10059–10068. https://doi.org/10.1021/jacs.0c01896.

(10) Joseph, C.; Cobb, C. R.; Rose, M. J. Single-Step Sulfur Insertions into Iron Carbide Carbonyl Clusters: Unlocking the Synthetic Door to FeMoco Analogues. *Angew. Chem. Int. Ed.* **2021**, *60* (7), 3433–3437. https://doi.org/10.1002/anie.202011517.

(11) Liu, L.; Rauchfuss, T. B.; Woods, T. J. Iron Carbide–Sulfide Carbonyl Clusters. *Inorg. Chem.* **2019**, *58* (13), 8271–8274. https://doi.org/10.1021/acs.inorgchem.9b01231.

(12) Ohta, S.; Ohki, Y.; Hashimoto, T.; Cramer, R. E.; Tatsumi, K. A Nitrogenase Cluster Model [Fe_8S_6O] with an Oxygen Unsymmetrically Bridging Two Proto-Fe_4S_3 Cubes: Relevancy to the Substrate Binding Mode of the FeMo Cofactor. *Inorg. Chem.* **2012**, *51* (21), 11217–11219. https://doi.org/10.1021/ic301348f.

(13) Ohki, Y.; Ikagawa, Y.; Tatsumi, K. Synthesis of New [8Fe-7S] Clusters: A Topological Link between the Core Structures of P-Cluster, FeMo-Co, and FeFe-Co of Nitrogenases. *J. Am. Chem. Soc.* **2007**, *129* (34), 10457–10465. https://doi.org/10.1021/ja072256b.

(14) Powers, T. M.; Betley, T. A. Testing the Polynuclear Hypothesis: Multielectron Reduction of Small Molecules by Triiron Reaction Sites. *J. Am. Chem. Soc.* **2013**, *135* (33), 12289–12296. https://doi.org/10.1021/ja405057n.

(15) Sridharan, A.; Brown, A. C.; Suess, D. L. M. A Terminal Imido Complex of an Iron–Sulfur Cluster. *Angew. Chem. Int. Ed.* **2021**, *60* (23), 12802–12806. https://doi.org/10.1002/anie.202102603.

(16) McSkimming, A.; Suess, D. L. M. Dinitrogen Binding and Activation at a Molybdenum–Iron–Sulfur Cluster. *Nat. Chem.* **2021**, *13* (7), 666–670. https://doi.org/10.1038/s41557-021-00701-6.

(17) DeRosha, D. E.; Chilkuri, V. G.; Van Stappen, C.; Bill, E.; Mercado, B. Q.; DeBeer, S.; Neese, F.; Holland, P. L. Planar Three-Coordinate Iron Sulfide in a Synthetic [4Fe-3S] Cluster with Biomimetic Reactivity. *Nat. Chem.* **2019**, *11* (11), 1019–1025. https://doi.org/10.1038/s41557-019-0341-7.

(18) Xu, G.; Zhou, J.; Wang, Z.; Holm, R. H.; Chen, X.-D. Controlled Incorporation of Nitrides into W-Fe-S Clusters. *Angew. Chem. Int. Ed.* **2019**, *58* (46), 16469–16473. https://doi.org/10.1002/anie.201908968.

(19) Lee, Y.; Sloane, F. T.; Blondin, G.; Abboud, K. A.; García-Serres, R.; Murray, L. J. Dinitrogen Activation Upon Reduction of a Triiron(II) Complex. *Angew. Chem. Int. Ed.* **2015**, *54* (5), 1499–1503. https://doi.org/10.1002/anie.201409676.

(20) Reiners, M.; Baabe, D.; Münster, K.; Zaretzke, M.-K.; Freytag, M.; Jones, P. G.; Coppel, Y.; Bontemps, S.; Rosal, I. del; Maron, L.; Walter, M. D. NH_3 Formation from N_2 and H_2 Mediated by Molecular Tri-Iron Complexes. *Nat. Chem.* **2020**, *12* (8), 740–746. https://doi.org/10.1038/s41557-020-0483-7.

(21) Reed, C. J.; Agapie, T. Tetranuclear Fe Clusters with a Varied Interstitial Ligand: Effects on the Structure, Redox Properties, and Nitric Oxide Activation. *Inorg. Chem.* **2017**, *56* (21), 13360–13367. https://doi.org/10.1021/acs.inorgchem.7b02114.

(22) Arnett, C. H.; Chalkley, M. J.; Agapie, T. A Thermodynamic Model for Redox-Dependent Binding of Carbon Monoxide at Site-Differentiated, High Spin Iron Clusters. *J. Am. Chem. Soc.* **2018**, *140* (16), 5569–5578. https://doi.org/10.1021/jacs.8b01825.

(23) Arnett, C. H.; Kaiser, J. T.; Agapie, T. Remote Ligand Modifications Tune Electronic Distribution and Reactivity in Site-Differentiated, High-Spin Iron Clusters: Flipping Scaling Relationships. *Inorg. Chem.* **2019**, *58* (23), 15971–15982. https://doi.org/10.1021/acs.inorgchem.9b02470.

(24) Joseph, C.; Kuppuswamy, S.; Lynch, V. M.; Rose, M. J. Fe_5Mo Cluster with Iron-Carbide and Molybdenum-Carbide Bonding Motifs: Structure and Selective Alkyne Reductions. *Inorg. Chem.* **2018**, *57* (1), 20–23. https://doi.org/10.1021/acs.inorgchem.7b02615.

(25) Churchill, M. R.; Wormald, J.; Knight, J.; Mays, M. J. Synthesis and Crystallographic Characterization of Bis(Tetramethylammonium) Carbidohexadecacarbonylhexaferrate, a Hexanuclear Carbidocarbonyl Derivative of Iron. *J. Am. Chem. Soc.* **1971**, *93* (12), 3073–3074. https://doi.org/10.1021/ja00741a058.

(26) McGale, J.; Cutsail, G. E.; Joseph, C.; Rose, M. J.; DeBeer, S. Spectroscopic X-Ray and Mössbauer Characterization of μ_6 and μ_5 Iron(Molybdenum)-Carbonyl Carbide Clusters: High Carbide-Iron Covalency Enhances Local Iron Site Electron Density Despite Cluster Oxidation. *Inorg. Chem.* **2019**, *58* (19), 12918–12932. https://doi.org/10.1021/acs.inorgchem.9b01870.

(27) Bradley, J. S.; Ansell, G. B.; Leonowicz, M. E.; Hill, E. W. Synthesis and Molecular Structure of μ_4-Carbido-μ_2-Carbonyl-Dodecacarbonyltetrairon, a Neutral Iron Butterfly Cluster Bearing an Exposed Carbon Atom. *J. Am. Chem. Soc.* **1981**, *103* (16), 4968–4970. https://doi.org/10.1021/ja00406a062.

(28) Arnett, C. H.; Bogacz, I.; Chatterjee, R.; Yano, J.; Oyala, P. H.; Agapie, T. Mixed-Valent Diiron μ-Carbyne, μ-Hydride Complexes: Implications for Nitrogenase. *J. Am. Chem. Soc.* **2020**, *142* (44), 18795–18813. https://doi.org/10.1021/jacs.0c05920.

(29) Spatzal, T.; Perez, K. A.; Howard, J. B.; Rees, D. C. Catalysis-Dependent Selenium Incorporation and Migration in the Nitrogenase Active Site Iron-Molybdenum Cofactor. *eLife* **2015**, *4*, e11620. https://doi.org/10.7554/eLife.11620.

(30) Spatzal, T.; Perez, K. A.; Einsle, O.; Howard, J. B.; Rees, D. C. Ligand Binding to the FeMo-Cofactor: Structures of CO-Bound and Reactivated Nitrogenase. *Science* **2014**, *345* (6204), 1620. https://doi.org/10.1126/science.1256679.

(31) Sippel, D.; Rohde, M.; Netzer, J.; Trncik, C.; Gies, J.; Grunau, K.; Djurdjevic, I.; Decamps, L.; Andrade, S. L. A.; Einsle, O. A Bound Reaction Intermediate Sheds Light on the Mechanism of Nitrogenase. *Science* **2018**, *359* (6383), 1484. https://doi.org/10.1126/science.aar2765.

(32) Xu, G.; Wang, Z.; Ling, R.; Zhou, J.; Chen, X.-D.; Holm, R. H. Ligand Metathesis as Rational Strategy for the Synthesis of Cubane-Type Heteroleptic Iron–Sulfur Clusters Relevant to the FeMo Cofactor. *Proc. Natl. Acad. Sci. U.S.A.* **2018**, *115* (20), 5089. https://doi.org/10.1073/pnas.1801025115.

(33) Fomitchev, D. V.; McLauchlan, C. C.; Holm, R. H. Heterometal Cubane-Type MFe_3S_4 Clusters (M = Mo, V) Trigonally Symmetrized with Hydrotris(Pyrazolyl)Borate(1−) and Tris(Pyrazolyl)Methanesulfonate(1−) Capping Ligands. *Inorg. Chem.* **2002**, *41* (4), 958–966. https://doi.org/10.1021/ic011106d.

(34) Hong, D.; Zhang, Y.; Holm, R. H. Heterometal Cubane-Type WFe_3S_4 and Related Clusters Trigonally Symmetrized with Hydrotris(3,5-Dimethylpyrazolyl)Borate. *Inorg. Chim. Acta* **2005**, *358* (7), 2303–2311. https://doi.org/10.1016/j.ica.2004.11.051.

(35) Lavallo, V.; Ishida, Y.; Donnadieu, B.; Bertrand, G. Isolation of Cyclopropenylidene–Lithium Adducts: The Weiss–Yoshida Reagent. *Angew. Chem. Int. Ed.* **2006**, *45* (40), 6652–6655. https://doi.org/10.1002/anie.200602701.

(36) Martinez, J. L.; Lin, H.-J.; Lee, W.-T.; Pink, M.; Chen, C.-H.; Gao, X.; Dickie, D. A.; Smith, J. M. Cyanide Ligand Assembly by Carbon Atom Transfer to an Iron Nitride. *J. Am. Chem. Soc.* **2017**, *139* (40), 14037–14040. https://doi.org/10.1021/jacs.7b08704.

(37) Deng, L.; Holm, R. H. Stabilization of Fully Reduced Iron−Sulfur Clusters by Carbene Ligation: The $[Fe_nS_n]^0$ Oxidation Levels (n = 4, 8). *J. Am. Chem. Soc.* **2008**, *130* (30), 9878–9886. https://doi.org/10.1021/ja802111w.

(38) Evans, M. E.; Li, T.; Jones, W. D. C−H vs C−C Bond Activation of Acetonitrile and Benzonitrile via Oxidative Addition: Rhodium vs Nickel and Cp* vs Tp′ (Tp′ = Hydrotris(3,5-Dimethylpyrazol-1-Yl)Borate, Cp* = η^5-Pentamethylcyclopentadienyl). *J. Am. Chem. Soc.* **2010**, *132* (45), 16278–16284. https://doi.org/10.1021/ja107927b.

(39) Kent, G. T.; Staun, S. L.; Wu, G.; Hayton, T. W. Reactivity of $[Ce(NR_2)_3]$ (R = $SiMe_3$) with Prospective Carbon Atom Transfer Reagents. *Organometallics* **2020**. https://doi.org/10.1021/acs.organomet.0c00186.

(40) Chu, C. T.-Wah.; Dahl, L. F. Structural Characterization of $[AsPh_4]^+[Fe_4(NO)_7(M_3\text{-}S)_3]^-$. Stereochemical and Bonding Relationship of the Roussin Black Monoanion with the Red Ethyl Ester, $Fe_2(NO)_4(\mu_2\text{-}SC_2H_5)_2$, and $Fe_4(NO)_4(\mu_3\text{-}S)_4$. *Inorg. Chem.* **1977**, *16* (12), 3245–3251. https://doi.org/10.1021/ic50178a052.

(41) Fritsch, J.; Scheerer, P.; Frielingsdorf, S.; Kroschinsky, S.; Friedrich, B.; Lenz, O.; Spahn, C. M. T. The Crystal Structure of an Oxygen-Tolerant Hydrogenase Uncovers a Novel Iron-Sulphur Centre. *Nature* **2011**, *479* (7372), 249–252. https://doi.org/10.1038/nature10505.

(42) Coucouvanis, D.; Han, J.; Moon, N. Synthesis and Characterization of Sulfur-Voided Cubanes. Structural Analogues for the $MoFe_3S_3$ Subunit in the Nitrogenase Cofactor. *J. Am. Chem. Soc.* **2002**, *124* (2), 216–224. https://doi.org/10.1021/ja0110832.

(43) Powers, T. M.; Fout, A. R.; Zheng, S.-L.; Betley, T. A. Oxidative Group Transfer to a Triiron Complex to Form a Nucleophilic μ_3-Nitride, $[Fe_3(\mu_3\text{-}N)]^-$. *J. Am. Chem. Soc.* **2011**, *133* (10), 3336–3338. https://doi.org/10.1021/ja2003445.

(44) Horitani, M.; Shisler, K.; Broderick, W. E.; Hutcheson, R. U.; Duschene, K. S.; Marts, A. R.; Hoffman, B. M.; Broderick, J. B. Radical SAM Catalysis via an Organometallic Intermediate with an Fe–[5′-C]-Deoxyadenosyl Bond. *Science* **2016**, *352* (6287), 822. https://doi.org/10.1126/science.aaf5327.

(45) Ye, M.; Thompson, N. B.; Brown, A. C.; Suess, D. L. M. A Synthetic Model of Enzymatic [Fe_4S_4]–Alkyl Intermediates. *J. Am. Chem. Soc.* **2019**. https://doi.org/10.1021/jacs.9b06975.

(46) Sherbow, T. J.; Zakharov, L. N.; Johnson, D. W.; Pluth, M. D. Hydrosulfide Oxidation at a Molybdenum Tetrasulfido Complex. *Inorg. Chem.* **2020**, *59* (21), 15574–15578. https://doi.org/10.1021/acs.inorgchem.0c02622.

(47) Kowalska, J. K.; Henthorn, J. T.; Van Stappen, C.; Trncik, C.; Einsle, O.; Keavney, D.; DeBeer, S. X-Ray Magnetic Circular Dichroism Spectroscopy Applied to Nitrogenase and Related Models: Experimental Evidence for a Spin-Coupled Molybdenum(III) Center. *Angew. Chem. Int. Ed.* **2019**, *58* (28), 9373–9377. https://doi.org/10.1002/anie.201901899.

(48) Majumdar, A.; Holm, R. H. Specific Incorporation of Chalcogenide Bridge Atoms in Molybdenum/Tungsten-Iron-Sulfur Single Cubane Clusters. *Inorg. Chem.* **2011**, *50* (21), 11242–11251. https://doi.org/10.1021/ic2018117.

(49) Colebatch, A. L.; Frogley, B. J.; Hill, A. F.; Onn, C. S. Pnictogen-Functionalised C1 Ligands: MC-AR_n (N=0, 1, 2, 3). *Chem. Eur. J.* **2021**, *27* (17), 5322–5343. https://doi.org/10.1002/chem.202004280.

(50) Spatzal, T.; Aksoyoglu, M.; Zhang, L.; Andrade, S. L. A.; Schleicher, E.; Weber, S.; Rees, D. C.; Einsle, O. Evidence for Interstitial Carbon in Nitrogenase FeMo Cofactor. *Science* **2011**, *334* (6058), 940. https://doi.org/10.1126/science.1214025.

(51) Tano, H.; Tajima, R.; Miyake, H.; Itoh, S.; Sugimoto, H. Selenidobis(Dithiolene)Metal(IV) Complexes (Metal M = Mo, W) Potentially Related to the Nicotinic Acid Hydroxylase Reaction Center: Redox Aspects in Electrochemistry and Oxygen Atom Transfer from Me_3NO to M^{IV} Centers. *Inorg. Chem.* **2008**, *47* (17), 7465–7467. https://doi.org/10.1021/ic8009942.

(52) Lever, A. B. P. Electrochemical Parametrization of Metal Complex Redox Potentials, Using the Ruthenium(III)/Ruthenium(II) Couple to Generate a Ligand Electrochemical Series. *Inorg. Chem.* **1990**, *29* (6), 1271–1285. https://doi.org/10.1021/ic00331a030.

(53) Čorić, I.; Holland, P. L. Insight into the Iron–Molybdenum Cofactor of Nitrogenase from Synthetic Iron Complexes with Sulfur, Carbon, and Hydride Ligands. *J. Am. Chem. Soc.* **2016**, *138* (23), 7200–7211. https://doi.org/10.1021/jacs.6b00747.

(54) Henthorn, J. T.; Arias, R. J.; Koroidov, S.; Kroll, T.; Sokaras, D.; Bergmann, U.; Rees, D. C.; DeBeer, S. Localized Electronic Structure of Nitrogenase FeMoco Revealed by Selenium K-Edge High Resolution X-Ray Absorption Spectroscopy. *J. Am. Chem. Soc.* **2019**, *141* (34), 13676–13688. https://doi.org/10.1021/jacs.9b06988.

(55) Scott, A. G.; Agapie, T. Synthesis of a Fe_3–Carbyne Motif by Oxidation of an Alkyl Ligated Iron–Sulfur (WFe_3S_3) Cluster. *J. Am. Chem. Soc.* **2023**, *145* (1), 2–6. https://doi.org/10.1021/jacs.2c04826.

(56) Speelman, A. L.; Čorić, I.; Van Stappen, C.; DeBeer, S.; Mercado, B. Q.; Holland, P. L. Nitrogenase-Relevant Reactivity of a Synthetic Iron–Sulfur–Carbon Site. *J. Am. Chem. Soc.* **2019**, *141* (33), 13148–13157. https://doi.org/10.1021/jacs.9b05353.

(57) Lavallo, V.; Canac, Y.; Donnadieu, B.; Schoeller, W. W.; Bertrand, G. Cyclopropenylidenes: From Interstellar Space to an Isolated Derivative in the Laboratory. *Science* **2006**, *312* (5774), 722. https://doi.org/10.1126/science.1126675.

(58) Burgmayer, S. J. N.; Kim, M.; Petit, R.; Rothkopf, A.; Kim, A.; BelHamdounia, S.; Hou, Y.; Somogyi, A.; Habel-Rodriguez, D.; Williams, A.; Kirk, M. L. Synthesis, Characterization, and Spectroscopy of Model Molybdopterin Complexes. *J. Inorg. Biochem* **2007**, *101* (11), 1601–1616. https://doi.org/10.1016/j.jinorgbio.2007.07.012.

(59) Shupp, J. P.; Rose, A. R.; Rose, M. J. Synthesis and Interconversions of Reduced, Alkali–Metal Supported Iron–Sulfur–Carbonyl Complexes. *Dalton Trans.* **2017**, *46* (28), 9163–9171. https://doi.org/10.1039/C7DT01506B.

(60) Seino, H.; Arai, Y.; Iwata, N.; Nagao, S.; Mizobe, Y.; Hidai, M. Preparation of Mononuclear Tungsten Tris(Sulfido) and Molybdenum Sulfido−Tetrasulfido Complexes with Hydridotris(Pyrazolyl)Borate Coligand and Conversion of the Former into Sulfido-Bridged Bimetallic Complex Having $Pt(\mu\text{-}S)_2WS$ Core. *Inorg. Chem.* **2001**, *40* (7), 1677–1682. https://doi.org/10.1021/ic0008823.

(61) Culmo, R. F.; Shelton, C. The Elemental Analysis of Various Classes of Chemical Compounds Using CHN. *Shelton, CT* **2013**.

(62) Bruker. APEX3, 2012.

(63) Bruker. SADABS, 2001.

(64) Sheldrick, G. SHELXT - Integrated Space-Group and Crystal-Structure Determination. *Acta Cryst. A* **2015**, *71* (1), 3–8.

(65) Altomare, A.; Cascarano, G.; Giacovazzo, C.; Guagliardi, A.; Burla, M. C.; Polidori, G.; Camalli, M. SIR92 - a Program for Automatic Solution of Crystal Structures by Direct Methods. *J. Appl. Crystallogr.* **1994**, *27* (3), 435.

(66) Palatinus, L.; Chapuis, G. SUPERFLIP - a Computer Program for the Solution of Crystal Structures by Charge Flipping in Arbitrary Dimensions. *J. Appl. Crystallogr.* **2007**, *40* (4), 786–790.

(67) Betteridge, P. W.; Carruthers, J. R.; Cooper, R. I.; Prout, K.; Watkin, D. J. CRYSTALS Version 12: Software for Guided Crystal Structure Analysis. *J. Appl. Crystallogr.* **2003**, *36* (6), 1487.

(68) Dolomanov, O. V.; Bourhis, L. J.; Gildea, R. J.; Howard, J. A. K.; Puschmann, H. OLEX2: A Complete Structure Solution, Refinement and Analysis Program. *J. Appl. Crystallogr.* **2009**, *42* (2), 339–341.

(69) Spek, A. PLATON SQUEEZE: A Tool for the Calculation of the Disordered Solvent Contribution to the Calculated Structure Factors. *Acta Cryst. C* **2015**, *71* (1), 9–18.

(70) Seino, H.; Iwata, N.; Kawarai, N.; Hidai, M.; Mizobe, Y. A Series of Dinuclear Homo- and Heterometallic Complexes with Two or Three Bridging Sulfido Ligands Derived from the Tungsten Tris(Sulfido) Complex $[Et_4N][(Me_2Tp)WS_3]$ (Me_2Tp = Hydridotris(3,5-Dimethylpyrazol-1-Yl)Borate). *Inorg. Chem.* **2003**, *42* (23), 7387–7395. https://doi.org/10.1021/ic030164r.

(71) Guo, J.-T.; Chen, X.-D. Templated Syntheses of Heterometal Tungsten–Cobalt–Sulfur Clusters with Different Nuclearities. *Dalton Trans.* **2020**, *49* (17), 5523–5530. https://doi.org/10.1039/D0DT00765J.

Chapter 3

HIGHLY ACTIVATED TERMINAL CARBON MONOXIDE LIGAND IN AN IRON–SULFUR CLUSTER MODEL OF FEMCO WITH INTERMEDIATE LOCAL SPIN STATE AT FE

Le, L. N. V.; Joyce, J. P.; Oyala, P. H.; DeBeer, S.; Agapie, T. Highly Activated Terminal Carbon Monoxide Ligand in an Iron–Sulfur Cluster Model of FeMco with Intermediate Local Spin State at Fe. *J. Am. Chem. Soc.* **2024**, *146* (8), 5045–5050. https://doi.org/10.1021/jacs.3c12025.

3.1 ABSTRACT

Nitrogenases, the enzymes that convert N_2 to NH_3, also catalyze the reductive coupling of CO to yield hydrocarbons. CO-coordinated species of nitrogenase clusters have been isolated and used to infer mechanistic information. However, synthetic FeS clusters displaying CO ligands remain rare, which limits benchmarking. Starting from a synthetic cluster that models a cubane portion of the FeMo cofactor (FeMoco), including a bridging carbyne ligand, we report a heterometallic tungsten–iron–sulfur cluster with a single terminal CO coordination in two oxidation states with a high level of CO activation (ν_{CO} = 1851 and 1751 cm^{-1}). The local Fe coordination environment (2S, 1C, 1CO) is identical to that in the protein making this system a suitable benchmark. Computational studies find an unusual intermediate spin electronic configuration at the Fe sites promoted by the presence of the carbyne ligand. This electronic feature is partly responsible for the high degree of CO activation in the reduced cluster. This work was done in collaboration with the DeBeer lab (calculations).

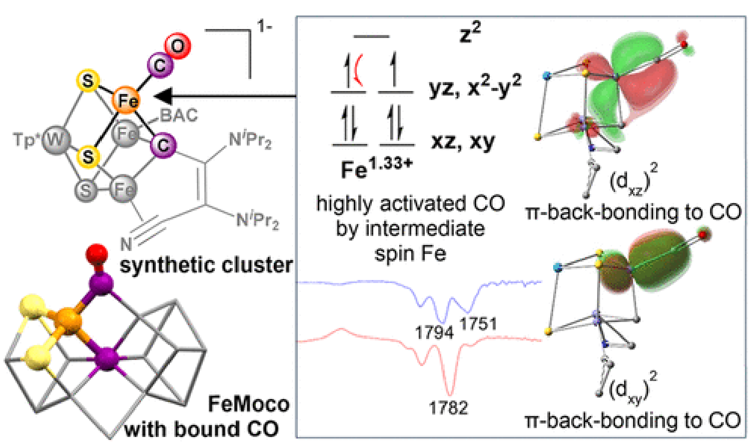

3.2 INTRODUCTION

Substrate activation at complex inorganic cofactors in enzyme active sites has raised fundamental questions about the role of the cluster structure on reactivity. For example, the challenging conversion of N_2 to NH_3 by nitrogenase enzymes occurs at FeMo cofactor (FeMoco) (M = Mo, V, or Fe), which comprises complex double cubane clusters with the MFe_7S_9C composition.[1,2] Nitrogenases also catalyze the reductive coupling of CO to form hydrocarbons for M = Mo and V.[3,4] Despite interest in these transformations, the characterization of substrate-bound clusters is very rare, which limits insight into the site of small molecule activation and reaction mechanism.[5–11] Only two CO-bound species of FeMoco and FeVco have been characterized structurally.[9,10,12,13] Structural characterization of N_2-derived species remains debated.[14–16]

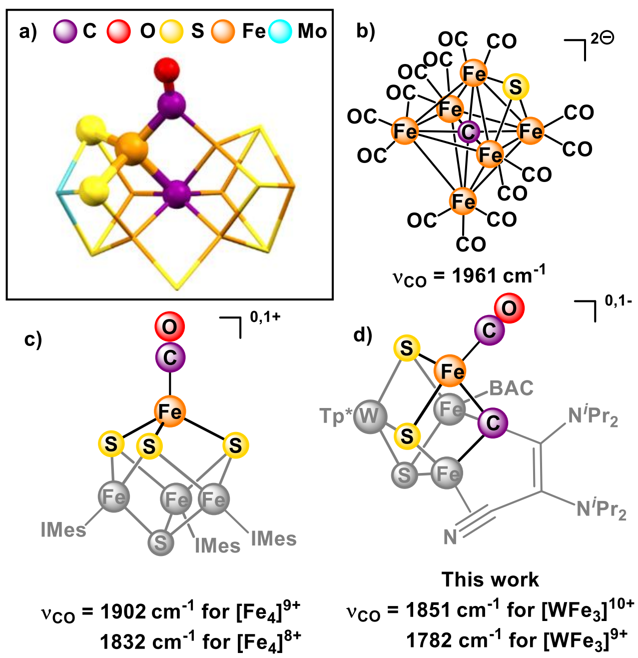

Figure 3.1. Structures of FeS clusters with CO coordination: (a) CO-bound FeMoco (PDB: 4TKV); (b) synthetic cluster with carbide ligand;[17,18] (c) Fe_4S_4 cluster with a single terminal CO;[19] (d) present report. Local coordination sphere of Fe–CO moiety highlighted in (a), (c), and (d).

Synthetic models promise to facilitate a better understanding of the impact of cluster structure on substrate binding and level of activation.[20–25] However, few examples of synthetic iron–sulfur clusters with terminal or bridging N_2 or CO ligands have been reported, many of which possess multiple CO ligands that drastically alter the electronic structure of the cluster and complicate comparisons to FeMoco (Figure 3.1).[17,18,26–30] Only one type of FeS cluster with a single terminal CO ligand has been characterized, ligated by three carbenes ligands.[19,31]

Having accessed a partial synthetic analog **3.1** of the cluster core of FeMoco displaying a μ_3-carbyne ligand with the WFe_3S_3CR composition, where W is the isoelectronic analogue of Mo,[32] we targeted the coordination of nitrogenase substrates (Figure 3.2).[33] Herein, we report the reactivity of **3.1** with isocyanides and CO, which affords an FeS cubane with a single terminal CO. We characterize this cluster in two oxidation states, which show a high level of CO activation, as observed in the low CO stretching frequency (1751–1851 cm^{-1}) by IR spectroscopy.

3.3 RESULTS AND DISCUSSION

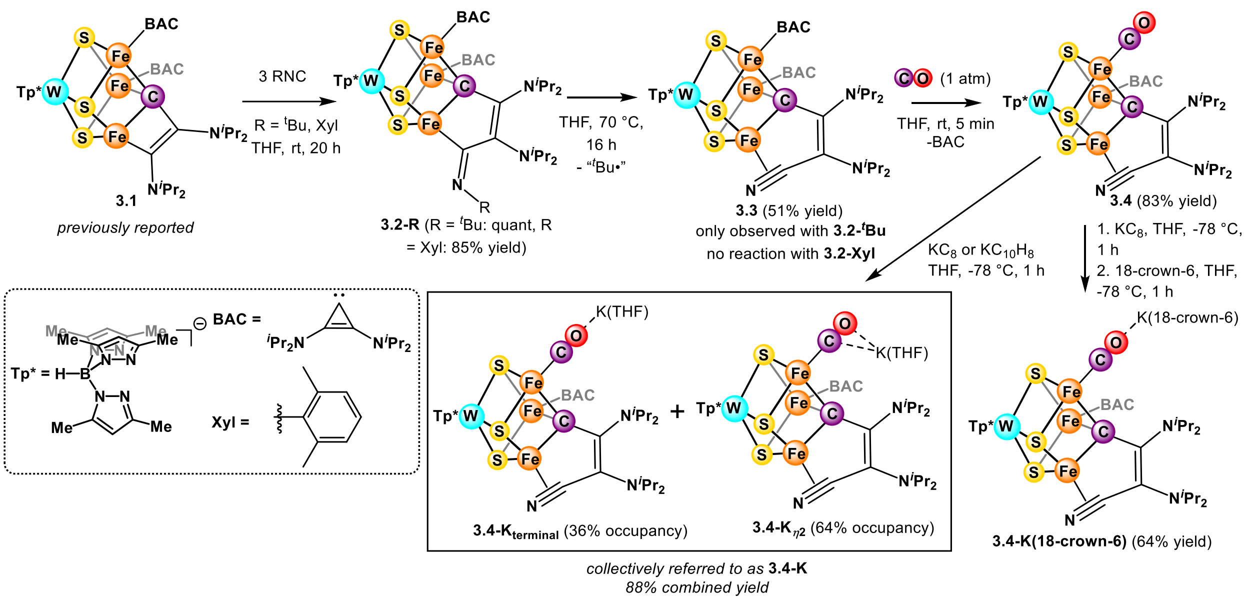

Figure 3.2. Syntheses of clusters.

We employed isocyanides as isoelectronic analogues of CO and substrates of nitrogenase[34] that also allow for a more controlled reactivity. Treating **3.1** with ^{t}BuNC or XylNC (Xyl = 2,6-dimethylphenyl) gives **3.2-^{t}Bu** or **3.2-Xyl** (Figure 3.2), respectively, through the insertion of isocyanide into the Fe–C(vinyl) bond, which demonstrates rare examples of C–C bond formation at an FeS cluster.[35–38] Heating **3.2-^{t}Bu** in THF at 70 °C for 16 h leads to the formation of **3.3**, where XRD and NMR studies are consistent with the loss of a ^{t}Bu radical (leaving an η^2-nitrile ligand). Vacuum transfer of volatiles from the synthesis of **3.3** allows for the identification of isobutane and isobutene, two expected products from the decomposition of the *ᵗ*Bu radical (see Figure 3.S14). While determining the protonation state of the N atom solely on the basis of XRD is inconclusive, the short C–N bond length of 1.205(6) Å compared with ~1.25 Å for η^2-iminoacyl (see Figure 3.S15 for additional support by ATR IR spectroscopy) is indicative of an η^2-nitrile motif.[39] An η^2-iminoacyl motif is expected to be substantially bent at C16 (Figure 3.3), with literature examples around 130°.[39] Side-bound organic nitriles are also significantly bent at C, but typically have more obtuse angles in non-chelated versions.[40] Chelated nitriles show much larger angles, above 140° with a Ru example of the same size chelate as **3.3** displaying a similarly obtuse angle (167.7°).[40] Cluster **3.3** displays a very similar C-N distance to the one observed (1.194(4) Å) in the only previously structurally characterized Fe analog.[41] This C-N distance, elongated from free nitrile (1.16 Å for CH_3CN),[42] is indicative of significant π-backbonding from Fe.

The loss of the ^{t}Bu radical suggests a propensity for side-on nitrile binding, which is an intriguing observation in the context of the nitrogenase substrates displaying triple bonds, including N_2, acetylene, and isocyanides.[43] The conversion from **3.2-^{t}Bu** to **3.3**, which involves the loss of a ^{t}Bu radical, formally represents one-electron oxidation of the WFe_3 metal core. In contrast to **3.2-^{t}Bu**, **3.2-Xyl** is stable under the same conditions, which is consistent with a lower tendency to lose the more reactive aryl radical.[44]

With **3.3** in hand, we explored reactions with CO. Cluster **3.3** reacts with 1 atm CO to form **3.4** within 5 min, which shows substitution of one bis(diisopropylamino)cyclopropenylidene (BAC) ligand with CO (83% yield, Figure 3.2) in an uncommon instance of carbene lability.[45] The average Fe–C(μ_3) distance remains similar to **3.2-^{t}Bu** and **3.3** at 1.95 Å, but the range for the individual bond lengths increases to 1.88–2.00 Å (compared with 1.92–1.95 Å in **3.2-^{t}Bu** and 1.95–1.96 Å in **3.3**), which suggests that the carbyne ligand, and potentially the carbide in FeMoco, has the ability to accommodate distinct electronic demands of different Fe centers through structural changes.[46] This is in contrast to spectroscopic studies suggesting that the central carbide serves to maintain the rigid core structure.[8,47]

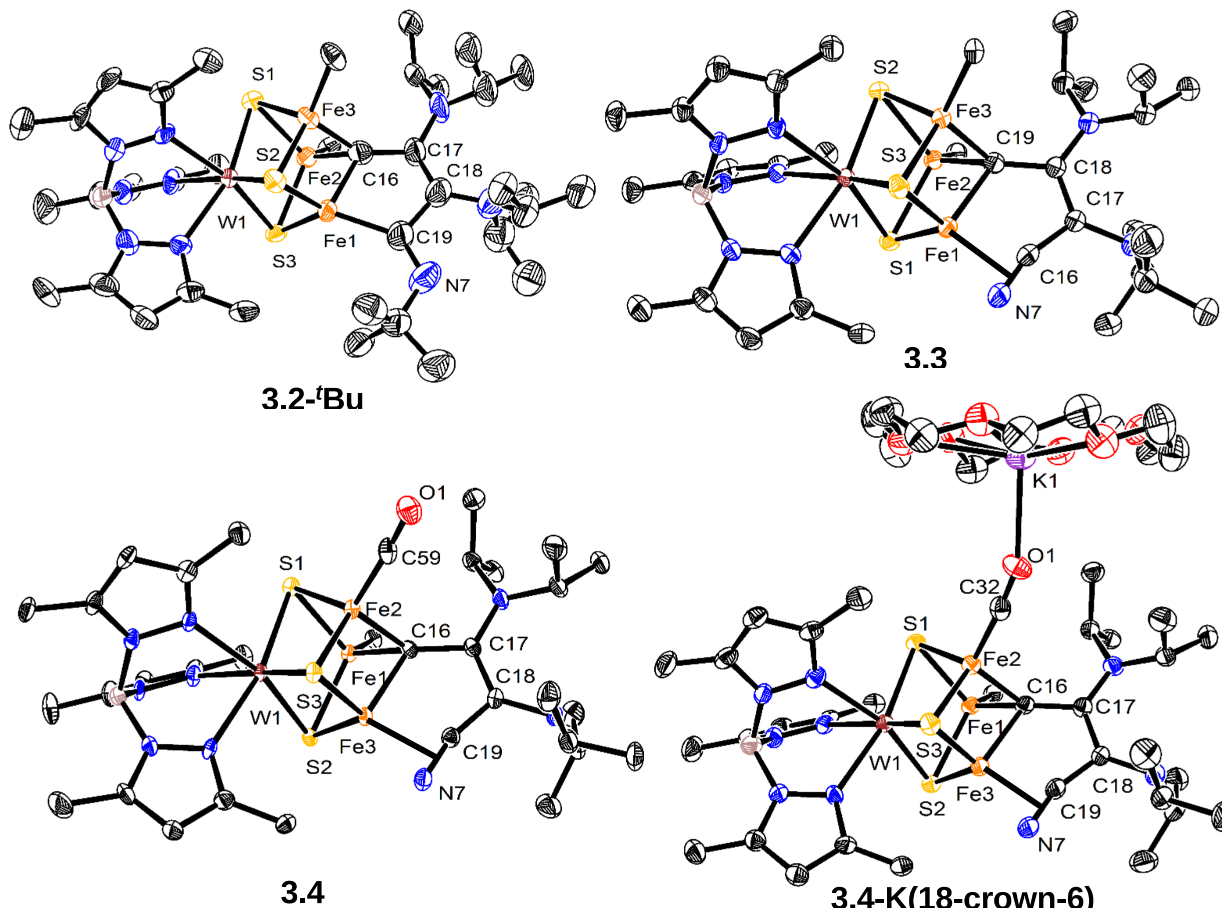

Figure 3.3. Crystal structures of **3.2-ᵗBu**, **3.3**, **3.4**, and **3.4-K(18-crown-6)**. Ellipsoids are shown at 50% probability level. Hydrogen atoms, solvent molecules, and the BAC ligand, except for the carbene C, are omitted for clarity.

In contrast, the Xyl-containing clusters exhibit different reactivities. As the loss of the Xyl radical is unfavorable, we attempted to mimic the transformation from **3.2-ᵗBu** to **3.3** with **3.2-Xyl** by employing an external oxidizing agent. Treatment of **3.2-Xyl** with AgOTf in THF at -78 °C leads to the clean formation of **3.5** as determined by XRD (Figure 3.4). The iminoacyl group in **3.5** coordinates to Fe in an η^2 manner, with the C-N distance of 1.266(7) Å within the range (1.26 – 1.28 Å) of previously reported complexes bearing η^2-iminoacyl moieties.[48–51] Moreover, this C-N distance is longer than in **3.3** (1.205(6) Å), consistent with a higher bond order in **3.3** and further supporting its assignment as a nitrile. Iminoacyl ligands coordinate to metals in η^1 or η^2 fashion depending on the nature of the metal center. [48,49,52] In **3.5**, the decrease in electron density at the iminoacyl-bound Fe center upon oxidation promotes binding of the N lone pair.

When treated with 1 atm CO over 24 h, **3.5** shows primarily starting material (Figure 3.4). The difference in reactivity between **3.3** and **3.5** is notable, given the same formal oxidation states, the same atoms in the first coordination sphere of the cluster, and the substitution of the same BAC ligand targeted. The divergence likely stems from the difference in the ligand on the Fe center remote from the CO-binding site. The two η^2-(N-C) ligands, formally $[\text{Xyl-C}\equiv\text{N-R}]^+$ in **3.5** and C≡N-R in **3.3**, have distinct electronic properties, with the nitrile being more electron releasing, resulting in a more electron rich Fe center. Indeed, Mössbauer measurements indicate that the Fe centers in **3.3** have a lower average oxidation state (δ_{ave} = 0.41 mm s^{-1} (**3.3**), δ_{ave} = 0.36 mm s^{-1} (**3.5**), Figure 3.S16). This difference promotes ligand substitution and CO binding in **3.3** and provides a demonstration of the impact of remote changes in cluster structure on reactivity.[53,54] Even **3.2-Xyl**, the reduced version of **3.5**, does not react with CO because changes in the binding mode of the iminoacyl ligand at the distal site still result in an increased average Fe oxidation state as supported by Mössbauer spectroscopy (δ_{ave} = 0.30 mm s^{-1}, Figure 3.S16).

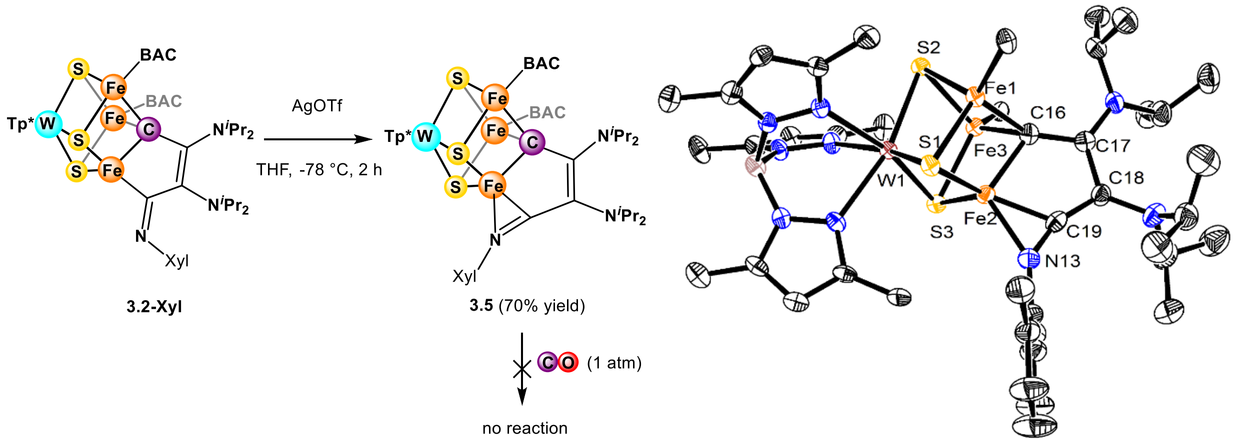

Figure 3.4. Oxidation of **3.2-Xyl** to **3.5** (Xyl = 2.6-dimethylphenyl) and crystal structure of **3.5**. Ellipsoids are shown at 50% probability level. Hydrogen atoms, counterions, solvent molecules, and the BAC ligand except for the carbene C are omitted for clarity.

To the best of our knowledge, **3.4** is the only well-characterized example of a heterometallic $MFe_3S_3(CR)$ cubane cluster bearing a single terminal CO ligand. This provides an opportunity for benchmarking the impact of structure and coordination environment relative to FeMoco. The THF solution IR spectrum of **3.4** displays a prominent peak at 1851 cm^{-1}, assigned as the C–O stretch

(Figure 3.5) and confirmed by ^{13}CO labeling ($\nu_{13CO\ exp}$ = 1807 cm^{-1}, $\nu_{13CO\ calc}$ = 1810 cm^{-1}), thereby suggesting highly activated CO.

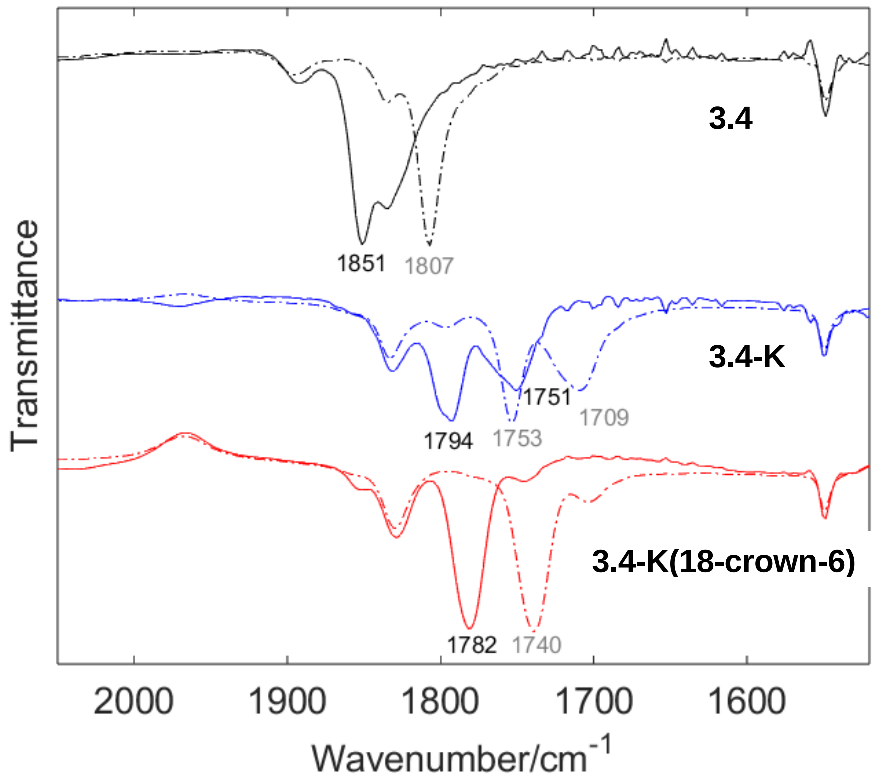

Figure 3.5. IR spectra of **3.4**, **3.4-K**, and **3.4-K(18-crown-6)** (THF solution) with ν_{CO} values shown. Dashed spectra correspond to ^{13}CO-labeled species with ν_{13CO} in gray. The feature at 1830 cm^{-1} unchanged upon ^{13}CO labeling is assigned to BAC.

To study the effects of cluster oxidation state on the level of CO activation, we reduced **3.4** with one equivalent of KC_8 or potassium naphthalenide to yield **3.4-K** (S = 3/2, see the Supporting Information) (Figure 3.2). As expected, the CO bond length increases upon reduction from 1.15(1) to 1.198(3) Å. The solution IR spectrum of **3.4-K** shows two C–O bands at 1794 and 1751 cm^{-1} (Figure 3.4), which is consistent with the crystal structure of **3.4-K** displaying CO–K^+ interactions disordered over two positions: terminal (36% occupancy) (assigned as **3.4-K$_{terminal}$**) and η^2 (64% occupancy) (assigned as **3.4-K$_{\eta2}$**). These isomers are collectively referred to as **3.4-K**. Chelation of K^+ with 18-crown-6 results in the formation of **3.4-K(18-crown-6)**. XRD shows that the K^+ ion is present in only one location and interacts end-on with the O atom of CO (Figure 3.3). In agreement, the IR spectrum shows a single band at 1782 cm^{-1} (Figure 3.5; $\nu_{13CO\ exp}$ = 1740 cm^{-1};

$\nu_{13CO\ calc}$ = 1742 cm^{-1}). The same band is observed upon treatment with [2.2.2]cryptand, thereby suggesting that the K^+ ion in **3.4-K(18-crown-6)** does not impact CO activation substantially.[55] The analogous Mo versions of the clusters, namely **3.2-Mo**, **3.3-Mo**, **3.4-Mo**, and **3.4-Mo-K(18-crown-6)**, have also been prepared similarly starting from **3.1-Mo**, and the CO-bound species exhibit similar ν_{CO} values to the W versions (Figure 3.S29).

Both **3.4-K** and **3.4-K(18-crown-6)** exhibit highly activated CO ligands coordinated to Fe in a terminal fashion. The interaction with K^+ in different binding modes affects the level of CO activation in the 1794 and 1751 cm^{-1} range. Previous computational work describes a semibridging CO ligand at Fe2 in FeMoco with a frequency of 1718 cm^{-1},[56] very close to that assigned to the bridging CO in lo-CO at 1715 cm^{-1}.[57] This is slightly lower than the typical values observed for μ_2-CO ligands, which lie in the 1720–1850 cm^{-1} range.[58] Hydrogen bonding between the carbonyl oxygen and the nearby His195 residue is proposed to further activate CO.[56] Similarly, in **3.4-K**, the K^+ cation can play the same role as the hydrogen bonding network and lower the C–O stretching frequency. Nevertheless, ν_{CO} values below 1800 cm^{-1} are unprecedented for FeS clusters. For comparison, the CO adducts of N-heterocyclic carbene (NHC)-supported Fe_4S_4 clusters reported by Suess and co-workers display C–O stretching frequencies of 1832 cm^{-1} for the $[Fe_4S_4]^0$ and 1902 cm^{-1} for the $[Fe_4S_4]^+$ states.[19] The local coordination environment at each Fe (FeS_2C in **3.4** and **3.4-K** and FeS_3 in $[Fe_4S_4]^{+,0}$) and oxidation state distribution between different metal sites can contribute to the level of diatomic activation.[19,53,59]

In order to understand the electronic structure origin of the profound CO activation in these clusters, we employed computational methods using broken symmetry density functional theory (BS-DFT) in collaboration with the DeBeer lab (Max Planck Institute for Chemical Energy Conversion). Our computational procedure detailed in the Supporting Information accurately assigns the geometric, Mössbauer, and vibrational properties of **3.4** and **3.4-K**. Here, we highlight the impact of the carbyne, W^{3+} center, and a K^+ countercation with respect to the strong CO activation in **3.4-K**.

The carbyne has three anionic lone pairs oriented along the Fe-bonding axes in its μ_3-binding mode. The localized orbitals characterize the carbyne lone pairs as σ-donors that stabilize the intermediate spin (IS) state of the three formal Fe^{2+} ($S = 1$) centers. Observing the IS state at the Fe sites that do not bind CO suggests that it is an innate property of the μ_3-carbyne ligand. The IS state in Fe^{2+} centers give full occupation of its π-backbonding orbitals, consistent with the increased CO activation in **3.4-K**. In agreement, hyperfine sublevel correlation (HYSCORE) spectra of **3.4-K(^{13}CO)** show small hyperfine coupling to the ^{13}C center of CO {$\boldsymbol{A}$(**^{13}C**) = [−0.5, 1.0, −0.5] MHz; see the Supporting Information}. A partially occupied Fe–CO backbonding orbital is expected to result in larger coupling.[5,60,61] In comparison, Fe centers in FeS clusters are routinely assigned as high-spin because of their weak ligand field environment, such as the $S = 3/2$ state assigned to the CO-bound Fe^{1+} by Suess and co-workers.[19]

Furthermore, the Fe centers are preferentially ferromagnetically coupled, which results in the equal delocalization of two electrons among the three Fe atoms (Figure 3.6). This formally lowers the oxidation state of the CO-bound Fe site from its formal 2+ to 1.33+ charge and proportionately increases the other Fe centers to 2.33+; their resonance states are illustrated in the Supporting Information. This is analogous to the net $Fe^{2.5+}$ oxidation state resulting from the equal delocalization of one electron between two Fe sites in formal Fe^{2+}–Fe^{3+} dimers.[62] This pairwise delocalization supports a reduced state at the CO-bound center that is otherwise inaccessible under biological conditions. Similarly, redox disproportionation has been proposed in previously reported [$Fe_6(\mu_6\text{-}C)(CO)_{18}$] and $Fe_4S_4(CO)(IMes)_3$ clusters, where Fe sites of different oxidation states are within close proximity.[19,63]

The anionic charge of **3.4**$^-$ supports strong noncovalent interactions with its countercation. The geometry optimization of **3.4-K** preferentially binds K^+ in an η^2-conformation with respect to the CO bond. The calculated CO stretching frequency decreases from 1800 cm^{-1} without K^+ to 1756 cm^{-1}, which is consistent with the distinct vibrational modes observed in the IR spectrum of **3.4-K**. The electronic structure of the cluster is not impacted by K coordination, thereby suggesting that it is a purely ionic interaction that stabilizes the π-bonding of the CO ligand.

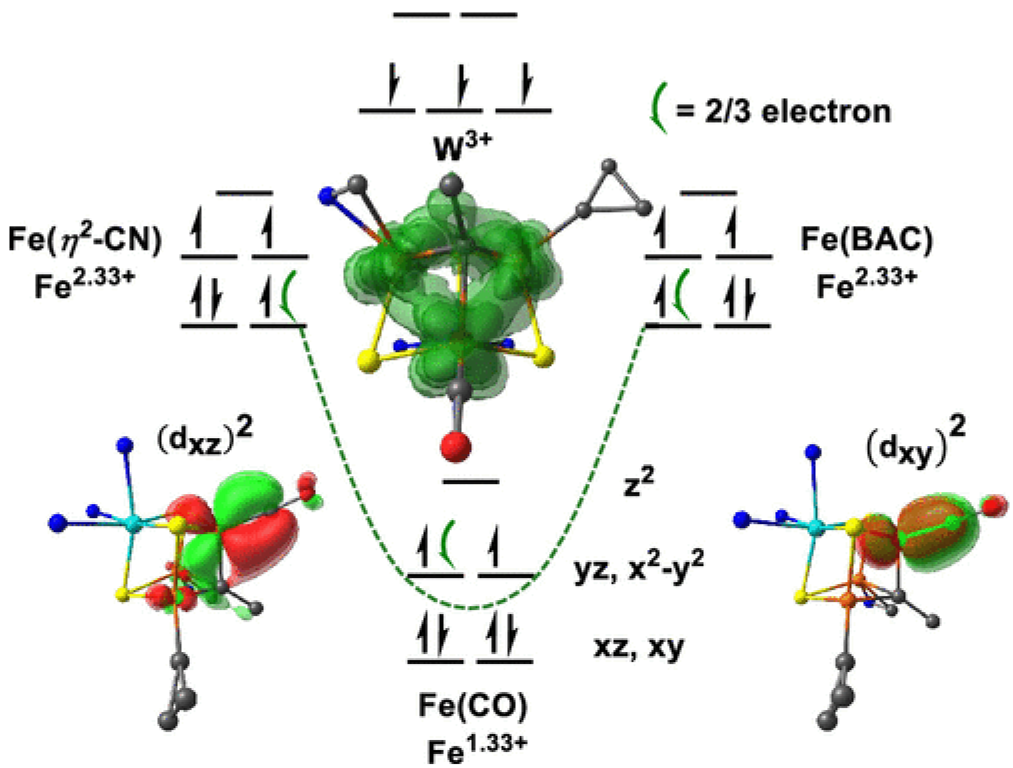

Figure 3.6. Local oxidation and spin states of the metal centers of **3.4**⁻ (S = 3/2) with respect to the Mulliken spin population of their PM-localized orbitals (Figures 3.S45 – 47).The curved green arrow denotes a pair of electrons that are equally delocalized among the Fe centers (illustrated in the inset) with respect to its localized spin density. The degenerate Fe–CO π-bonding interactions are shown at the bottom with respect to their localized orbitals.

The CO lone pair can overlap with orbitals arising from the Fe–W interaction assigned as purely covalent in **3.4**⁻ on the basis of the localized orbitals (see Figure 3.S45 for a graphical representation). The Fe–W covalent interaction redistributes electron density between the metal centers promoting the electrostatic attraction with the CO lone pair and consequently also enhances the π*-backbonding discussed above.[64,65] The other Fe centers exhibit bonding characters that are intermediate of a covalent and magnetic interaction, analogous to bonding properties detailed in the Mo^{3+} heteroatom of FeMoco.[66,67] In contrast, this is not observed for the cluster reported by Suess and co-workers[19] because of the comparatively weak bonding interactions between Fe sites. Overall, these factors contribute to the stronger CO activation in **3.4**⁻ compared with these reported clusters with an average metal oxidation state of 2+, despite the higher average metal oxidation state of 2.25+ in **3.4**⁻.[19]

3.4 CONCLUSION

In summary, we have reported a series of heterometallic WFe_3S_3CR cubanes and demonstrated several types of organometallic transformations and binding modes that are rare for iron–sulfur clusters. These compounds show C–C coupling, along with side-on binding of an organic nitrile moiety at one Fe site. Furthermore, we characterized the first example of a heterometallic iron–sulfur cluster with a single terminally bound, highly activated CO ligand in two oxidation states. Computation suggests an unusual carbyne-promoted intermediate spin electronic configuration at all Fe sites, along with a low oxidation state of 1.33+ for Fe(CO) in **3.4**$^{-}$. This electron configuration affords full occupancy of the two π-back-bonding orbitals to CO, which are responsible for the high level of CO activation in the reduced clusters. The negative charge of the cluster and the metal–metal covalency were found computationally to also impact CO activation. These findings provide a set of parameters to evaluate in future studies for the conversion of substrates in nitrogenase.

3.5 SUPPORTING INFORMATION

A) Synthetic details and characterization

1. General considerations:

All reactions were performed at room temperature in a N_2-filled MBraun glovebox or using standard Schlenk techniques unless otherwise specified. Glassware was oven-dried at 140 °C for at least 2 h prior to use and allowed to cool under vacuum. **3.1** and **3.1-Mo** were prepared according to literature procedures.[33] Diethyl ether, benzene, tetrahydrofuran (THF), and pentane were dried by sparging with N_2 for at least 15 min and then passing through a column of activated A2 alumina under positive N_2 pressure, and stored over 3 Å molecular sieves prior to use. ^{1}H spectra were recorded on a Varian 300 MHz spectrometer. Deuterated benzene (C_6D_6) was purchased from Cambridge Isotope Laboratories, dried over sodium/benzophenone ketyl, degassed by three freeze–pump–thaw cycles, and vacuum-transferred prior to use. IR spectra were obtained as either solution samples using a KBr window cell on a Thermo Scientific Nicolet 6700 FT-IR spectrometer or thin films formed by evaporation of solutions using a Bruker Alpha Platinum ATR spectrometer with OPUS software in a glovebox under an N_2 atmosphere.

2. Procedures:

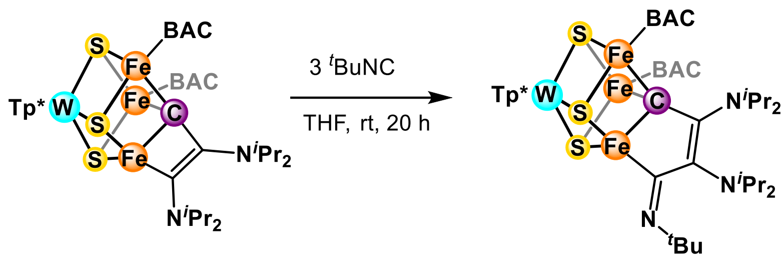

3.1 **3.2-ᵗBu**

Synthesis of **3.2-ᵗBu**. In a glovebox, **3.1** (300.0 mg, 0.206 mmol, 1 equiv) was dissolved in THF (15 mL). To this solution, ᵗBuNC (70 µL, 0.619 mmol, 3 equiv) was added to the reaction using a microsyringe. The reaction was stirred at room temperature for 20 h, after which the volatiles were removed *in vacuo*. The crude material was used without further purification. Yield: 317 mg (quant). X-ray quality crystals of **3.2-ᵗBu** were grown by first washing the crude material with pentane and Et_2O, extracting the product into C_6H_6 and diffusing HMDSO into a concentrated C_6H_6 solution for several days. ^{1}H NMR (400 MHz, THF-h_8, solvent suppression) δ 12.91, 7.28, 6.89, 6.14, 5.56, 5.13, 0.42, -1.57, -2.77, -2.95, -3.35, -3.76, -4.98, -6.36. Anal. calcd (%) $C_{65}H_{115}BFe_3N_{13}S_3W$ (M_r = 1537.09): C, 50.79; H, 7.54; N, 11.85. Found: C, 50.55; H, 8.44; N, 11.54.

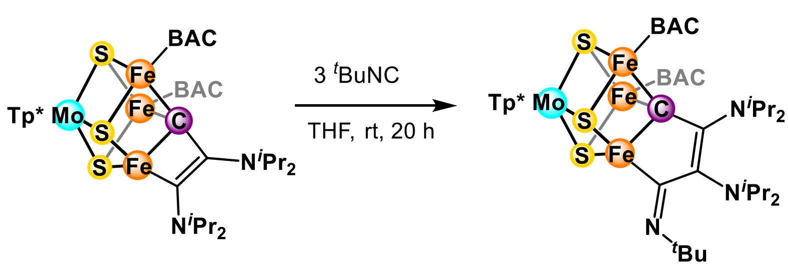

3.1-Mo **3.2-Mo-ᵗBu**

Synthesis of **3.2-Mo-ᵗBu**. In a glovebox, **3.1-Mo** (30.0 mg, 0.022 mmol, 1 equiv) was dissolved in THF (2 mL). To this solution, ᵗBuNC (7 µL, 0.066 mmol, 3 equiv) was added to the reaction using a microsyringe. The reaction was stirred at room temperature for 20 h, after which the volatiles were removed *in vacuo*. The crude material was used without further purification. Yield: 32 mg (quant). The cluster does not crystallize well but its structure was assigned based on similarities in the NMR spectrum compared to the W version. ^{1}H NMR (400 MHz, THF-h_8, solvent suppression) δ 12.24, 9.09, 7.62, 6.98, 6.37, 6.05, 5.82, 5.70, 0.46, -0.23, -1.58, -1.74, -1.89, -5.16, -5.72, -7.52.

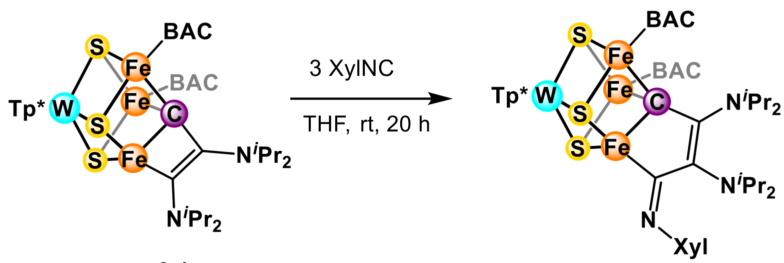

3.1 3.2-Xyl

Synthesis of **3.2-Xyl**. In a glovebox, **3.1** (210.0 mg, 0.144 mmol, 1 equiv) and XylNC (56.8 mg, 0.433 mmol, 3 equiv) were combined in THF (5 mL). The reaction was stirred at room temperature for 20 h, after which the volatiles were removed *in vacuo*. The crude material was triturated three times with Et_2O and washed with Et_2O. The solid was redissolved in a minimal amount of THF, filtered and crystallized by THF/pentane vapor diffusion. Yield: 195 mg (85%). X-ray quality crystals were grown by diffusing Et_2O into a concentrated solution of **3.2-Xyl** in THF. ^{1}H NMR (400 MHz, THF-h_8, solvent suppression) δ 15.53, 11.59, 11.10, 9.63, 7.26, 6.99, 6.45, 6.01, 5.54, 0.24, -0.66, -1.80, -1.86, -2.77, -3.36. Anal. calcd (%) $C_{69}H_{115}BFe_3N_{13}S_3W$ (M_r = 1585.14): C, 52.28; H, 7.31; N, 11.49. Found: C, 51.24; H, 7.35; N, 12.44.

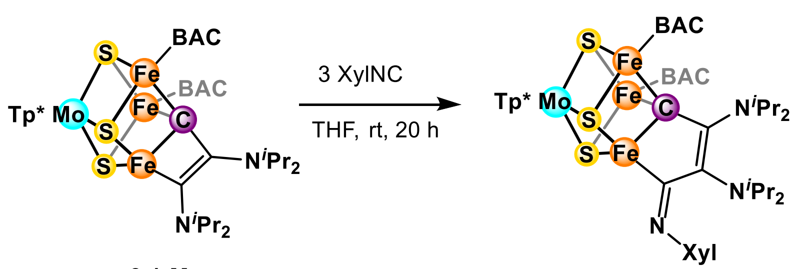

3.1-Mo 3.2-Mo-Xyl

Synthesis of **3.2-Mo-Xyl**. In a glovebox, **3.1-Mo** (20.0 mg, 0.015 mmol, 1 equiv) and XylNC (5.8 mg, 0.045 mmol, 3 equiv) were combined in THF (2 mL). The reaction was stirred at room temperature for 20 h, after which the volatiles were removed *in vacuo*. The crude material was triturated three times with Et_2O and washed with Et_2O. The solid was redissolved in a minimal amount of THF, filtered and crystallized by THF/pentane vapor diffusion. The crystals obtained from C_6H_6/Et_2O vapor diffusion diffract weakly but a connectivity can be established. 1H NMR (400 MHz, THF-h_8, solvent suppression) δ 14.54, 10.06, 8.89, 7.25, 7.07, 6.75, 6.11, 5.31, 4.24, 0.18, -0.82, -0.98, -1.07, -1.70, -1.90.

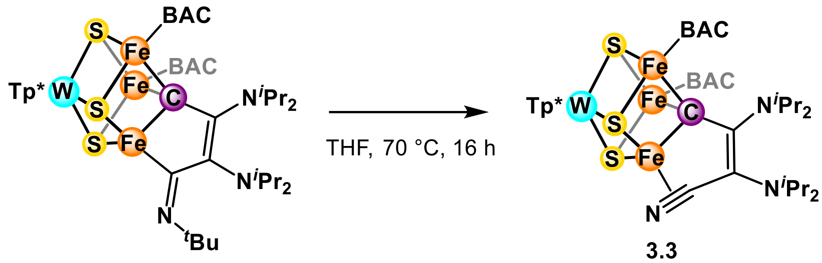

3.2-^{t}Bu

3.3

Synthesis of **3.3**. In a glovebox, crude **3.2-^{t}Bu** (300.0 mg, 0.195 mmol) was added to a Schlenk tube and dissolved in THF (6 mL). The tube was capped, taken out of the box and heated in an oil bath at 70 °C for 16 h. The tube must be closed while heated to give **3.3** (***NOTE: heating a closed system can lead to an explosion, so make sure the amount of solvent is much smaller than the flask volume and that the reaction does not boil). The tube was then cooled, brought back into the box and the solvent removed *in vacuo*. The resultant solid was triturated in pentane, washed with pentane and Et_2O, then redissolved in THF and crystallized by THF/pentane vapor diffusion to yield X-ray quality crystals. Yield: 148 mg (51%). The mother liquor still contains some **3.3** although less pure, but it can be used to prepare **3.4**. ^{1}H NMR (400 MHz, THF-h$_8$, solvent suppression) δ 14.89, 8.24, 6.91, 6.43, 5.16, 1.31, 1.07, 0.84, 0.59, 0.02, -0.58, -3.17, -3.48, -4.48. Anal. calcd (%) $C_{61}H_{106}BFe_3N_{13}S_3W{\cdot}THF$ (M_r = 1552.08): C, 50.30; H, 7.40; N, 11.73. Found: C, 50.17; H, 7.80; N, 11.04.

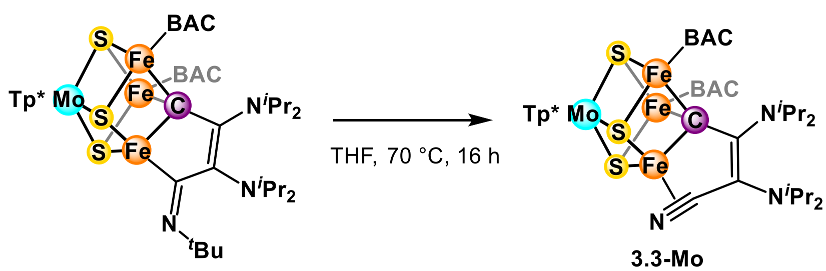

3.2-Mo-^{t}Bu

3.3-Mo

Synthesis of **3.3-Mo**. In a glovebox, crude **3.2-Mo-^{t}Bu** (344.8 mg, 0.238 mmol) was added to a Schlenk tube and dissolved in THF (6 mL). The tube was capped, taken out of the box and heated in an oil bath at 70 °C for 16 h. The tube must be closed while heated to give **3.3-Mo** (***NOTE: heating a closed system can lead to an explosion, so make sure the amount of solvent is much smaller than the flask volume and that the reaction does not boil). The tube was then cooled, brought back into the box and the solvent removed *in vacuo*. The resultant solid was triturated in pentane, washed with pentane and Et_2O, then redissolved in THF and crystallized by THF/pentane vapor diffusion to yield X-ray quality crystals. Yield: 256 mg (77%). ^1H NMR (400 MHz, THF-h_8, solvent suppression) δ 10.63, 7.94, 7.54, 6.58, 4.77, 4.28, 2.79, 0.97, 0.13, -1.79, -3.35, -4.86. Anal. calcd (%) $C_{61}H_{106}BFe_3N_{13}S_3Mo{\cdot}THF$ (M_r = 1466.20): C, 53.25; H, 7.97; N, 12.42. Found: C, 52.65; H, 8.18; N, 12.08.

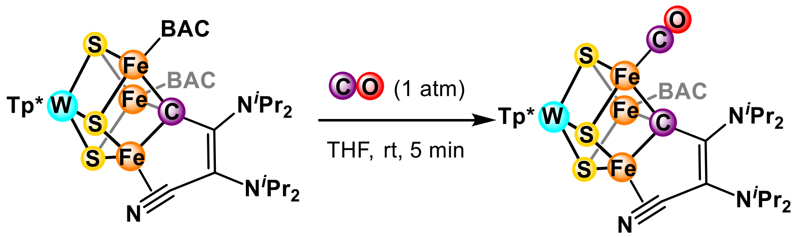

Synthesis of **3.4**. In a glovebox, **3.3** (132.0 mg, 0.089 mmol) was added to a Schlenk tube and dissolved in THF (5 mL). The tube was capped and degassed by three freeze-pump-thaw cycles on a Schlenk line. Then, the headspace of the tube was pressurized with 1 atm CO. The tube was capped again and inverted over a period of 5 minutes, after which the solution changed from green-brown to red-brown. NMR spectroscopy typically indicates the complete consumption of **3.3** at this point. The volatiles were removed *in vacuo* and the tube was brought back into the box. The resultant solid was washed with Et_2O then redissolved in THF to crystallize by THF/pentane vapor diffusion. Yield: 94.2 mg (83%). X-ray quality crystals can be grown by washing the crude material with C_6H_6, followed by vapor diffusion of Et_2O into a concentrated solution of **3.4** in THF. ^1H NMR (400 MHz, THF-h_8, solvent suppression) δ 10.18, 8.48, 7.24, 6.91, 6.81, 5.81, 5.58, 1.40, 1.23, 1.10, 1.06, 0.83, -0.28, -1.58, -3.73. Anal. calcd (%) $C_{47}H_{78}BFe_3N_{11}OS_3W$ (M_r = 1271.58): C, 44.39; H, 6.18; N, 12.12. Found: C, 44.49; H, 6.91; N, 11.15.

Synthesis of **3.4** with ^{13}CO. In a glovebox, **3.3** (20.0 mg, 0.013 mmol) was added to a 20 mL Schlenk tube with a stir bar and dissolved in THF (2 mL). The tube was capped and degassed by three freeze-pump-thaw cycles on a Schlenk line, capped tightly, then connected to one end of a glass solvent transfer bridge (as small as possible to minimize the amount of unused ^{13}CO), which is connected to the Schlenk line. The other end of the tube was connected to a ^{13}CO flask (~1 atm in 500 mL). The system was evacuated, then the solution was frozen in liquid nitrogen to prevent solvent contamination to the ^{13}CO flask. Then, the transfer bridge was closed to vacuum (similarly to a solvent vacuum transfer), and the ^{13}CO flask was opened to fill the system with ^{13}CO. The reaction tube was opened for about 5 minutes to fill the headspace with ^{13}CO while still frozen, then capped again and thawed while stirring vigorously. The solution changed from green-brown to red-brown after about 10 minutes. The tube was left to stir for 2 h, after which the volatiles were removed *in vacuo* and the tube was brought back into the box. The resultant solid was washed with Et_2O then redissolved in THF to crystallize by THF/pentane vapor diffusion. Yield: 7.1 mg (41%). NMR data are identical to **3.4** prepared from regular CO.

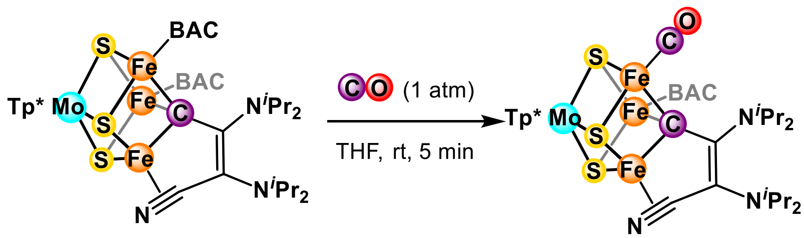

3.3-Mo **3.4-Mo**

Synthesis of **3.4-Mo**. In a glovebox, **3.3-Mo** (130.0 mg, 0.093 mmol) was added to a Schlenk tube and dissolved in THF (5 mL). The tube was capped and degassed by three freeze-pump-thaw cycles on a Schlenk line. Then, the headspace of the tube was pressurized with 1 atm CO. The tube was capped again and inverted over a period of 5 minutes, after which the solution changed from green-brown to red-brown. NMR spectroscopy typically indicates the complete consumption of **3.3-Mo** at this point. The volatiles were removed *in vacuo* and the tube was brought back into the box. The resultant solid was washed with Et_2O then redissolved in THF to crystallize by THF/pentane vapor diffusion. Yield: 84 mg (76%). X-ray quality crystals can be grown by vapor diffusion of Et_2O into a concentrated solution of **3.4-Mo** in THF. ν_{CO} = 1858 cm^{-1}. ^{1}H NMR (400 MHz, THF-h_8, solvent suppression) δ 7.53, 6.92, 6.65, 6.17, 5.66, 1.47, 1.37, 1.26, 1.22, 1.09, 0.86, 0.38, -0.28, -3.46. Anal. calcd (%) $C_{47}H_{78}BFe_3N_{11}OS_3Mo\cdot THF$ (M_r = 1241.81): C, 49.33; H, 7.14; N, 12.41. Found: C, 48.51; H, 7.29; N, 11.52.

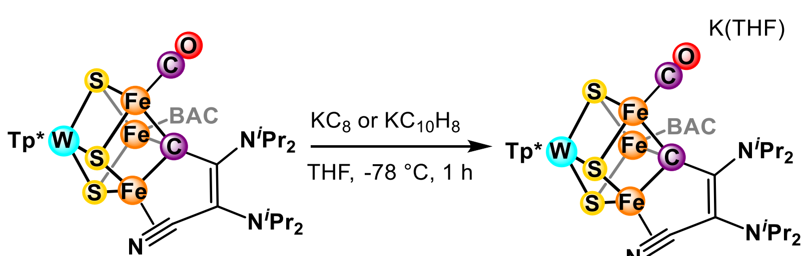

3.4 **3.4-K**

Synthesis of **3.4-K**. In a glovebox, **3.4** (20.0 mg, 0.016 mmol, 1 equiv) was dissolved in THF (2 mL) in a 20 mL scintillation vial with a pre-reduced Teflon stir bar to form a dark red-brown solution and cooled to -78 °C in the cold well. To this solution was added KC_8 (2.5 mg, 0.019 mmol, 1.2 equiv) or potassium naphthalenide (0.157 mL, 0.1 M in THF, 0.016 mmol, 1 equiv) and the dark green-brown reaction was stirred at -78 °C. After 2 h, the solution was filtered through Celite and the solvent removed *in vacuo*. The resultant solid was washed with Et_2O, then redissolved in THF and crystallized by THF/pentane vapor diffusion. Yield: 19 mg (88%). X-ray quality crystals were grown by vapor diffusion of Et_2O into a concentrated solution of **3.4-K** in THF. ^1H NMR (400 MHz, THF-h_8, solvent suppression) δ 15.24, 14.71, 10.86, 8.88, 6.43, 6.12, 5.13, 2.83, 2.42, 1.04, 0.79, 0.10, -0.42, -3.31, -8.89, -12.96. Anal. calcd (%) $C_{47}H_{78}BFe_3N_{11}OS_3WK{\cdot}THF$ (M_r = 1382.79): C, 44.30; H, 6.27; N, 11.14. Found: C, 44.82; H, 6.30; N, 10.96. The ^{13}CO-labeled version was prepared identically from ^{13}CO-labeled **3.4** for IR spectroscopy.

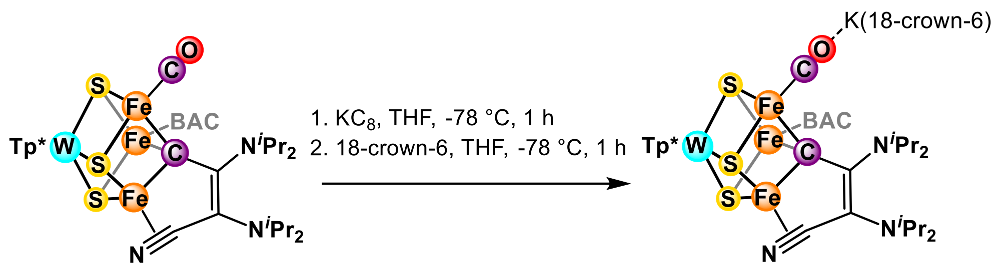

Synthesis of **3.4-K(18-crown-6)**. In a glovebox, **3.4** (12.8 mg, 0.010 mmol, 1 equiv) was dissolved in THF (2 mL) in a 20 mL scintillation vial with a pre-reduced Teflon stir bar to form a dark red-brown solution and cooled to -78 °C in the cold well. To this solution was added excess KC_8 (2.3 mg, 0.020 mmol, 2 equiv) and the dark green-brown reaction was stirred at -78 °C. After 2 h, IR spectroscopy indicated the disappearance of the starting material, and excess 18-crown-6 (5.4 mg, 0.020 mmol, 2 equiv) was added to the reaction. The solution was stirred at -78 °C for another 2 h before taking an aliquot for IR spectroscopy and concentrated under vacuum, then filtered through Celite and crystallized by THF/pentane vapor diffusion. Yield: 10 mg (64%). X-ray quality crystals were grown by vapor diffusion of Et_2O into a concentrated solution of **3.4-K(18-crown-6)** in DME. ^1H NMR (400 MHz, THF-h_8, solvent suppression) δ 19.10, 11.39, 9.07, 6.44, 6.04, 5.41, 2.94, 2.54, 1.07, 0.84, 0.10, -0.64, -3.82, -9.78, -14.87. Anal. calcd (%) $C_{59}H_{102}BFe_3KN_{11}O_7S_3W$

(M_r = 1575.00): C, 44.99; H, 6.53; N, 9.78. Found: C, 43.14; H, 6.31; N, 9.57. The ^{13}CO-labeled version was prepared identically from ^{13}CO-labeled **3.4**.

The reaction was also carried out identically using [2.2.2]cryptand instead of 18-crown-6 for IR spectroscopy, which shows the same C-O stretch.

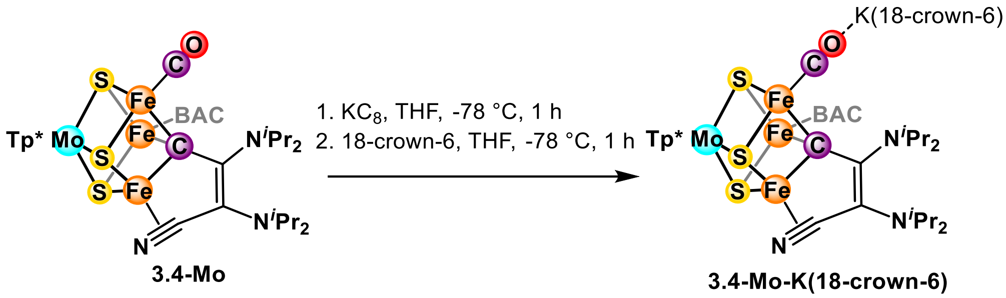

Synthesis of **3.4-Mo-K(18-crown-6)**. In a glovebox, **3.4-Mo** (40.0 mg, 0.034 mmol, 1 equiv) was dissolved in THF (2 mL) in a 20 mL scintillation vial with a pre-reduced Teflon stir bar to form a dark red-brown solution and cooled to -78 °C in the cold well. To this solution was added excess KC_8 (9.1 mg, 0.068 mmol, 2 equiv) and the dark green-brown reaction was stirred at -78 °C. After 2 h, excess 18-crown-6 (17.8 mg, 0.068 mmol, 2 equiv) was added to the reaction. The solution was stirred at -78 °C for another 2 h before taking an aliquot for IR spectroscopy and concentrated under vacuum, then filtered through Celite and purified by THF/pentane vapor diffusion. Yield: 48 mg (96%). The cluster does not crystallize well but its structure was assigned based on similarities in the NMR spectrum compared to the W version. ν_{CO} = 1786 cm^{-1}. ^{1}H NMR (400 MHz, THF-h_8, solvent suppression) δ 12.12, 8.28, 6.36, 5.91, 0.95, 0.75, 0.32, -0.08, -2.13, -3.09, -11.07.

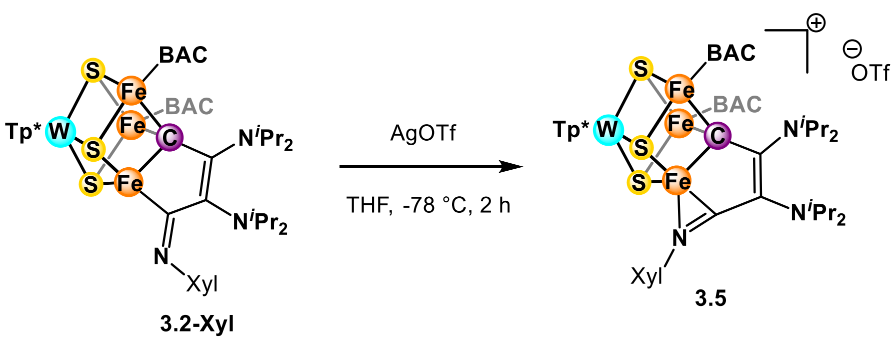

Synthesis of **3.5**. In a glovebox, **3.2-Xyl** (52.1 mg, 0.033 mmol, 1 equiv) was dissolved in THF (2 mL) in a 20 mL scintillation vial with a stir bar to form a dark green-brown solution and cooled to -78 °C in the cold well. To this solution was added AgOTf (8.4 mg, 0.033 mmol, 1 equiv) and the dark red-brown reaction was stirred at -78 °C. After 2 h, the solution was filtered through Celite and the solvent removed *in vacuo*. The resultant solid was washed with Et_2O, then redissolved in THF and crystallized by THF/pentane vapor diffusion. Yield: 40 mg (70%). X-ray quality crystals were grown by vapor diffusion of $^{i}Pr_2O$ into a concentrated solution of **3.5** in THF. ^{1}H NMR (400 MHz, THF-h_8, solvent suppression) δ 13.29, 11.09, 10.22, 7.33, 6.97, 6.38, 5.88, 5.75, 4.99, 1.08, 0.38, -0.27, -1.10, -1.88. Anal. calcd (%) $C_{70}H_{115}BFe_3N_{13}S_4F_3O_3W$ (M_r = 1734.20): C, 48.48; H, 6.68; N, 10.50. Found: C, 48.71; H, 6.60; N, 12.91.

The following cluster was not discussed in the main text but was also isolated to provide more support for reactivity pattern.

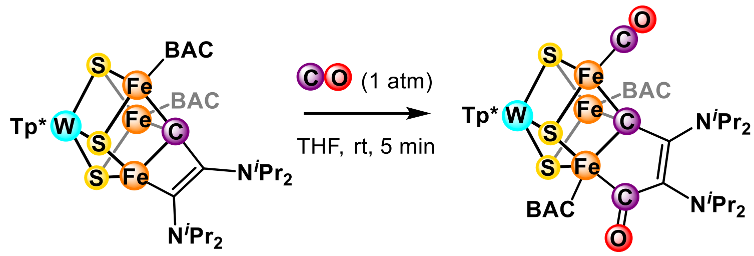

3.1 **3.6**

(structured determined by X-ray crystallography)

Reaction of **3.1** *with 1 atm CO*. Treatment of **3.1** with 1 atm CO results in a complex reaction mixture by ^{1}H NMR spectroscopy (see SI), but one product could be characterized by crystallography. In a glovebox, **3.1** (20.0 mg, 0.014 mmol) was dissolved in THF (0.7 mL) and transferred to a J. Young NMR tube. The tube was capped and degassed by three freeze-pump-thaw cycles on a Schlenk line. Then, the headspace of the tube was pressurized with 1 atm CO. The tube was capped again and inverted over a period of 5 minutes, after which NMR spectroscopy indicated the complete consumption of **3.1** and the appearance of new peaks between -2 and -12 ppm. The tube was brought back into the glovebox and the solvent was removed *in vacuo* to yield a dark film. The film was washed with pentane and the product was extracted into Et_2O and filtered through a pad of Celite before the solvent was removed *in vacuo*. The resultant material was redissolved in a minimal amount of Et_2O and placed at -35 °C for several days to yield X-ray quality crystals, whose structure is determined to be **3.6**. Despite multiple trials, only a few crystals of **3.6** were observed each time, which precludes bulk characterization.

For all the reactions that result in products that can be isolated and characterized, spectroscopic yields were also measured by NMR spectroscopy. Each reaction was carried out on a small scale, and a known amount of an internal standard (4-phenylbenzaldehyde or cobaltocene) was added at the end of the reaction mixture without working up. Separately, a known amount of the same internal standard was added to a known amount of purified material. Comparison of the integrations between a pair of non-overlapping peaks (one each for the standard and the analyte) in both cases allows for the determination of reaction yields by NMR spectroscopy. The table below displays the results.

Table 3.S1. Measured NMR spectroscopic yields for reactions

Product	Spectroscopic yield/%	Isolated yield/%	Standard
3.2-^{t}Bu	98	Quant	4-phenylbenzaldehyde
3.2-Xyl	94	85	4-phenylbenzaldehyde
3.3	61	51	4-phenylbenzaldehyde
3.4	87	83	4-phenylbenzaldehyde
3.4-K	90	88	cobaltocene
3.4-K(18-crown-6)	92	64	cobaltocene
3.5	93	70	4-phenylbenzaldehyde

3. NMR spectra:

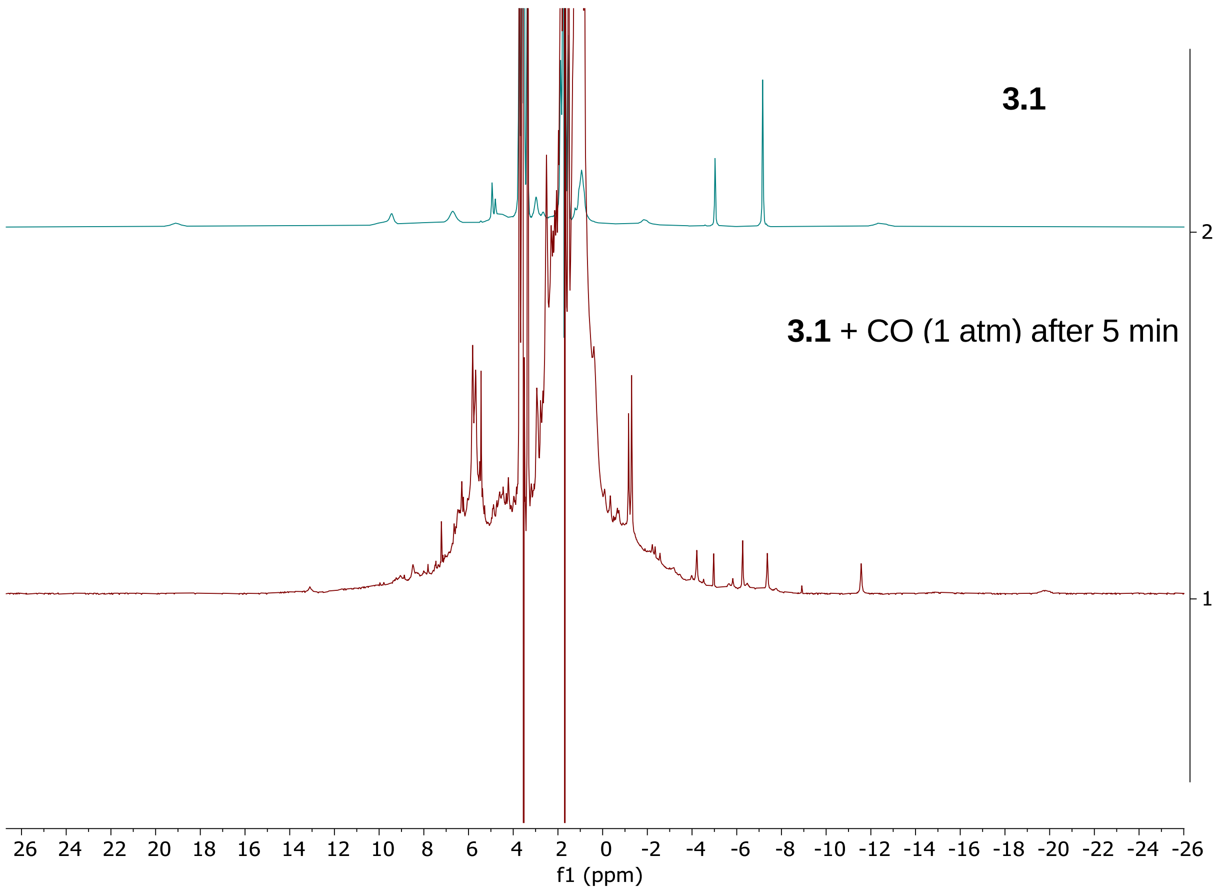

Figure 3.S1. ^{1}H NMR spectrum (400 MHz, THF-h_8, solvent suppression) of **3.1** (top) and **3.1** + CO (1 atm) after mixing for 5 min (bottom). The peaks corresponding to the starting material disappear and new peaks appear within the -2 to -12 ppm region, assigned to **3.6** (structure below as determined by X-ray crystallography).

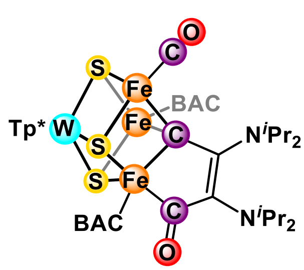

3.6

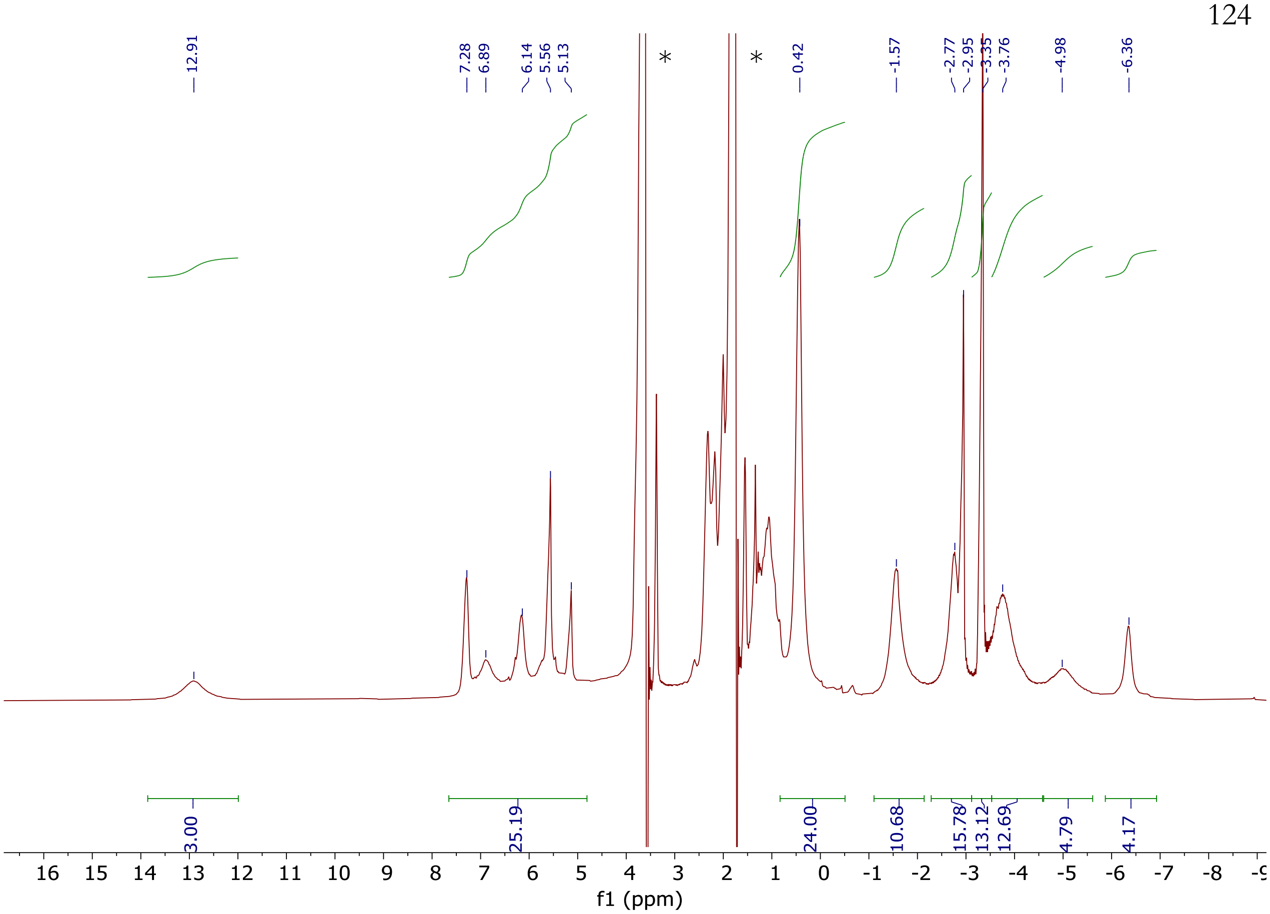

Figure 3.S2. ^{1}H NMR spectrum (400 MHz, THF-h_8, solvent suppression) of **3.2-*^{t}*Bu**. Solvent peaks are indicated by asterisks (*).

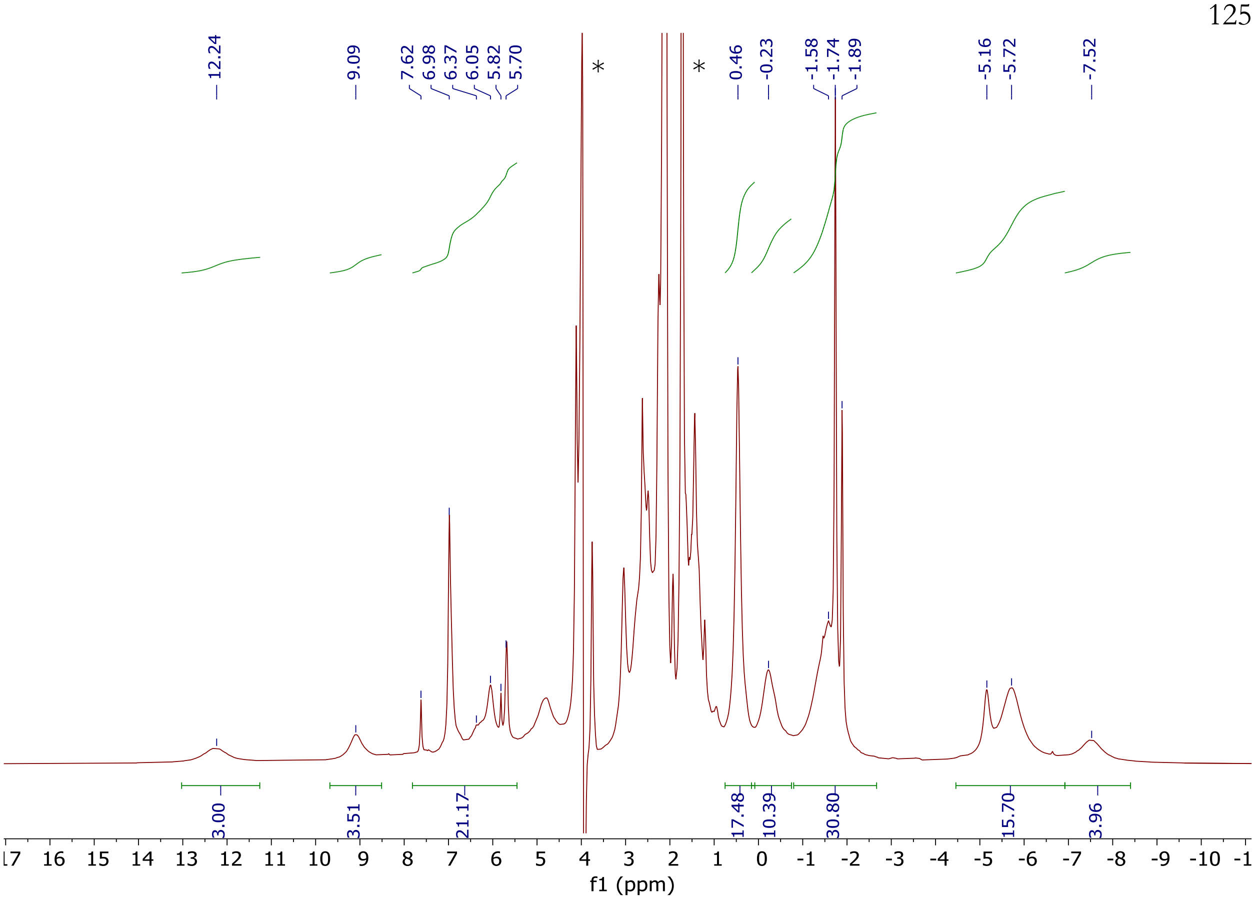

Figure 3.S3. ^{1}H NMR spectrum (400 MHz, THF-h_8, solvent suppression) of **3.2-Mo-^{t}Bu**. Solvent peaks are indicated by asterisks (*).

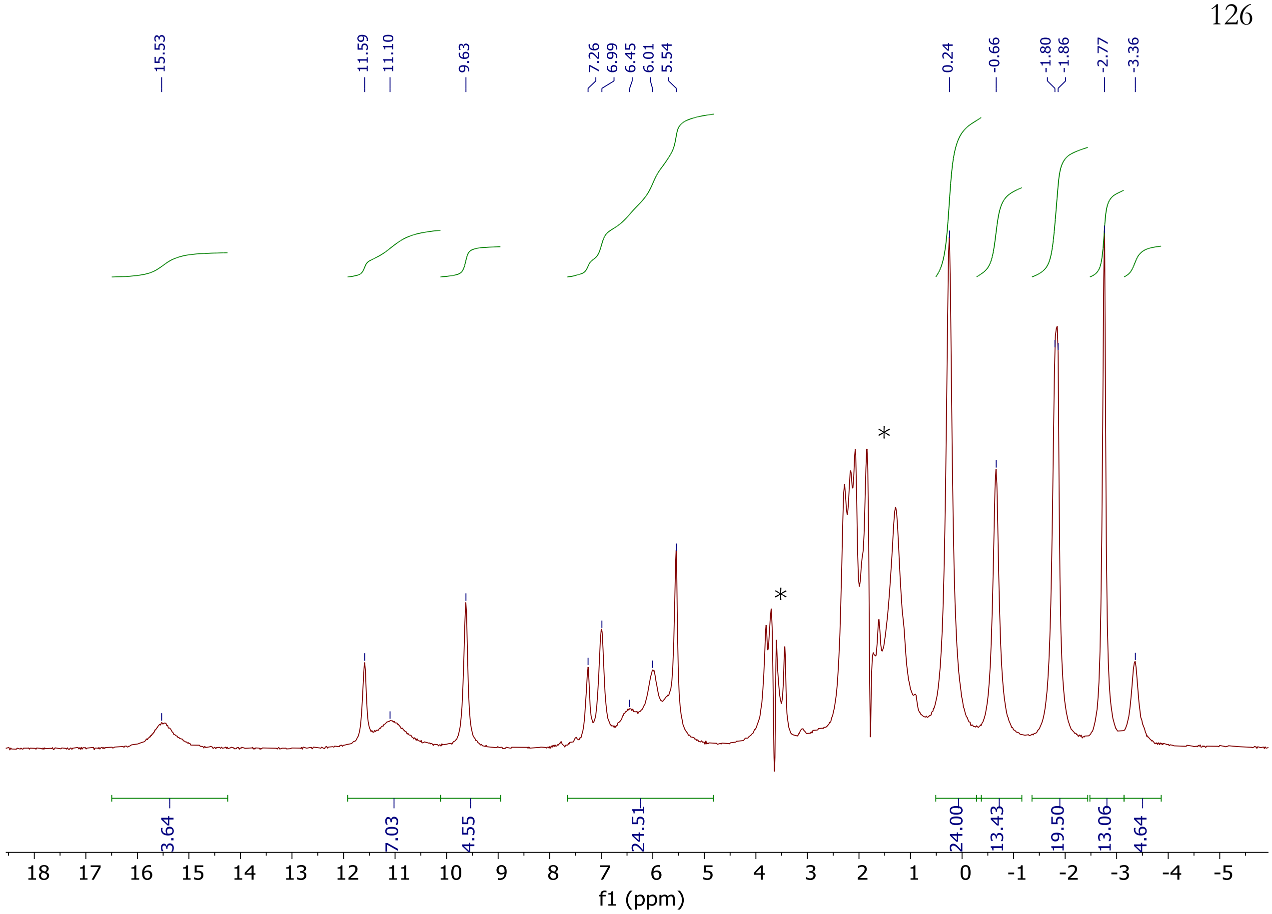

Figure 3.S4. [1]H NMR spectrum (400 MHz, THF-h_8, solvent suppression) of **3.2-Xyl**. Solvent peaks are indicated by asterisks (*).

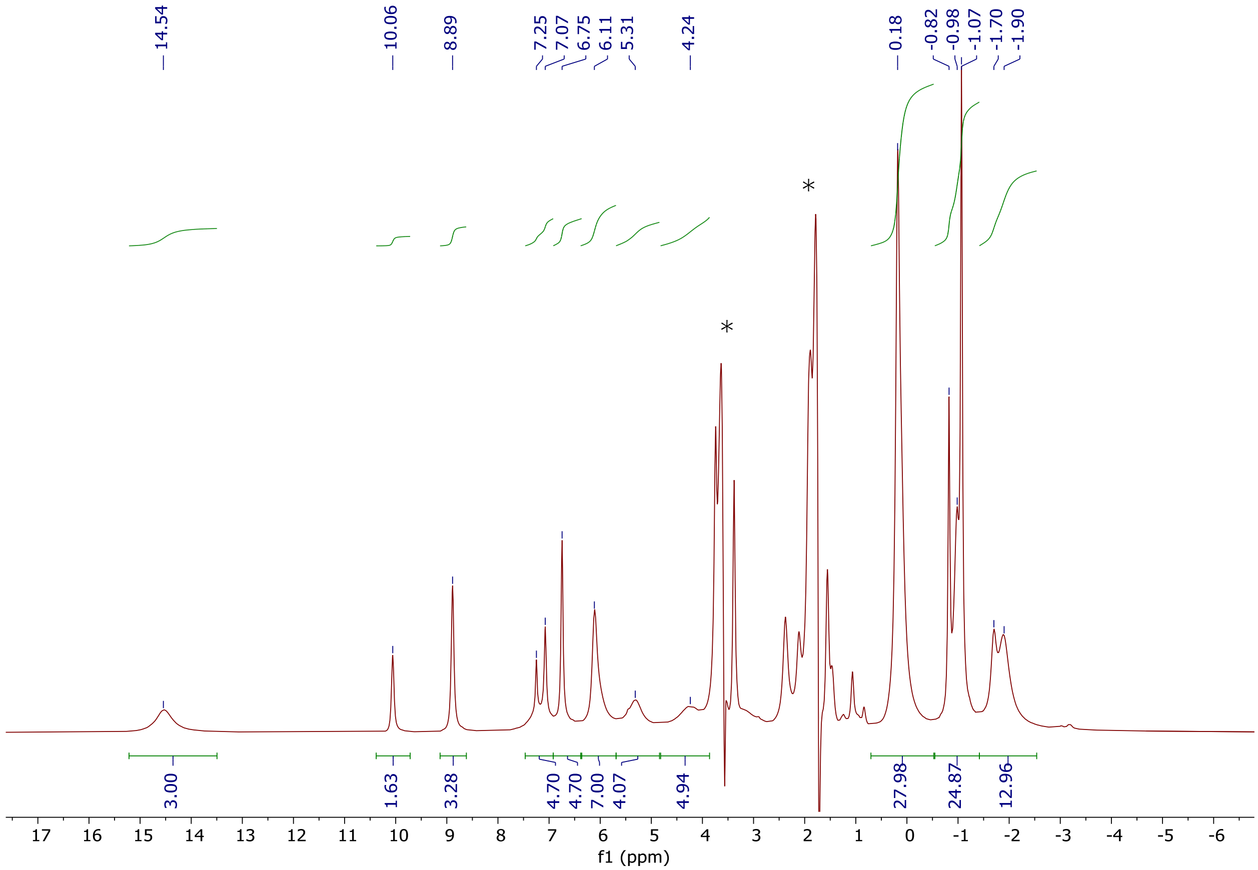

Figure 3.S5. ^{1}H NMR spectrum (400 MHz, THF-h_8, solvent suppression) of **3.2-Mo-Xyl**. Solvent peaks are indicated by asterisks (*).

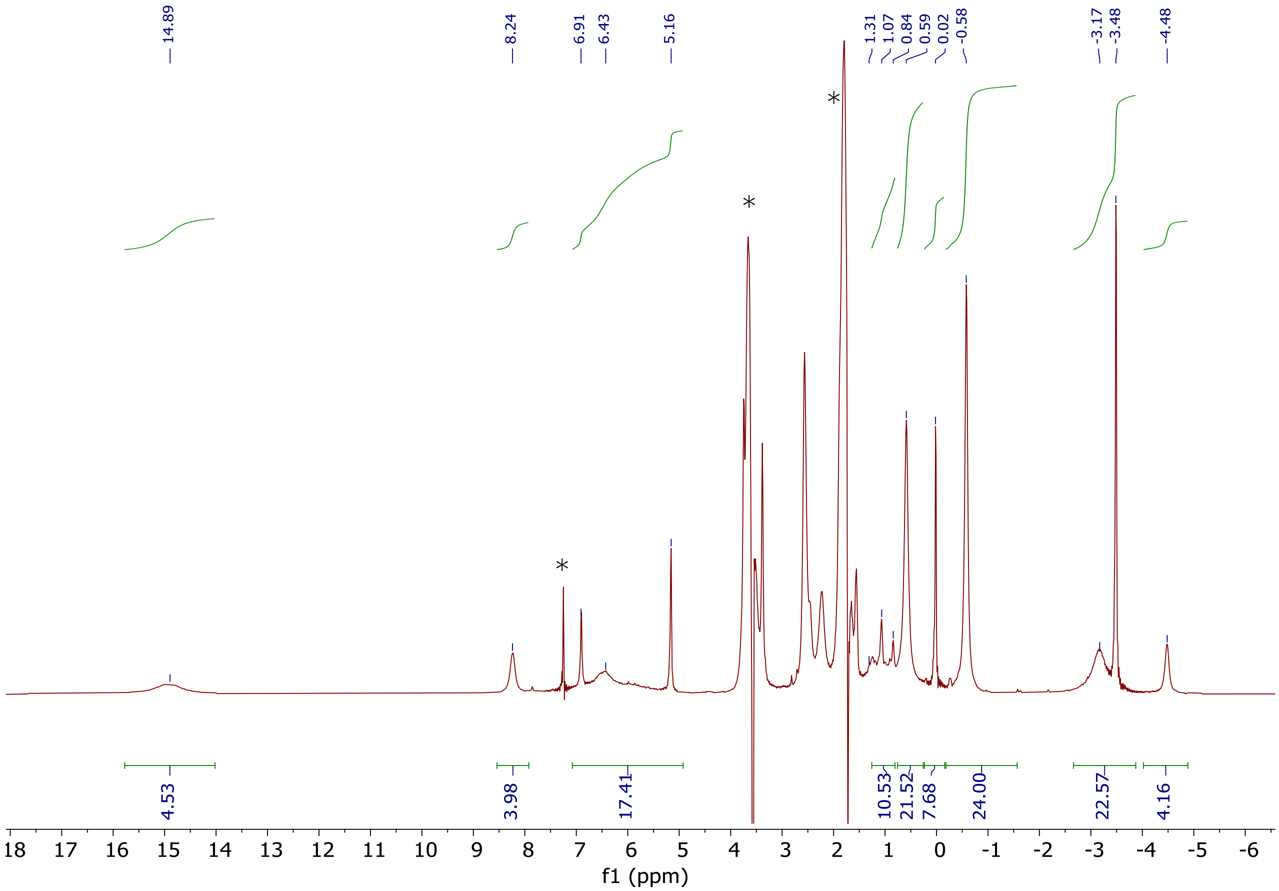

Figure 3.S6. ^{1}H NMR spectrum (400 MHz, THF-h_8, solvent suppression) of **3.3**. Solvent peaks are indicated by asterisks (*).

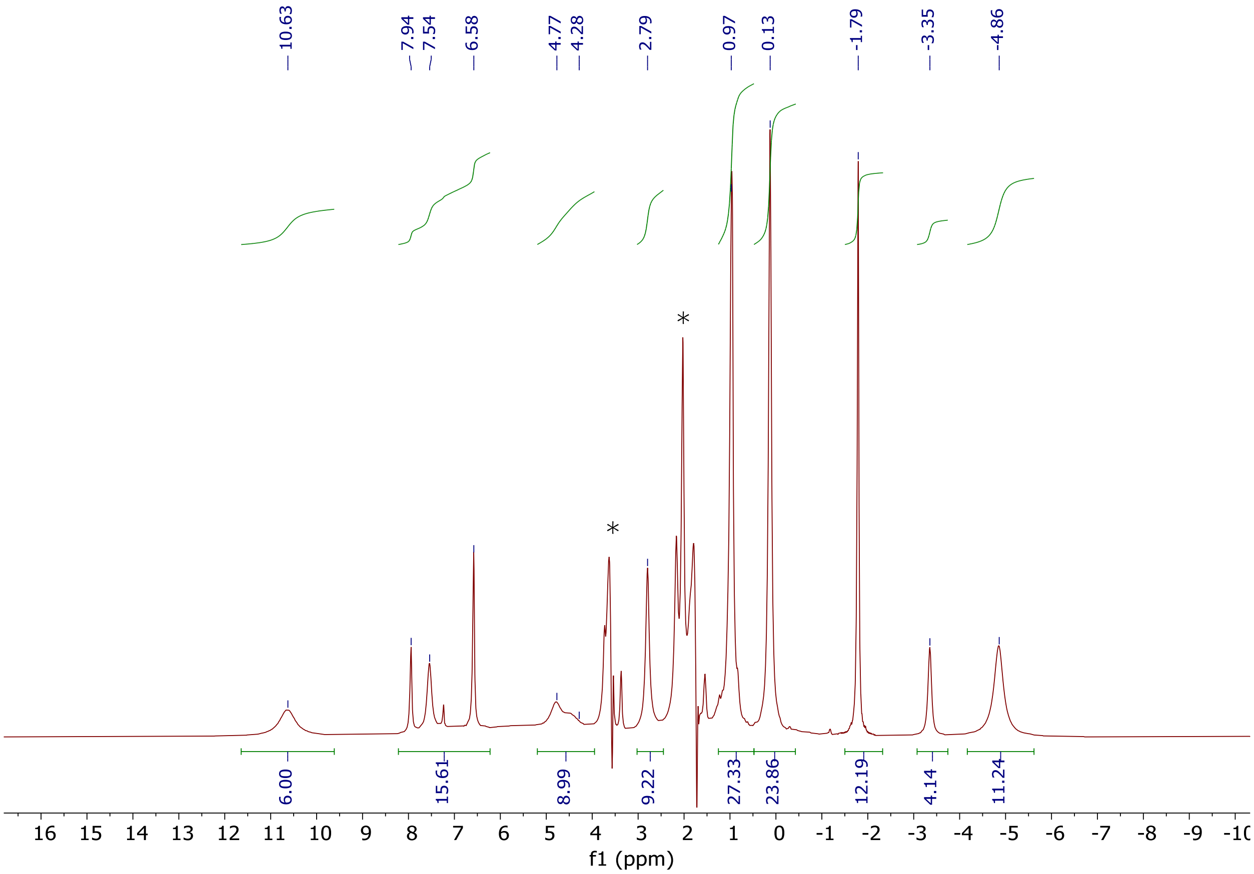

Figure 3.S7. ^{1}H NMR spectrum (400 MHz, THF-h_8, solvent suppression) of **3.3-Mo**. Solvent peaks are indicated by asterisks (*).

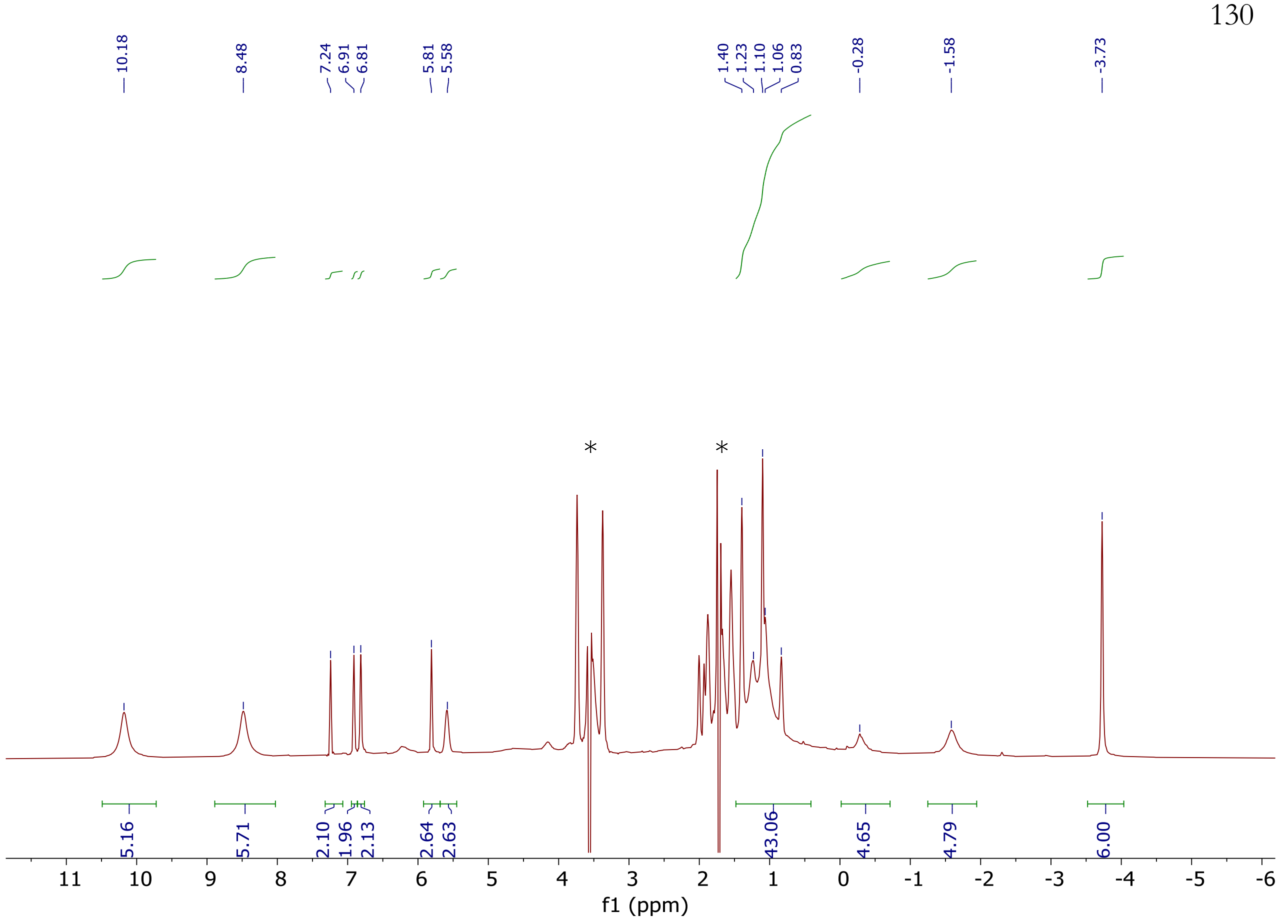

Figure 3.S8. ^{1}H NMR spectrum (400 MHz, THF-h_8, solvent suppression) of **3.4**. Solvent peaks are indicated by asterisks (*).

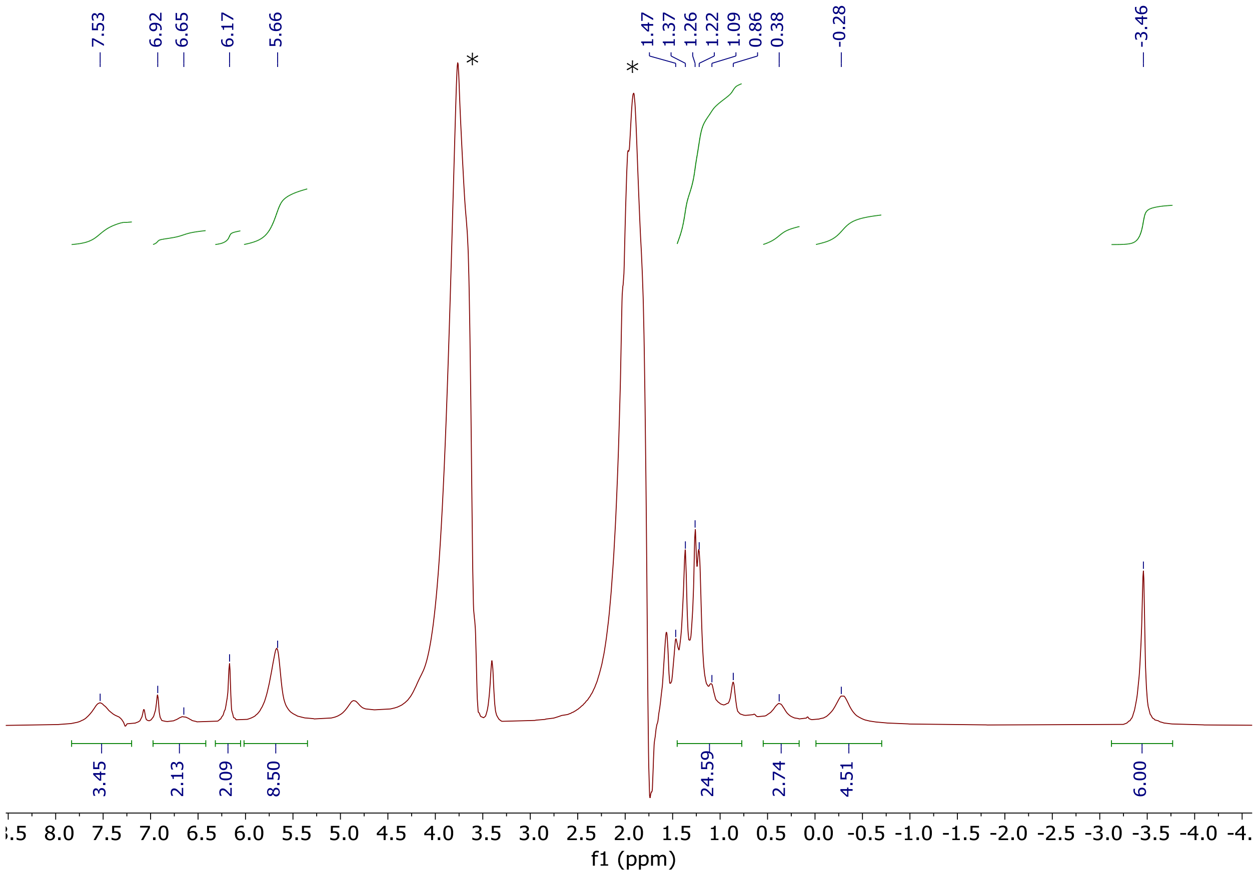

Figure 3.S9. ^{1}H NMR spectrum (400 MHz, THF-h_8, solvent suppression) of **3.4-Mo**. Solvent peaks are indicated by asterisks (*).

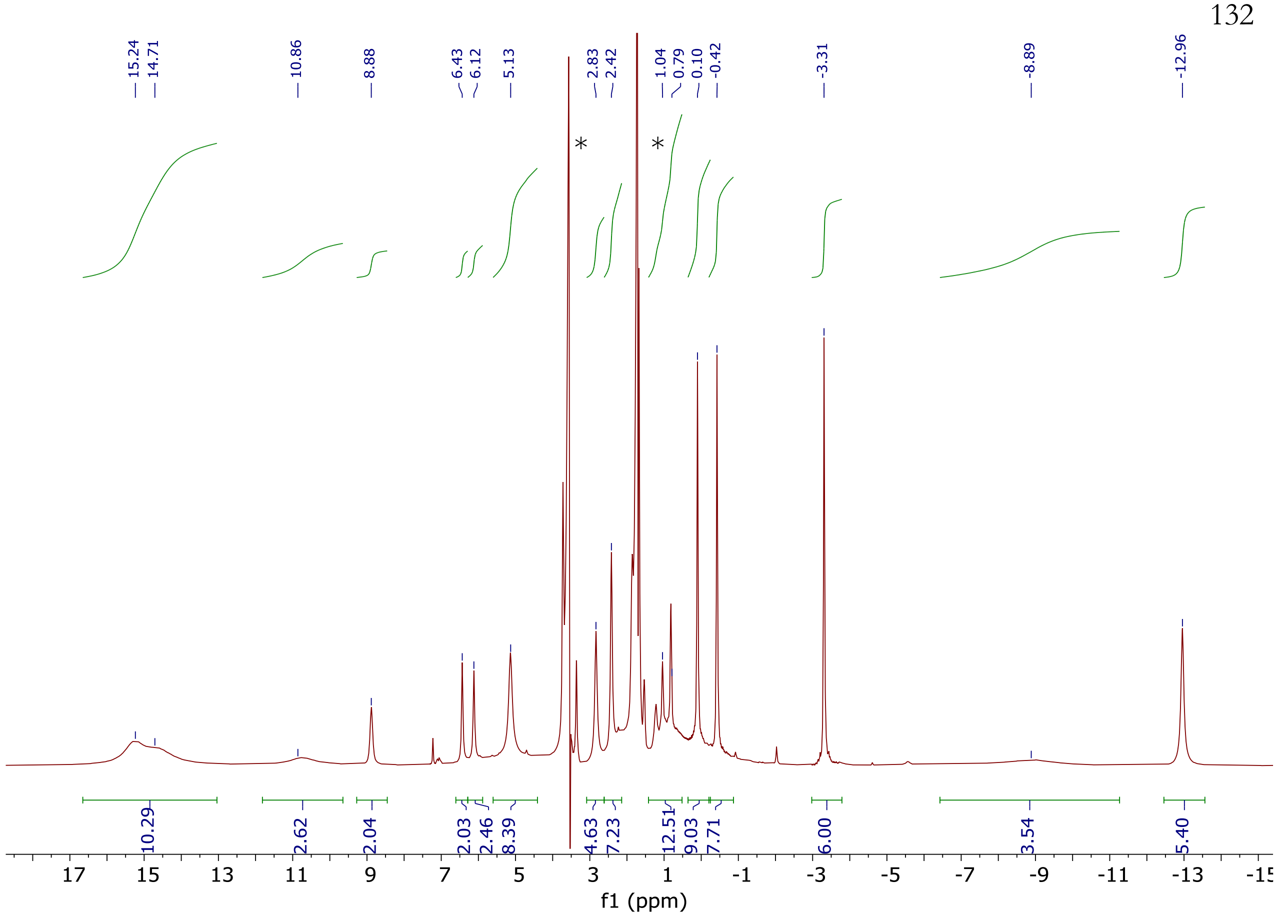

Figure 3.S10. ^{1}H NMR spectrum (400 MHz, THF-h_8, solvent suppression) of **3.4-K**. Solvent peaks are indicated by asterisks (*).

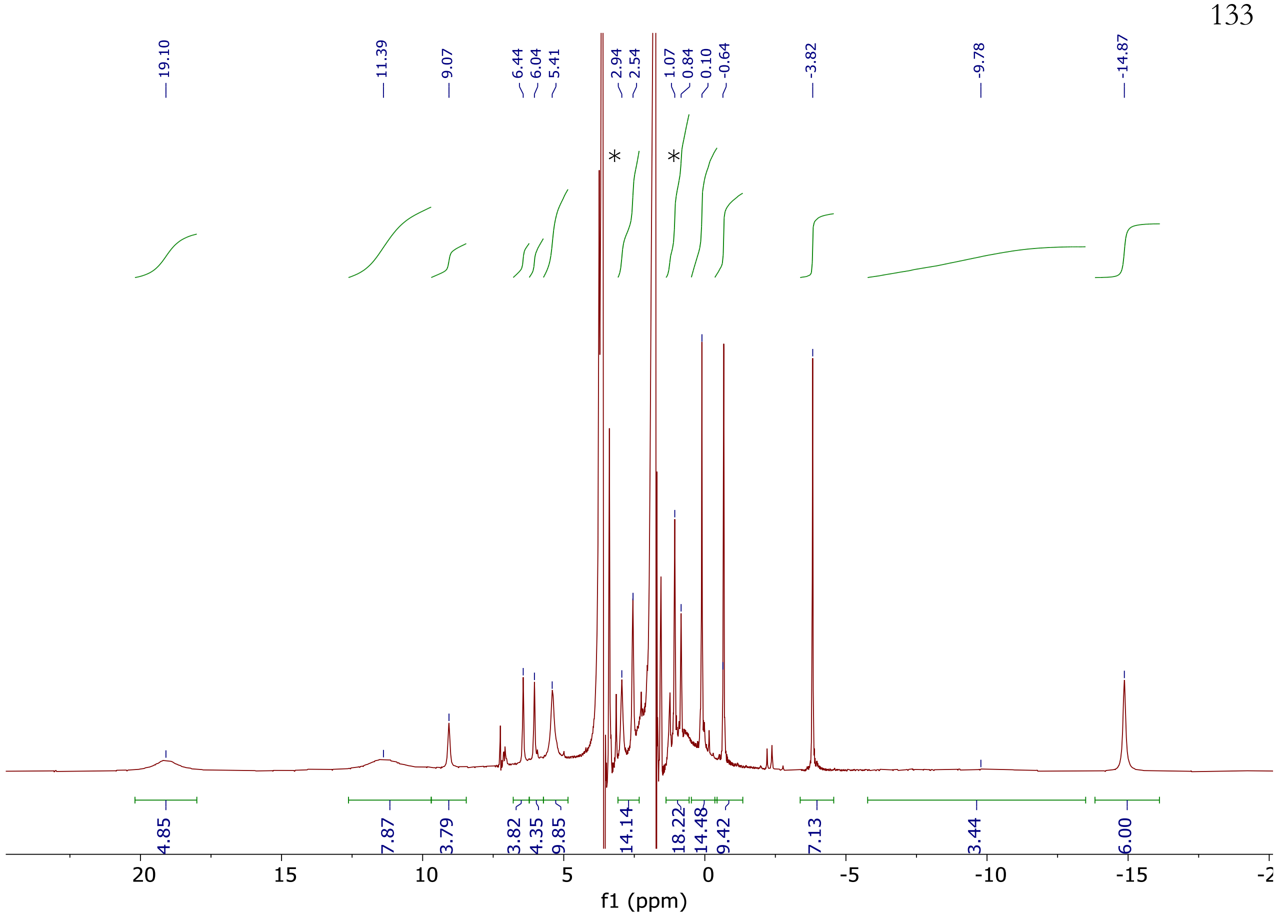

Figure 3.S11. ¹H NMR spectrum (400 MHz, THF-h_8, solvent suppression) of **3.4-K(18-crown-6)**. Solvent peaks are indicated by asterisks (*).

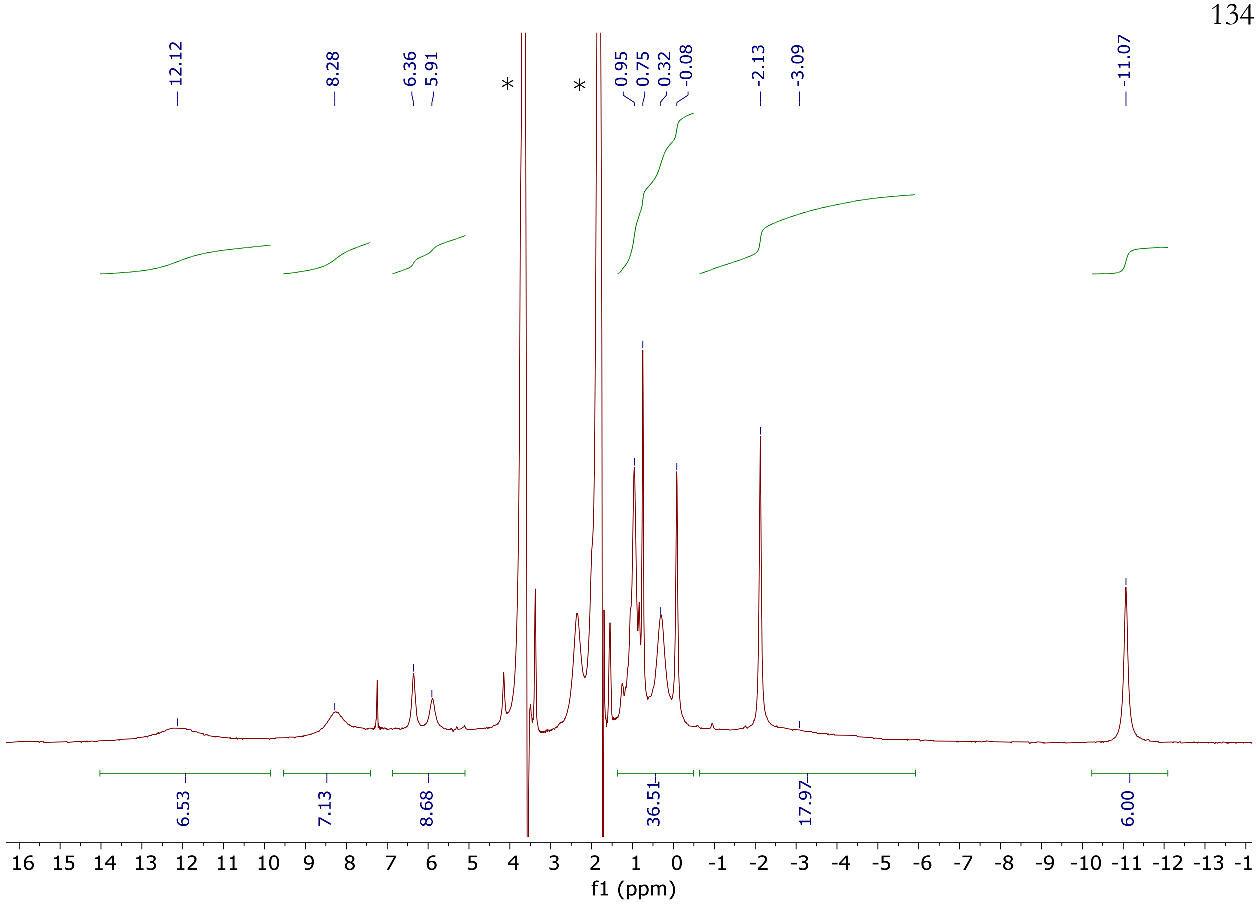

Figure 3.S12. [1]H NMR spectrum (400 MHz, THF-h_8, solvent suppression) of **3.4-Mo-K(18-crown-6)**. Solvent peaks are indicated by asterisks (*).

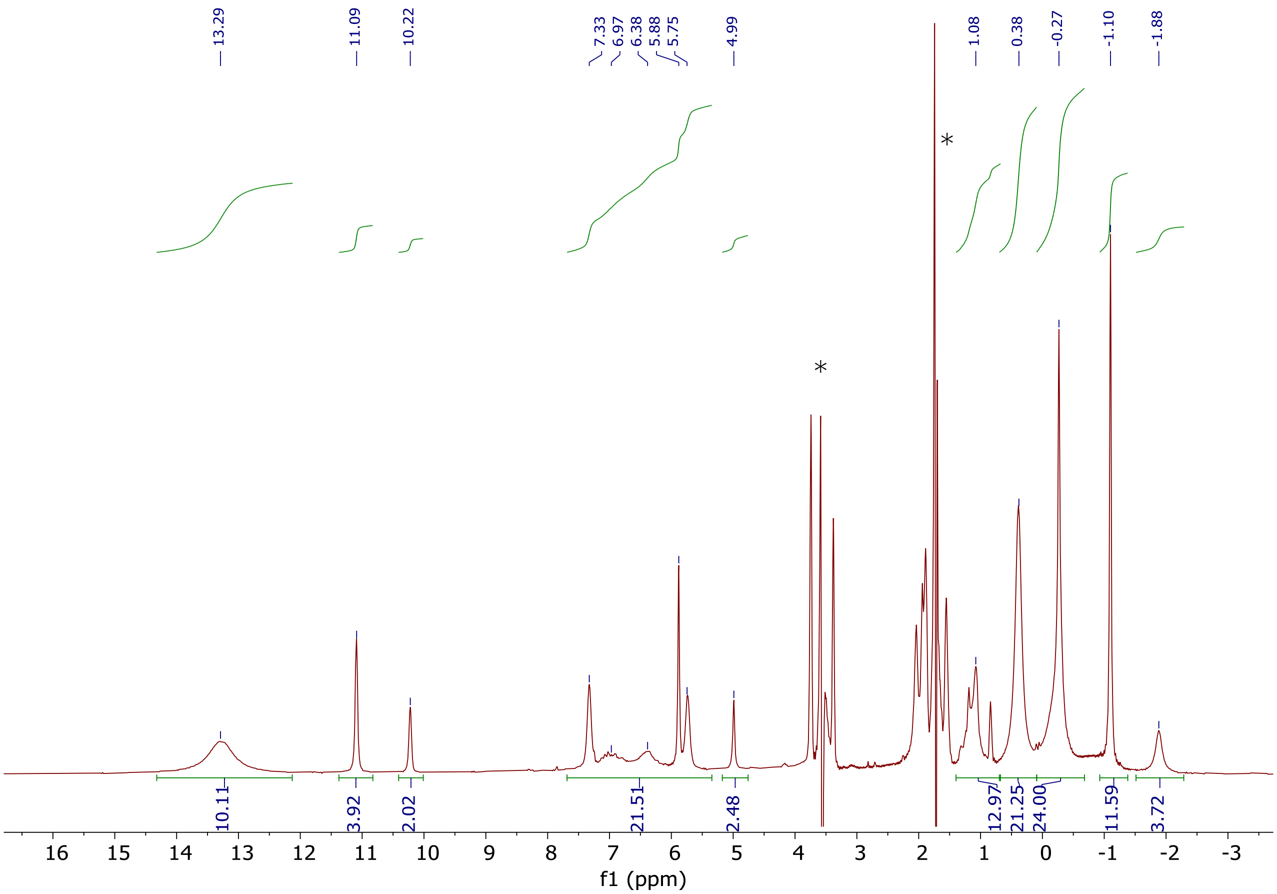

Figure 3.S13. [1]H NMR spectrum (400 MHz, THF-h_8, solvent suppression) of **3.5**. Solvent peaks are indicated by asterisks (*).

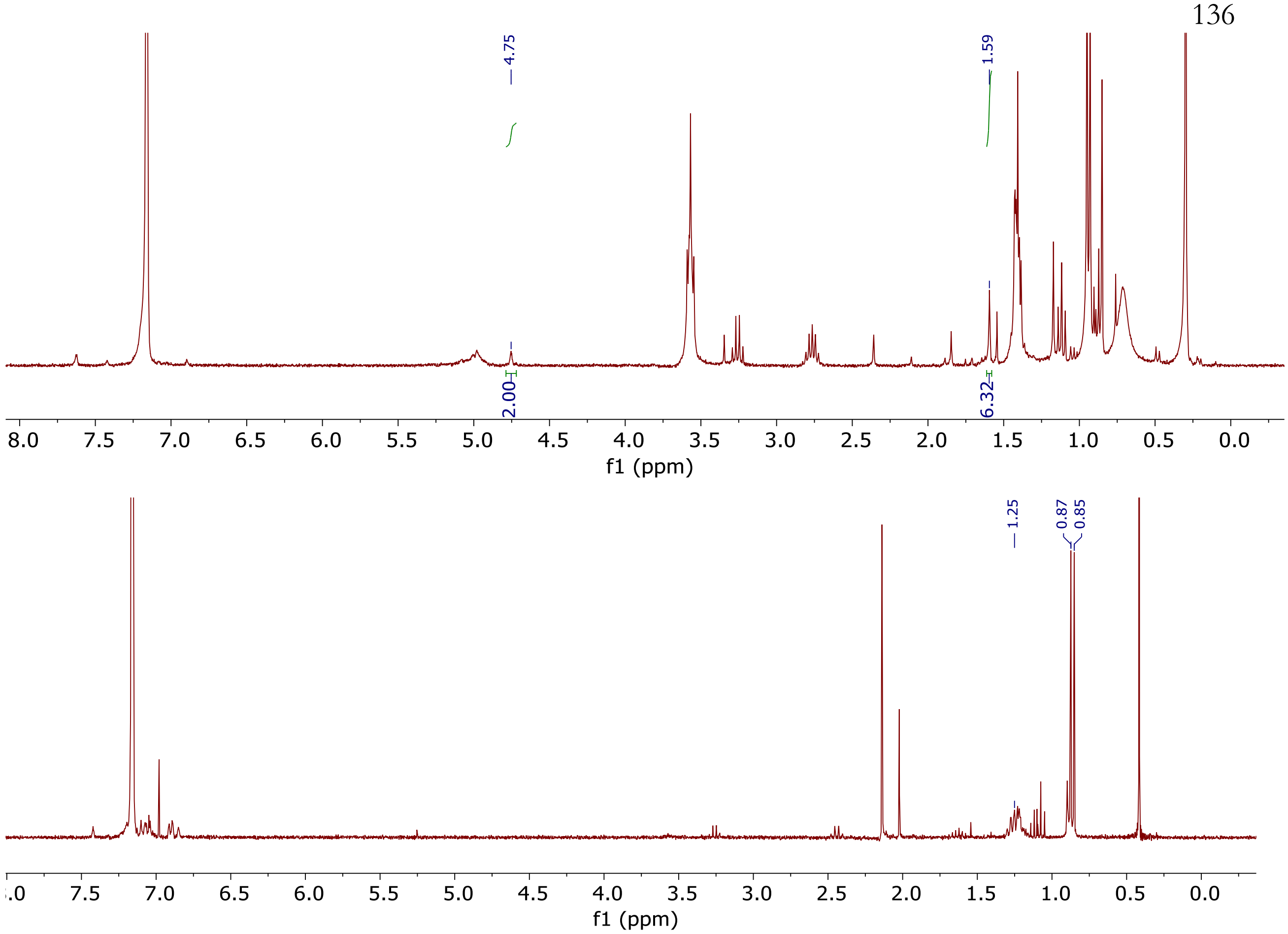

Figure 3.S14. Top: A sample of **3.2-*t*Bu** (25 mg) in C_6D_6 (0.7 mL) was heated at 70 °C for 16 h, after which the entire content was vacuum transferred into an empty J. Young tube cooled in liquid N_2. The ^1H NMR spectrum (300 MHz, C_6D_6) of the J. Young tube was recorded, where the labeled peaks are assigned to isobutene, but isobutane cannot be identified due to the various side products due to undesired reactions. Bottom: A sample of **3.2-*t*Bu** (40 mg) in xylenes (5 mL) was heated at 70 °C for 16 h (the reaction is somewhat cleaner when diluted, to avoid side products when vacuum transferred), after which the reaction flask was cooled to 0 °C to minimize xylenes transfer, and the volatiles were vacuum transferred onto a J. Young tube containing degassed C_6D_6 (0.7 mL) cooled in liquid N_2. The ^1H NMR spectrum (300 MHz, C_6D_6) of the J. Young tube was recorded, where the labeled peaks are assigned to isobutane. Isobutene was not observed, which could be because it still remained in the original reaction flask, as only part of the reaction products could be transferred.

4. IR spectroscopy supporting side-on nitrile assignment for **3.3***:*

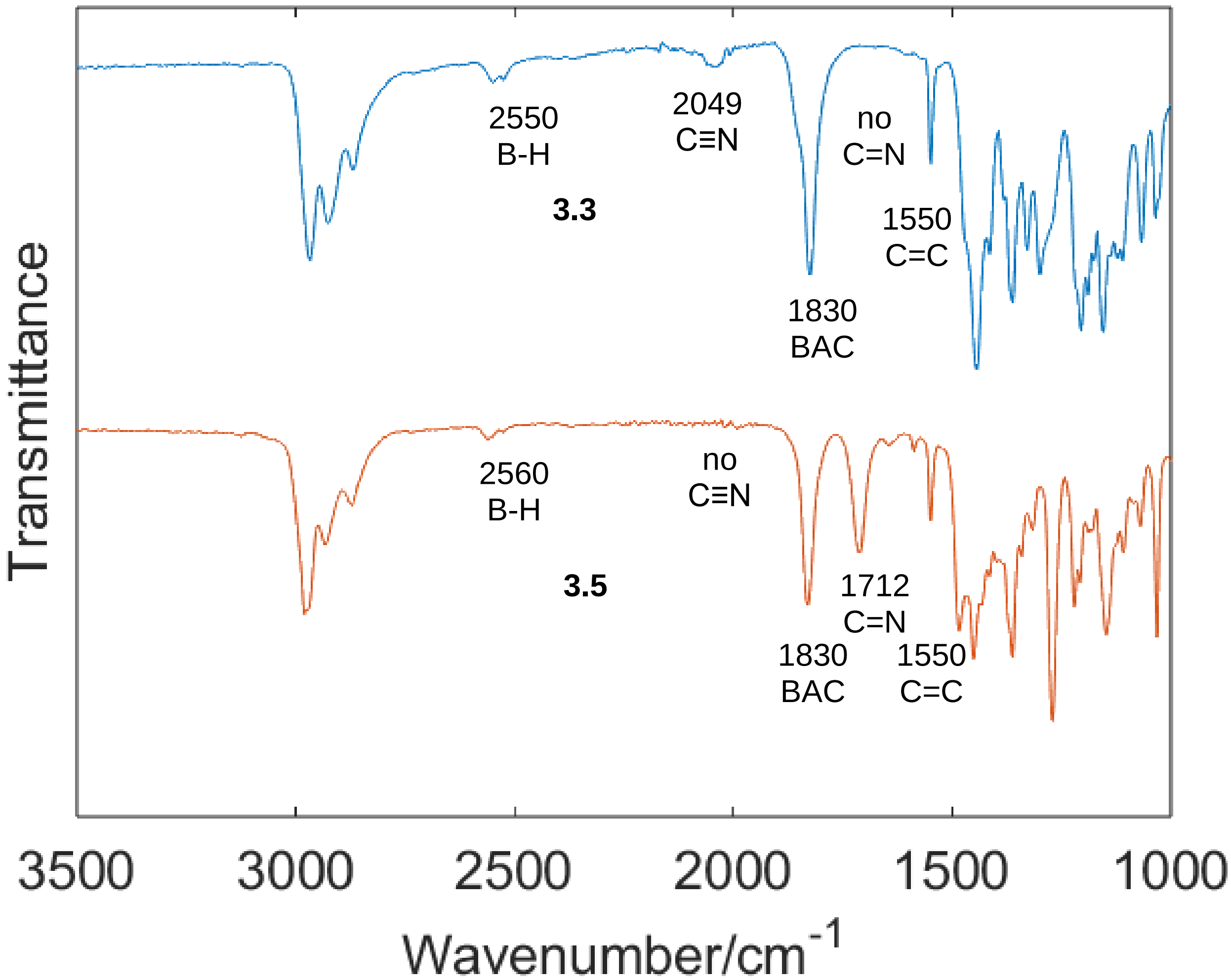

Figure 3.S15. ATR-IR spectra of **3.3** (top, blue) and **3.5** (bottom, orange).

The IR spectra of **3.3** and **3.5** (thin film, ATR mode, Figure 3.S15) are consistent with the structural assignments. For **3.3**, a feature at 2049 cm^{-1} assigned to the C≡N motif is observed.[40] In contrast, for **3.5**, no peak in this region is seen but instead a peak at 1712 cm^{-1} is present, assigned to the C=N motif.

5. Physical methods:

Mössbauer spectroscopy

Zero field ^{57}Fe Mössbauer spectra were recorded in constant acceleration at 80 K on a spectrometer from See Co (Edina, MN) equipped with an SVT-400 cryostat (Janis, Woburn, MA). The quoted isomer shifts are relative to the centroid of the spectrum of α-Fe foil at room temperature. Samples were ground with boron nitride into a fine powder and transferred to a Delrin cup. The data were fitted to Lorentzian lineshapes using the program WMOSS (www.wmoss.org).

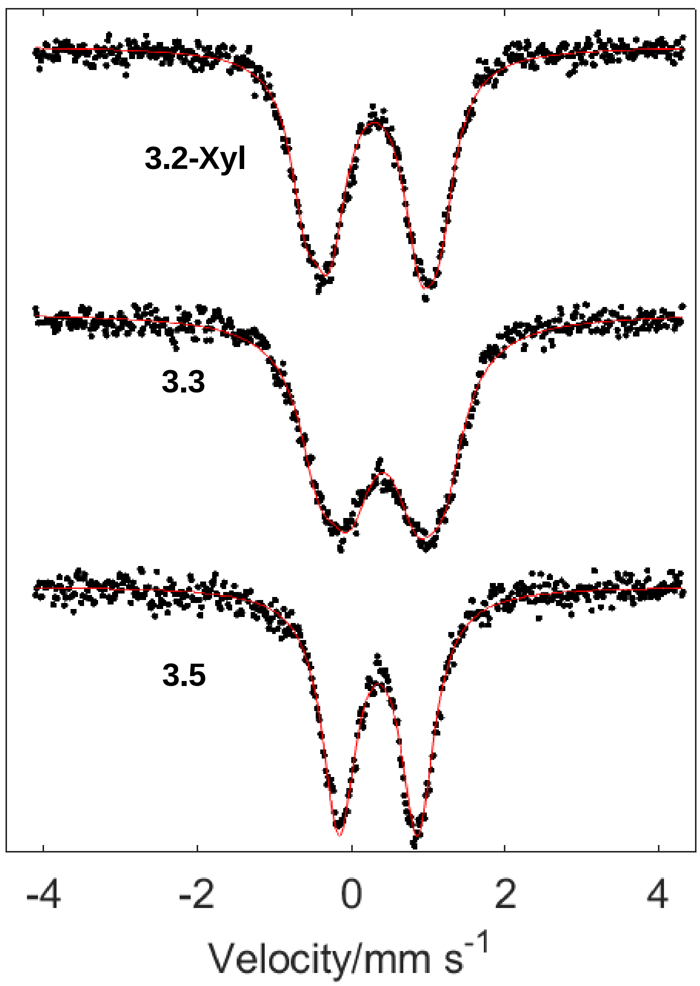

Figure 3.S16. Mössbauer spectra of **3.2-Xyl**, **3.3**, and **3.5** (80 K, no applied field). Average isomer shifts: δ_{ave} = 0.30 mm s^{-1} (**3.2-Xyl**), δ_{ave} = 0.41 mm s^{-1} (**3.3**), δ_{ave} = 0.36 mm s^{-1} (**3.5**).

The Mössbauer spectra of **3.2-Xyl**, **3.3**, and **3.5** consist of broad quadrupole doublets (Figure 3.S16), owing to valence delocalization on the Mössbauer timescale that does not resolve the individual Fe signals. This has been observed for other synthetic iron-sulfur clusters,[19,43] and because the broadness precludes the definite assignment of isomer shifts, we focus instead on the average shift δ_{ave} that is representative of all the Fe sites regardless of the simulation. The δ_{ave} value of 0.41 mm s^{-1} for **3.3** is higher than that for **3.5** (0.36 mm s^{-1}), which is in turn higher than that for **3.2-Xyl** (0.30 mm s^{-1}), suggesting the following order in terms of increasing average electron density on the Fe sites of the cluster: **3.2-Xyl** < **3.5** < **3.3**.

Mössbauer fit parameters:

For **3.2-Xyl**: The Mössbauer spectrum of **3.2-Xyl** can be fit with a two-site model using the following parameters:

Site 1: δ = 0.282 mm s^{-1} $|E_Q|$ = 1.759 mm s^{-1} Linewidth = 0.463 mm s^{-1} Area = 35%

Site 2: δ = 0.309 mm s^{-1} $|E_Q|$ = 1.191 mm s^{-1} Linewidth = 0.554 mm s^{-1} Area = 65%

For **3.3**: The Mössbauer spectrum of **3.3** can be fit with a two-site model using the following parameters:

Site 1: δ = 0.397 mm s^{-1} $|E_Q|$ = 1.657 mm s^{-1} Linewidth = 0.586 mm s^{-1} Area = 31%

Site 2: δ = 0.418 mm s^{-1} $|E_Q|$ = 0.901 mm s^{-1} Linewidth = 0.812 mm s^{-1} Area = 69%

For **3.5**: The Mössbauer spectrum of **3.5** can only be fit satisfactorily with a one-site model using the following parameters:

δ = 0.355 mm s^{-1} $|E_Q|$ = 1.022 mm s^{-1} Linewidth = 0.525 mm s^{-1}

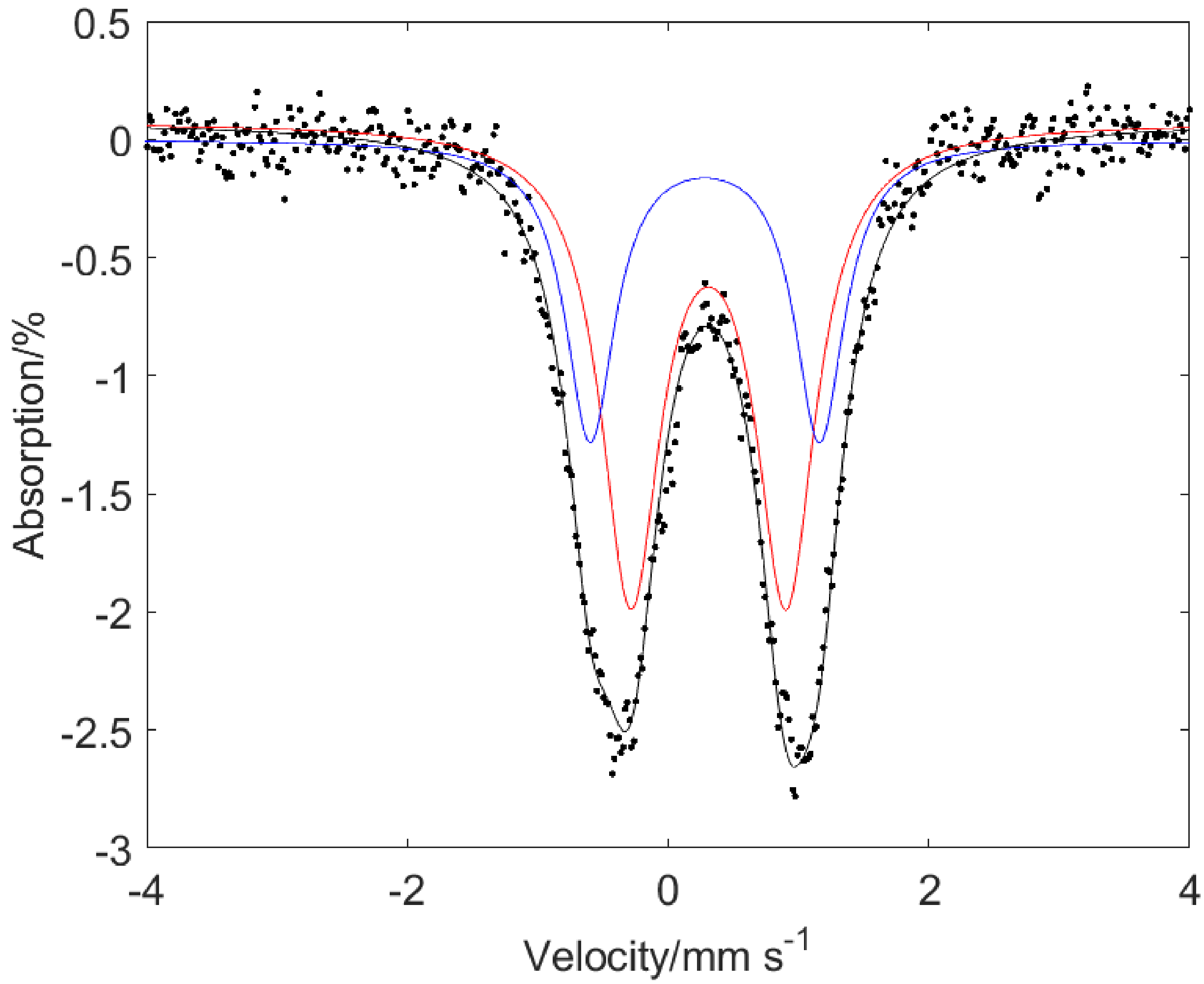

Figure 3.S17. Fitting for the Mössbauer spectrum of **3.2-Xyl** (80 K, no applied field) using a two-site model, with the total fit shown by the black trace.

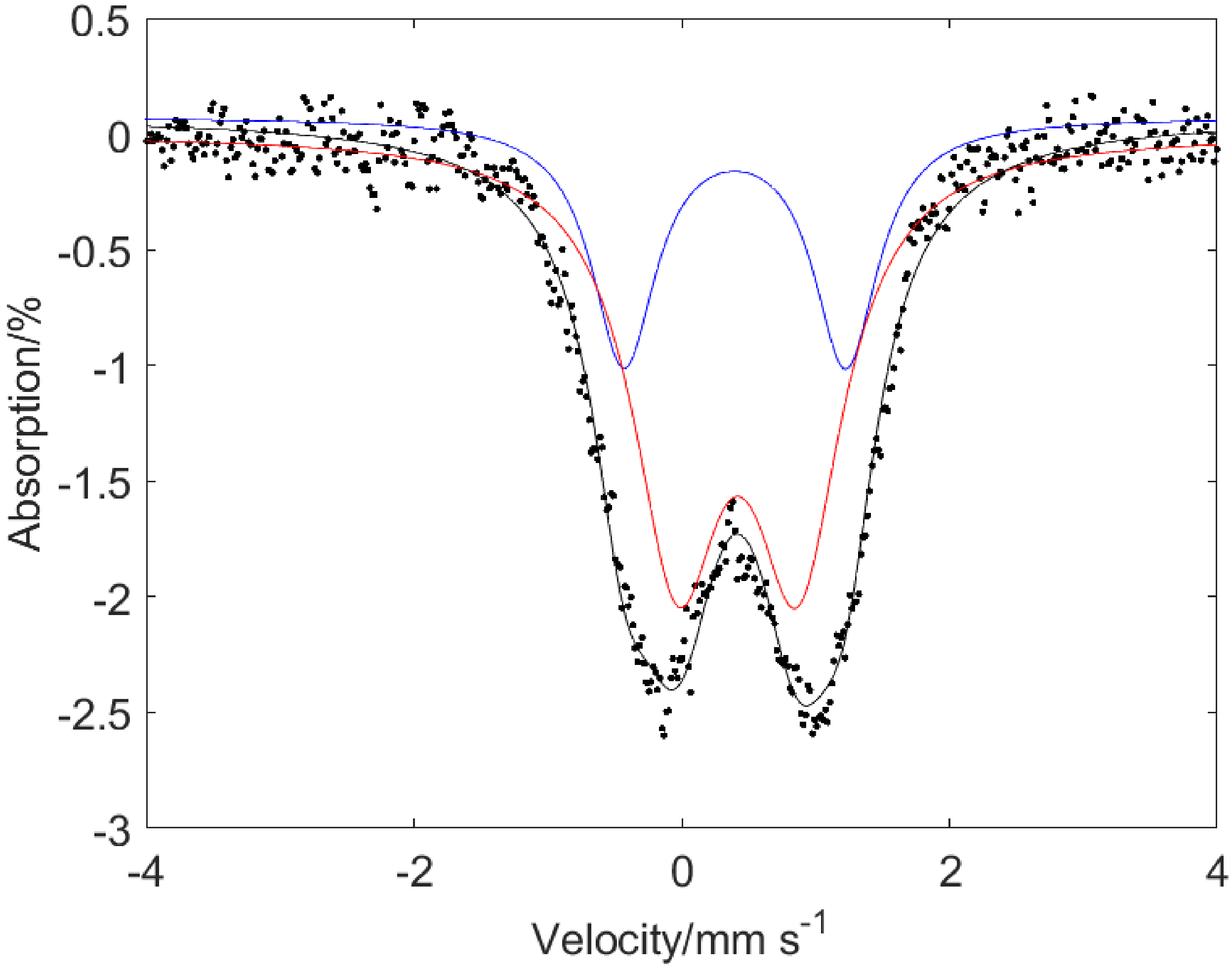

Figure 3.S18. Fitting for the Mössbauer spectrum of **3.3** (80 K, no applied field) using a two-site model, with the total fit shown by the black trace.

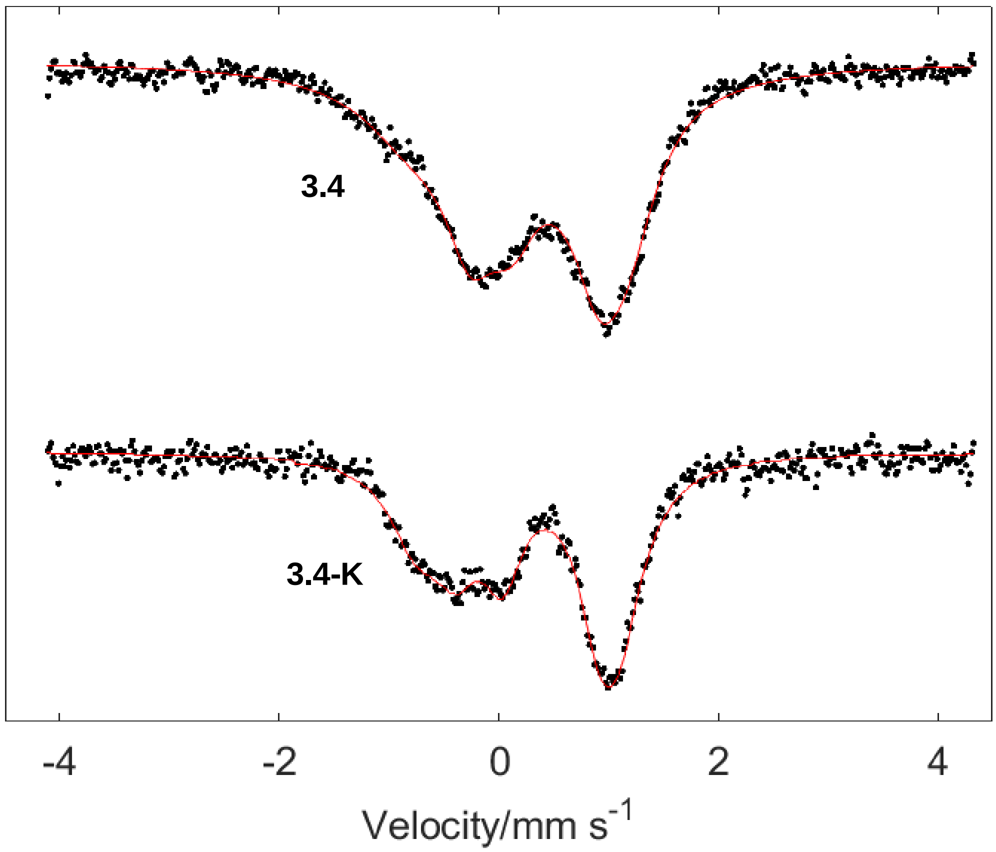

Figure 3.S19. Mössbauer spectra of **3.4** and **3.4-K** (80 K, no applied field). Average isomer shifts: δ_{ave} = 0.33 mm s^{-1} for both clusters.

The Mössbauer spectra of **3.4** and **3.4-K** consist of broad quadrupole doublets (Figure 3.S19), owing to valence delocalization on the Mössbauer timescale that does not resolve the individual Fe signals. This has been observed for other synthetic iron-sulfur clusters,[19,43] and because the broadness precludes the definite assignment of isomer shifts, we only present one set of values for the fit parameters. Other fits are possible for both systems.

Mössbauer fit parameters:

For **3.4**: The Mössbauer spectrum of **3.4** can be fit with a three-site model using the following parameters:

Site 1: δ = 0.02 mm s^{-1} $|E_Q|$ = 1.57 mm s^{-1} Linewidth = 1.14 mm s^{-1} Area = 33%

Site 2: δ = 0.65 mm s^{-1} $|E_Q|$ = 1.07 mm s^{-1} Linewidth = 0.64 mm s^{-1} Area = 33%

Site 3: δ = 0.33 mm s^{-1} |E_Q| = 1.19 mm s^{-1} Linewidth = 0.56 mm s^{-1} Area = 33%

For **3.4-K**: The Mössbauer spectrum of **3.4-K** can be fit with a three-site model using the following parameters:

Site 1: δ = 0.47 mm s^{-1} |E_Q| = 0.87 mm s^{-1} Linewidth = 0.45 mm s^{-1} Area = 33%

Site 2: δ = 0.17 mm s^{-1} |E_Q| = 1.84 mm s^{-1} Linewidth = 0.60 mm s^{-1} Area = 33%

Site 3: δ = 0.35 mm s^{-1} |E_Q| = 1.47 mm s^{-1} Linewidth = 0.54 mm s^{-1} Area = 33%

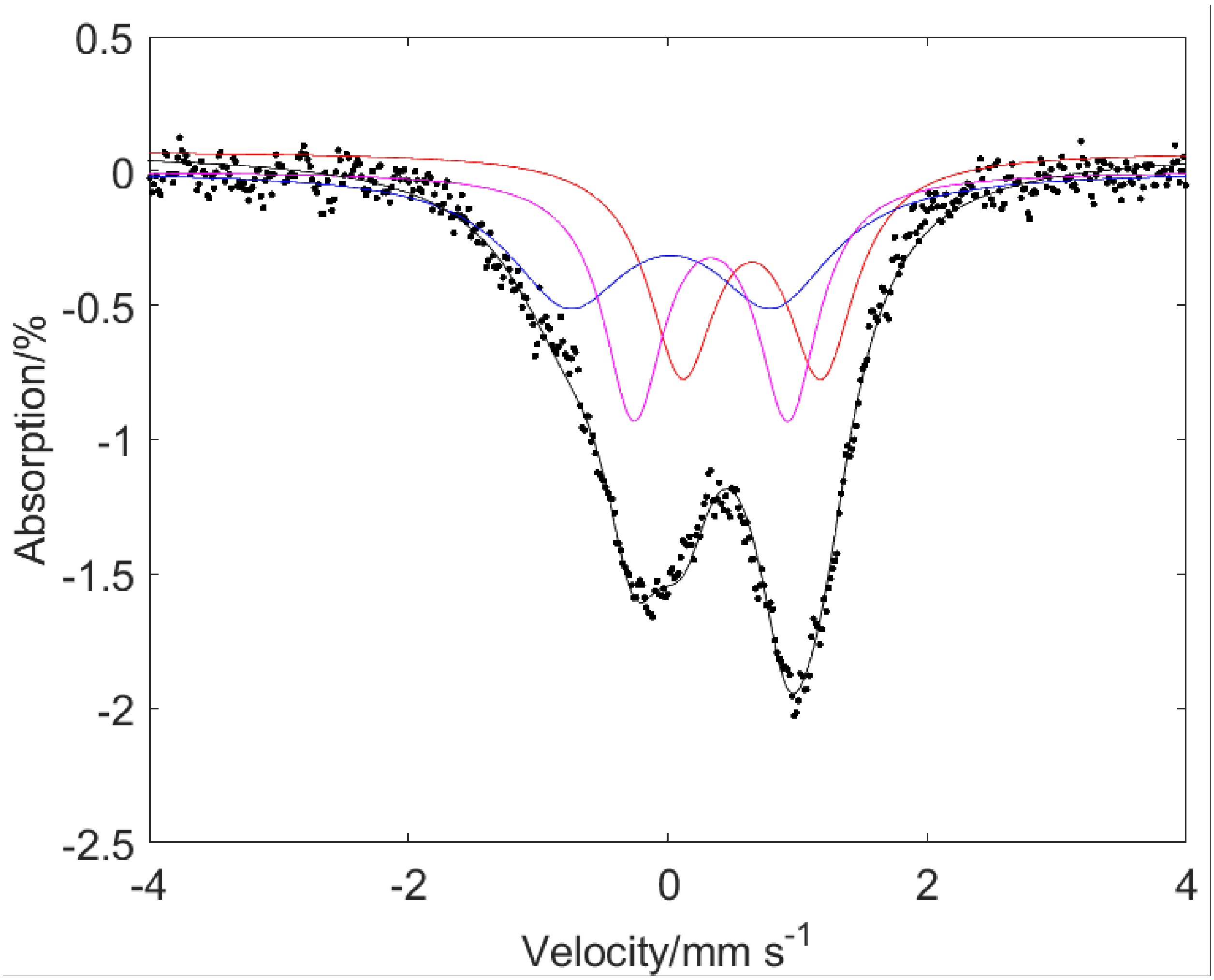

Figure 3.S20. Fitting for the Mössbauer spectrum of **3.4** (80 K, no applied field) using a three-site model, with the total fit shown by the black trace.

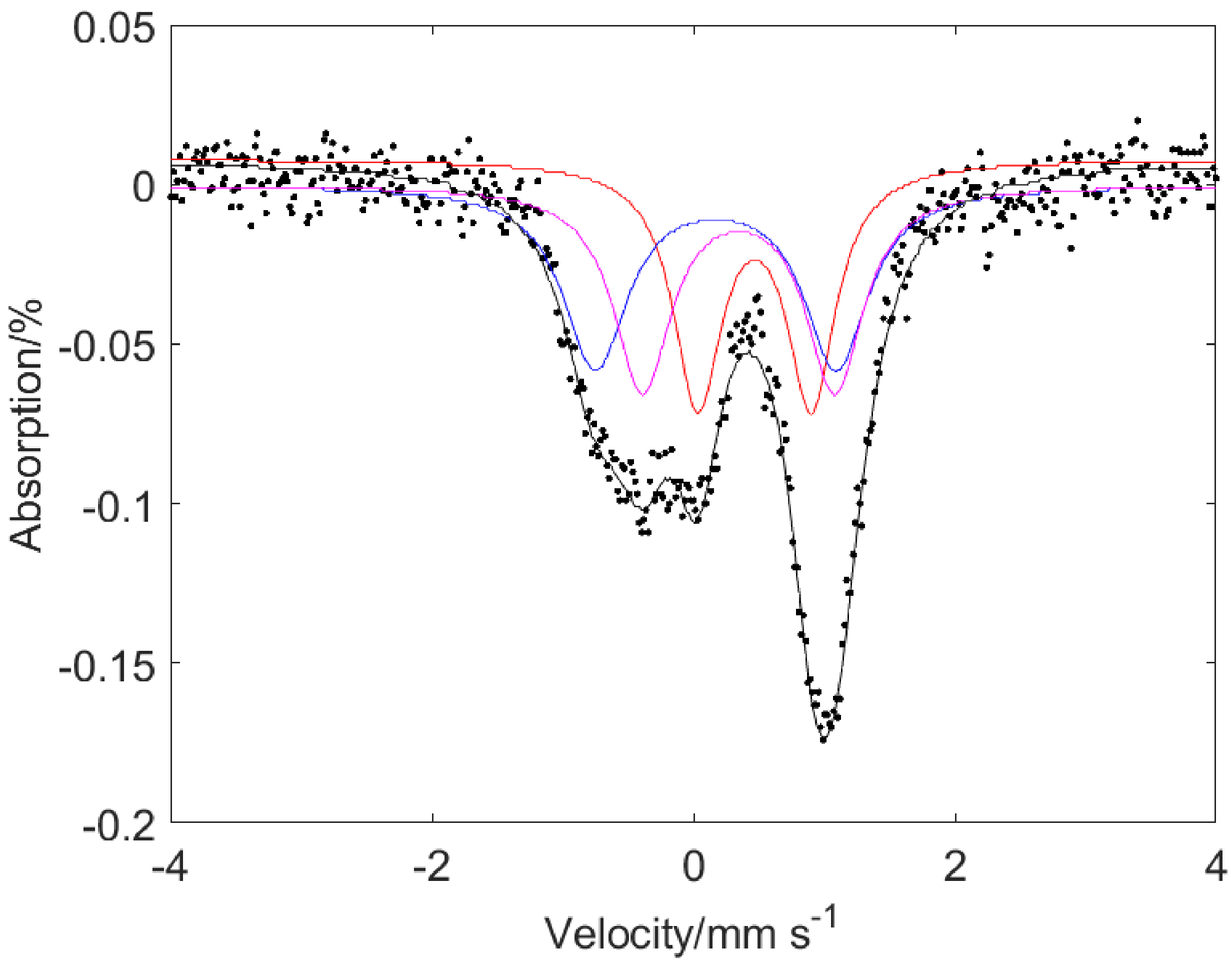

Figure 3.S21. Fitting for the Mössbauer spectrum of **3.4-K** (80 K, no applied field) using a three-site model, with the total fit shown by the black trace.

Electrochemical measurements

Cyclic voltammetry experiments were performed with a Pine Instrument Company AFCBP1 biopotentiostat with the *AfterMath* software package. All measurements were performed in a three-electrode cell, which consisted of glassy carbon (working; ⌀ = 3.0 mm), Ag wire (reference), and bare Pt wire (counter), in a N_2-filled MBraun glovebox at room temperature. Dry CH_3CN that contained ~0.2 M $[Bu_4N][PF_6]$ was used as the electrolyte solution. Redox potentials are reported relative to the ferrocene/ferrocenium redox wave (Fc^+/Fc; ferrocene added as an internal standard). The open circuit potential was measured prior to each voltammogram being collected. Voltammograms were scanned reductively in order to minimize the oxidative damage that was frequently observed on scanning more oxidatively.

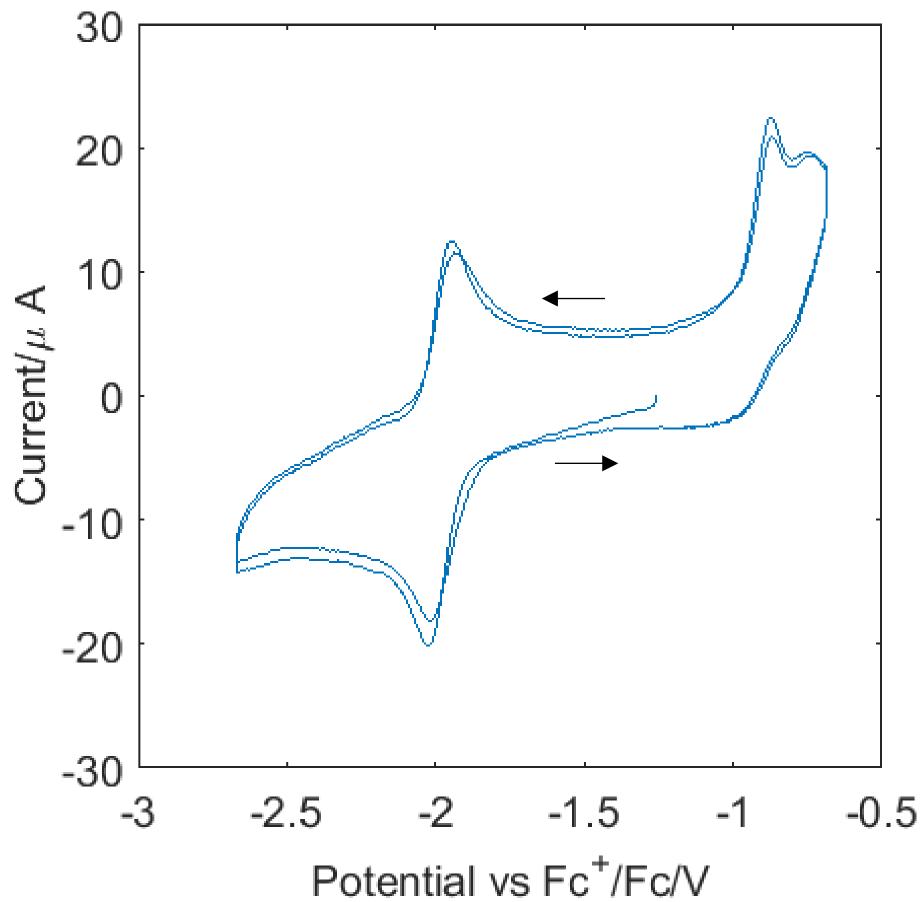

Figure 3.S22. Cyclic voltammetry (CV) scan for **3.4**, starting from the open circuit potential, showing the reversible feature at -1.99 V vs. Fc^{+}/Fc. Conditions: 2.5 mM cluster in MeCN with 0.2 M $TBAPF_6$, scan rates of 200 mV s^{-1}.

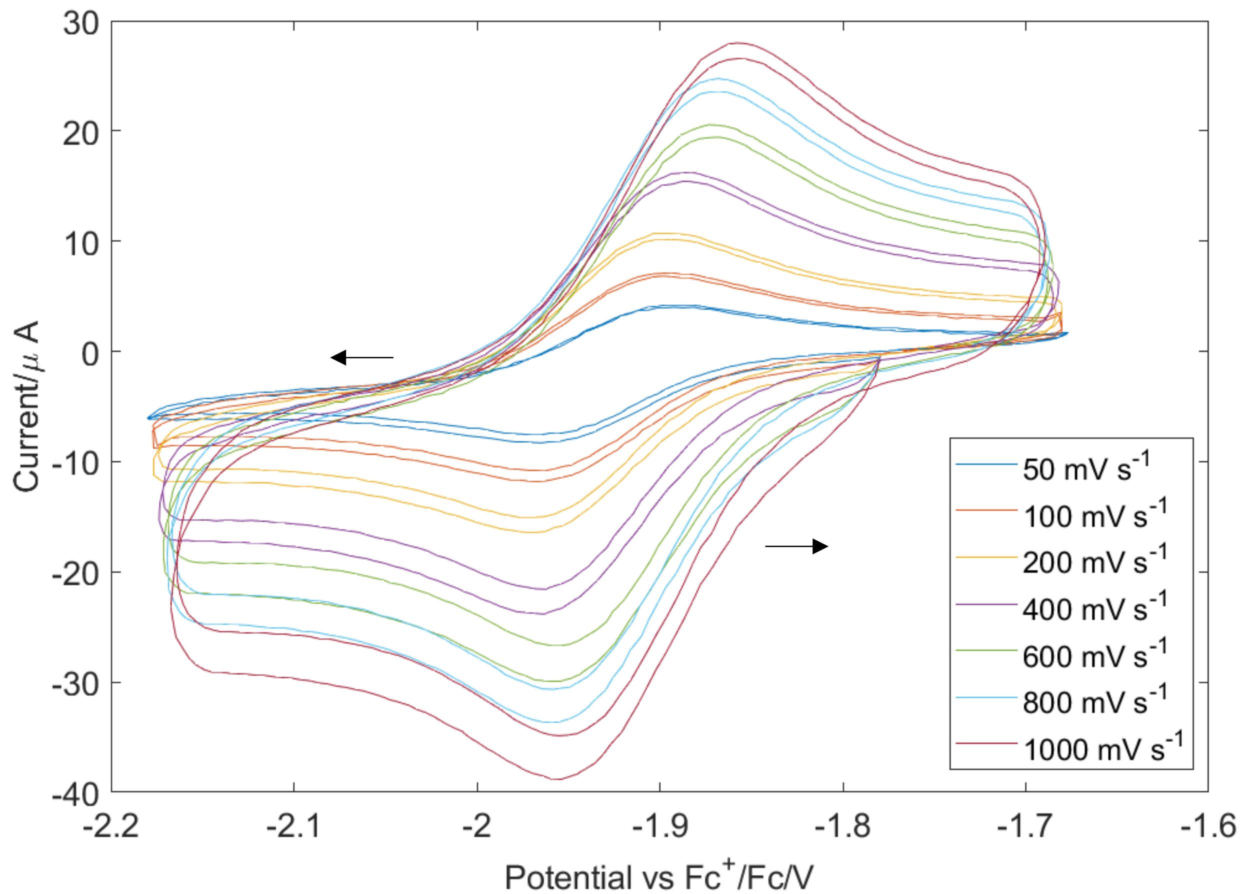

Figure 3.S23. CV of **3.4** at different scan rates, showing the reversible redox event.

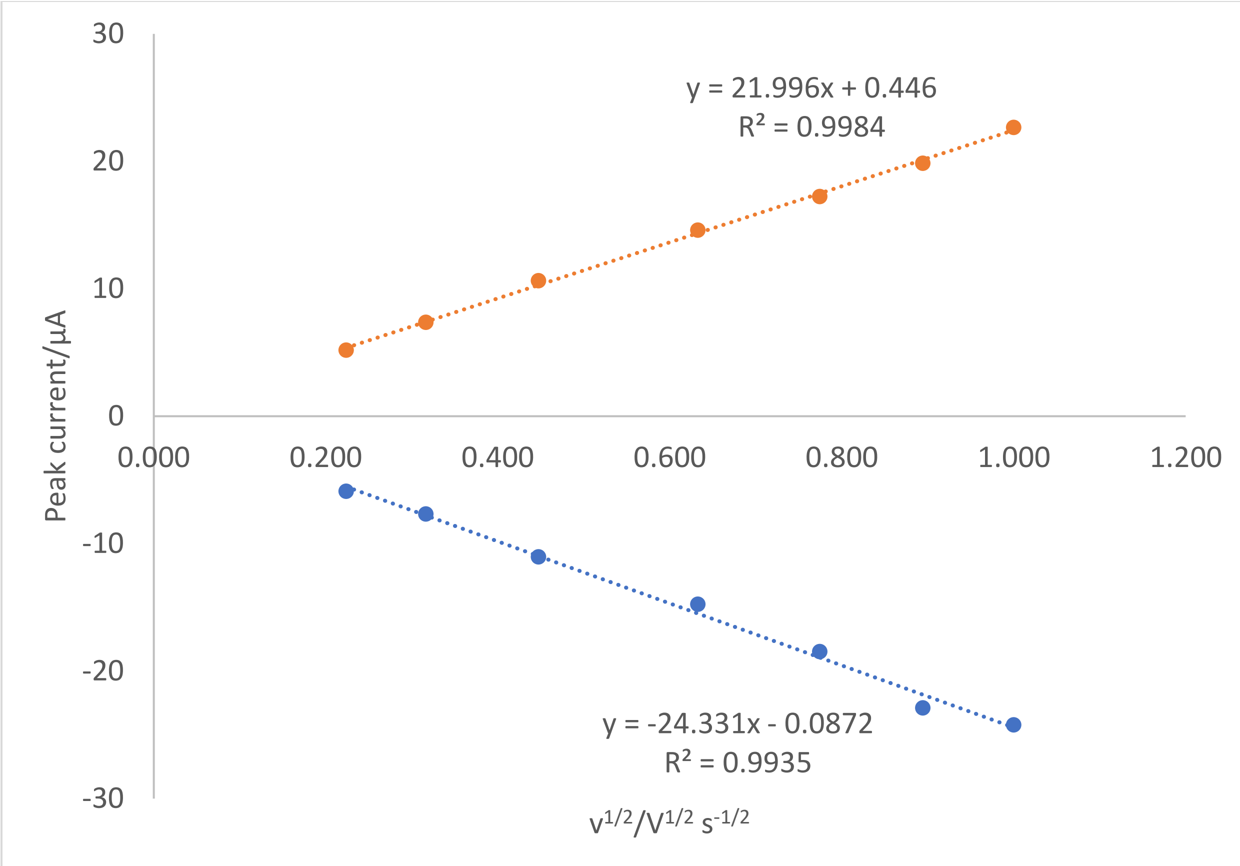

Figure 3.S24. Peak current vs. square root of scan rate for the reversible redox feature in **3.4**.

Additional IR spectra

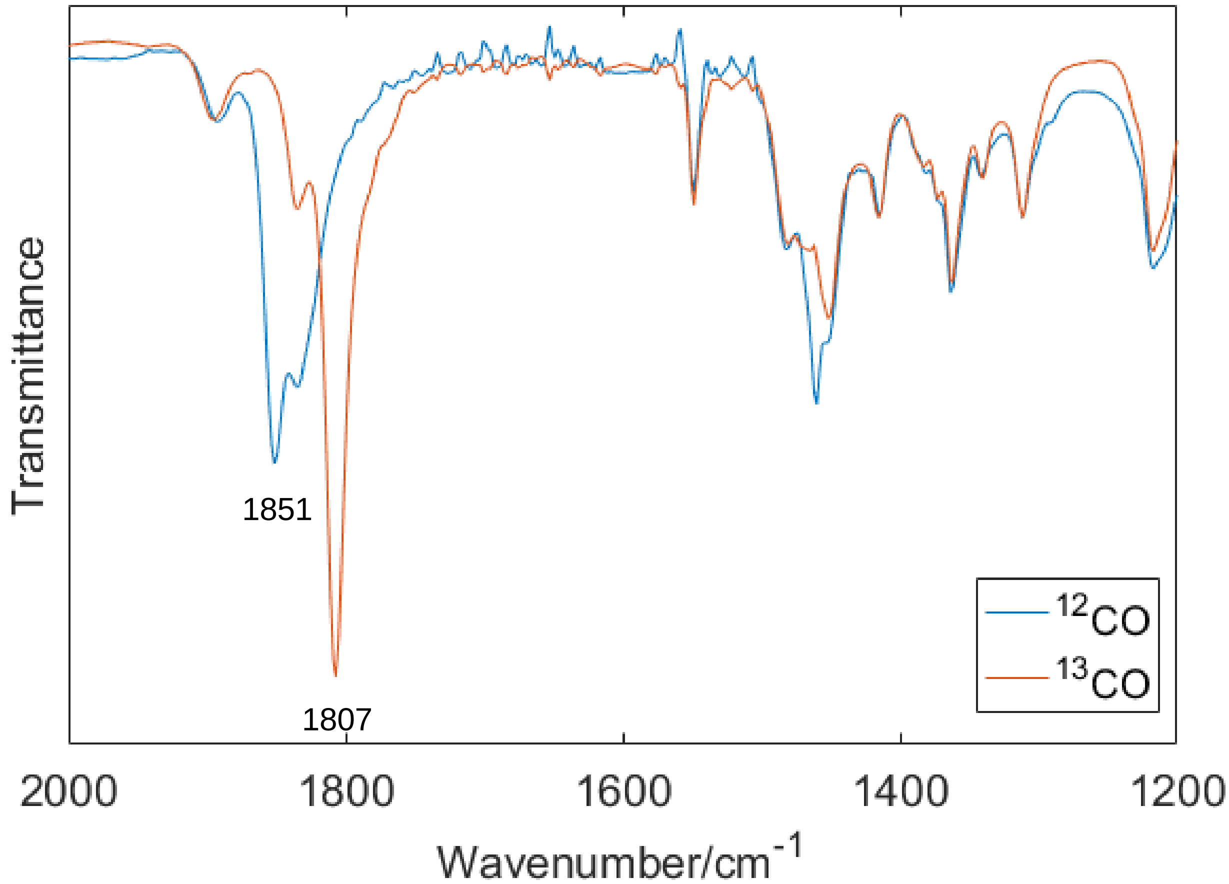

Figure 3.S25. IR spectra of **3.4** in THF with ^{12}CO and ^{13}CO over a wider window, with the CO peaks indicated.

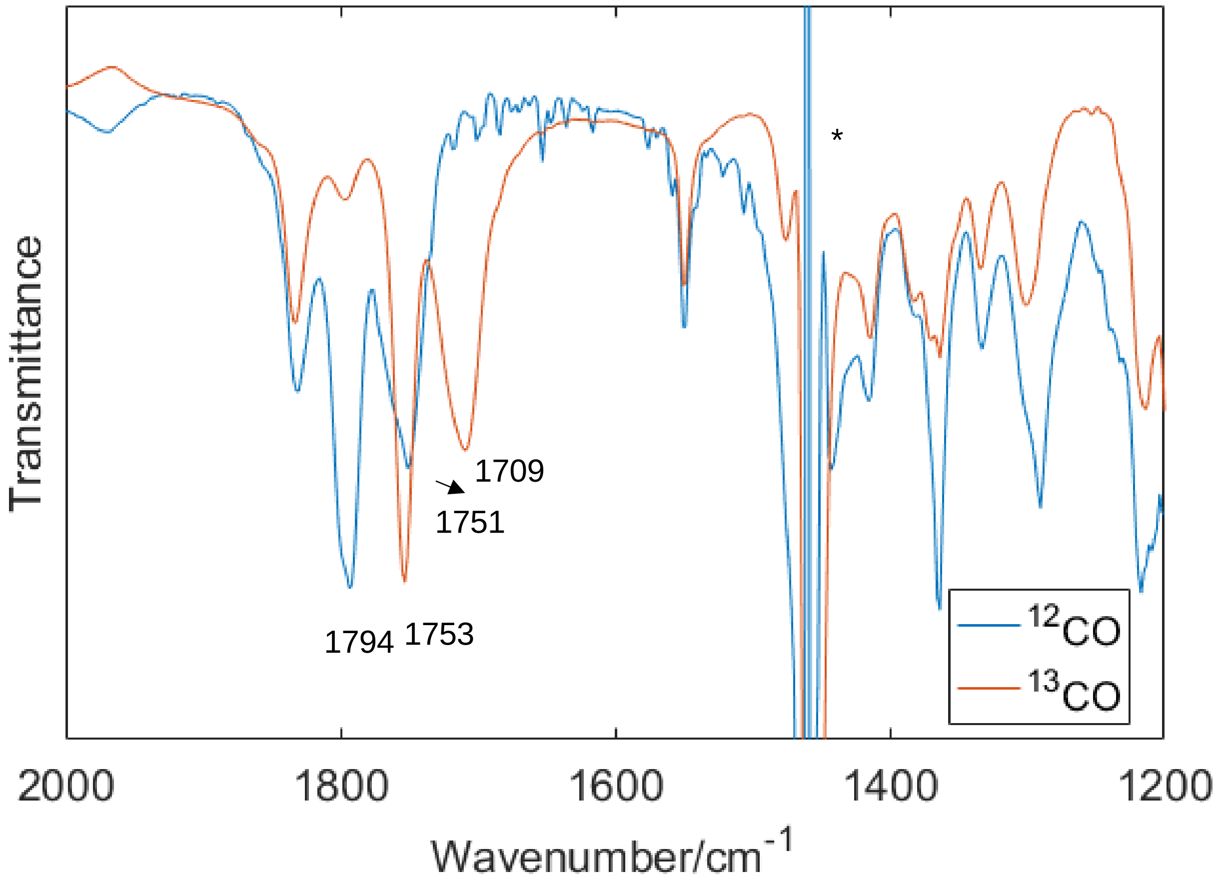

Figure 3.S26. IR spectra of **3.4-K** in THF with ^{12}CO and ^{13}CO over a wider window, with the CO peaks indicated. The feature marked with an asterisk (*) is an artifact due to the solvent.

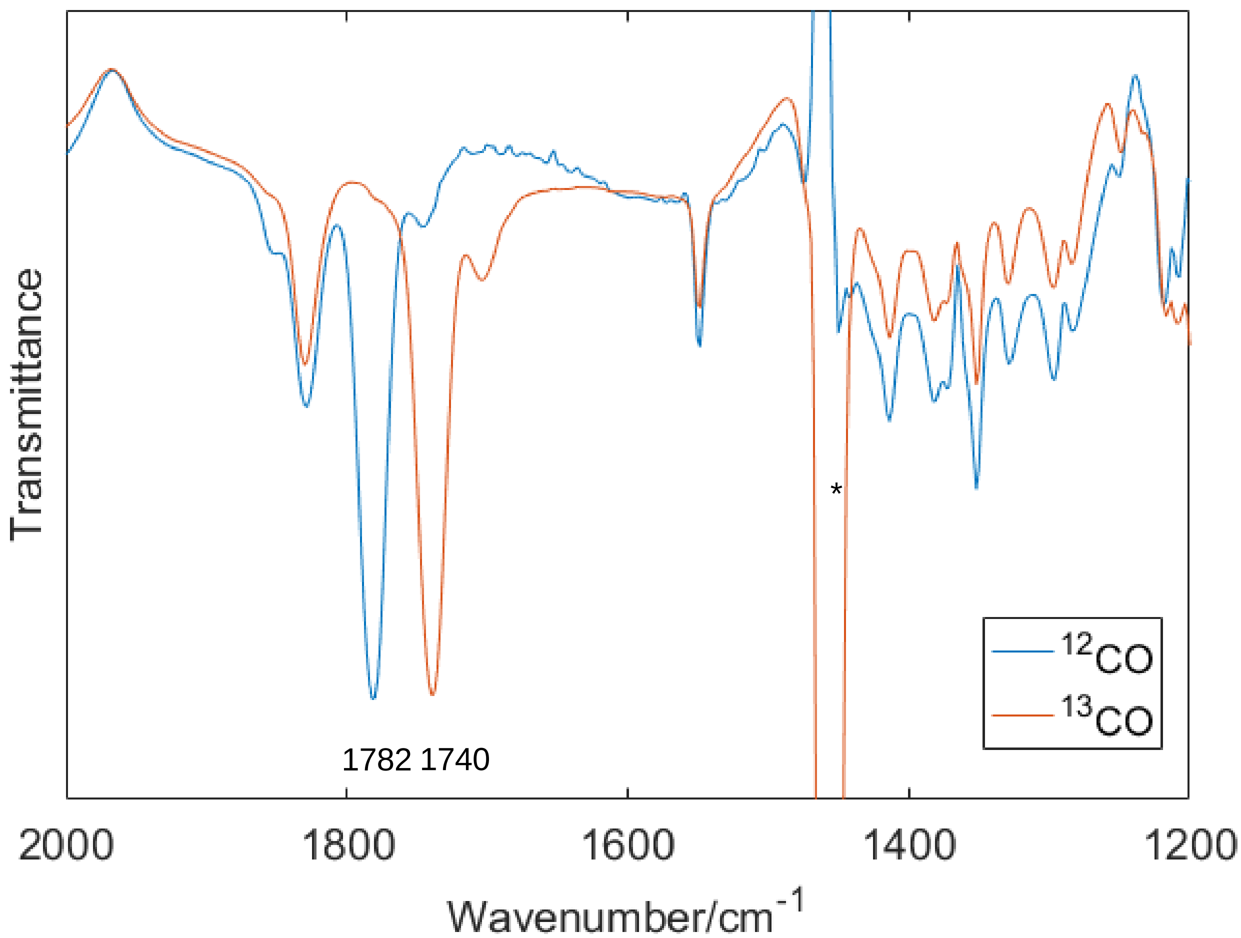

Figure 3.S27. IR spectra of **3.4-K(18-crown-6)** in THF with ^{12}CO and ^{13}CO over a wider window, with the CO peaks indicated. The feature marked with an asterisk (*) is an artifact due to the solvent.

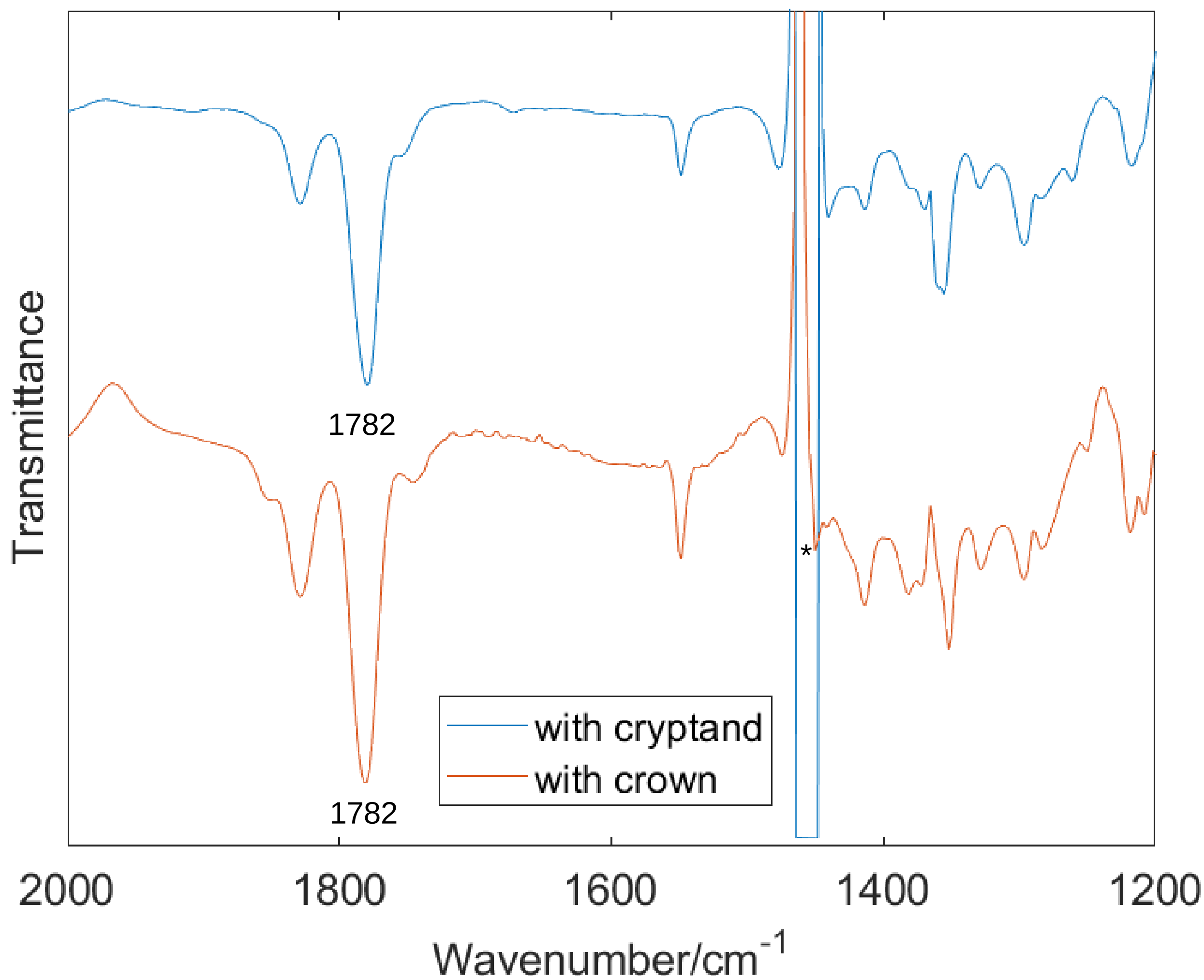

Figure 3.S28. IR spectra of **3.4-K** in the presence of 18-crown-6 and [2.2.2]cryptand in THF, with the CO peaks indicated. The feature marked with an asterisk (*) is an artifact due to the solvent.

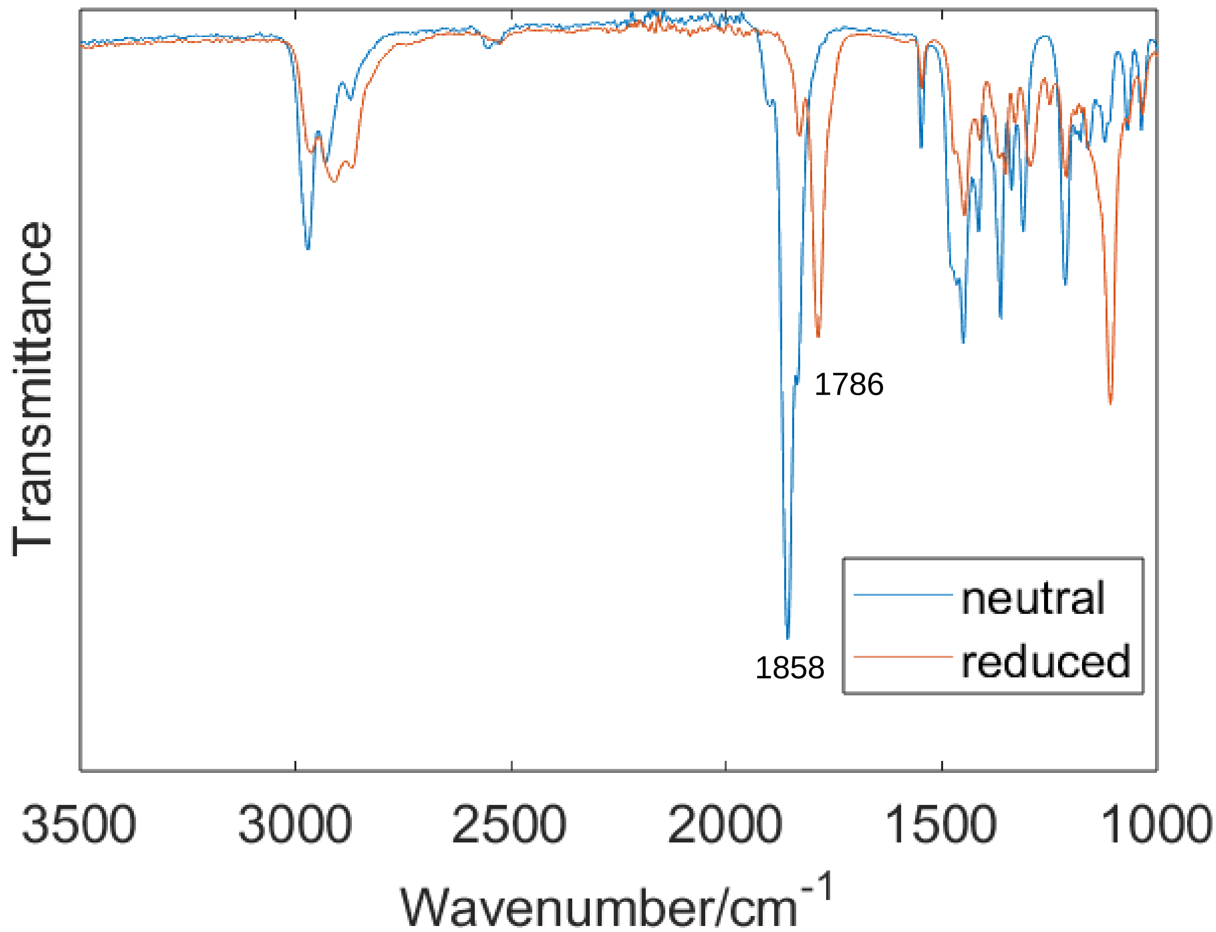

Figure 3.S29. ATR-IR spectra of the neutral **3.4-Mo** (blue) and reduced **3.4-Mo-K(18-crown-6)** (orange), with ν_{CO} highlighted.

Table 3.S2. Summary of CO stretching frequencies and comparison with calculated values

Cluster	ν_{12CO}/cm^{-1}	ν_{13CO}/cm^{-1} (exp)	ν_{13CO}/cm^{-1} (calc from harmonic oscillator model)
3.4	1851	1807	1810
3.4-K	1794, 1751	1753, 1709	1754, 1712
3.4-K(18-crown-6)	1782	1740	1742

Evans method for 3.4

The magnetic susceptibility of **3.4** was measured using Evans method on a THF solution of the cluster with 3% added C_6H_6 as a reference between 25 °C and -100 °C. The variable-temperature data suggest that the cluster possesses a spin state of S = 1 (theoretical $\mu_{eff} = 2.83\mu_B$).

Table 3.S3. Variable-temperature Evans method data for **3.4**

Temperature/°C	Measured μ_{eff}/μ_B
25	2.71
0	2.78
-20	2.71
-40	2.79
-60	2.72
-80	2.69
-100	2.61

The μ_{eff} value for **3.4-Mo** at room temperature measured using the identical procedure is $\mu_{eff} = 2.56\mu_B$, also suggesting S = 1 (theoretical $\mu_{eff} = 2.83\mu_B$).

EPR spectroscopy

Samples were prepared as solutions (ca. 2 mM) in 2-MeTHF and rapidly cooled in liquid nitrogen to form a frozen glass. All X-band EPR experiments presented in this study were acquired at the Caltech EPR facility. X-band CW EPR spectra were acquired on a Bruker (Billerica, MA) EMX spectrometer using Bruker Xenon software (ver. 1.2). Temperature control was achieved using liquid helium and an Oxford Instruments (Oxford, UK) ESR-900 cryogen flow cryostat and an ITC-503 temperature controller. Spectra were simulated using EasySpin5 (release 5.2.35)[68] with Matlab R2021b.

EPR spectroscopy was employed to determine the spin state of odd-electron clusters **3.4-K** and **3.4-K(18-crown-6)**. Both species possess a spin state of S = 3/2, with very similar spectra.

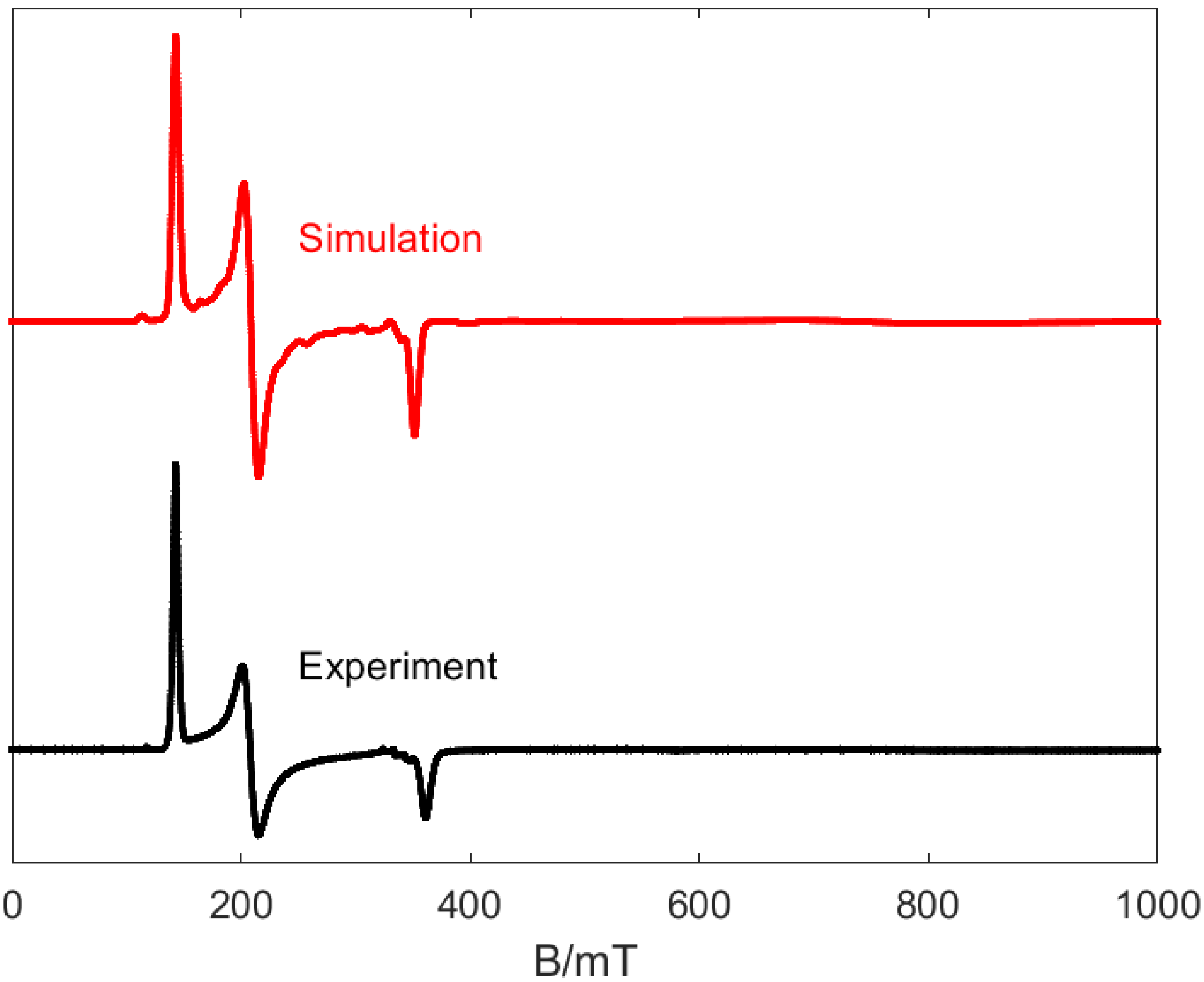

Figure 3.S30. X-band EPR spectrum of **3.4-K** as a frozen glass in 2-MeTHF at 5 K. Acquisition parameters: frequency = 9.64 MHz, power = 2.18 mW, conversion time = 10 ms, modulation amplitude = 8 G. Simulation parameters: S = 3/2, g = 2.05, large D (D = 2 cm^{-1}), E/D = 0.13, DStrain = 0.047 cm^{-1}.

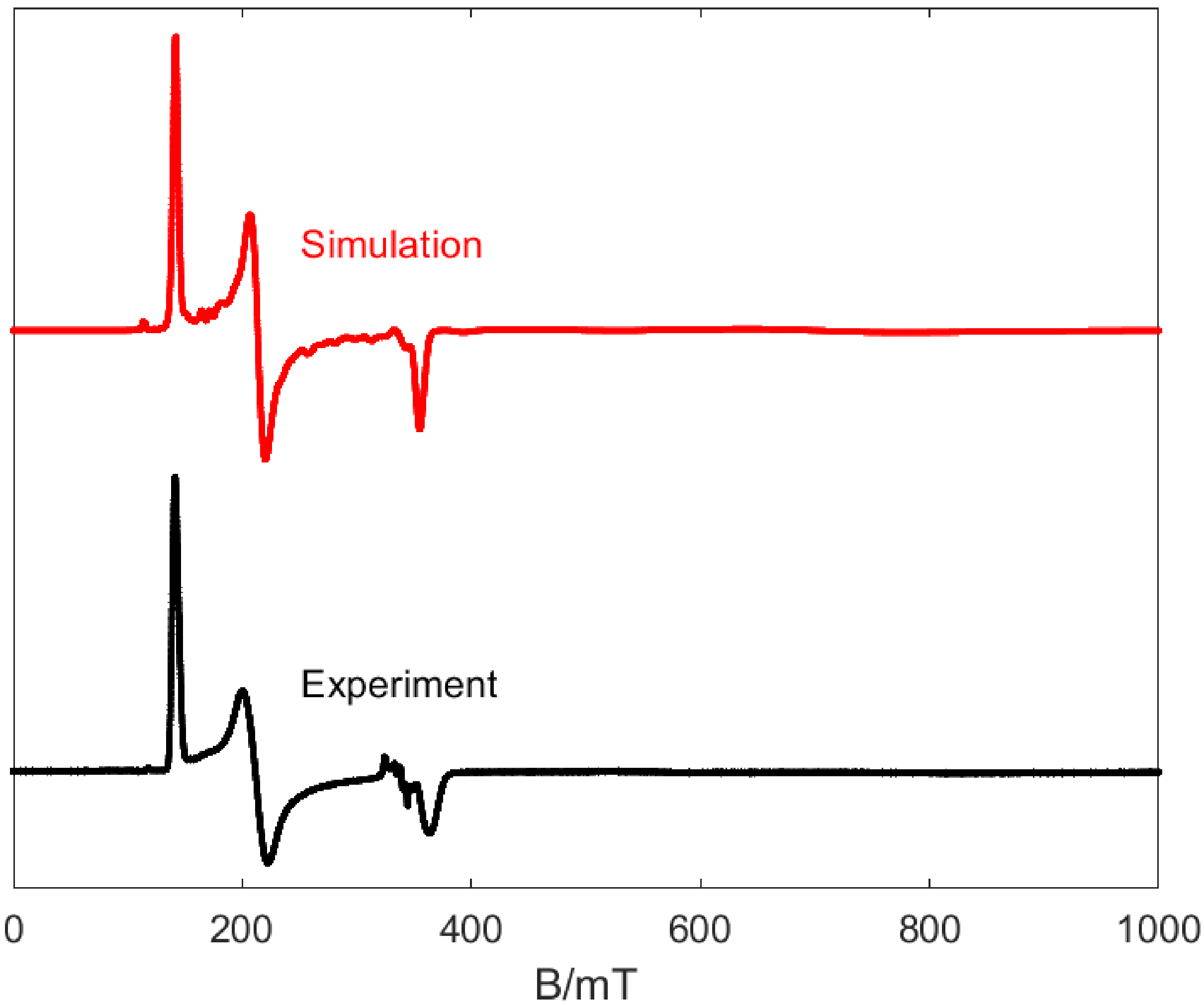

Figure 3.S31. X-band EPR spectrum of **3.4-K(18-crown-6)** as a frozen glass in 2-MeTHF at 5 K. Acquisition parameters: frequency = 9.64 MHz, power = 2.18 mW, conversion time = 10 ms, modulation amplitude = 8 G. Simulation parameters: S = 3/2, g = 2.05, large D (D = 2 cm^{-1}), E/D = 0.14, DStrain = 0.054 cm^{-1}.

Pulse EPR spectroscopy. All pulse EPR and electron nuclear double resonance (ENDOR) experiments were acquired using a Bruker (Billerica, MA) ELEXSYS E580 pulse EPR spectrometer. All X-band data was acquired using a Bruker MD-4 resonator. Temperature control was achieved using an Oxford Instruments CF935 and Mercury ITC.

X-band HYSCORE spectra were acquired using the 4-pulse sequence ($\pi/2 - \tau - \pi/2 - t_1 - \pi - t_2 - \pi/2$ – echo), where τ is a fixed delay, while t_1 and t_2 are independently incremented by Δt_1 and Δt_2, respectively. At each field, the fixed delay τ was selected to be a multiple of the time interval equivalent to the inverse of the ^{1}H Larmor frequency, in order to selectively suppress contributions from solvent matrix protons. A 16-step phase cycle was used to eliminate contributions from secondary/tertiary spin echoes and associated artifacts in the time domain. The time domain data was baseline-corrected (third-order polynomial) to eliminate the exponential decay in the echo intensity, apodized with a Hamming window function, zero-filled to eight-fold points, and fast Fourier-transformed to yield the 2-dimensional frequency domain. For ^{13}C-minus-Natural Abundance (N.A). difference spectra, the time domain of the HYSCORE spectrum of the sample prepared using natural abundance CO was subtracted from that of the ^{13}CO sample, and the same data processing procedure detailed above was used to generate the frequency spectrum. Contour plots of the 2D frequency spectra are plotted in logarithmic scale, with contours plotted in colors ranging from blue → yellow → red in increasing intensity.

In general, the ENDOR spectrum for a given nucleus with spin I = 1/2 (^{1}H, ^{13}C, ^{31}P) coupled to the S = 1/2 electron spin exhibits a doublet at frequencies

$$\nu_{\pm} = \left|\frac{A}{2} \pm \nu_N\right| \tag{1}$$

Where ν_N is the nuclear Larmor frequency and A is the hyperfine coupling. For nuclei with $I \geq 1$ (^{14}N, ^{2}H), an additional splitting of the $\nu_{\pm}$ manifolds is produced by the nuclear quadrupole interaction (P)

$$\nu_{\pm,m_I} = \left|\nu_N \pm \frac{3P(2m_I - 1)}{2}\right| \tag{2}$$

In HYSCORE spectra, these signals manifest as cross-peaks or ridges in the 2-D frequency spectrum which are generally symmetric about the diagonal of a given quadrant. This technique allows hyperfine levels corresponding to the same electron-nuclear submanifold to be differentiated, as well as separating features from hyperfine couplings in the weak-coupling regime ($|A| < 2|\nu_I|$) in the (+,+) quadrant from those in the strong coupling regime ($|A| > 2|\nu_I|$) in the (−,+) quadrant. The (−,−) and (+,−) quadrants of these frequency spectra are symmetric to the (+,+) and (−,+) quadrants, thus only two of the quadrants are typically displayed in literature.

For systems with appreciable hyperfine anisotropy in frozen solutions or solids, HYSCORE spectra typically do not exhibit sharp cross peaks, but show ridges that represent the sum of cross peaks from selected orientations within the excitation bandwidth of the MW pulses at the magnetic field position at which the spectrum is collected. The length and curvature of these correlation ridges can allow for the separation and estimation of the magnitude of the isotropic and dipolar components of the hyperfine tensor, as shown in Figure 3.S32.

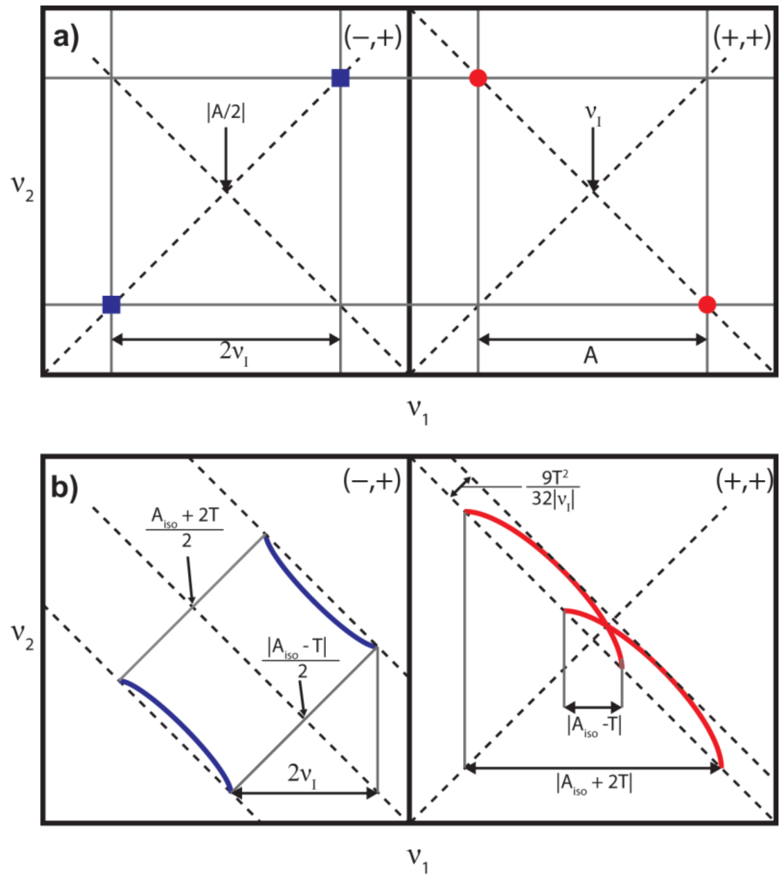

Figure 3.S32. a) HYSCORE powder patterns for an S = 1/2, I = 1/2 spin system with an isotropic hyperfine tensor A. b) HYSCORE powder patterns for an S = 1/2, I = 1/2 spin system with an axial hyperfine tensor that contains isotropic (a_{iso}) and dipolar (T) contributions. Blue correlation ridges represent the strong coupling case; red correlation ridges represent the weak coupling case.

EPR Simulations. Simulations of all CW and pulse EPR data were achieved using the EasySpin simulation toolbox (release 5.2.25)[68] with Matlab 2019a using the following Hamiltonian:

$$\hat{H} = \mu_B \vec{B}_0 g \hat{S} + \mu_N g_N \vec{B}_0 \hat{I} + h\hat{S} \cdot \boldsymbol{A} \cdot \hat{I} + h\hat{I} \cdot \boldsymbol{P} \cdot \hat{I} \quad (3)$$

In this expression, the first term corresponds to the electron Zeeman interaction term where μ_B is the Bohr magneton, g is the electron spin g-value matrix with princial components $\mathbf{g} = [g_{xx}\ g_{yy}\ g_{zz}]$, and $\hat{S}$ is the electron spin operator; the second term corresponds to the nuclear Zeeman interaction term where μ_N is the nuclear magneton, g_N is the characteristic nuclear g-value for each nucleus (e.g. ^{1}H, ^{13}C) and $\hat{I}$ is the nuclear spin operator; the third term corresponds to the electron-nuclear hyperfine term, where $\boldsymbol{A}$ is the hyperfine coupling tensor with principal components $\boldsymbol{A}$ = [A_{xx}, A_{yy}, A_{zz}]; and for nuclei with $I \geq 1$, the final term corresponds to the nuclear quadrupole (NQI) term which arises from the interaction of the nuclear quadrupole moment with the local electric field gradient (efg) at the nucleus, where $\boldsymbol{P}$ is the quadrupole coupling tensor. In the principal axis system (PAS), $\boldsymbol{P}$ is traceless and parametrized by the quadrupole coupling constant e^2Qq/h and the asymmetry parameter η such that:

$$\boldsymbol{P} = \begin{pmatrix} P_{xx} & 0 & 0 \\ 0 & P_{yy} & 0 \\ 0 & 0 & P_{zz} \end{pmatrix} = \frac{e^2Qq/h}{4I(2I-1)} \begin{pmatrix} -(1-\eta) & 0 & 0 \\ 0 & -(1+\eta) & 0 \\ 0 & 0 & 2 \end{pmatrix} \quad (4)$$

where $\frac{e^2Qq}{h} = 2I(2I-1)P_{zz}$ and $\eta = \frac{P_{xx}-P_{yy}}{P_{zz}}$. The asymmetry parameter may have values between 0 and 1, with 0 corresponding to an electric field gradient (EFG) with axial symmetry and 1 corresponding to a fully rhombic EFG.

The orientations between the hyperfine and NQI tensor principal axis systems and the g-matrix reference frame are defined by the Euler angles (α, β, γ), with rotations performed within the zyz convention where α rotates xyz counterclockwise about z-axis to give x'y'z', β rotates x'y'z' counterclockwise about y'-axis to give x",y",z", γ rotates x"y"z" counterclockwise about z"-axis to give final frame orientation.

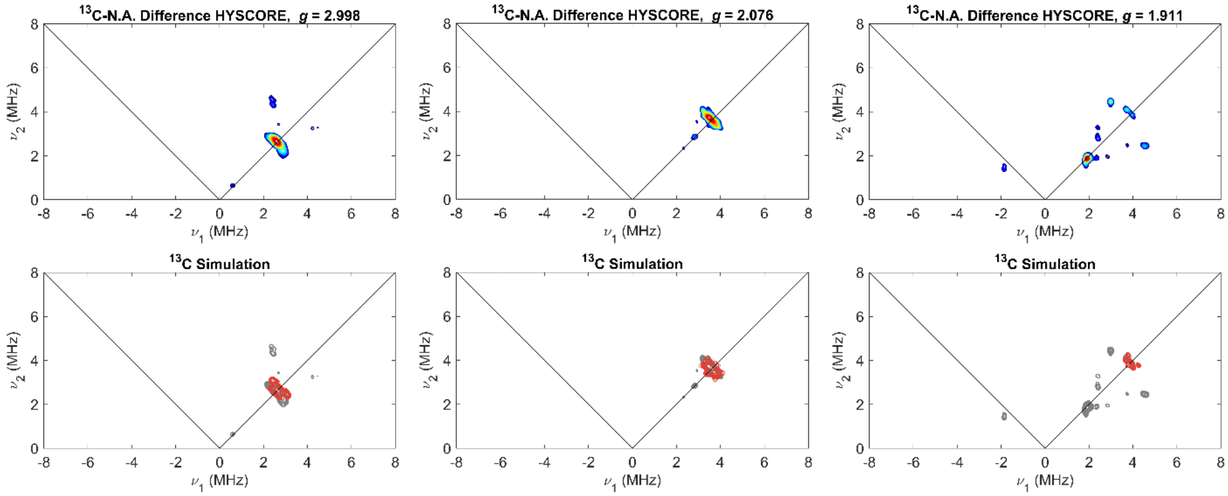

Figure 3.S33. Top Panels: Field-dependent X-band ^{13}C-minus-Natural Abundance (N.A.) HYSCORE of **3.4-K(^{13}CO)**. Bottom Panels: Experimental HYSCORE spectrum (gray contours) with overlay of simulated ^{13}C HYSCORE spectrum (***A*(^{13}C)** = [-0.5, 1.0, -0.5] MHz) in red. Acquisition parameters: Temperature = 3.6 K; B_0 = 242 mT (*g* = 2.998), 335 mT (*g* = 2.076), 364 mT (*g* = 1.911); MW Frequency = 9.736 GHz; MW pulse lengths $(\pi/2, \pi)$ = 8 ns, 16 ns; τ = 98 ns (*g* = 2.998), 140 ns (*g* = 2.076), 130 ns (*g* = 1.911); $t_1 = t_2$ = 100 ns; $\Delta t_1 = \Delta t_2$ =12 ns; shot repetition time (srt) = 1 ms.

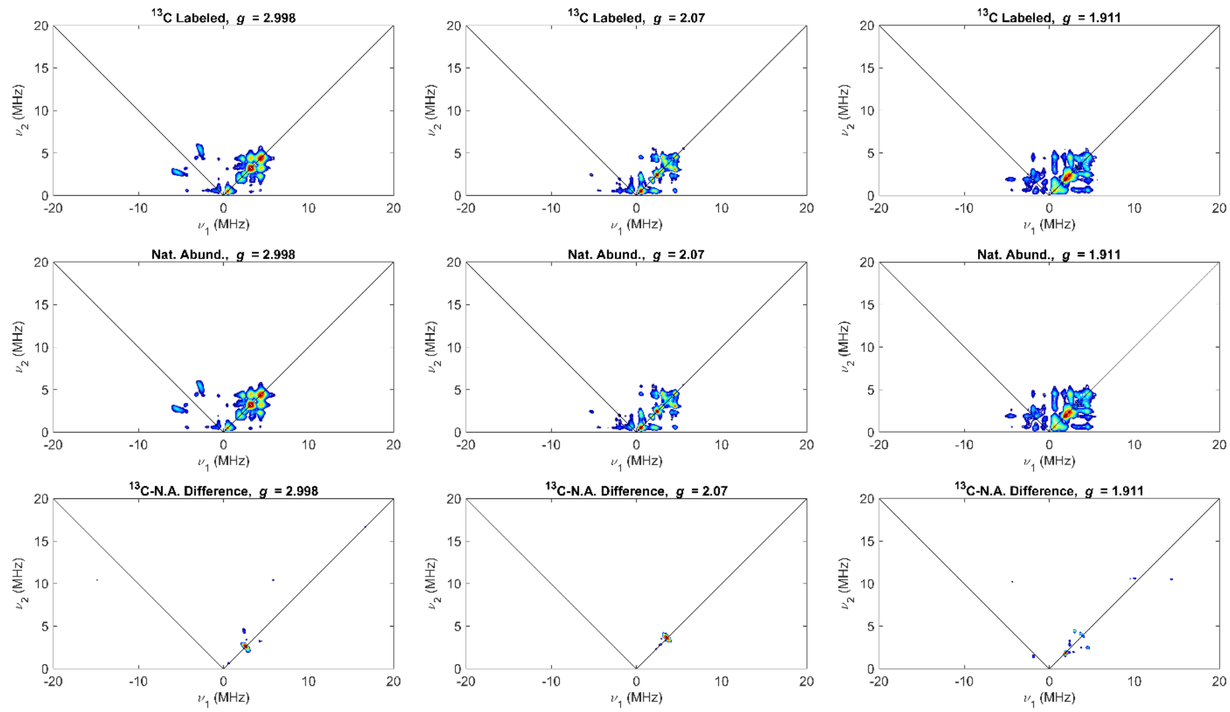

Figure 3.S34. Field-dependent X-band HYSCORE of **3.4-K(^{13}CO)** (top panels)**, 3.4-K** (middle panels), and the ^{13}C-N.A. difference spectra plotted in the bottom panels. Acquisition parameters: Temperature = 3.6 K; B_0 = 242 mT (g = 2.998), 335 mT (g = 2.076), 364 mT (g = 1.911); MW Frequency = 9.736 GHz; MW pulse lengths $(\pi/2, \pi)$ = 8 ns, 16 ns; τ = 98 ns (g = 2.998), 140 ns (g = 2.076), 130 ns (g = 1.911); $t_1 = t_2$ = 100 ns; $\Delta t_1 = \Delta t_2$ =12 ns; shot repetition time (srt) = 1 ms.

B) Crystallographic information:

1. X-ray crystallography:

XRD data were collected at 100 K on a Bruker AXS D8 KAPPA or Bruker AXS D8 VENTURE diffractometer [microfocus sealed X-ray tube, λ(Mo Kα) = 0.71073 Å or λ(Cu Kα) = 1.54178 Å]. All manipulations, including data collection, integration, and scaling, were carried out using the Bruker *APEX3* software.[69] Absorption corrections were applied using *SADABS*.[70] Structures were solved by direct methods using *Sir92*[71] or *SUPERFLIP*[72] and refined using full-matrix least-squares on *CRYSTALS*[73] to convergence. All non-H atoms were refined using anisotropic displacement parameters. H atoms were placed in idealized positions and refined using a riding model. Because of the size of the compounds some crystals included solvent-accessible voids that contained disordered solvent. The solvent could be either modeled satisfactorily or accounted for using either the *SQUEEZE* procedure in the *PLATON* software package.[74]

2. Additional information:

Special refinement details for **3.2-^{t}Bu**. The asymmetric unit of the structure contains three co-crystallized C_6H_6 solvent molecules, which can be modeled satisfactorily using bond lengths and similarity restraints for anisotropic displacement parameters (ADPs). The backbone of the five-membered chelate portion containing the two N^{i}Pr$_2$ groups is disordered over two positions, with occupancies of 43% and 57%.

Special refinement details for **3.3**. The asymmetric unit of the structure contains two co-crystallized THF solvent molecules which can be modeled satisfactorily using bond lengths and similarity restraints for ADPs. Two N^{i}Pr fragments on one BAC ligand are disordered over two positions, with occupancies of 38% and 62%, and 33% and 67%.

Special refinement details for **3.3-Mo**. The asymmetric unit of the structure contains one co-crystallized pentane and one co-crystallized Et_2O solvent molecules, which can be modeled satisfactorily using bond lengths and similarity restraints for ADPs.

Special refinement details for **3.4**. The asymmetric unit of the structure contains half of a co-crystallized C_6H_6 and two Et_2O solvent molecules, which can be modeled satisfactorily using bond lengths and similarity restraints for ADPs.

Special refinement details for **3.4-Mo**. The asymmetric unit of the structure contains one co-crystallized THF solvent molecule, which can be modeled satisfactorily using bond lengths and similarity restraints for ADPs. The remaining solvent molecules are heavily disordered and cannot be modeled satisfactorily. Therefore, the electron density for co-crystallized solvent molecules were accounted for using the *SQUEEZE* procedure in *PLATON*,[74] whereby 531 electrons were found in a volume of 2240 Å^3, consistent with the presence of 1.5[$C_4H_{10}O$] in the asymmetric unit.

Special refinement details for **3.4-K**. The asymmetric unit of the structure contains two co-crystallized Et_2O solvent molecules, which can be modeled satisfactorily using bond lengths and similarity restraints for ADPs. The K(THF) fragments are disordered over two positions, with occupancies of 36% and 64%. In one position, the positions of the atoms within the THF molecule tend to oscillate, so a shift-limiting restrain was applied to stabilize them.

Special refinement details for **3.4-K(18-crown-6)**. The asymmetric unit of the structure contains heavily disordered solvent molecules and cannot be modeled satisfactorily. Therefore, the electron density for co-crystallized solvent molecules were accounted for using the *SQUEEZE* procedure in *PLATON*,[74] whereby 37 electrons were found in a volume of 235 Å^3, consistent with the presence of 0.5[$C_4H_{10}O$] in the asymmetric unit.

Special refinement details for **3.5**. The asymmetric unit of the structure contains two co-crystallized THF solvent molecules, which can be modeled satisfactorily using bond lengths and similarity restraints for ADPs.

Special refinement details for **3.6**. The asymmetric unit of the structure contains one co-crystallized Et_2O solvent molecule, which can be modeled satisfactorily using bond lengths and similarity restraints for ADPs. The remaining solvent molecules are heavily disordered and cannot be modeled satisfactorily. Therefore, the electron density for co-crystallized solvent molecules were accounted for using the *SQUEEZE* procedure in *PLATON*,[74] whereby 42 electrons were found in a volume of 474 Å^3, consistent with the presence of 0.5[$C_4H_{10}O$] in the asymmetric unit.

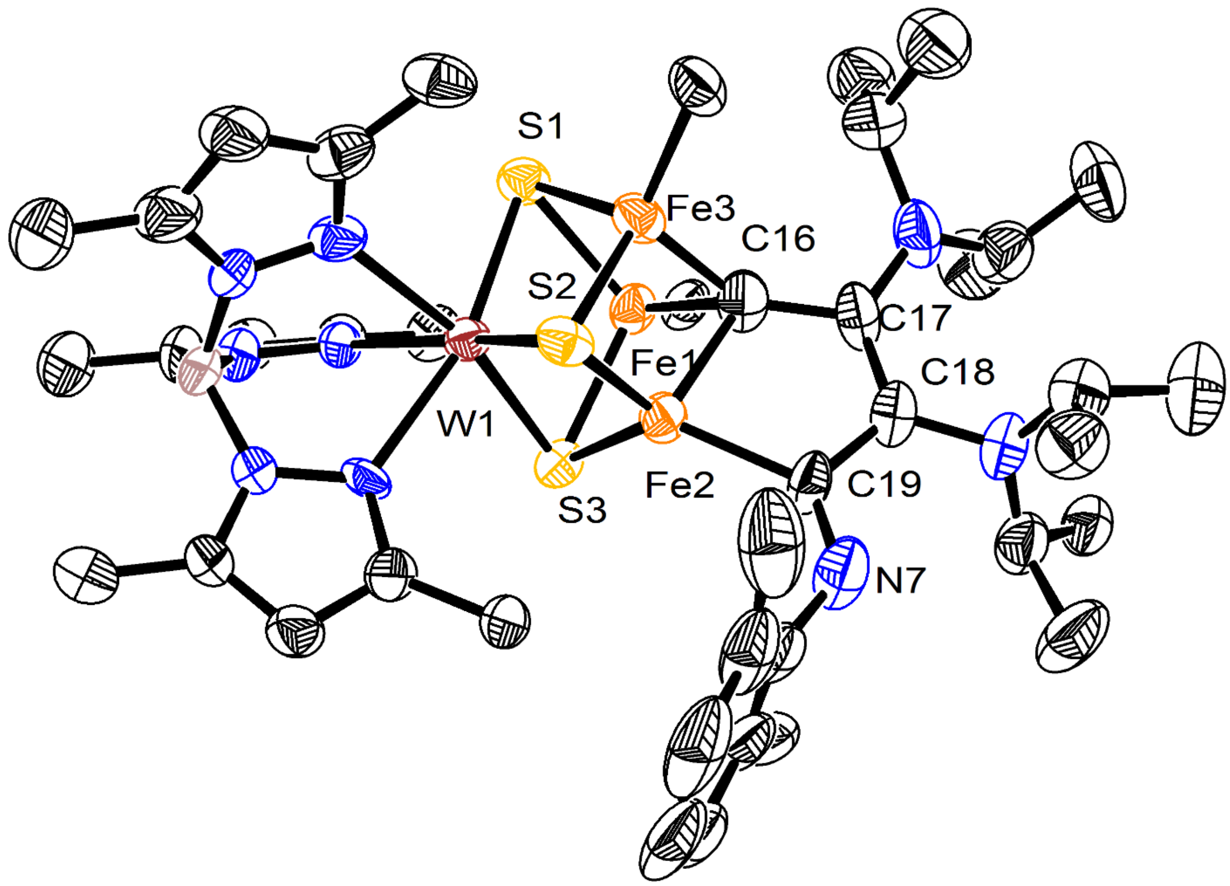

Figure 3.S35. Crystal structure of **3.2-Xyl**. Ellipsoids are shown at 50% probability level. Hydrogen atoms, solvent molecules, and the BAC ligand except for the carbene C are omitted for clarity.

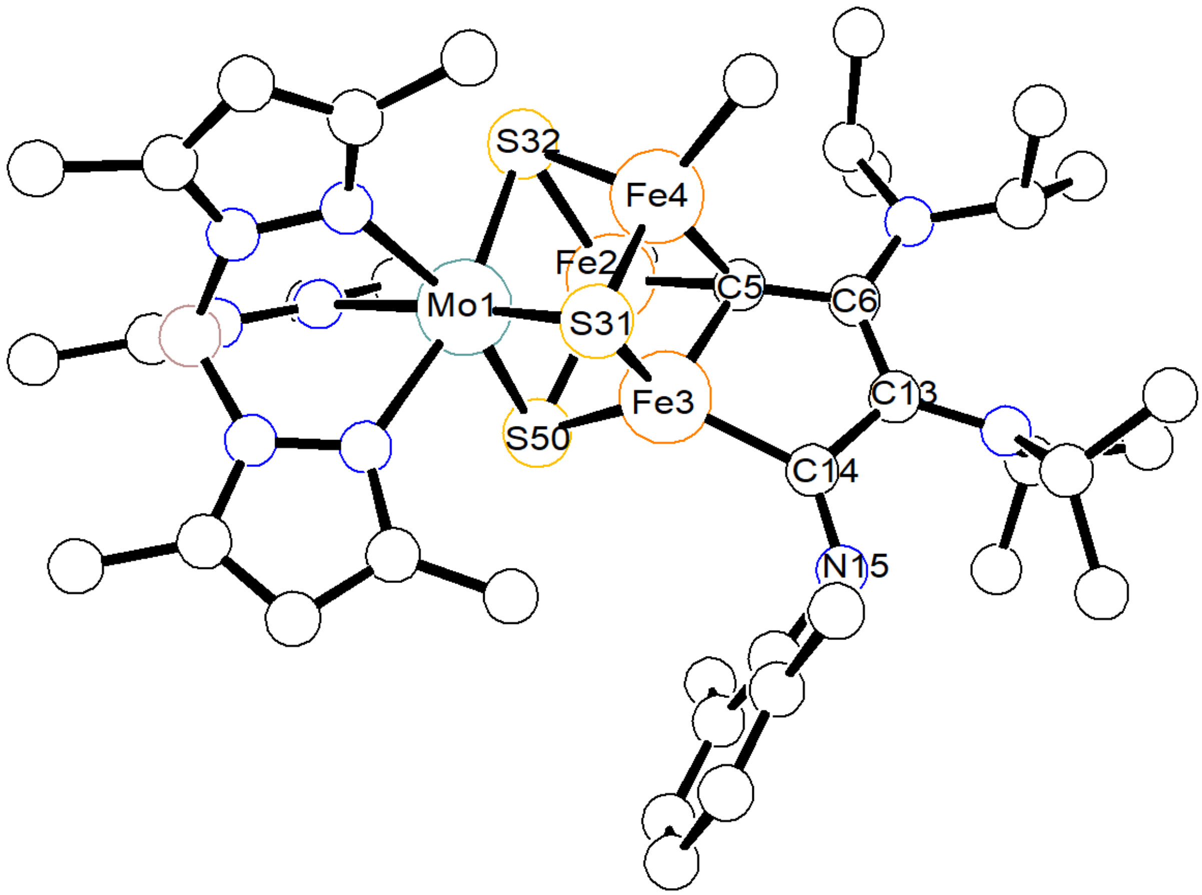

Figure 3.S36. Connectivity of **3.2-Mo-Xyl**. Spheres are shown at 50% probability level. Hydrogen atoms, solvent molecules, and the BAC ligand except for the carbene C are omitted for clarity.

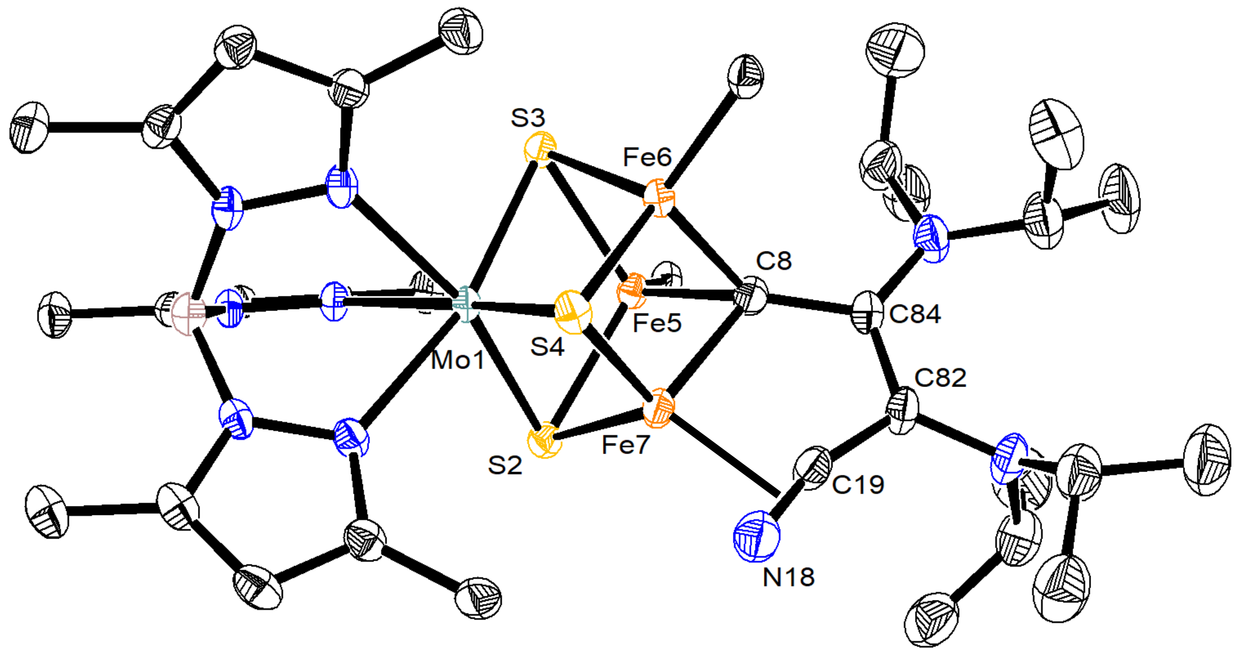

Figure 3.S37. Crystal structure of **3.3-Mo**. Ellipsoids are shown at 50% probability level. Hydrogen atoms, solvent molecules, and the BAC ligand except for the carbene C are omitted for clarity.

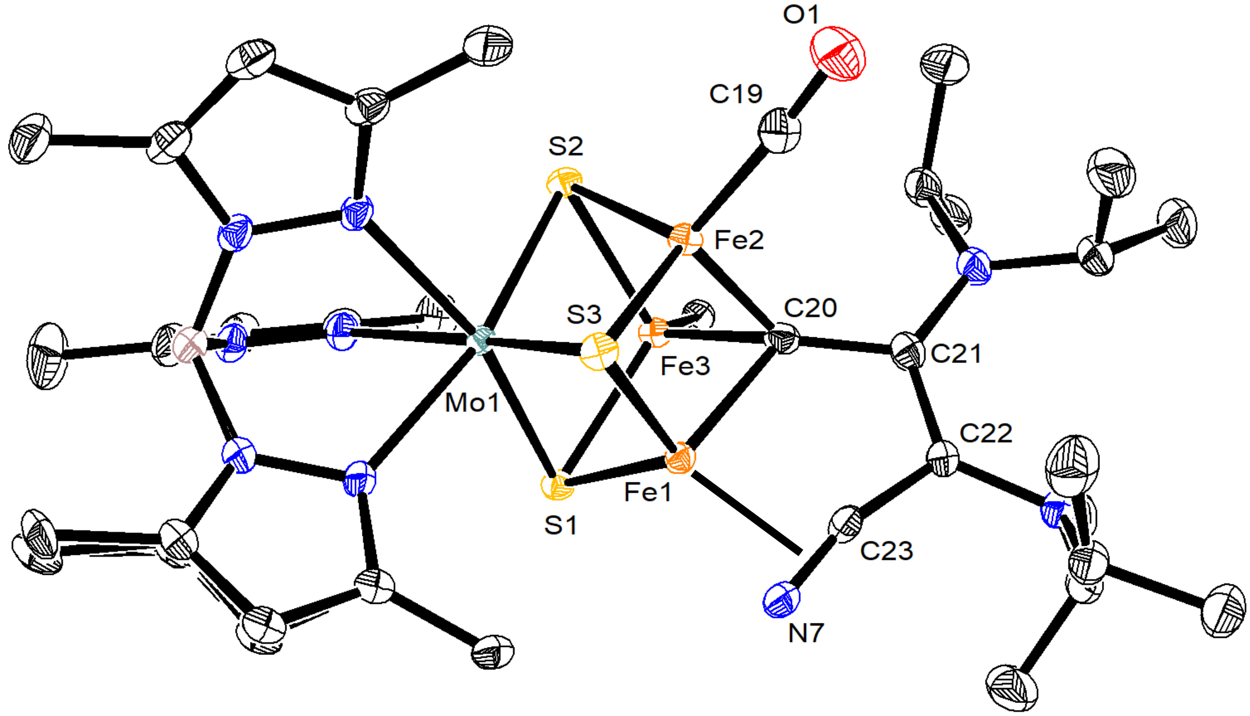

Figure 3.S38. Crystal structure of **3.4-Mo**. Ellipsoids are shown at 50% probability level. Hydrogen atoms, solvent molecules, and the BAC ligand except for the carbene C are omitted for clarity.

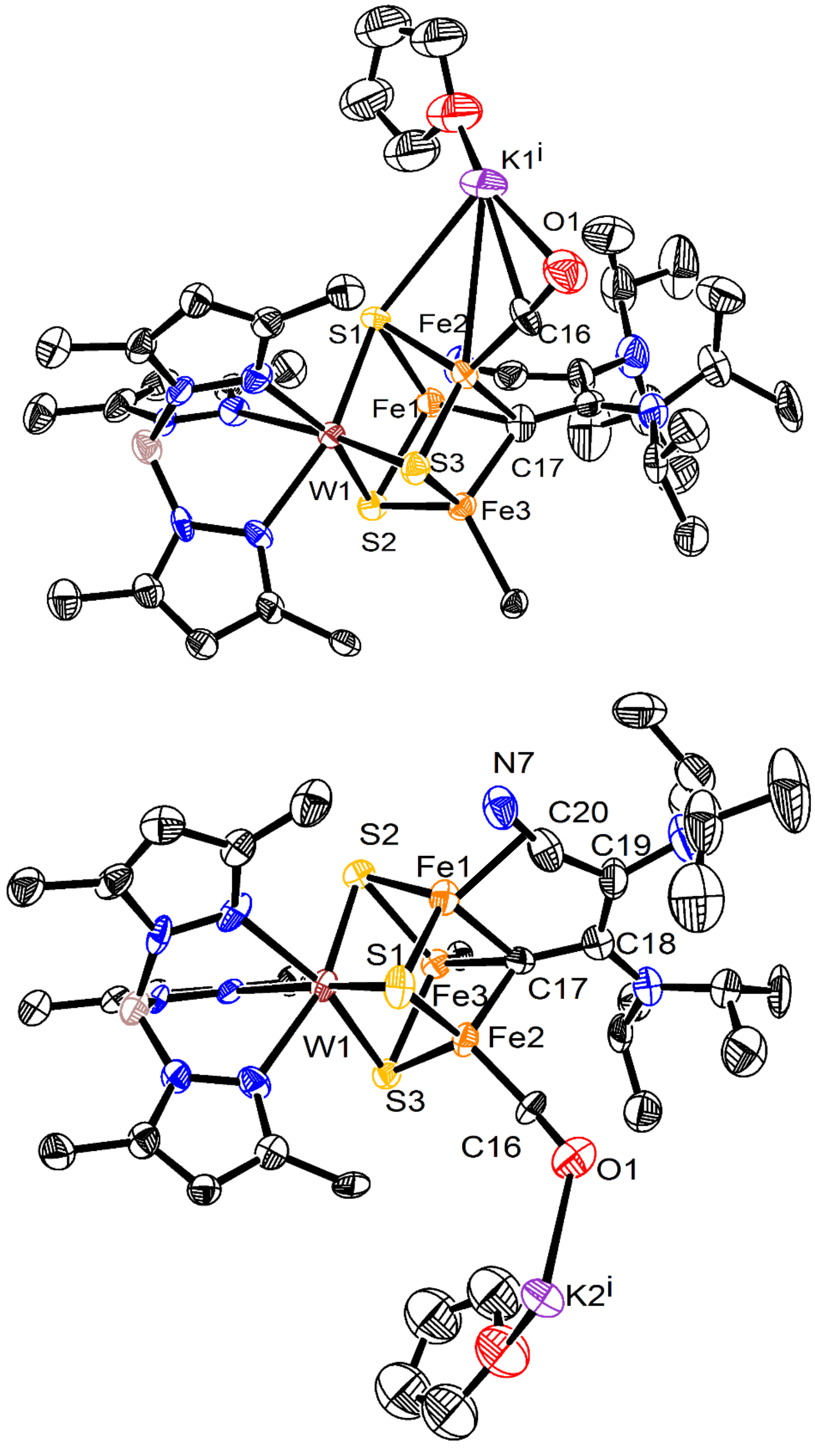

Figure 3.S39. Crystal structure of **3.4-K** in two views showing the two disordered positions of the K atom. Ellipsoids are shown at 50% probability level. Hydrogen atoms, solvent molecules, and the BAC ligand except for the carbene C are omitted for clarity.

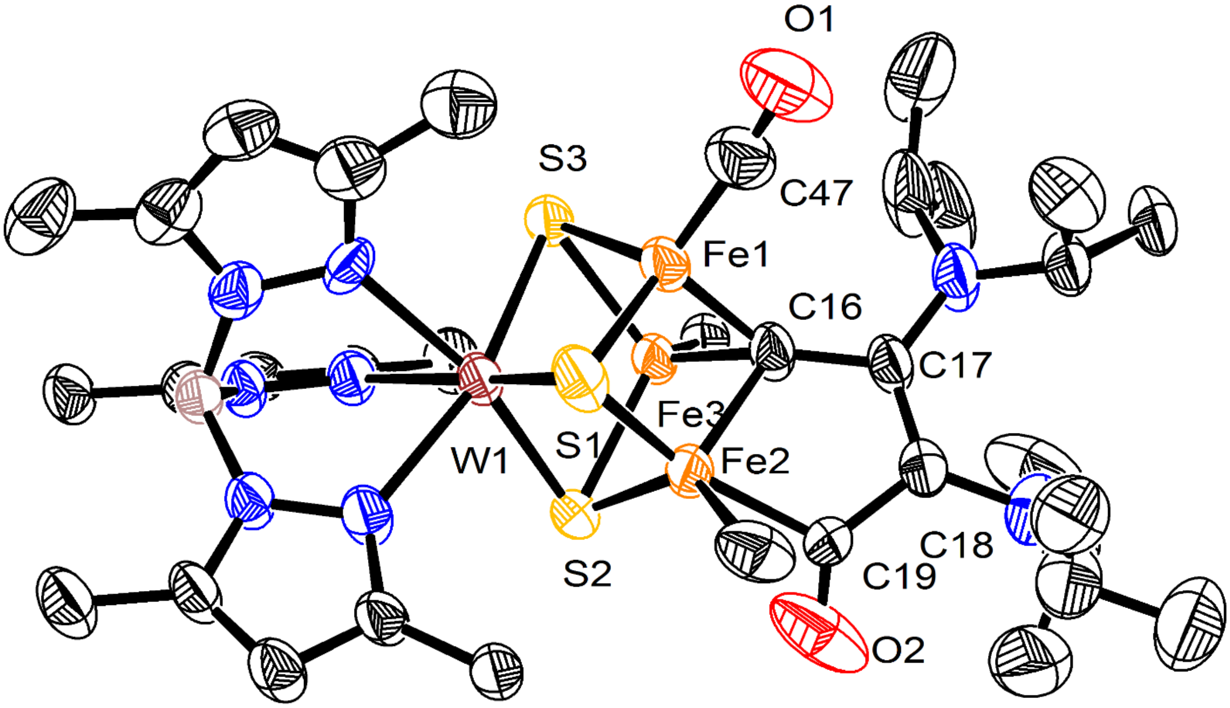

Figure 3.S40. Crystal structure of **3.6**. Ellipsoids are shown at 50% probability level. Hydrogen atoms, solvent molecules, and the BAC ligand except for the carbene C are omitted for clarity.

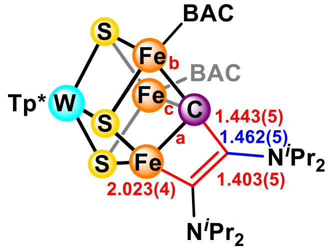

3.1

a = 1.943(3)
b = 1.958(4)
c = 1.945(3)

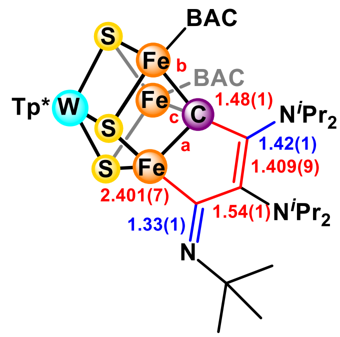

3.2-^{t}Bu

a = 1.919(6)
b = 1.944(8)
c = 1.953(7)

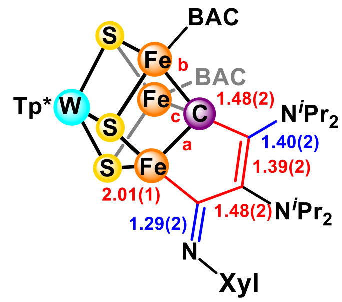

3.2-Xyl

a = 1.91(1)
b = 1.92(1)
c = 1.93(1)

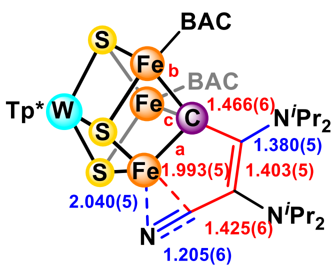

3.3

a = 1.988(4)
b = 1.939(4)
c = 1.930(4)

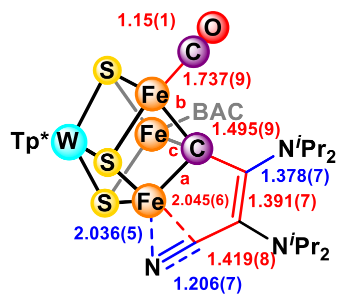

3.4

a = 2.009(6)
b = 1.880(8)
c = 1.953(8)

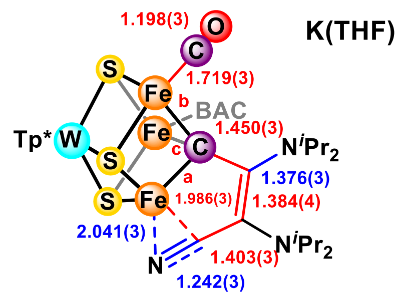

3.4-K

a = 2.046(3)
b = 1.908(2)
c = 1.955(4)

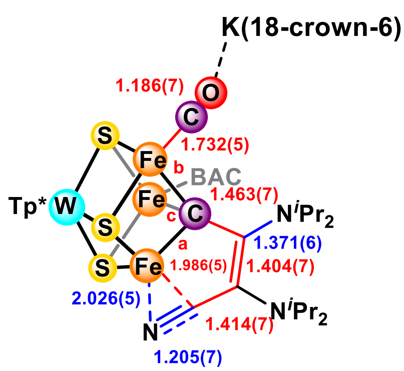

3.4-K(18-crown-6)

a = 2.021(5)
b = 1.900(7)
c = 1.961(4)

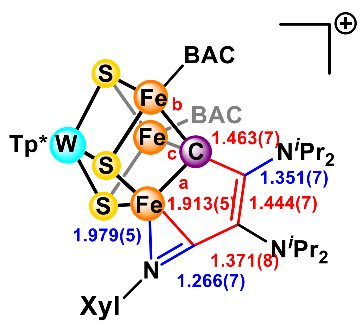

3.5

a = 1.945(5)
b = 1.961(5)
c = 1.948(5)

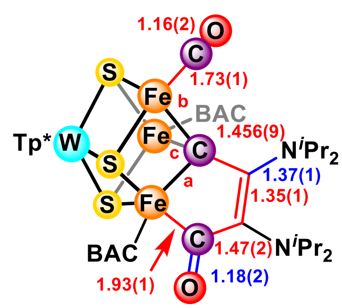

3.6

a = 1.943(7)
b = 1.956(8)
c = 1.907(8)

Figure 3.S41. Bond length comparisons in Å for the clusters reported for selected bonds. The abbreviations a, b, and c refer to the three Fe-C(μ_3) distances as labeled in the structures.

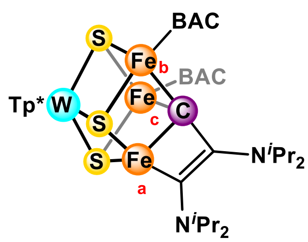

3.1

W-Fe(a) = 2.7203(5)
W-Fe(b) = 2.7089(5)
W-Fe(c) = 2.6934(5)
av. W-Fe = 2.7075
Fe(a)-Fe(b) = 2.5122(6)
Fe(b)-Fe(c) = 2.5186(7)
Fe(c)-Fe(a) = 2.4854(7)
av. Fe-Fe = 2.5054

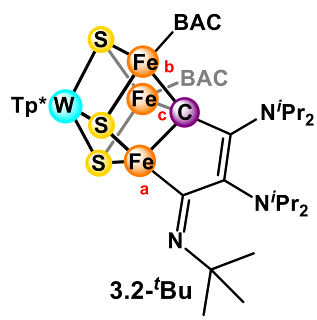

3.2-^{t}Bu

W-Fe(a) = 2.713(3)
W-Fe(b) = 2.720(3)
W-Fe(c) = 2.781(2)
av. W-Fe = 2.738
Fe(a)-Fe(b) = 2.514(2)
Fe(b)-Fe(c) = 2.535(4)
Fe(c)-Fe(a) = 2.526(3)
av. Fe-Fe = 2.525

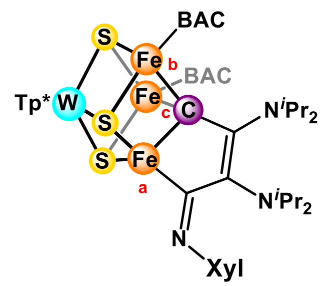

3.2-Xyl

W-Fe(a) = 2.687(2)
W-Fe(b) = 2.708(2)
W-Fe(c) = 2.705(2)
av. W-Fe = 2.700
Fe(a)-Fe(b) = 2.519(2)
Fe(b)-Fe(c) = 2.528(3)
Fe(c)-Fe(a) = 2.486(2)
av. Fe-Fe = 2.511

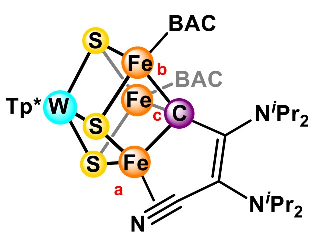

3.3

W-Fe(a) = 2.6790(9)
W-Fe(b) = 2.7200(9)
W-Fe(c) = 2.715(1)
av. W-Fe = 2.705
Fe(a)-Fe(b) = 2.5708(9)
Fe(b)-Fe(c) = 2.5373(9)
Fe(c)-Fe(a) = 2.541(1)
av. Fe-Fe = 2.550

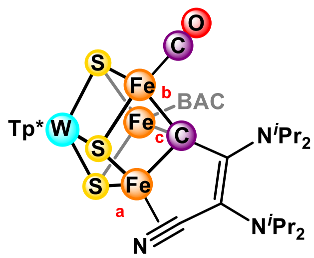

3.4

W-Fe(a) = 2.6786(9)
W-Fe(b) = 2.657(1)
W-Fe(c) = 2.727(1)
av. W-Fe = 2.688
Fe(a)-Fe(b) = 2.512(1)
Fe(b)-Fe(c) = 2.501(2)
Fe(c)-Fe(a) = 2.566(1)
av. Fe-Fe = 2.526

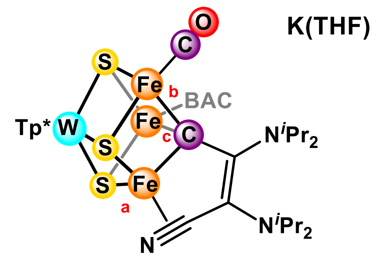

3.4-K

W-Fe(a) = 2.698(2)
W-Fe(b) = 2.711(1)
W-Fe(c) = 2.735(2)
av. W-Fe = 2.715
Fe(a)-Fe(b) = 2.549(2)
Fe(b)-Fe(c) = 2.530(2)
Fe(c)-Fe(a) = 2.587(3)
av. Fe-Fe = 2.555

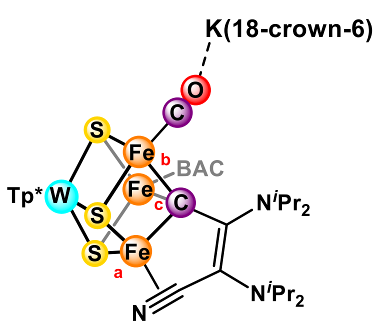

3.4-K(18-crown-6)

W-Fe(a) = 2.658(1)
W-Fe(b) = 2.715(1)
W-Fe(c) = 2.730(1)
av. W-Fe = 2.701
Fe(a)-Fe(b) = 2.541(1)
Fe(b)-Fe(c) = 2.519(2)
Fe(c)-Fe(a) = 2.585(1)
av. Fe-Fe = 2.548

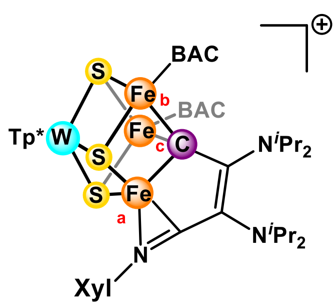

3.5

W-Fe(a) = 2.7263(9)
W-Fe(b) = 2.7421(9)
W-Fe(c) = 2.7243(8)
av. W-Fe = 2.7309
Fe(a)-Fe(b) = 2.520(1)
Fe(b)-Fe(c) = 2.554(1)
Fe(c)-Fe(a) = 2.546(1)
av. Fe-Fe = 2.540

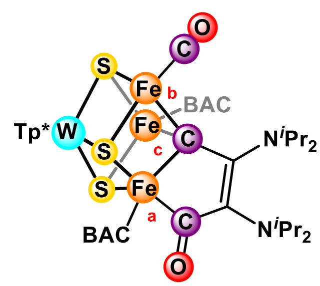

3.6

W-Fe(a) = 2.811(1)
W-Fe(b) = 2.692(1)
W-Fe(c) = 2.706(1)
av. W-Fe = 2.736
Fe(a)-Fe(b) = 2.498(2)
Fe(b)-Fe(c) = 2.500(2)
Fe(c)-Fe(a) = 2.571(2)
av. Fe-Fe = 2.523

Figure 3.S42. Metal-metal distances in Å for the clusters reported.

Table 3.S4. Summary of statistics for diffraction data for clusters **3.2** to **3.4**

Cluster	**3.2-^{t}Bu**	**3.2-Xyl**	**3.3**	**3.4**
CCDC	2130433	2233067	2233068	2130436
Empirical formula	$C_{83}H_{133}BFe_3N_{13}S_3W$	$C_{73}H_{125}BFe_3N_{13}OS_3W$	$C_{69}H_{122}BFe_3N_{13}O_2S_3W$	$C_{58}H_{101}BFe_3N_{11}O_3S_3W$
Formula weight	1771.45	1659.28	1624.21	1458.91
Temperature/K	100	100	100	100
Crystal system	Monoclinic	Triclinic	Monoclinic	Monoclinic
Space group	Cc	P-1	$P2_1/n$	C2/c
a/Å	23.8881(12)	14.394(2)	20.374(7)	40.500(3)
b/Å	15.1745(7)	16.501(2)	17.922(3)	16.2716(10)
c/Å	26.2682(14)	17.357(4)	21.852(6)	24.9399(16)
α/°	90	76.625(13)	90	90
β/°	111.144(5)	81.965(6)	101.54(2)	125.5559(16)
γ/°	90	87.939(10)	90	90
Volume/Å^3	8880.9(8)	3971.5(12)	7818(4)	13370.9(15)
Z	4	2	4	8
ρ_{calc}/g cm^{-3}	1.325	1.387	1.380	1.449
μ/mm^{-1}	7.209	8.030	8.155	2.496
F(000)	3708.0	1734.0	14202.0	6040.0
Crystal size/mm^3	0.05 × 0.06 × 0.10	0.01 × 0.05 × 0.20	0.02 × 0.08 × 0.16	0.05 × 0.05 × 0.10
Radiation	Cu Kα	Cu Kα	Cu Kα	Mo Kα
θ_{max}/°	80.685	74.820	74.820	33.976
Index ranges	$-30 \le h \le 27$, $-19 \le k \le 19$, $-32 \le l \le 32$	$-15 \le h \le 17$, $-20 \le k \le 20$, $-21 \le l \le 21$	$-25 \le h \le 25$, $-22 \le k \le 22$, $-27 \le l \le 27$	$-55 \le h \le 63$, $-25 \le k \le 25$, $-39 \le l \le 39$
Reflections measured	91969	91921	139311	136877
Independent reflections	17918	16152	15954	27087
Restraints/Parameters	324/1082	0/856	234/903	104/726
GOF on F^2	0.992	0.969	1.006	1.003
R-factor	0.0564	0.0941	0.0410	0.0783
Weighted R-factor	0.1463	0.2556	0.1078	0.1939
Largest diff. peak/hole/e Å^{-3}	0.79/-1.24	2.90/-4.85	1.79/-1.11	4.75/-6.37

Table 3.S5. Summary of statistics for diffraction data for clusters **3.4-K** to **3.6**

Cluster	3.4-K	3.4-K(18-crown-6)	3.5	3.6
CCDC	2233070	2233072	2233069	2130434
Empirical formula	$C_{59}H_{106}BFe_3KN_{11}O_4S_3W$	$C_{59}H_{102}BFe_3KN_{11}O_7S_3W$	$C_{78}H_{131}BF_3Fe_3N_{13}O_5S_4W$	$C_{66}H_{116}BFe_3N_{12}O_3S_3W$
Formula weight	1531.06	1575.03	1878.44	1584.12
Temperature/K	100	100	100	100
Crystal system	Monoclinic	Triclinic	Monoclinic	Triclinic
Space group	$P2_1/c$	P-1	$P2_1/c$	P-1
a/Å	16.2062(5)	13.942(4)	15.131(3)	13.4439(6)
b/Å	31.3345(9)	16.201(5)	25.397(3)	16.4143(6)
c/Å	14.0576(5)	17.697(7)	23.235(6)	19.0773(7)
α/°	90	73.25(2)	90	97.603(2)
β/°	93.6639(18)	69.84(2)	95.143(12)	103.792(2)
γ/°	90	79.89(3)	90	97.819(3)
Volume/Å^3	7124.0(4)	3580(2)	8893(3)	3990.6(3)
Z	4	2	4	2
ρ_{calc}/g cm^{-3}	1.427	1.461	1.403	1.318
μ/mm^{-1}	9.441	9.444	7.538	7.981
F(000)	3172.0	1626.0	3912.0	1650.0
Crystal size/mm^3	0.02 × 0.09 × 0.12	0.02 × 0.05 × 0.06	0.08 × 0.12 × 0.20	0.05 × 0.10 × 0.15
Radiation	Cu Kα	Cu Kα	Cu Kα	Cu Kα
θ_{max}/°	74.616	76.224	74.636	80.292
Index ranges	$-20 \le h \le 19$, $-39 \le k \le 38$, $-17 \le l \le 17$	$-16 \le h \le 17$, $-19 \le k \le 20$, $-22 \le l \le 22$	$-18 \le h \le 18$, $-31 \le k \le 30$, $-28 \le l \le 29$	$-17 \le h \le 16$, $-20 \le k \le 20$, $-24 \le l \le 24$
Reflections measured	99392	93037	131294	76077
Independent reflections	14543	14706	18124	17199
Restraints/Parameters	758/803	0/775	65/973	64/802
GOF on F^2	1.054	0.971	1.025	0.978
R-factor	0.1067	0.0508	0.0559	0.0769
Weighted R-factor	0.2314	0.1513	0.1252	0.2179
Largest diff. peak/hole/e Å^{-3}	5.47/-3.19	5.02/-2.54	3.47/-1.98	4.25/-2.23

Table 3.S6. Summary of statistics for diffraction data for Mo-containing clusters

Cluster	3.3-Mo	3.4-Mo
Empirical formula	$C_{70}H_{128}BFe_3Mo N_{13}OS_3$	$C_{51}H_{88}BFe_3Mo N_{11}O_2S_3$
Formula weight	1538.36	1257.82
Temperature/K	100	100
Crystal system	Monoclinic	Monoclinic
Space group	$P2_1/n$	C2/c
a/Å	15.521(6)	40.599(3)
b/Å	24.225(5)	16.2980(12)
c/Å	21.870(9)	24.9810(15)
α/°	90	90
β/°	102.38(3)	125.715(4)
γ/°	90	90
Volume/Å^3	8032(5)	13420.8(18)
Z	4	8
ρ_{calc}/g cm^{-3}	1.272	1.245
μ/mm^{-1}	6.598	7.791
F(000)	3280.0	5280.0
Crystal size/mm^3	0.02 × 0.10 × 0.10	0.02 × 0.13 × 0.18
Radiation	Cu Kα	Cu Kα
θ_{max}/°	74.587	74.580
Index ranges	$-19 \leq h \leq 18$ $-30 \leq k \leq 29$ $-27 \leq l \leq 27$	$-50 \leq h \leq 50$ $-20 \leq k \leq 20$ $-31 \leq l \leq 31$
Reflections measured	110505	124119
Independent reflections	16425	13737
Restraints/Parameters	31/829	95/677
GOF on F^2	0.972	0.996
R-factor	0.0478	0.0364
Weighted R-factor	0.1283	0.0959
Largest diff. peak/hole/e Å^{-3}	2.30/-2.00	1.12/-1.25

C) Computational details

Computational procedure

The r^2SCAN[75] density functional was used that has been benchmarked[76] with respect to the structural properties of analogous Fe-S containing systems. The r^2SCAN functional does not include Hartree-Fock exchange so that it is less costly and facilitates the characterization of large chemical systems. The defgrid2 integration grid in ORCA was used for the geometry optimizations. The D4 empirical dispersion developed by Grimme[77] with respect to parameters reported by Brandenburg.[78] The relativistically contracted ZORA-def2-TZVP[79,80] basis set was used for all eligible elements. The all-electron SARC-ZORA-TZVP[81] basis was used for W. The CPCM[82] solvation model was used with respect to the dielectric constant and refractive index of THF.

The structures were optimized with respect to the broken symmetry solution of the stated multiplicity. The six distinct broken symmetry solutions that can result from the magnetic coupling between four open-shell centers were considered with the SpinFlip module in ORCA. We found that all calculations converged to an identical wavefunction.

The local spin states and pairwise electronic interactions of the metal centers were assigned with interpretation of their Pipek-Mezey (PM) localization method.[83]

The CO vibrational frequencies were calculated from the partial Hessian of the CO and coordinating Fe center.

The Mössbauer isomer shift (δ) were calculated from the electron densities of the Fe nuclei (ρ_0) that have a linear relationship with respect to the empirical parameters α, β, and C.[84,85] The parameters for their linear relationship were calibrated with respect to Fe-carbonyl compounds whose experimental Mössbauer properties[86] are provided in Table S11. The optimized geometries were obtained from the same computational procedure and their coordinates are provided. The quadrupole splitting (ΔE_Q) was calculated separately with a CP(PPP) basis set[87] applied to the Fe-centers. The defgrid3 integration grid was used for calculating the Mössbauer parameters.

All calculations were done with the ORCA v5.03 quantum chemistry code.[88]

Geometry optimizations

Table 3.S7. The comparison of the experimental metal-metal bond lengths of **3.4-K(18-crown-6)** and the optimized quartet state of its charged, **3.4**$^{-}$, and neutral, **3.4-K**, states. The RMSD is provided separately for the W-Fe and Fe-Fe bonds.

Bond	**3.4-K(18-crown-6) (Å)**	**3.4^{-} (Å)**	**3.4-K (Å)**
W-Fe(CO)	2.72	2.63	2.64
W-Fe(BAC)	2.73	2.66	2.67
W-Fe(CN)	2.66	2.62	2.62
Fe(CO)-Fe(BAC)	2.52	2.52	2.52
Fe(CO)-Fe(CN)	2.54	2.53	2.52
Fe(BAC)-Fe(CN)	2.59	2.57	2.57
RMSD(W-Fe)		0.07	0.07
RMSD(Fe-Fe)		0.01	0.02

Table 3.S8. The comparison of the experimental metal-metal bond lengths of **3.4** and the optimized quintet and triplet state. The RMSD is provided separately for the W-Fe and Fe-Fe bonds.

Bond	**3.4 (Å)**	**$M_s = 2$ (Å)**	**$M_s = 1$ (Å)**
W-Fe(CO)	2.66	2.64	2.64
W-Fe(BAC)	2.73	2.67	2.64
W-Fe(CN)	2.68	2.61	2.61
Fe(CO)-Fe(BAC)	2.51	2.46	2.51
Fe(CO)-Fe(CN)	2.51	2.51	2.52
Fe(BAC)-Fe(CN)	2.57	2.53	2.45
RMSD(W-Fe)		0.05	0.06
RMSD(Fe-Fe)		0.03	0.07

CO vibrational mode

Table 3.S9. The experimental and calculated CO vibrational mode of **3.4**, **3.4⁻**, and **3.4-K**. We consider both the K^+ and $K(18\text{-crown-}6)^+$ salts and the bare anion for **3.4⁻**. The calculated vibrational mode is reported for both the quintet and triplet state for **3.4**. We do not apply a scaling factor to the calculated vibrational modes.

Cluster	Experimental ν_{CO} (cm^{-1})	Calculated ν_{CO} (cm^{-1})
3.4-K(18-crown-6)	1782	
3.4-K	1794 1751	1756
3.4^-		1802
3.4	1851	1880 ($M_s = 2$) 1866 ($M_s = 1$)

Mössbauer parameters

Table 3.S10. The experimental and calculated Mössbauer isomer shifts (δ) for **3.4^-** and **3.4-K**. The experimental values are reported with respect to the K^+-salt at 80 K. The parameters for calculating the isomer shifts are collected in Figure S43.

Site	Experimental 3.4-K δ ($mm\ s^{-1}$)	Calculated 3.4^- δ ($mm\ s^{-1}$)	Calculated 3.4-K δ($mm\ s^{-1}$)
Fe(CO)	0.17	0.12	0.12
Fe(BAC)	0.35	0.33	0.33
Fe(CN)	0.47	0.49	0.48
Avg.	0.33	0.32	0.31

Table 3.S11. The experimental and calculated Mössbauer isomer shifts (δ) for **3.4**. The values are presented for both the quintet and triplet state. The parameters for calculating the isomer shifts are collected in Figure S43.

Site	Experimental 3.4 δ (mm s^{-1})	Calculated 3.4 ($M_s = 2$) δ (mm s^{-1})	Calculated 3.4 ($M_s = 1$) δ (mm s^{-1})
Fe(CO)	0.02	0.11	0.15
Fe(BAC)	0.33	0.39	0.26
Fe(CN)	0.65	0.56	0.40
Avg.	0.33	0.35	0.27

Table 3.S12. The experimental and calculated absolute Mössbauer quadrupole splitting ($|\Delta E_Q|$) for **3.4**$^-$. The experimental values are reported with respect to the K^+-salt at 80 K.

Site	Experimental 3.4-K $|\Delta E_Q|$ (mm s^{-1})	Calculated 3.4$^-$ $|\Delta E_Q|$ (mm s^{-1})	Calculated 3.4-K $|\Delta E_Q|$ (mm s^{-1})
Fe(CO)	1.84	1.62	1.38
Fe(BAC)	1.47	1.57	1.61
Fe(CN)	0.87	0.60	0.61

Table 3.S13. The experimental and calculated absolute Mössbauer quadrupole splitting ($|\Delta E_Q|$) for **3.4**. The values are presented for both the quintet and triplet state.

Site	Experimental 3.4 $|\Delta E_Q|$ (mm s^{-1})	Calculated 3.4 ($M_s = 2$) $|\Delta E_Q|$ (mm s^{-1})	Calculated 3.4 ($M_s = 1$) $|\Delta E_Q|$ (mm s^{-1})
Fe(CO)	1.57	1.63	2.69
Fe(BAC)	1.19	0.90	1.54
Fe(CN)	1.07	0.65	0.99

Table 3.S14. The experimental Mössbauer parameters (δ and $|\Delta E_Q|$) for the Fe-carbonyl compounds[86] that set the empirical parameters for the linear relationship between the calculated Fe-nuclear electron densities and isomer shift.

Compound	δ (mm s^{-1})	$|\Delta E_Q|$ (mm s^{-1})
$Fe(CO)_5$	-0.09	2.57
$Fe_2(CO)_9$	0.16	0.42
$Fe_3(CO)_{12}$	0.11 (66 %) 0.05 (33 %)	1.13 (66 %) 0.13 (33 %)
$[Fe(CO)_4]^{2-}$	-0.18	0
$[Fe_2(CO)_8]^{2-}$	-0.08	2.22
$[Fe_4(CO)_{13}]^{2-}$	0.02	0.27
$[Fe(CO)_4H]^{2-}$	-0.17	1.36
$[Fe_2(CO)_8H]^{2-}$	0.07	0.50
$[Fe_3(CO)_{11}H]^{2-}$	0.04 (66 %) 0.02 (33 %)	1.41 (66 %) 0.16 (33 %)
$Fe(Cp)(CO)_2I$	0.23	1.83

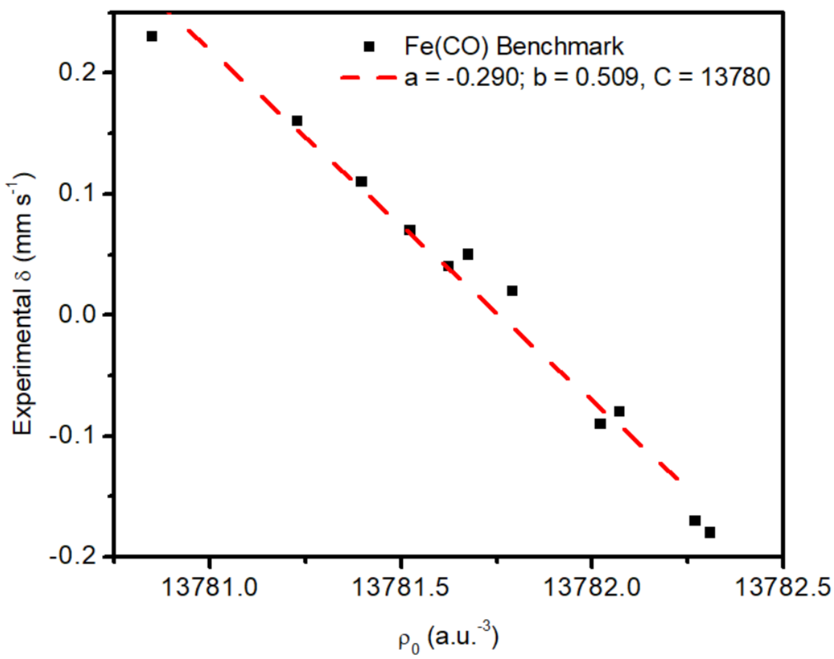

Figure 3.S43. The linear relationship (R^2 = 0.975) between the calculated Fe-nuclear electron densities (ρ_0) and the experimental isomer shifts (δ). The empirical parameters 'a', 'b', and 'C' are presented with respect to the detailed computational procedure.

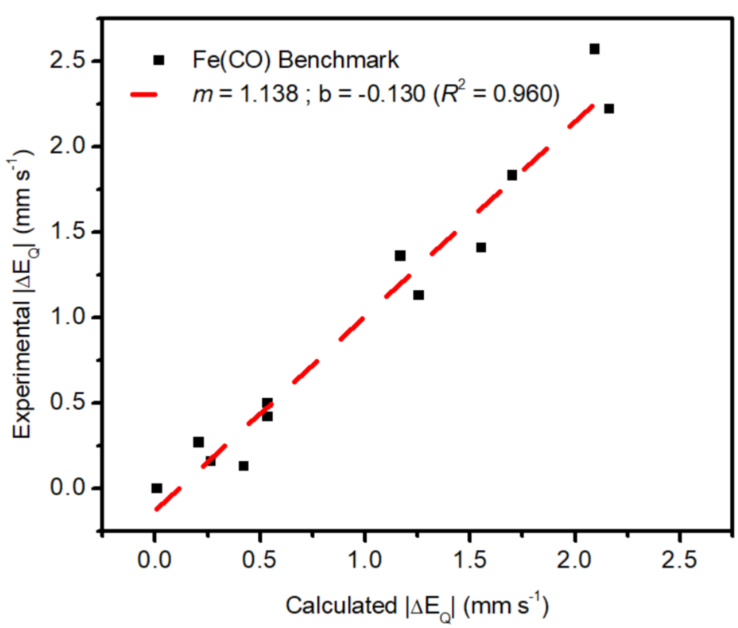

Figure 3.S44. The linear relationship (R^2 = 0.975) between the experimental and calculated absolute quadrupole splitting ($|\Delta E_Q|$).

Localized orbital analysis of 3.4⁻

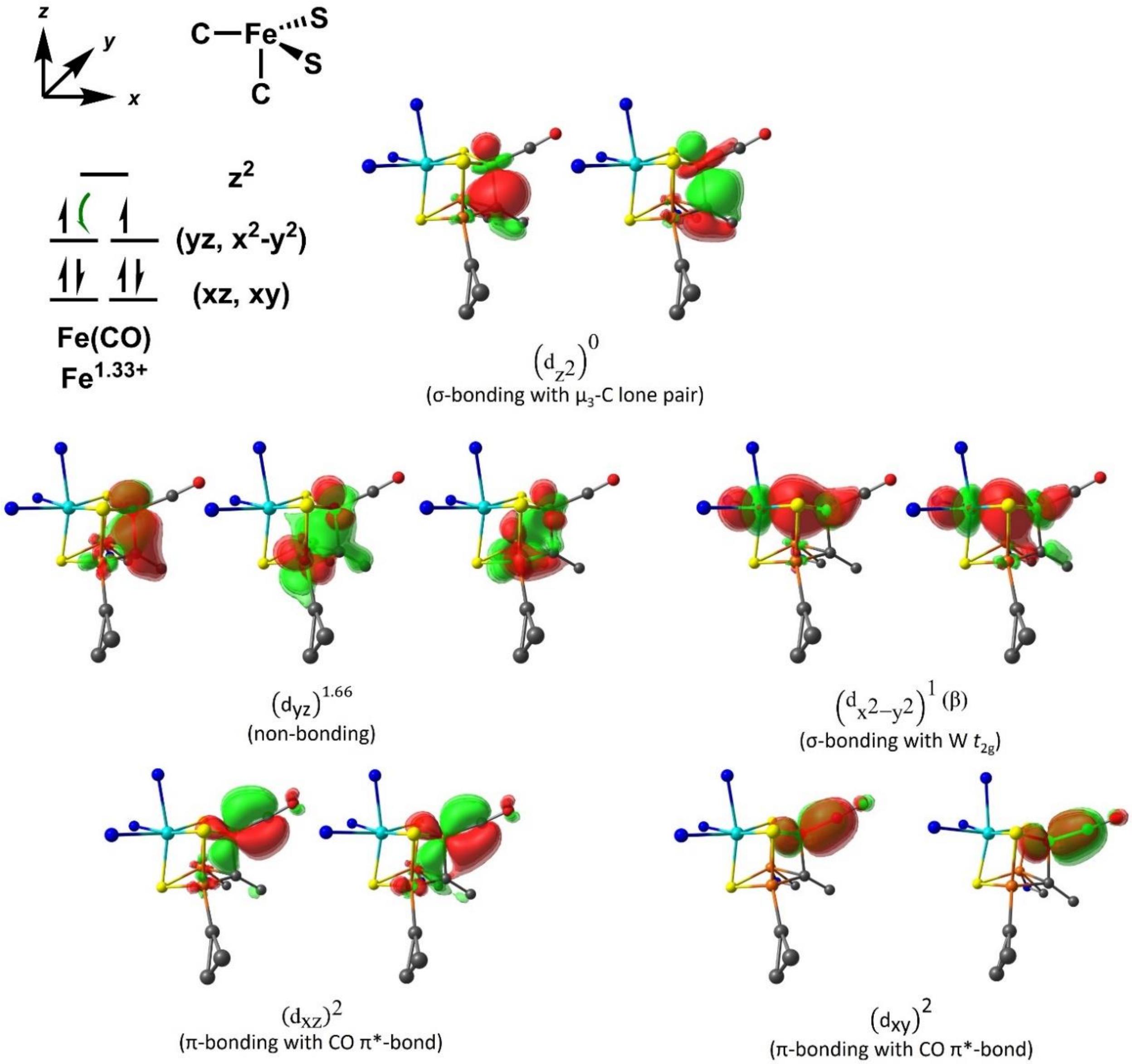

Figure 3.S45. The PM localized orbitals for the Fe(CO) center in **3.4**$^{-}$. The z-axis is oriented parallel to the Fe-carbyne bond. The electronic populations are specific to their α- or β-spin. The overall electronic configuration is included where the green arrow assigns 2/3 of an electron from delocalization.

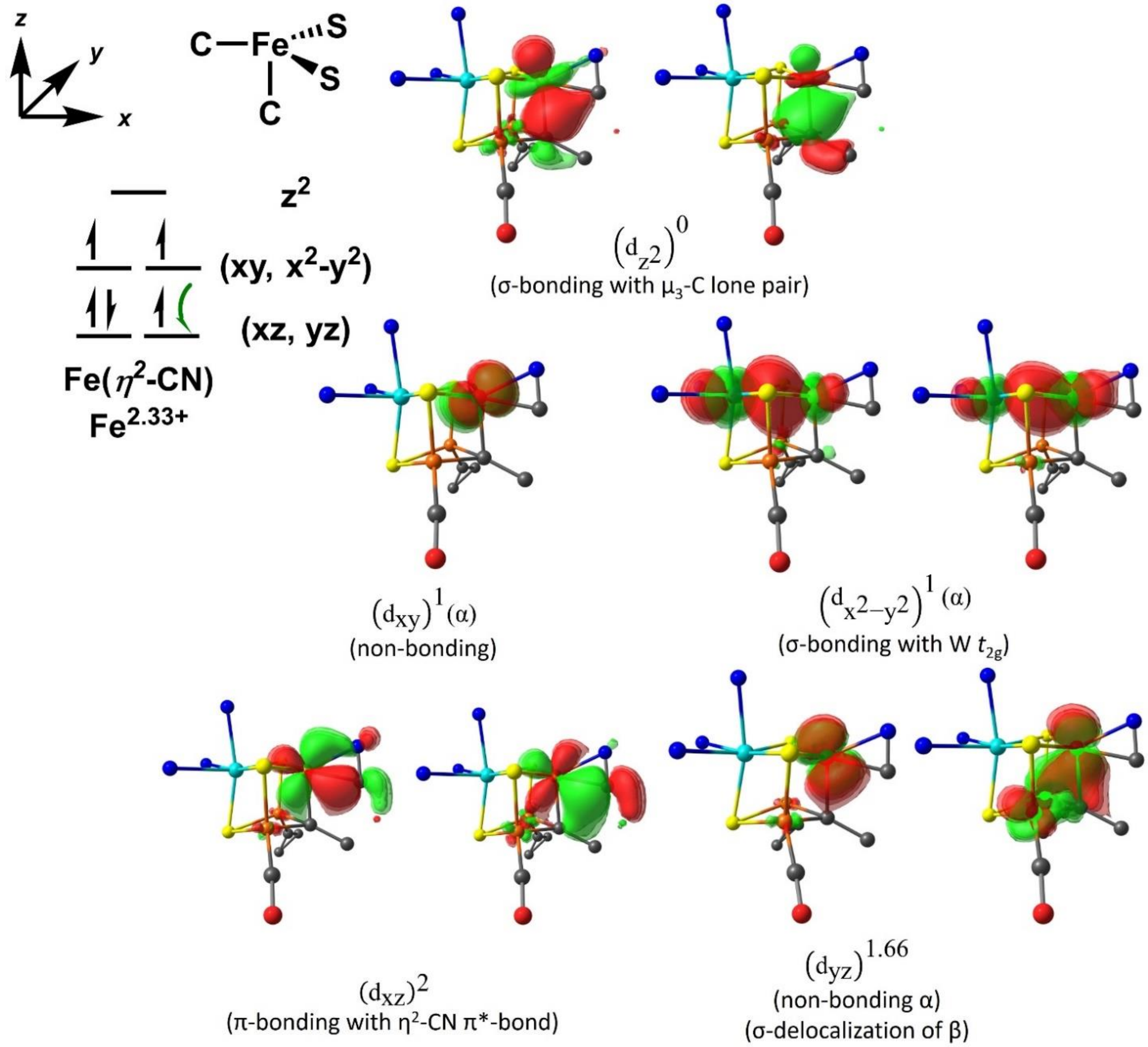

Figure 3.S46. The PM localized orbitals for the Fe(η^2-CN) center in **3.4**$^-$. The z-axis is oriented parallel to the Fe-carbyne bond. The electronic populations are specific to their α- or β-spin. The overall electronic configuration is included where the green arrow assigns 2/3 of an electron from delocalization.

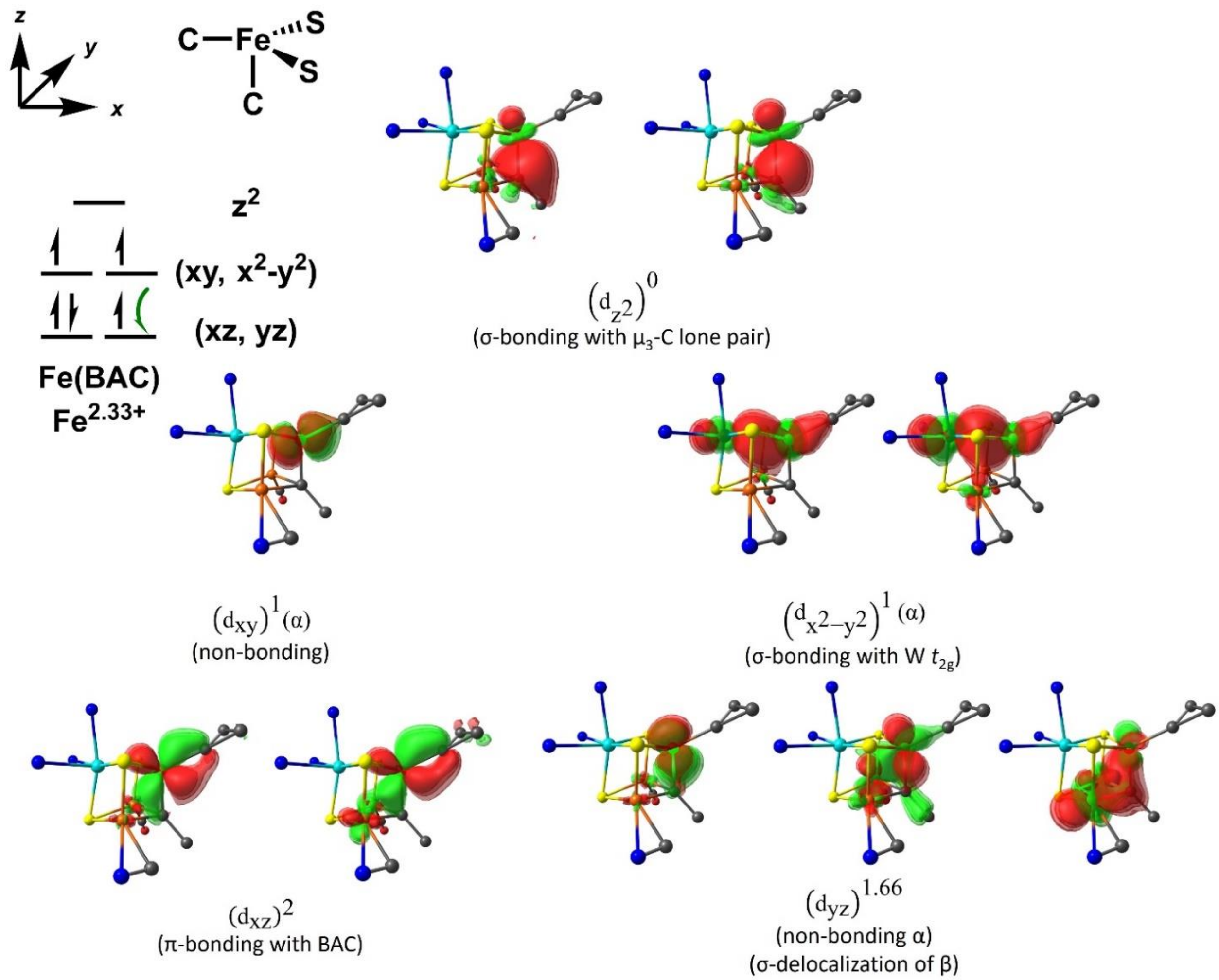

Figure 3.S47. The PM localized orbitals for the Fe(BAC) center in **3.4**$^-$. The z-axis is oriented parallel to the Fe-carbyne bond. The electronic populations are specific to their α- or β-spin. The overall electronic configuration is included where the green arrow assigns 2/3 of an electron from delocalization.

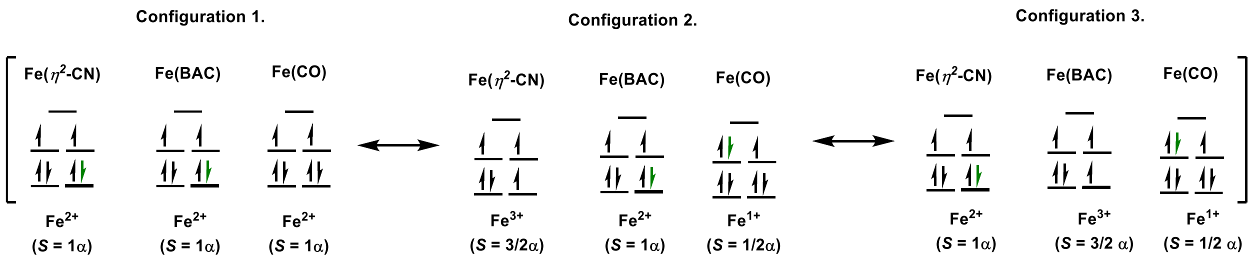

Figure 3.S48. The three equivalent resonance structures associated with the ferromagnetic coupling between the three Fe-centers in **3.4**⁻. The green arrow denotes the electrons that are delocalized between the resonance conformations. The oxidation and spin state are included.

3.6 REFERENCES

(1) Spatzal, T.; Schlesier, J.; Burger, E.-M.; Sippel, D.; Zhang, L.; Andrade, S. L. A.; Rees, D. C.; Einsle, O. Nitrogenase FeMoco Investigated by Spatially Resolved Anomalous Dispersion Refinement. *Nat. Commun.* **2016**, *7* (1), 10902. https://doi.org/10.1038/ncomms10902.

(2) Sippel, D.; Einsle, O. The Structure of Vanadium Nitrogenase Reveals an Unusual Bridging Ligand. *Nat. Chem. Biol.* **2017**, *13* (9), 956–960. https://doi.org/10.1038/nchembio.2428.

(3) Hu, Y.; Lee, C. C.; Ribbe, M. W. Extending the Carbon Chain: Hydrocarbon Formation Catalyzed by Vanadium/Molybdenum Nitrogenases. *Science* **2011**, *333* (6043), 753. https://doi.org/10.1126/science.1206883.

(4) Lee, C. C.; Hu, Y.; Ribbe, M. W. Catalytic Reduction of $CN^−$, CO, and CO_2 by Nitrogenase Cofactors in Lanthanide-Driven Reactions. *Angew. Chem. Int. Ed.* **2015**, *54* (4), 1219–1222. https://doi.org/10.1002/anie.201410412.

(5) Lee, H.-I.; Cameron, L. M.; Hales, B. J.; Hoffman, B. M. CO Binding to the FeMo Cofactor of CO-Inhibited Nitrogenase: ^{13}CO and ^{1}H Q-Band ENDOR Investigation. *J. Am. Chem. Soc.* **1997**, *119* (42), 10121–10126. https://doi.org/10.1021/ja9715096.

(6) George, S. J.; Ashby, G. A.; Wharton, C. W.; Thorneley, R. N. F. Time-Resolved Binding of Carbon Monoxide to Nitrogenase Monitored by Stopped-Flow Infrared Spectroscopy. *J. Am. Chem. Soc.* **1997**, *119* (27), 6450–6451. https://doi.org/10.1021/ja971088s.

(7) Davis, L. C.; Henzl, M. T.; Burris, R. H.; Orme-Johnson, W. H. Iron-Sulfur Clusters in the Molybdenum-Iron Protein Component of Nitrogenase. Electron Paramagnetic Resonance of the Carbon Monoxide Inhibited State. *Biochemistry* **1979**, *18* (22), 4860–4869. https://doi.org/10.1021/bi00589a014.

(8) Pérez-González, A.; Yang, Z.-Y.; Lukoyanov, D. A.; Dean, D. R.; Seefeldt, L. C.; Hoffman, B. M. Exploring the Role of the Central Carbide of the Nitrogenase Active-Site FeMo-

Cofactor through Targeted ^{13}C Labeling and ENDOR Spectroscopy. *J. Am. Chem. Soc.* **2021**, *143* (24), 9183–9190. https://doi.org/10.1021/jacs.1c04152.

(9) Rohde, M.; Grunau, K.; Einsle, O. CO Binding to the FeV Cofactor of CO-Reducing Vanadium Nitrogenase at Atomic Resolution. *Angew. Chem. Int. Ed.* **2020**, *59* (52), 23626–23630. https://doi.org/10.1002/anie.202010790.

(10) Rohde, M.; Laun, K.; Zebger, I.; Stripp, S. T.; Einsle, O. Two Ligand-Binding Sites in CO-Reducing V Nitrogenase Reveal a General Mechanistic Principle. *Sci. Adv.* **2021**, *7* (22), eabg4474. https://doi.org/10.1126/sciadv.abg4474.

(11) Van Stappen, C.; Decamps, L.; Cutsail, G. E.; Bjornsson, R.; Henthorn, J. T.; Birrell, J. A.; DeBeer, S. The Spectroscopy of Nitrogenases. *Chem. Rev.* **2020**, *120* (12), 5005–5081. https://doi.org/10.1021/acs.chemrev.9b00650.

(12) Spatzal, T.; Perez, K. A.; Einsle, O.; Howard, J. B.; Rees, D. C. Ligand Binding to the FeMo-Cofactor: Structures of CO-Bound and Reactivated Nitrogenase. *Science* **2014**, *345* (6204), 1620. https://doi.org/10.1126/science.1256679.

(13) Buscagan, T. M.; Perez, K. A.; Maggiolo, A. O.; Rees, D. C.; Spatzal, T. Structural Characterization of Two CO Molecules Bound to the Nitrogenase Active Site. *Angew. Chem. Int. Ed.* **2021**, *60* (11), 5704–5707. https://doi.org/10.1002/anie.202015751.

(14) Kang, W.; Lee, C. C.; Jasniewski, A. J.; Ribbe, M. W.; Hu, Y. Structural Evidence for a Dynamic Metallocofactor during N_2 Reduction by Mo-Nitrogenase. *Science* **2020**, *368* (6497), 1381. https://doi.org/10.1126/science.aaz6748.

(15) Peters, J. W.; Einsle, O.; Dean, D. R.; DeBeer, S.; Hoffman, B. M.; Holland, P. L.; Seefeldt, L. C. Comment on "Structural Evidence for a Dynamic Metallocofactor during N_2 Reduction by Mo-Nitrogenase." *Science* **2021**, *371* (6530), eabe5481. https://doi.org/10.1126/science.abe5481.

(16) Kang, W.; Lee, C. C.; Jasniewski, A. J.; Ribbe, M. W.; Hu, Y. Response to Comment on "Structural Evidence for a Dynamic Metallocofactor during N_2 Reduction by Mo-Nitrogenase." *Science* **2021**, *371* (6530), eabe5856. https://doi.org/10.1126/science.abe5856.

(17) Liu, L.; Rauchfuss, T. B.; Woods, T. J. Iron Carbide–Sulfide Carbonyl Clusters. *Inorg. Chem.* **2019**, *58* (13), 8271–8274. https://doi.org/10.1021/acs.inorgchem.9b01231.

(18) Joseph, C.; Cobb, C. R.; Rose, M. J. Single-Step Sulfur Insertions into Iron Carbide Carbonyl Clusters: Unlocking the Synthetic Door to FeMoco Analogues. *Angew. Chem. Int. Ed.* **2021**, *60* (7), 3433–3437. https://doi.org/10.1002/anie.202011517.

(19) Brown, A. C.; Thompson, N. B.; Suess, D. L. M. Evidence for Low-Valent Electronic Configurations in Iron–Sulfur Clusters. *J. Am. Chem. Soc.* **2022**, *144* (20), 9066–9073. https://doi.org/10.1021/jacs.2c01872.

(20) McSkimming, A.; Suess, D. L. M. Dinitrogen Binding and Activation at a Molybdenum–Iron–Sulfur Cluster. *Nat. Chem.* **2021**, *13* (7), 666–670. https://doi.org/10.1038/s41557-021-00701-6.

(21) Sridharan, A.; Brown, A. C.; Suess, D. L. M. A Terminal Imido Complex of an Iron–Sulfur Cluster. *Angew. Chem. Int. Ed.* **2021**, *60* (23), 12802–12806. https://doi.org/10.1002/anie.202102603.

(22) Anderton, K. J.; Knight, B. J.; Rheingold, A. L.; Abboud, K. A.; García-Serres, R.; Murray, L. J. Reactivity of Hydride Bridges in a High-Spin $[Fe_3(\mu\text{-}H)_3]^{3+}$ Cluster: Reversible H_2/CO Exchange and Fe–H/B–F Bond Metathesis. *Chem. Sci.* **2017**, *8* (5), 4123–4129. https://doi.org/10.1039/C6SC05583D.

(23) Arnett, C. H.; Agapie, T. Activation of an Open Shell, Carbyne-Bridged Diiron Complex Toward Binding of Dinitrogen. *J. Am. Chem. Soc.* **2020**, *142* (22), 10059–10068. https://doi.org/10.1021/jacs.0c01896.

(24) Arnett, C. H.; Bogacz, I.; Chatterjee, R.; Yano, J.; Oyala, P. H.; Agapie, T. Mixed-Valent Diiron μ-Carbyne, μ-Hydride Complexes: Implications for Nitrogenase. *J. Am. Chem. Soc.* **2020**, *142* (44), 18795–18813. https://doi.org/10.1021/jacs.0c05920.

(25) Ohki, Y.; Munakata, K.; Matsuoka, Y.; Hara, R.; Kachi, M.; Uchida, K.; Tada, M.; Cramer, R. E.; Sameera, W. M. C.; Takayama, T.; Sakai, Y.; Kuriyama, S.; Nishibayashi, Y.; Tanifuji, K. Nitrogen Reduction by the Fe Sites of Synthetic $[Mo_3S_4Fe]$ Cubes. *Nature* **2022**, *607* (7917), 86–90. https://doi.org/10.1038/s41586-022-04848-1.

(26) Tyson, M. A.; Coucouvanis, D. New Fe/Mo/S Clusters with $MoFe_3S_3$ Cuboidal Cores Similar to the One in the Fe/Mo Cofactor of Nitrogenase. Synthesis and Structural Characterization of the $(C_{14}\text{-Cat})MoFe_3S_3(PEt_3)_2(CO)_6$ and $(C_{14}\text{-Cat})Mo(O)Fe_3S_3(PEt_3)_3(CO)_5$ Clusters. *Inorg. Chem.* **1997**, *36* (18), 3808–3809. https://doi.org/10.1021/ic970761b.

(27) Han, J.; Beck, K.; Ockwig, N.; Coucouvanis, D. Synthetic Analogs for the $MoFe_3S_3$ Subunit of the Nitrogenase Cofactor: Structural Features Associated with the Total Number of Valence Electrons and the Possible Role of M−M and Multiple M−S Bonding in the Function of Nitrogenase. *J. Am. Chem. Soc.* **1999**, *121* (44), 10448–10449. https://doi.org/10.1021/ja991880o.

(28) Coucouvanis, D.; Han, J.; Moon, N. Synthesis and Characterization of Sulfur-Voided Cubanes. Structural Analogues for the $MoFe_3S_3$ Subunit in the Nitrogenase Cofactor. *J. Am. Chem. Soc.* **2002**, *124* (2), 216–224. https://doi.org/10.1021/ja0110832.

(29) Brunner, H.; Janietz, N.; Wachter, J.; Zahn, T.; Ziegler, M. L. Novel MoFeS Clusters from $[(C_5Me_5)_2Mo_2S_4]$ and $Fe(CO)_5$ or $Fe_2(CO)_9$. *Angew. Chem., Int. Ed. Engl.* **1985**, *24* (2), 133–135. https://doi.org/10.1002/anie.198501331.

(30) Joseph, C.; Shupp, J. P.; Cobb, C. R.; Rose, M. J. Construction of Synthetic Models for Nitrogenase-Relevant NifB Biogenesis Intermediates and Iron-Carbide-Sulfide Clusters. *Catalysts* **2020**, *10* (11). https://doi.org/10.3390/catal10111317.

(31) Brown, A. C.; Suess, D. L. M. An Iron–Sulfur Cluster with a Highly Pyramidalized Three-Coordinate Iron Center and a Negligible Affinity for Dinitrogen. *J. Am. Chem. Soc.* **2023**, *145* (36), 20088–20096. https://doi.org/10.1021/jacs.3c07677.

(32) Holm, R. H.; Solomon, E. I.; Majumdar, A.; Tenderholt, A. Comparative Molecular Chemistry of Molybdenum and Tungsten and Its Relation to Hydroxylase and Oxotransferase Enzymes. *Coord. Chem. Rev.* **2011**, *255* (9), 993–1015. https://doi.org/10.1016/j.ccr.2010.10.017.

(33) Le, L. N. V.; Bailey, G. A.; Scott, A. G.; Agapie, T. Partial Synthetic Models of FeMoco with Sulfide and Carbyne Ligands: Effect of Interstitial Atom in Nitrogenase Active Site. *Proc. Natl. Acad. Sci. U.S.A.* **2021**, *118* (49), e2109241118. https://doi.org/10.1073/pnas.2109241118.

(34) Seefeldt, L. C.; Yang, Z.-Y.; Duval, S.; Dean, D. R. Nitrogenase Reduction of Carbon-Containing Compounds. *Biochim. Biophys. Acta - Bioenerg.* **2013**, *1827* (8), 1102–1111. https://doi.org/10.1016/j.bbabio.2013.04.003.

(35) Brown, A. C.; Suess, D. L. M. Reversible Formation of Alkyl Radicals at [Fe_4S_4] Clusters and Its Implications for Selectivity in Radical SAM Enzymes. *J. Am. Chem. Soc.* **2020**, *142* (33), 14240–14248. https://doi.org/10.1021/jacs.0c05590.

(36) Lichtenberg, C.; Garcia Rubio, I.; Viciu, L.; Adelhardt, M.; Meyer, K.; Jeschke, G.; Grützmacher, H. A Low-Valent Iron Imido Heterocubane Cluster: Reversible Electron Transfer and Catalysis of Selective C–C Couplings. *Angew. Chem. Int. Ed.* **2015**, *54* (44), 13012–13017. https://doi.org/10.1002/anie.201505668.

(37) Muñoz, S. B.; Daifuku, S. L.; Brennessel, W. W.; Neidig, M. L. Isolation, Characterization, and Reactivity of $Fe_8Me_{12}^-$: Kochi's S = 1/2 Species in Iron-Catalyzed Cross-Couplings with MeMgBr and Ferric Salts. *J. Am. Chem. Soc.* **2016**, *138* (24), 7492–7495. https://doi.org/10.1021/jacs.6b03760.

(38) Bradley, J. S.; Ansell, G. B.; Hill, E. W. Homogeneous Carbon Monoxide Hydrogenation on Multiple Sites: A Dissociative Pathway to Oxygenates. *J. Am. Chem. Soc.* **1979**, *101* (24), 7417–7419. https://doi.org/10.1021/ja00518a055.

(39) Lis, Edward C.; Delafuente, D. A.; Lin, Y.; Mocella, C. J.; Todd, M. A.; Liu, W.; Sabat, M.; Myers, W. H.; Harman, W. D. The Uncommon Reactivity of Dihapto-Coordinated Nitrile, Ketone, and Alkene Ligands When Bound to a Powerful π-Base. *Organometallics* **2006**, *25* (21), 5051–5058. https://doi.org/10.1021/om060434o.

(40) Arikawa, Y.; Asayama, T.; Itatani, K.; Onishi, M. N−C Bond Formation of NO Ligands on Ruthenium Complexes with Concurrent Vinylic C−H Activation and Subsequent Proton-

Induced Reactivities of the Resulting Nitrosovinyl Species. *J. Am. Chem. Soc.* **2008**, *130* (32), 10508–10509. https://doi.org/10.1021/ja804095u.

(41) Cowley, R. E.; Christian, G. J.; Brennessel, W. W.; Neese, F.; Holland, P. L. A Reduced (β-Diketiminato)Iron Complex with End-On and Side-On Nitriles: Strong Backbonding or Ligand Non-Innocence? *Eur. J. Inorg. Chem.* **2012**, *2012* (3), 479–483. https://doi.org/10.1002/ejic.201100787.

(42) Pyykkö, P.; Riedel, S.; Patzschke, M. Triple-Bond Covalent Radii. *Chem. Eur. J.* **2005**, *11* (12), 3511–3520. https://doi.org/10.1002/chem.200401299.

(43) Brown, A. C.; Suess, D. L. M. Valence Localization in Alkyne and Alkene Adducts of Synthetic $[Fe_4S_4]^+$ Clusters. *Inorg. Chem.* **2022**. https://doi.org/10.1021/acs.inorgchem.2c01353.

(44) Peters, J. C.; Johnson, A. R.; Odom, A. L.; Wanandi, P. W.; Davis, W. M.; Cummins, C. C. Assembly of Molybdenum/Titanium μ-Oxo Complexes via Radical Alkoxide C−O Cleavage. *J. Am. Chem. Soc.* **1996**, *118* (42), 10175–10188. https://doi.org/10.1021/ja960564w.

(45) Crudden, C. M.; Allen, D. P. Stability and Reactivity of N-Heterocyclic Carbene Complexes. *Coord. Chem. Rev.* **2004**, *248* (21), 2247–2273. https://doi.org/10.1016/j.ccr.2004.05.013.

(46) Rittle, J.; Peters, J. C. Fe–N_2/CO Complexes That Model a Possible Role for the Interstitial C Atom of FeMo-Cofactor (FeMoco). *Proc. Natl. Acad. Sci. U.S.A.* **2013**, *110* (40), 15898. https://doi.org/10.1073/pnas.1310153110.

(47) Lukoyanov, D. A.; Yang, Z.-Y.; Pérez-González, A.; Raugei, S.; Dean, D. R.; Seefeldt, L. C.; Hoffman, B. M. ^{13}C ENDOR Characterization of the Central Carbon within the Nitrogenase Catalytic Cofactor Indicates That the CFe6 Core Is a Stabilizing "Heart of Steel." *J. Am. Chem. Soc.* **2022**, *144* (40), 18315–18328. https://doi.org/10.1021/jacs.2c06149.

(48) Chen, J.; Chen, T.; Norton, J. R.; Rauch, M. Insertion of Isonitriles into the Zr–CH_3 Bond of $Cp^*{}_2Zr(CH_3)_2$ and Electrophilic Cleavage of the Remaining Methyl Group. *Organometallics* **2018**, *37* (23), 4424–4430. https://doi.org/10.1021/acs.organomet.8b00690.

(49) Valadez, T. N.; Norton, J. R.; Neary, M. C.; Quinlivan, P. J. Reaction of $Cp^*{}_2Zr$(2,3-Dimethylbutadiene) with Isonitriles and CO. *Organometallics* **2016**, *35* (18), 3163–3169. https://doi.org/10.1021/acs.organomet.6b00522.

(50) Klose, A.; Solari, E.; Ferguson, R.; Floriani, C.; Chiesi-Villa, A.; Rizzoli, C. Insertion Reactions of Isocyanides and Nitriles into Unsupported Iron-Aryl Bonds: The Synthesis of a Dimeric Iron(II) Homoleptic Iminoacyl Complex. *Organometallics* **1993**, *12* (7), 2414–2416. https://doi.org/10.1021/om00031a006.

(51) Klose, A.; Solari, E.; Floriani, C.; Chiesi-Villa, A.; Rizzoli, C.; Re, N. Magnetic Properties Diagnostic for the Existence of Iron(II)-Iron(II) Bonds in Dinuclear Complexes Which

Derive from Stepwise Insertion Reactions on Unsupported Iron-Aryl Bonds. *J. Am. Chem. Soc.* **1994**, *116* (20), 9123–9135. https://doi.org/10.1021/ja00099a030.

(52) Boyarskiy, V. P.; Bokach, N. A.; Luzyanin, K. V.; Kukushkin, V. Yu. Metal-Mediated and Metal-Catalyzed Reactions of Isocyanides. *Chem. Rev.* **2015**, *115* (7), 2698–2779. https://doi.org/10.1021/cr500380d.

(53) Arnett, C. H.; Kaiser, J. T.; Agapie, T. Remote Ligand Modifications Tune Electronic Distribution and Reactivity in Site-Differentiated, High-Spin Iron Clusters: Flipping Scaling Relationships. *Inorg. Chem.* **2019**, *58* (23), 15971–15982. https://doi.org/10.1021/acs.inorgchem.9b02470.

(54) Reed, C. J.; Agapie, T. Tetranuclear Fe Clusters with a Varied Interstitial Ligand: Effects on the Structure, Redox Properties, and Nitric Oxide Activation. *Inorg. Chem.* **2017**, *56* (21), 13360–13367. https://doi.org/10.1021/acs.inorgchem.7b02114.

(55) Joseph, C.; Kuppuswamy, S.; Lynch, V. M.; Rose, M. J. Fe_5Mo Cluster with Iron-Carbide and Molybdenum-Carbide Bonding Motifs: Structure and Selective Alkyne Reductions. *Inorg. Chem.* **2018**, *57* (1), 20–23. https://doi.org/10.1021/acs.inorgchem.7b02615.

(56) Spiller, N.; Bjornsson, R.; DeBeer, S.; Neese, F. Carbon Monoxide Binding to the Iron–Molybdenum Cofactor of Nitrogenase: A Detailed Quantum Mechanics/Molecular Mechanics Investigation. *Inorg. Chem.* **2021**, *60* (23), 18031–18047. https://doi.org/10.1021/acs.inorgchem.1c02649.

(57) Gee, L. B.; Myers, W. K.; Nack-Lehman, P. A.; Scott, A. D.; Yan, L.; George, S. J.; Dong, W.; Dapper, C. H.; Newton, W. E.; Cramer, S. P. Nitrogenase Chemistry at 10 Kelvin─Phototautomerization and Recombination of CO-Inhibited α-H195Q Enzyme. *Inorg. Chem.* **2022**, *61* (30), 11509–11513. https://doi.org/10.1021/acs.inorgchem.2c00818.

(58) Crabtree, R. H. Chapter 4: Carbonyls, Phosphines, and Substitution. In *The Organometallic Chemistry of the Transition Metals*; John Wiley & Sons, Inc.: Hoboken, New Jersey, 2004; pp 98–133.

(59) Arnett, C. H.; Chalkley, M. J.; Agapie, T. A Thermodynamic Model for Redox-Dependent Binding of Carbon Monoxide at Site-Differentiated, High Spin Iron Clusters. *J. Am. Chem. Soc.* **2018**, *140* (16), 5569–5578. https://doi.org/10.1021/jacs.8b01825.

(60) Bailey, G. A.; Buss, J. A.; Oyala, P. H.; Agapie, T. Terminal, Open-Shell Mo Carbide and Carbyne Complexes: Spin Delocalization and Ligand Noninnocence. *J. Am. Chem. Soc.* **2021**, *143* (33), 13091–13102. https://doi.org/10.1021/jacs.1c03806.

(61) Rao, G.; Britt, R. D. Electronic Structure of Two Catalytic States of the [FeFe] Hydrogenase H-Cluster As Probed by Pulse Electron Paramagnetic Resonance Spectroscopy. *Inorg. Chem.* **2018**, *57* (17), 10935–10944. https://doi.org/10.1021/acs.inorgchem.8b01557.

(62) Soncini, A.; Mallah, T.; Chibotaru, L. F. Molecular Spintronics in Mixed-Valence Magnetic Dimers: The Double-Exchange Blockade Mechanism. *J. Am. Chem. Soc.* **2010**, *132* (23), 8106–8114. https://doi.org/10.1021/ja101887f.

(63) Kuppuswamy, S.; Wofford, J. D.; Joseph, C.; Xie, Z.-L.; Ali, A. K.; Lynch, V. M.; Lindahl, P. A.; Rose, M. J. Structures, Interconversions, and Spectroscopy of Iron Carbonyl Clusters with an Interstitial Carbide: Localized Metal Center Reduction by Overall Cluster Oxidation. *Inorg. Chem.* **2017**, *56* (10), 5998–6012. https://doi.org/10.1021/acs.inorgchem.7b00741.

(64) Loipersberger, M.; Mao, Y.; Head-Gordon, M. Variational Forward–Backward Charge Transfer Analysis Based on Absolutely Localized Molecular Orbitals: Energetics and Molecular Properties. *J. Chem. Theory Comput.* **2020**, *16* (2), 1073–1089. https://doi.org/10.1021/acs.jctc.9b01168.

(65) Lupinetti, A. J.; Fau, S.; Frenking, G.; Strauss, S. H. Theoretical Analysis of the Bonding between CO and Positively Charged Atoms. *J. Phys. Chem. A* **1997**, *101* (49), 9551–9559. https://doi.org/10.1021/jp972657l.

(66) Bjornsson, R.; Lima, F. A.; Spatzal, T.; Weyhermüller, T.; Glatzel, P.; Bill, E.; Einsle, O.; Neese, F.; DeBeer, S. Identification of a Spin-Coupled Mo(III) in the Nitrogenase Iron–Molybdenum Cofactor. *Chem. Sci.* **2014**, *5* (8), 3096–3103. https://doi.org/10.1039/C4SC00337C.

(67) Bjornsson, R.; Neese, F.; Schrock, R. R.; Einsle, O.; DeBeer, S. The Discovery of Mo(III) in FeMoco: Reuniting Enzyme and Model Chemistry. *J. Biol. Inorg. Chem.* **2015**, *20* (2), 447–460. https://doi.org/10.1007/s00775-014-1230-6.

(68) Stoll, S.; Schweiger, A. EasySpin, a Comprehensive Software Package for Spectral Simulation and Analysis in EPR. *J. Magn. Reson.* **2006**, *178* (1), 42–55. https://doi.org/10.1016/j.jmr.2005.08.013.

(69) Bruker. APEX3, 2012.

(70) Bruker. SADABS, 2001.

(71) Altomare, A.; Cascarano, G.; Giacovazzo, C.; Guagliardi, A.; Burla, M. C.; Polidori, G.; Camalli, M. SIR92 - a Program for Automatic Solution of Crystal Structures by Direct Methods. *J. Appl. Crystallogr.* **1994**, *27* (3), 435.

(72) Palatinus, L.; Chapuis, G. SUPERFLIP - a Computer Program for the Solution of Crystal Structures by Charge Flipping in Arbitrary Dimensions. *J. Appl. Crystallogr.* **2007**, *40* (4), 786–790.

(73) Betteridge, P. W.; Carruthers, J. R.; Cooper, R. I.; Prout, K.; Watkin, D. J. CRYSTALS Version 12: Software for Guided Crystal Structure Analysis. *J. Appl. Crystallogr.* **2003**, *36* (6), 1487.

(74) Spek, A. PLATON SQUEEZE: A Tool for the Calculation of the Disordered Solvent Contribution to the Calculated Structure Factors. *Acta Cryst. C* **2015**, *71* (1), 9–18.

(75) Furness, J. W.; Kaplan, A. D.; Ning, J.; Perdew, J. P.; Sun, J. Accurate and Numerically Efficient r^{2}SCAN Meta-Generalized Gradient Approximation. *J. Phys. Chem. Lett.* **2020**, *11* (19), 8208–8215. https://doi.org/10.1021/acs.jpclett.0c02405.

(76) Benediktsson, B.; Bjornsson, R. Analysis of the Geometric and Electronic Structure of Spin-Coupled Iron–Sulfur Dimers with Broken-Symmetry DFT: Implications for FeMoco. *J. Chem. Theory Comput.* **2022**, *18* (3), 1437–1457. https://doi.org/10.1021/acs.jctc.1c00753.

(77) Caldeweyher, E.; Bannwarth, C.; Grimme, S. Extension of the D3 Dispersion Coefficient Model. *J. Chem. Phys.* **2017**, *147* (3), 034112. https://doi.org/10.1063/1.4993215.

(78) Ehlert, S.; Huniar, U.; Ning, J.; Furness, J. W.; Sun, J.; Kaplan, A. D.; Perdew, J. P.; Brandenburg, J. G. r^{2}SCAN-D4: Dispersion Corrected Meta-Generalized Gradient Approximation for General Chemical Applications. *J. Chem. Phys.* **2021**, *154* (6), 061101. https://doi.org/10.1063/5.0041008.

(79) Weigend, F.; Ahlrichs, R. Balanced Basis Sets of Split Valence, Triple Zeta Valence and Quadruple Zeta Valence Quality for H to Rn: Design and Assessment of Accuracy. *Phys. Chem. Chem. Phys.* **2005**, *7* (18), 3297–3305. https://doi.org/10.1039/B508541A.

(80) Pantazis, D. A.; Chen, X.-Y.; Landis, C. R.; Neese, F. All-Electron Scalar Relativistic Basis Sets for Third-Row Transition Metal Atoms. *J. Chem. Theory Comput.* **2008**, *4* (6), 908–919. https://doi.org/10.1021/ct800047t.

(81) Rolfes, J. D.; Neese, F.; Pantazis, D. A. All-Electron Scalar Relativistic Basis Sets for the Elements Rb–Xe. *J. Comput. Chem.* **2020**, *41* (20), 1842–1849. https://doi.org/10.1002/jcc.26355.

(82) Barone, V.; Cossi, M. Quantum Calculation of Molecular Energies and Energy Gradients in Solution by a Conductor Solvent Model. *J. Phys. Chem. A* **1998**, *102* (11), 1995–2001. https://doi.org/10.1021/jp9716997.

(83) Pipek, J.; Mezey, P. G. A Fast Intrinsic Localization Procedure Applicable for Ab Initio and Semiempirical Linear Combination of Atomic Orbital Wave Functions. *J. Chem. Phys.* **1989**, *90* (9), 4916–4926. https://doi.org/10.1063/1.456588.

(84) Römelt, M.; Ye, S.; Neese, F. Calibration of Modern Density Functional Theory Methods for the Prediction of ^{57}Fe Mössbauer Isomer Shifts: Meta-GGA and Double-Hybrid Functionals. *Inorg. Chem.* **2009**, *48* (3), 784–785. https://doi.org/10.1021/ic801535v.

(85) Neese, F. Prediction and Interpretation of the ^{57}Fe Isomer Shift in Mössbauer Spectra by Density Functional Theory. *Inorg. Chim. Acta* **2002**, *337*, 181–192. https://doi.org/10.1016/S0020-1693(02)01031-9.

(86) Greatrex, R.; Greenwood, N. N. Mössbauer Spectra, Structure, and Bonding in Iron Carbonyl Derivatives. *Discuss. Faraday Soc.* **1969**, *47* (0), 126–135. https://doi.org/10.1039/DF9694700126.

(87) Sinnecker, S.; Slep, L. D.; Bill, E.; Neese, F. Performance of Nonrelativistic and Quasi-Relativistic Hybrid DFT for the Prediction of Electric and Magnetic Hyperfine Parameters in ^{57}Fe Mössbauer Spectra. *Inorg. Chem.* **2005**, *44* (7), 2245–2254. https://doi.org/10.1021/ic048609e.

(88) Neese, F.; Wennmohs, F.; Becker, U.; Riplinger, C. The ORCA Quantum Chemistry Program Package. *J. Chem. Phys.* **2020**, *152* (22), 224108. https://doi.org/10.1063/5.0004608.

Chapter 4

MOLYBDENUM-IRON-SULFUR CLUSTERS WITH A BRIDGING CARBIDE LIGAND

4.1 ABSTRACT

The active site of the nitrogenase enzyme which catalyzes the reduction of atmospheric N_2 to NH_3 contains a complex Fe-M (M = Mo, Fe, or V) cofactor (FeMco), with eight metal centers bridged by sulfides and a carbide in a MFe_7S_8C composition. The role of the unusual carbide ligand, as well as its effects on the metal centers, remains poorly understood. No synthetic iron-sulfur clusters aimed at replicating the FeMco structure have successfully incorporated a carbide ligand. Here, we report the transfer of a carbide ligand to a $MoFe_3S_3$ cluster supported by a bisphenoxide ligand using a previously reported terminal Mo carbide complex to yield a pentametallic cluster of the [$MoFe_3Mo$] composition. This cluster also displays a bridging CO that resembles the lo-CO form of nitrogenase, and an S = 1/2 state amenable to studies by pulse EPR spectroscopy (in collaboration with Tianyi He and Dr. Paul Oyala). This provides a strategy for the synthesis of carbide-containing iron-sulfur clusters relevant to nitrogenase modeling, as well as opportunities for benchmarking the metal-carbon interactions by EPR methods.

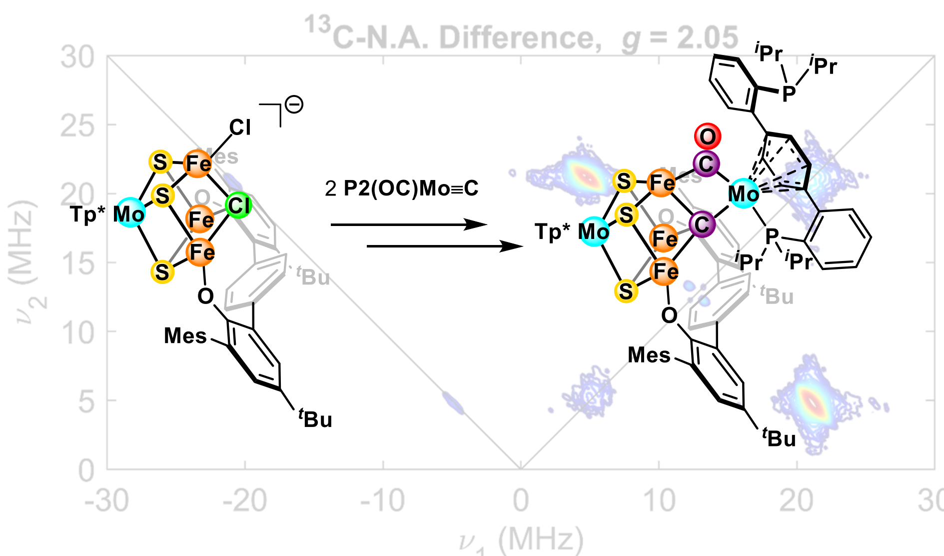

4.2 INTRODUCTION

The nitrogenase enzyme, capable of converting atmospheric N_2 into NH_3, contains the remarkably complex iron-sulfur cluster FeMco of the MFe_7S_9C composition (M = Mo, V, Fe) at the active site.[1–3] A striking feature in the enzyme is the inclusion of an unusual interstitial carbide ligand,[1,4,5] which is a rare motif in both synthetic chemistry and biology.[6] In addition, the function of the carbide in nitrogenase remains largely unclear. Studies on N_2 binding in monometallic model complexes containing a Fe-C interaction suggest that the interstitial carbide might help maintain the flexibility of the cluster, stabilizing the different geometries at substrate-bound Fe sites during various steps of the catalytic cycle.[7–9] Furthermore, the carbide can also modulate the Fe-C covalency, reducing excess charge at Fe to favor multielectron processes.[10] In an extreme case, computational modeling suggests that the carbon atom is highly dynamic and undergoes protonation to form a methyl ligand during N_2 reduction.[11] In contrast, comparison of ^{13}C pulse EPR parameters for different FeMoco intermediates reveals very similar coupling constants and geometries, indicating that the carbide instead stabilizes the rigid core structure.[12,13]

Despite efforts in synthetic chemistry to replicate the FeMco architecture,[14–20] none has successfully incorporated a bridging carbide ligand into an iron-sulfur cluster structure (Figure 4.1). A few reported Fe clusters contain a bridging sulfide and an interstitial carbide,[21–23] but the metal sites are ligated by many strong-field CO ligands that are electronically different from the weak-field sulfides in FeMco. Our group has described examples of MFe_3S_3C (M = Mo, W) cubane-type clusters with C-based ligands bound in a μ_3 fashion to the Fe sites to replicate half of FeMoco, but all are carbyne motifs instead of carbide.[24–26] Thus, this motivates us to improve our models to include a carbide ligand in an iron-sulfur cluster.

The most straightforward strategy to access a bridging carbide complex involves the direct metalation of a terminal carbide ligand.[6] For instance, the carbide complexes **$(Cy_3P)_2Cl_2Ru{\equiv}C$** (Figure 4.1) and **$[Tp^*(OC)_2M{\equiv}C]^-$** (M = Mo, W) can react with a number of metal precursors to yield complexes containing a μ_2-carbide motif.[27–37] Our laboratory has reported a terminal Mo carbide **P2(OC)Mo≡C** supported by a terphenyl diphosphine **P2** ligand (Figure 4.1),[38–41] which undergoes C-C coupling between the carbide and an external CO fragment after the addition of a hydride and proton source to release ethyl acetate as the product.[39] While **P2(OC)Mo≡C** acts as a

C-atom transfer reagent to form an organic product in this case, it has not been used for carbide transfer in an inorganic complex. Here, we report the synthesis and characterization by EPR spectroscopy of a molybdenum-iron-sulfur cluster with a μ_4-carbide ligand using **P2(OC)Mo≡C** as a carbide-containing model relevant to nitrogenase.

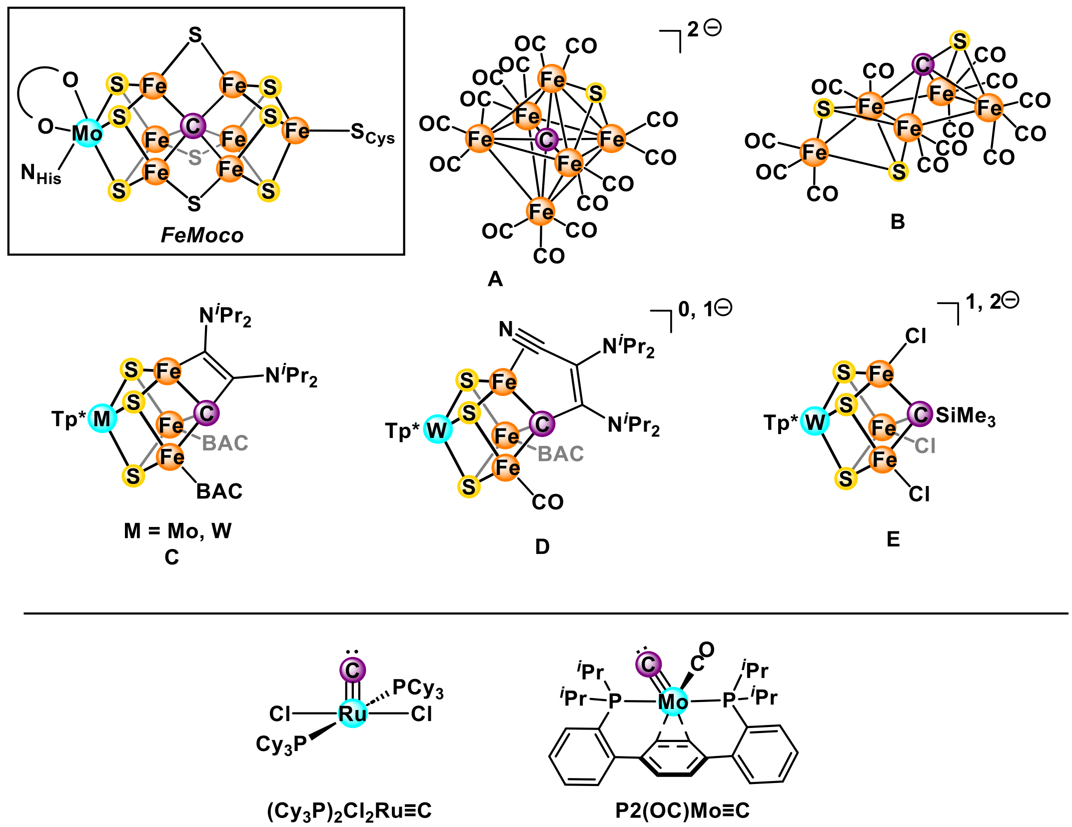

Figure 4.1. Top: Structures of FeMoco (boxed), Fe clusters containing an interstitial carbide (**A**, **B**), and iron-sulfur clusters with a μ_3-carbyne ligand (**C** – **E**). BAC = bis(diisopropylamino)cyclopropenylidene, Tp* = tris(3,5-dimethyl-1-pyrazolyl)borate. Bottom: Structures of **$(Cy_3P)_2Cl_2Ru$≡C** and **P2(OC)Mo≡C**.

4.3 RESULTS AND DISCUSSION

We envision the construction of a desymmetrized $MoFe_3$ cluster, where two Fe sites are blocked by a bidentate ligand, to deliver the C atom to the more open third Fe site in a more controlled manner. Subsequent transformations can allow the C atom to substitute labile ligands at the bridging position. A starting material such as the known cubane[20,24] **4.1** (Figure 4.2) is an ideal candidate, as it possesses both terminal and bridging Cl atoms that can be substituted with a bidentate ligand or a carbide. In addition, a bisphenoxide ligand based on a terphenyl backbone has an O-O distance of about 6.7 Å,[42–44] far enough to accommodate a $MoFe_3$ cubane cluster between the two O atoms.

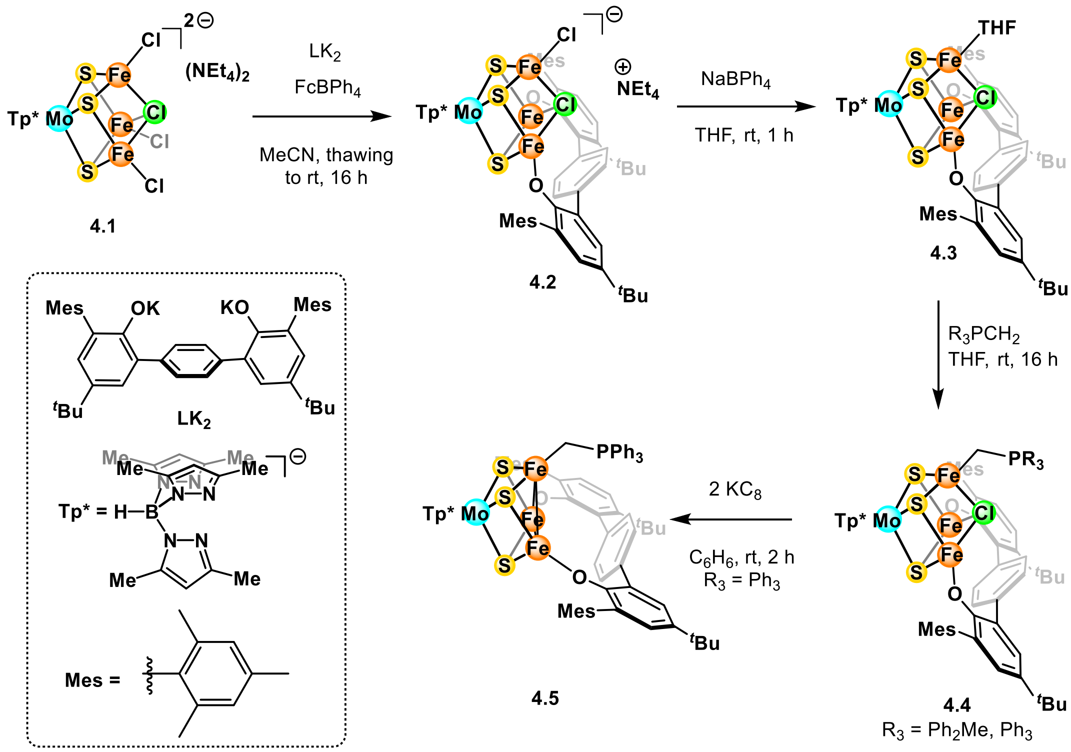

Figure 4.2. Syntheses of clusters **4.3** to **4.5**.

While the reaction between **4.1** and the bisphenoxide **LK₂** results in an intractable mixture, adding **LK₂** to a thawing solution of **4.1** in MeCN in the presence of ferrocenium tetraphenylborate ($FcBPh_4$) as an oxidant results in the formation of one major species with paramagnetically shifted peaks by ^1H NMR spectroscopy (Figure 4.S1). The product obtained crystallizes poorly, but the atomic connectivity was established by X-ray crystallography, confirming the binding of the bisphenoxide fragment to the $MoFe_3$ cubane (Figure 4.S19), with the structure assigned as **4.2** (Figure 4.2). Two terminal Cl ligands have been substituted by the bisphenoxide, where the third terminal Cl and the μ_3-Cl are intact. The cleaner reaction between **4.1** and **LK₂** when an oxidant is present may stem from stronger bonds between the electron-rich phenoxides and Fe sites on a more electron-poor cluster.

Since **4.2** contains potentially labile Cl ligands, we attempted to remove them in order to install a carbide moiety. Adding $NaBPh_4$ as a halide abstracting reagent to a THF solution of **4.2** with stirring results in the formation of a new paramagnetic species by ^1H NMR spectroscopy (Figure 4.S3), along with the concomitant appearance of a white solid assigned as NaCl.[24] While the product also does not crystallize well, its NMR spectrum resembles that of **4.2** where similar diagnostic peaks are detected with different chemical shifts, suggesting analogous structures between the two clusters. Therefore, we assigned the product as **4.3** (Figure 4.2), with the unique Fe site ligated by a THF solvent molecule after the removal of the terminal Cl by $NaBPh_4$.

We envision delivering a C-based ligand to the unique Fe site to replace the solvent molecule and subsequently transfer it to the bridging position. One such reagent is the phosphorus ylide R_3PCH_2, which acts as a CH_2 synthon after the loss of the stable phosphine PR_3 fragment.[45] Reacting **4.3** (generated *in situ*) with one equivalent of Ph_3PCH_2 or Ph_2MePCH_2 leads to the disappearance of the starting material and the formation of a new species with similar NMR features but different chemical shifts compared to **4.2** and **4.3**, suggesting their closely related structures with the product. X-ray crystallography of crystals from the reaction with Ph_2MePCH_2 allows for the assignment of the product as **4.4** (Figure 4.3), where the ylide coordinates to the unique Fe through the C atom and substitutes for the THF ligand in **4.3**.

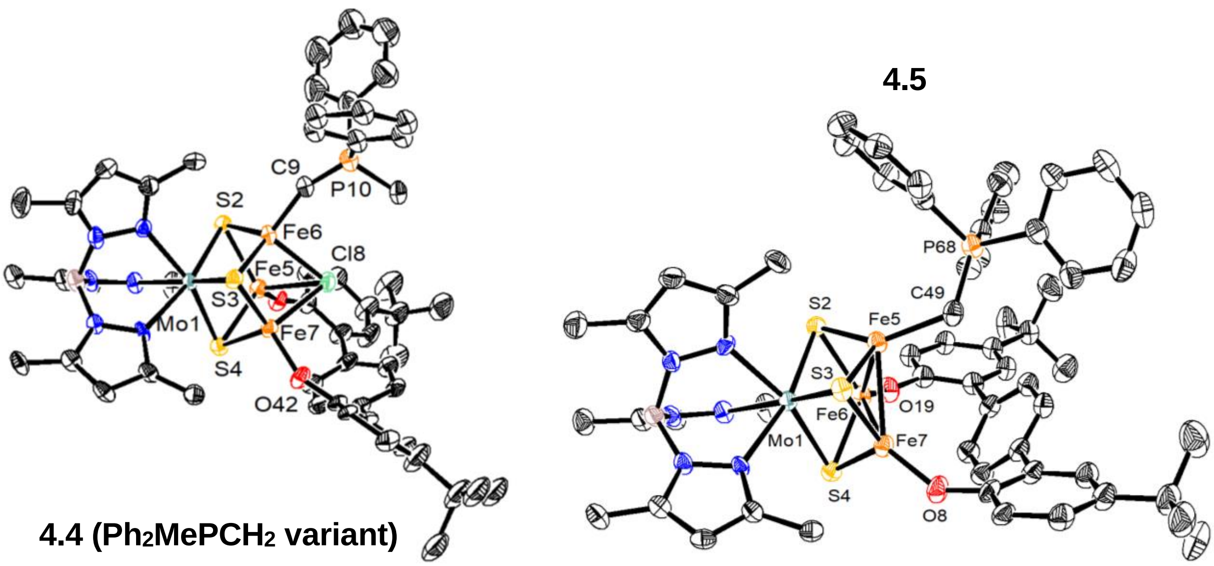

Figure 4.3. Crystal structures of **4.4** (Ph_2MePCH_2 variant) and **4.5**. Ellipsoids are shown at 50% probability level. Hydrogen atoms, solvent molecules, and part of the bisphenoxide ligand are omitted for clarity.

Next, we attempted to remove the μ_3-Cl ligand to transfer the ylide carbon to the bridging position by reduction, as this has been successfully achieved with previously reported carbene-containing clusters.[24] However, reacting **4.4** with strong reducing agents like KC_8 leads to intractable mixtures. With the Ph_3PCH_2-bound version, extracting the crude mixture into Et_2O and storing the solution at -35 °C over several weeks led to the formation of some X-ray quality crystals, which establish the structure of the product as **4.5** (Figure 4.3). In this case, the μ_3-Cl ligand has been lost as expected to yield an incomplete cubane, but no transfer of the ylide carbon to the bridging position is observed. Interestingly, the bisphenoxide ligand moves upward compared to **4.2**, likely to offer steric protection to the open Fe_3 face.

Consequently, we developed an alternative strategy to deliver a carbide motif directly using a metal carbide complex. Cluster **4.3** remains unreacted even when stirred for 24 h at room temperature when the Ru carbide **$(Cy_3P)_2Cl_2Ru{\equiv}C$** is added, and decomposes when the reaction is heated at 80 °C. In contrast, **4.3** reacts quickly when one equivalent of the Mo carbide **P2(OC)Mo≡C** (generated *in situ*) is added. After 1 h, ^{1}H NMR spectroscopy indicates the complete disappearance of **4.3** and the formation of a new product. Crystallization in C_6H_6/pentane vapor diffusion results in dark plates, whose structure is determined by single-crystal X-ray diffraction (XRD) as **4.6** (Figures 4.4 and 4.5). In this cluster, the **P2(OC)Mo≡C** moiety coordinates to the unique Fe through the C atom, resulting in a μ_2-C ligand that bridges between the Fe and Mo centers. The bonding motif is reminiscent of **$(Cy_3P)_2Cl_2Ru{\equiv}C$** acting as a terminal ligand to the heterometal M' vertex of a M_3S_4M' cubane cluster (M = Mo, W; M' = Pd, Pt).[28] Notably, within these clusters, the authors observe relatively short distances between the μ_2-C and the heterometal compared to typical heterometal-carbon bonds. This has been explained by the strong π-accepting nature of terminal carbide complexes as ligands, comparable to a CO fragment.[27,28] In contrast, the Fe-(μ_2-C) distance of 1.992(5) Å in **4.6** is much longer than the median Fe-C bond lengths from the Cambridge Structural Database (CSD) of 1.80 Å (Figure 4.S23). Possibly, the electron-rich late metals Pd and Pt in the M' site of the aforementioned M_3S_4M' clusters lead to greater degrees of π-backbonding to the bound carbide complex, compared to the less electron-rich Fe site in **4.6**.

Having demonstrated the delivery of a carbide ligand to one Fe vertex, we attempted to remove the μ_3-Cl atom in **4.6** and transfer the carbide to the bridging position. Previous work suggests that Cl removal can be achieved with reduction,[24] while the installation of a μ_3-C atom is possible with oxidation.[25] However, both reduction and oxidation of **4.6** by chemical methods result in intractable mixtures, with free phosphine ligand observed by ^{31}P NMR spectroscopy in some cases, denoting decomposition.

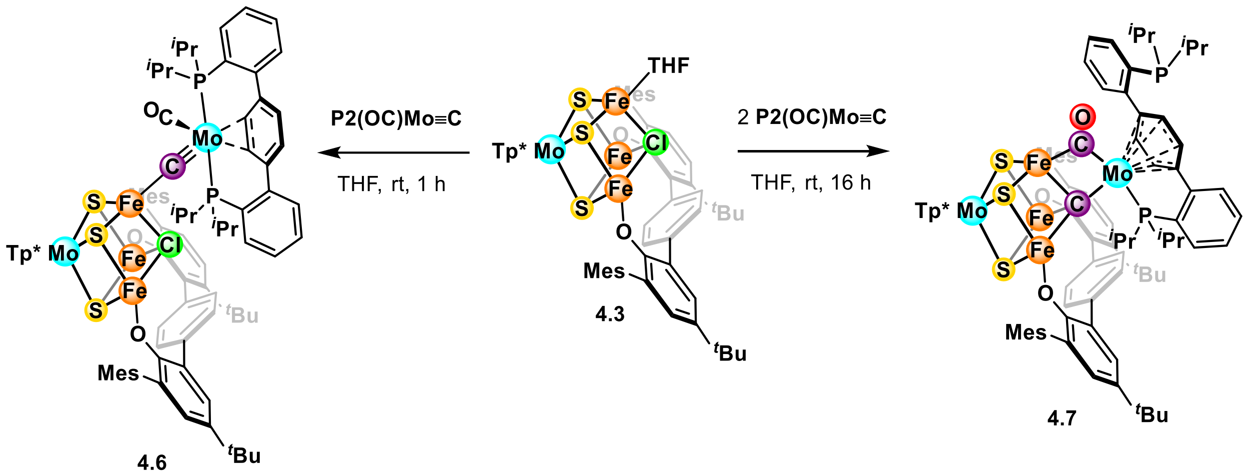

Figure 4.4. Syntheses of carbide-containing clusters **4.6** and **4.7**.

Unexpectedly, changing the reaction conditions in the synthesis of **4.6** leads to the delivery of a carbide ligand to the bridging position. With two equivalents of **P2(OC)Mo≡C** and longer reaction time (16 h), a new species is cleanly generated as indicated by ^{1}H NMR spectroscopy with a greater number of peaks than **4.6**, suggesting a highly asymmetrical geometry. XRD studies of crystals grown by diffusing pentane into a concentrated C_6H_6 solution of the crude product reveals its structure as **4.7** (Figure 4.4). In this case, the carbide now binds in a μ_4 manner to the Fe sites and the Mo atom from **P2(OC)Mo≡C**, displacing the μ_3-Cl ligand. The conversion from **4.6** to **4.7** involves a one-electron reduction, which might be accomplished by the extra equivalent of **P2(OC)Mo≡C**. In addition, the **P2** ligand only coordinates to the Mo center through one phosphine arm, while the other arm does not bind to any metal, likely because of the steric crowding around the Mo atom. This arm-on arm-off binding mode has been observed for **P2(OC)Mo≡C**, where long reaction times promote the dissociation of the second phosphine arm.[39]

While the Mo-(μ_4-C) bond length of 1.744(5) Å in **4.6** is consistent with a triple bond,[38–40] the corresponding distance in **4.7** is much longer at 2.026(3) Å, indicative of a single bond. The average Fe-(μ_4-C) distance of 1.95 Å is in good agreement with the reported carbyne-containing clusters,[24–26] although the wide range of individual bond lengths between 1.87 and 2.03 Å suggests that the carbide can accommodate flexible Fe-C interactions.[7] Compared to FeMoco with an average Fe-carbide bond of 2.00 Å,[1] the corresponding distance in **4.7** is slightly shorter, possibly due to the lack of two additional metal sites around the carbon atom.

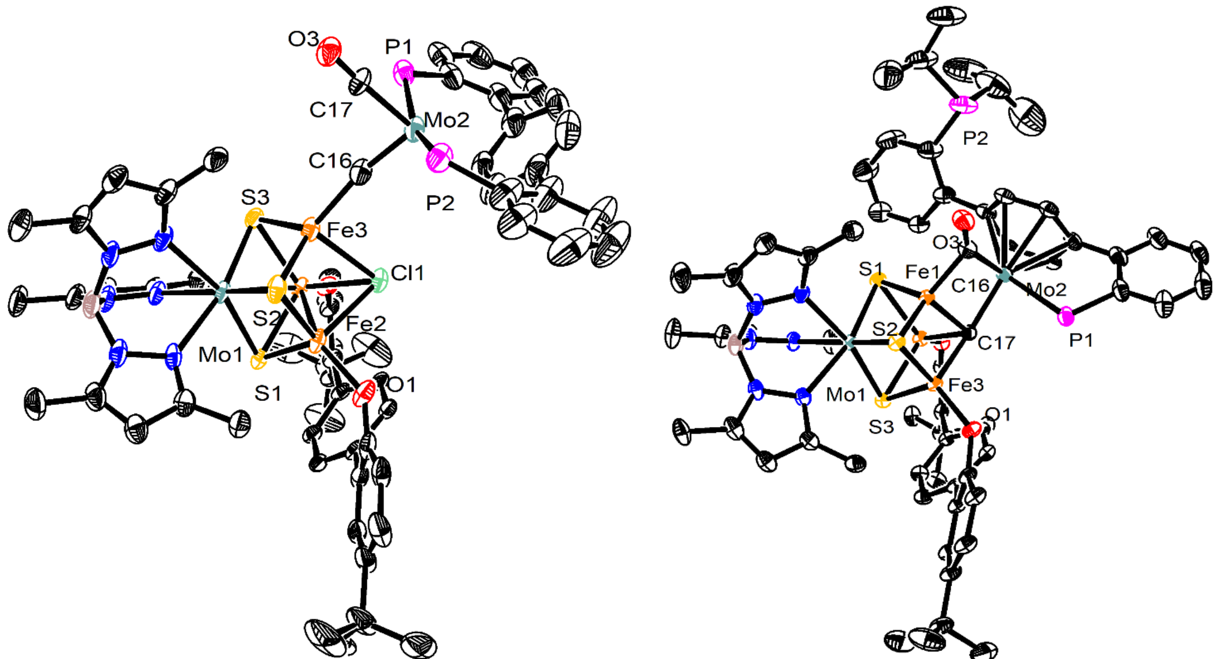

4.6 **4.7**

Figure 4.5. Crystal structures of **4.6** and **4.7**. Ellipsoids are shown at 50% probability level. Hydrogen atoms, solvent molecules, and part of the bisphenoxide and the phosphine ligands are omitted for clarity.

In addition, the CO ligand on the Mo carbide fragment forms a bridge between the Mo atom and one Fe site. The C-O bond length of 1.172(5) in **4.7** is longer than that in **4.6** at 1.159(5), consistent with greater CO activation due to backbonding from two metal centers. In the IR spectrum, this μ_2-CO stretch is assigned to a peak at 1750 cm^{-1}. Thus, **4.7** highly resembles the structure of lo-CO, where one CO molecule has replaced a belt sulfide in FeMoco to form a bridge between Fe2 and Fe6.[46] Here, we have successfully reproduced both the carbide and bridging CO motifs, albeit with only four metal centers, one of which is Mo instead of Fe.

Cluster **4.7**, with the formal metal charges of $[MoFe_3Mo]^{13+}$, possesses a half-integer spin state suitable for studies by EPR spectroscopy. Additionally, a ^{13}C-labeled version was prepared starting from **P2(O^{13}C)Mo≡^{13}C** for pulse EPR studies to understand the nature of metal-carbon bonding in the CO and carbide ligands. Notably, **4.7** provides an opportunity for comparison with pulse

EPR data reported for FeMoco, as only two examples of synthetic systems containing Fe-C interaction with ^{13}C labeling have been interrogated by pulse EPR methods.[10,47]

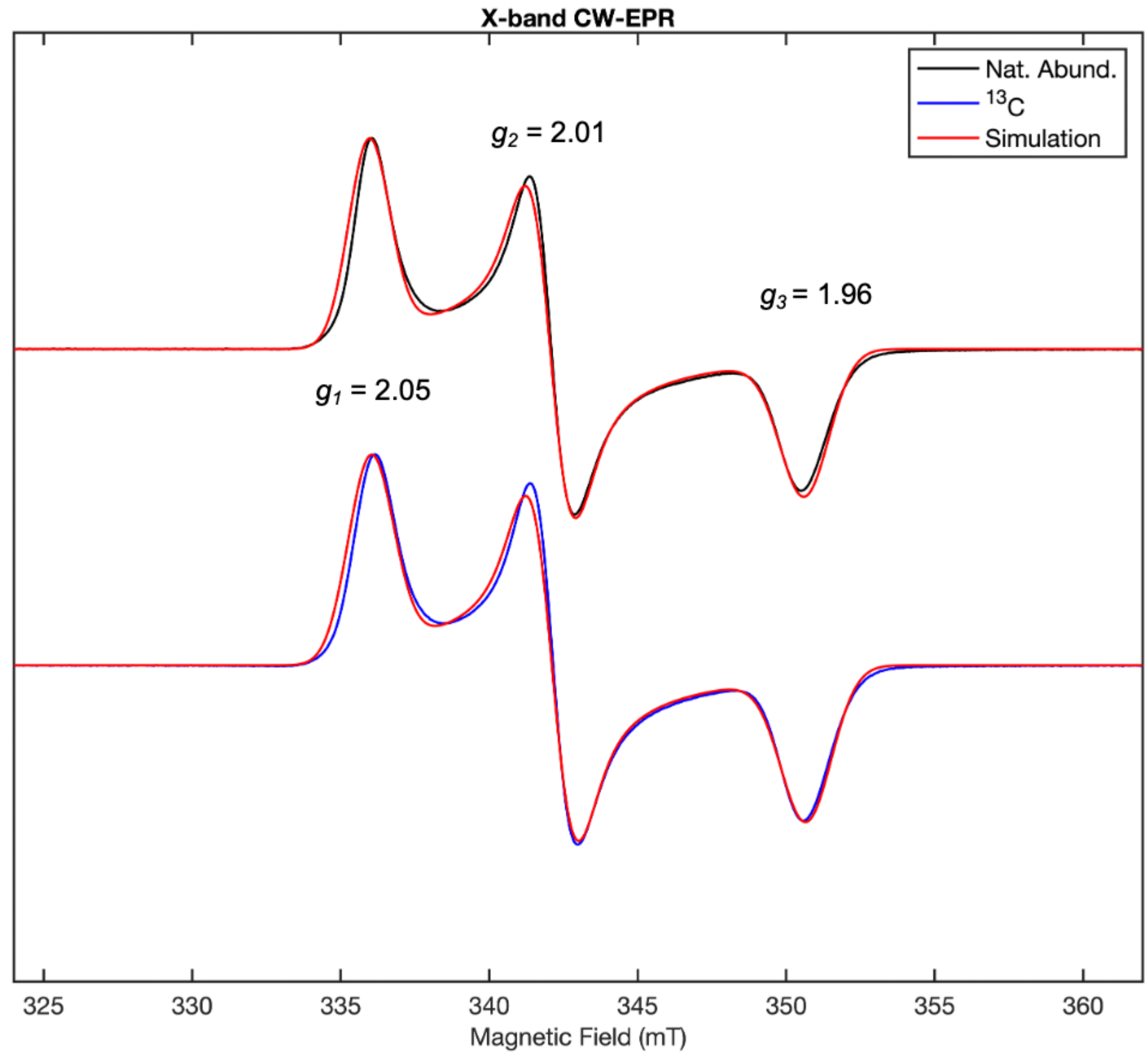

Figure 4.6. Experimental (black and blue) and simulated X-band CW-EPR of **4.7** at 15 K in a frozen toluene glass. Acquisition parameters: MW frequency: 9.64 GHz; MW power = 35 μW; modulation amplitude: 0.2 mT (**4.7**), 0.8 mT (**4.7-^{13}C,^{13}CO**); conversion time = 10 ms; time constant = 10.24 ms;

The X-band CW-EPR spectrum of **4.7** at 15 K (Figure 4.6) revealed an S = 1/2 ground state with a rhombic *g*-tensor of [2.05 2.01 1.96] that was further resolved in the Q-band ESE-EPR spectrum (Figure 4.7). There was no discernable difference between the X-band CW-EPR and Q-band ESE-

EPR between **4.7** and **4.7-^{13}C,^{13}CO** (Figures 4.S15 and 4.S16), except for the slightly different linewidths at g_2 = 2.01.

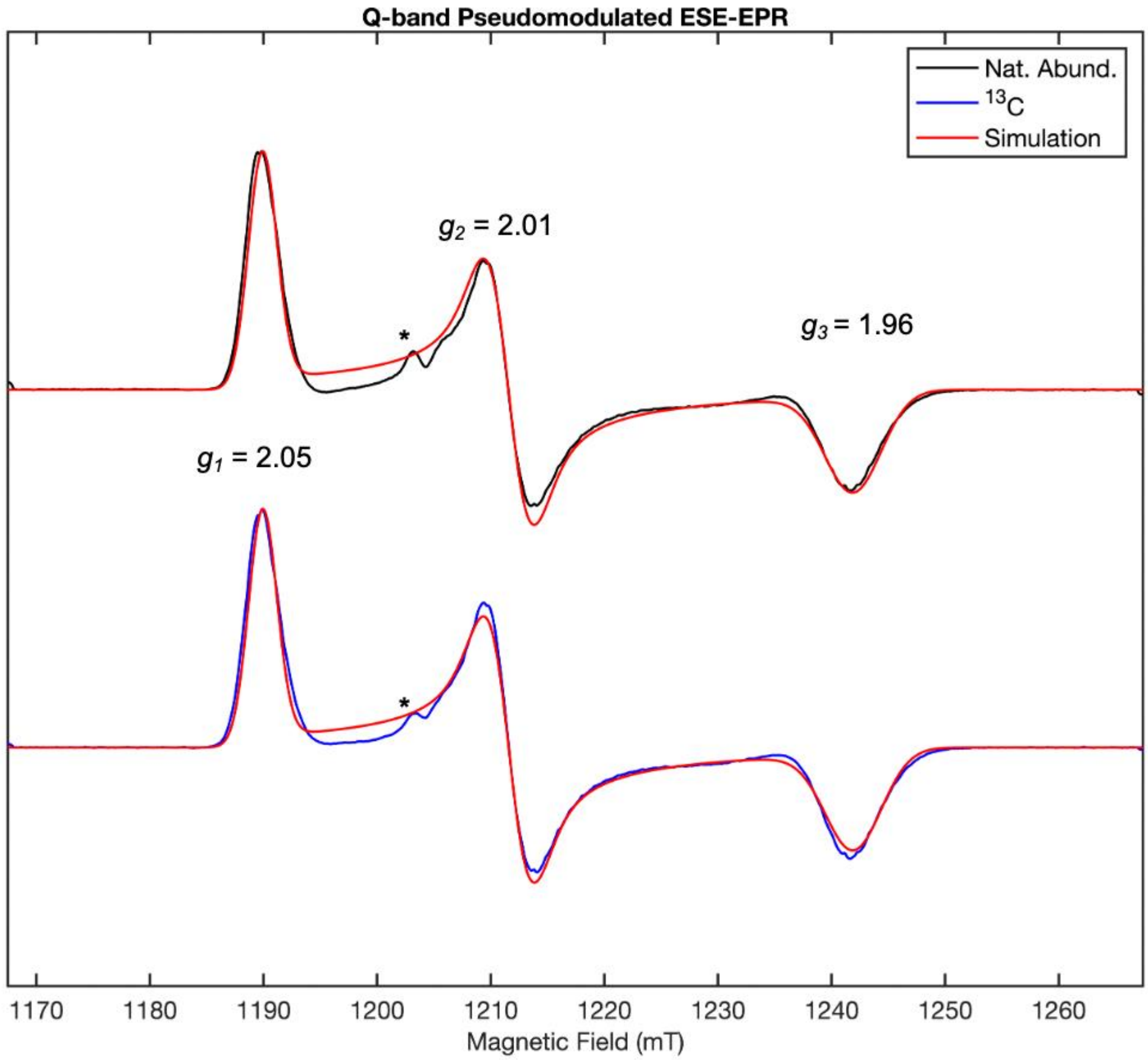

Figure 4.7. Experimental (black and blue) and simulated Q-band pseudomodulated ESE-EPR spectra of **4.7** at 15 K in a frozen toluene glass. Asterisk denotes a background signal in the Q-band resonator; Acquisition parameters: MW frequency = 33.7 GHz (**4.7**) 34.1 GHz (**4.7-^{13}C,^{13}CO**); MW power = 8 mW; pseudomodulation = 1 mT.

Q-band ENDOR was employed to further understand the local hyperfine coupling tensor of the interstitial carbide and the bridging CO. Q-band Davies ENDOR of **4.7** revealed two distinct classes of weakly-coupled ^{31}P nuclei, consistent with the arm-on/arm-off configuration of the diphosphine ligand in the solid-state structure of **4.7**. Q-band Davies ENDOR of **4.7-^{13}C,^{13}CO** revealed two distinct classes of weakly-coupled ^{13}C signals (Figure 4.8, middle). Selective ^{13}C labeling at the CO position starting from **P2(O^{13}C)Mo≡C** to form **4.7-^{13}CO** revealed that the ^{13}C signal with smaller coupling was from ^{13}CO, whereas the larger coupling corresponds to the interstitial carbide (Figure 4.S17).

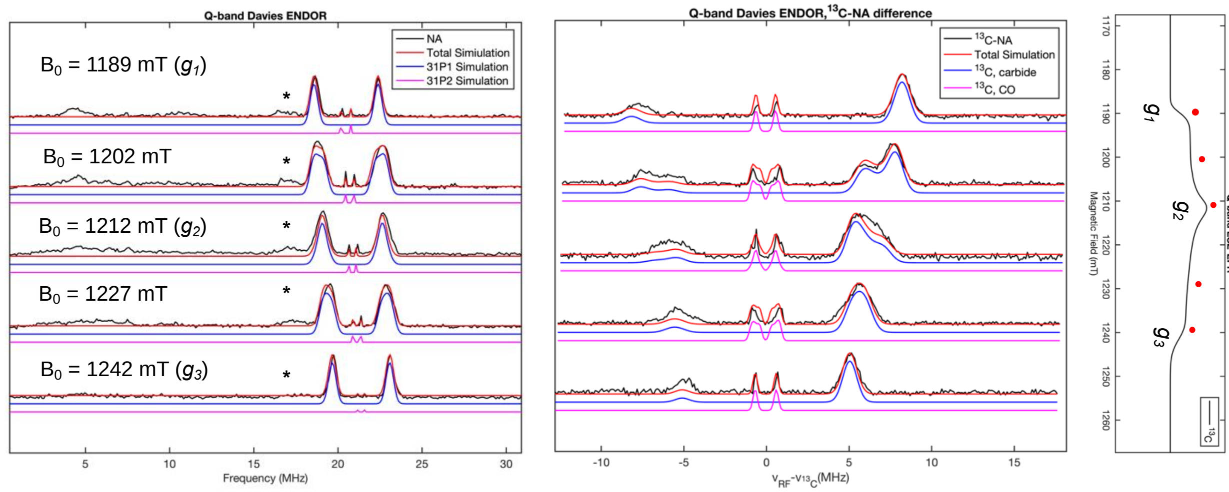

Figure 4.8. Pulse EPR spectroscopy. Left: Field-dependent Q-band Davies ENDOR of **4.7** at various field with simulations overlaid (parameters in Table 4.1); Middle: Field-dependent Q-band Davies ENDOR difference spectra of **4.7-^{13}C,^{13}CO** and **4.7**; Right: Q-band ESE-EPR with red circles highlighting field positions at which field-dependent Q-band Davies ENDOR was acquired. Asterisks denote 3rd harmonic of ^{1}H ENDOR. Acquisition parameters: temperature = 12 K; MW frequency = 34.1 GHz; MW π pulse length = 160 ns; π_{RF} pulse length = 60 μs; T_{RF} delay = 2 μs; shot repetition time (srt) = 20 ms.

Table 4.1. Hyperfine coupling tensors for simulation.

Nucleus	***A* (MHz)**
^{13}C, carbide	[10.2 10.1 17.2]
^{13}C, CO	[1.89 1.30 0.43]
^{31}P1	[4.56 3.61 2.59]
^{31}P2	[0.36 0.46 0.58]

Q-band Davies ENDOR for both **4.7** and **4.7-^{13}C,^{13}CO** were simulated with parameters in Table 4.1. The hyperfine coupling tensor of ^{13}C of the CO ligand can be decomposed into its isotropic and anisotropic components $\boldsymbol{A}(^{13}\mathbf{C,CO}) = \boldsymbol{a_{iso}} + \boldsymbol{T_{obs}} = \mathbf{1.21 + [0.68\ 0.09\ -0.78]\ MHz}$. The rhombicity of $\boldsymbol{A_{aniso}}$ **(^{13}C,CO)** is reminiscent of that of the lo-CO form of FeMoco with a μ_2-CO bridge, $\boldsymbol{A}(^{13}\mathbf{CO,\ lo\text{-}CO}) = \mathbf{1.2 + [-3.2\ 2.3\ 0.8]\ MHz}$, where the rhombicity of the anisotropic component of the hyperfine coupling tensor was attributed to the non-coaxial contributions between the two metal ions which the μ_2-CO bridges.[48,49]

Table 4.2. Comparison between ^{13}C components of the hyperfine coupling tensors of interstitial carbides across **4.7-^{13}C,^{13}CO** and the E_0, hi-CO, E_4(4H)/α-Ile[70], E_4(2H)*/α-Ile[70], PA in α-Ala[70] states of the FeMo cofactor in nitrogenase.[12,13]

Species	$\boldsymbol{a_{iso}}$ **(MHz)**	$\boldsymbol{T_{obs}}$ **(MHz)**
4.7-^{13}C,^{13}CO	12.5	[-2.3 -2.4 4.7]
E_0	0.86	[2.24 -0.43 -1.81]
hi-CO	-1.81	[4.5 -2.1 -2.4]
E_4(4H)/α-Ile[70]	2.7	[3.6 -2.7 -0.8]
E_4(2H)*/α-Ile[70]	0.9	[2.7 -0.1 -2.5]
PA in α-Ala[70]	2.3	[3.2 -1.0 -2.3]

The hyperfine coupling tensor of the interstitial carbide can be likewise decomposed into its isotropic and anisotropic components $\boldsymbol{A}(^{13}\mathbf{C,carbide}) = \mathbf{12.5 + [-2.3\ -2.4\ 4.7]\ MHz}$. Compared to the small isotropic components of the carbide hyperfine coupling tensor observed in different states of the nitrogenase,[12,13] **4.7-^{13}C,^{13}CO** exhibits a larger isotropic component a_{iso}, whereas the anisotropic contributions $\boldsymbol{T_{obs}}$ is similar in magnitude to those observed in different states of the nitrogenase (Table 4.2). Previous work on protein systems has suggested that the small isotropic coupling in nitrogenase species could arise from one of two reasons: i) the Fe-C(carbide) interaction is largely ionic, with little spin delocalization from the anionic carbide onto the Fe atoms, or ii) the Fe-C(carbide) interaction is strongly covalent, but antiferromagnetic coupling of the Fe sites in FeMoco (3↑/3↓ for the Fe_6 core) results in a net near-zero a_{iso} by canceling individual contributions from each Fe-C bond.[3-4] The authors favor the second explanation mainly based on computational rationale, but the difficulty in constructing an asymmetric biological system to remove the geometric effects precludes direct experimental evidence. In contrast, using

4.7 as an asymmetric synthetic system lacking the three other belt Fe centers, we provided definitive proof of a strong Fe-C(carbide) interaction by EPR spectroscopy, which is likely also present in FeMoco.

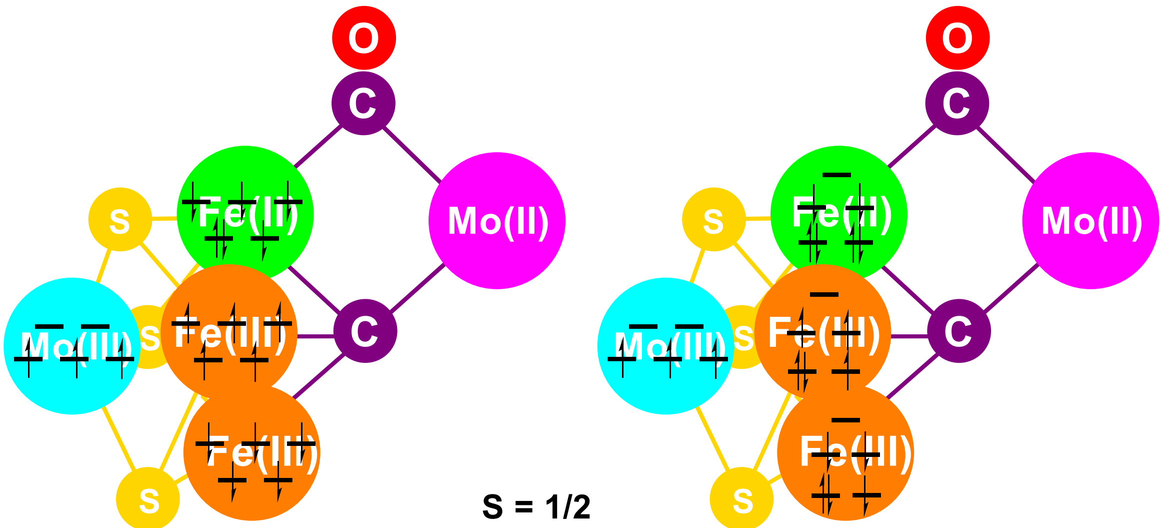

Figure 4.9. Proposed exchange-coupling schemes of **4.7** with high spin (left) or intermediate spin (right) configurations at Fe.

Intriguingly, the S = 1/2 ground state in **4.7** is unusual for clusters based on the [$Tp^*MS_3Fe_3$] scaffolds.[24–26] A general description of the exchange-coupling between metal centers in **4.7** is therefore desirable. First, the Mo center supported by the terphenyl diphosphine ligand is considered. Open-shell Mo complexes supported by this ligand scaffold bearing M≡E multiple bonds (E = C, P) have been extensively studied,[40,50] where a significant spin density on Mo typically displays large ^{31}P couplings with $a_{iso}(^{31}P)$ > 40 MHz.[40,50] For example, **[P2Mo(≡C)CO][BAr$^F_{24}$]** (BAr^F_{24} = tetrakis(3,5-bistrifluoromethylphenyl)borate) was shown to exhibit an average $a_{iso}(^{31}P)$ = 60 MHz where ρ_{Mo} = 0.58 e^-.[40] In comparison, **[K][P2Mo(≡C)CO]** was shown to exhibit a much lower $a_{iso}(^{31}P)$ = 5.2 MHz, presumably because of the diminished spin density on Mo (ρ_{Mo} = 0.12-0.20 e^-).[40] Based on the small ^{31}P coupling observed in **4.7**, the Mo center ligated by the diphosphine ligand was assigned to be diamagnetic. While direct determination of oxidation state of the **P2**-supported Mo center was not feasible with current data, the Mo center was assigned to be a diamagnetic Mo^{II} based on the average crystallographic bond length of Mo-C(central arene), where Mo-C_{avg}(central arene) = 2.351Å is in good agreement with an average Mo-central arene bond distance of 2.351Å in **[P2Mo^{II}(CO)$_2$][OTf]$_2$**.[51] Assuming diamagnetic Mo^{II}, two exchange-coupling schemes were proposed in Figure 4.9 to rationalize the S = 1/2 ground state, with either a conventional high spin configuration at each tetrahedral Fe site, or an intermediate spin state at the Fe atoms resulting from the strong Fe-C(carbide) interaction.[26] In addition, a combination of intermediate spin (at Fe(CO)) and high spin (at other Fe sites) states is also possible.

In order to install a second cluster to achieve the octametallic core of FeMoco, the **MoP2** moiety needs to be removed. Preliminary results suggest that the Mo-C(carbide) bond can be cleaved, although the highly reactive carbide generated tends to undergo undesired side reactions. For instance, oxidation of **4.7** with I_2 leads to a complex mixture, but some low-quality crystals obtained from extracting the crude product into Et_2O and crystallizing by Et_2O/pentane vapor diffusion suggest that the **MoP2** fragment has been lost, while the carbide undergoes C-C bond formation with the bridging CO to form a metallaketene ligand in **4.8** (Figures 4.10 and 4.S20). The Mo-C(carbide) bond can also be cleaved using $Fe_3(CO)_{12}$ to form **4.9**, where C-C coupling is also observed between the carbide C and a CO moiety (Figures 4.10 and 4.S21). Current efforts focus on alternative strategies to remove the **MoP2** fragment while preventing side reactions at the carbide ligand.

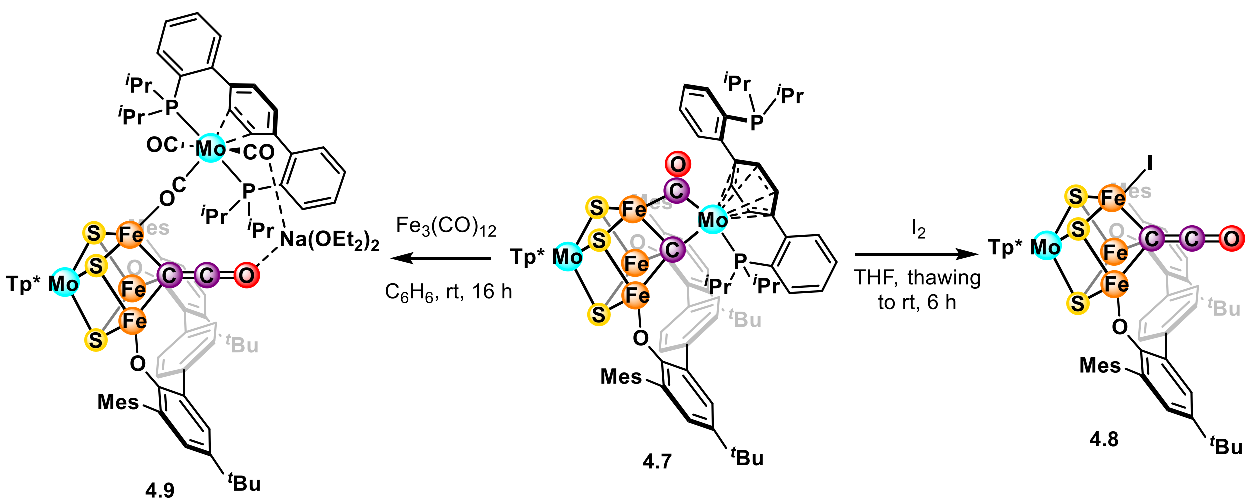

Figure 4.10. Attempts to remove the **MoP2** fragment in **4.7**. The cation in **4.9** is modeled as Na since Na was present in previous steps in the synthetic route, but it could also be Fe with partial occupancy, although there is insufficient data to conclusively assign its identity.

4.4 CONCLUSION

We have demonstrated the binding of a bisphenoxide ligand to a $MoFe_3$ cubane cluster to protect two Fe sites, leaving a third Fe site open for further reactivity in a controlled manner. Using this strategy, we showed that a carbide motif can be installed on the cluster using the previously reported terminal carbide complex **P2(OC)Mo≡C**, yielding a $MoFe_3$ cluster with a carbide ligand in a μ_2 or μ_4 binding mode. Notably, the μ_4-carbide cluster **4.7**, possessing a bridging CO ligand that resembles the lo-CO state, also exhibits an S = 1/2 state suitable for pulse EPR studies to understand the degree of interaction between the C-based ligands and the metal centers. This report presents a new synthetic strategy to access iron-sulfur clusters with bridging carbide ligands relevant to the modeling of nitrogenase.

4.5 SUPPORTING INFORMATION

A) Synthetic details and characterization

1. General considerations:

All reactions were performed at room temperature in a N_2-filled MBraun glovebox or using standard Schlenk techniques unless otherwise specified. Glassware was oven-dried at 140 °C for at least 2 h prior to use and allowed to cool under vacuum. **4.1**,[24] KBn,[52] $FcBPh_4$,[53] Ph_2MePCH_2,[54] Ph_3PCH_2,[54] and **P2(OC)Mo≡C** were prepared[39] according to literature procedures. **LH_2** was prepared analogously to the anthracene-bridged version previously reported.[55] Pentane, diethyl ether, benzene, toluene, and tetrahydrofuran (THF) were dried by sparging with N_2 for at least 15 min and then passing through a column of activated A2 alumina under positive N_2 pressure and stored over 3 Å molecular sieves prior to use. ^1H spectra were recorded on a Varian 300 MHz spectrometer. Deuterated benzene (C_6D_6) was purchased from Cambridge Isotope Laboratories, dried over sodium/benzophenone ketyl, degassed by three freeze–pump–thaw cycles, and vacuum-transferred prior to use. IR spectra were obtained as thin films formed by evaporation of solutions using a Bruker Alpha Platinum ATR spectrometer with OPUS software in a glovebox under an N_2 atmosphere.

2. Procedures:

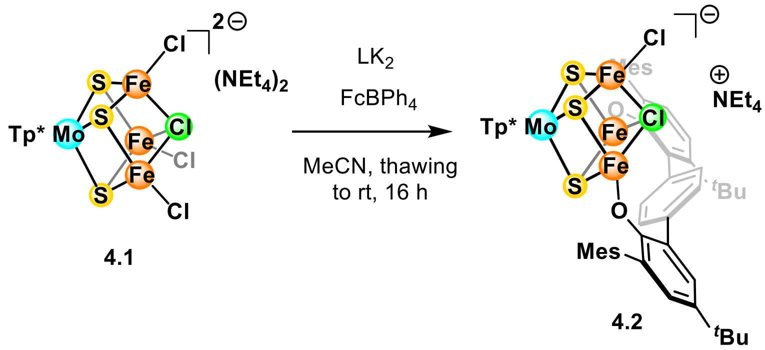

Synthesis of **4.2**. In a glovebox, **4.1** (775 mg, 0.732 mmol, 1 equiv) was dissolved in 30 mL MeCN to form a dark blue solution and frozen in a cold well cooled in liquid N_2. In a separate vial, **LH_2** (335 mg, 0.549 mmol, 0.75 equiv) was dissolved in THF (15 mL) to form a colorless solution and frozen in the cold well. KBn (143 mg, 1.098 mmol, 1.50 equiv) was added to the thawing solution of **LH_2** with stirring to form a fluorescent yellow solution. The reaction was stirred at room temperature for about 10 min to form **LK_2** then concentrated to about 5 mL. To the frozen solution of **4.1** was added $FcBPh_4$ (370 mg, 0.732 mmol, 1 equiv) followed by the solution of **LK_2**. The reaction was allowed to warm and stirred at room temperature inside the box for 16 h, resulting in a dark yellow/brown solution. Then, the reaction was filtered, and the solvent removed *in vacuo*. The resulting dark solid was washed extensively with pentane to remove ferrocene until the washing was no longer yellow. The product was extracted into C_6H_6 and lyophilized to yield a brown powder. The crude material was used without further purification since it does not crystallize well, and NMR spectroscopy indicates small peaks from small amounts of impurities that cannot be removed. Crude yield: 730 mg (91%). Some low-quality crystals of **4.2** were grown by vapor diffusion of pentane into a solution of **4.2** in Et_2O at room temperature over several weeks. ^1H NMR (400 MHz, THF-h_8, solvent suppression) δ 137.12, 80.39, 71.91, 70.61, 10.06, 7.58, 7.25, 6.87, 4.71, 4.34, 4.06, 2.32, 1.29, 0.06, -4.60, -18.38, -18.79.

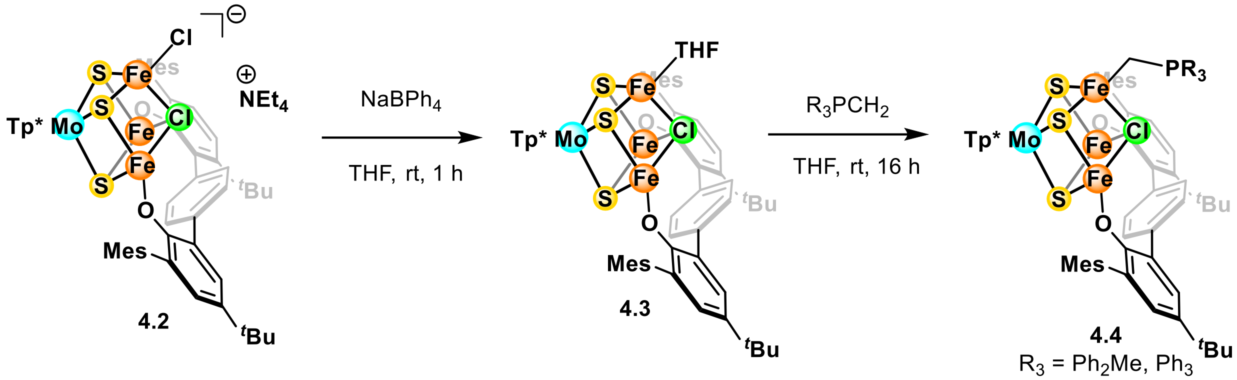

Syntheses of **4.3** and **4.4**. In a glovebox, **4.2** (15.0 mg, 0.0102 mmol, 1 equiv) and $NaBPh_4$ (3.5 mg, 0.0102 mmol, 1 equiv) were combined in THF (2 mL). The dark brown reaction was stirred at room temperature for 1 h, after which the white precipitate formed was removed by filtration. The filtrate containing **4.3** and NEt_4BPh_4 as the side product was used without further purification. ^{1}H NMR (400 MHz, THF-h_8, solvent suppression) δ 142.97, 81.92, 72.85, 70.13, 10.02, 7.58, 4.84, 1.29, 1.06, -1.22, -1.90, -4.70, -18.78, -18.85.

To this solution of **4.3** was added Ph_2MePCH_2 (2.2 mg, 0.0102 mmol, 1 equiv) or Ph_3PCH_2 (2.8 mg, 0.0102 mmol, 1 equiv) and the reaction was stirred at room temperature inside the glovebox for 16 h. The solvent was removed *in vacuo* and the crude product was washed with pentane, followed by extraction into C_6H_6 and lyophilization to yield a brown powder. Only the Ph_2MePCH_2 version provides X-ray quality crystals that can be grown from vapor diffusion of pentane into a concentrated solution of the cluster in Et_2O at room temperature. ^{1}H NMR (400 MHz, THF-h_8, solvent suppression) Ph_2MePCH_2 variant: δ 157.25, 88.29, 77.86, 69.81, 10.39, 7.85, 5.28, -4.78, -18.82, -20.08. Ph_3PCH_2 variant: δ 110.89, 75.74, 73.47, 67.37, 23.70, 9.96, 7.91, 7.46, 7.36, 7.23, 7.12, 6.73, 5.90, 4.48, 4.05, 2.21, 1.23, 1.05, 0.82, -3.91, -15.51, -16.90.

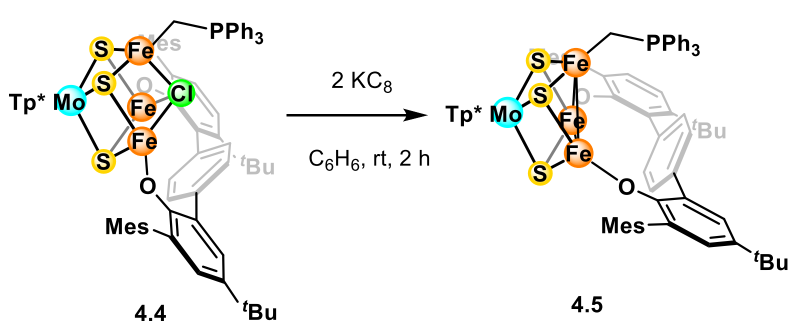

Formation of **4.5**. In a glovebox, **4.4** (Ph_3PCH_2 variant) (19.0 mg, 0.012 mmol, 1 equiv) and KC_8 (3.4 mg, 0.024 mmol, 2 equiv) were combined in C_6H_6 (2 mL). The dark green-brown reaction was stirred at room temperature for 2 h, after which it was filtered through Celite and the solvent removed *in vacuo*. The crude product was extracted into Et_2O, filtered through Celite, and placed in the freezer at -35 °C. Only some X-ray quality crystals of **4.5** were obtained after several days, which precludes bulk characterization.

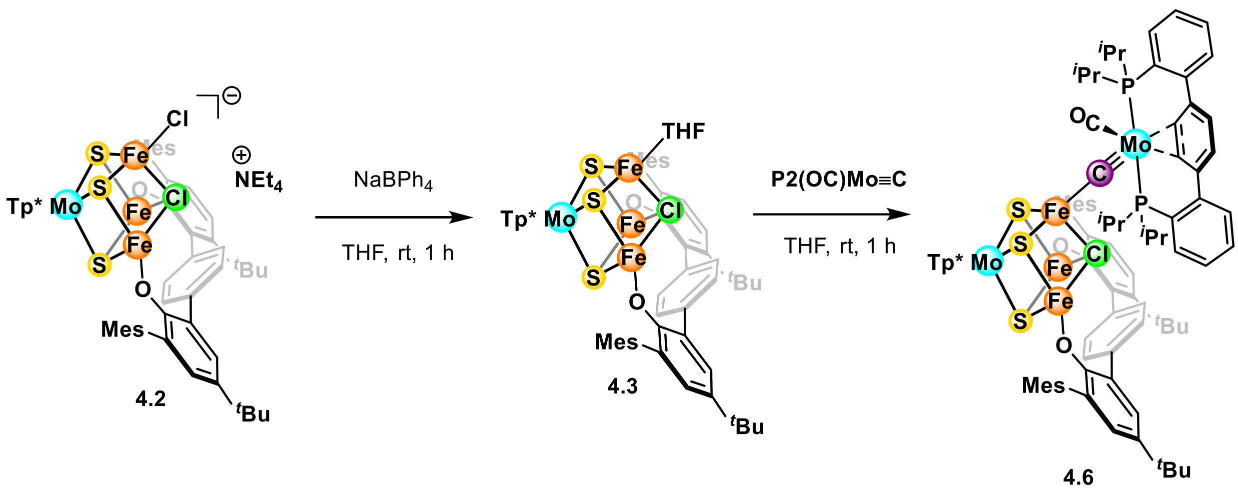

Synthesis of **4.6**. In a glovebox, **4.2** (30.0 mg, 0.0205 mmol, 1 equiv) and $NaBPh_4$ (7.0 mg, 0.0205 mmol, 1 equiv) were combined in THF (2 mL) to form **4.3**. The dark brown reaction was stirred at room temperature for 1 h, after which the white precipitate formed was removed by filtration. To this solution, a deep red/orange solution of **P2(OC)Mo≡C** in 2 mL THF (prepared *in situ* as previously described from **P2(OC)Mo(CH)Cl**, 13.0 mg, 0.0205 mmol, 1 equiv and KBn, 2.7 mg, 0.0205 mmol, 1 equiv) was added at room temperature. The reaction was stirred for 1 h, when ^{1}H NMR spectroscopy indicates the complete disappearance of **4.3**. The content of the vial was filtered through a pad of Celite and the solvent removed *in vacuo* to yield a dark film. The film was washed with pentane, extracted into C_6H_6, and crystallized by C_6H_6/pentane vapor diffusion to yield X-ray quality crystals. However, NMR spectroscopy still indicates the presence of an impurity that cannot be removed, so the peaks assigned are based on the major species. Yield: 22.9 mg (59%). ^{1}H NMR (400 MHz, THF-h_8, solvent suppression) δ 70.63, 65.66, 61.84, 60.67, 31.47, 8.53, 6.76, 0.81, 0.75, -0.55, -9.24, -14.99.

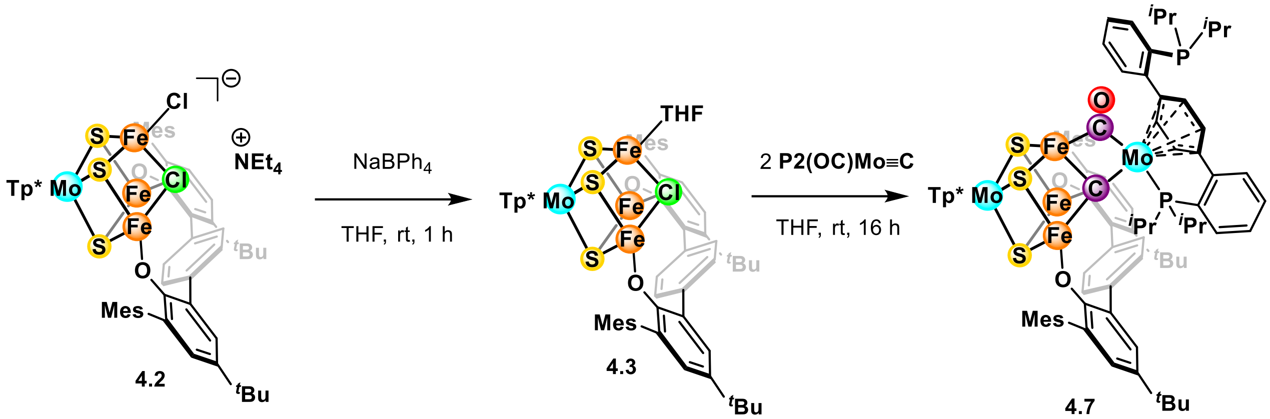

Synthesis of **4.7**. In a glovebox, **4.2** (75.0 mg, 0.0510 mmol, 1 equiv) and $NaBPh_4$ (17.5 mg, 0.0510 mmol, 1 equiv) were combined in THF (4 mL). The dark brown reaction was stirred at room temperature for 1 h, after which the white precipitate formed was removed by filtration. To this solution, a deep red/orange solution of **P2(OC)Mo≡C** in 4 mL THF (prepared *in situ* as previously described from **P2(OC)Mo(CH)Cl**, 64.9 mg, 0.1020 mmol, 2 equiv and KBn, 13.3 mg, 0.1020 mmol, 2 equiv) was added at room temperature. The reaction was stirred for 16 h, after which the solvent was removed *in vacuo* to yield a dark solid. The product was extracted into Et_2O, evaporated to dryness, and crystallized by C_6H_6/pentane vapor diffusion to yield X-ray quality crystals. Yield: 60.0 mg (64%). ^1H NMR (400 MHz, THF-h_8, solvent suppression) δ 57.63, 44.53, 40.87, 36.36, 19.04, 17.40, 13.63, 11.28, 9.24, 9.14, 8.45, 8.16, 7.86, 7.54, 7.36, 7.24, 7.11, 6.99, 6.78, 6.65, 6.16, 6.05, 5.54, 4.90, 2.96, 2.70, 2.28, 2.22, 1.01, 0.95, 0.63, 0.35, -1.03. Anal. calcd (%) $C_{91}H_{110}BFe_3Mo_2N_6O_3P_2S_3$ (M_r = 1864.29): C, 58.62; H, 5.95; N, 4.51. Found: C, 54.71; H, 5.85; N, 4.94. The low C content could be due to incomplete carbon combustion, a known problem for the analysis of metal complexes by combustion analysis.[56] The labeled clusters were prepared identically starting from **P2(O^{13}C)Mo(^{13}CH)Cl** or **P2(O^{13}C)Mo(CH)Cl**.

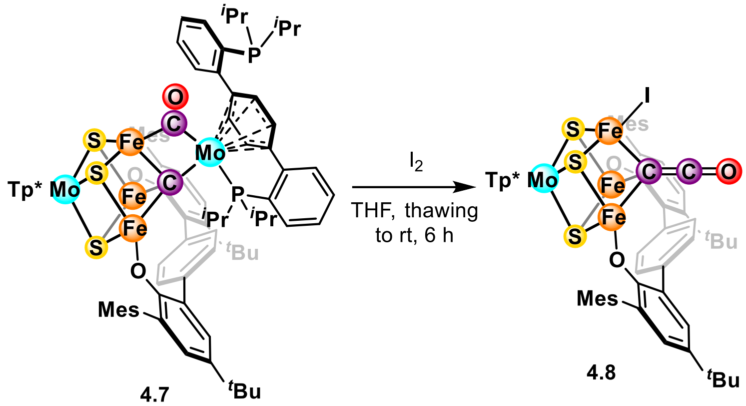

Formation of **4.8**. In a glovebox, **4.7** (12.0 mg, 0.0064 mmol, 1 equiv) was dissolved in THF (2 mL) and frozen in the cold well. To the thawing reaction was added I_2 (1.6 mg, 0.0064 mmol, 1 equiv) and the dark brown reaction was stirred at room temperature for 6 h. The solution was filtered through Celite and the solvent was removed *in vacuo*. The crude product was extracted into Et_2O, filtered through Celite, and crystallized by Et_2O/pentane vapor diffusion. Only some X-ray quality crystals of **4.8** were obtained after several days, which precludes bulk characterization.

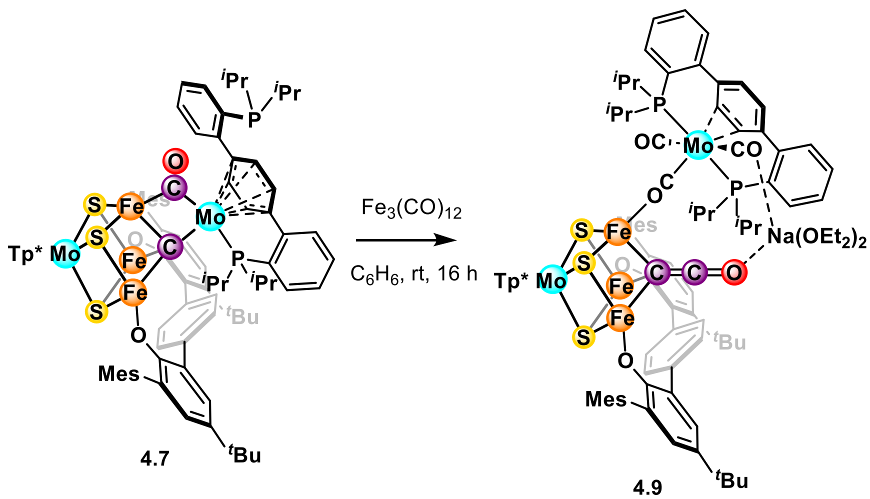

Synthesis of **4.9**. In a glovebox, **4.7** (10.0 mg, 0.0054 mmol, 1 equiv) and $Fe_3(CO)_{12}$ (2.7 mg, 0.0054 mmol, 1 equiv) were combined in C_6H_6 (2 mL) and stirred at room temperature for 16 h. The reaction was filtered through a pad of Celite and the solvent removed *in vacuo* to yield a dark film. The crude product was extracted into Et_2O and crystallized by Et_2O/pentane vapor diffusion to yield X-ray quality crystals. ^1H NMR (400 MHz, C_6H_6, solvent suppression) δ 31.29, 28.48, 28.33, 15.37, 8.91, 8.63, 5.83, 4.73, 3.54, 2.92, 2.25, 2.15, 2.09, 1.94, 1.90, 1.85, 1.79, 1.67, 1.27, -2.41, -3.34, -12.03.

Modified syntheses of the precursors to **P2(OC)Mo≡C**:

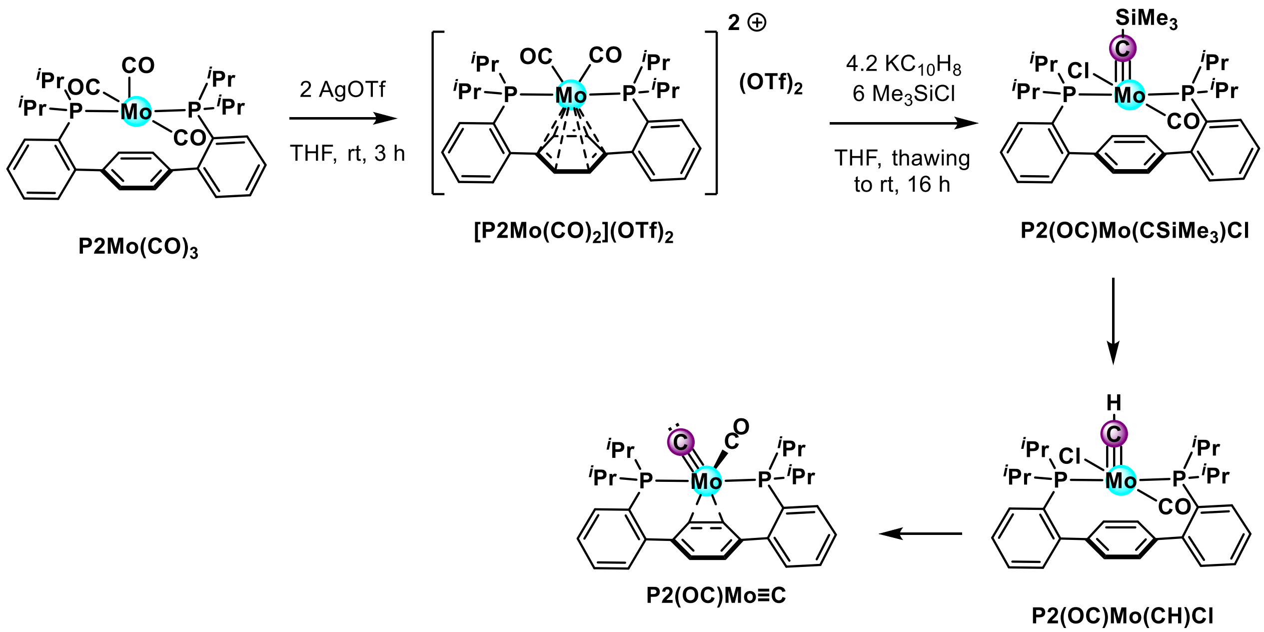

Modified synthesis of **[P2Mo(CO)₂](OTf)₂**. In a glovebox, **P2Mo(CO)₃** (prepared as previously described)[51] (2.94 g, 4.57 mmol, 1 equiv) was dissolved in THF (150 mL) in a Schlenk tube to form an orange solution. AgOTf (2.46 g, 9.60 mmol, 2.1 equiv) was dissolved in THF (50 mL) and added to the tube, and the reaction was stirred at room temperature for 3 h. The light brown solid was collected by filtration and washed with THF (100 mL). Then, MeCN (250 mL) was added in portions to dissolve the crude product and collected by filtration until the filtrate is no longer colored. The dark yellow/brown solution was concentrated in vacuo to about half of the original volume, after which about 2 times the volume of Et_2O was added to precipitate the product as a bright yellow microcrystalline solid. The product was collected by filtration, washed with Et_2O, and dried under vacuum. Yield: 3.62 g (87%). NMR data are identical to previously reported samples.[51]

Modified synthesis of **P2(OC)Mo(CSiMe₃)Cl**. In a glovebox, **[P2Mo(CO)₂](OTf)₂** (2.62 g, 2.87 mmol, 1 equiv) was suspended in THF (70 mL) with a pre-reduced Teflon stir bar and frozen in liquid N_2 in a cold well. To the thawing reaction was added $KC_{10}H_8$ (4.2 equiv, prepared by stirring 0.47 g K with 1.55 g naphthalene in 30 mL THF for 1 h) with stirring. The solution quickly becomes dark red/orange. Stirring was continued for about 10 min until the flask warmed to room temperature, after which it was frozen again in the cold well. To the thawing reaction was added a thawing solution of excess Me_3SiCl (1.87 g, 17.22 mmol, 6 equiv) dissolved in THF (5 mL) with stirring. The reaction was allowed to stir for 16 h at room temperature inside the glovebox, after which the volatiles were removed *in vacuo* to yield a red/orange powder. The powder was triturated in hexanes 2 times and washed with pentane until the washing was colorless to remove an orange impurity. The remaining red solid was washed with HMDSO (10 mL), then extracted into C_6H_6 and lyophilized to give **P2(OC)Mo(CSiMe$_3$)Cl**. Yield: 1.39 g (69%). NMR data are identical to previously reported samples.[38]

The subsequent species **P2(OC)Mo(CH)Cl** and **P2(OC)Mo≡C** were prepared as previously reported.[39]

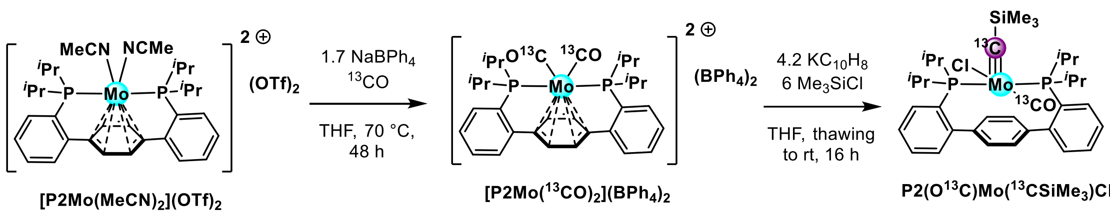

Modified synthesis of **[P2Mo(^{13}CO)$_2$]$^{2+}$**. The procedure was modified from a reported protocol.[38] In a glovebox, **[P2Mo(MeCN)$_2$](OTf)$_2$** (prepared as previously described)[51] (952 mg, 1.01 mmol, 1 equiv) and $NaBPh_4$ (590 mg, 1.72 mmol, 1.70 equiv) were added to THF (40 mL) in a 200 mL Schlenk tube to form a dark purple suspension. The tube was capped tightly, taken out of the box and degassed by 3 cycles of freeze-pump-thaw on the Schlenk line and immersed in liquid N_2. On a high vacuum line with a mercury manometer, ^{13}CO (0.17 atm = 130 mmHg) was admitted to the tube. The reaction was sealed and allowed to warm to room temperature (resulting in ^{13}CO pressure of 0.68 atm), then heated at 70 °C with stirring for 48 h. After this period, a copious amount of light yellow precipitate formed, with an orange solution. The tube was cooled and brought into the glovebox. The solid was collected by filtration, washed with THF, then redissolved in MeCN and filtered again. The MeCN solution was concentrated *in vacuo* until some solid forms, then 2 – 3 times the volume of Et_2O was added to precipitate the product **[P2Mo(^{13}CO)$_2$](BPh$_4$)$_2$** as a yellow solid. The solid was collected, washed with Et_2O, and dried under vacuum. Yield: 633 mg (50%). The ^{31}P NMR data are identical to previously reported samples,[38] while the ^{1}H NMR data show slight shifts.[51] ^{1}H NMR (300 MHz, CD_3CN) δ 7.87 (m, 2H, aryl-*H*), 7.78 (m, 2H, aryl-*H*), 7.67 (m, 2H, aryl-*H*), 7.28 (m, 8H, BPh_4 aryl-*H*), 7.01 (m, 12H, BPh_4 aryl-*H* and central arene-*H*), 6.86 (m, 4 H, BPh_4 aryl-*H*), 3.27 (m, 4H, C*H*(CH_3)$_2$), 1.29 – 1.44 (m, 24H, CH(C*H*$_3$)$_2$).

Modified synthesis of **P2(O^{13}C)Mo(^{13}CSiMe$_3$)Cl**. In a glovebox, **[P2Mo(^{13}CO)$_2$](BPh$_4$)$_2$** (150 mg, 0.120 mmol, 1 equiv) was suspended in THF (3 mL) with a pre-reduced Teflon stir bar and frozen in liquid N_2 in a cold well. To the thawing reaction was added $KC_{10}H_8$ (4.2 equiv, prepared by stirring 19.6 mg K with 64.3 mg naphthalene in 2 mL THF for 1 h) with stirring. The reaction quickly becomes dark red/orange with a large amount of white insoluble solid, assigned as $KBPh_4$. An additional 5 mL THF was added to break up the insoluble clumps and stirring was continued for about 10 min until the vial warmed to room temperature, after which it was frozen again in the cold well. To the thawing reaction was added a thawing solution of excess Me_3SiCl (91 mg, 0.72 mmol, 6 equiv) dissolved in THF (5 mL) with stirring. The reaction was allowed to stir at room temperature for 16 h inside the glovebox. Then, it was filtered to remove the white solid, after which the volatiles were removed *in vacuo* to yield a red/orange powder. The powder was triturated in hexanes 2 times and washed with pentane until the washing was colorless to remove an orange impurity. The remaining red solid was washed with HMDSO (1 mL), then extracted into C_6H_6 and lyophilized to give **P2(O^{13}C)Mo(^{13}CSiMe$_3$)Cl**. Yield: 50.6 mg (60%). NMR data are identical to previously reported samples.[38]

The selectively labeled complex **P2(O^{13}C)Mo≡C** was prepared *in situ* from **P2(O^{13}C)Mo(CH)Cl**, which was in turn prepared from **P2(O^{13}C)Mo(CSiMe$_3$)Cl** provided by Tianyi He using the reported route.[39] The ^{1}H NMR spectrum of **P2(O^{13}C)Mo(CH)Cl** (Figure 4.S12) shows a quartet instead of triplet (seen in the natural abundance version) or a doublet of triplet (seen in **P2(O^{13}C)Mo(^{13}CH)Cl**) for the methylidyne proton, while the ^{31}P NMR spectrum (Figure 4.S13) shows a triplet instead of a singlet (seen in the natural abundance version) or a doublet of doublet (seen in **P2(O^{13}C)Mo(^{13}CH)Cl**).

3. NMR spectra:

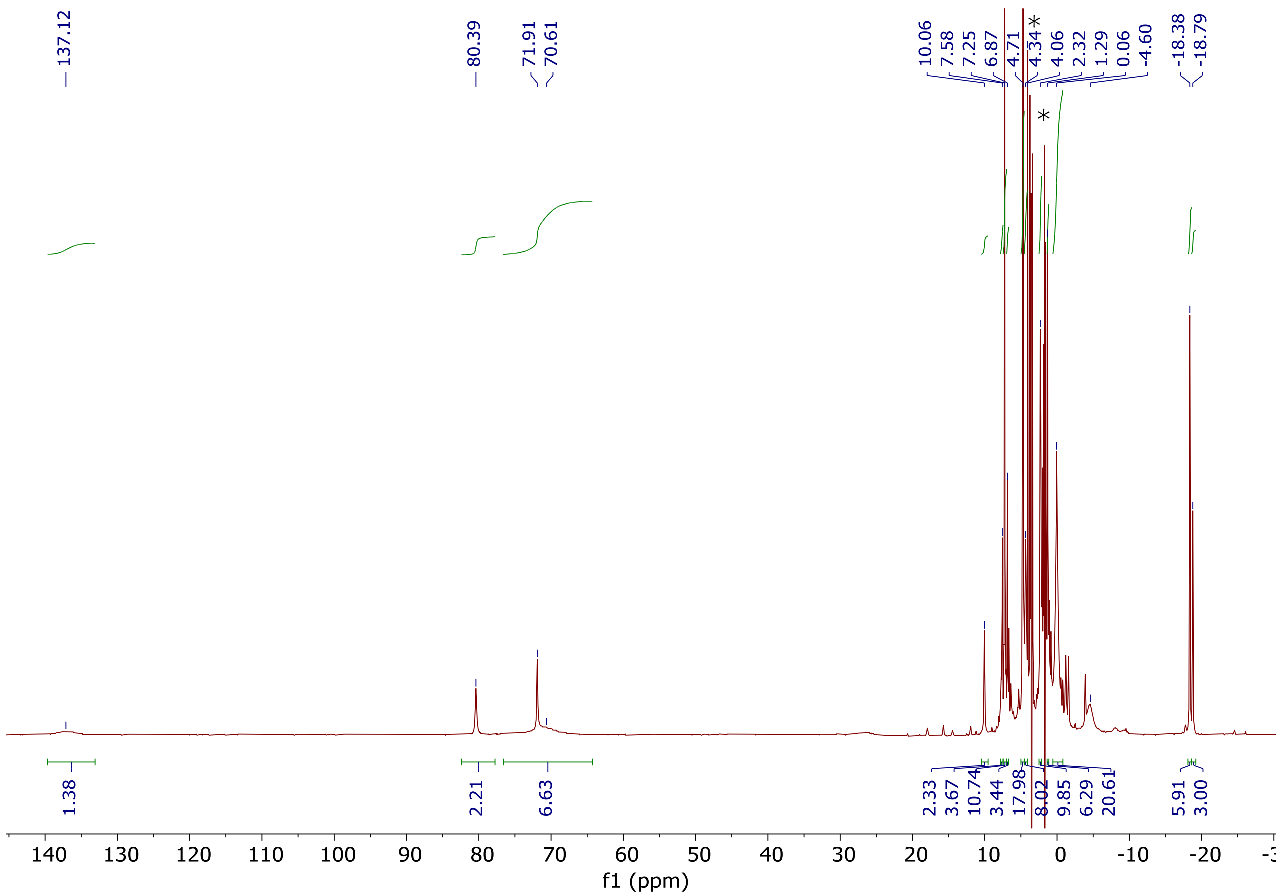

Figure 4.S1. ^{1}H NMR spectrum (400 MHz, THF-h_8, solvent suppression) of **4.2**. Solvent peaks are indicated by asterisks (*).

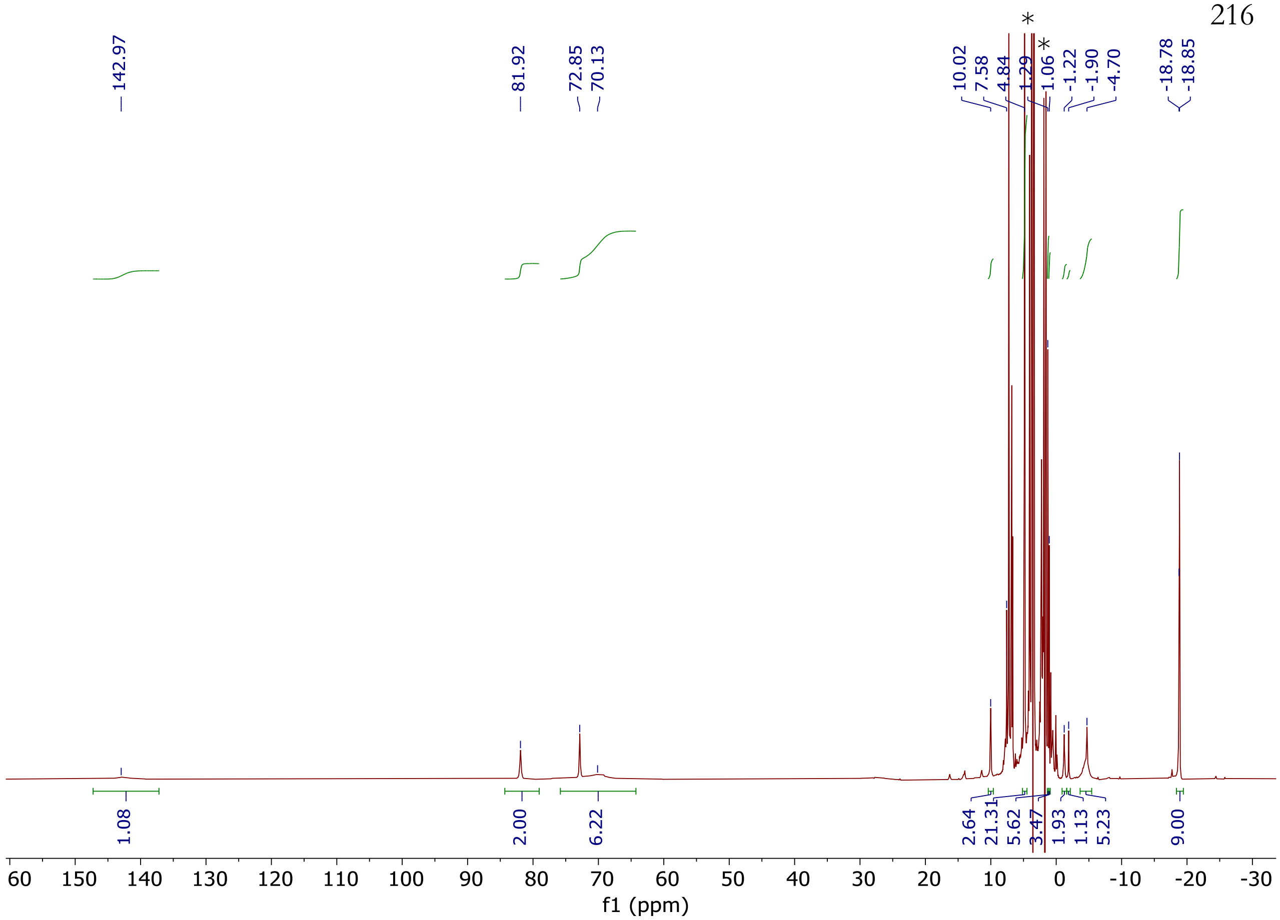

Figure 4.S2. ^{1}H NMR spectrum (400 MHz, THF-h_8, solvent suppression) of **4.3**. Solvent peaks are indicated by asterisks (*).

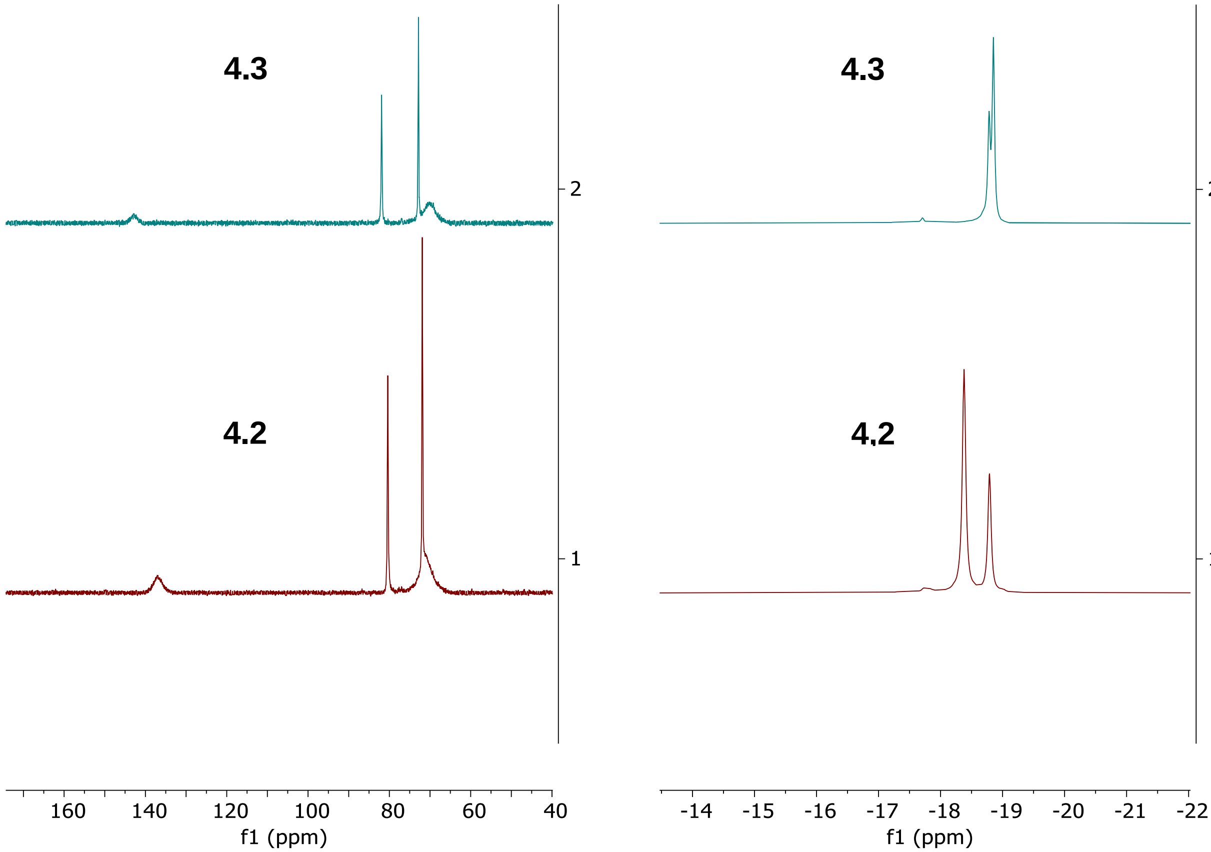

Figure 4.S3. Comparison of [1]H NMR spectra (400 MHz, THF-h_8, solvent suppression) showing the shifts in the diagnostic peaks between **4.2** and **4.3**.

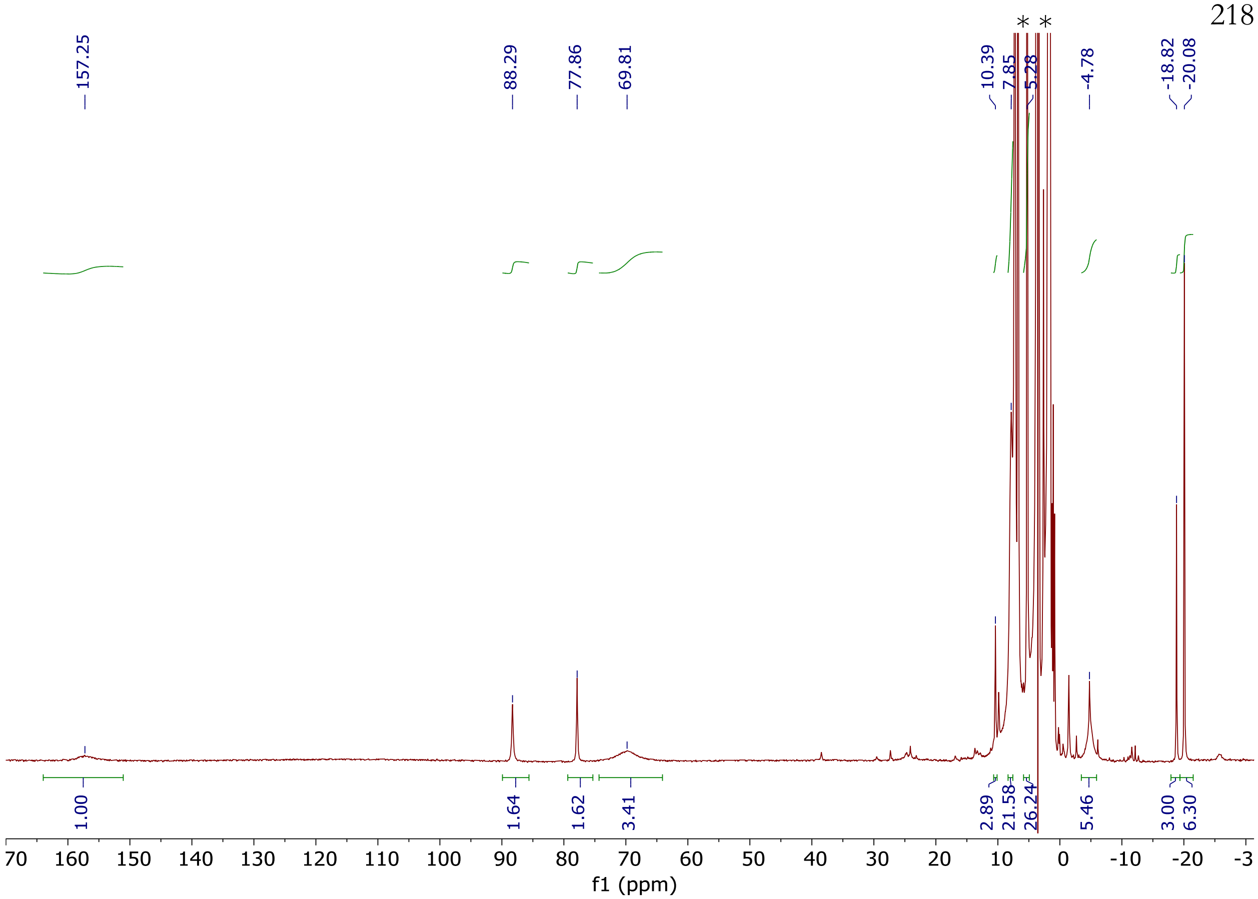

Figure 4.S4. ^{1}H NMR spectrum (400 MHz, THF-h_8, solvent suppression) of crude **4.4**, Ph_2MePCH_2 variant. Solvent peaks are indicated by asterisks (*).

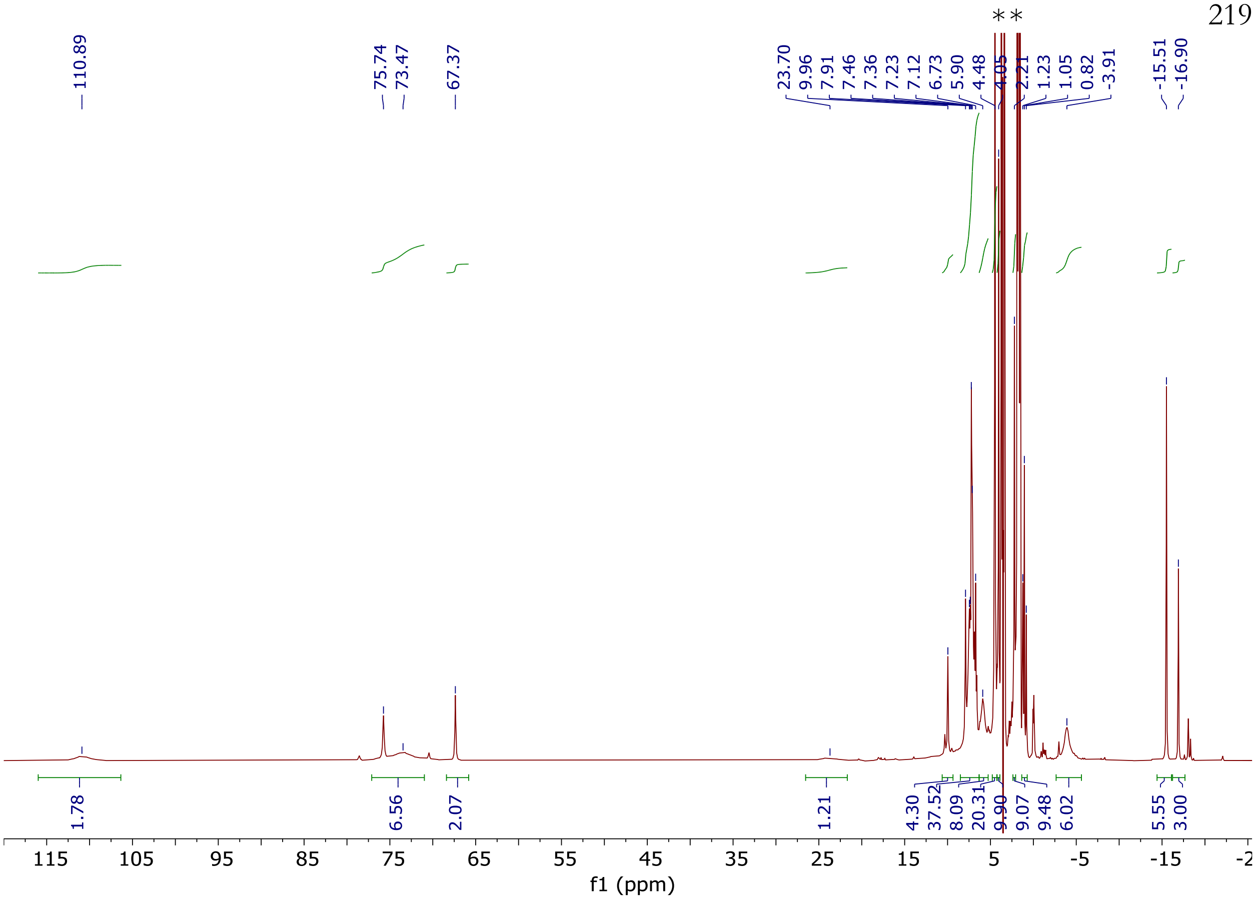

Figure 4.S5. ^{1}H NMR spectrum (400 MHz, THF-h_8, solvent suppression) of crude **4.4**, Ph_3PCH_2 variant. Solvent peaks are indicated by asterisks (*).

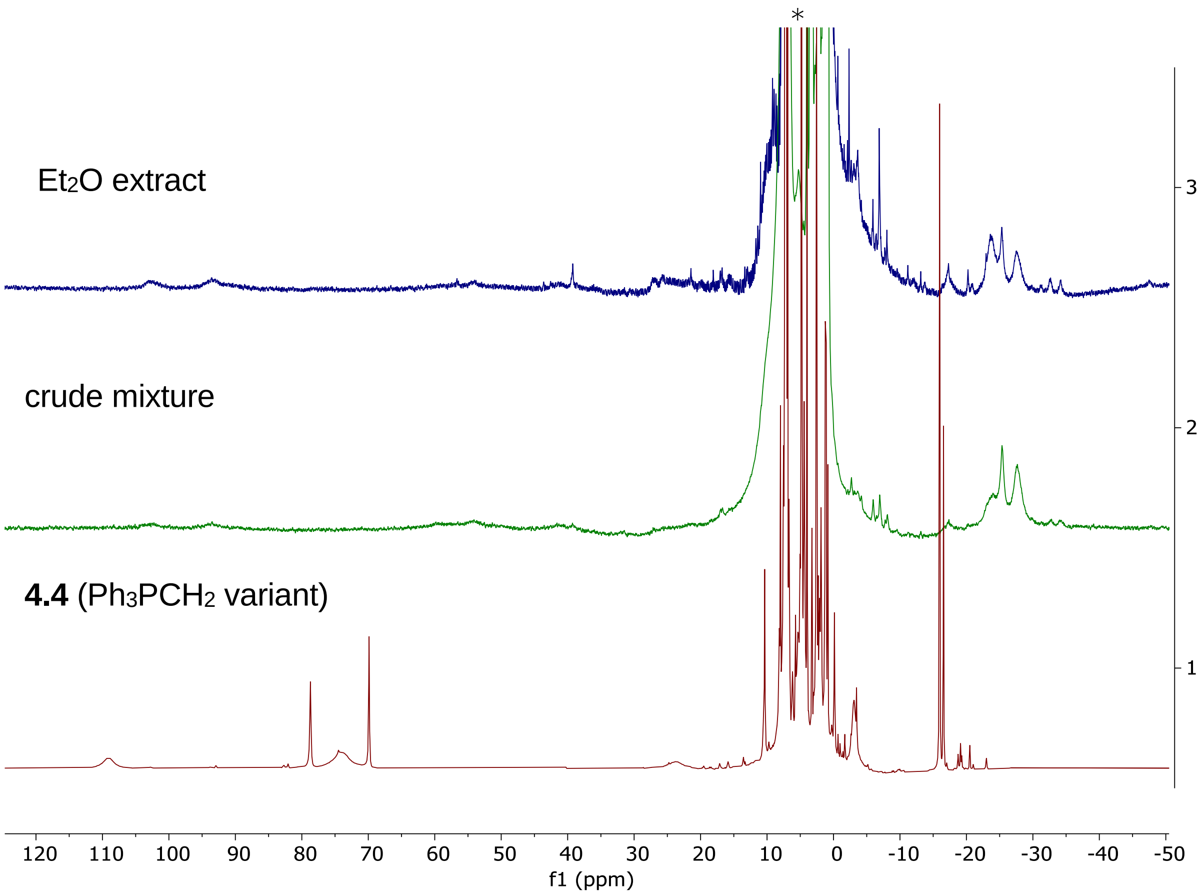

Figure 4.S6. ^{1}H NMR spectra (400 MHz, C_6H_6, solvent suppression) of crude **4.4** (Ph_3PCH_2 variant) (bottom), crude reaction mixture with KC_8 (middle), and Et_2O extract (top). Solvent peaks are indicated by asterisks (*).

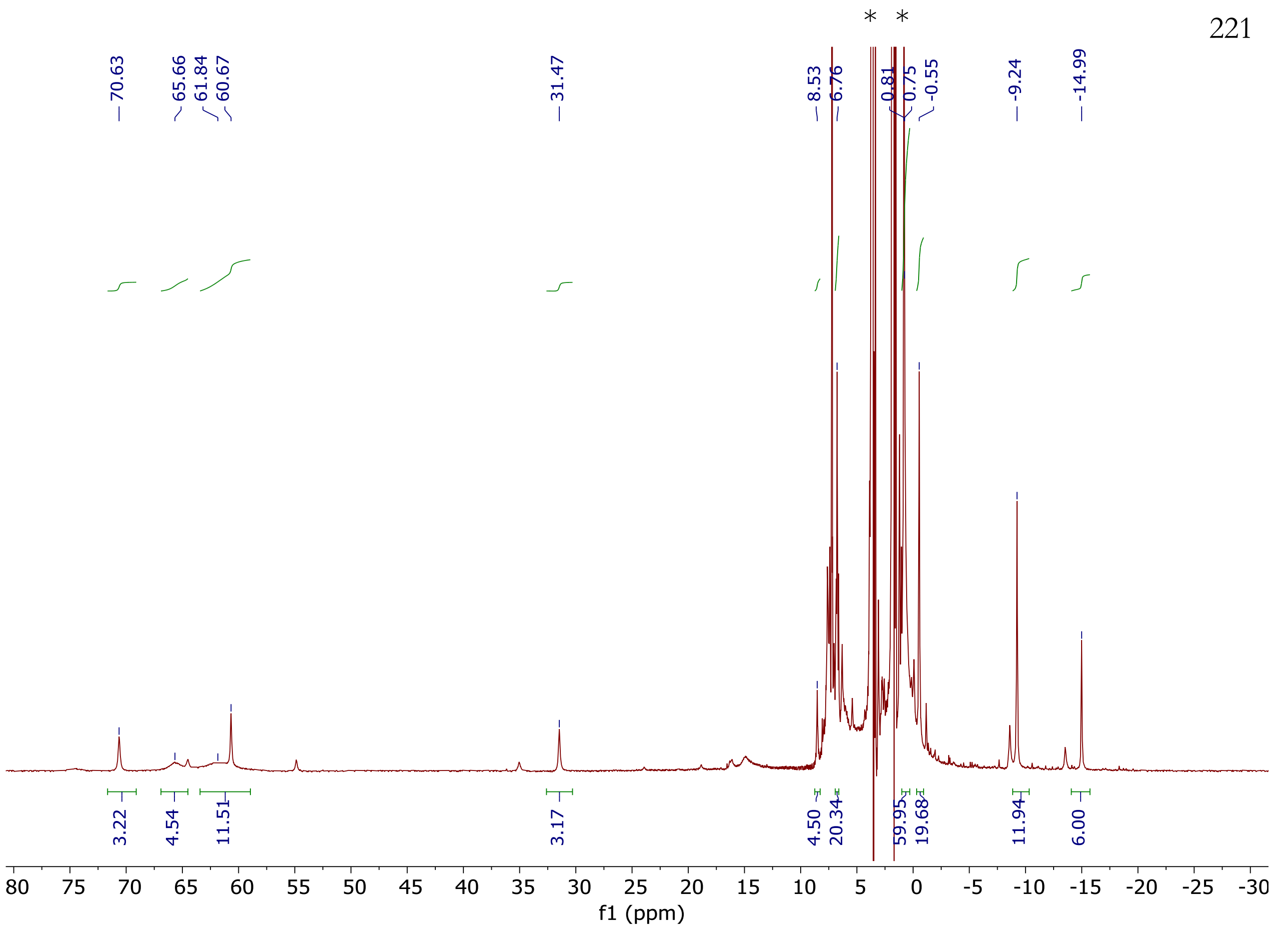

Figure 4.S7. ^{1}H NMR spectrum (400 MHz, THF-h_8, solvent suppression) of crude **4.6**. Solvent peaks are indicated by asterisks (*).

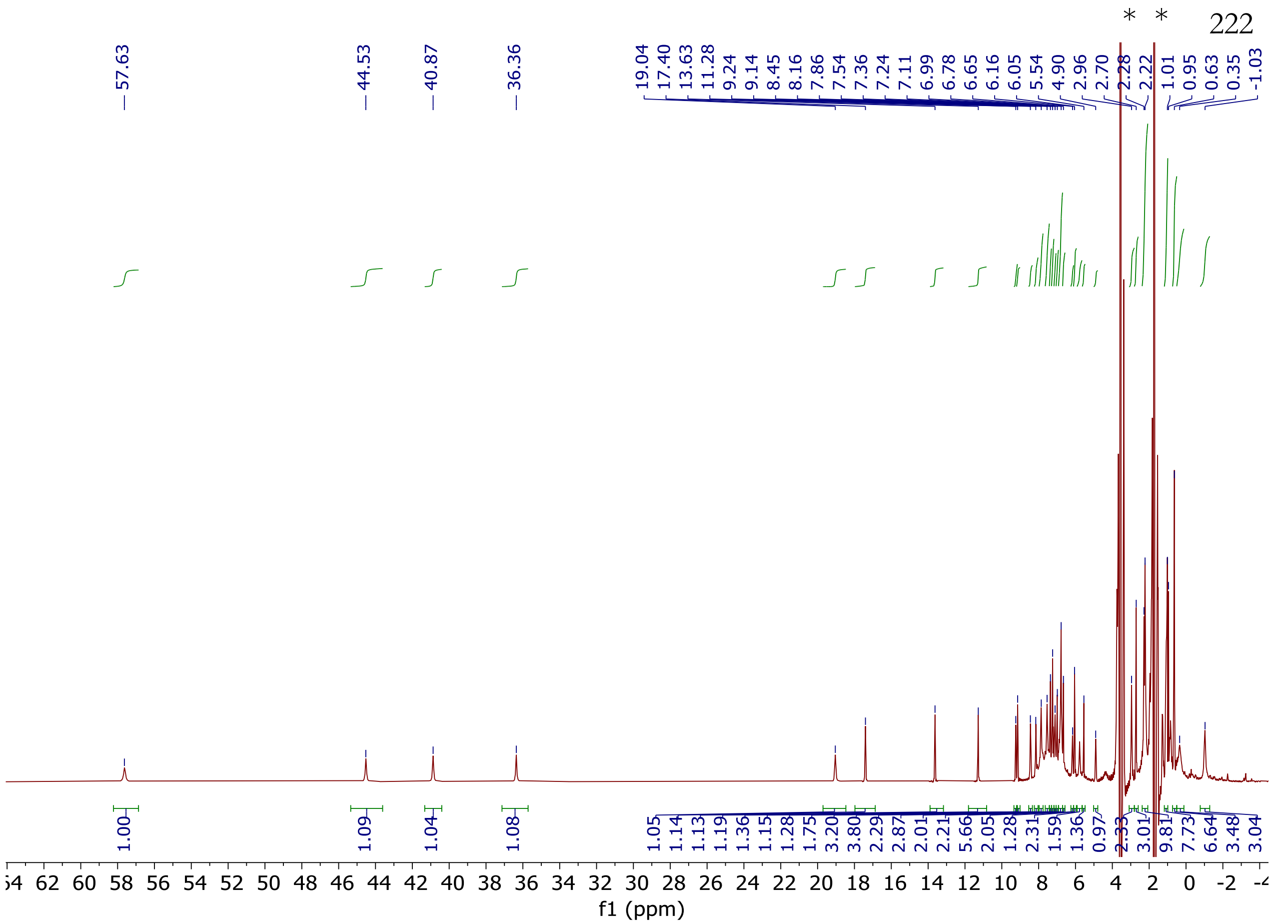

Figure 4.S8. ^{1}H NMR spectrum (400 MHz, THF-h_8, solvent suppression) of **4.7**. Solvent peaks are indicated by asterisks (*).

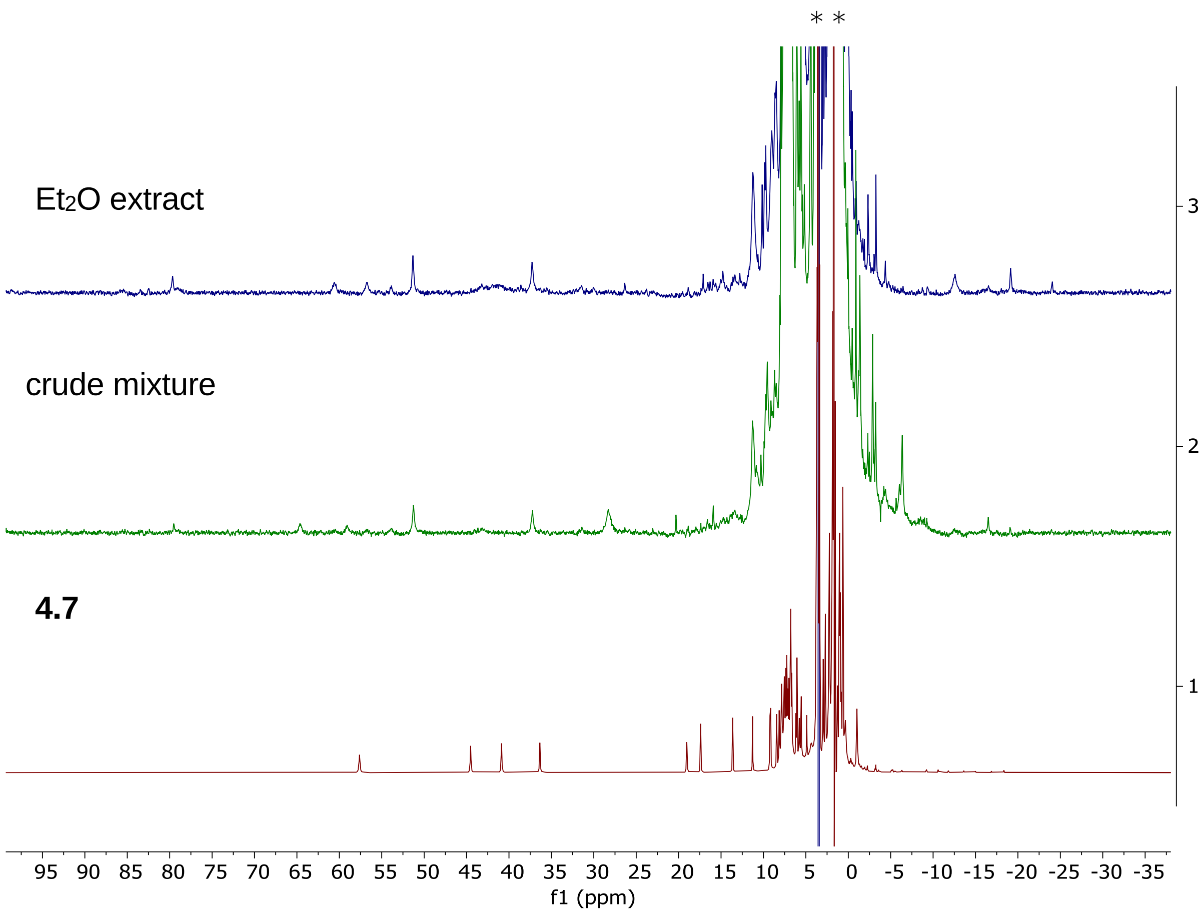

Figure 4.S9. ^{1}H NMR spectra (400 MHz, THF-h_8, solvent suppression) of **4.7** (bottom), crude reaction mixture with I_2 (middle), and Et_2O extract (top). Solvent peaks are indicated by asterisks (*).

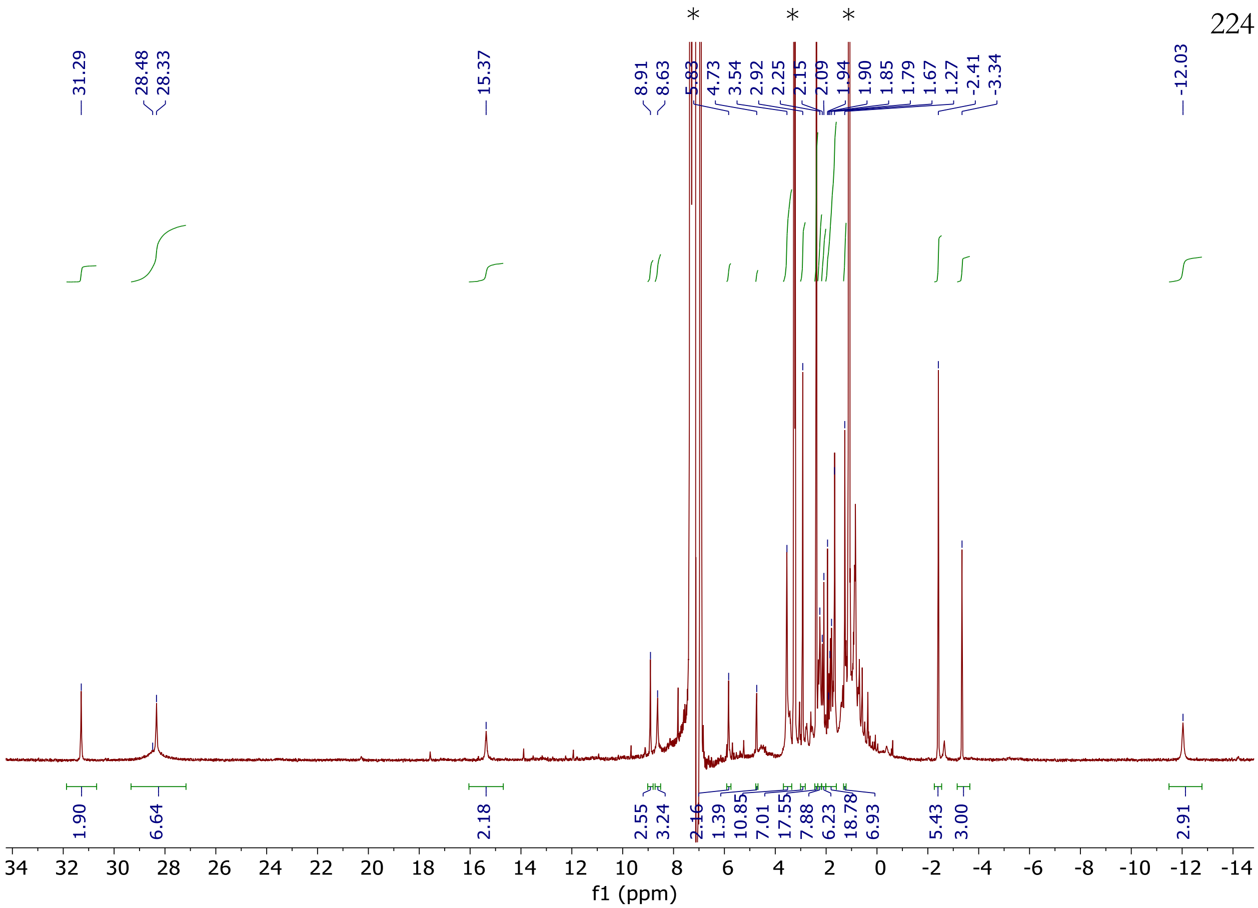

Figure 4.S10. ^{1}H NMR spectrum (400 MHz, C_6H_6, solvent suppression) of crude **4.9**. Solvent peaks are indicated by asterisks (*).

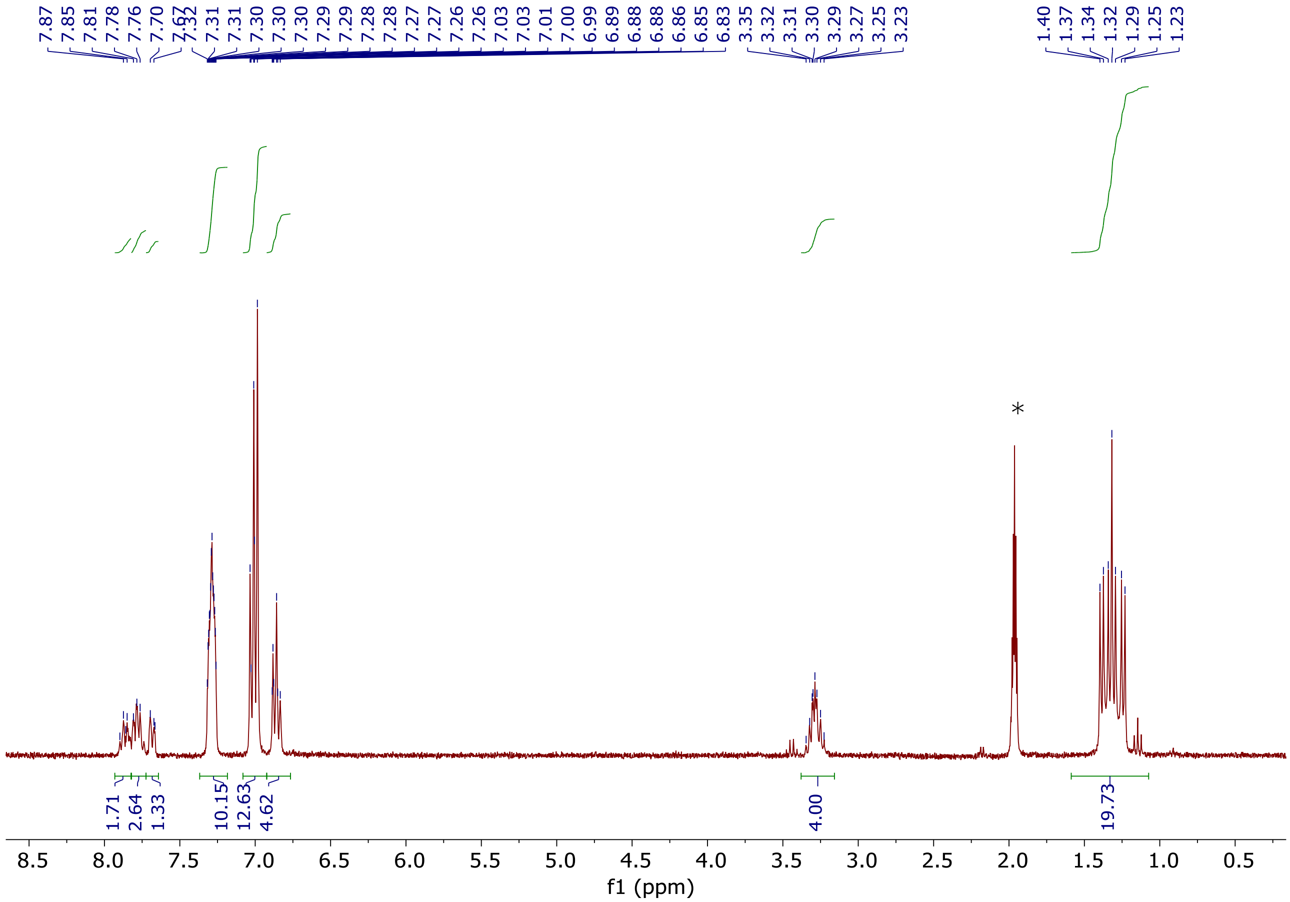

Figure 4.S11. ^{1}H NMR spectrum (300 MHz, CD_3CN) of **[P2Mo(^{13}CO)$_2$](BPh$_4$)$_2$**. Solvent peak is indicated by asterisk (*).

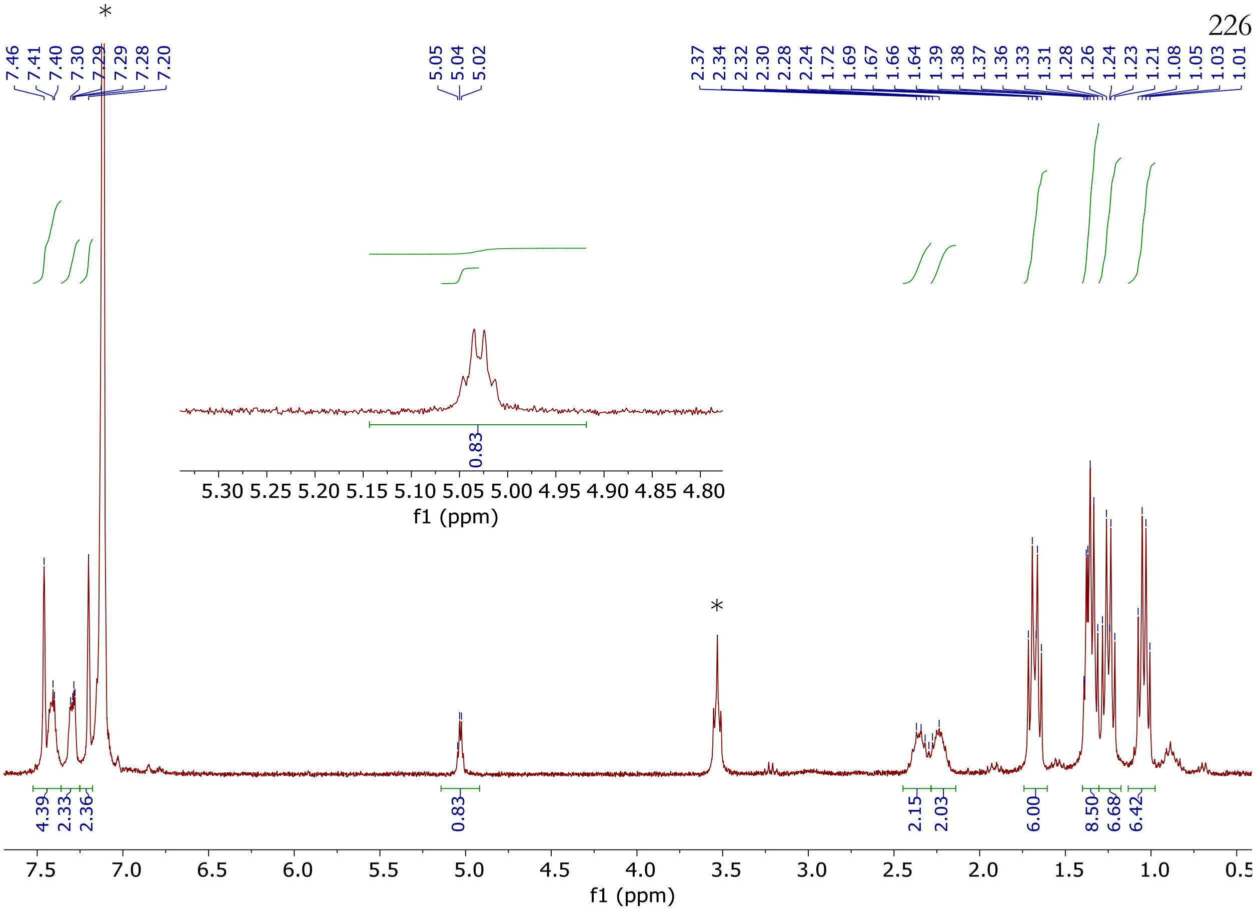

Figure 4.S12. ^{1}H NMR spectrum (300 MHz, C_6D_6) of **P2(O^{13}C)Mo(CH)Cl**, with the methylidyne proton shown in the inset. Solvent peaks are indicated by asterisks (*).

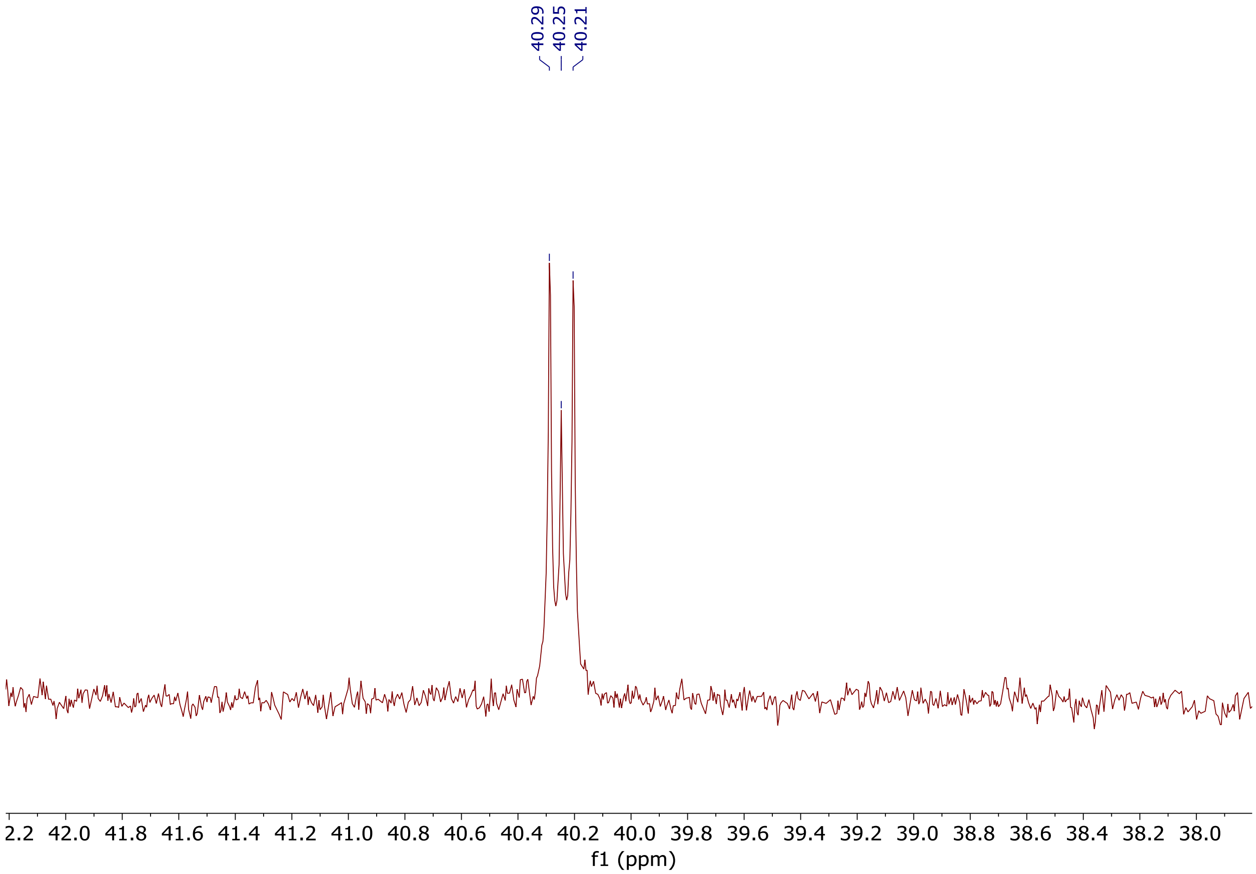

Figure 4.S13. ^{31}P NMR spectrum (121 MHz, C_6D_6) of **P2(O^{13}C)Mo(CH)Cl**.

4. IR spectroscopy:

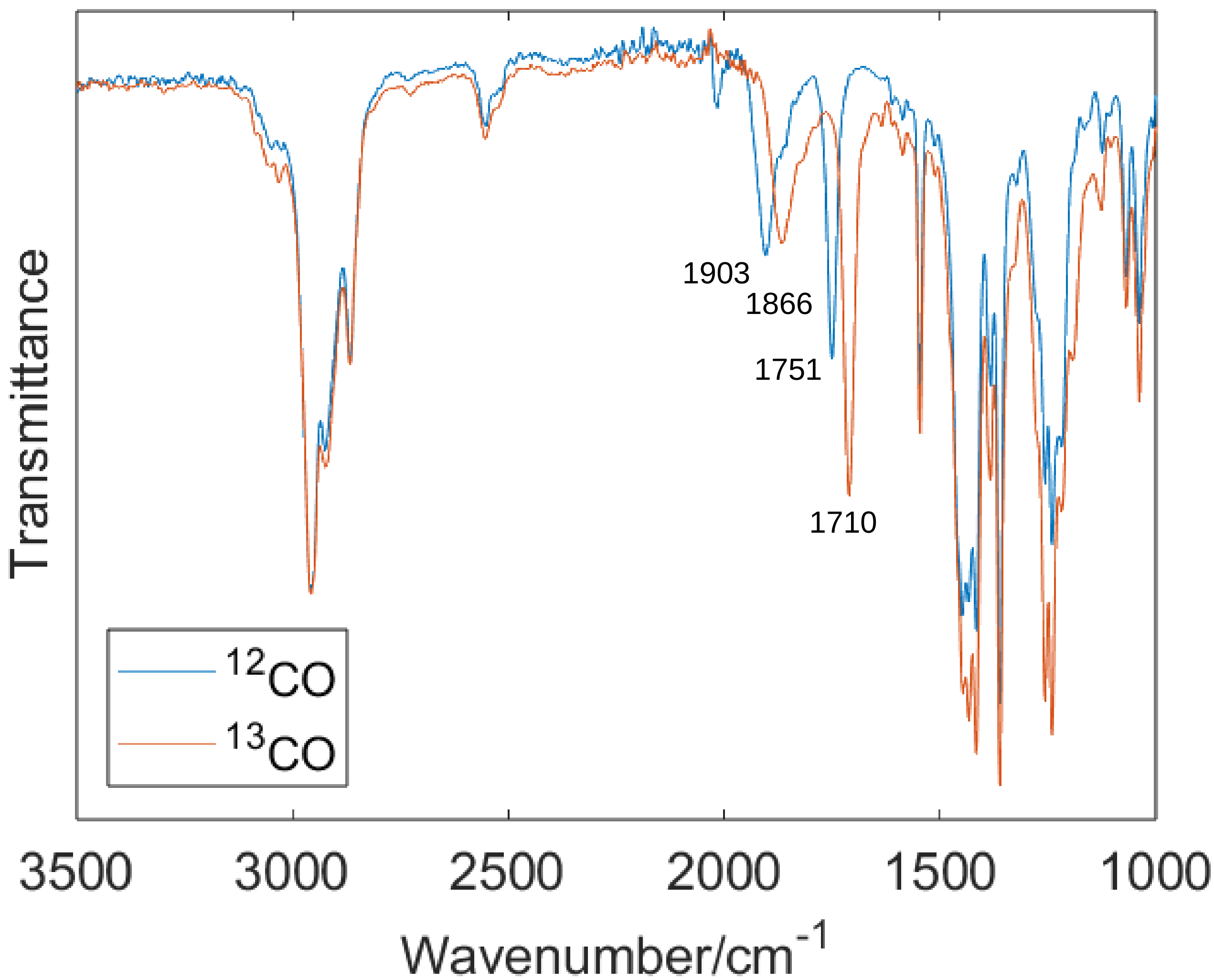

Figure 4.S14. ATR-IR spectra of **4.7** with ^{12}CO and ^{13}CO.

The bridging CO stretch is assigned to the peak at 1751 cm^{-1}, which shifts to 1710 cm^{-1} upon ^{13}C labeling. Another broad peak at 1903 cm^{-1} also shifts to 1866 cm^{-1} upon ^{13}C labeling, which may correspond to a terminal CO ligand. This may suggest a very fast isomerization process that is not resolved by NMR spectroscopy or X-ray crystallography, where the CO ligand moves between a bridging position between Fe and Mo and a terminal position to Mo, with a possible η^2 interaction with Fe. Some CO complexes have been shown to be fluxional even in the solid state,[57] and in this case the interconversion between the two forms only involves a vibration along the Fe-C vector.

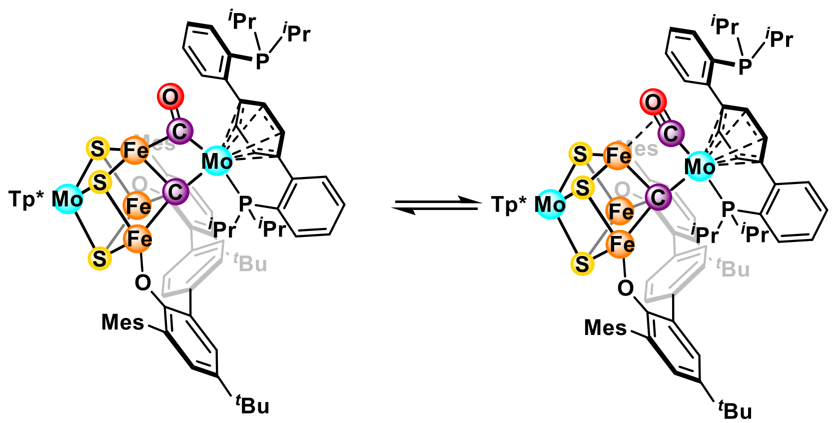

5. EPR spectroscopy:

Samples were prepared as solutions (c.a. 2 mM) in PhMe and rapidly cooled in liquid nitrogen to form a frozen glass. All X-band and Q-band EPR experiments presented in this study were acquired at the Caltech EPR facility. X-band CW EPR spectra were acquired on a Bruker (Billerica, MA) EMX spectrometer using Bruker Xenon software (ver. 1.2). Temperature control was achieved using liquid helium and an Oxford Instruments (Oxford, UK) ESR-900 cryogen flow cryostat and an ITC-503 temperature controller. Pulse EPR and electron nuclear double resonance (ENDOR) experiments were acquired using a Bruker ELEXSYS E580 pulse EPR spectrometer using a Bruker D2 pulse ENDOR resonator for Q-band experiments. Temperature control was achieved using an Oxford Instruments CF-935 helium flow cryostat and a Mercury ITC temperature controller. Spectra were simulated using EasySpin5 (release 5.2.36) with Matlab R2020b. Acquisition parameters for Q-band Davies ENDOR: pulse sequence π-tRF-πRF-tRF-π/2-τ–π–τ-echo. The frequency of the RF pulse was randomly sampled to minimize nuclear spin saturation. Acquisition parameters for Q-band Mims ENDOR: pulse sequence π/2-τ-π/2- tRF-πRF-tRF-π/2-τ-echo. The frequency of the RF pulse was randomly sampled to minimize nuclear spin saturation.

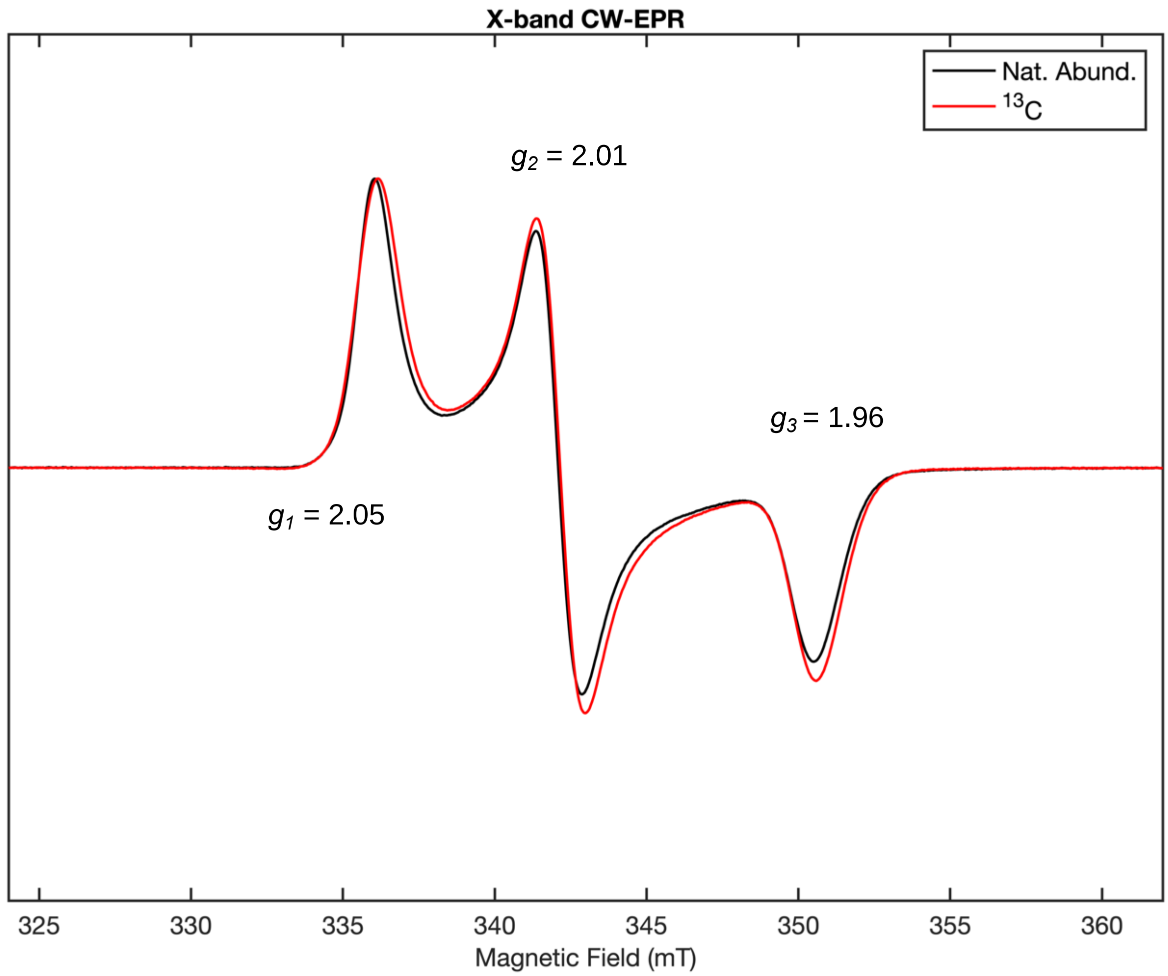

Figure 4.S15. X-band CW-EPR of **4.7** (black) and **4.7-^{13}C,^{13}CO** (red) at 15 K in a frozen toluene glass. Acquisition parameters: MW frequency: 9.64 GHz; MW power = 35 μW; modulation amplitude: 0.2 mT (**4.7**), 0.8 mT (**4.7-^{13}C,^{13}CO**); conversion time = 10 ms; time constant = 10.24 ms.

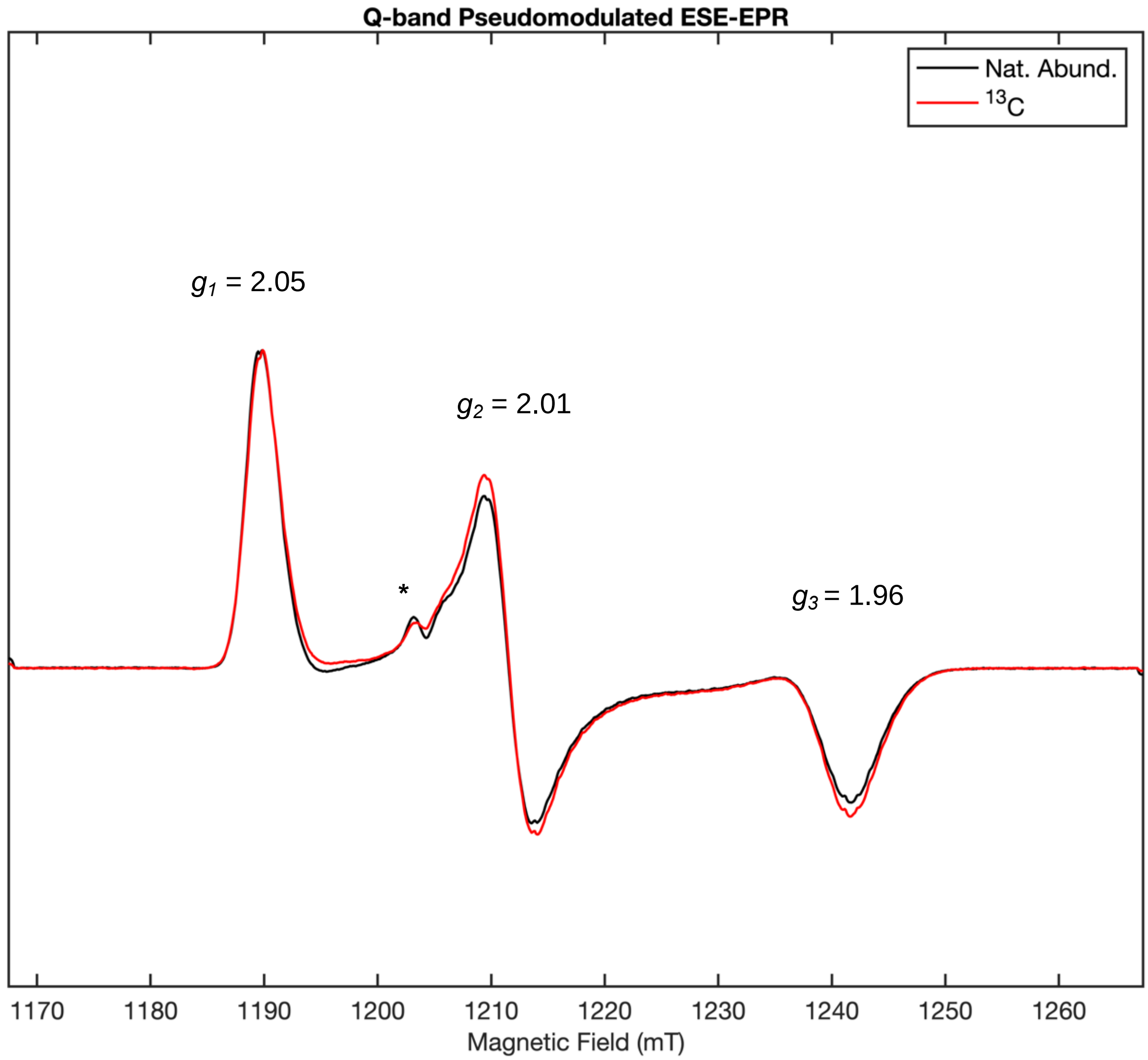

Figure 4.S16. Q-band pseudomodulated ESE-EPR spectra of **4.7** (black) and **4.7-^{13}C,^{13}CO** (red) at 15 K in a frozen toluene glass. Asterisk denotes a background signal in the Q-band resonator; Acquisition parameters: MW frequency = 33.7 GHz (**4.7**) 34.1 GHz (**4.7-^{13}C,^{13}CO**); MW power = 8 mW; pseudomodulation = 1 mT.

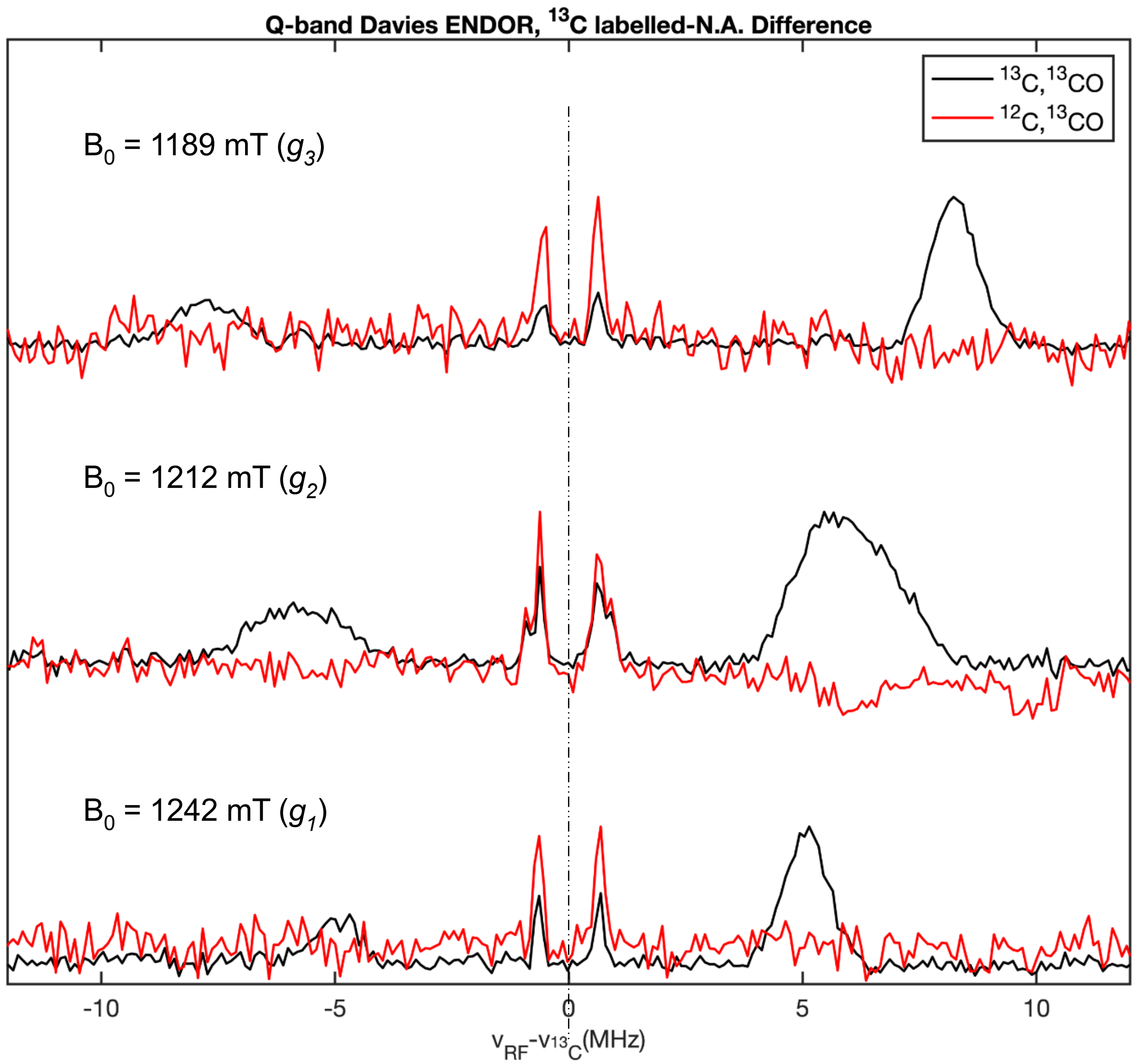

Figure 4.S17. Field-dependent Q-band Davies ENDOR difference spectra of **4.7-^{13}C,^{13}CO** and **4.7-^{13}CO**.

6. Mössbauer spectroscopy:

Zero field ^{57}Fe Mössbauer spectra were recorded in constant acceleration at 80 K on a spectrometer from See Co (Edina, MN) equipped with an SVT-400 cryostat (Janis, Woburn, MA). The quoted isomer shifts are relative to the centroid of the spectrum of α-Fe foil at room temperature. Samples were ground with boron nitride into a fine powder and transferred to a Delrin cup. The data were fit to Lorentzian lineshapes using the program WMOSS (www.wmoss.org).

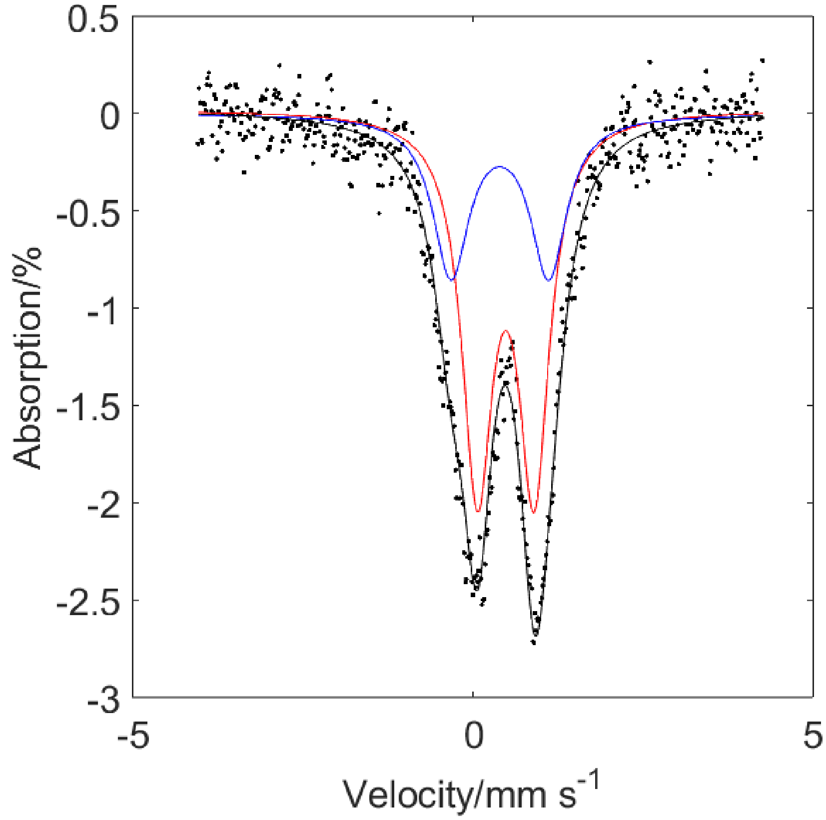

Figure 4.S18. Fitting for the Mössbauer spectrum of **4.7** (80 K, no applied field) using a two-site model, with the total fit shown by the black trace.

The Mössbauer spectrum of **4.7** can be fit with a two-site model using the following parameters:

Site 1: δ = 0.482 mm s^{-1} $|E_Q|$ = 0.833 mm s^{-1} Linewidth = 0.547 mm s^{-1} Area = 66%

Site 2: δ = 0.396 mm s^{-1} $|E_Q|$ = 1.435 mm s^{-1} Linewidth = 0.644 mm s^{-1} Area = 34%

B) Crystallographic information

1. X-ray crystallography:

XRD data were collected at 100 K on a Bruker AXS D8 VENTURE diffractometer [microfocus sealed X-ray tube, λ(Cu Kα) = 1.54178 Å]. All manipulations, including data collection, integration, and scaling, were carried out using the Bruker *APEX3* software.[58] Absorption corrections were applied using *SADABS*.[59] Structures were solved by direct methods using *Sir92*[60] or *SUPERFLIP*[61] and refined using full-matrix least-squares on *CRYSTALS*[62] to convergence. All non-H atoms were refined using anisotropic displacement parameters. H atoms were placed in idealized positions and refined using a riding model. Because of the size of the compounds some crystals included solvent-accessible voids that contained disordered solvent, which could be modeled satisfactorily.

2. *Additional information:*

Special refinement details for **4.4** (Ph_2MePCH_2 variant). The asymmetric unit of the structure contains one co-crystallized pentane solvent molecule, which can be modeled satisfactorily using bond lengths and similarity restraints for anisotropic displacement parameters (ADPs). The remaining solvent molecules are heavily disordered and cannot be modeled satisfactorily. Therefore, the electron density for co-crystallized solvent molecules were accounted for using the *SQUEEZE* procedure in *PLATON*,[63] whereby 530 electrons were found in a volume of 2665 Å^3, consistent with the presence of 1.5[$C_4H_{10}O$] in the asymmetric unit. One Ph group of the Ph_2MePCH_2 ligand is disordered over two positions, with occupancies of 49% and 51%, and one ^{t}Bu group is disordered over two positions, with occupancies of 31% and 69%.

Special refinement details for **4.5**. The asymmetric unit of the structure contains four co-crystallized Et_2O solvent molecules, which can be modeled satisfactorily using bond lengths and similarity restraints for ADPs.

Special refinement details for **4.6**. The asymmetric unit of the structure contains 2.5 co-crystallized C_6H_6 solvent molecules, which can be modeled satisfactorily using bond lengths and similarity restraints for ADPs. One Mes group is disordered over two positions, with occupancies of 45% and 55%.

Special refinement details for **4.7**. The asymmetric unit of the structure contains three co-crystallized pentane solvent molecules, which can be modeled satisfactorily using bond lengths and similarity restraints for ADPs.

Special refinement details for **4.9**. The asymmetric unit of the structure contains two co-crystallized pentane solvent molecules, which can be modeled satisfactorily without restraints.

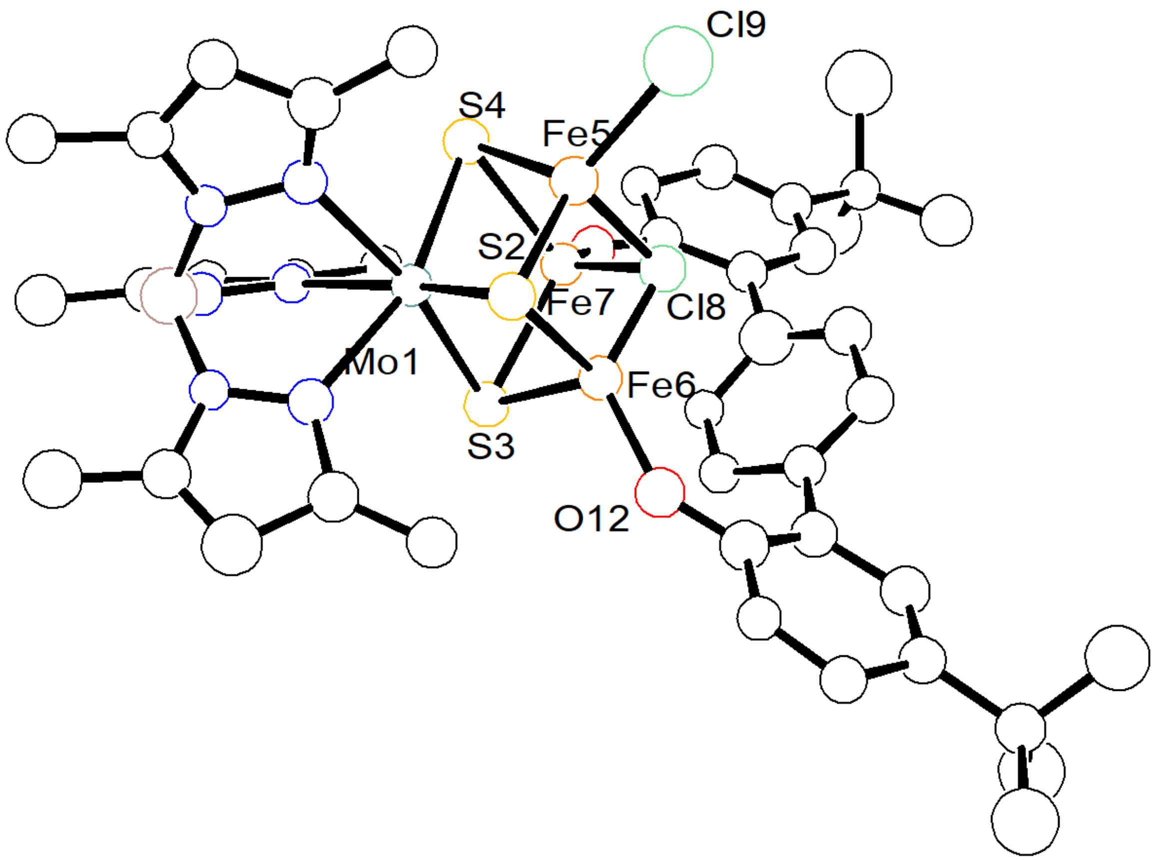

Figure 4.S19. Connectivity of **4.2** to confirm the binding of the bisphenoxide ligand. Spheres are shown at 50% probability level. Hydrogen atoms, solvent molecules, counterions, and part of the bisphenoxide ligand are omitted for clarity.

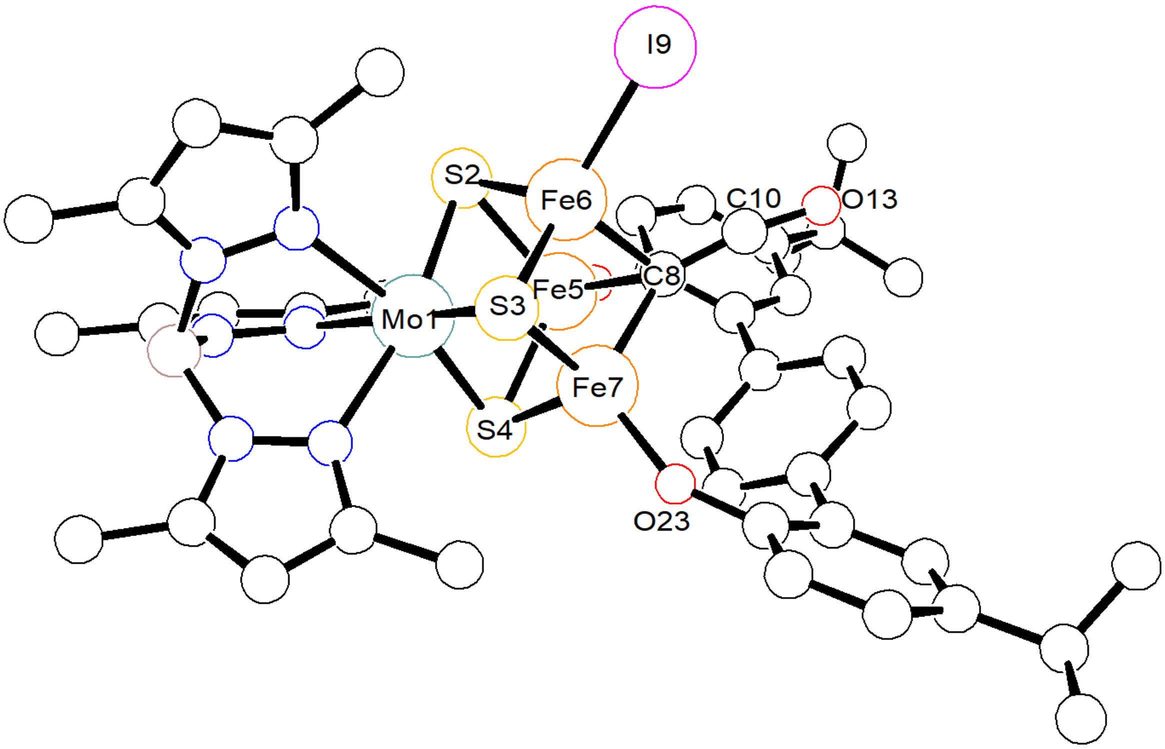

Figure 4.S20. Connectivity of **4.8**. Spheres are shown at 50% probability level. Hydrogen atoms, solvent molecules, and part of the bisphenoxide ligand are omitted for clarity.

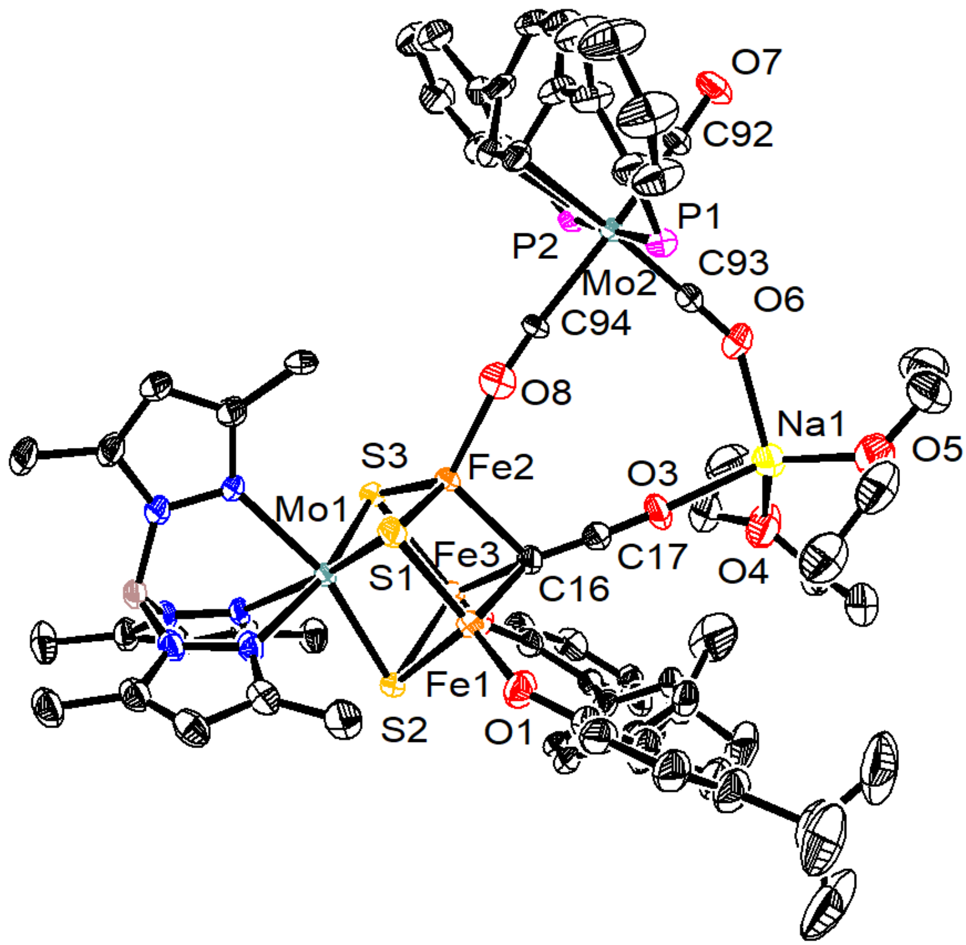

Figure 4.S21. Crystal structures of **4.9**. Ellipsoids are shown at 50% probability level. Hydrogen atoms, solvent molecules, and part of the bisphenoxide and the phosphine ligands are omitted for clarity.

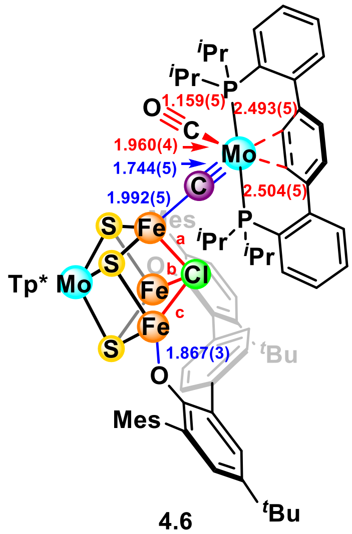

a = 2.454(1)
b = 2.439(1)
c = 2.430(1)

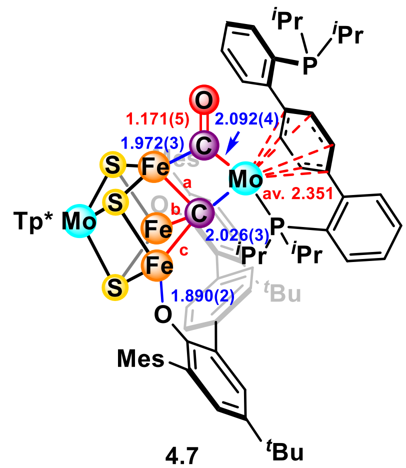

a = 1.869(3)
b = 1.975(3)
c = 2.028(4)

Figure 4.S22. Bond length comparisons in Å for **4.6** and **4.7** for selected bonds. The abbreviations a, b, and c refer to the three Fe-C(μ_3) distances as labeled in the structures.

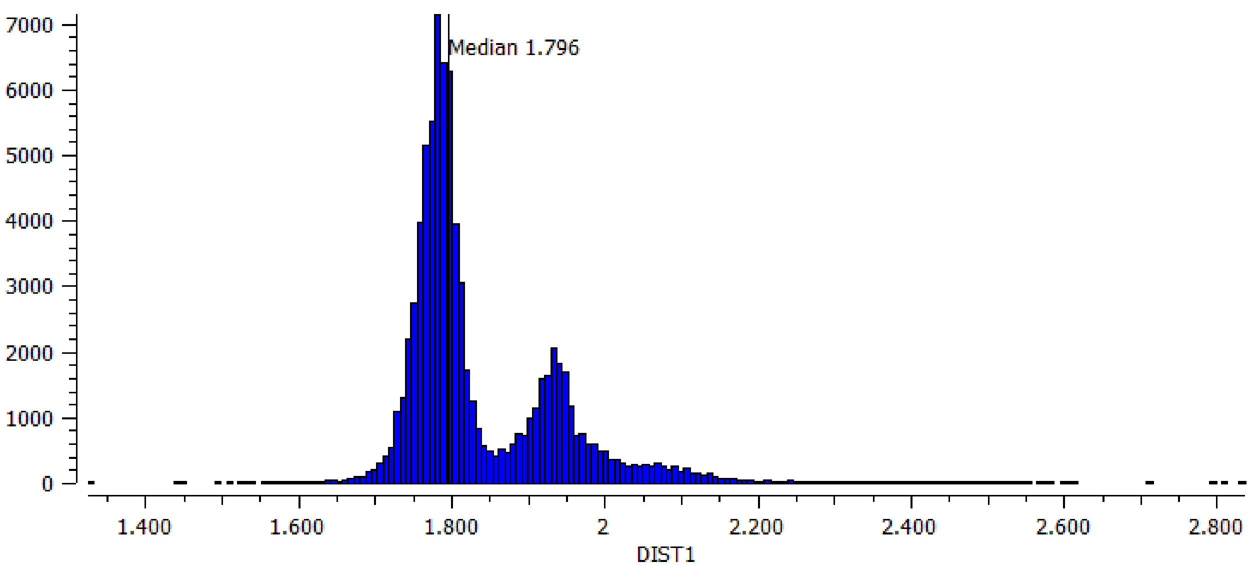

Figure 4.S23. Histogram with Fe-C distances from the Cambridge Structural Database.

Table 4.S1. Summary of statistics for diffraction data for clusters **4.4** (Ph_2MePCH_2 variant) to **4.7** and **4.9**

Cluster	**4.4** (Ph_2MePCH_2)	**4.5**	**4.6**	**4.7**	**4.9**
Empirical formula	$C_{78}H_{97}BClFe_3MoN_6O_2PS_3$	$C_{94}H_{127}BFe_3MoN_6O_6PS_3$	$C_{106}H_{125}BClFe_3Mo_2N_6O_3P_2S_3$	$C_{106}H_{146}BFe_3Mo_2N_6O_3P_2S_3$	$C_{112}H_{154}BFe_3Mo_2N_6NaO_8P_2S_3$
Formula weight	1587.58	1838.54	2095.03	2080.66	2263.87
Temperature/K	100	100	100	100	100
Crystal system	Orthorhombic	Monoclinic	Monoclinic	Triclinic	Monoclinic
Space group	Pbcn	$P2_1/c$	$P2_1/n$	P-1	$P2_1/c$
a/Å	29.475(3)	15.989(5)	15.8008(13)	16.4619(16)	28.323(3)
b/Å	21.6710(18)	26.434(16)	28.085(2)	17.2522(18)	24.751(4)
c/Å	26.861(5)	22.459(14)	23.982(2)	19.6375(19)	16.3335(13)
α/°	90	90	90	93.328(12)	90
β/°	90	92.26(2)	107.099(5)	109.542(11)	91.532(15)
γ/°	90	90	90	90.474(9)	90
Volume/Å^3	17158(4)	9485(9)	10172.0(15)	5244.7(10)	11446(2)
Z	8	4	4	2	4
ρ_{calc}/g cm^{-3}	1.229	1.287	1.368	1.317	1.314
μ/mm^{-1}	6.639	5.855	6.831	6.387	5.965
F(000)	6624.0	3876.0	4356.0	2186.0	4752.0
Crystal size/mm^3	0.07 × 0.18 × 0.20	0.05 × 0.08 × 0.15	0.04 × 0.14 × 0.18	0.03 × 0.05 × 0.17	0.07 × 0.13 × 0.14
Radiation	Cu Kα	Cu Kα	Cu Kα	Cu Kα	Cu Kα
θ_{max}/°	74.765	74.675	74.608	74.671	74.884
Index ranges	$-36 \le h \le 36, -26 \le k \le 27, -30 \le l \le 33$	$-16 \le h \le 19, -33 \le k \le 33, -28 \le l \le 28$	$-19 \le h \le 19, -35 \le k \le 35, -28 \le l \le 29$	$-20 \le h \le 20, -21 \le k \le 21, -24 \le l \le 24$	$-35 \le h \le 35, -30 \le k \le 30, -20 \le l \le 20$
Reflections measured	281021	172055	178784	138427	198169
Independent reflections	17591	19386	20787	21436	23397
Restraints/Parameters	297/957	134/1036	182/1190	76/1135	0/1243
GOF on F^2	1.021	1.021	1.029	0.993	1.003
R-factor	0.1148	0.0831	0.0579	0.0440	0.0529
Weighted R-factor	0.2468	0.2037	0.1435	0.1285	0.1352
Largest diff. peak/hole/e Å^{-3}	2.56/-2.06	1.74/-1.72	1.58/-1.38	1.67/-1.20	2.34/-1.12

4.6 REFERENCES

(1) Spatzal, T.; Aksoyoglu, M.; Zhang, L.; Andrade, S. L. A.; Schleicher, E.; Weber, S.; Rees, D. C.; Einsle, O. Evidence for Interstitial Carbon in Nitrogenase FeMo Cofactor. *Science* **2011**, *334* (6058), 940. https://doi.org/10.1126/science.1214025.

(2) Jasniewski, A. J.; Lee, C. C.; Ribbe, M. W.; Hu, Y. Reactivity, Mechanism, and Assembly of the Alternative Nitrogenases. *Chem. Rev.* **2020**, *120* (12), 5107–5157. https://doi.org/10.1021/acs.chemrev.9b00704.

(3) Eady, R. R. Structure−Function Relationships of Alternative Nitrogenases. *Chem. Rev.* **1996**, *96* (7), 3013–3030. https://doi.org/10.1021/cr950057h.

(4) Rees, J. A.; Bjornsson, R.; Schlesier, J.; Sippel, D.; Einsle, O.; DeBeer, S. The Fe–V Cofactor of Vanadium Nitrogenase Contains an Interstitial Carbon Atom. *Angew. Chem. Int. Ed.* **2015**, *54* (45), 13249–13252. https://doi.org/10.1002/anie.201505930.

(5) Schmidt, F. V.; Schulz, L.; Zarzycki, J.; Prinz, S.; Oehlmann, N. N.; Erb, T. J.; Rebelein, J. G. Structural Insights into the Iron Nitrogenase Complex. *Nat. Struct. Mol. Biol.* **2024**, *31* (1), 150–158. https://doi.org/10.1038/s41594-023-01124-2.

(6) Reinholdt, A.; Bendix, J. Transition Metal Carbide Complexes. *Chem. Rev.* **2022**, *122* (1), 830–902. https://doi.org/10.1021/acs.chemrev.1c00404.

(7) Rittle, J.; Peters, J. C. Fe–N_2/CO Complexes That Model a Possible Role for the Interstitial C Atom of FeMo-Cofactor (FeMoco). *Proc. Natl. Acad. Sci. U.S.A.* **2013**, *110* (40), 15898. https://doi.org/10.1073/pnas.1310153110.

(8) Creutz, S. E.; Peters, J. C. Catalytic Reduction of N_2 to NH_3 by an Fe–N_2 Complex Featuring a C-Atom Anchor. *J. Am. Chem. Soc.* **2014**, *136* (3), 1105–1115. https://doi.org/10.1021/ja4114962.

(9) Čorić, I.; Mercado, B. Q.; Bill, E.; Vinyard, D. J.; Holland, P. L. Binding of Dinitrogen to an Iron–Sulfur–Carbon Site. *Nature* **2015**, *526* (7571), 96–99. https://doi.org/10.1038/nature15246.

(10) Arnett, C. H.; Bogacz, I.; Chatterjee, R.; Yano, J.; Oyala, P. H.; Agapie, T. Mixed-Valent Diiron μ-Carbyne, μ-Hydride Complexes: Implications for Nitrogenase. *J. Am. Chem. Soc.* **2020**, *142* (44), 18795–18813. https://doi.org/10.1021/jacs.0c05920.

(11) Siegbahn, P. E. M. Model Calculations Suggest That the Central Carbon in the FeMo-Cofactor of Nitrogenase Becomes Protonated in the Process of Nitrogen Fixation. *J. Am. Chem. Soc.* **2016**, *138* (33), 10485–10495. https://doi.org/10.1021/jacs.6b03846.

(12) Pérez-González, A.; Yang, Z.-Y.; Lukoyanov, D. A.; Dean, D. R.; Seefeldt, L. C.; Hoffman, B. M. Exploring the Role of the Central Carbide of the Nitrogenase Active-Site FeMo-Cofactor through Targeted ^{13}C Labeling and ENDOR Spectroscopy. *J. Am. Chem. Soc.* **2021**, *143* (24), 9183–9190. https://doi.org/10.1021/jacs.1c04152.

(13) Lukoyanov, D. A.; Yang, Z.-Y.; Pérez-González, A.; Raugei, S.; Dean, D. R.; Seefeldt, L. C.; Hoffman, B. M. ^{13}C ENDOR Characterization of the Central Carbon within the Nitrogenase Catalytic Cofactor Indicates That the CFe_6 Core Is a Stabilizing "Heart of Steel." *J. Am. Chem. Soc.* **2022**, *144* (40), 18315–18328. https://doi.org/10.1021/jacs.2c06149.

(14) Lee, S. C.; Lo, W.; Holm, R. H. Developments in the Biomimetic Chemistry of Cubane-Type and Higher Nuclearity Iron–Sulfur Clusters. *Chem. Rev.* **2014**, *114* (7), 3579–3600. https://doi.org/10.1021/cr4004067.

(15) Tanifuji, K.; Ohki, Y. Recent Advances in the Chemical Synthesis of Nitrogenase Model Clusters. In *Metallocofactors that Activate Small Molecules: With Focus on Bioinorganic Chemistry*; Ribbe, M. W., Ed.; Structure and Bonding; Springer International Publishing: Cham, 2019; pp 33–61. https://doi.org/10.1007/430_2018_26.

(16) Lee, S. C. Synthetic Models of the Nitrogenase Clusters. In *Molybdenum and Tungsten Enzymes: Bioinorganic Chemistry*; Hille, R., Schulzke, C., Kirk, M. L., Eds.; The Royal Society of Chemistry, 2016; pp 130–165.

(17) McSkimming, A.; Suess, D. L. M. Dinitrogen Binding and Activation at a Molybdenum–Iron–Sulfur Cluster. *Nat. Chem.* **2021**, *13* (7), 666–670. https://doi.org/10.1038/s41557-021-00701-6.

(18) Ohki, Y.; Munakata, K.; Matsuoka, Y.; Hara, R.; Kachi, M.; Uchida, K.; Tada, M.; Cramer, R. E.; Sameera, W. M. C.; Takayama, T.; Sakai, Y.; Kuriyama, S.; Nishibayashi, Y.; Tanifuji, K. Nitrogen Reduction by the Fe Sites of Synthetic [Mo_3S_4Fe] Cubes. *Nature* **2022**, *607* (7917), 86–90. https://doi.org/10.1038/s41586-022-04848-1.

(19) Tanifuji, K.; Sickerman, N.; Lee, C. C.; Nagasawa, T.; Miyazaki, K.; Ohki, Y.; Tatsumi, K.; Hu, Y.; Ribbe, M. W. Structure and Reactivity of an Asymmetric Synthetic Mimic of Nitrogenase Cofactor. *Angew. Chem. Int. Ed.* **2016**, *55* (50), 15633–15636. https://doi.org/10.1002/anie.201608806.

(20) He, J.; Wei, J.; Xu, G.; Chen, X.-D. Stepwise Construction of Mo–Fe–S Clusters Using a LEGO Strategy. *Inorg. Chem.* **2022**, *61* (9), 4150–4158. https://doi.org/10.1021/acs.inorgchem.1c03998.

(21) Liu, L.; Rauchfuss, T. B.; Woods, T. J. Iron Carbide–Sulfide Carbonyl Clusters. *Inorg. Chem.* **2019**, *58* (13), 8271–8274. https://doi.org/10.1021/acs.inorgchem.9b01231.

(22) Joseph, C.; Cobb, C. R.; Rose, M. J. Single-Step Sulfur Insertions into Iron Carbide Carbonyl Clusters: Unlocking the Synthetic Door to FeMoco Analogues. *Angew. Chem. Int. Ed.* **2021**, *60* (7), 3433–3437. https://doi.org/10.1002/anie.202011517.

(23) Joseph, C.; Shupp, J. P.; Cobb, C. R.; Rose, M. J. Construction of Synthetic Models for Nitrogenase-Relevant NifB Biogenesis Intermediates and Iron-Carbide-Sulfide Clusters. *Catalysts* **2020**, *10* (11). https://doi.org/10.3390/catal10111317.

(24) Le, L. N. V.; Bailey, G. A.; Scott, A. G.; Agapie, T. Partial Synthetic Models of FeMoco with Sulfide and Carbyne Ligands: Effect of Interstitial Atom in Nitrogenase Active Site. *Proc. Natl. Acad. Sci. U.S.A.* **2021**, *118* (49), e2109241118. https://doi.org/10.1073/pnas.2109241118.

(25) Scott, A. G.; Agapie, T. Synthesis of a Fe_3–Carbyne Motif by Oxidation of an Alkyl Ligated Iron–Sulfur (WFe3S3) Cluster. *J. Am. Chem. Soc.* **2023**, *145* (1), 2–6. https://doi.org/10.1021/jacs.2c04826.

(26) Le, L. N. V.; Joyce, J. P.; Oyala, P. H.; DeBeer, S.; Agapie, T. Highly Activated Terminal Carbon Monoxide Ligand in an Iron–Sulfur Cluster Model of FeMco with Intermediate Local Spin State at Fe. *J. Am. Chem. Soc.* **2024**, *146* (8), 5045–5050. https://doi.org/10.1021/jacs.3c12025.

(27) Reinholdt, A.; Vibenholt, J. E.; Morsing, T. J.; Schau-Magnussen, M.; Reeler, N. E. A.; Bendix, J. Carbide Complexes as π-Acceptor Ligands. *Chem. Sci.* **2015**, *6* (10), 5815–5823. https://doi.org/10.1039/C5SC02077H.

(28) Reinholdt, A.; Herbst, K.; Bendix, J. Delivering Carbide Ligands to Sulfide-Rich Clusters. *Chem. Commun.* **2016**, *52* (10), 2015–2018. https://doi.org/10.1039/C5CC08918B.

(29) Reinholdt, A.; Bendix, J. Weakening of Carbide–Platinum Bonds as a Probe for Ligand Donor Strengths. *Inorg. Chem.* **2017**, *56* (20), 12492–12497. https://doi.org/10.1021/acs.inorgchem.7b01956.

(30) Reinholdt, A.; Majer, S. H.; Gelardi, R. M.; MacMillan, S. N.; Hill, A. F.; Wendt, O. F.; Lancaster, K. M.; Bendix, J. An Approach to Carbide-Centered Cluster Complexes. *Inorg. Chem.* **2019**, *58* (8), 4812–4819. https://doi.org/10.1021/acs.inorgchem.8b03222.

(31) Reinholdt, A.; Bendix, J. Platinum(II) as an Assembly Point for Carbide and Nitride Ligands. *Chem. Commun.* **2019**, *55* (57), 8270–8273. https://doi.org/10.1039/C9CC03411K.

(32) Colebatch, A. L.; Cordiner, R. L.; Hill, A. F.; Nguyen, K. T. H. D.; Shang, R.; Willis, A. C. A Bis-Carbyne (Ethanediylidyne) Complex via the Catalytic Demercuration of a Mercury Bis(Carbido) Complex. *Organometallics* **2009**, *28* (15), 4394–4399. https://doi.org/10.1021/om900462p.

(33) Hill, A. F.; Sharma, M.; Willis, A. C. Heterodinuclear Bridging Carbido and Phosphoniocarbyne Complexes. *Organometallics* **2012**, *31* (7), 2538–2542. https://doi.org/10.1021/om201057c.

(34) Borren, E. S.; Hill, A. F.; Shang, R.; Sharma, M.; Willis, A. C. A Golden Ring: Molecular Gold Carbido Complexes. *J. Am. Chem. Soc.* **2013**, *135* (13), 4942–4945. https://doi.org/10.1021/ja400128h.

(35) Frogley, B. J.; Hill, A. F. Flexible Platinum(0) Coordination to a Ditungsten Ethanediylidyne. *Angew. Chem. Int. Ed.* **2019**, *58* (24), 8044–8048. https://doi.org/10.1002/anie.201902116.

(36) Frogley, B. J.; Hill, A. F. Tungsten–Platinum μ-Carbido and μ-Methylidyne Complexes. *Chem. Commun.* **2019**, *55* (82), 12400–12403. https://doi.org/10.1039/C9CC06472A.

(37) Hejl, A.; Trnka, T. M.; Day, M. W.; Grubbs, R. H. Terminal Ruthenium Carbido Complexes as σ-Donor Ligands. *Chem. Commun.* **2002**, No. 21, 2524–2525. https://doi.org/10.1039/B207903H.

(38) Buss, J. A.; Agapie, T. Four-Electron Deoxygenative Reductive Coupling of Carbon Monoxide at a Single Metal Site. *Nature* **2016**, *529* (7584), 72–75. https://doi.org/10.1038/nature16154.

(39) Buss, J. A.; Bailey, G. A.; Oppenheim, J.; VanderVelde, D. G.; Goddard, W. A.; Agapie, T. CO Coupling Chemistry of a Terminal Mo Carbide: Sequential Addition of Proton, Hydride, and CO Releases Ethenone. *J. Am. Chem. Soc.* **2019**, *141* (39), 15664–15674. https://doi.org/10.1021/jacs.9b07743.

(40) Bailey, G. A.; Buss, J. A.; Oyala, P. H.; Agapie, T. Terminal, Open-Shell Mo Carbide and Carbyne Complexes: Spin Delocalization and Ligand Noninnocence. *J. Am. Chem. Soc.* **2021**, *143* (33), 13091–13102. https://doi.org/10.1021/jacs.1c03806.

(41) Bailey, G. A.; Agapie, T. Terminal Mo Carbide and Carbyne Reactivity: H_2 Cleavage, B–C Bond Activation, and C–C Coupling. *Organometallics* **2021**, *40* (16), 2881–2887. https://doi.org/10.1021/acs.organomet.1c00336.

(42) Radlauer, M. R.; Agapie, T. Bimetallic Zirconium Amine Bis(Phenolate) Polymerization Catalysts: Enhanced Activity and Tacticity Control for Polyolefin Synthesis. *Organometallics* **2014**, *33* (13), 3247–3250. https://doi.org/10.1021/om500608j.

(43) Sampson, J.; Choi, G.; Akhtar, M. N.; Jaseer, E. A.; Theravalappil, R.; Al-Muallem, H. A.; Agapie, T. Olefin Polymerization by Dinuclear Zirconium Catalysts Based on Rigid Teraryl Frameworks: Effects on Tacticity and Copolymerization Behavior. *Organometallics* **2017**, *36* (10), 1915–1928. https://doi.org/10.1021/acs.organomet.7b00015.

(44) Radlauer, M. R.; Buckley, A. K.; Henling, L. M.; Agapie, T. Bimetallic Coordination Insertion Polymerization of Unprotected Polar Monomers: Copolymerization of Amino Olefins and Ethylene by Dinickel Bisphenoxyiminato Catalysts. *J. Am. Chem. Soc.* **2013**, *135* (10), 3784–3787. https://doi.org/10.1021/ja4004816.

(45) Zatsepin, P.; Ahn, S.; Pudasaini, B.; Gau, M. R.; Baik, M.-H.; Mindiola, D. J. Conversion of Methane to Ethylene Using an Ir Complex and Phosphorus Ylide as a Methylene Transfer Reagent. *Chem. Commun.* **2019**, *55* (13), 1927–1930. https://doi.org/10.1039/C8CC08761J.

(46) Spatzal, T.; Perez, K. A.; Einsle, O.; Howard, J. B.; Rees, D. C. Ligand Binding to the FeMo-Cofactor: Structures of CO-Bound and Reactivated Nitrogenase. *Science* **2014**, *345* (6204), 1620. https://doi.org/10.1126/science.1256679.

(47) Citek, C.; Oyala, P. H.; Peters, J. C. Mononuclear Fe(I) and Fe(II) Acetylene Adducts and Their Reductive Protonation to Terminal Fe(IV) and Fe(V) Carbynes. *J. Am. Chem. Soc.* **2019**. https://doi.org/10.1021/jacs.9b06987.

(48) Lee, H.-I.; Cameron, L. M.; Hales, B. J.; Hoffman, B. M. CO Binding to the FeMo Cofactor of CO-Inhibited Nitrogenase: ^{13}CO and ^{1}H Q-Band ENDOR Investigation. *J. Am. Chem. Soc.* **1997**, *119* (42), 10121–10126. https://doi.org/10.1021/ja9715096.

(49) Van Stappen, C.; Decamps, L.; Cutsail, G. E.; Bjornsson, R.; Henthorn, J. T.; Birrell, J. A.; DeBeer, S. The Spectroscopy of Nitrogenases. *Chem. Rev.* **2020**, *120* (12), 5005–5081. https://doi.org/10.1021/acs.chemrev.9b00650.

(50) Buss, J. A.; Oyala, P. H.; Agapie, T. Terminal Molybdenum Phosphides with d Electrons: Radical Character Promotes Coupling Chemistry. *Angew. Chem. Int. Ed.* **2017**, *56* (46), 14502–14506. https://doi.org/10.1002/anie.201707921.

(51) Buss, J. A.; Edouard, G. A.; Cheng, C.; Shi, J.; Agapie, T. Molybdenum Catalyzed Ammonia Borane Dehydrogenation: Oxidation State Specific Mechanisms. *J. Am. Chem. Soc.* **2014**, *136* (32), 11272–11275. https://doi.org/10.1021/ja5059923.

(52) Schlosser, M.; Hartmann, J. Transmetalation and Double Metal Exchange: A Convenient Route to Organolithium Compounds of the Benzyl and Allyl Type. *Angew. Chem., Int. Ed. Engl.* **1973**, *12* (6), 508–509. https://doi.org/10.1002/anie.197305082.

(53) Piglosiewicz, I. M.; Beckhaus, R.; Wittstock, G.; Saak, W.; Haase, D. Selective Oxidation and Reduction of Trinuclear Titanium(II) Hexaazatrinaphthylene ComplexesSynthesis, Structure, and Electrochemical Investigations. *Inorg. Chem.* **2007**, *46* (18), 7610–7620. https://doi.org/10.1021/ic701009u.

(54) Transue, W. J.; Yang, J.; Nava, M.; Sergeyev, I. V.; Barnum, T. J.; McCarthy, M. C.; Cummins, C. C. Synthetic and Spectroscopic Investigations Enabled by Modular Synthesis of Molecular Phosphaalkyne Precursors. *J. Am. Chem. Soc.* **2018**, *140* (51), 17985–17991. https://doi.org/10.1021/jacs.8b09845.

(55) Low, C. H.; Rosenberg, J. N.; Lopez, M. A.; Agapie, T. Oxidative Coupling with Zr(IV) Supported by a Noninnocent Anthracene-Based Ligand: Application to the Catalytic Cotrimerization of Alkynes and Nitriles to Pyrimidines. *J. Am. Chem. Soc.* **2018**, *140* (38), 11906–11910. https://doi.org/10.1021/jacs.8b07418.

(56) Culmo, R. F.; Shelton, C. The Elemental Analysis of Various Classes of Chemical Compounds Using CHN. *Shelton, CT* **2013**.

(57) Dorn, H.; Hanson, B. E.; Motell, E. Triiron Dodecacarbonyl Revisited: Fluxionality in the Solid State. *Inorg. Chim. Acta.* **1981**, *54*, L71–L73. https://doi.org/10.1016/S0020-1693(00)95389-1.

(58) Bruker. APEX3, 2012.

(59) Bruker. SADABS, 2001.

(60) Altomare, A.; Cascarano, G.; Giacovazzo, C.; Guagliardi, A.; Burla, M. C.; Polidori, G.; Camalli, M. SIR92 - a Program for Automatic Solution of Crystal Structures by Direct Methods. *J. Appl. Crystallogr.* **1994**, *27* (3), 435.

(61) Palatinus, L.; Chapuis, G. SUPERFLIP - a Computer Program for the Solution of Crystal Structures by Charge Flipping in Arbitrary Dimensions. *J. Appl. Crystallogr.* **2007**, *40* (4), 786–790.

(62) Betteridge, P. W.; Carruthers, J. R.; Cooper, R. I.; Prout, K.; Watkin, D. J. CRYSTALS Version 12: Software for Guided Crystal Structure Analysis. *J. Appl. Crystallogr.* **2003**, *36* (6), 1487.

(63) Spek, A. PLATON SQUEEZE: A Tool for the Calculation of the Disordered Solvent Contribution to the Calculated Structure Factors. *Acta Cryst. C* **2015**, *71* (1), 9–18.

Chapter 5

SYNTHESIS AND REACTIVITY OF BISPHENOXIDE-BOUND DESYMMETRIZED MOFE$_3$S$_3$ CLUSTERS WITH AN FE-ANTHRACENE INTERACTION

5.1 ABSTRACT

Biological nitrogen fixation occurs at an Fe-M (M = Mo, Fe, or V) cofactor (FeMco) of nitrogenase, which displays eight metal centers bridged by sulfides and a carbide having the MFe$_7$S$_8$C cluster composition. Different mechanisms have been proposed, with different substrate binding modes, but few relevant intermediates have been isolated to verify these hypotheses, one of which is a protonated cluster. Desymmetrized synthetic iron-sulfur cluster models serve as potential candidates for reactivity studies, as they provide a unique site for small molecule binding. We report a group of cubane-type MoFe$_3$S$_3$ cluster that mimic half of FeMoco, where two Fe sites are stabilized by a chelating bisphenoxide ligand, and the third Fe site is ligated with a labile Cl ligand. Upon reduction, the anthracene-bridged bisphenoxide cluster loses all halide ligands, where the unique Fe site interacts with the arene. This cluster catalyzes the electrochemical proton reduction of an externally added acid, possibly through a protonated cluster intermediate. This demonstrates the ability of synthetic clusters to catalyze reactions relevant to nitrogenase like proton reduction, as well as avenues to study protonated iron-sulfur clusters.

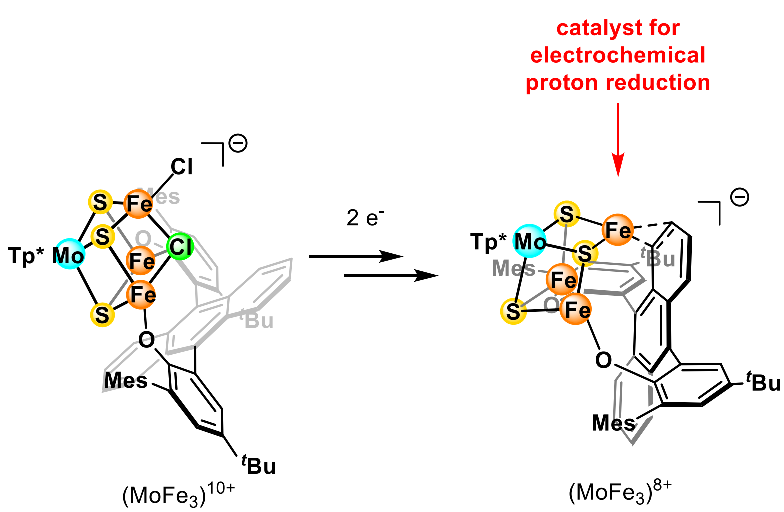

5.2 INTRODUCTION

Nitrogenase refers to a class of enzymes in microorganism capable of catalyzing the reduction of atmospheric N_2 into NH_3.[1] The site of N_2 reduction in the nitrogenase enzyme is the heterometallic MFe cluster cofactor (M = Mo, V, Fe), where the most efficient version, the iron-molybdenum cofactor (FeMoco), contains molybdenum.[2] This complex cluster consists of a Fe_4S_3 and a $MoFe_3S_3$ partial cubanes, joined together by an unusual interstitial μ_6-C atom (Figure 5.1).[3–5]

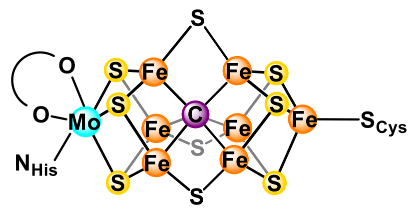

Figure 5.1. Structure of FeMoco in Mo-dependent nitrogenase (PDB 3U7Q).

The reduction of N_2 to NH_3 in nitrogenase is proposed to proceed through an eight-step cycle described by the Lowe-Thorneley scheme (Figure 5.2).[2] The FeMoco cluster undergoes eight consecutive reduction and protonation reactions, cycling through the eight E states E_0 to E_7. In addition, N_2 binds to the cluster at the E_4 state, accompanied by the release of one molecule of H_2.

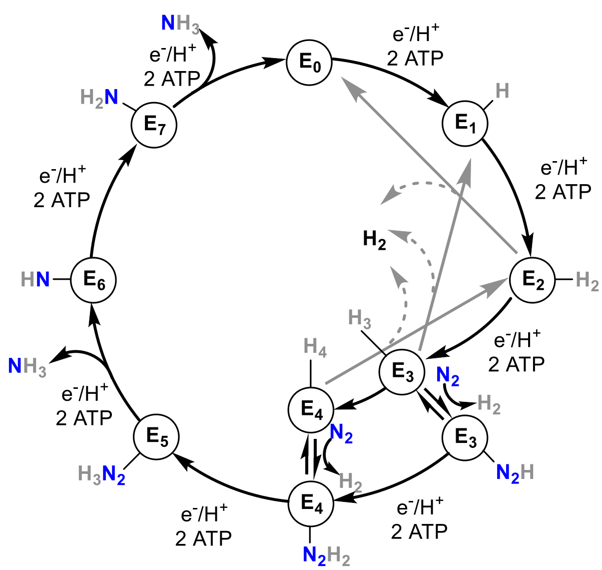

Figure 5.2. The Lowe-Thorneley kinetic scheme for N_2 reduction to NH_3. Adapted from reference.[6]

Despite intensive studies, few intermediates of N_2 reduction have been characterized. One crystal structure of FeVco with a small ligand that bridges between two Fe sites has been reported, assigned to NH that possibly formed during the conversion of N_2 to NH_3.[7] Another crystal structure was described for FeMoco where a diatomic ligand bridges between two Fe atoms, displacing a belt sulfide, although the authors' assignment of the ligand as N_2 is highly debated.[8–10] Likewise, apart from characterization of the resting state E_0,[11–14] only E_1,[15–17] E_2,[18,19] and E_4 states[20–25] in the Lowe-Thorneley scheme have been studied *in situ* by spectroscopic methods.

The presence of hydride ligands has been invoked in the structures of E_1 to E_4,[15–25] as a result of the accumulation of protons before the binding of N_2. For example, in the E_4 state, two hydrides are proposed to bridge between two pairs of Fe sites, and the remaining two protons are bound to the bridging sulfides as SH ligands.[26] However, the exact structure has not been confirmed, as these reactive species have not been isolated, rendering it difficult for further studies using methods like neutron scattering that can locate hydrogen atoms.[27]

In comparison, synthetic models aspire to replicate the chemistry of complex biological cofactors, and reactivity studies on these systems can provide insights into similar pathways in natural clusters. However, protonation of synthetic iron-sulfur clusters has not been well-studied, due to the ease of cluster degradation and ligand exchange on addition of acid.[28–31] Furthermore, the observation of additional protons on these platforms encounter several spectroscopic challenges, such as the broadness in ^{1}H NMR peaks due to paramagnetic broadening and chemical exchange of labile protons.[28] Here, we report the synthesis of a $MoFe_3S_3$ partial cubane cluster featuring a bisphenoxide ligand that functions as an electrocatalyst for H_2 evolution from acid in an organic solvent, which may proceed through a protonated intermediate. This provides a design to study protonated iron-sulfur clusters, especially in terms of locating the proton using methods such as neutron diffraction.

5.3 RESULTS AND DISCUSSION

In order to offer protection to the cluster **5.1** while directing further reactivity to a more accessible metal site, we employed bisphenoxide **LK_2** (Figure 5.3) to chelate two Fe atoms. As rotation is possible around the aryl bridge, an anthracene linker increases the thermal barrier to this isomerization, allowing the two isomers where the substituents are *syn* and *anti* to be separated at room temperature.[32] We targeted the *syn* isomer, as this conformation enforces the phenoxides to bind to two Fe sites across a cluster, instead of bridging two Fe sites of two different clusters that can occur with the *anti* isomer. In addition, when oxygen atoms on the *syn* isomer are located on the two phenyl rings at the position *ortho* to the anthracene bridge, their large separation (~6.0 Å)[32] can accommodate a $MoFe_3$ unit.

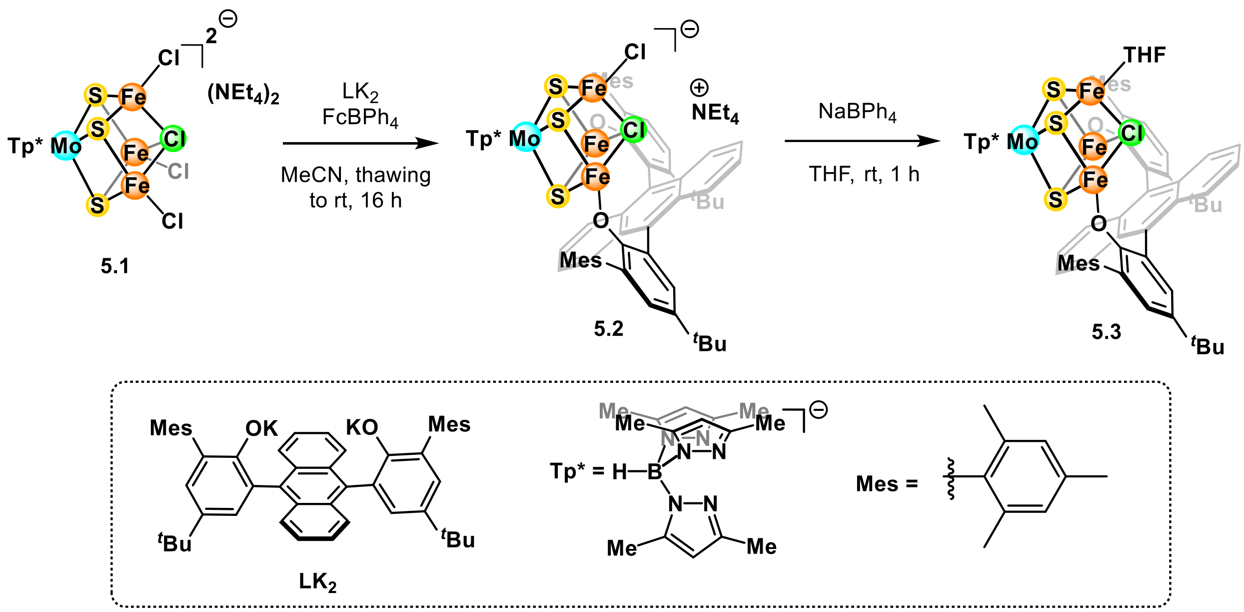

Figure 5.3. Syntheses of **5.1** to **5.3**.

Similarly to the phenylene-bridged version (Chapter 4), **LK**$_2$ reacts with **5.1** in the presence of ferrocenium tetraphenylborate ($FcBPh_4$) as an oxidant. While the product does not form high-quality crystals, its atomic connectivity can be established by X-ray crystallography as **5.2** (Figure 5.4), confirming the binding of the bisphenoxide to two Fe sites on the cluster. The third Fe site still retains a terminal Cl ligand, while the μ_3-Cl atom is also intact.

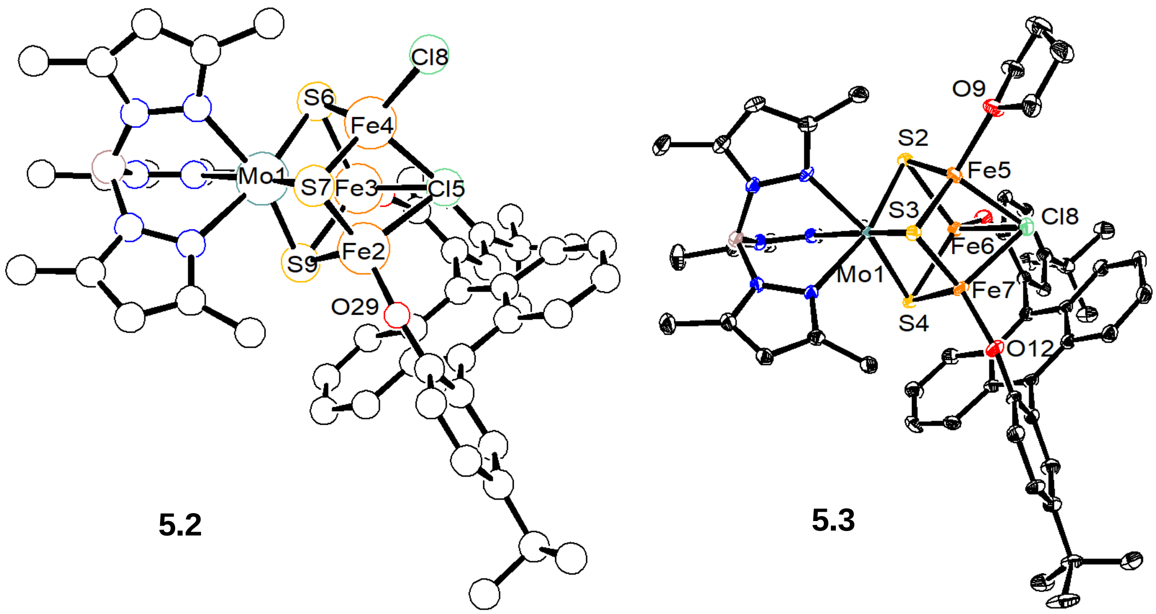

Figure 5.4. Connectivity of **5.2** (left) and crystal structure of **5.3** (right). Spheres and ellipsoids are shown at 50% probability level. Hydrogen atoms, solvent molecules, counterions, and part of the bisphenoxide ligand are omitted for clarity.

A halide abstracting reagent can potentially remove the terminal Cl ligand within **5.2**,[33–35] generating an open coordination site for further functionalization of the cluster with relevant small molecule substrates. Adding one equivalent of $NaBPh_4$ to a solution of **5.2** in THF leads to the precipitation of a white solid, assigned as NaCl, and a new species as observed by ^1H NMR spectroscopy. The resulting cluster is stable after removal of the solvent under vacuum and reconstitution in THF but attempts at purification to remove the THF-soluble NEt_4BPh_4 by extraction into other solvents like Et_2O and C_6H_6 lead to decomposition (Figure 5.5), suggesting the crucial role of THF in stabilizing the unique Fe site after Cl removal.

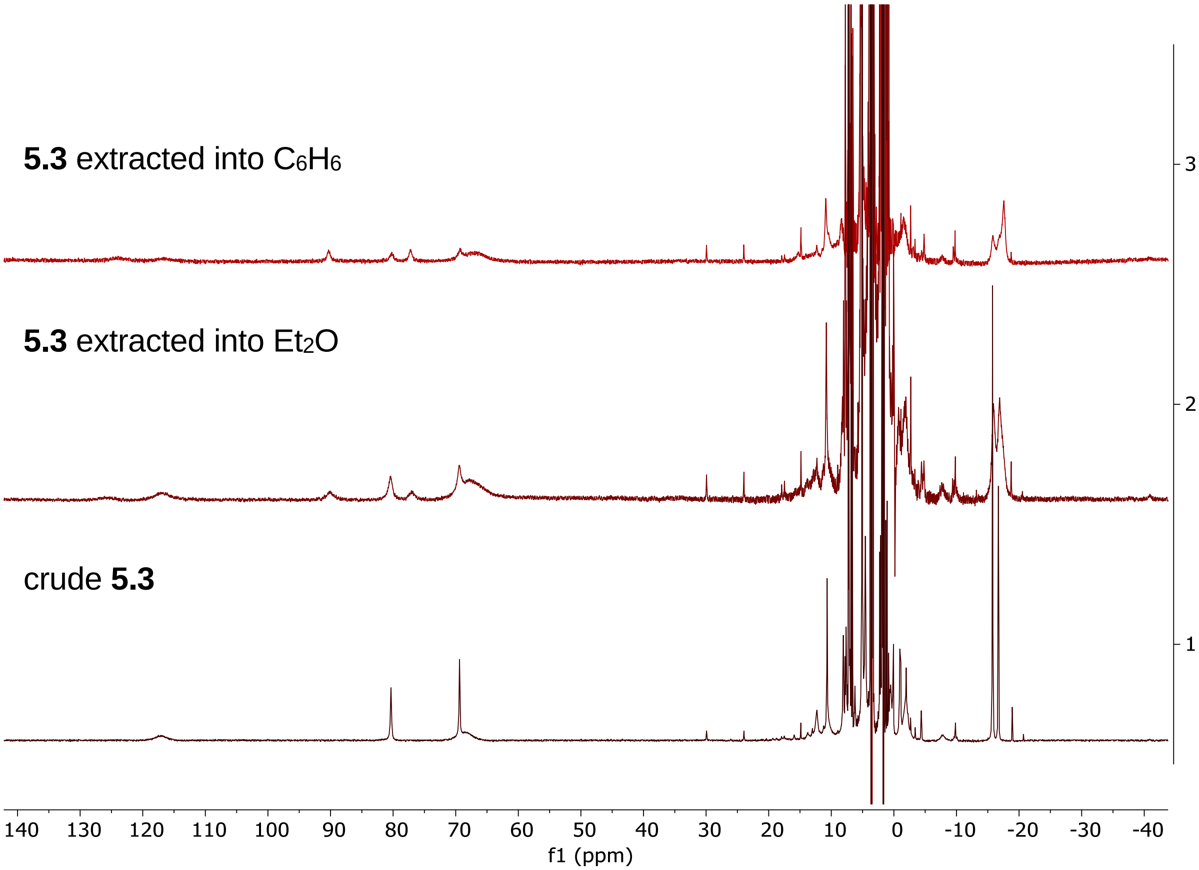

Figure 5.5. Comparison of ^{1}H NMR spectra (400 MHz, THF-h_8, solvent suppression) of crude **5.3** and after extraction into Et_2O and C_6H_6.

An aliquot of the reaction in THF after filtration produced dark crystals by vapor diffusion of pentane after several weeks, along with some white powder assigned as NEt_4BPh_4. X-ray crystallography reveals the structure of these crystals as the neutral cluster **5.3**, where the Fe site that formerly contained a terminal Cl ligand is now coordinated by a THF molecule (Figure 5.4). In addition, the less labile μ_3-Cl atom is not abstracted by $NaBPh_4$. The good quality of the crystal allows for discussion of the bond metrics within the cluster. The Fe-O(THF) bond length of 2.011(2) Å is similar to that in a previously reported Fe_4S_4 cluster with a bound ether,[36] suggesting the presence of a Fe^{2+} ion at this site. The Fe-O(phenoxide) bond distances of 1.825(2) and 1.834(2) are much shorter than those observed in high-spin tetrahedral Fe^{II} complexes with phenoxide ligands at around 1.90 – 2.00 Å,[37–39] suggesting that these sites likely possess oxidation states above +2. In comparison, Fe-O(phenoxide) bonds in high-spin tetrahedral Fe^{II} compounds lie between 1.83 and 1.86 Å.[40–42] Thus, the data indicates that the oxidation states of the phenoxide-bound Fe atoms could be +3 or an intermediate value between +2 and +3. Given the prevalence of Mo^{III} in synthetic $MoFe_3$ clusters,[12] it is likely that these Fe sites possess an oxidation state of 2.5+ to account for the $(MoFe_3)^{10+}$ formal metal charges.

In an attempt to deliver a carbon-based ligand to solvent-bound site and incorporate it into the bridging position at a later stage, we reacted **5.3** (generated *in situ*) with the ylides Ph_2MePCH_2 or Ph_3PCH_2. Upon mixing the reactants, a new species quickly formed as indicated by ^1H NMR spectroscopy. The similarities in the spectra compared to those of **5.2** and **5.3** suggest that the new clusters have an analogous structure, where the bisphenoxide remains bound to two Fe sites and ligand binding occurs at the remaining Fe site. A low-quality crystal allows us to establish the of the product as **5.4**, where the ylide coordinates to the unique Fe site through the C atom (see Figure 5.6 for the Ph_2MePCH_2 variant and Figure 5.S14 for the Ph_3PCH_2 variant), suggesting that the reaction is a redox-neutral substitution process.

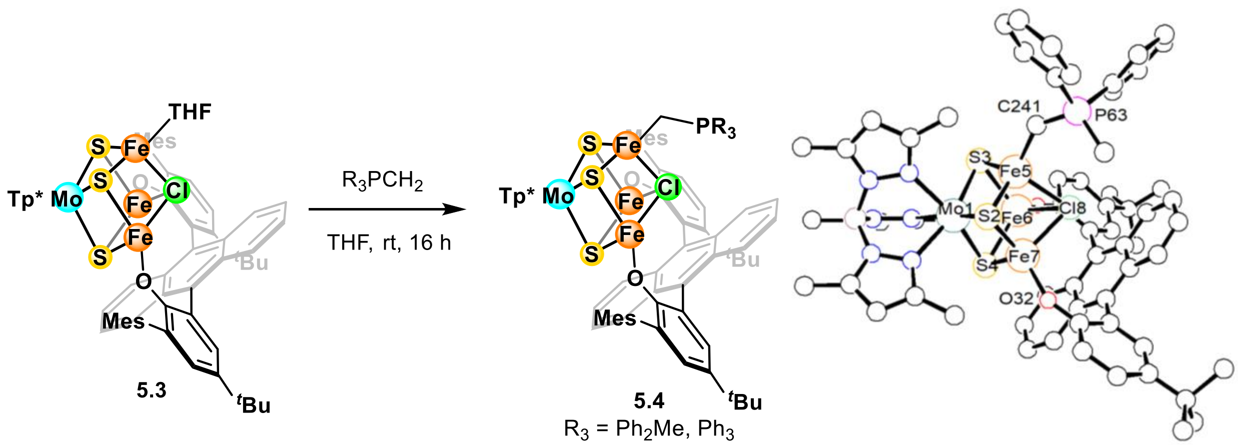

Figure 5.6. Synthesis of **5.4** and its atomic connectivity for the Ph_2MePCH_2 variant. Spheres are shown at 50% probability level. Hydrogen atoms, solvent molecules, and part of the bisphenoxide ligand are omitted for clarity.

Next, we targeted a more electron-rich cluster, to facilitate both the removal of the bridging Cl to deliver a bridging C-based ligand[35] and the coordination and activation of multiply-bonded small molecules like N_2. Reduction of **5.3** and **5.4** with one equivalent of a strong reductant such as potassium naphthalenide leads to the formation of the same major species and side products, indicating that the ylide ligand dissociates instead of delivering a CH_2 group or binding in a μ_3

manner. Using two equivalents of potassium naphthalenide leads to a cleaner reaction, with the same major species and few cluster byproducts in the ^{1}H NMR spectrum.

However, the resulting cluster forms very small crystals from various crystallization conditions, precluding its characterization in the solid state. We turned to other spectroscopic methods to gain insight into the structure of the reduced cluster. Both IR and Raman spectroscopy reveal no noticeable features in the 1800 – 2200 cm^{-1}, ruling out the presence of a bound terminal or bridging N_2 ligand (Figure 5.7).

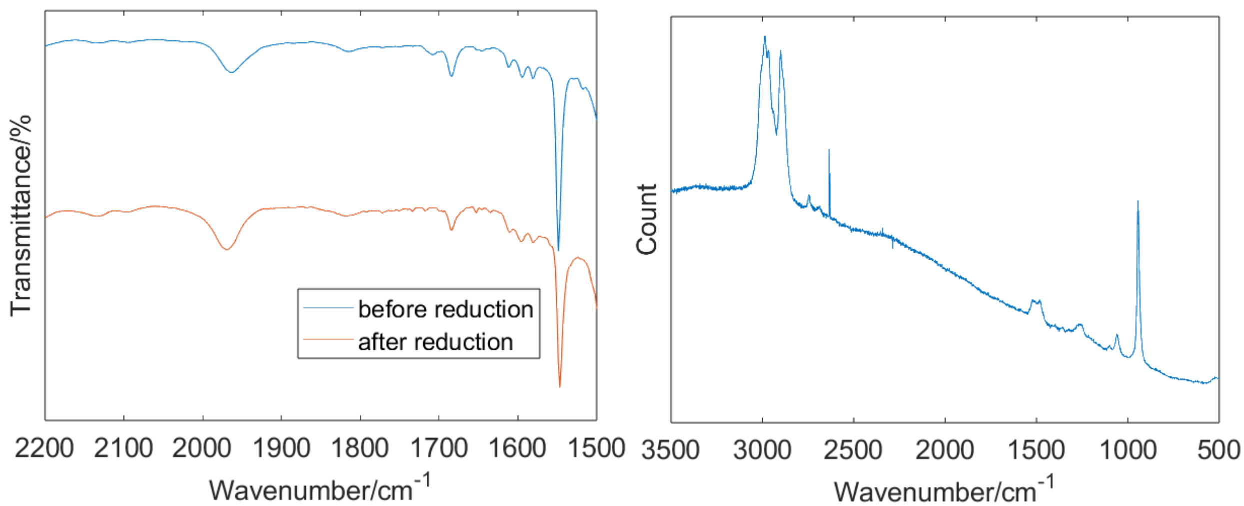

Figure 5.7. IR spectrum of **5.3** before and after reduction (left) and Raman spectrum of **5.3** after reduction (right), where the peaks seen arise from the solvent THF.

The clean formation of the new cluster with two equivalents of reductant suggests that the reaction is a two-electron process. With the first reducing equivalent, the bridging Cl ligand can be lost, and the second reducing equivalent will lead to an anionic cluster. Thus, we reasoned that changing the cation in the reductant may allow the product to crystallize better. No improvement was observed with sodium naphthalenide, $LiBHEt_3$ or $CoCp^*_2$. However, using potassium naphthalenide in the presence of 18-crown-6 leads to the formation of dark crystals from C_6H_6/pentane vapor diffusion. X-ray crystallography reveals the structure of the product as **5.5** (Figure 5.8), where the bridging Cl ligand has been removed as anticipated (Figure 5.9). Unexpectedly, the anthracene bridge moves closer to the cluster, resulting in the coordination of a double bond on the ring to the unique Fe site. Cluster **5.5** adds to the list of very rare examples of iron-sulfur clusters bearing multiply-bonded system coordinating in an η^2 fashion to a Fe site.[43,44] In addition, the ligation sphere around the unique Fe in **5.5** resembles that of a thiolate-bound monometallic Fe complex possessing an η^6 interaction with a benzene ring in the ligand backbone, which binds N_2 upon reduction.[45] Further studies toward developing similar reactivities are under investigation.

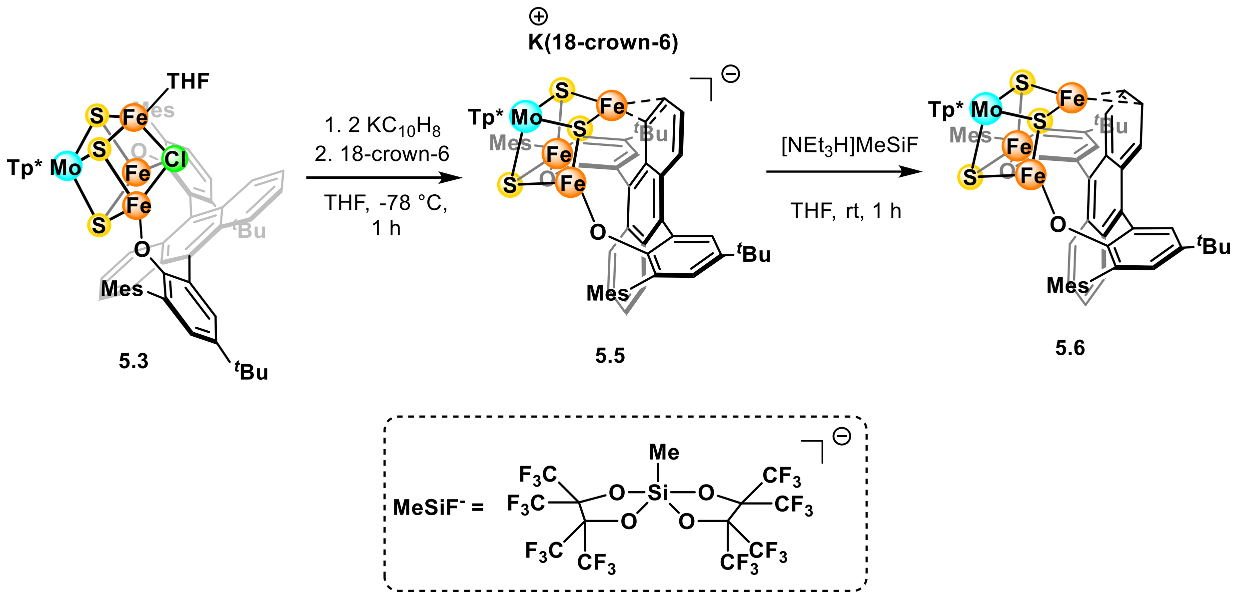

Figure 5.8. Syntheses of **5.5** and **5.6**.

Compared to **5.3**, the geometry around the Mo center remains unperturbed, suggesting that reduction occurs at the Fe site. Indeed, the Fe-O distances in **5.5** are longer at 1.88 Å, implying an oxidation state closer to Fe^{II}. With a total metal formal charge of $(MoFe_3)^{8+}$, a Mo^{III} center indicates at least one highly reduced Fe site below the +2 oxidation state. The average Fe-Fe distance decreases from 2.76 Å in **5.3** to 2.65 Å in **5.5** upon reduction and loss of the μ_3-Cl, similarly to the reported carbene-ligated clusters,[35] suggesting an increased level of Fe-Fe interaction. This observation corroborates previous results in a WFe_2Ni cluster, where short metal-metal bonds from high metal-metal interactions are proposed to store redox equivalents and stabilize low-valent metal centers.[46]

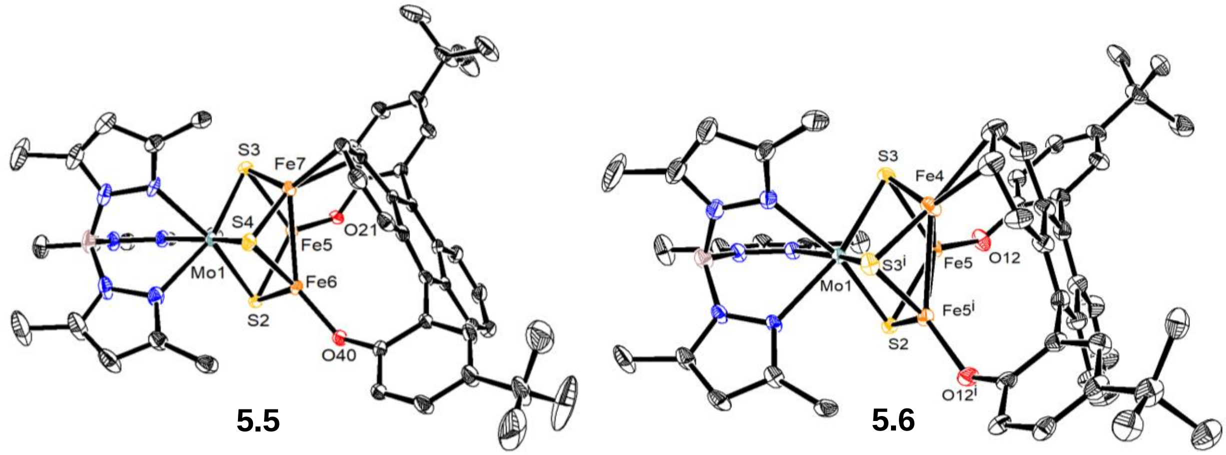

Figure 5.9. Crystal structures of **5.5** (left) and **5.6** (right). Ellipsoids are shown at 50% probability level. Hydrogen atoms, solvent molecules, counterions, and part of the bisphenoxide ligand are omitted for clarity.

Having isolated the highly reduced cluster **5.5**, we explored its role in reactions relevant to nitrogenase. When one equivalent of the acid $[NEt_3H]MeSiF$ (prepared by Tianyi He) is added to a dark green THF solution of **5.5** at room temperature, the reaction quickly turns dark brown, and ^1H NMR spectroscopy indicates the disappearance of the starting material after 1 h with the formation of a new major species. The C_6H_6-soluble crude material gave dark crystals from C_6H_6/pentane vapor diffusion. Analysis by X-ray crystallography reveals that the product has the same connectivity as **5.5**, except for the absence of the K(18-crown-6) counterion. When **5.5** is reacted with one equivalent of a chemical oxidant like AgOTf, a similar species is observed by NMR spectroscopy (Figure 5.S8). In addition, the same species forms when a different acid like lutidinium triflate is employed (Figure 5.S9). It is challenging to distinguish between oxidized and protonated forms of **5.5**, as protons are difficult to locate on iron-sulfur clusters by spectroscopic methods such as NMR or IR spectroscopy due to the broadening of paramagnetic NMR peaks or weak absorption of Fe-H and S-H vibrations.[28] The Fe-O distances of 1.851(4) Å in the product is slightly shorter than those in **5.5** suggesting some level of oxidation, although the average Fe-Fe distances of 2.66 Å does not deviate greatly from **5.5**. Furthermore, the Mössbauer spectrum of **5.5** shows an average isomer shift of 0.55 mm s^{-1}, while that of the product is 0.45 mm s^{-1}, signifying a lower electron density (Figures 5.S12 and 5.S13). Here, we tentatively assign the structure of the product as the neutral cluster **5.6** (Figure 5.8), although we cannot disregard a protonated cluster.

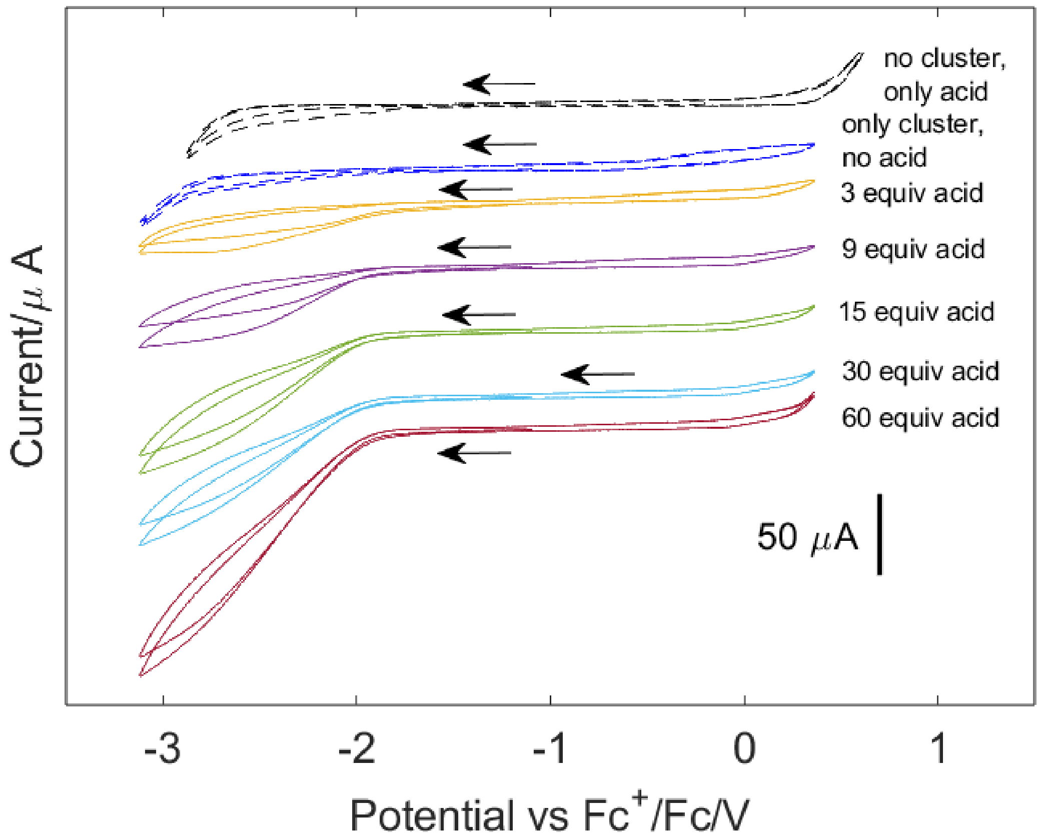

Figure 5.10. CV of $[NEt_3H]MeSiF$, **5.5**, and **5.5** with 3, 6, 9, 15, 30, and 60 equivalents of $[NEt_3H]MeSiF$. Conditions: ~2.5 mM cluster in THF with 0.2 M $TBAPF_6$, scan rates of 200 mV s^{-1}

Given the possibility of oxidizing **5.5** by an acid, a negatively applied potential can regenerate the cluster and **5.5** may serve as a system for electrocatalytic proton reduction, similarly to how nitrogenase catalyzes H_2 evolution. The cyclic voltammogram (CV) of **5.5** in THF shows no prominent redox feature (Figure 5.10). Upon adding 3 equivalents of $[NEt_3H]MeSiF$ and sweeping negatively, we observed a feature appearing at around -2 V vs. Fc^+/Fc. With more $[NEt_3H]MeSiF$ added up to 60 equivalents, this feature continues to increase in intensity. In comparison, the CV of $[NEt_3H]MeSiF$ under the same condition shows no redox features. This behavior suggests an electrochemical proton reduction reaction catalyzed by **5.5**, which may proceed through a reactive protonated cluster intermediate. A bulk electrolysis experiment with 20 equivalents of acid confirms the generation of H_2 by gas chromatography of a sample of the headspace (Figure 5.S11).

While proton reduction occurs at relatively negative potentials in this case, it still demonstrates a reaction relevant to nitrogenase, providing an opportunity to study possible protonated intermediates. The use of iron-sulfur clusters in electrocatalytic H_2 production is limited, with examples of Fe_4S_4-type clusters[47,48] and none with heterometals like the $MoFe_3$ structure in our report. In addition, protonated clusters have been invoked as intermediates for various transformations, but their properties and reactivities have not been well-explored, likely due to their propensity to degrade upon reaction with acids. A chelating environment like in **5.5** and **5.6**, where the ligand interacts with all three Fe centers, can play a role in preventing ligand dissociation and decomposition of the cluster.[28–31]

5.4 CONCLUSION

We have demonstrated the desymmetrization of a $MoFe_3$ cluster with a bisphenoxide ligand bearing an anthracene bridge, where the phenoxide O atoms coordinate to two Fe sites, leaving a third Fe site with a labile terminal Cl ligand. After halide abstraction and reduction, the anthracene bridge moves closer to the unique Fe site, leading to a highly reduced cluster **5.5** bearing an Fe-anthracene interaction. This cluster can catalyze the electrochemical reduction of proton using an added acid, which may proceed through a protonated cluster intermediate. This system demonstrates the biologically relevant proton reduction reaction observed for nitrogenase, providing an opportunity for further investigation on this reactivity with synthetic clusters. Current work focuses on exploring small molecule activation with **5.5** and further characterization of the protonated species, especially in terms of determining the location of the added proton.

5.5 SUPPORTING INFORMATION

A) Synthetic details and characterization

1. General considerations:

All reactions were performed at room temperature in a N_2-filled MBraun glovebox or using standard Schlenk techniques unless otherwise specified. Glassware was oven-dried at 140 °C for at least 2 h prior to use and allowed to cool under vacuum. **5.1**,[35] KBn,[49] $FcBPh_4$,[50] Ph_2MePCH_2,[51] Ph_3PCH_2,[51] and **LH_2** were prepared according to literature procedures.[52] $[NEt_3H]MeSiF$ was prepared by Tianyi He. Pentane, diethyl ether, benzene, toluene, and tetrahydrofuran (THF) were dried by sparging with N_2 for at least 15 min and then passing through a column of activated A2 alumina under positive N_2 pressure and stored over 3 Å molecular sieves prior to use. ^1H spectra were recorded on a Varian 400 MHz spectrometer. Deuterated benzene (C_6D_6) was purchased from Cambridge Isotope Laboratories, dried over sodium/benzophenone ketyl, degassed by three freeze–pump–thaw cycles, and vacuum-transferred prior to use. IR spectra were obtained as thin films formed by evaporation of solutions using a Bruker Alpha Platinum ATR spectrometer with OPUS software in a glovebox under an N_2 atmosphere.

2. Procedures:

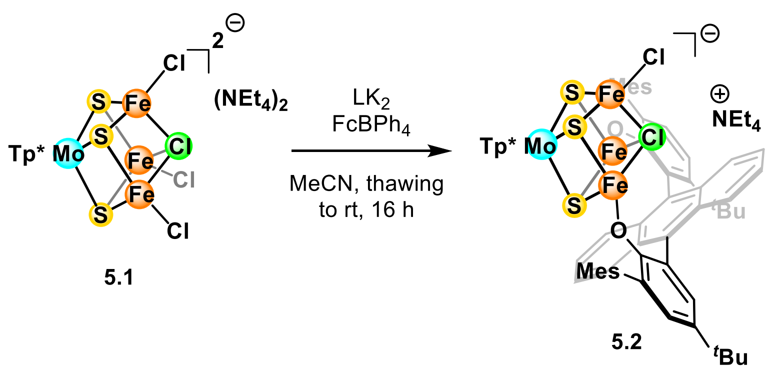

Synthesis of **5.2**. In a glovebox, **5.1** (505 mg, 0.48 mmol, 1 equiv) was dissolved in 25 mL MeCN to form a dark blue solution and frozen in a cold well cooled in liquid N_2. In a separate vial, **LH_2** (254 mg, 0.36 mmol, 0.75 equiv) was dissolved in THF (12 mL) to form a colorless solution and frozen in the cold well. KBn (93 mg, 0.72 mmol, 1.50 equiv) was added to the thawing solution of

LH_2 with stirring to form an orange solution. The reaction was stirred at room temperature for about 10 min to form **LK_2** then concentrated to about 5 mL. To the frozen solution of **5.1** was added $FcBPh_4$ (241 mg, 0.48 mmol, 1 equiv) followed by the solution of **LK_2**. The reaction was allowed to warm and stirred at room temperature inside the box for 16 h, resulting in a dark yellow/brown solution. Then, the reaction was filtered, and the solvent removed *in vacuo*. The resulting dark solid was washed extensively with pentane to remove ferrocene until the washing was no longer yellow. The product was extracted into C_6H_6 and lyophilized to yield a brown powder. The crude material was used without further purification since it does not crystallize well, and NMR spectroscopy indicates small peaks from small amounts of impurities that cannot be removed. Crude yield: 619 mg (83%). Some low-quality crystals of **5.2** were grown by vapor diffusion of pentane into a solution of **5.2** in Et_2O at room temperature over several days. ^1H NMR (400 MHz, thf-H_8, solvent suppression) δ 117.17, 79.67, 70.42, 69.09, 11.97, 10.61, 5.02, -0.06, -0.93, -1.80, -3.54, -7.74, -9.56, -15.63, -16.79. Note: a slight excess of **5.1** and $FcBPh_4$ compared to the ligand gives a cleaner reaction than using equimolar amounts.

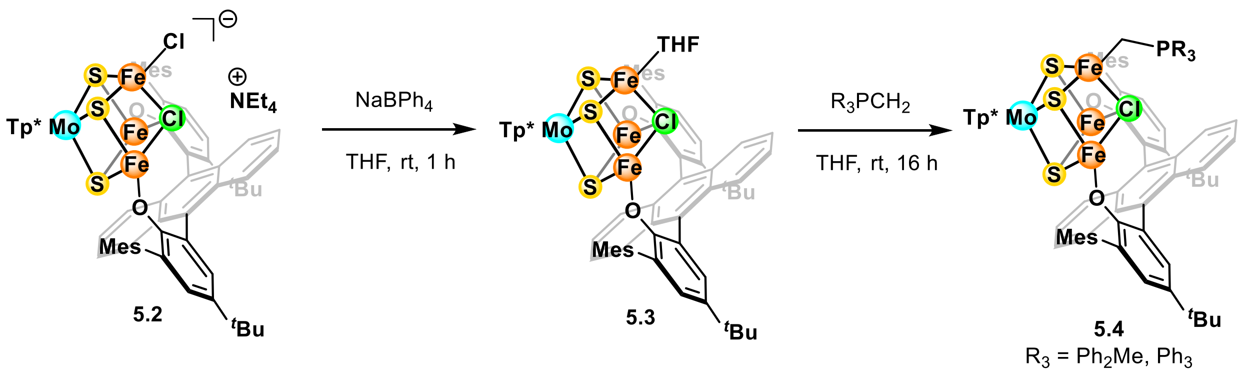

Syntheses of **5.3** and **5.4**. In a glovebox, **5.2** (40.0 mg, 0.026 mmol, 1 equiv) and $NaBPh_4$ (8.7 mg, 0.026 mmol, 1 equiv) were combined in THF (2 mL). The dark brown reaction was stirred at room temperature for 1 h, after which the white precipitate formed was removed by filtration. The filtrate containing **5.3** and NEt_4BPh_4 as the side product was used without further purification. X-ray quality crystals of **5.3** were grown by vapor diffusion of pentane into a filtered aliquot of the reaction at room temperature over several weeks. ^1H NMR (400 MHz, THF-h_8, solvent suppression) δ 116.90, 80.31, 69.34, 68.42, 12.33, 10.66, 5.06, 4.56, -0.95, -1.98, -7.86, -9.87, -15.76, -16.67.

To this solution of **5.3**, Ph_2MePCH_2 (5.5 mg, 0.026 mmol, 1 equiv) or Ph_3PCH_2 (7.1 mg, 0.026 mmol, 1 equiv) was added at room temperature and stirred for 16 h. The content of the vial was filtered through a pad of Celite and the solvent removed *in vacuo* to yield a dark film. The crude product was extracted into Et_2O and the solvent removed *in vacuo* to yield a dark solid. Yield: 38.0 mg (92%). Some low-quality crystals of **5.4** were grown by vapor diffusion of pentane into a solution of the cluster in *o*-difluorobenzene at -35 °C over several weeks for the Ph_2MePCH_2 variant, or by vapor diffusion of pentane into a solution of the cluster in C_6H_6 at room temperature for the Ph_3PCH_2 variant. ^1H NMR (400 MHz, THF-h_8, solvent suppression) Ph_2MePCH_2 variant: δ 149.94, 86.93, 74.30, 71.41, 13.05, 11.28, 10.05, 9.60, 8.49, 8.20, 7.78, 7.02, 5.44, 4.66, 1.06, -1.60, -2.55, -16.76, -17.62. Ph_3PCH_2 variant: δ 90.09, 77.26, 69.76, 67.01, 12.30, 10.50, 9.73, 8.40, 7.70, 7.50, 6.72, 4.85, -12.86, -15.60.

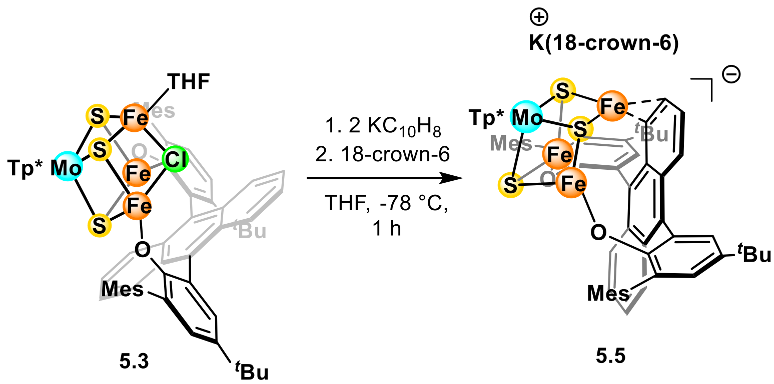

Synthesis of **5.5**. In a glovebox, **5.2** (200 mg, 0.13 mmol, 1 equiv) and $NaBPh_4$ (43.7 mg, 0.13 mmol, 1 equiv) were combined in THF (5 mL). The dark brown reaction was stirred at room temperature for 1 h, after which the white precipitate formed was removed by filtration. A pre-reduced Teflon stir bar was added to the dark brown filtrate and the reaction was cooled to -78 °C in the cold well. To this solution was added $KC_{10}H_8$ (0.1 M in THF, 2.55 mL, 0.26 mmol, 2 equiv). The reaction quickly changed to dark green with a small amount of precipitate. The reaction was stirred for 1 h at -78 °C, after which the precipitate was removed by filtration. The filtrate was cooled to -78 °C and 18-crown-6 (33.7 mg, 0.13 mmol, 1 equiv) was added along with a pre-reduced Teflon stir bar. The reaction was stirred at -78 °C for 1 h, then the solvent was removed *in vacuo*. The resulting dark green solid was washed with pentane to remove naphthalene, then extracted into C_6H_6 and crystallized by vapor diffusion of pentane to yield X-ray quality crystals. Yield: 150 mg (70%). ^1H NMR (400 MHz, THF-h_8, solvent suppression) δ 80.25, 66.11, 45.90, 41.15, 15.63, 13.01, 9.68, 7.96, 7.14, 6.81, 6.73, 6.58, 5.16, 1.24, 1.06, 0.84, -2.11, -6.86, -15.32, -17.07. Evans method: $\mu = 8.42\ \mu_B$, suggesting S = 4. Anal. calcd (%) $C_{79}H_{98}BFe_3KN_6O_8S_3Mo$ (M_r = 1669.26): C, 56.84; H, 5.92; N, 5.03. Found: C, 57.03; H, 5.73; N, 4.96.

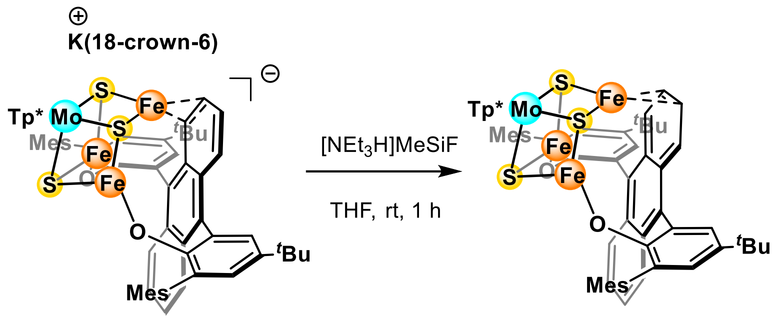

5.5 5.6

Formation of **5.6**. In a glovebox, **5.5** (15.0 mg, 0.009 mmol, 1 equiv) and [NEt$_3$H]MeSiF (7.3 mg, 0.009 mmol, 1 equiv) were combined in THF (2 mL). The solution quickly changed from dark green to dark brown. The reaction was stirred at room temperature for 2 h, after which solvent was removed *in vacuo*. The resulting solid was washed with Et_2O to remove a dark impurity, then extracted into C_6H_6 and crystallized by vapor diffusion of pentane to yield X-ray quality crystals. This material still contains some other species as observed by ^{1}H NMR spectroscopy, so only characteristic peaks are reported. ^{1}H NMR (400 MHz, THF-h_8, solvent suppression) δ 100.41, 98.14, 84.33, 80.94, -16.53, -19.85.

3. NMR spectra:

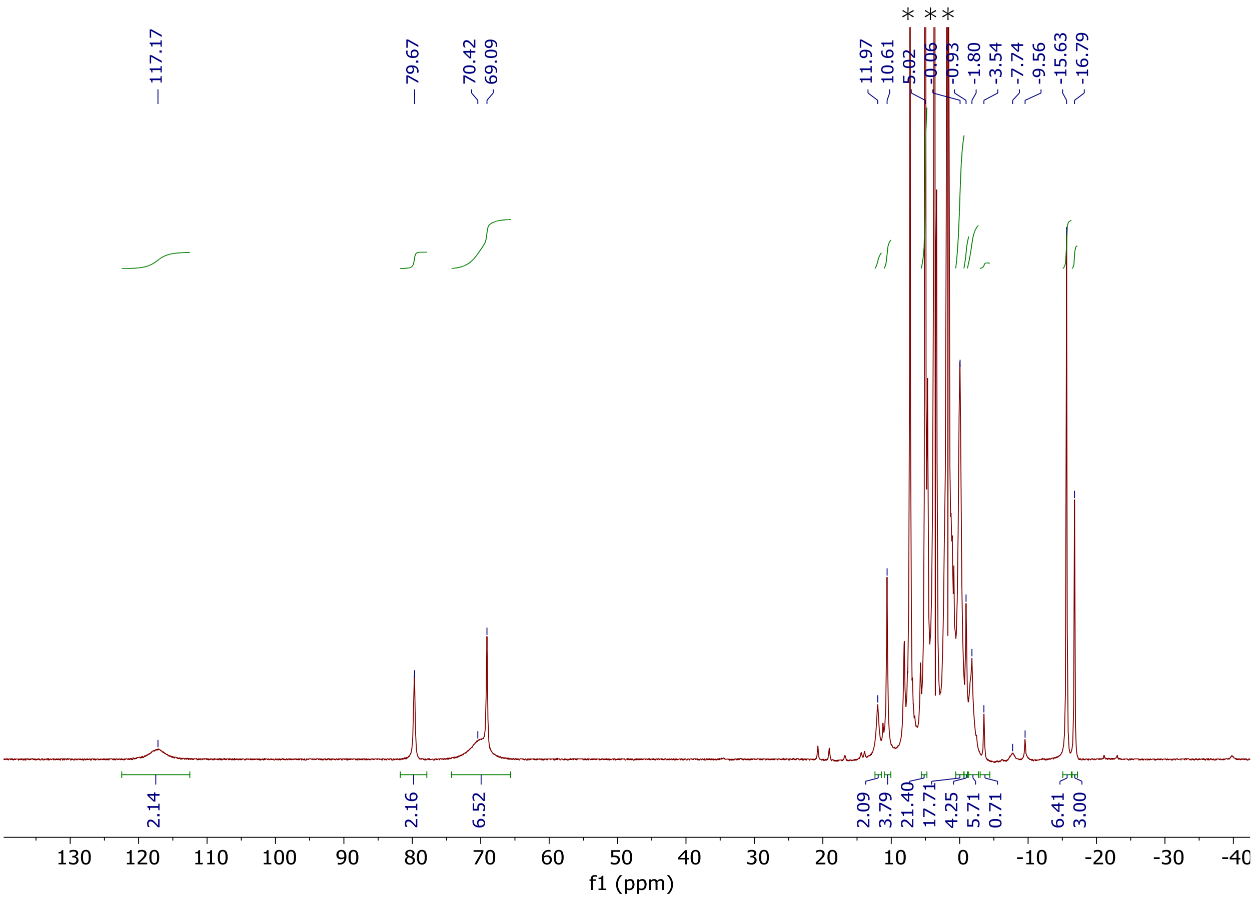

Figure 5.S1. ^{1}H NMR spectrum (400 MHz, THF-h_8, solvent suppression) of **5.2**. Solvent peaks are indicated by asterisks (*).

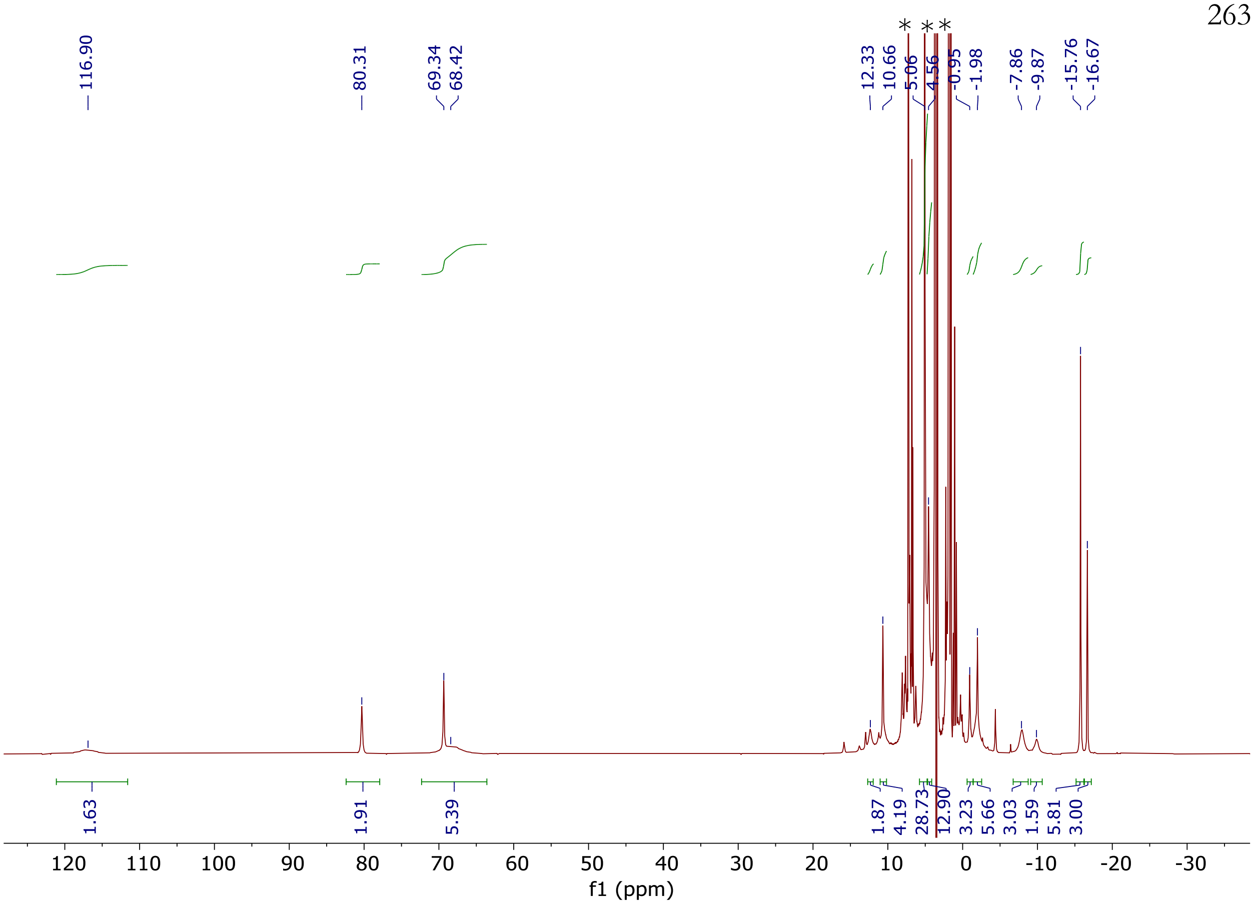

Figure 5.S2. ^{1}H NMR spectrum (400 MHz, THF-h_8, solvent suppression) of **5.3**. Solvent peaks are indicated by asterisks (*).

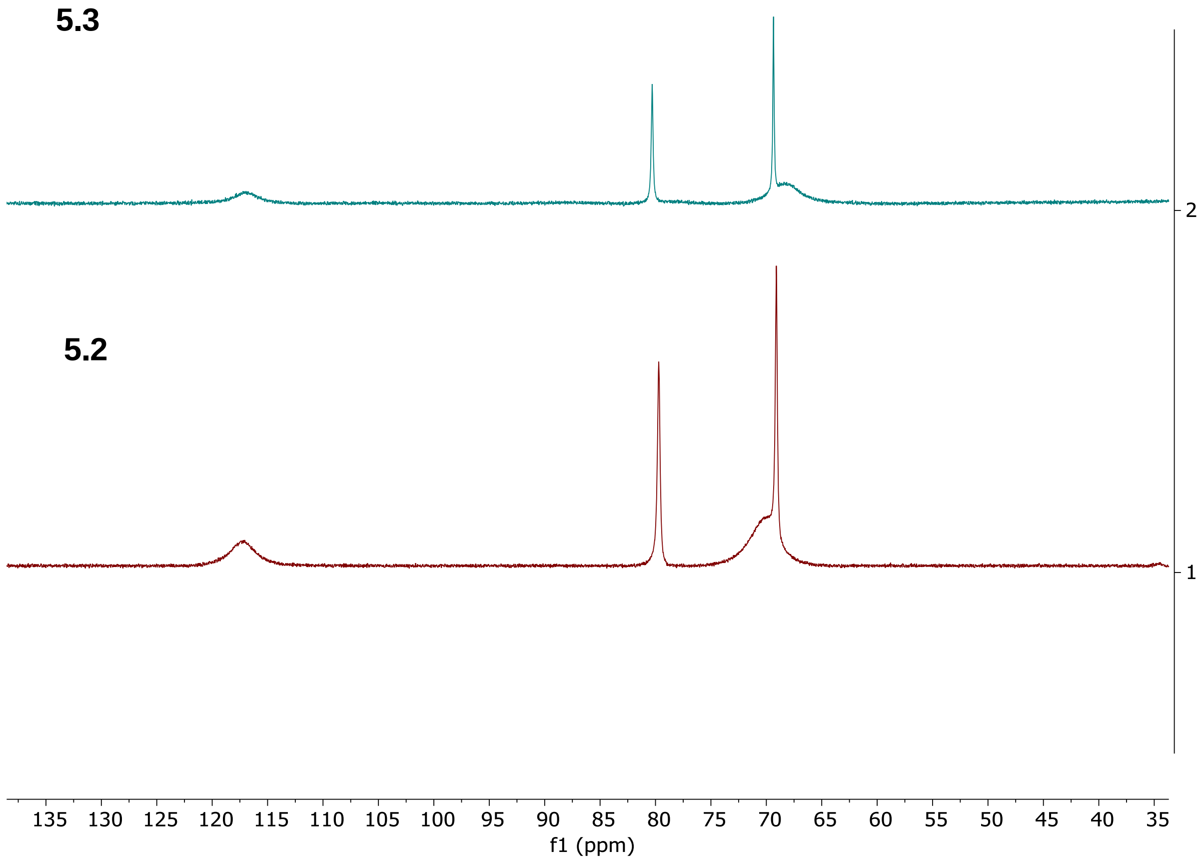

Figure 5.S3. Comparison of ^{1}H NMR spectra (400 MHz, THF-h_8, solvent suppression) of **5.2** and **5.3**, showing the characteristic peak shifts.

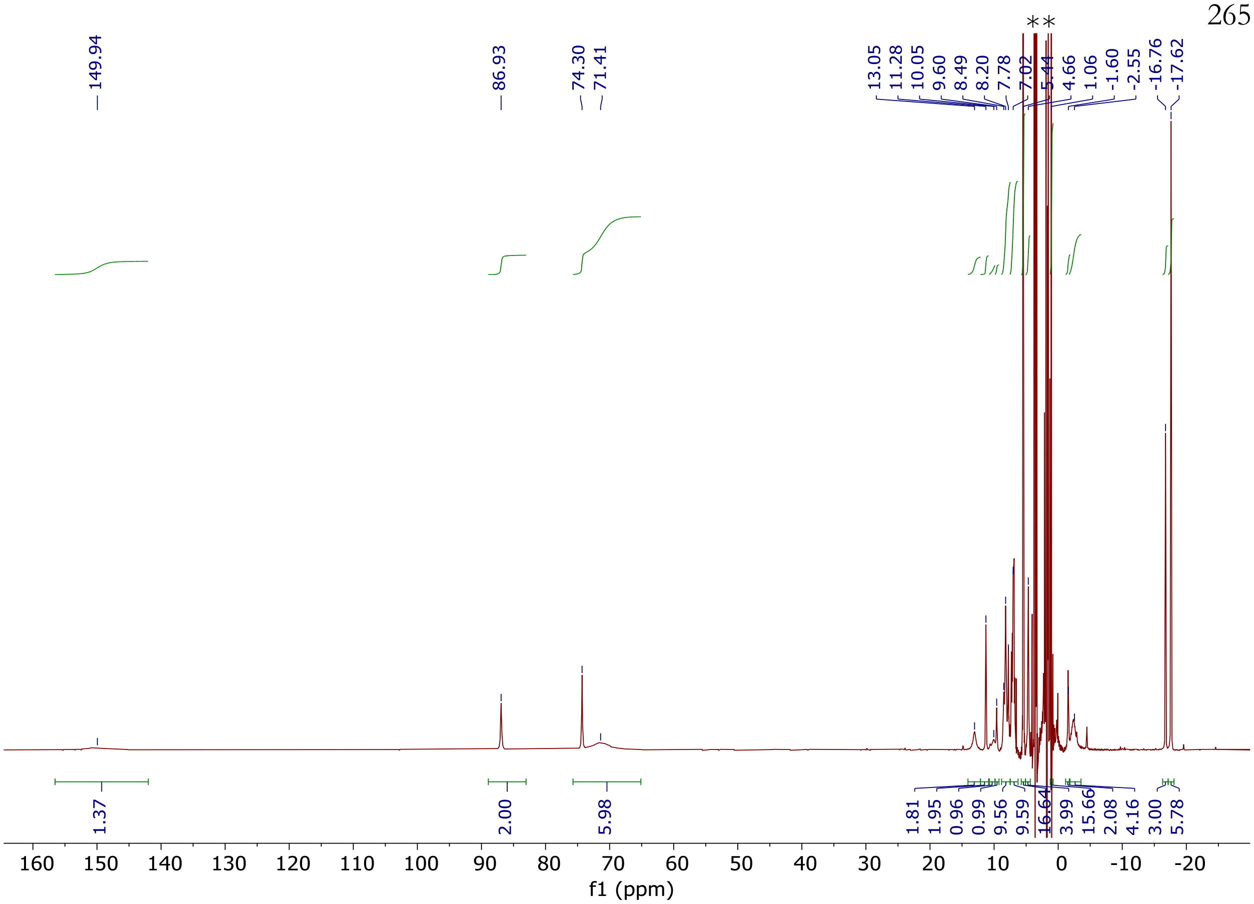

Figure 5.S4. ^{1}H NMR spectrum (400 MHz, THF-h_8, solvent suppression) of **5.4** (Ph_2MePCH_2 variant). Solvent peaks are indicated by asterisks (*).

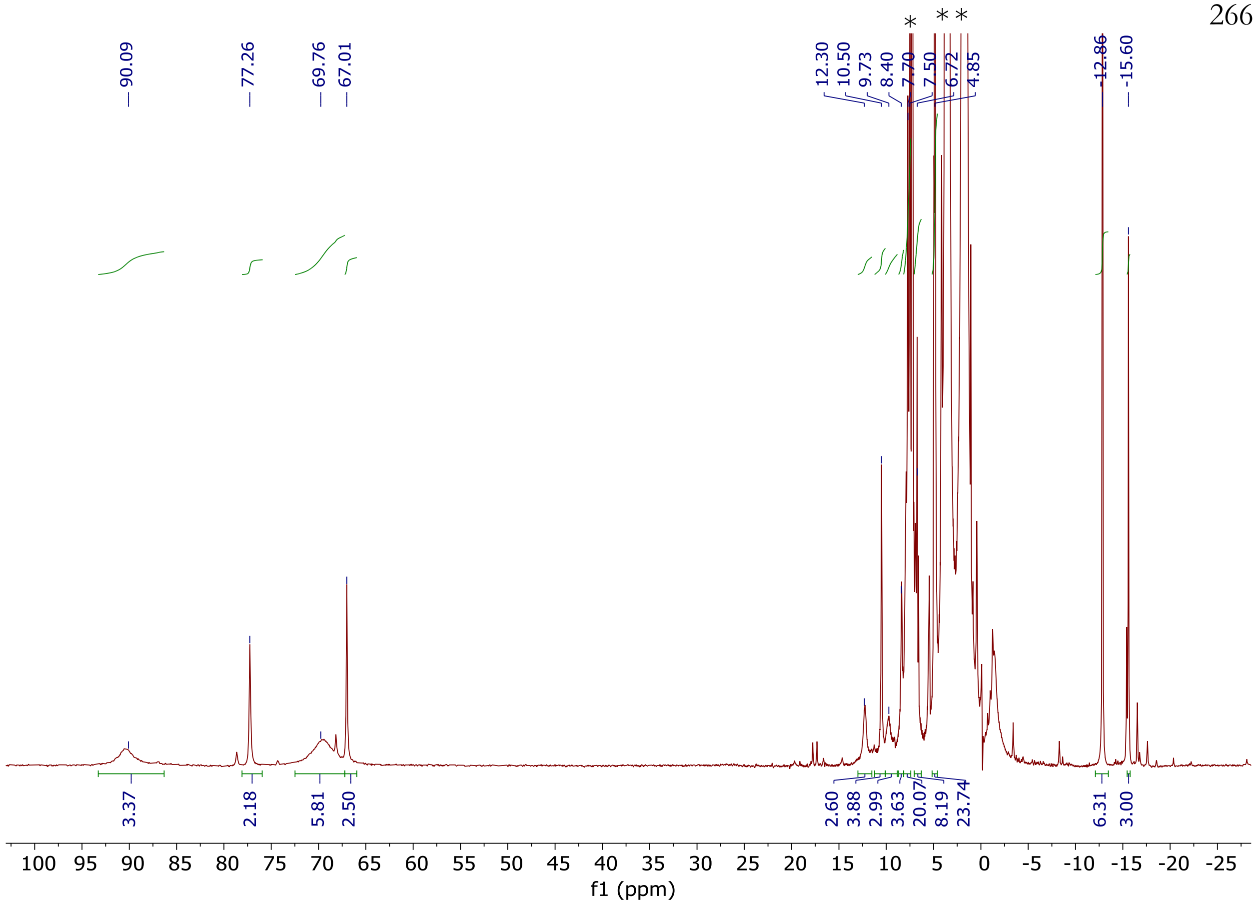

Figure 5.S5. ^{1}H NMR spectrum (400 MHz, THF-h_8, solvent suppression) of crude **5.4** (Ph_3PCH_2 variant). Solvent peaks are indicated by asterisks (*).

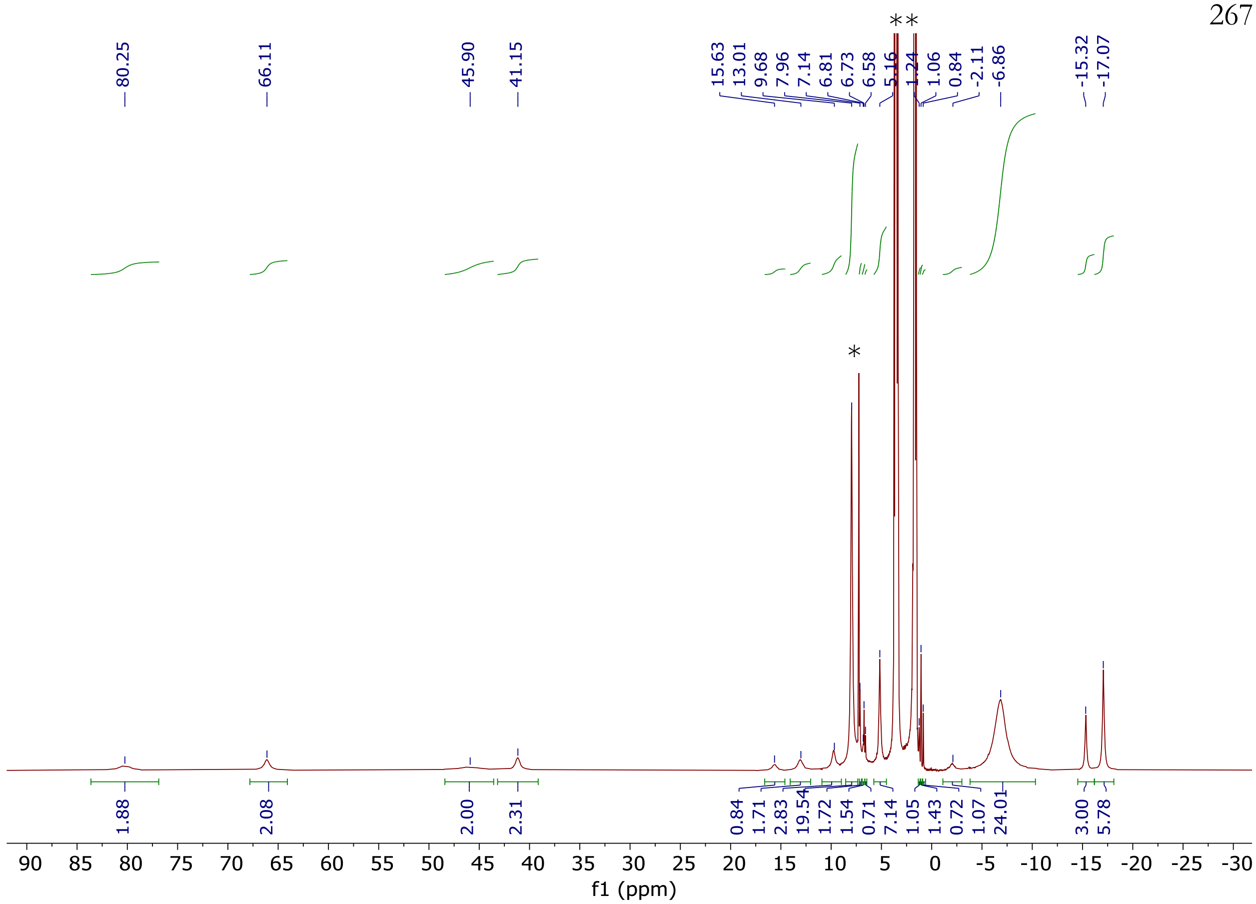

Figure 5.S6. ^{1}H NMR spectrum (400 MHz, THF-h_8, solvent suppression) of **5.5**. Solvent peaks are indicated by asterisks (*).

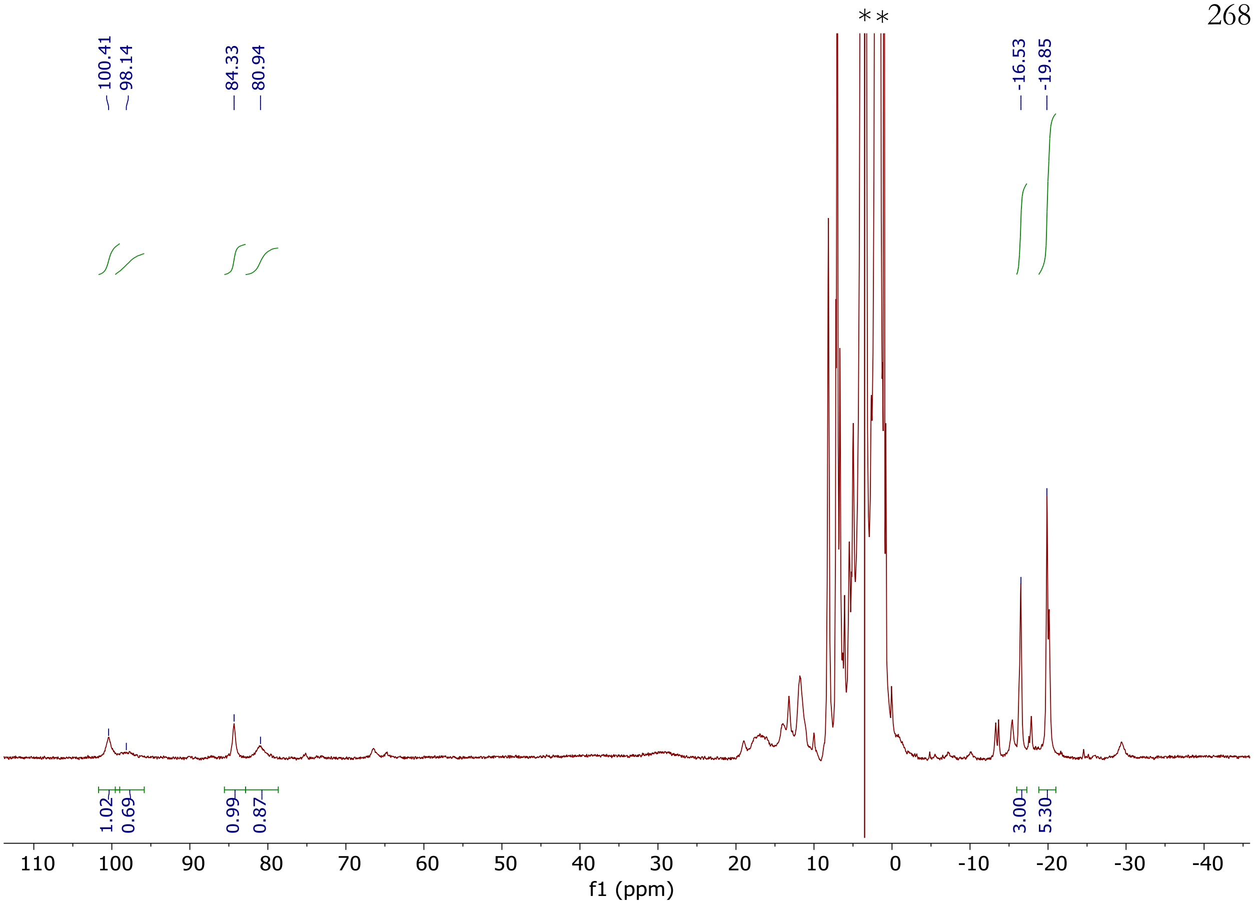

Figure 5.S7. ^{1}H NMR spectrum (400 MHz, THF-h_8, solvent suppression) of **5.6** with impurities present. Solvent peaks are indicated by asterisks (*).

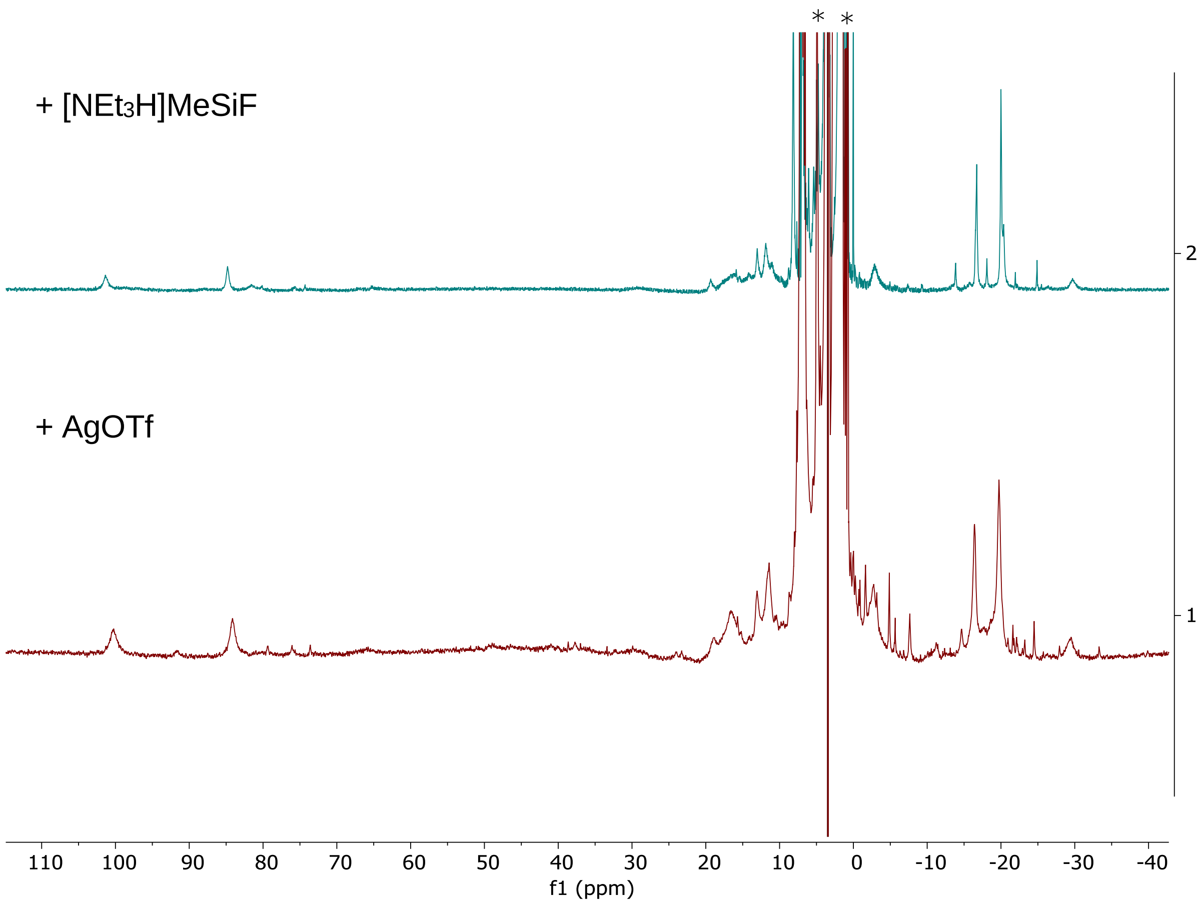

Figure 5.S8. ^{1}H NMR spectra (400 MHz, THF-h_8, solvent suppression) of the product when **5.5** is reacted with [NEt$_3$H]MeSiF (top) and AgOTf (bottom). Solvent peaks are indicated by asterisks (*).

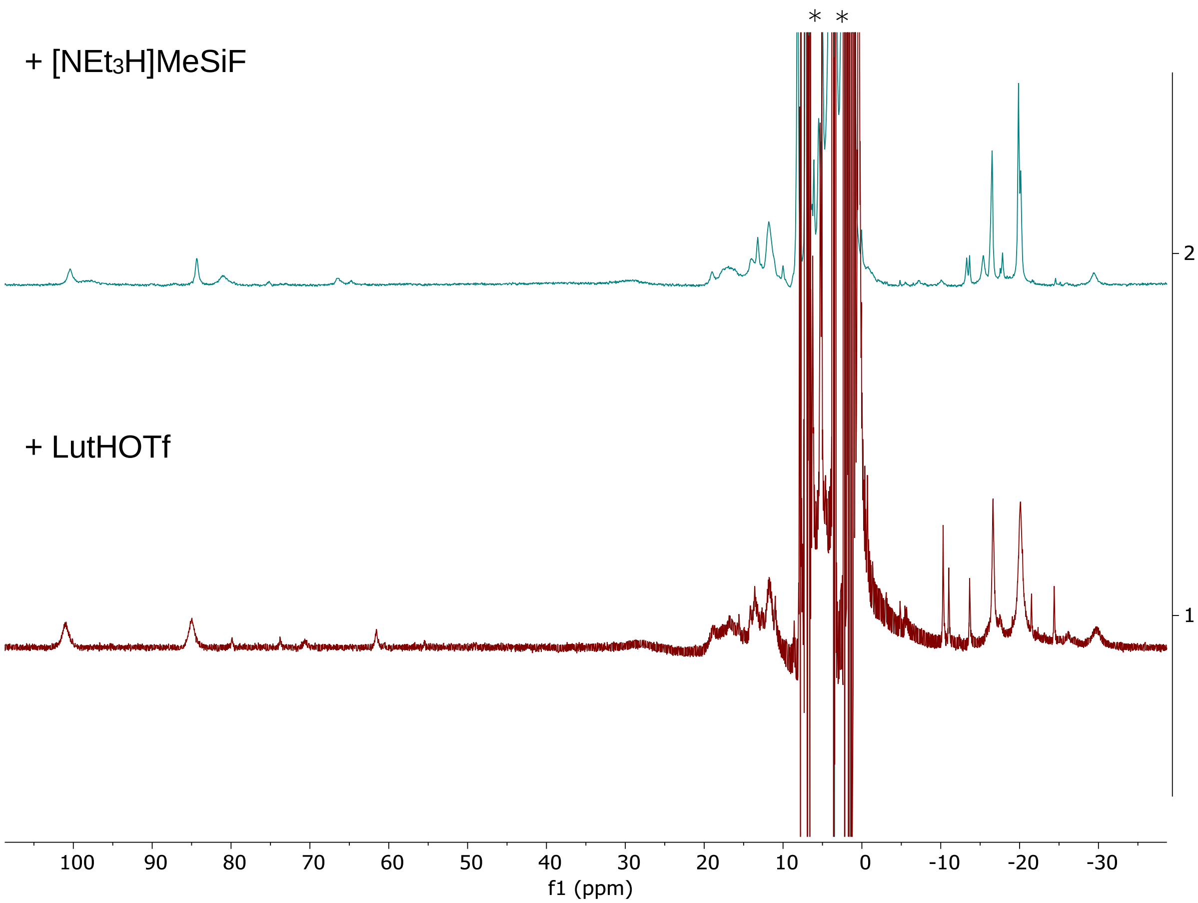

Figure 5.S9. ^{1}H NMR spectrum (400 MHz, THF-h_8, solvent suppression) of the product when **5.5** is reacted with $[NEt_3H]MeSiF$ (top) and lutidinium triflate (bottom). Solvent peaks are indicated by asterisks (*).

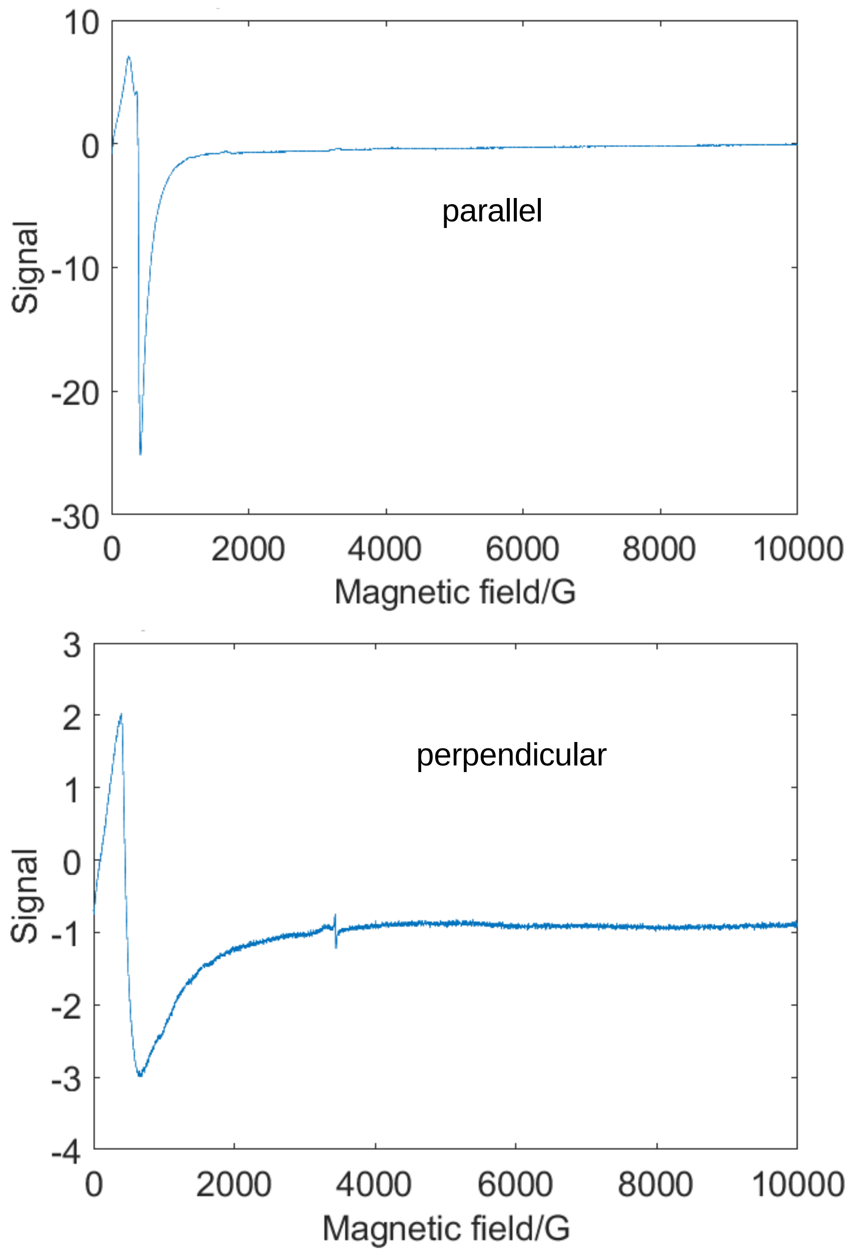

Figure 5.S10. X-band EPR spectra of **5.5** in toluene at 4 K in parallel (top) and perpendicular (bottom) modes.

B) Electrochemical information

Cyclic voltammetry experiments were performed with a Pine Instrument Company AFCBP1 biopotentiostat with the *AfterMath* software package. All measurements were performed in a three-electrode cell, which consisted of glassy carbon (working; ⌀ = 3.0 mm), Ag wire (reference), and bare Pt wire (counter), in a N_2-filled MBraun glovebox at room temperature. Dry THF that contained ~0.2 M $[Bu_4N][PF_6]$ was used as the electrolyte solution. Redox potentials are reported relative to the ferrocene/ferrocenium redox wave (Fc/Fc^+; ferrocene added as an internal standard). The open circuit potential was measured prior to each voltammogram being collected. Voltammograms were scanned reductively in order to minimize the oxidative damage that was frequently observed on scanning more oxidatively.

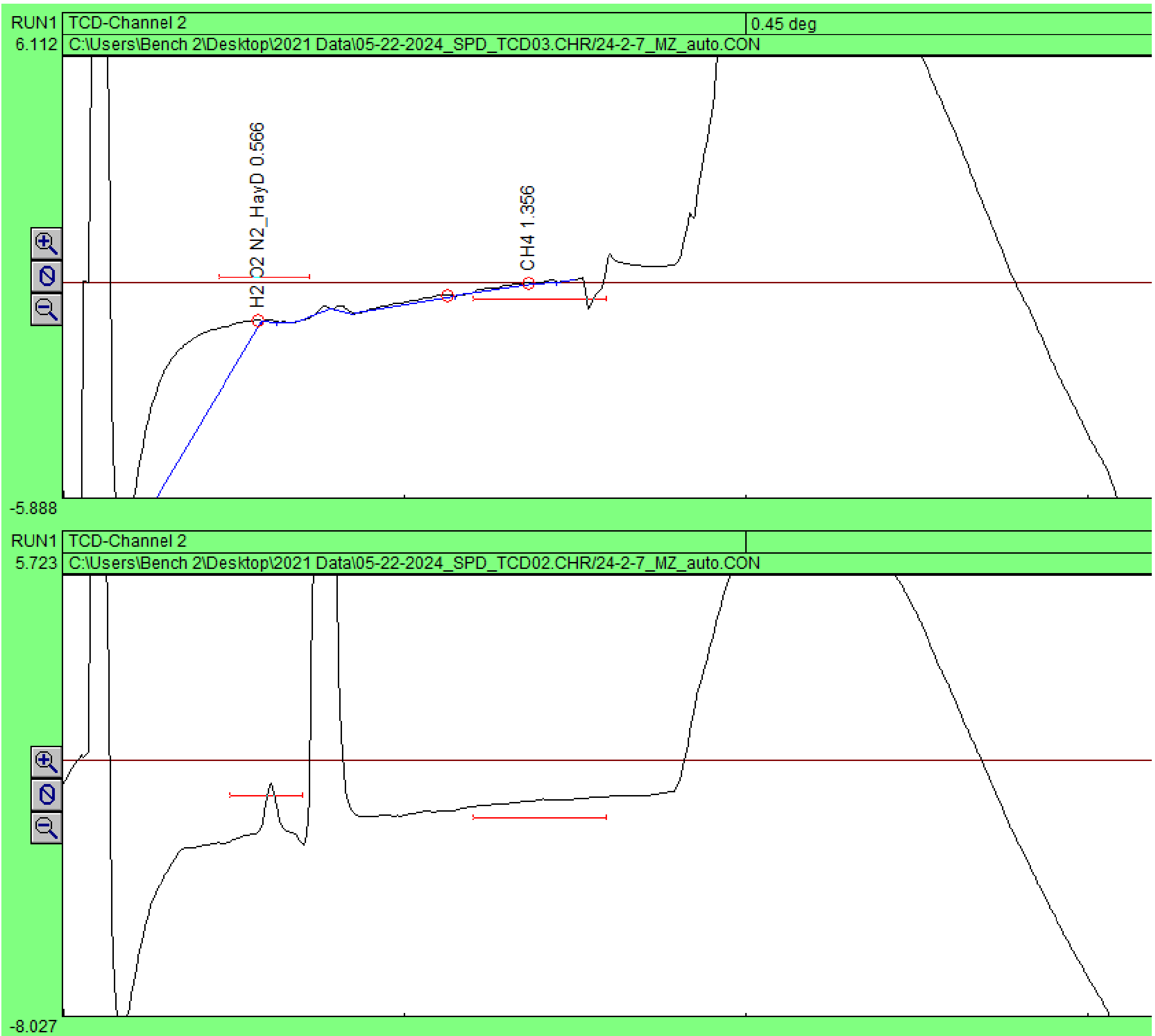

Figure 5.S11. Gas chromatogram of the headspace after bulk electrolysis with 20 equivalents $[NEt_4][MeSiF]$ at -2.5 V vs. Fc^+/Fc (bottom), showing a peak assigned to H_2 at 0.566 min, and no H_2 in the blank sample (top). The other prominent peaks are N_2 and CO_2 in order of increasing retention time.

C) Mossbauer spectroscopy

Zero field ^{57}Fe Mössbauer spectra were recorded in constant acceleration at 80 K on a spectrometer from See Co (Edina, MN) equipped with an SVT-400 cryostat (Janis, Woburn, MA). The quoted isomer shifts are relative to the centroid of the spectrum of α-Fe foil at room temperature. Samples were ground with boron nitride into a fine powder and transferred to a Delrin cup. The data were fit to Lorentzian lineshapes using the program WMOSS (www.wmoss.org).

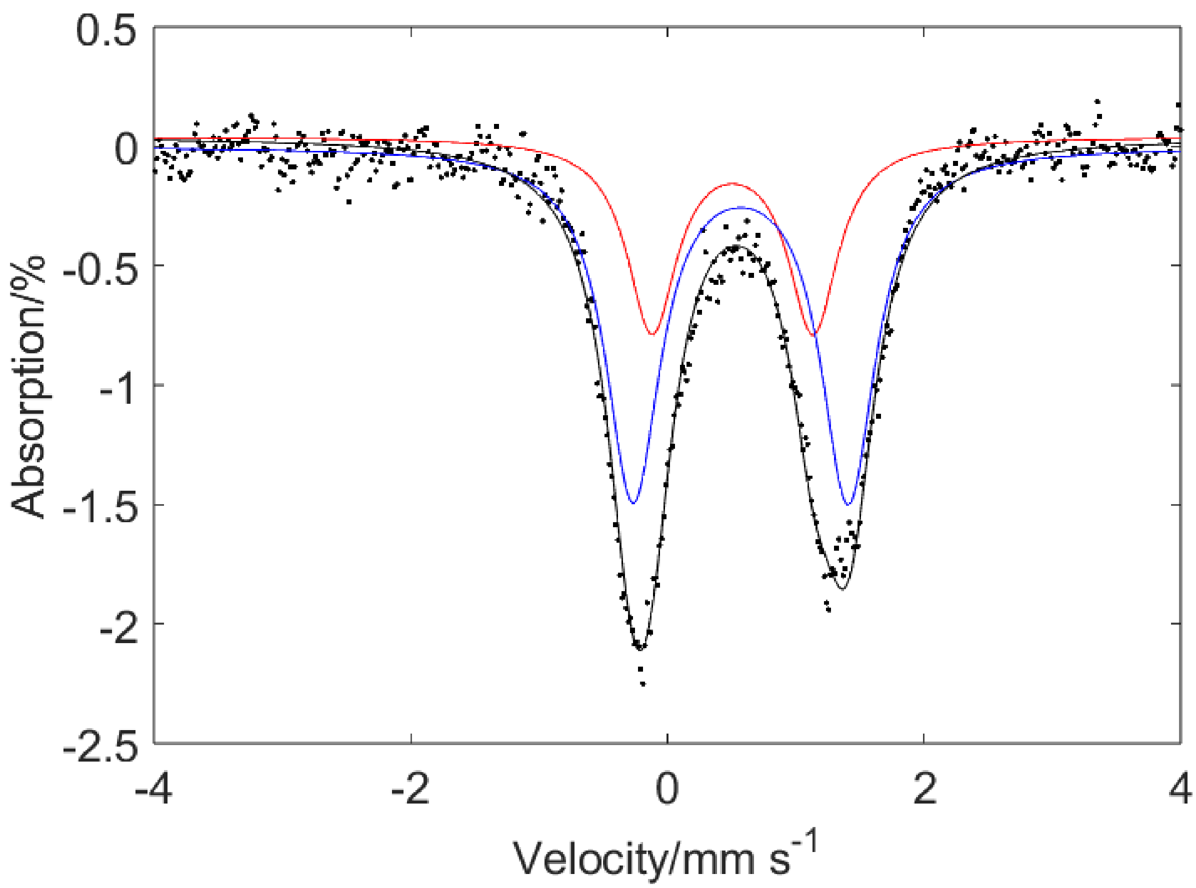

Figure 5.S12. Fitting for the Mössbauer spectrum of **5.5** (80 K, no applied field) using a two-site model, with the total fit shown by the black trace.

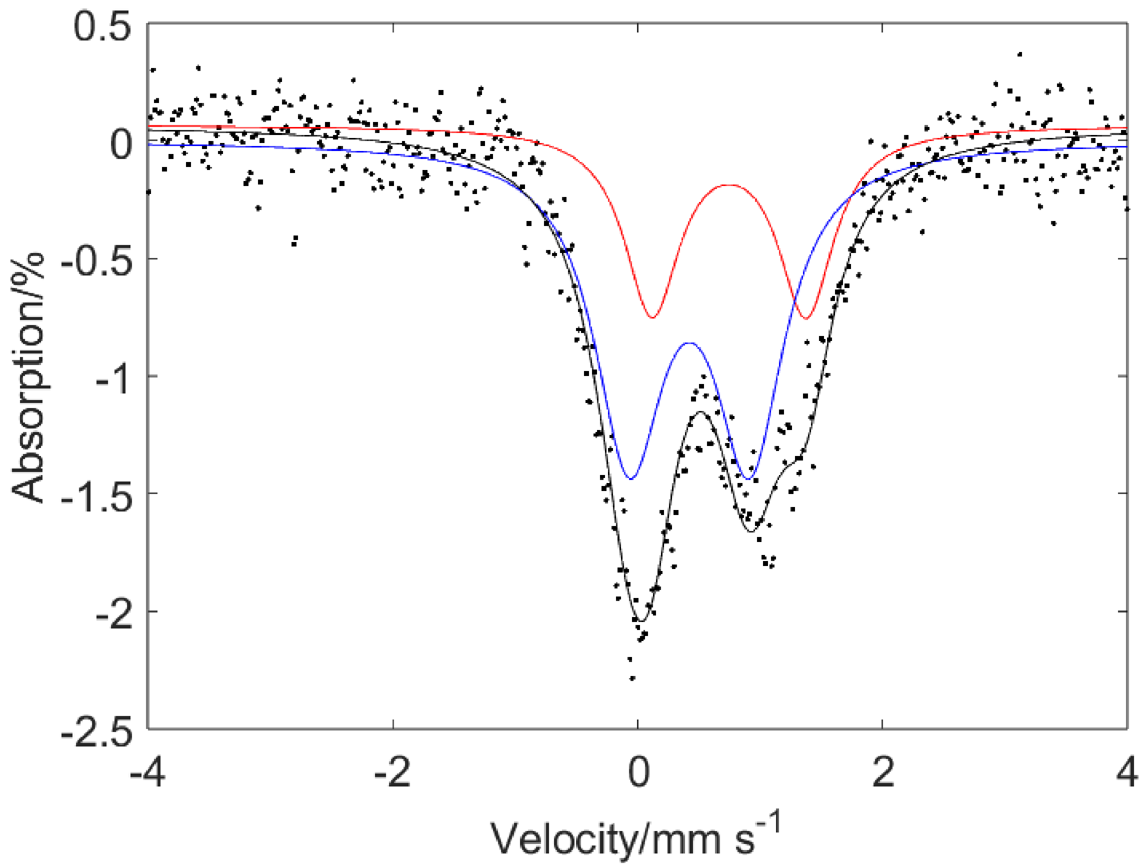

Figure 5.S13. Fitting for the Mössbauer spectrum of **5.6** (80 K, no applied field) using a two-site model, with the total fit shown by the black trace.

Mössbauer fit parameters:

For **5.5**: The Mössbauer spectrum of **5.5** can be fit with a two-site model using the following parameters:

Site 1: δ = 0.51 mm s^{-1} $|E_Q|$ = 1.26 mm s^{-1} Linewidth = 0.47 mm s^{-1} Area = 33%

Site 2: δ = 0.57 mm s^{-1} $|E_Q|$ = 1.68 mm s^{-1} Linewidth = 0.52 mm s^{-1} Area = 67%

For **5.6**: The Mössbauer spectrum of **5.6** can be fit with a two-site model using the following parameters:

Site 1: δ = 0.40 mm s^{-1} $|E_Q|$ = 1.44 mm s^{-1} Linewidth = 0.64 mm s^{-1} Area = 34%

Site 2: δ = 0.48 mm s^{-1} $|E_Q|$ = 0.83 mm s^{-1} Linewidth = 0.55 mm s^{-1} Area = 66%

D) Crystallographic information

1. X-ray crystallography:

XRD data were collected at 100 K on a Bruker AXS D8 KAPPA or Bruker AXS D8 VENTURE diffractometer [microfocus sealed X-ray tube, λ(Mo Kα) = 0.71073 Å or λ(Cu Kα) = 1.54178 Å]. All manipulations, including data collection, integration, and scaling, were carried out using the Bruker *APEX3* software.[53] Absorption corrections were applied using *SADABS*.[54] Structures were solved by direct methods using *Sir92*[55] or *SUPERFLIP*[56] and refined using full-matrix least-squares on *CRYSTALS*[57] to convergence. All non-H atoms were refined using anisotropic displacement parameters. H atoms were placed in idealized positions and refined using a riding model. Because of the size of the compounds most crystals included solvent-accessible voids that contained a disordered solvent. The solvent could be either modeled satisfactorily, or accounted for using either the *SQUEEZE* procedure in the *PLATON* software package.[58]

2. Additional information:

Special refinement details for **5.3**. The asymmetric unit contains two co-crystallized pentane solvent molecules, which can be modeled satisfactorily using bond lengths and similarity restraints for ADPs. The coordinated THF molecule is disordered over two positions, with occupancies of 48% and 52%.

Special refinement details for **5.5**. The asymmetric unit of the structure contains one co-crystallized pentane and two halves of C_6H_6 solvent molecules, which can be modeled satisfactorily using bond lengths and similarity restraints for ADPs.

Special refinement details for **5.6**. The asymmetric unit contains half of a cluster. One ^{t}Bu group is disordered over two positions, with occupancies of 46% and 54%. The solvent molecules are heavily disordered and cannot be modeled satisfactorily. Therefore, the electron density for co-crystallized solvent molecules were accounted for using the *SQUEEZE* procedure in *PLATON*,[58] whereby 108 electrons were found in a volume of 421 Å^3, consistent with the presence of 1[C_5H_{12}] in the asymmetric unit.

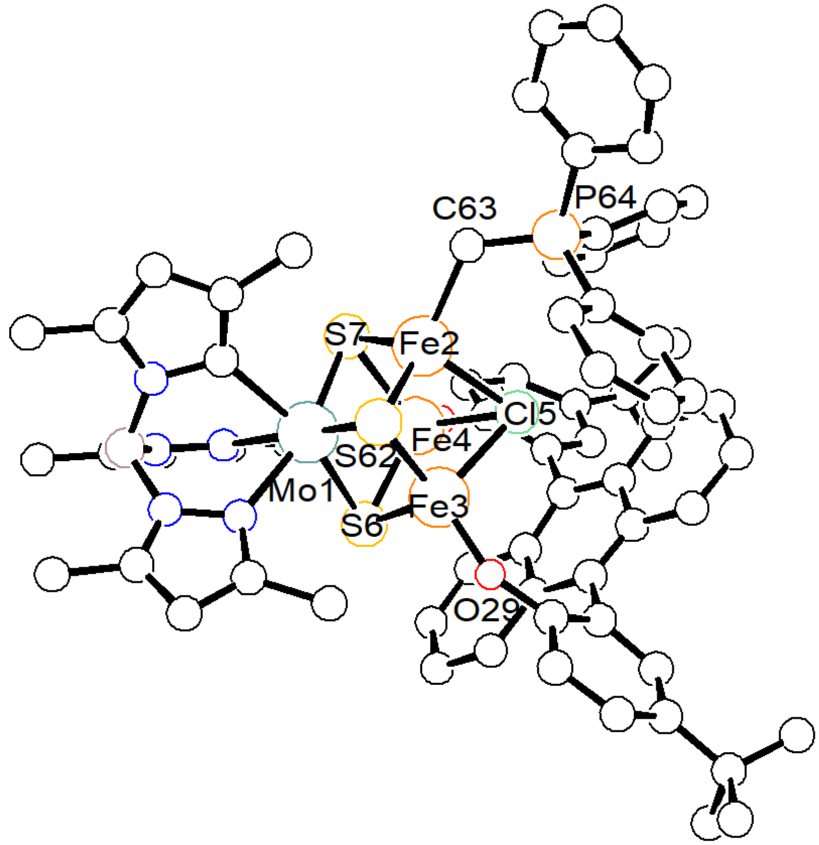

Figure 5.S14. Connectivity of **5.4** (Ph_3PCH_2 variant). Spheres are shown at 50% probability level. Hydrogen atoms, solvent molecules, and part of the bisphenoxide ligand are omitted for clarity.

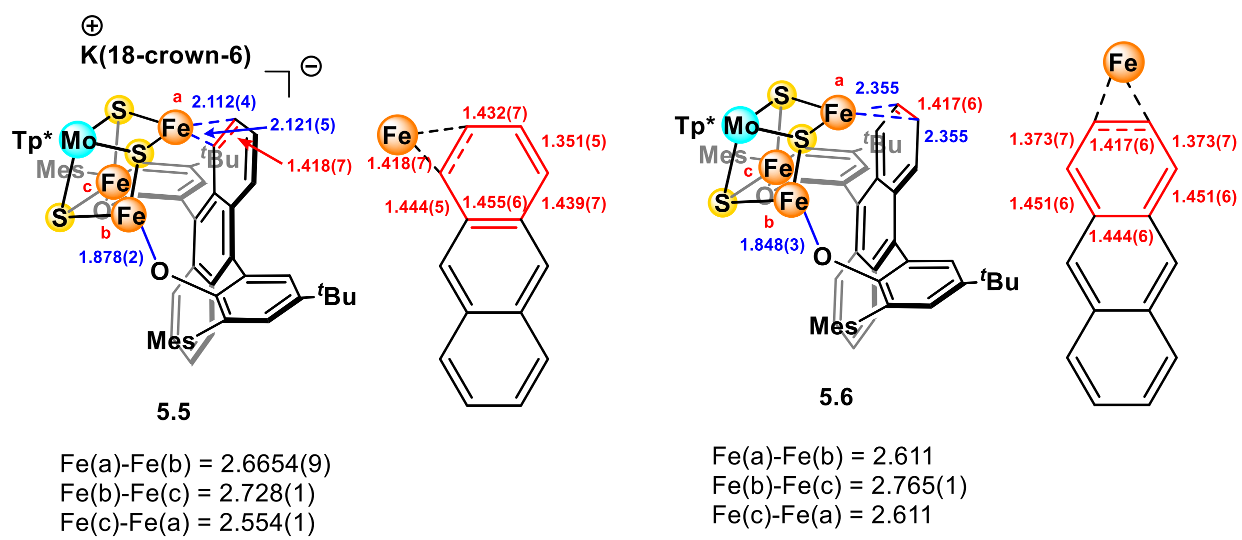

Figure 5.S15. Bond length comparisons in Å for **5.5** and **5.6** for selected bonds.

Table 5.S1. Summary of statistics for diffraction data for **5.3**, **5.5** and **5.6**

Cluster	5.3	5.5	5.6
Empirical formula	$C_{81}H_{106}BClFe_3MoN_6O_3S_3$	$C_{96}H_{122}BFe_3KMoN_6O_8S_3$	$C_{67}H_{74}BFe_3MoN_6O_2S_3$
Formula weight	1617.71	1897.65	1365.80
Temperature/K	100	100	100
Crystal system	Monoclinic	Triclinic	Orthorhombic
Space group	$P2_1/c$	P-1	$Pmn2_1$
a/Å	16.802(2)	13.4861(7)	21.873(3)
b/Å	18.478(4)	17.0587(11)	8.321(1)
c/Å	25.856(4)	21.5941(14)	18.7200(17)
α/°	90	106.717(4)	90
β/°	97.909(5)	96.994(4)	90
γ/°	90	100.418(4)	90
Volume/Å^3	7951(2)	4599.1(5)	3407.1(6)
Z	4	2	2
ρ_{calc}/g cm^{-3}	1.351	1.370	1.335
μ/mm^{-1}	6.997	6.311	7.706
F(000)	3392.0	1992.0	1422.0
Crystal size/mm^3	0.09 × 0.19 × 0.24	0.09 × 0.10 × 0.23	0.07 × 0.07 × 0.10
Radiation	Cu Kα	Cu Kα	Cu Kα
θ_{max}/°	74.824	72.795	75.040
Index ranges	$-20 \leq h \leq 20$, $-23 \leq k \leq 23$, $-32 \leq l \leq 29$	$-16 \leq h \leq 16$, $-21 \leq k \leq 20$, $0 \leq l \leq 26$	$-25 \leq h \leq 27$, $-10 \leq k \leq 10$, $-22 \leq l \leq 23$
Reflections measured	188687	195844	36522
Independent reflections	16249	18211	6396
Restraints/Parameters	46/911	140/1072	57/424
GOF on F^2	1.000	1.002	0.994
R-factor	0.0431	0.0630	0.0373
Weighted R-factor	0.1071	0.1688	0.0994
Largest diff. peak/hole/e Å^{-3}	1.03/-0.93	2.33/-1.94	0.84/-0.48

5.6 REFERENCES

(1) Howard, J. B.; Rees, D. C. Structural Basis of Biological Nitrogen Fixation. *Chem. Rev.* **1996**, *96* (7), 2965–2982. https://doi.org/10.1021/cr9500545.

(2) Burgess, B. K.; Lowe, D. J. Mechanism of Molybdenum Nitrogenase. *Chem. Rev.* **1996**, *96* (7), 2983–3012. https://doi.org/10.1021/cr950055x.

(3) Spatzal, T.; Aksoyoglu, M.; Zhang, L.; Andrade, S. L. A.; Schleicher, E.; Weber, S.; Rees, D. C.; Einsle, O. Evidence for Interstitial Carbon in Nitrogenase FeMo Cofactor. *Science* **2011**, *334* (6058), 940. https://doi.org/10.1126/science.1214025.

(4) Einsle, O.; Tezcan, F. A.; Andrade, S. L. A.; Schmid, B.; Yoshida, M.; Howard, J. B.; Rees, D. C. Nitrogenase MoFe-Protein at 1.16 Å Resolution: A Central Ligand in the FeMo-Cofactor. *Science* **2002**, *297* (5587), 1696. https://doi.org/10.1126/science.1073877.

(5) Lancaster, K. M.; Roemelt, M.; Ettenhuber, P.; Hu, Y.; Ribbe, M. W.; Neese, F.; Bergmann, U.; DeBeer, S. X-Ray Emission Spectroscopy Evidences a Central Carbon in the Nitrogenase Iron-Molybdenum Cofactor. *Science* **2011**, *334* (6058), 974. https://doi.org/10.1126/science.1206445.

(6) Einsle, O.; Rees, D. C. Structural Enzymology of Nitrogenase Enzymes. *Chem. Rev.* **2020**, *120* (12), 4969–5004. https://doi.org/10.1021/acs.chemrev.0c00067.

(7) Sippel, D.; Rohde, M.; Netzer, J.; Trncik, C.; Gies, J.; Grunau, K.; Djurdjevic, I.; Decamps, L.; Andrade, S. L. A.; Einsle, O. A Bound Reaction Intermediate Sheds Light on the Mechanism of Nitrogenase. *Science* **2018**, *359* (6383), 1484. https://doi.org/10.1126/science.aar2765.

(8) Kang, W.; Lee, C. C.; Jasniewski, A. J.; Ribbe, M. W.; Hu, Y. Structural Evidence for a Dynamic Metallocofactor during N_2 Reduction by Mo-Nitrogenase. *Science* **2020**, *368* (6497), 1381. https://doi.org/10.1126/science.aaz6748.

(9) Peters, J. W.; Einsle, O.; Dean, D. R.; DeBeer, S.; Hoffman, B. M.; Holland, P. L.; Seefeldt, L. C. Comment on “Structural Evidence for a Dynamic Metallocofactor during N_2 Reduction by Mo-Nitrogenase.” *Science* **2021**, *371* (6530), eabe5481. https://doi.org/10.1126/science.abe5481.

(10) Kang, W.; Lee, C. C.; Jasniewski, A. J.; Ribbe, M. W.; Hu, Y. Response to Comment on “Structural Evidence for a Dynamic Metallocofactor during N_2 Reduction by Mo-Nitrogenase.” *Science* **2021**, *371* (6530), eabe5856. https://doi.org/10.1126/science.abe5856.

(11) Münck, E.; Rhodes, H.; Orme-Johnson, W. H.; Davis, L. C.; Brill, W. J.; Shah, V. K. Nitrogenase. VIII. Mössbauer and EPR Spectroscopy. The MoFe Protein Component from *Azotobacter vinelandii* OP. *Biochim. Biophys. Acta, Protein Struct.* **1975**, *400* (1), 32–53. https://doi.org/10.1016/0005-2795(75)90124-5.

(12) Bjornsson, R.; Lima, F. A.; Spatzal, T.; Weyhermüller, T.; Glatzel, P.; Bill, E.; Einsle, O.; Neese, F.; DeBeer, S. Identification of a Spin-Coupled Mo(III) in the Nitrogenase Iron–Molybdenum Cofactor. *Chem. Sci.* **2014**, *5* (8), 3096–3103. https://doi.org/10.1039/C4SC00337C.

(13) Spatzal, T.; Schlesier, J.; Burger, E.-M.; Sippel, D.; Zhang, L.; Andrade, S. L. A.; Rees, D. C.; Einsle, O. Nitrogenase FeMoco Investigated by Spatially Resolved Anomalous Dispersion Refinement. *Nat. Commun.* **2016**, *7* (1), 10902. https://doi.org/10.1038/ncomms10902.

(14) Castillo, R. G.; Hahn, A. W.; Van Kuiken, B. E.; Henthorn, J. T.; McGale, J.; DeBeer, S. Probing Physical Oxidation State by Resonant X-Ray Emission Spectroscopy: Applications to Iron Model Complexes and Nitrogenase. *Angewandte Chemie International Edition* **2021**, *60* (18), 10112–10121. https://doi.org/10.1002/anie.202015669.

(15) Christiansen, J.; Tittsworth, R. C.; Hales, B. J.; Cramer, S. P. Fe and Mo EXAFS of Azotobacter Vinelandii Nitrogenase in Partially Oxidized and Singly Reduced Forms. *J. Am. Chem. Soc.* **1995**, *117* (40), 10017–10024. https://doi.org/10.1021/ja00145a012.

(16) Yoo, S. J.; Angove, H. C.; Papaefthymiou, V.; Burgess, B. K.; Münck, E. Mössbauer Study of the MoFe Protein of Nitrogenase from Azotobacter Vinelandii Using Selective 57Fe Enrichment of the M-Centers. *J. Am. Chem. Soc.* **2000**, *122* (20), 4926–4936. https://doi.org/10.1021/ja000254k.

(17) Van Stappen, C.; Davydov, R.; Yang, Z.-Y.; Fan, R.; Guo, Y.; Bill, E.; Seefeldt, L. C.; Hoffman, B. M.; DeBeer, S. Spectroscopic Description of the E1 State of Mo Nitrogenase Based on Mo and Fe X-Ray Absorption and Mössbauer Studies. *Inorg. Chem.* **2019**, *58* (18), 12365–12376. https://doi.org/10.1021/acs.inorgchem.9b01951.

(18) Lukoyanov, D.; Barney, B. M.; Dean, D. R.; Seefeldt, L. C.; Hoffman, B. M. Connecting Nitrogenase Intermediates with the Kinetic Scheme for N_2 Reduction by a Relaxation Protocol and Identification of the N_2 Binding State. *Proc. Natl. Acad. Sci. U.S.A.* **2007**, *104* (5), 1451–1455. https://doi.org/10.1073/pnas.0610975104.

(19) Lukoyanov, D.; Yang, Z.-Y.; Duval, S.; Danyal, K.; Dean, D. R.; Seefeldt, L. C.; Hoffman, B. M. A Confirmation of the Quench-Cryoannealing Relaxation Protocol for Identifying Reduction States of Freeze-Trapped Nitrogenase Intermediates. *Inorg. Chem.* **2014**, *53* (7), 3688–3693. https://doi.org/10.1021/ic500013c.

(20) Igarashi, R. Y.; Laryukhin, M.; Dos Santos, P. C.; Lee, H.-I.; Dean, D. R.; Seefeldt, L. C.; Hoffman, B. M. Trapping H- Bound to the Nitrogenase FeMo-Cofactor Active Site during H2 Evolution: Characterization by ENDOR Spectroscopy. *J. Am. Chem. Soc.* **2005**, *127* (17), 6231–6241. https://doi.org/10.1021/ja043596p.

(21) Hoeke, V.; Tociu, L.; Case, D. A.; Seefeldt, L. C.; Raugei, S.; Hoffman, B. M. High-Resolution ENDOR Spectroscopy Combined with Quantum Chemical Calculations Reveals the Structure of Nitrogenase Janus Intermediate E4(4H). *J. Am. Chem. Soc.* **2019**. https://doi.org/10.1021/jacs.9b04474.

(22) Lukoyanov, D.; Yang, Z.-Y.; Dean, D. R.; Seefeldt, L. C.; Hoffman, B. M. Is Mo Involved in Hydride Binding by the Four-Electron Reduced (E_4) Intermediate of the Nitrogenase MoFe Protein? *J. Am. Chem. Soc.* **2010**, *132* (8), 2526–2527. https://doi.org/10.1021/ja910613m.

(23) Doan, P. E.; Telser, J.; Barney, B. M.; Igarashi, R. Y.; Dean, D. R.; Seefeldt, L. C.; Hoffman, B. M. ^{57}Fe ENDOR Spectroscopy and 'Electron Inventory' Analysis of the Nitrogenase E4 Intermediate Suggest the Metal-Ion Core of FeMo-Cofactor Cycles Through Only One Redox Couple. *J. Am. Chem. Soc.* **2011**, *133* (43), 17329–17340. https://doi.org/10.1021/ja205304t.

(24) Lukoyanov, D.; Yang, Z.-Y.; Khadka, N.; Dean, D. R.; Seefeldt, L. C.; Hoffman, B. M. Identification of a Key Catalytic Intermediate Demonstrates That Nitrogenase Is Activated by the Reversible Exchange of N_2 for H_2. *J. Am. Chem. Soc.* **2015**, *137* (10), 3610–3615. https://doi.org/10.1021/jacs.5b00103.

(25) Lukoyanov, D.; Khadka, N.; Dean, D. R.; Raugei, S.; Seefeldt, L. C.; Hoffman, B. M. Photoinduced Reductive Elimination of H_2 from the Nitrogenase Dihydride (Janus) State Involves a FeMo-Cofactor-H_2 Intermediate. *Inorg. Chem.* **2017**, *56* (4), 2233–2240. https://doi.org/10.1021/acs.inorgchem.6b02899.

(26) Lukoyanov, D.; Khadka, N.; Yang, Z.-Y.; Dean, D. R.; Seefeldt, L. C.; Hoffman, B. M. Reductive Elimination of H_2 Activates Nitrogenase to Reduce the N≡N Triple Bond: Characterization of the E_4(4H) Janus Intermediate in Wild-Type Enzyme. *J. Am. Chem. Soc.* **2016**, *138* (33), 10674–10683. https://doi.org/10.1021/jacs.6b06362.

(27) Blakeley, M. P.; Langan, P.; Niimura, N.; Podjarny, A. Neutron Crystallography: Opportunities, Challenges, and Limitations. *Curr. Opin. Struct. Biol.* **2008**, *18* (5), 593–600. https://doi.org/10.1016/j.sbi.2008.06.009.

(28) Henderson, R. A. Proton Transfer to Synthetic Fe–S-Based Clusters. *Coord. Chem. Rev.* **2005**, *249* (17), 1841–1856. https://doi.org/10.1016/j.ccr.2004.12.021.

(29) Saouma, C. T.; Morris, W. D.; Darcy, J. W.; Mayer, J. M. Protonation and Proton-Coupled Electron Transfer at S-Ligated [4Fe-4S] Clusters. *Chem. Eur. J.* **2015**, *21* (25), 9256–9260. https://doi.org/10.1002/chem.201500152.

(30) Johnson, R. W.; Holm, R. H. Reaction Chemistry of the Iron-Sulfur Protein Site Analogs $[Fe_4S_4(SR)_4]^{2-}$. Sequential Thiolate Ligand Substitution Reactions with Electrophiles. *J. Am. Chem. Soc.* **1978**, *100* (17), 5338–5344. https://doi.org/10.1021/ja00485a014.

(31) Henderson, R. A.; Oglieve, K. E. Protonation of the Iron–Sulfur Core in $[Fe_4S_4X_4]^{2-}$(X = Cl or Br): Chemical Precedent for the Elementary Reaction of the Hydrogenases and Nitrogenases. *J. Chem. Soc., Chem. Commun.* **1994**, No. 4, 377–379. https://doi.org/10.1039/C39940000377.

(32) Zehm, D.; Fudickar, W.; Hans, M.; Schilde, U.; Kelling, A.; Linker, T. 9,10-Diarylanthracenes as Molecular Switches: Syntheses, Properties, Isomerisations and Their Reactions with Singlet Oxygen. *Chem. Eur. J.* **2008**, *14* (36), 11429–11441. https://doi.org/10.1002/chem.200801355.

(33) Brown, A. C.; Suess, D. L. M. Controlling Substrate Binding to Fe_4S_4 Clusters through Remote Steric Effects. *Inorg. Chem.* **2019**, *58* (8), 5273–5280. https://doi.org/10.1021/acs.inorgchem.9b00360.

(34) Brown, A. C.; Thompson, N. B.; Suess, D. L. M. Evidence for Low-Valent Electronic Configurations in Iron–Sulfur Clusters. *J. Am. Chem. Soc.* **2022**, *144* (20), 9066–9073. https://doi.org/10.1021/jacs.2c01872.

(35) Le, L. N. V.; Bailey, G. A.; Scott, A. G.; Agapie, T. Partial Synthetic Models of FeMoco with Sulfide and Carbyne Ligands: Effect of Interstitial Atom in Nitrogenase Active Site. *Proc. Natl. Acad. Sci. U.S.A.* **2021**, *118* (49), e2109241118. https://doi.org/10.1073/pnas.2109241118.

(36) Ye, M.; Brown, A. C.; Suess, D. L. M. Reversible Alkyl-Group Migration between Iron and Sulfur in [Fe_4S_4] Clusters. *J. Am. Chem. Soc.* **2022**, *144* (29), 13184–13195. https://doi.org/10.1021/jacs.2c03195.

(37) Torzilli, M. A.; Colquhoun, S.; Kim, J.; Beer, R. H. Structural and ^{1}H NMR Spectroscopic Characterization of Bis(*N*-Isopropylsalicylaldiminato)Iron(II). *Polyhedron* **2002**, *21* (7), 705–713. https://doi.org/10.1016/S0277-5387(02)00837-9.

(38) Cantalupo, S. A.; Ferreira, H. E.; Bataineh, E.; King, A. J.; Petersen, M. V.; Wojtasiewicz, T.; DiPasquale, A. G.; Rheingold, A. L.; Doerrer, L. H. Synthesis with Structural and Electronic Characterization of Homoleptic Fe(II)- and Fe(III)-Fluorinated Phenolate Complexes. *Inorg. Chem.* **2011**, *50* (14), 6584–6596. https://doi.org/10.1021/ic2003782.

(39) Houghton, J.; Simonovic, S.; Whitwood, A. C.; Douthwaite, R. E.; Carabineiro, S. A.; Yuan, J.-C.; Marques, M. M.; Gomes, P. T. Transition-Metal Complexes of Phenoxy-Imine Ligands Modified with Pendant Imidazolium Salts: Synthesis, Characterisation and Testing as Ethylene Polymerisation Catalysts. *J. Organomet. Chem.* **2008**, *693* (4), 717–724. https://doi.org/10.1016/j.jorganchem.2007.11.060.

(40) Qian, X.; Dawe, L. N.; Kozak, C. M. Catalytic Alkylation of Aryl Grignard Reagents by Iron(III) Amine-Bis(Phenolate) Complexes. *Dalton Trans.* **2011**, *40* (4), 933–943. https://doi.org/10.1039/C0DT01239D.

(41) Marlin, D. S.; Olmstead, M. M.; Mascharak, P. K. Chemistry of Iron(III) Complexes of *N,N′*-Bis(2-Hydroxyphenyl)-Pyridine-2,6-Dicarboxamide: Seven-Coordinate Iron(III) Complexes Ligated to Deprotonated Carboxamido Nitrogens. *Inorg. Chim. Acta.* **2000**, *297* (1), 106–114. https://doi.org/10.1016/S0020-1693(99)00291-1.

(42) Chard, E. F.; Thompson, J. R.; Dawe, L. N.; Kozak, C. M. Synthesis and Structure of Iron(III) Complexes of Amine-Bis(Phenolate) Ligands. *Can. J. Chem.* **2014**, *92* (8), 758–764. https://doi.org/10.1139/cjc-2014-0043.

(43) Brown, A. C.; Suess, D. L. M. Valence Localization in Alkyne and Alkene Adducts of Synthetic [Fe_4S_4]$^+$ Clusters. *Inorg. Chem.* **2022**. https://doi.org/10.1021/acs.inorgchem.2c01353.

(44) Le, L. N. V.; Joyce, J. P.; Oyala, P. H.; DeBeer, S.; Agapie, T. Highly Activated Terminal Carbon Monoxide Ligand in an Iron–Sulfur Cluster Model of FeMco with Intermediate Local Spin State at Fe. *J. Am. Chem. Soc.* **2024**, *146* (8), 5045–5050. https://doi.org/10.1021/jacs.3c12025.

(45) Speelman, A. L.; Čorić, I.; Van Stappen, C.; DeBeer, S.; Mercado, B. Q.; Holland, P. L. Nitrogenase-Relevant Reactivity of a Synthetic Iron–Sulfur–Carbon Site. *J. Am. Chem. Soc.* **2019**, *141* (33), 13148–13157. https://doi.org/10.1021/jacs.9b05353.

(46) Wilson, D. W. N.; Fataftah, M. S.; Mathe, Z.; Mercado, B. Q.; DeBeer, S.; Holland, P. L. Three-Coordinate Nickel and Metal–Metal Interactions in a Heterometallic Iron–Sulfur Cluster. *J. Am. Chem. Soc.* **2024**. https://doi.org/10.1021/jacs.3c12157.

(47) Begum, A.; Sheikh, A. H.; Moula, G.; Sarkar, S. Fe_4S_4 Cubane Type Cluster Immobilized on a Graphene Support: A High Performance H2 Evolution Catalysis in Acidic Water. *Sci. Rep.* **2017**, *7* (1), 16948. https://doi.org/10.1038/s41598-017-17121-7.

(48) Alenezi, K.; Alshammari, H. Electrocatalytic Production of Hydrogen Using Iron Sulfur Cluster. *Int. J. Chem.* **2017**, *9* (2), p52. https://doi.org/10.5539/ijc.v9n2p52.

(49) Schlosser, M.; Hartmann, J. Transmetalation and Double Metal Exchange: A Convenient Route to Organolithium Compounds of the Benzyl and Allyl Type. *Angew. Chem., Int. Ed. Engl.* **1973**, *12* (6), 508–509. https://doi.org/10.1002/anie.197305082.

(50) Piglosiewicz, I. M.; Beckhaus, R.; Wittstock, G.; Saak, W.; Haase, D. Selective Oxidation and Reduction of Trinuclear Titanium(II) Hexaazatrinaphthylene ComplexesSynthesis, Structure, and Electrochemical Investigations. *Inorg. Chem.* **2007**, *46* (18), 7610–7620. https://doi.org/10.1021/ic701009u.

(51) Transue, W. J.; Yang, J.; Nava, M.; Sergeyev, I. V.; Barnum, T. J.; McCarthy, M. C.; Cummins, C. C. Synthetic and Spectroscopic Investigations Enabled by Modular Synthesis of Molecular Phosphaalkyne Precursors. *J. Am. Chem. Soc.* **2018**, *140* (51), 17985–17991. https://doi.org/10.1021/jacs.8b09845

(52) Low, C. H.; Rosenberg, J. N.; Lopez, M. A.; Agapie, T. Oxidative Coupling with Zr(IV) Supported by a Noninnocent Anthracene-Based Ligand: Application to the Catalytic Cotrimerization of Alkynes and Nitriles to Pyrimidines. *J. Am. Chem. Soc.* **2018**, *140* (38), 11906–11910. https://doi.org/10.1021/jacs.8b07418.

(53) Bruker. APEX3, 2012.

(54) Bruker. SADABS, 2001.

(55) Altomare, A.; Cascarano, G.; Giacovazzo, C.; Guagliardi, A.; Burla, M. C.; Polidori, G.; Camalli, M. SIR92 - a Program for Automatic Solution of Crystal Structures by Direct Methods. *J. Appl. Crystallogr.* **1994**, *27* (3), 435.

(56) Palatinus, L.; Chapuis, G. SUPERFLIP - a Computer Program for the Solution of Crystal Structures by Charge Flipping in Arbitrary Dimensions. *J. Appl. Crystallogr.* **2007**, *40* (4), 786–790.

(57) Betteridge, P. W.; Carruthers, J. R.; Cooper, R. I.; Prout, K.; Watkin, D. J. CRYSTALS Version 12: Software for Guided Crystal Structure Analysis. *J. Appl. Crystallogr.* **2003**, *36* (6), 1487.

(58) Spek, A. PLATON SQUEEZE: A Tool for the Calculation of the Disordered Solvent Contribution to the Calculated Structure Factors. *Acta Cryst. C* **2015**, *71* (1), 9–18.

Appendix A

MISCELLANEOUS CRYSTAL STRUCTURES

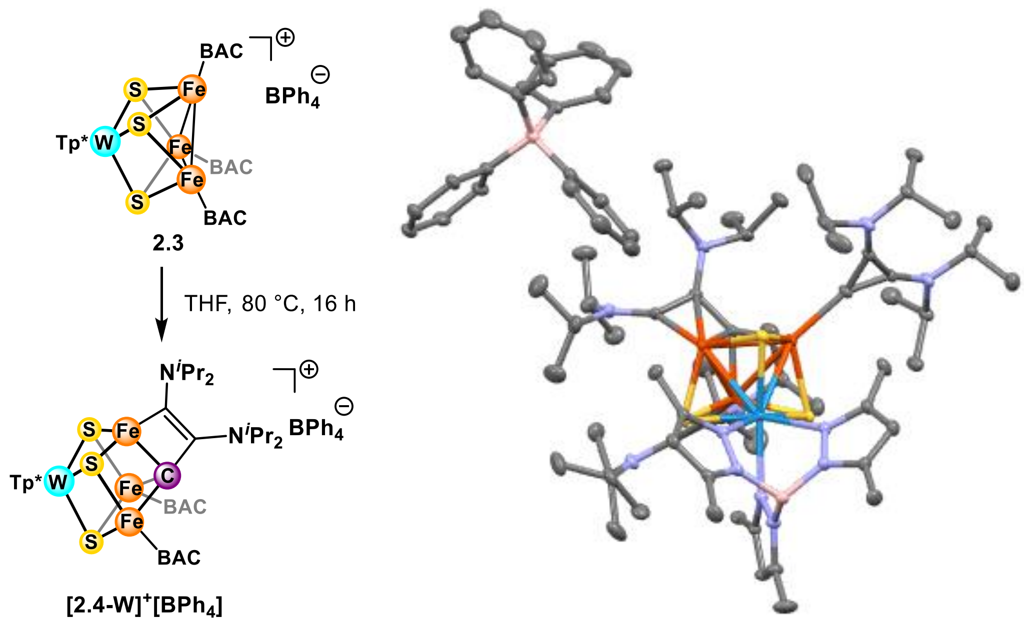

Figure A1. Crystal structure of **[2.4-W][BPh$_4$]** from heating of **2.3** (data set v20113).

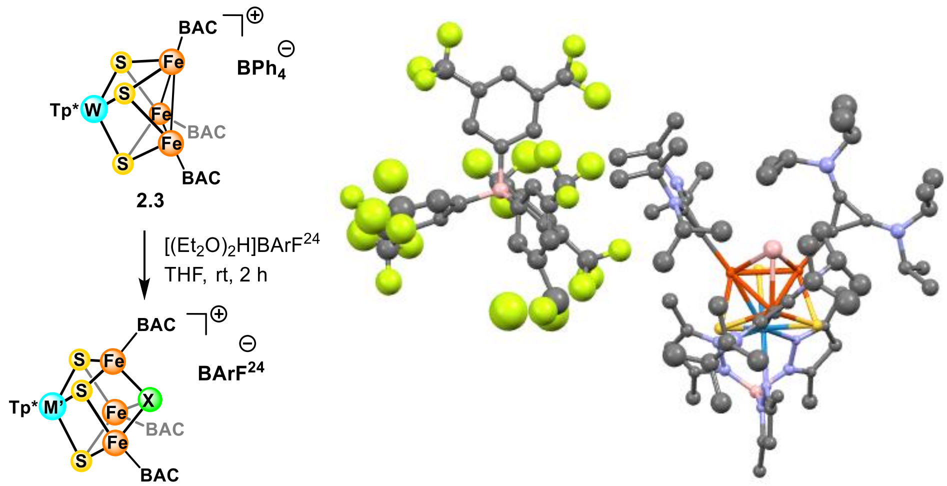

Figure A2. Crystal structure of the product from the reaction between **2.3** and [(Et_2O)$_2$H][BArF^{24}] after extracting into Et_2O and crystallizing by C_6H_6/pentane or Et_2O/pentane vapor diffusion (data set v20115). The data quality is not enough to determine the identity of X.

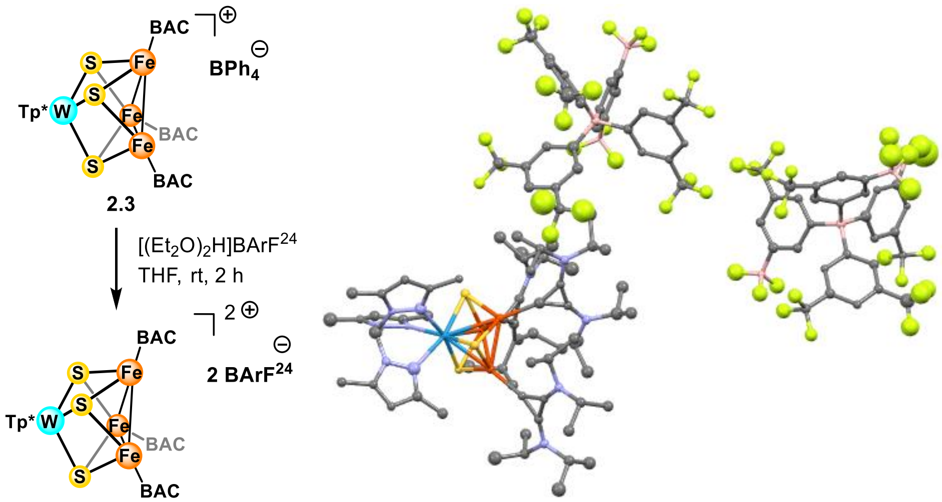

Figure A3. Crystal structure of the product from the reaction between **2.3** and [(Et_2O)$_2$H][BArF^{24}] after extracting into Et_2O and crystallizing by Et_2O slow evaporation (data set v20117).

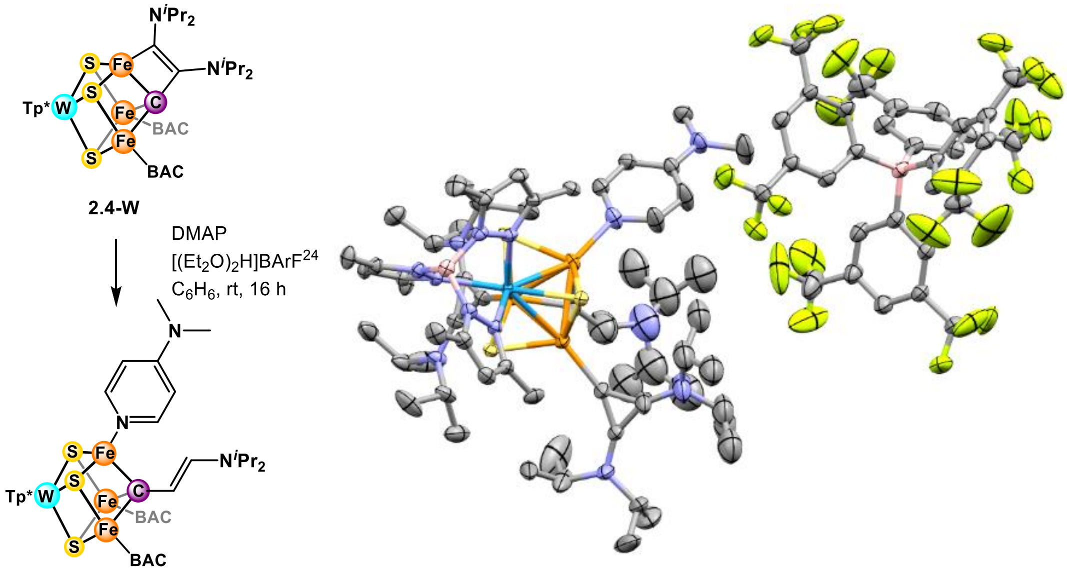

Figure A4. Crystal structure of the product from the reaction between **2.4-W**, [(Et_2O)$_2$H][BArF^{24}], and DMAP (data set v20127).

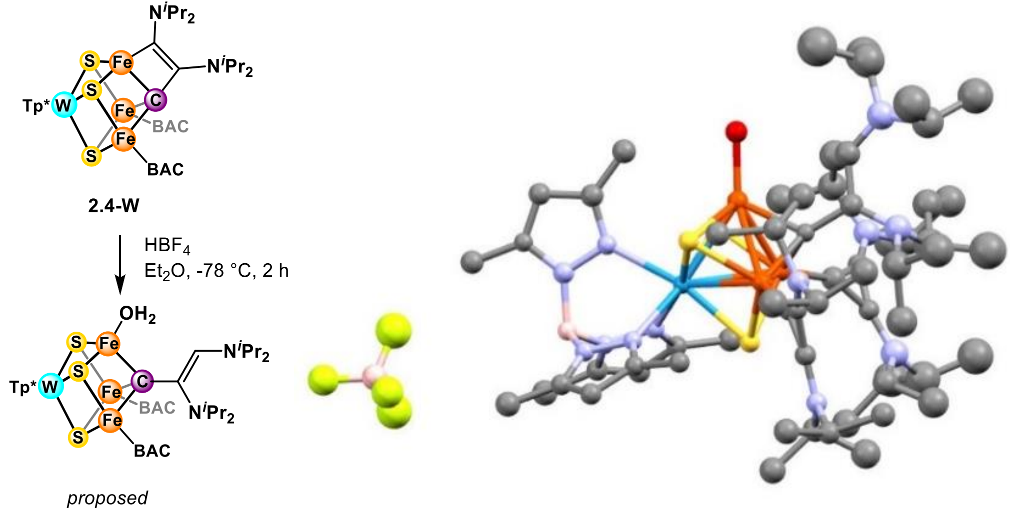

Figure A5. Crystal structure of the product from the reaction between **2.4-W** and HBF_4 (data set v20163).

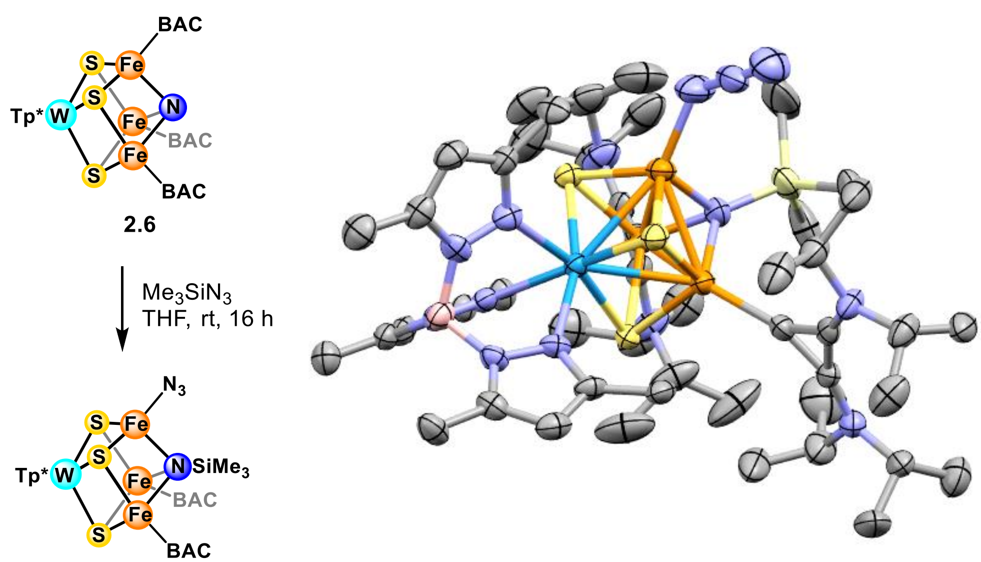

Figure A6. Crystal structure of the product from the reaction between **2.6** and Me_3SiN_3 (data set v20216).

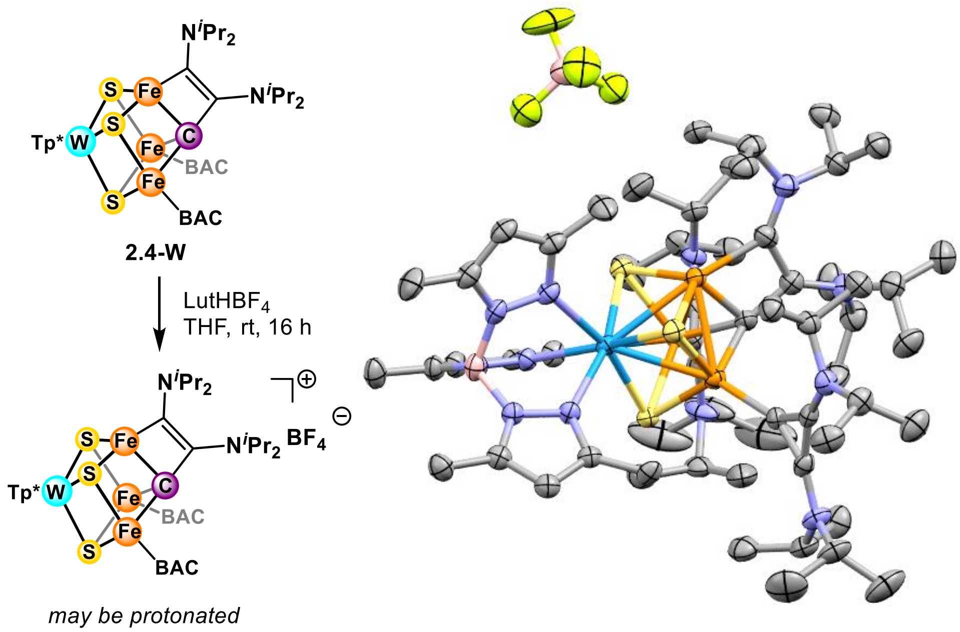

Figure A7. Crystal structure of the product from the reaction between **2.4-W** and $LutHBF_4$ (data set v20224).

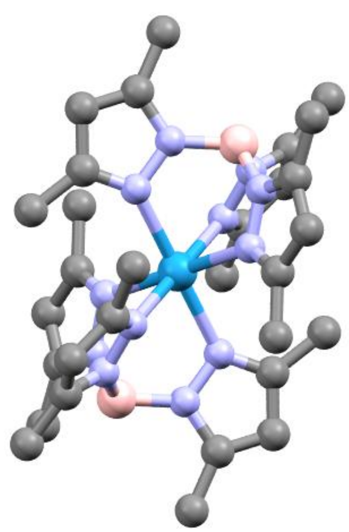

Figure A8. Crystal structure of **Tp*$_2$W** as a side product from heating **3.2** to form **3.3** (data set v21334).

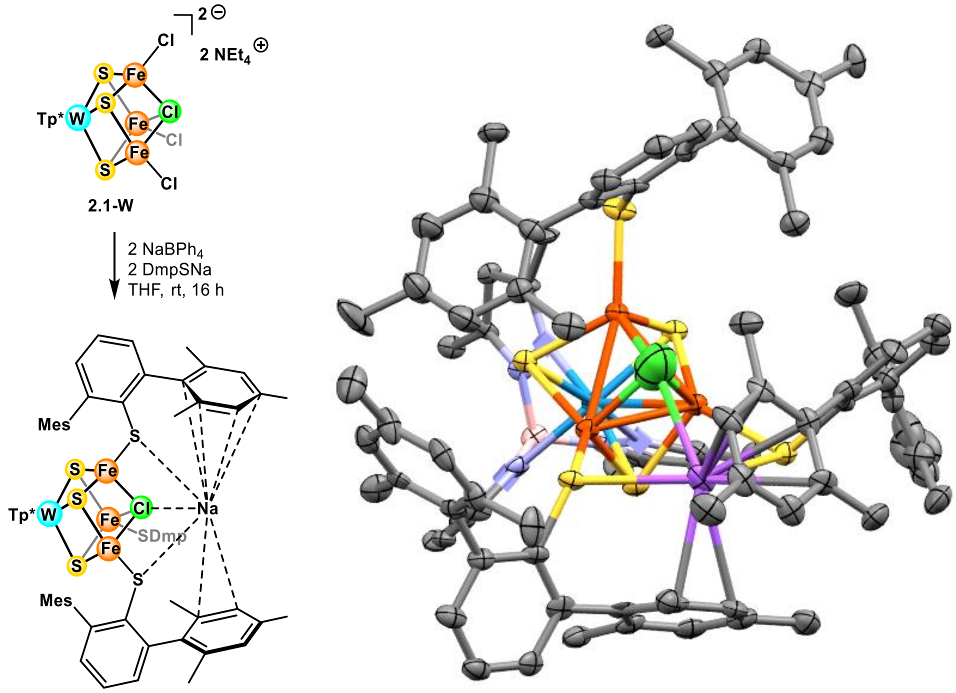

Figure A9. Crystal structure of the product from reaction of **2.1-W** with DmpSNa (Dmp = 2,6-(mesityl)$_2$C$_6$H$_3$) and NaBPh$_4$ (data set v21387 and v22197).

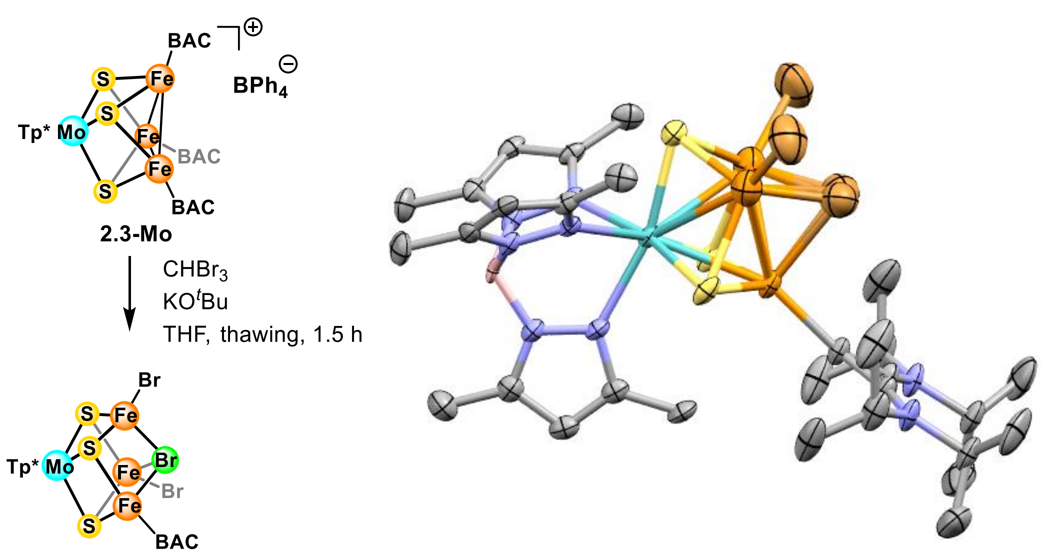

Figure A10. Crystal structure of the product from the reaction between the Mo analog **2.3-Mo**, CHBr$_3$, and KO^{t}Bu (data set v22020).

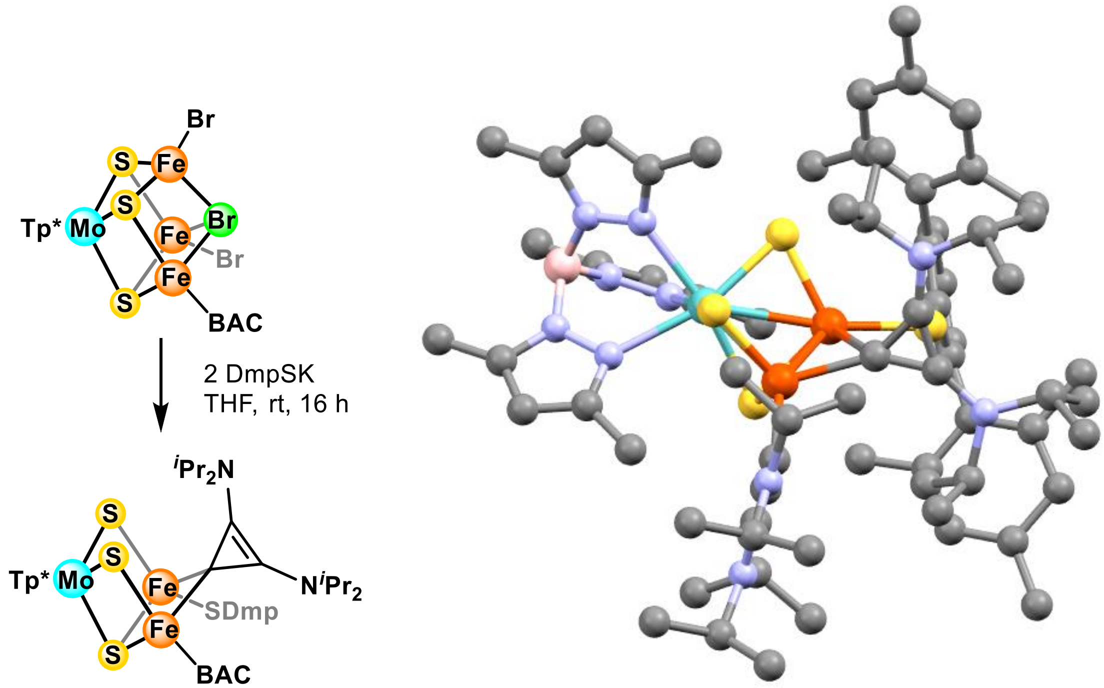

Figure A11. Crystal structure of the product from the reaction between the cluster in Figure A10 and DmpSK (data set v22040).

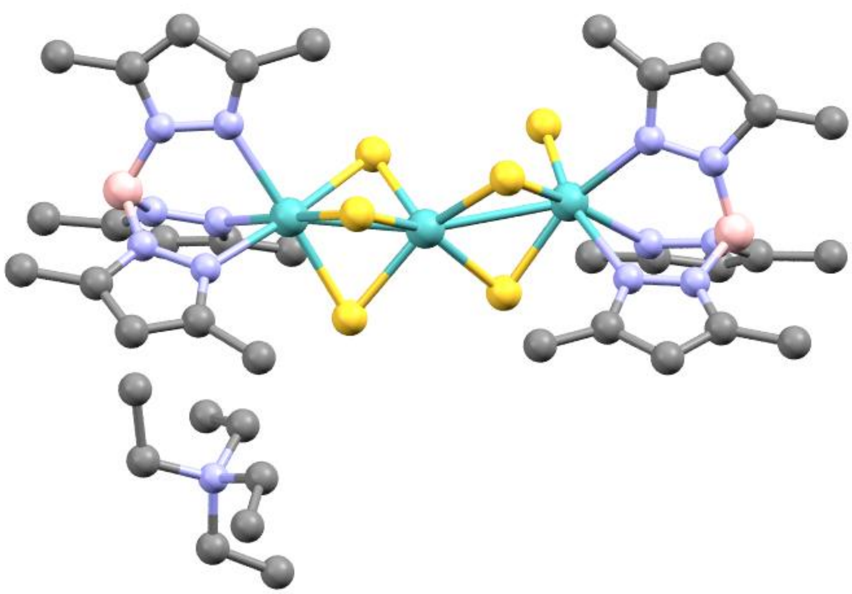

[NEt_4][Tp*MoS_3MoS_3MoTp*]

Figure A12. Crystal structure of the product from the reaction between **[NEt_4][Tp*MoS_5]** and an excess (3 equiv) of PPh_3 (data set v22055).

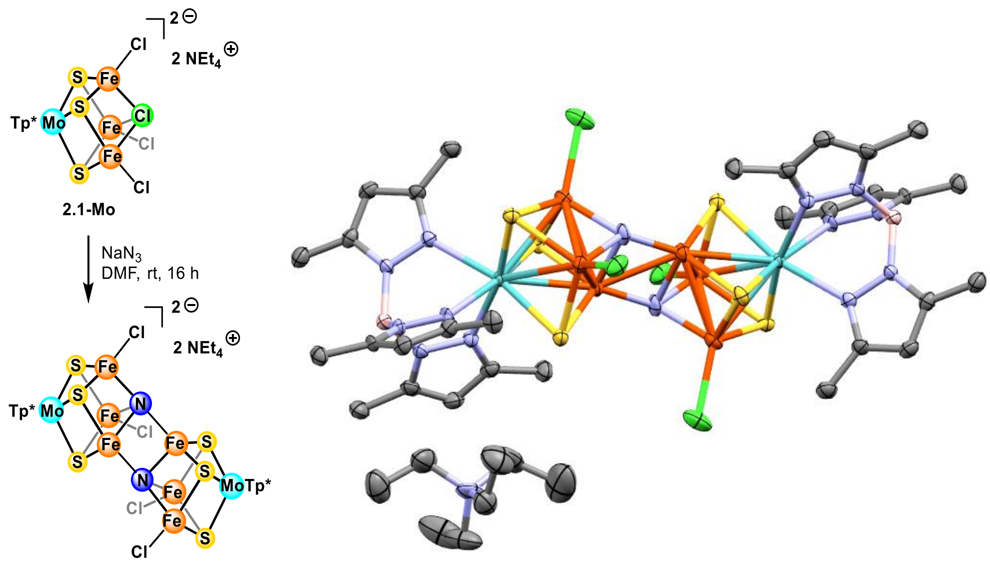

Figure A13. Crystal structure of the product from the reaction between **2.1-Mo** and NaN_3 (data set v22089).

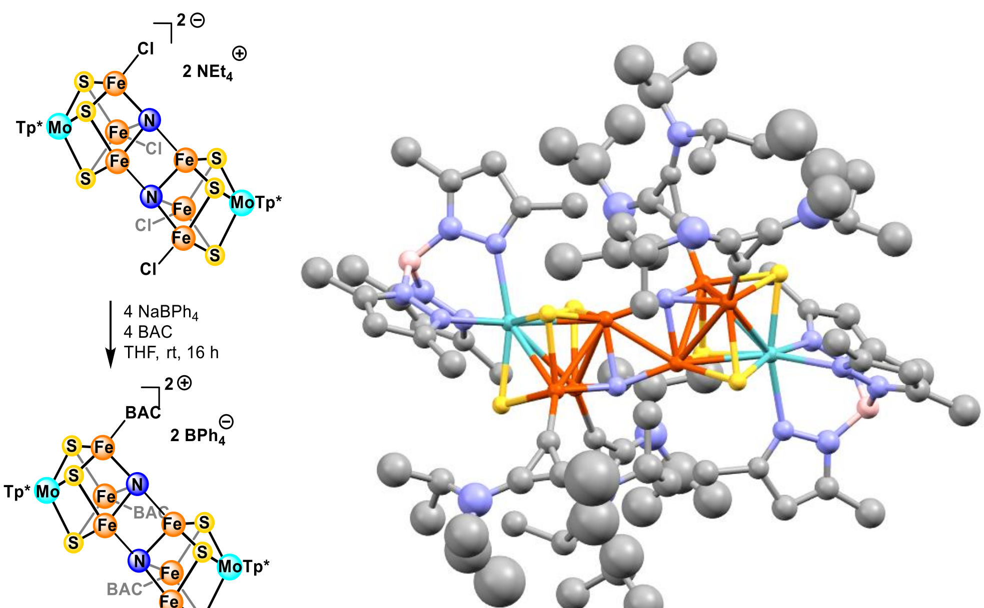

Figure A14. Crystal structure of the product from the reaction between the cluster in Figure A19, BAC, and $NaBPh_4$ (data set v22155).

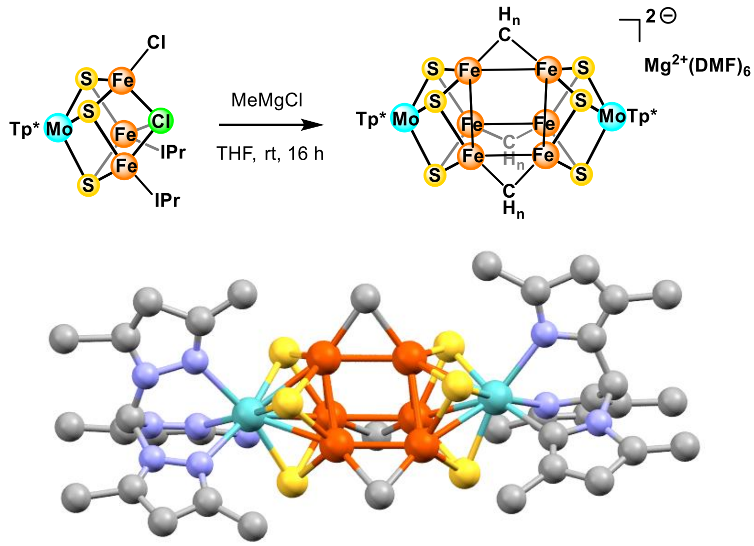

Figure A15. Crystal structure of the product in the DMF fraction from the reaction between **Tp*MoFe₃S₃(μ₃-Cl)IPr₂Cl** and MeMgCl (IPr = 1,3-bis(2,6-diisopropylphenyl)imidazol-2-ylidene) (n is undetermined) (data set v22164).

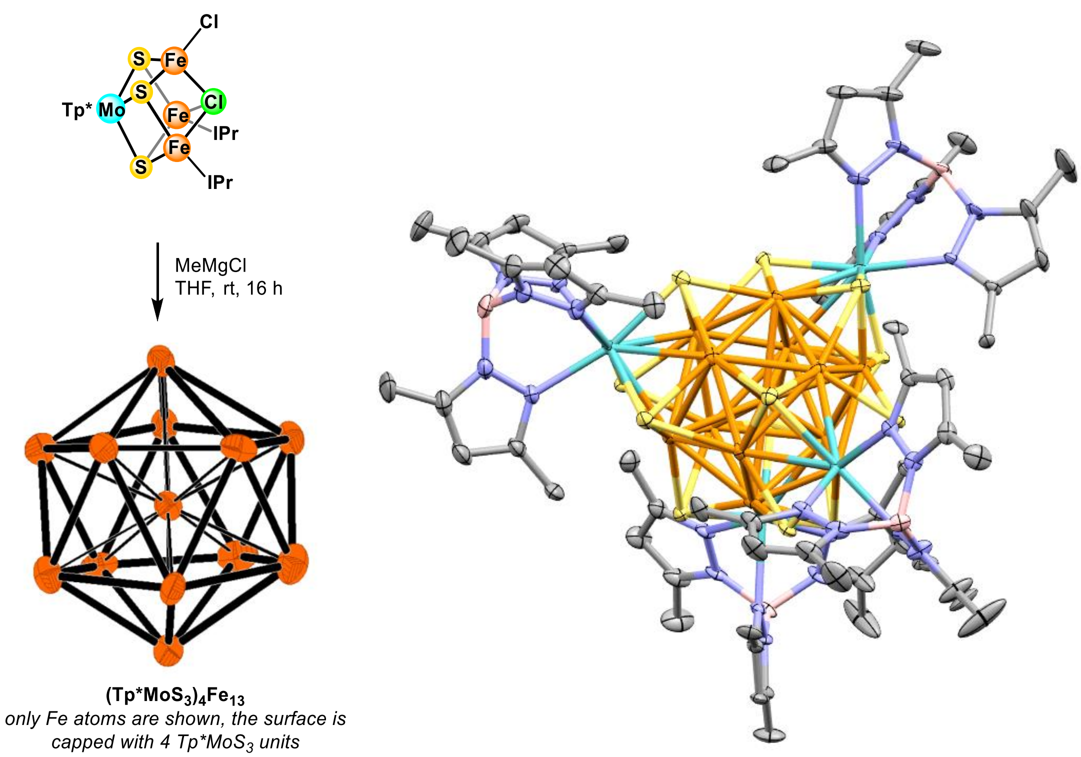

Figure A16. Crystal structure of the product in the MeCN fraction from the reaction between **Tp*MoFe₃S₃(μ₃-Cl)IPr₂Cl** and MeMgCl (data set v22171).

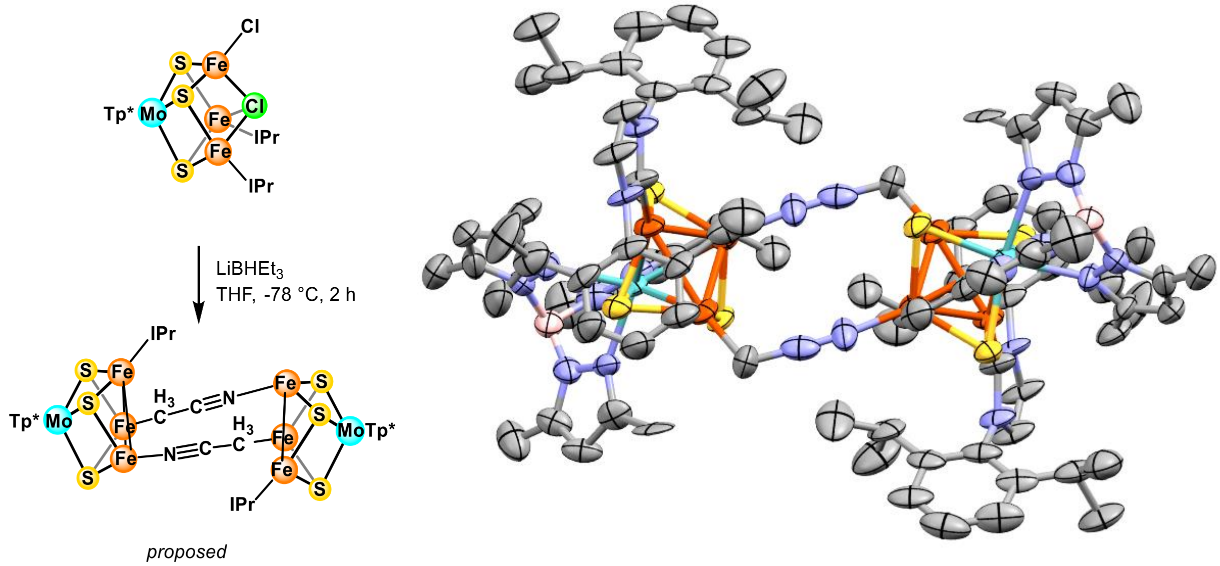

Figure A17. Crystal structure of the product from the reaction between **Tp*MoFe$_3$S$_3$(μ$_3$-Cl)IPr$_2$Cl** and LiBHEt$_3$ (data set v22195).

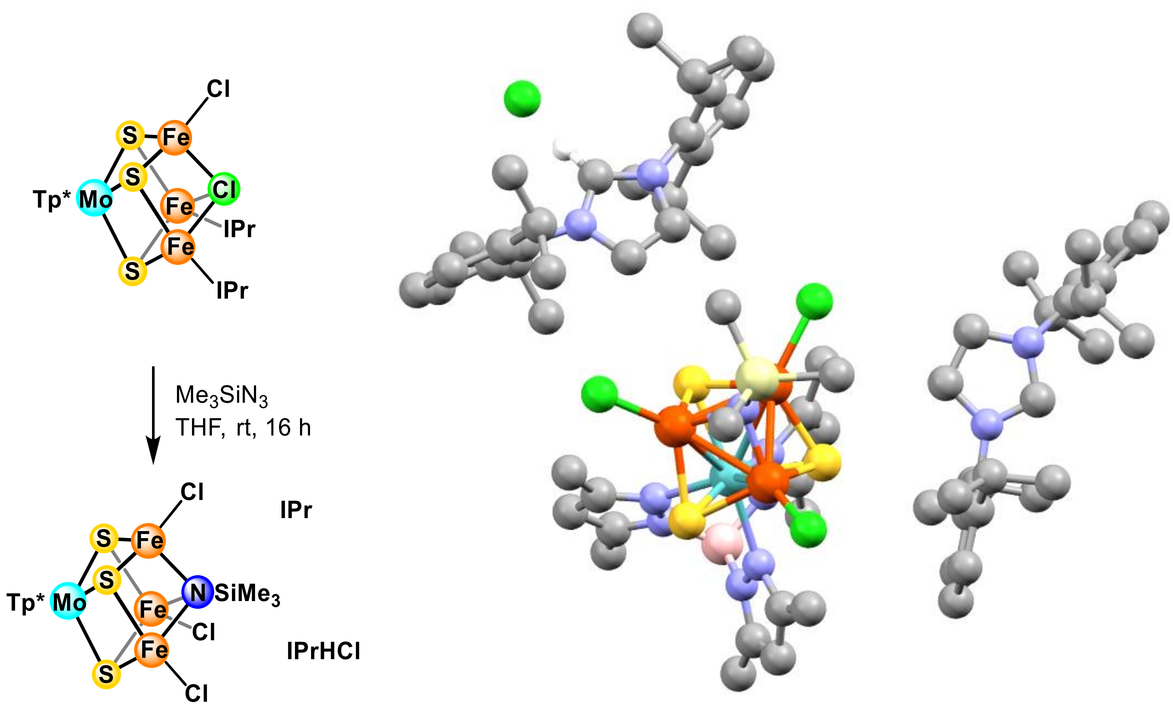

Figure A18. Crystal structure of the product from the reaction between **Tp*MoFe$_3$S$_3$(μ$_3$-Cl)IPr$_2$Cl** and SiMe$_3$N$_3$ (data set v22206).

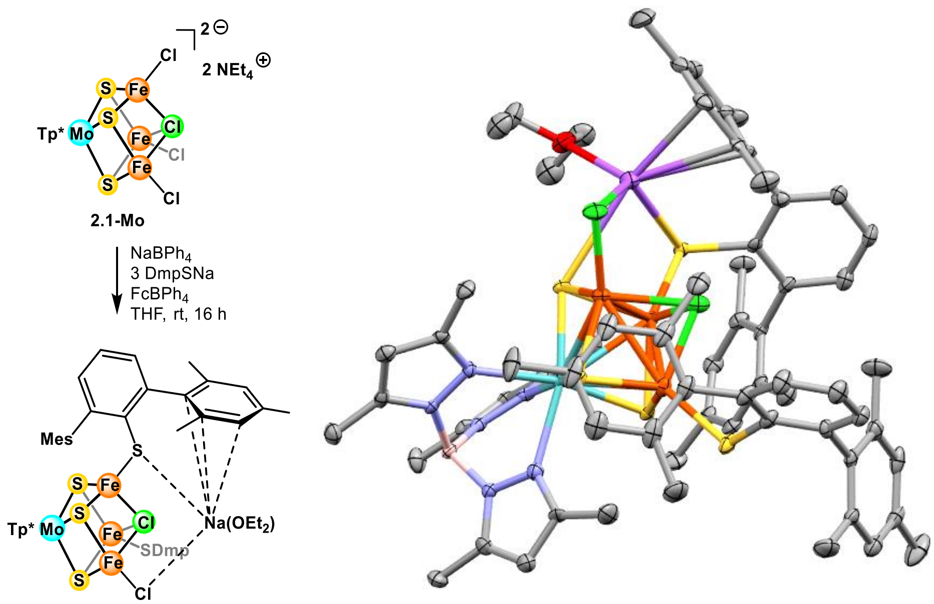

Figure A19. Crystal structure of the product extracted into Et_2O from reaction of **2.1-Mo** with DmpSNa (Dmp = 2,6-(mesityl)$_2C_6H_3$), $NaBPh_4$, and $FcBPh_4$ (data set v22216).

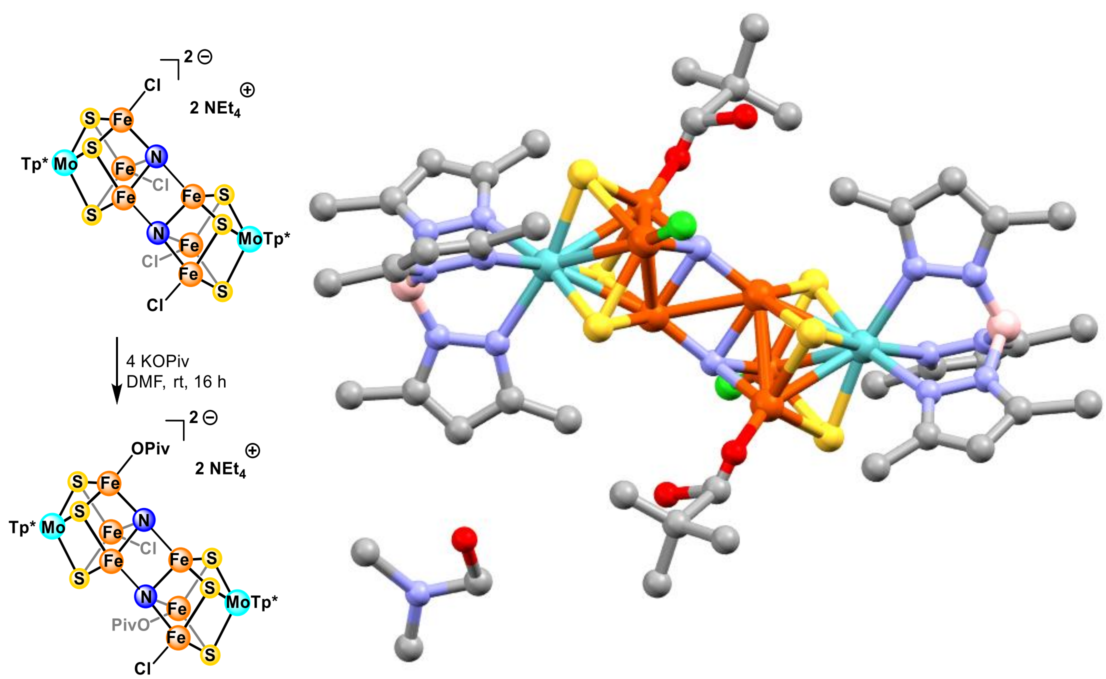

Figure A20. Crystal structure of the product from the reaction between the cluster in Figure A10 and potassium pivalate (data set v22255).

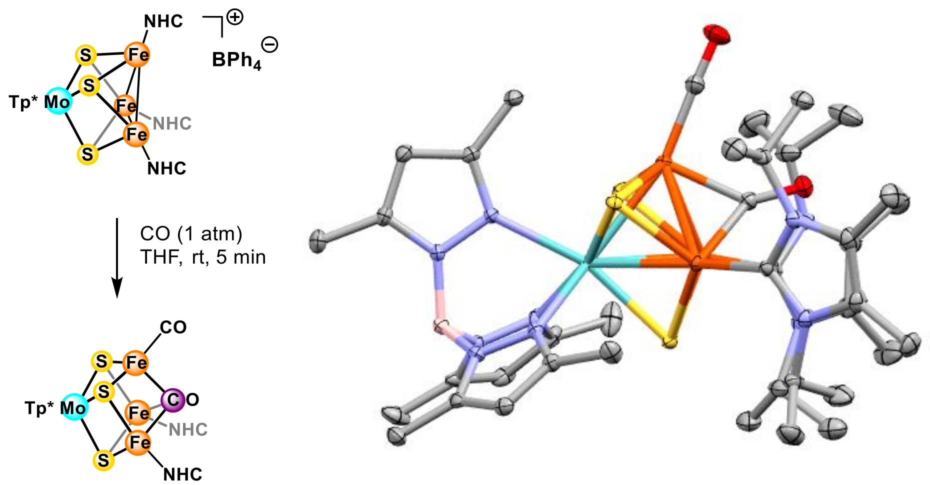

Figure A21. Crystal structure of the product from the reaction between **[Tp*MoFe$_3$S$_3$(NHC)$_3$][BPh$_4$]** (NHC = 1,3-bis(isopropyl)-4,5(dimethyl)imidazol-2-ylidene) and 1 atm CO (data set v22272).

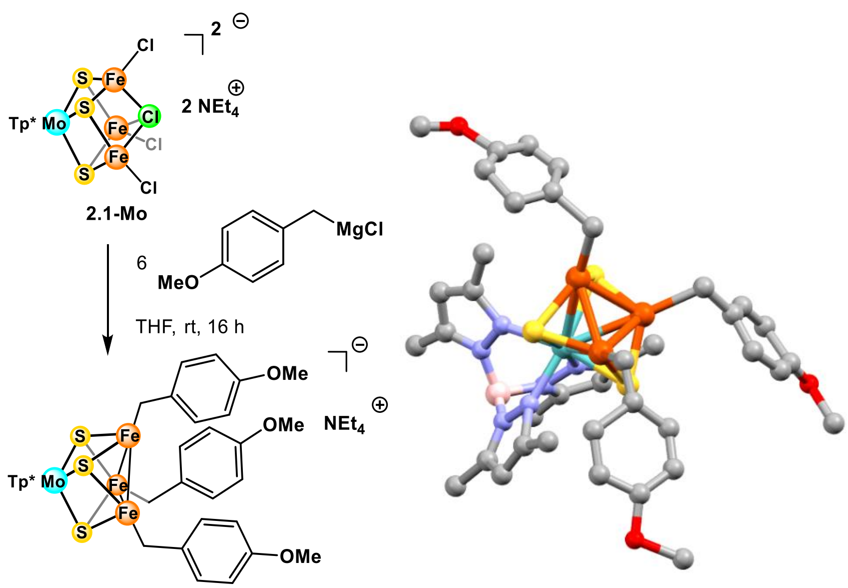

Figure A22. Crystal structure of the product from the reaction between **2.1-Mo** and (4-MeOPh)CH$_2$MgCl (data set v22302).

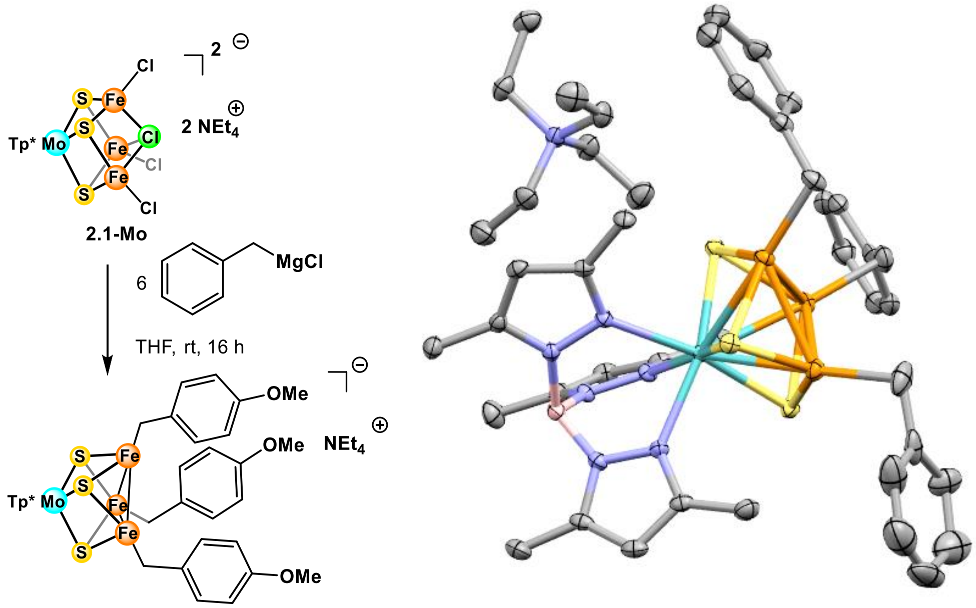

Figure A23. Crystal structure of the product from the reaction between **2.1-Mo** and $PhCH_2MgCl$ (data set v22368).

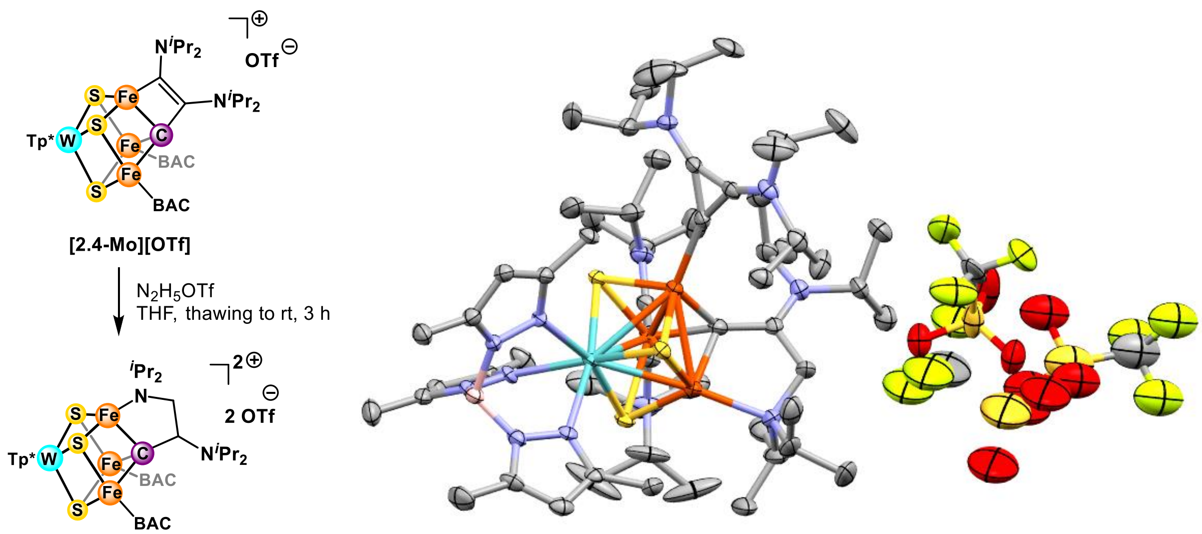

Figure A24. Crystal structure of the product from the reaction between [**2.4-Mo][OTf]** and N_2H_5OTf, where the double bond seems to have been hydrogenated (data set v22455).

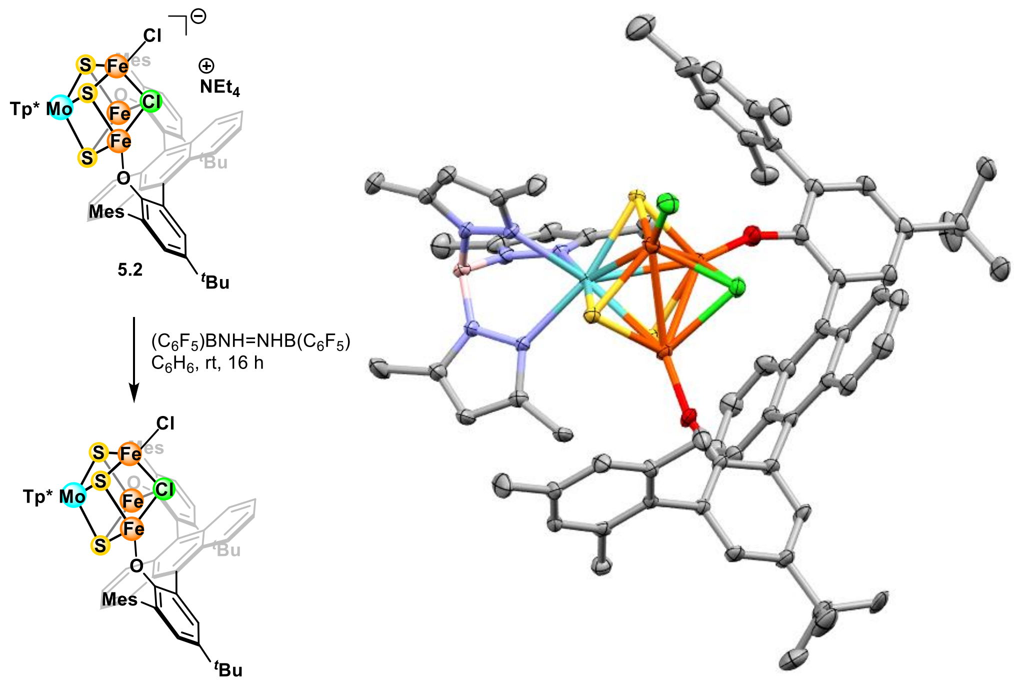

Figure A25. Crystal structure of the one-electron oxidized **5.2** with $(C_6F_5)BNH{=}NHB(C_6F_5)$ (data set v23015).

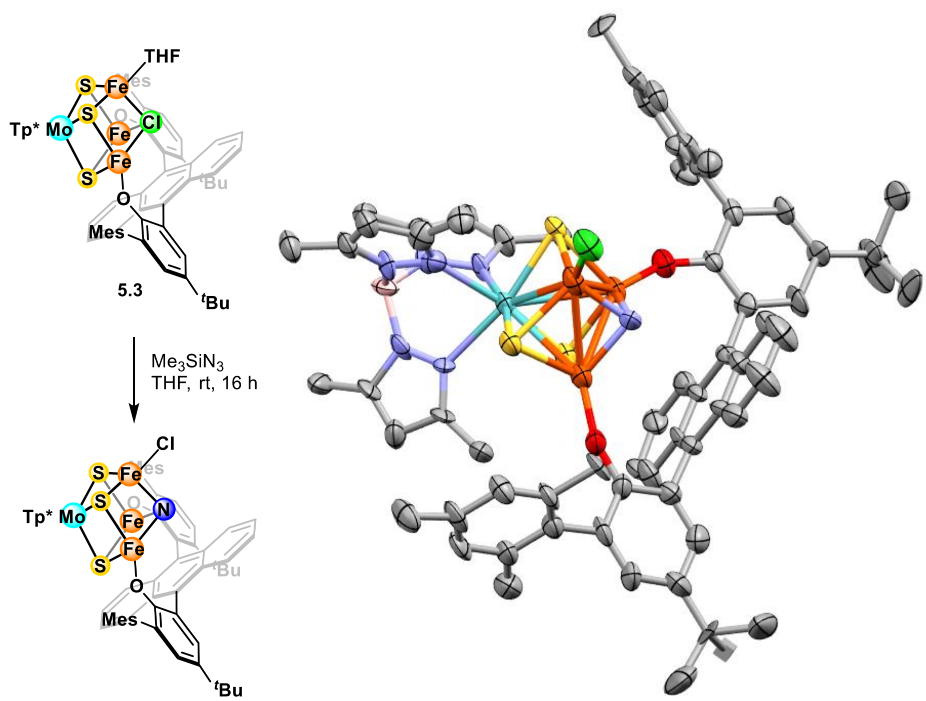

Figure A26. Crystal structure of the product from the reaction between **5.3** and Me_3SiN_3 (data set v23088).

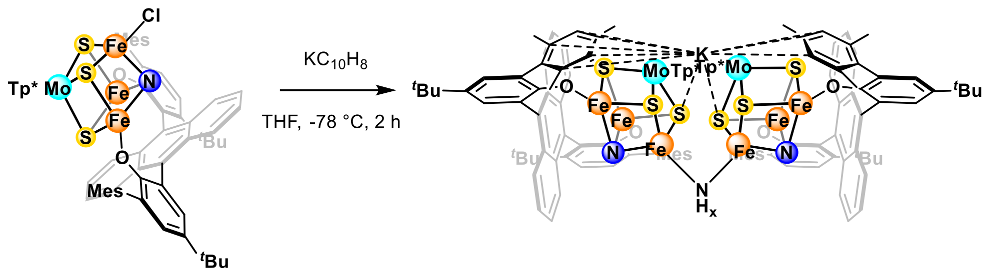

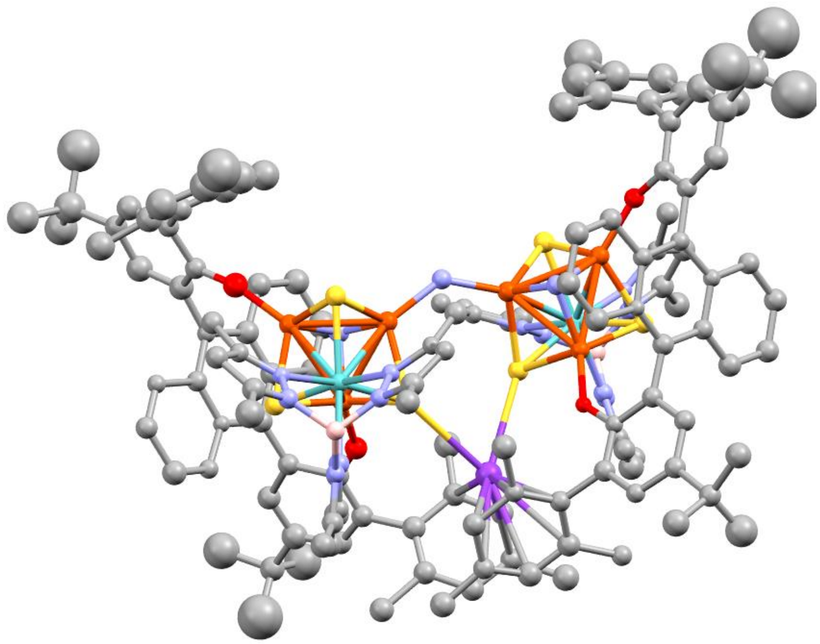

Figure A27. Crystal structure of the product from the reaction between the cluster in Figure A26 and potassium naphthalenide (x is undetermined) (data set v23120).

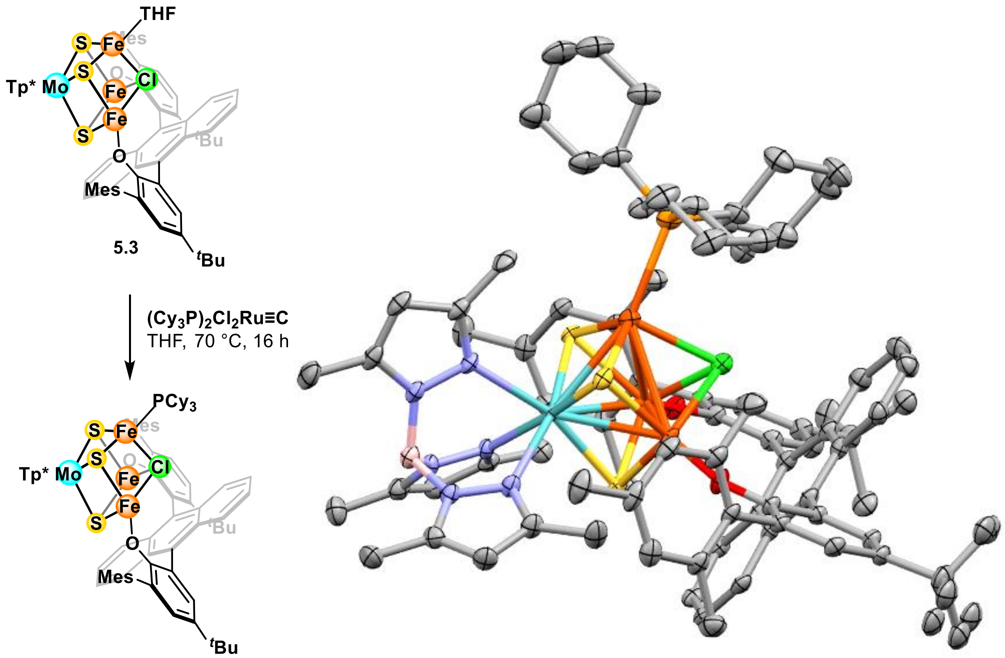

Figure A28. Crystal structure of the product from the reaction between **5.3** and **$(Cy_3P)_2Cl_2Ru{\equiv}C$** at 70 °C for 16 h (data set v23217).

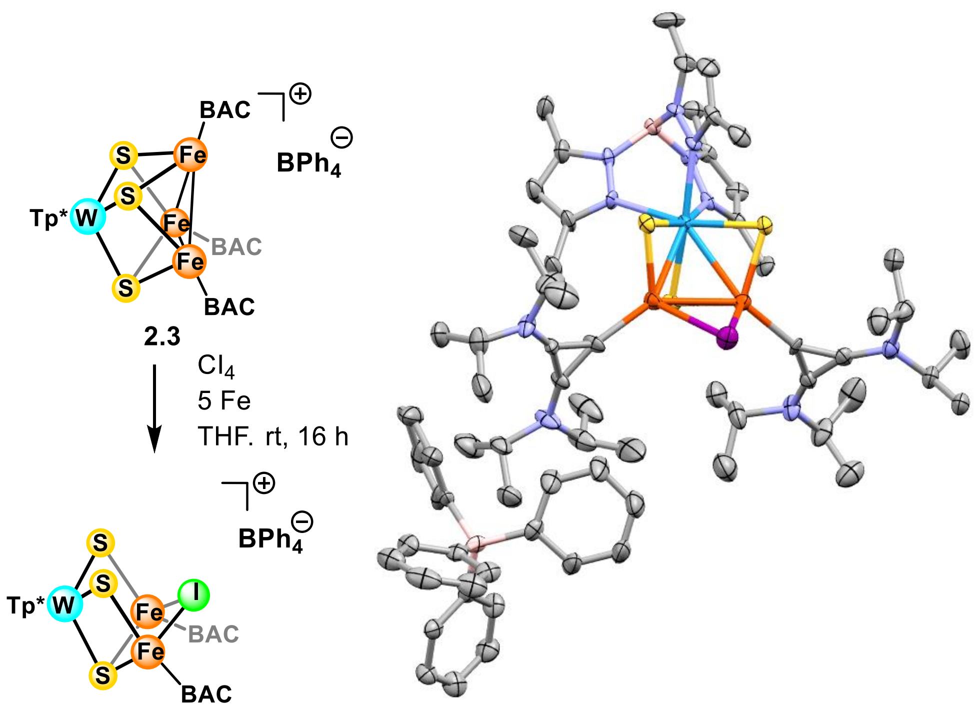

Figure A29. Crystal structure of the product from the reaction between **2.3**, CI_4, and Fe powder (data set v23232).

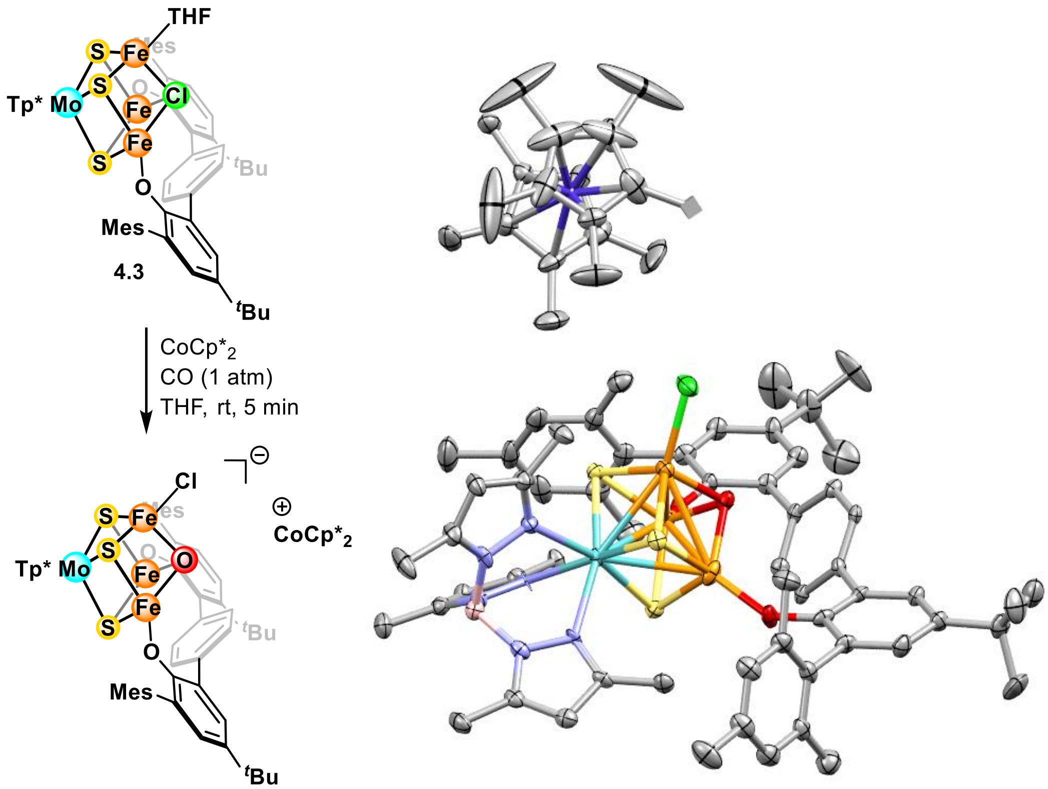

Figure A30. Crystal structure of the product from the reaction between **4.3**, $CoCp*_2$, and 1 atm CO (data set v23366).

ABOUT THE AUTHOR

Linh Nguyen Vuong Le was born on March 31, 1995 in Hanoi, Vietnam. He lived there until age 14, when he moved to Singapore on November 2, 2009 under the A*STAR School-Based Scholarship. There, he attended Anglo-Chinese School (Independent) (ACS(I)) and obtained the International Baccalaureate (IB) Diploma in 2014. He participated in many math and science competitions in Singapore and won several medals, most notably Gold Medals at the Singapore Junior Chemistry Olympiad (SJChO) in 2011 and the Singapore Chemistry Olympiad (SChO) in 2012. Linh also conducted scientific research while in Singapore, working at the Nanyang Technological University (NTU) on organic solar cells and the Bioprocessing Technology Institute (BTI) on mass spectrometric methods to study lipids. He then attended Colgate University in Hamilton, NY for his undergraduate studies, earning Bachelor of Arts degrees in Chemistry and Physics in 2018. There, he worked with Professor Anthony Chianese on ruthenium pincer catalysts for ester hydrogenation for most of his undergraduate career, except for a study abroad program at Cardiff University in Wales in Spring 2017 and a research experience at Princeton University in the lab of Professor Brad Carrow in Summer 2017. Then, he moved to Pasadena in 2018 to earn his PhD with Professor Theodor Agapie at the California Institute of Technology, studying cluster synthetic models of nitrogenase. When not in lab, Linh enjoys listening to music, watching movies, and hanging out with friends in Southern California.